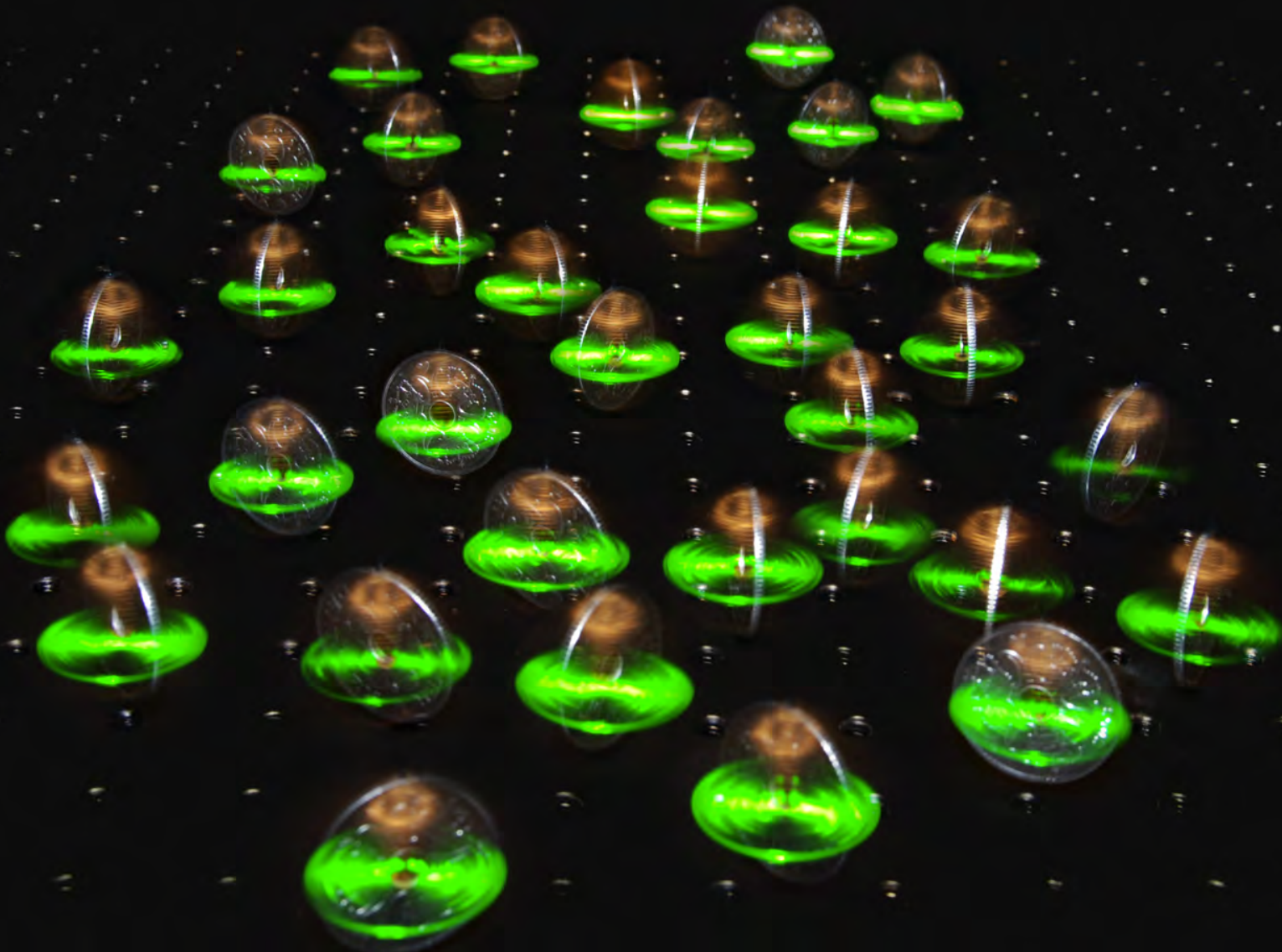


QUANTOP - NIELS BOHR INSTITUTE
FACULTY OF SCIENCE
UNIVERSITY OF COPENHAGEN



PhD thesis
Daniel Oblak

Quantum State Engineering in Cold Caesium Atoms
An entangled tale of non-destructively induced collapse and squeezing of atomic states



Principal academic advisor: Eugene S. Polzik

Submitted: 18/12/2009

PhD thesis

Daniel Oblak

Quantum State Engineering in Cold Caesium Atoms

An entangled tale of non-destructively induced collapse and squeezing of atomic states

Danish National Research Foundation Centre for Quantum Optics (QUANTOP)
Niels Bohr Institute
Graduate School of Science
Faculty of Science
University of Copenhagen

Daniel Oblak
Version 2.0 (defence version),
Copenhagen, July 5, 2010
Copyright ©2009. All rights reserved.

Cover photo: Niels Kjærgaard, Daniel Oblak, and Ulrich B. Hoff

Principal academic supervisor: Eugene S. Polzik

Additional academic supervisors: Carlos L. Garrido Alzar
Jörg H. Müller
Niels Kjærgaard
Anders S. Sørensen
Jürgen Appel

PhD committee:

NBI local head :

External experts :

Prof. Lene Oddershede

Dr. Pierre Lemonde

Prof. Arno Rauschenbeutel

Thesis submitted :

21st of December 2009

Defence date :

1st of February 2010

Abstract

Quantum mechanics is characterised by several strange features, which include quantum uncertainty, quantum measurements, and entanglement. This thesis involves all three of these. The quantum uncertainty poses a fundamental standard quantum limit (SQL) in applications where quantum systems are used to gauge some quantity. A prime example is that of atomic frequency standards, which with unprecedented precision measure an atomic quantum state. Quantum measurements in the form of Quantum Non-Demolition (QND) measurements can be engineered so as to overcome the SQL by redistributing quantum uncertainty amongst different variables of the system. Such squeezed spin-states rely on inter-atomic correlation, which goes by the name of entanglement.

In this work we present a detailed description of how we have implemented a QND measurement with laser pulses in a Mach-Zehnder Interferometer (MZI) and demonstrate that we can engineer a squeezed state in a cold trapped ensemble of Cs atoms. We verify that the squeezing is useful for improving the precision of atomic clocks. Along the way, we also investigate several remarkable features of the interaction, by which atoms and light-particles (photons) exchange phase-shifts.

Sammendrag

Karakteristisk for den kvantemekaniske beskrivelse af verden er en række besynderlige fænomener såsom kvanteubestemthed, kvante-målinger samt kvantesammenfiltrering. Ubestemthedsprincippet sætter en grundlæggende standard kvantegrænse (SQL) for præcisionen med hvilken et kvantesystem kan måle en eller anden størrelse. Et fremtrædende eksempel på en kvantestøjs begrænset måling er frekvens-standards eksperimenter, også kendt som atomure, hvor evolutionen af en atomar kvantetilstand måles med uovertruffen præcision. Ved hjælp af ikke-destruktive kvantemålinger er det muligt at omfordele ubestemtheden mellem systemets forskellige variable og derved frembringe kvante-tilstande som kan bruges til at overskride standard kvantegrænsen i f.eks. atomure. Disse såkaldte klemte kvante-tilstande afhænger af atomernes indbyrdes korrelation, hvilken i kvante-sprog går under navnet sammenfiltrering.

I dette væk giver vi en uddybende beskrivelse af vores implementering af en QND måling ved brug af laser pulser i et Mach-Zehnder Interferometer (MZI), hvormed vi har frembragt klemte spin-tilstande i et ensemble af kolde Cs atomer. Vi efterprøver tillige at kvante-tilstanden er tilstrækkeligt klemt til at ville kunne forbedre præcisionen af et atomur. I den forbindelse undersøger vi grundigt en hel række egenskaber QND vekselvirkningen som gør at atomer og lys-partikler (fotoner) udveksler faseskift.

Sažetak

Kvantna mehanika se odlikuje sa nekoliko osobitih mogućnosti, koje uključuju kvantne neodređenosti, kvantna mjerenja, i sprežanja. U ovom radu su opisane sve tri. U koristi gdje su kvantni sustavi mjerac neke količine, kvantna neodređenost je temeljno ograničenje. Jedan primjer je, mjerenje frekvencije atoma kao standard (atomske satovi), u kojem se određuje kvantno stanje atoma s nevidjenom preciznošću. Kvantna mjerenja u obliku ne-rušenja kvantnih stanja (QND), mogu se shvatiti i izvesti tako da se može preći standardna kvantna granica, po preraspodjeli kvantnih neodređenosti među različitim varijablama sustava. Takva stisnuta spin-stanja oslanjaju se na među-atomske korelacije, koje nazivamo sprežanje.

U ovom radu ćemo predstaviti detaljan opis kako smo proveli QND mjerenja sa laserskim pulsevima u Mach-Zehnder Interferometru (MZI) i pokazati da možemo postići stisnuto stanje u ansamblu hladnih i zarobljenih Cs atoma. Potvrdili smo da su stisnuta stanja korisna za poboljšanje preciznosti atomskih satova. U isto vrijeme, također smo istraživali nekoliko izvanrednih mogućnosti interakcije, po kojoj atomi i čestice svjetla (fotoni) izmjenjuju smjene faza.

In memory of Damir Kosec, "Tata"
★ 1947 – † 2009

Preface

Genesis of an experiment In the beginning vast public funding created heavenly lab-space on earth. Now the labs were formless and empty and the spirited physicists were contemplating over their future experiments. And they said let there be light and they built a grating stabilised external cavity diode laser. And they said let there be an optical table to separate the floor from the ceiling. And it was bought. And they browsed through catalogues from Thorlabs, MiniCircuits, and Farnell and populated the optical table and the racks above it and the entire floor-space below it. And they said let us invite some graduate students who are like us and let them screw, turn, solder, align, and calibrate all the equipment on the optical table, the racks above it and the entire floor-space below it. They saw all that they had made and it was very good; so they tried to optimise it to make it even better and at the end nothing worked as it should. Finally, they rested with a cup of coffee conversing about all the time they had spent, sang and played merry tunes, while at the back of their minds a certain guilt of missed-publication arose.

Once upon a time farther west The quantum optics lab under the auspices of Eugene Polzik have been the frame for most of my research life ever since a long time ago in Aarhus I opted for a Bachelor's project with the famed cell experiment. As this experience did not scare me away, I decided that quantum optics, besides its catchy name, might be an interesting field to spend a year of my Master's thesis on. One year became two and Aarhus was exchanged for Copenhagen, but at the end of it all I produced a thesis on the preliminary steps of spin squeezing on the Cs clock transition. As my lab efforts did not scare off Eugene, I was encouraged by him to continue my work on the experiment until in the future — one that turned out to be rather distant — it would demonstrate spin squeezing. By now, I have been a part of the quantum optics lab endeavour for so long that I'm only a few months short of making it onto the inventory list. Over this time I have worked alongside over a dozen colleagues mostly in a pattern where I have been part of a lab tripod with periods of overlap and increased lab population. I believe the many years spent on the clock-experiment grants me a privileged insight into its evolution. Though this insight may also be considered rather pointless I decided that it should not part with me and consequently at the end of the Introduction chapter I include what I have named an *experimental timeline* (sec. 1).

Thank'ya all Physics has been just one of the blessing of being part of the Quantop gang. The many outings, activities and daily coffee breaks has turned the research group into a group of friends. So it has been during all the years I have been a member and it is surely a thing I will miss. Alas, I will meet some again and some maybe not. To all the people I have worked and during some of the extended experimental runs almost lived with... thanks for your

company =;). It is always nice to see ones name following a "thanks" so as a token of appreciation to my co-workers on the experiment I wish to thank Wolfgang Tittel, Jens Lykke Sørensen, Plamen Petrov, Carlos Garrido Alzar, Niels Kjærgaard, Patrick Windpassinger, Marcin Kubasik, Mark Saffman, Jürgen Appel, Anne Lauchet-Chauvet, and Jelmer Renema. On the inner title page I have accredited Carlos Garrido Alzar, Jörg Helge Müller, Niels Kjærgaard, Anders Sørensen, Jürgen Appel as "additional academic advisors". These nominations are based on my overall professional relationship with them being characterised by me having a question and them having the answer. Particularly I thank Niels Kjærgaard for his camera expertise on the cover photo, his Mathematica code on which the Bloch-sphere drawings are based, and his large role in the preparation of several of my manuscripts. In addition I am grateful for all the clues and assistance I have received from all my colleagues. For more specialised assistance I thank my office mate Andrew Hilliard for serving as a live English dictionary, and Inge Florjančič for editing of the Croatian abstract. Likewise the technical and administrative support staff at the NBI deserve credit for facilitating all the aspects of experimental endeavour.

I've had the privilege to visit the quantum optics group at the Australian National University in Canberra. I wish to extend my thanks to Hans Bachor for granting me this opportunity and to my lab-mates Ping Koy Lam, Ben Buchler, Magnus Hsu, Oliver Glöckl, and Gabriel Hëtet. A special note of gratitude to Massimiliano Colla, whom I shared an office with, for his nearly unlimited practical support during my stay in Canberra. Both professionally and personally my visit to Australia was a great experience and I will always have the fondest memories of that time and the people there — unbelievably I also terribly miss cockatoos!

All physicist need to be extremely thankful to their families, who are forced to allot so much patience for a cause they often do not see any point in. I thank for the love, encouragement and understanding of my wife Suratsawadee "Emma" and my daughter Anais Thima I thank for just being herself. I will end my credits in the same way as in my master's thesis by proclaiming "thank God I made it!"

Contents

Abstract	iii
Preface	vii
Publications	xiii
Abbreviations and Acronyms	xv
1 Introduction	1
I Theory	17
2 Probe light pulses	19
2.1 Photonic operators	19
2.1.1 Schwinger operators	21
2.2 Quantum shot noise	22
2.3 Mode configurations	23
2.3.1 Mach-Zehnder interferometer configuration	23
3 Atomic ensemble	31
3.1 Atomic variables	31
3.2 The atom	33
3.3 Pseudo-spin	35
3.3.1 Bloch sphere representation	35
3.4 Quantum projection noise	37
3.5 Squeezed states	41
3.5.1 Spin squeezed states	42
3.6 Entanglement and squeezing	44
3.7 Decoherence and squeezing	45
3.7.1 Coherence time	45
3.7.2 Squeezing affected by generic loss and decoherence	46
4 Atom light interaction	49
4.1 Effective Interaction Hamiltonian	50
4.2 Phase-shift and absorption	52
4.3 Evolution of the atomic population	54
4.3.1 Rate of excitations	55
4.4 Input-output relations	56
4.5 Decoherence due to probing	58
4.5.1 Experimental examples	60

5	QND measurements and squeezing	67
5.1	QND measurements	67
5.1.1	Squeezing by QND measurements	69
5.2	Atom light interaction and QND measurement squeezing	72
5.2.1	QND measurement as projection on Dicke-state basis	73
5.2.2	Relation between coupling strength and real transitions	76
5.3	QND and squeezing in experimental probing configurations	78
5.3.1	Monochromatic MZI	78
5.3.2	Dichromatic 1 and 2-input MZI	81
5.4	Full ensemble squeezing	88
6	Noise sensitivity	89
6.1	Classical interferometer noise	89
6.1.1	Laser intensity noise	91
6.1.2	Laser frequency/phase noise	91
6.1.3	Acoustic noise	92
6.2	Classical noise in atomic state measurement	94
6.2.1	Atom number fluctuations	95
6.2.2	Coupling strength fluctuations	95
II	Experiment	99
7	Overview of setup	101
7.1	Layout, instrumentation and control system	101
8	MZI performance	105
8.1	Probe laser layout	105
8.1.1	Frequency locked grating stabilised diode lasers	105
8.1.2	Absorption saturation locking	107
8.1.3	Beat-note locking	109
8.2	Pulsed acquisition	114
8.2.1	Pulsed photo-detector	114
8.2.2	Digitisation and storage	114
8.3	MZI layout	118
8.4	Alignment	121
8.4.1	White light positioning	122
8.4.2	Mode overlap in 2-input configuration	124
8.5	Fringe calibration	124
8.6	Locking MZI path-length	125
8.6.1	Counter propagating CW laser	126
8.6.2	Co propagating modulated laser	126
8.6.3	Power stabilisation and path-length wiggling	127
8.6.4	Lock-point offset	130
8.7	Quantum and classical noise characteristics	131
8.7.1	1-input configuration	131
8.7.2	2-input configuration	135
9	Sample preparation and characterisation	139
9.1	Atom trapping setup and control	139
9.1.1	Magneto-optical trap	140
9.1.2	Far Off Resonant Trap	143
9.2	Non-destructive trap characterisation	147
9.2.1	Loading and lifetime	147
9.2.2	Trap frequency	149
9.2.3	Temperature	152
9.3	Effects from FORT	153
9.3.1	Light-shift and dephasing	153

10 State preparation and characterisation	157
10.1 Optical pumping	157
10.1.1 Principles and theory	157
10.1.2 Optical pumping setup	159
10.1.3 Efficiency and dependence on parameters	161
10.2 Microwave interaction	163
10.2.1 Principles and theory	164
10.2.2 Microwave Setup	172
10.2.3 Rabi, Ramsey, and spin echo sequences	180
10.2.4 Relationship with coherence measurements	186
11 Atomic interaction and characterisation	191
11.1 Probe light shift observations	192
11.1.1 Rabi oscillations	193
11.1.2 Ramsey fringes	197
11.2 Light shift cancellation	198
11.2.1 Ramsey spin-echo re-phasing method	199
11.2.2 Light-shift re-phasing in light of atomic motion	200
11.2.3 2-input method and equivalents	205
11.3 Spontaneous scattering decoherence	209
12 QND measurements and squeezing	213
12.1 General procedures	213
12.1.1 General QND measurement sequence	214
12.2 Analysis methods	216
12.2.1 Correlation	217
12.2.2 Data organisation and correction	221
12.2.3 Conditioning data	223
12.3 State destruction	225
12.4 Spin squeezing experiments - approaches and results	225
12.4.1 One-input MZI with reference pulses	226
12.4.2 One input MZI — what now?	229
12.4.3 Two-input MZI	230
12.4.4 Two-input equivalent MZI	237
12.5 Squeezing lifetime	239
12.6 State tomography and anti-squeezing	243
III Outlook and Applications	251
13 Conclusion	253
14 Next steps and improvements	255
14.1 What to improve	255
14.1.1 Limitations	256
14.2 What to do next	257
14.2.1 Running a squeezed clock	257
14.2.2 Single atom excitations	257
15 Applications	259
15.1 Atomic clocks	259
16 Review of experiments	263

IV Appendices	267
A Optical field and operator transformations	269
A.1 Fields and operators	269
A.2 Distribution in Fock-basis	269
A.3 Elements	269
A.3.1 Beamsplitter	269
A.3.2 Free propagation	270
A.3.3 Losses	270
A.3.4 Mode overlap	271
A.4 Full MZI	272
A.4.1 Ideal loss-less MZI	272
A.4.2 Loss-less MZI with imperfect mode overlap	273
A.4.3 Near real life MZI	274
A.5 MZI sensitivity to phase displacements	275
A.6 Sideband interferometer configuration	276
A.6.1 QND and squeezing in sideband interferometer	278
B Atomic operator variances, correlations, and decoherence	279
B.0.2 Quantum projection noise	279
B.0.3 Squeezing affected by generic loss and decoherence	280
B.0.4 Decoherence due to probing	283
C Full ensemble squeezing – influence of geometry	285
D Atomic constants and properties	293
D.1 Expressing the coupling-strength	293
D.2 Cs atom constants	295
D.2.1 D-line constants	295
E Simulations of trapped atomic ensemble	299
E.1 Initial distribution	299
E.1.1 Detection	301
E.2 Single atom phase-space trajectories	301
E.3 Light-shift phase imprints	302
F Measures of oscillator (in)stability	305
G Inventory	307
H Experimental techniques	311
H.0.1 Background field nulling	311
List of Figures	313
Bibliography	319

Publications

Peer reviewed

1. Jörg H. Müller, Plamen G. Petrov, Daniel Oblak, Carlos L. Garrido Alzar, Sebastian R. de Echaniz and Eugene S. Polzik,
Diffraction effects on light-atomic ensemble quantum interface
Physical Review A 71, 033803 (2005)
2. Daniel Oblak, Plamen G. Petrov, Carlos L. Garrido Alzar, Jens K. Mikkelsen, Wolfgang Tittel, Anton K. Vershovski, Jens L. Sørensen and Eugene S. Polzik,
Quantum noise limited interferometric measurement of atomic noise: towards spins squeezing on the Cs clock transition
Physical Review A 71, 043807 (2005)
3. Plamen G. Petrov, Daniel Oblak, Carlos L. Garrido Alzar, Niels Kjærgaard, Patrick Windpassinger, and Eugene S. Polzik,
Non-destructive characterization of an atomic dipole-force trap
Physical Review A 75, 033803 (2007)
4. Patrick J. Windpassinger, Daniel Oblak, Plamen G. Petrov, Marcin Kubasik, Mark Saffman, Carlos L. Garrido Alzar, Jürgen Appel, Jörg H. Müller, Niels Kjærgaard, and Eugene S. Polzik,
Dispersive probing of rabi oscillations on the clock transition near the standard quantum limit
Physical Review Letters, 100, 103601 (2008)
5. Patrick J. Windpassinger, Daniel Oblak, Ulrich B. Hoff, Jürgen Appel, Niels Kjærgaard, and Eugene S. Polzik,
Inhomogeneous light shift effects on atomic quantum state evolution in non-destructive measurements
New Journal of Physics 10, 053032 (2008)
6. Hanna Krauter, Jacob Sherson, Kasper Jensen, Thomas Fernholz, Daniel Oblak, Patrick J. Windpassinger, Niels Kjærgaard, Jonas S. Neergaard-Nielsen, Bo Melholt-Nielsen, Andrew Hilliard, Christina Olausson, Jörg H. Müller, and Eugene S. Polzik.
Quantum interface between light and atomic ensembles
in *Proceedings of the XVIII International Conference on Laser Spectroscopy (ICOLS) 2007*, Leo Hollberg, Jim Bergquist, Mark Kasevich, Eds. World Scientific (2008).
7. Daniel Oblak, Jürgen Appel, Patrick J. Windpassinger, Ulrich B. Hoff, Niels Kjærgaard, and Eugene S. Polzik,
Echo spectroscopy of atomic dynamics in a Gaussian trap via phase imprints
European Physics Journal D 50, 67 (2008)

8. Gabriel Hétet, Mahdi Hosseini, Ben Sparkes, Daniel Oblak, Ping Koy Lam and Ben C. Buchler
Photon echoes generated by reversing magnetic field gradients in a rubidium vapour
Optics Letters 33, 2323 (2008)
9. Mark Saffman, Daniel Oblak, Jürgen Appel and Eugene S. Polzik,
Spin squeezing of atomic ensembles by multicolor quantum non-demolition measurements
Physical Review A 79, 023831 (2009)
10. Jürgen Appel, Patrick J. Windpassinger, Daniel Oblak, Ulrich B. Hoff, Niels Kjærgaard, and Eugene S. Polzik,
Mesoscopic atomic entanglement for precision measurements beyond the standard quantum limit
Proceedings of the National Academy of Sciences 106, 27, 10960 (2009)
11. Patrick J. Windpassinger, Daniel Oblak, Ulrich B. Hoff, Anne Louchet, Jürgen Appel, Niels Kjærgaard, and Eugene S. Polzik.
Squeezing of Atomic Quantum Projection Noise
Journal of Modern Optics 56, 1993 (2009)
12. Daniel Oblak, Patrick J. Windpassinger, Ulrich B. Hoff, Jürgen Appel, Niels Kjærgaard, and Eugene S. Polzik.
Establishing the projection noise in a quantum non-demolition measurement on the caesium clock transition
(submitted to Journal of Physics D).
13. Anne Louchet-Chauvet, Jürgen Appel, Jelmer J. Renema, Daniel Oblak, and Eugene S. Polzik.
Projection noise limited and entanglement assisted atomic clock
(submitted to special issue of New Journal of Physics)

Other

13. Carlos L. Garrido Alzar, Plamen G. Petrov, Daniel Oblak, Jörg H. Müller and Eugene S. Polzik,
Compensation of eddy-current induced magnetic field transients in a MOT
ArXiv/physics/0701251 (2006)
14. Kasper Jensen, Daniel Oblak og Eugene S. Polzik,
Kvanteinformation og kommunikation: den næste kvanterevolution.
in Københavns Universitetets Almanak, Skrive- og Rejse-Kalender for år 2010 (2009)

Abbreviations and Acronyms

AC	Alternating Current
ADC	Analogue to Digital Converter
AMC	American Microwave Corporation (business)
AOI	Angle Of Incidence
AOM	Acousto-Optic Modulator
ATM	Advanced Technical Materials (business)
BNC	Bayonet Neill Concelman (connector)
BS	Beam Splitter
BW	Band-Width
CCD	Charge Coupled Device
CSS	Coherent Spin State
CW	Continuous Wave
DAC	Digital to Analogue Converter
DC	Direct Current
DDS	Digital Digital Synthesiser
DIO	Digital Input/Output
DRO	Digital Resonant Oscillator
DSO	Digital Storage Oscilloscope
EM	Electro-Magnetic (field)
ELS	Elektronik Laser System GmbH (business)
FIFO	First-In-First-Out (memory)
FOD	Fibre Optical Devices (business)
FORT	Far-Off-Resonant Trap
FPGA	Field Programmable Gate-Array
FWHM	Full Width Half Maximum
GPIO	General Purpose Interface Bus
GPS	Global Positioning System
GPSDO	GPS Disciplined Oscillator
IL	Insertion Loss
LED	Light Emitting Diode
LPF	Low-Pass Filter
MOT	Magneto-Optical Trap
MZI	Mach Zehnder Interferometer
NaN	Not a Number (data value)
NBI	Niels Bohr Institute (organisation)
OCXO	Oven Controlled Crystal Oscillator

OI Optical Isolator

PBS Polarising Beam Splitter

PCI Peripheral Component Interconnect (connector/bus)

PLL Phase Locked Loop

PN Projection Noise

PNL Projection Noise Level

PPG Programmable Phase Generator

PSI Poseidon Scientific Instruments (business)

QND Quantum Non-Demolition

QUANTOP Danish National Research Foundation Centre for Quantum Optics
(organisation)

RIN Relative Intensity Noise

RTSI Real Time System Integration (bus)

SA Spectrum Analyser

SBI Sideband Interferometer

SN Shot Noise

SNL Shot Noise Level

SMA SubMiniature version A (connector)

SNR Signal to Noise Ratio

SPDT Single Pole Double Throw (switch)

SQL Standard Quantum Limit

SSS Squeezed Spin State

TTL Transistor-Transistor Logic

VCO Voltage Controlled Oscillator

Introduction

This account brings together some of the most intriguing quantum mechanical concepts, *quantum uncertainty*, *(non-destructive) quantum measurements*, and *entanglement*. The quantum uncertainty reflects that the outcome of a measurement of a quantum variable \hat{A} can generally only be predicted with a certain probability. This is an intrinsic property of the quantum mechanical description of systems in terms of wave-functions, which represent a form of probability distribution in the generalised variable space, the Hilbert space. It is possible for a wave function of a system to prescribe a single well defined value of a variable, whereby we say that the system is in an eigen-state of that variable. So, quantum uncertainty should be viewed in a broader sense, which brings one to Heisenberg's uncertainty relation. The uncertainty relation states that $\langle(\Delta\hat{A})^2\rangle\langle(\Delta\hat{B})^2\rangle \geq |\langle[\hat{A},\hat{B}]\rangle|^2/4$, i.e., the product of the variances of a set of operators must be equal to or exceed the norm-squared value of their mutual commutator. Hence, the relation does not limit the uncertainty of a variable by itself, but only relative to any other non-commuting variable. As it happens, any straight forward preparation of a quantum system tends to produce states that are symmetric in the distribution of uncertainty, in the sense that they have $\langle(\Delta\hat{A})^2\rangle = \langle(\Delta\hat{B})^2\rangle$.¹ A good example is that of the three components of an angular momentum operator $\hat{\mathbf{F}} = \hat{F}_x, \hat{F}_y, \hat{F}_z$. For these the uncertainty relation prescribes $\langle(\Delta\hat{F}_i)^2\rangle\langle(\Delta\hat{F}_j)^2\rangle \geq |\langle\hat{F}_k\rangle|^2/4$. If one defines the coordinates such that the \hat{F}_k is the only component with non-zero mean value then $\langle(\Delta\hat{F}_i)^2\rangle = \langle(\Delta\hat{F}_j)^2\rangle$. This state, often referred to as Coherent Spin State (CSS), can be depicted as in fig. 1.1 with a circular uncertainty blob at the tip of the spin-vector. The blob signifies that one does not know with certainty exactly in which direction the spin points, only that it is most likely to be somewhere within the blob.

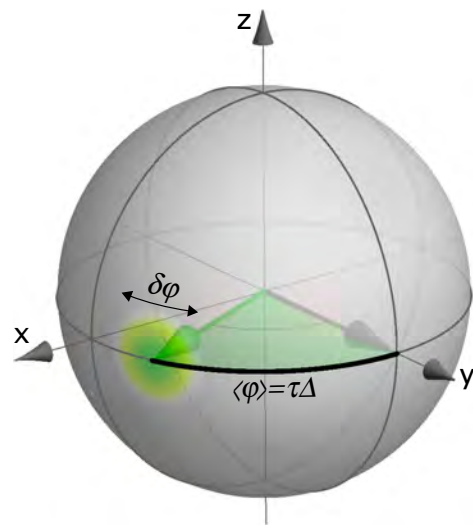


Figure 1.1: Quantum uncertainty in spectroscopy

¹for the moment, please accept this somewhat ambiguous statement

Besides being of fundamental interest the uncertainty of the quantum state has implications for various applications. In extremely sensitive measurements, such as performed in gravitational wave detectors, atomic clocks and other forms of spectroscopy, the quantum uncertainty appears as a noise in the quantity than one is measuring. Thus, in spectroscopic measurements the ultimate precision obtainable using classical resources is the standard quantum limit (SQL). At this limit, the measurement precision is limited only by the quantum noise of the system. This point is also illustrated in fig. 1.1: In many cases an atomic spin is used to measure some perturbation, as in magnetometers, or as a reference to some external sources. In clock experiments the atoms act as a reference to an external frequency source. The difference between the atomic and external frequency Δ is gauged by the angle ϕ that the atomic spin precesses during some interrogation time τ . The quantum mechanical expectation value of this precession angle is of course well determined, but the outcome of a single measurement is contaminated by an uncertainty $\delta\phi$, which arises from the pointing uncertainty of the spin.

The SQL can, however, be surpassed by using spin states which have the uncertainty of one of its components smaller than the SQL. This class of states is referred to as squeezed spin states (SSS) — a prime example is depicted in fig. 1.2, where the uncertainty blob has been drawn as an ellipse. Due to the smaller angular uncertainty of the SSS the precision of the spectroscopic measurement is improved.

The problem of squeezed states is that they are not *off-the-shelf* quantum states. Whether the squeezing be of optical or atomic systems, e.g. of spins, considerable effort goes in to engineering them. Squeezed states can be created by various non-linear interactions of the different variables within the system it self or it can be generated by coupling to an auxiliary system. The latter is what brings us to the topic of *non-destructive quantum measurements*. This squeezing approach involves quantum non-demolition (QND) measurements where a variable of a target quantum system is coupled to a meter variable. The understanding of what makes a measurement is probably one of the most contended in quantum theory. Non-demolition measurements are particularly interesting because they require a proper and fully quantum mechanical treatment and thus open to a host of quantum phenomena. With relation to spectroscopy at the SQL, a QND measurement of the before mentioned meter variable increases the knowledge about the target variable and reduces its quantum uncertainty. Obviously, it is essential that the meter does not couple back to the measured target variable — termed *back-action evasion* — as this would yield the knowledge gained about it obsolete. It is also essential that the target variable is coupled with sufficient strength that its value can be discerned in the meter detection. Thus, if a QND measurement can achieve a sensitivity at the SQL the target system ends up in a squeezed state.

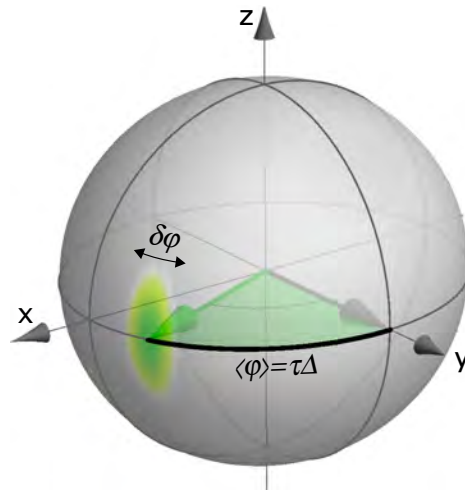


Figure 1.2: Quantum uncertainty in spectroscopy using a SSS.

In fig. 1.3 we draw a small cartoon of a QND measurement between spins of a light/photonic and an atomic quantum system. In the figure the moving photons

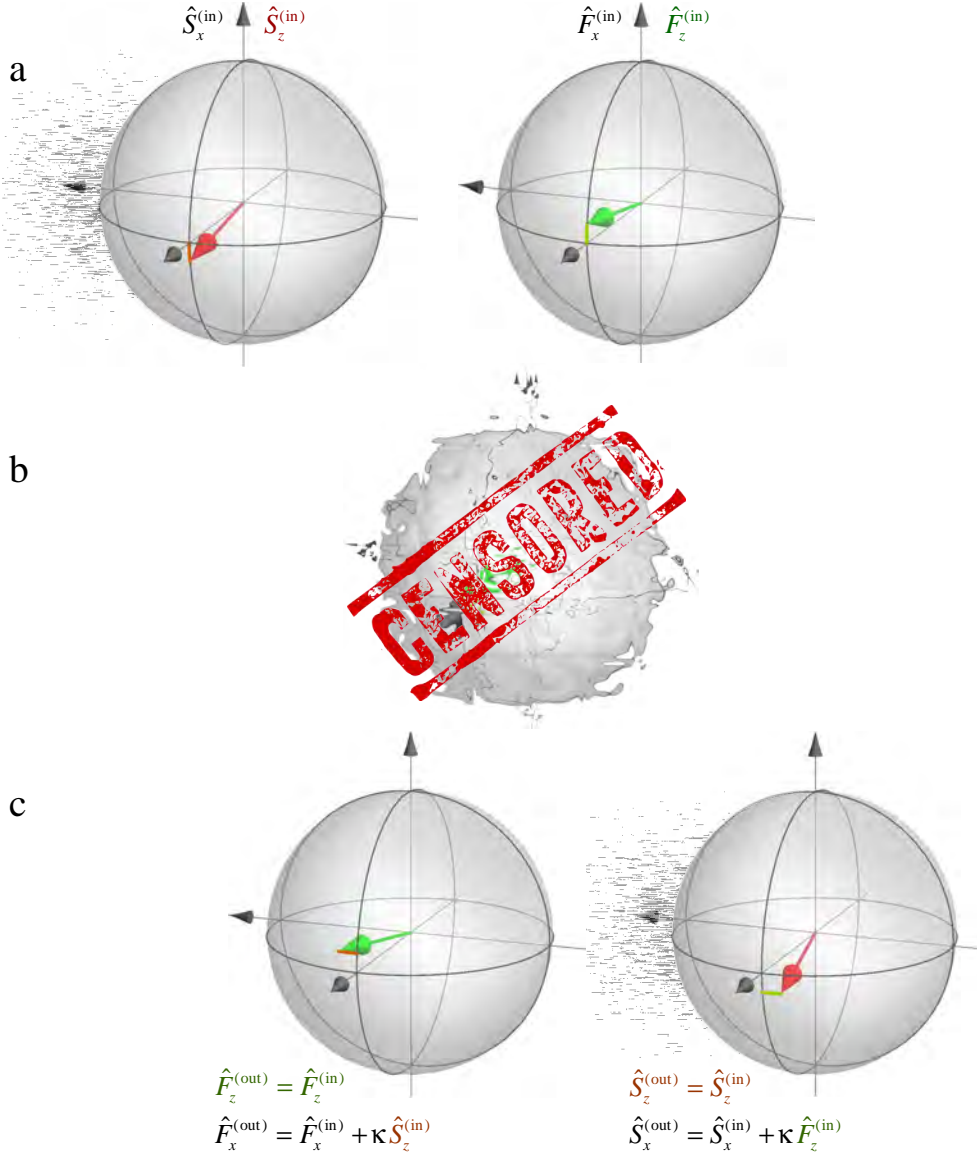


Figure 1.3: QND interaction between light and atomic pseudo-spin

are described by $\hat{\mathbf{S}} = \{\hat{S}_x, \hat{S}_y, \hat{S}_z\}$ and the stationary atoms by $\hat{\mathbf{F}} = \{\hat{F}_x, \hat{F}_y, \hat{F}_z\}$, where we take \hat{F}_z as the target variable. Before the QND interaction the quantum uncertainty of \hat{F}_z and \hat{S}_z may result in them being displaced by some small amount given by the green and orange line segments respectively (fig. 1.3a). During the interaction the two systems exchange information about each others' quantum states (fig. 1.3b). This is done in a way that the the target variable \hat{F}_z is unaffected but \hat{S}_x is perturbed by the value of \hat{F}_z (fig. 1.3c). This evolution follows from an interaction Hamiltonian on the form $\hat{H}_{\text{int}} = \tilde{\kappa} \hat{S}_z \hat{F}_z$, which in the literature is often referred to as a QND Hamiltonian. In this way \hat{S}_x records the value of \hat{F}_z and if subsequently \hat{S}_x is detected (either destructively or non-destructively) we can gain knowledge on \hat{F}_z and as argued above reduce its uncertainty. Heisenberg's uncertainty relation demands that the uncertainty in \hat{F}_x be increased simultaneously. This is indeed a natural result of the light-atom interaction which also involves \hat{F}_x recording \hat{S}_z . Since the value of \hat{S}_z is uncertain it will add to the uncertainty of \hat{F}_x . This embodies the back-action of the QND measurement.

The above picture is convenient for illustrating what we require from the QND measurement, but at the same time it is misleading because it gives the impres-

sion that from the beginning the spins actually had some well determined values \hat{F}_z and \hat{S}_z . We as observes, just didn't know these values beforehand, but by the QND measurement they were revealed to us. This picture is referred to as the *hidden variable* assumption, which is not the essence of quantum mechanics. In the correct picture the values of \hat{F}_z and \hat{S}_z are completely undetermined before the QND measurement. When the two systems interact they exchange some of their quantum variables whereby the systems become correlated a.k.a. entangled. It is in fact not until the very measurement that the SSS is created and a particular measurement value is realised.

This leads us to the concept of entanglement, which actually appears in two respects. First of all, the QND interaction entangles the target and meter systems so that the two are no longer separable. Hence, the detection of the light involves tracing out the photonic part of the entangled quantum state, which again results in the remaining atomic part ending up in a squeezed state. The second way that entanglement enters the discussion is in the squeezed state itself. The only way that atomic state can have less fluctuations in one variable is if the atoms are mutually correlated, that is, entangled. Being entangled means that the individual atoms do not behave independently, but the "action" of one atoms entails the some "action" of other atoms. We now turn to reflect on some more practical aspects of how to implement a QND measurement in order to engineer an SSS.

Practical considerations for SSSs engineered by QND measurements

From a pragmatic perspective there are three main experimental tasks to perform in order to claim that one has engineered a squeezed spin-state by a QND measurement:

1. Establishing the standard quantum limit (SQL).
2. Verifying quantum correlation of a spin component.
3. Determining the level of spin vector demolition.

This point-by-point structure also dictates the composition of [Appel09], where we report our spin-squeezing demonstration. As it turns out the second task, though it may appear complicated, is in fact the most straight forward to perform as we "just" have to measure correlation between two subsequent measurement of a spin component. The key to the ease of this task, is the fact that it requires establishment of the statistics of a relative measurement i.e. the difference between to measurements. Thereby, one automatically avoids many technical sources of noise that would otherwise mask the statistics of the quantum state. To establish the projection noise we need to measure the statistics of the quantum state w.r.t. to an absolute reference level. Hereby, the measurement becomes highly susceptible to classical sources of noise and only by arduous perfection of the experimental setup and sequences is it possible to resolve the projection noise. The third and final task of deducing the spin-vector is marred by a host of complications, which depending on the experimental setup may be of varying significance. In our case the AC Stark shift or light-shift of the atomic energy levels additionally perturbs the atomic state, and only by eliminating this effect are we able to faithfully measure the irreversible demolition of the quantum state. In the literature of claimed spin-squeezing experiments one of these tasks is often neglected — typically ascertaining the level of spontaneous-scattering is missed (see chapt. 16).

Returning to the demanding task of stabilising the absolute reference for measurement of the initial atomic state and thereby being able to see the quantum projection noise of it. Experimentally, the main factor characterising the measurement is its signal to noise ratio (SNR), which depends on both the achievable coupling strength as well as the level of limiting noise influences. In systems, such as ours, where a light meter reads out an atomic target variable, large coupling can be achieved by using dense ensembles or invoking cavity enhanced measurements. Owing to the general direction of research in our group we follow the ensemble path. The feat of stabilising the meter variable detection to the required level can be approached from various angles. One may focus on the inherent stability to ensure that no elements source noise to the meter and its detection. Alternatively, instead of eliminating the noise one can try to trace the fluctuations and compensate for them in the data analysis. Finally, one may construct a system which is immune to particular limiting sources of noise. The two alternative configurations discussed in this thesis embody the second and third approach, respectively.

Theses

Below I state the main theses that I aim to demonstrate in the remainder of this account. Since this is an experimental investigation it is understood that the successful demonstration should be based on empirical evidence, though the derivation of a theoretical basis is to be seen as an important attribute.

- A spin squeezed state can be engineered by means of a quantum non-demolition measurement.
- Probing in 2-input Mach-Zehnder interferometer configuration has several practical advantages for MZI stability
- Probing in 2-input Mach-Zehnder interferometer configuration affords the most effective cancellation of inhomogeneous light shift due to probing
- Dichromatic probing near cycling transitions suppresses the effect of spontaneous scattering

Our results put in context

The notion that it should be possible to measure a quantum system without actually destroying it surfaced already in the early days of quantum mechanics [Landau31, Neumann32, Bohm51]. However, the concept was given limited attention until it was seen to have prospects for application to gravity wave detection. Thus much of the early work on QND was devoted to gravity wave detection [Braginsky74, Braginsky77, Unruh78, Thorne78, Braginsky80], however much of this work also included general considerations about the nature of QND measurements coupled with attempts to define *what* they are. Comprehensive reviews of the QND measurement concept and the, to that date, limited number of experimental realisations can be found in [Braginsky80, Poizat94, Braginsky96]. More recent experimental developments are reviewed in [Bachor04, chapt. 11]. The initial experimental realisations were indeed not performed in relation to gravity-wave detection, but in non-linear optical materials [Braginsky77, Imoto85, Friberg92, Levenson93, Schiller96]. In these the

information about a target beam is relayed to a meter beam whilst they propagate through a medium with non-linear refractive index. A similar coupling has been achieved in Na in a room temperature vapour or in a laser cooled cloud [Grangier91, Poizat93, Roch97]. Another, approach to QND is to take a beam of light and split off half of the light on a beamsplitter. If the other input of the beamsplitter is "illuminated" with a squeezed vacuum field one can avoid adding vacuum noise to the target quadrature of the output fields which should thus be perfectly correlated. Detecting one output amounts to a QND measurement of the other output [Shapiro80, Bruckmeier97]. All these demonstrations have involved purely optical target and meter systems. Performing QND measurements in a mixed atom-photon system has taken longer to realise. A neat result comes from an experiment where atoms propagate through a microwave cavity and depending on the number of photons inside the cavity the atom receive a certain phase shift but do not permanently absorb any of the photons. Then detection of the atoms after passing the cavity can reveal the phase-shift and thus the photon number [Varcoe00, Bertet02]. This puts us at the edge of discussing the generation of squeezed states in atoms, but before jumping into that we review the experimental development towards squeezing in general.

Squeezing of quantum uncertainties hinges upon the Heisenberg relation only limiting the value of the product of a set of uncertainties. Thus, squeezed states of a set of conjugate operators can be prepared in both optical, atomic or any other quantum system. Nevertheless, the way to generate squeezing depends strongly on the type of system. Squeezed states have a far longer track record in optical than in atomic systems. The earliest modest demonstration of squeezing used four-wave-mixing in atomic beams [Slusher85]. These were followed by demonstrations of somewhat larger noise reduction by degenerate parametric down-conversion in OPO/OPA operated below threshold thus generating squeezed vacuum states [Wu86]. The Kerr-effect has also provided a path to generate squeezed states either inside optical fibres [Levenson85, Milburn87] or in a cold atomic cloud [Lambrecht95]. Atomic systems have been used to generate squeezed light by other means such as polarisation self rotation in vapours [Ries03] or through the non-linear interaction of atoms inside cavities [Orozco87]. Amplitude squeezed light can be generated by second harmonic generation (SHG) [Pereira88] or in the difference intensity of twin beams output from an OPO either in CW [Heidmann87] or pulsed [Aytür90, Nabors90] operation. Finally, regular diode lasers can become sources of amplitude squeezed light by driving them with a sub-Poissonian current. This has been used to produce intensity squeezed laser beams [Richardson91, Inoue92] and later also operating in single mode [Freeman93, Wang93].

Squeezing of angular momentum or spins was treated in [Wódkiewicz85b] with an implementation in Josephson junctions discussed in [Wódkiewicz85a]. More elaborate treatment of the requirements for a spins to be squeezed was done in [Yurke86, Wineland92, Kitagawa93, Wineland94] where the focus was put on applications in spectroscopy/interferometry. These papers will form the backbone for our approach to verify and gauge the spin squeezing in the experiment. There are two main currents in the approach to generate the squeezed states. The first relies on some form of non-linear interaction between different spin-components [Kitagawa93] while the other is based on QND measurements [Kuzmich99]. The first experimental demonstration of spin-squeezing actually falls outside the two approaches, as it was achieved by illuminating a Rb MOT sample with a beam of squeezed light [Hald99]. In line with the non-linear interaction approach, specific theoretical suggestions for generating squeezed atomic states started to develop. Initial proposals dealt with the usual

suspects namely the position and momentum observables of trapped and laser cooled ions [Heinzen90, Cirac93]. Other proposals involve the dipole interaction between Rydberg atoms [Bouchoule02b] or collisional interactions in BECs [Sørensen01a]. Experimental reports have shown increased sensitivity in Ramsey measurements using squeezed state of two ${}^9\text{Be}^+$ ions [Meyer01]. This result was extended to three ions in two simultaneous demonstrations [Roos04, Leibfried04]. There have been a number of experiments in BECs showing either increased fluctuations [Jo07] in the phase or suppression of atom number fluctuations between BEC separated in potential wells [Orzel01, Gerbier06]. A recent experimental report [Estève08] showed how squeezing of the atom-number difference between two BECs in separate potential wells could be achieved by means of the tunnelling interaction between the wells (see chapt. 16).

The other basic idea is that of inducing a partial projection of the particle wavefunction and thereby reduce the statistics of the state. To induce this partial wave-function collapse without destroying the atomic coherence is no easy feat, and only possible if the projection is done in a non-destructive fashion. This brings us back to the QND measurements. Kuzmich et al. in [Kuzmich98, Kuzmich99] introduced different forms of QND interactions between light and atomic spins that would result in the creation of a spin-squeezed state. This was followed by the first demonstration of QND measurement induced spin-squeezing in a room-temperature vapour cell [Kuzmich00]. The light-atom interaction in that experiment was in the form of the Faraday rotation of the probe beam polarisation by a spin polarised atomic sample in a static magnetic field. The Faraday interaction was also used to squeeze the combined collective spin of two Cs vapour cells [Julsgaard01]. The potentially long coherence times and high atomic densities possible for cold trapped atomic samples has resulted in a large interest to create spin squeezed states in such systems. A publication [Geremia04] seemed to demonstrate very impressive amount of spin-squeezing in a Rb MOT again by using the Faraday interaction. This article has, however, later been retracted [Geremia08]. Another QND measurement based on the Faraday rotation of the probe beam during passage through a Rb MOT was demonstrated in [Smith06]. In [Chaudhury07] squeezing induced by a non-destructive Faraday rotation measurement was reported in the same experimental setup. The squeezing did however not involve any inter-atomic correlation, but relied on correlation between the atomic sub-levels. Recent Faraday rotation experiments documented in [Takano09b, Takano09c] have shown signs of spin-squeezing in cold ${}^{171}\text{Yb}$ atoms.

Outside the realm of Faraday rotation measurements an alternative scheme involves the measurement of the optical phase-shift of a probe beam. This phase-shift is caused by the index of refraction of an atomic medium. Since the phase-shift depends on the internal atomic state the probe will be able to detect this state. The phase-shift can be detected either by the resonance-shift in an optical cavity or by an interferometer. A detailed analysis of the QND interaction in an interferometric setup was performed in [Bouchoule02a]. Subsequently this proposal has been taken up in [Oblak05, Saffman09]. The non-destructive atom detection capabilities of a Mach-Zehnder Interferometer (MZI) were established in [Petrov07, Windpassinger08c], with the latter report indicating sensitivity of the measurement at the SQL. These reports were followed by an article demonstrating spin-squeezing by a dichromatic MZI based measurement [Appel09]. Simultaneously, the results from two independent experiments using cavity based phase-shift measurements were released. The first [Schleier-Smith08, Leroux09] gives a clear demonstration of spin-squeezing in a FORT of Rb atoms. The phase-shift is measured by the change in the cavity mode with resulting perturbation of

the cavity transmission. The other [Teper08] only uses the cavity to enhance the coupling between the probe light and the Rb MOT. The report shows significant noise reduction and anti-squeezing that agrees with the prediction. However, the experiment comes just short of showing actual spin squeezing. In chapt. 16 we go in to some of the details of a number of key experimental results connected to squeezing in atomic systems.

At the very beginning of this introduction we emphasised the limitations that the quantum noise sets in spectroscopic applications [Wineland94] — referred to as the Standard Quantum Limit (SQL). At the time when this issue was foreseen, clock experiments were not yet operating at the SQL, but by 1999 they were [Santarelli99]. This boosted the interest in spin squeezing as a means to overcome the SQL. Hence, *spin-squeezing* and *clock (transition)* have featured together as catch-phrases in several publication titles and/or abstracts [Oblak05, Windpassinger08c, Meiser08, Teper08, Leroux09]. As noted above the clock-transition spin-squeezing was only realised by 2008 [Appel09, Schleier-Smith09] and still later the first results of applying the squeezed states in a clock-sequence were announced [Louchet-Chauvet09]. By now much of the focus within the frequency-standards field is moving towards optical clocks, and the spin squeezing between the hyperfine ground states is perhaps not at the top of the agenda. On the other hand spin-squeezing can be equally relevant for frequency standards based on optical transitions [Meiser08]. At the moment, the optical clocks are several orders of magnitude away from the SQL, but this is much like the state of microwave clocks when spin-squeezing was first suggested for spectroscopic applications. We would emphasise, that the particular configuration in our experiment where we rely on two lasers each probing a separate hyperfine level makes it in principle independent of the splitting of the probed levels. Thus, levels separated by an optical wavelength could equally well be squeezed in this setup. Finally, we note a very important advantage of the non-destructive probing that does not require squeezing. The non-destructiveness of the state detection simply means that the repetition rate of a frequency comparison between the atomic reference and the external microwave oscillator can be increased. This is expected to decrease the influence of the Dick effect [Dick90] and it has been demonstrated to work in a ^{87}Sr optical clock [Lodewyck09].

Since interferometers are so dear to our heart we reserve a few lines to note other MZI based experiments in quantum optics. In [Lye03] various approaches for non-destructive detection of BEC was investigated with the aim of being able to do feedback to the BEC. The MZI for that purpose was realised and characterised in [Fig106], but without demonstration of atomic detection. An MZI has also been used to detect the phase-shift of a single atom in a tightly focused Far of Resonant Trap (FORT) [Tey08].

Layout of thesis

I might be accused of adhering to the naive assumption that making the thesis comprehensive it cannot at the same time be incomprehensible. Certainly, I for my own part tend to prefer accounts to be as detailed as for all ambiguity to be removed. Another, concern is pedagogy. It has been my aim to structure the thesis in a logical order clearly highlighting the rationale and progression from one section to the other. furthermore, the reader may be either delighted or displeased with the thorough cross-referencing of sections, figures, and equations. To be sure of reaching both the target of clarity and pedagogy, I may state the same facts or elucidate the same points more than once, thereby adding to the length of this work.

The body of the thesis is divided into three parts covering the theoretical basis, the experimental demonstration, and the ramifications of our work. The theory progressively involves all the aspects needed to understand how a QND measurement arises from our system and how the result, under the right circumstances, should be the creation of a spin-squeezed state. To that end, I first introduce the two main players, the optical probe pulses in chapt. 2 and the atomic sample in chapt. 3. A crux in these sections is to cast the photonic and atomic variables in the form of "angular momentum like" operators and to make some simple concessions for the spatial distribution of the systems. In these sections I also look at the quantum statistical properties as incarnated by the shot noise of light and projection noise of atoms. W.r.t. the latter I introduce the concept of squeezed states and very importantly determine how they should be gauged. I also start developing the rather intricate theory of how the correlation is impacted by decoherence. The first step to make these two systems truly interesting is to let them interact, and that is exactly the topic of chapt. 4. From a very basic description of the dipole interaction I develop a formulation of the effective interaction which relates to the pseudo-spin operators. I also relate the interaction directly to more intuitive features such as the phase-shift and absorption of the light and the light-shift and spontaneous scattering of the atoms. I draw a parallel from the spontaneous scattering to the decoherence of the atomic state. In chapt. 5 I commence the discussion on QND measurements aiming to explain the foundations of the concept. This naturally leads to the engineering of spin-squeezed states by QND measurements and I present two related proofs of principle. A substantial number of pages is then devoted to a complete integration of the QND measurement induced spin-squeezing concept with the MZI based detection of the atomic pseudo-spin. In this treatment I go in depth with the parameters determining the amount of squeezing generated, be it the arrangement of the MZI, probe detunings, spontaneous scattering and more. In the final part of the theory chapt. 6 we already start transitioning to the experimental section, in that we discuss the various imperfections of the MZI based QND detection. This will lead to a number of pragmatic insights, which will be of great value for the design of the experimental setup.

In the experimental part the various elements of the setup are subjects of dedicated chapters. The treatment in these follows somewhat in line with theory, going from properties of the probe, over the preparation of the atomic ensemble, and finally indulging with their mutual interaction. In more detail, the chapters go through, first, a round up of the computer based control system, which regulates the operation and timing of all the other parts (chapt. 7). Hence, the control system inter-links the whole setup. Secondly, in chapt. 8 we detail the intrinsic properties of the MZI setup without any explicit reference to the atomic sample. The preparation of the atomic ensemble is discussed in the following chapters starting with the sample trapping in the MOT and dipole trap (chapt. 9). This involves the non-destructive MZI based characterisation of a number of trap parameters. Next, in chapt. 10 we discuss the two steps in the state preparation namely the optical pumping (sec. 10.1) and microwave rotations of the pseudo-spin vector (sec. 10.2). Both steps are characterised, and we put particular attention to the microwave interaction since it is a crucial tool for manipulating the atomic state also for other purposes than the state preparation. Moreover, the Rabi and Ramsey spectroscopy experiments that we perform reveal much about the various sources of decoherence of the atomic state. The following chapter (chapt. 11) gives a detailed account of the many precautionary measures needed to make the QND measurement usable for engineering spin-squeezed states. The key issue will be the AC-stark/light shift of the atomic state including methods

to revert or completely cancel the shift. With that in hand we proceed in the remaining chapt. 12 to discuss actual QND experiments in the framework of the QND atom-light interaction described in the theory. In the QND measurement chapter I have tried to present the data in a consistent form both in terms of the parameters presented and the visual layout. Admittedly, not all the figures are strictly necessary to understand the data. Then again, my aim has been to facilitate an easy comparison between the data.

In the last part, I sum up the results reported in this work and give some suggestions for desirable improvements to the setup. This is closely linked to the future fate of the experiment. I top off with a discussion of how the work is related to various applications and also draw parallels to similar results.

Scattered around the thesis pages are a few *yellow boxes*, which contain non-essential/anecdotal data or theoretical results and representations. Since the boxes can all be fitted into a single page I found it excessive to put them in to proper appendices. Nevertheless, the boxes may be treated as appended material. Lastly, the actual date of acquiring the experimental data presented in the figures is noted in the list of figures on 313. This chronological information in combination with the timeline below should make it a bit easier to track the changes and experimental setups corresponding to a given data set.

Notation

I afford a few lines to clarify some principles of the notation. I use the Dirac bra-ket notation for quantum states. Though it is quite tedious at times I have stuck to the convention of giving all quantum mechanical operators hats, i.e., $\hat{\cdot}$. Expectation values without are written as bra-kets, e.g. $\langle \hat{n}_{\text{ph}} \rangle = n_{\text{ph}}$, where the be-hatted symbol should automatically be taken as an expectation value. Vectors are in bold e.g. \mathbf{r} for the Cartesian coordinate. Notationally, I do not distinguish between between an experimental estimate of the variance $\langle (\Delta \cdot)^2 \rangle$ and the actual variance $\langle (\Delta \cdot)^2 \rangle$ nor whether it is the result of a classical probability distribution or of the quantum uncertainty inherent in the wave-function. To avoid some of the most common mistakes, I have tried — but probably failed in places — to keep all formulas involving frequencies in angular units, i.e., ω instead of ν .

Oh, and I use British spelling conventions so don't be alarmed when bumping into *colours, synthesisers, fibres, centres, caesium* and many more. Come to think of it one *should* be alarmed by an encounter with caesium... and preferably seek medical treatment.

Experimental timeline

Here comes a timeline of the experimental developments over the time the I have been a part of the clock spin squeezing endeavour. To structure the timeline the entries are colour coded according to

Human resources	Setup and equipment	Observations and measurements	Publications
-----------------	---------------------	-------------------------------	--------------

I include only important revisions or improvements of the setup. The same applies to measurements and observations and generally only the first instance is given an entry.

1-Nov-2000	Anton Vershovski joins the lab team
1-Jan-2002	Plamen Georgiev Petrov joins the lab team
1-Jan-2002	Wolfgang Tittel joins the lab team
1-Jan-2002	Jens Christian Mikkelsen joins the lab team
29-Aug-2002	New MOT coils of water cooled hollow copper wire made and put on chamber
1-Sep-2002	Daniel Oblak joins the lab team
20-Sep-2002	Fakuli (PC) enters service
5-Sep-2002	CCD camera for observing MOT set up
31-Oct-2002	Anton Vershovski leaves the lab team
1-Dec-2002	Fibre MZI built and white-light aligned
12-Dec-2002	Absorption imaging of MOT fails to work
20-Dec-2002	Wolfgang Tittel leaves the lab team
1-Jan-2003	Change from counter to co-propagating probe/lock and to equal polarisation with chromatic filtering
1-Jan-2003	Carlos Leonardo Garrido Alzar joins the lab team
20-Jan-2003	Shot noise operation of MZI up to 1000 nW (maximal power used) 2 μ s pulses on 7 μ s timescale
23-Jan-2003	Observing MOT phase-shift and atomic noise
29-Jan-2003	Observation of atomic noise (presumably classical MOT loading statistics)
4-Feb-2003	Move to NBI
4-Feb-2003	Jens Christian Mikkelsen leaves the lab team
4-Feb-2003	Jens Lykke Sørensen leaves the lab team
1-Mar-2003	Attempts to vacuum seal titanium chamber windows fail
2-Mar-2003	Attempts to un-mount titanium chamber windows fail
1-Apr-2003	Decision taken to shift to free-space MZI and quartz-cell MOT setup
1-May-2003	Free space MZI frame and base-plate setup done
11-Jul-2003	MOT anti-Helmholtz coils installed in MZI setup
23-Jul-2003	MOT collimators installed on MZI base-plate
1-Aug-2003	MOT observed in quartz-cell setup
29-Oct-2003	First noise measurement in free-space MZI setup with LeCroy
11-Nov-2003	FORT laser (ELS VersaDisk) arrives and is mounted on MZI table
2-Dec-2003	Replace LeCroy scope with integrator chip and acquire on PC card
9-Dec-2003	Shot noise operation of free-space MZI on short timescale
11-Dec-2003	White light alignment by minimisation of MZI signal variance induced by modulation of probe frequency
16-Jan-2004	Saturation absorption set up to monitor MOT slave lasers
10-Feb-2004	First observation of MOT phase-shift in free-space MZI
20-Feb-2004	First observation of atomic noise in free-space MZI setup
20-Mar-2004	Discovery of huge MOT-coil switching induced noise in MZI signal
24-May-2004	MOT/FORT imaging camera arrives
1-Jun-2004	FORT laser pulsing enabled by insertion of AOM

2-Jul-2004	Effect of MOT-coil switching removed
5-Sep-2004	Camera set up for observing FORT installed
20-Sep-2004	Microwave phase-shifter arrives
28-Sep-2004	FORT laser moved to separate table because of vibrations
9-Nov-2004	Attempts to gauge Stark shift from MOT cooler and repump
10-Nov-2004	Synchronising PC-card counters
18-Dec-2004	Fluorescence from FORT trapped atoms observed
4-Feb-2005	First observation of phase-shift from FORT trapped atoms
7-Mar-2005	PRA 71, 033803: Diffraction effects on light-atomic ensemble quantum interface
6-Apr-2005	First try on microwave spectroscopy with horn-antenna
11-Apr-2005	PRA 71, 043807: Quantum-noise-limited interferometric measurement of atomic noise: Towards spin squeezing on the Cs clock transition
13-Apr-2005	Niels Kjærgaard joins the lab team
20-Apr-2005	Carlos Leonardo Garrido Alzar leaves the lab team
15-Jul-2005	Narda microwave amplifier arrives
9-Sep-2005	Ukfuto (PC) enters service
20-Sep-2005	Horn antenna replaced by sawed-off wave-guide
20-Sep-2005	Patrick Joachim Windpassinger joins the lab team
11-Oct-2005	Optical pumping implemented (only $4 \rightarrow 4'$)
17-Oct-2005	Apply bias field along z-axis
19-Oct-2005	Full optical pumping implemented (adding the $3 \rightarrow 4'$ re-pump)
5-Feb-2006	Doku-Wiki initialised
21-Feb-2006	Novel shutters (based on stripped PC hard-drives) tested and installed
27-Feb-2006	Bias field switching implemented
6-Mar-2006	$3 \rightarrow 2'$ probe adjusted to the right frequency
30-Mar-2006	First dichromatic probe measurement of atomic superposition state noise: mostly quadratic noise above a large electronic noise floor
11-May-2006	DIO-64 card enters service with new control program
1-Jun-2006	First acquisition with scope (borrowed LeCroy)
20-Jun-2006	Plamen Georgiev Petrov leaves the lab team
14-Jul-2006	Agilent scope arrives
2-Aug-2006	Hyperfine level cleaning (blow-away) implemented
16-Nov-2006	Noise measurement using parallel scope channels
22-Nov-2006	FORT laser collimation - telescope in beam
11-Dec-2006	Direct measurement of optical depth via probe-beam absorption
13-Dec-2006	First noise measurement with up-down-superposition scheme
12-Jan-2007	AMC microwave switch enters operation
31-Jan-2007	Gamera (PC) enters service
7-Feb-2007	First clear observation of quantum projection noise in u-d-sp scheme
6-Mar-2007	PRA 75, 033803: Nondestructive interferometric characterization of an optical FORT

13-Apr-2007	Changing MZI cat-eye and output coupler (on Meier mount)
1-May-2007	Fakuli (PC) becomes Godzilla
1-May-2007	New lock for MZI installed
9-May-2007	New QND detector installed (3.44 times gain + lower electronic noise)
1-Jun-2007	Jürgen Appel joins the lab team
1-Aug-2007	Ulrich Busk Hoff joins the lab team
17-Aug-2007	New power reference detector (lower noise than original Thorlabs)
23-Aug-2007	Discovery of incoherent background light on 4 → 5' probe - insert filter
1-Sep-2007	New MZI locking scheme implemented (modulated lock beam co-propagating with probe and detected on QND detector)
18-Sep-2007	Second Cs dispenser enters service
25-Sep-2007	Thorough investigation and characterisation of probe light shift
8-Oct-2007	First noise measurement with reference pulses
9-Nov-2007	Thorough Ramsey spin-echo investigation of decoherence
14-Nov-2007	Increase to four state preparations per FORT loading
16-Nov-2007	AMC microwave switch breakdown
27-Nov-2007	Kahuna (PC) enters service
28-Nov-2007	Optical pump derived from 0'th order of MOT cooler slave
29-Jan-2008	Kuhne 4 W microwave amplifier installed - π pulse from 28 μ s → 8 μ s
30-Jan-2008	Trap dynamics and light shift phase imprints studied thoroughly
10-Feb-2008	Probe frequencies doubled (to see if probe frequency noise influence goes down)
12-Feb-2008	Measuring FORT light shift of probe transitions
18-Feb-2008	First measurements to find magical probe frequency combination
14-Mar-2008	PRL 100 , 103601: Nondestructive Probing of Rabi Oscillations on the Cesium Clock Transition near the Standard Quantum Limit
1-Apr-2008	New formulation of experimentalist life-time using atomic destiny operators
3-Apr-2008	Power reference detector placed in probe arm
14-Apr-2008	Probe arm attenuated
8-May-2008	Minimising RF noise in pulsing AOMs shot noise operation in 2 input configuration is achieved
20-May-2008	Discovery of beat signal between probe lasers (due to 9 GHz sideband)
28-May-2008	NJP 10 053032: Inhomogeneous light shift effects on atomic quantum state evolution in non-destructive measurements
8-Jun-2008	D1 line optical pumping tried out (5% better efficiency)
10-Jun-2008	First noise measurement in 2-input scheme
30-Jun-2008	First noise measurement indicating spin squeezing (\sim 3dB)

7-Jul-2008	3rd observation of squeezing, now with setup re-aligned from scratch
1-Aug-2008	Squeezing observed with stronger attenuation on probe arm
1-Sep-2008	Anne Marie Marthe Louchet joins the lab team
14-Oct-2008	Clock-frequency with GPS referenced synthesiser -Ramsey spectr
18-Oct-2008	EJPD 50, 67: Echo Spectroscopy of Atomic Dynamics in a Gaussian Trap via Phase Imprints
31-Oct-2008	Attempts on state tomography fail due to excess noise in either mw-source or clock level splitting
11-Nov-2008	Thorough characterisation of decoherence in 2-input configuration
10-Dec-2008	First observation of 2-photon $\Delta m = 2$ microwave transitions
20-Dec-2008	Patrick Joachim Windpassinger leaves the lab team
4-Feb-2009	Frequency chain from 500 MHz to 9.2 GHz incorporating the DDS is assembled and tested
4-Feb-2009	500 MHz OXCO source assembled
9-Feb-2009	Noise of CSS with/without $\pi/2$ rotation around pseudo-spin axis using new frequency chain and Rohde-Schwarz 500 MHz source. Classical MW phase-noise with $\pi/2$ rotation.
18-Feb-2009	Noise of CSS with/without $\pi/2$ rotation around pseudo-spin axis using new frequency chain and OXCO 500 MHz source. Both resolving projection noise.
3-Mar-2009	Phase-noise of OXCO based MW source measured by Ramsey sequence. Large excess classical noise for $\tau_R > 10 \mu\text{s}$.
11-Mar-2009	First SSS tomography attempt ($0-\pi/2$) showing huge noise increase when state is rotated.
25-Mar-2009	Reconfigure MZI to 2-input equivalent configuration of orthogonally polarised probe lasers entering same input and phase-shifted by $\pi/2$ by PBS at MZI input.
1-Apr-2009	Ulrich Busk Hoff leaves the lab team
1-Apr-2009	Observation of torroidial FORT laser transverse mode
15-Apr-2009	FORT laser setup re-alignment. FORT waist $23 \mu\text{m}$.
16-Apr-2009	Enclosure and setup for single photon detection assembled and aligned.
24-Apr-2009	Align FORT to probe by observing FORT AC-Stark shift when probe is set on resonance of MOT cloud (MOT turned off briefly during probing)
7-May-2009	First clock measurement for up to $40 \mu\text{s}$ interrogation time, showing noise reduction though not spectroscopic squeezing.
15-May-2009	Niels Kjærgaard leaves the lab team
22-May-2009	MZI balancing by feedback to memory-wire attached to wave-plate
1-Jun-2009	Homebuilt automatic refilling of FORT laser chiller water supply installed
10-Jun-2009	Align and test polarisation filtering and fibre link for detection of single photon from decay of single atomic excitation.

26-Jun-2009	Switching between profiles stored in DDS RAM incorporated in to scope program.
26-Jun-2009	Tomography of CSS with random switching between rotation angles. Signal mean value oscillates with angle due to MW intensity inhomogeneity.
1-Jul-2009	J. Mod. Opt.: Squeezing of Atomic Quantum Projection Noise
8-Jul-2009	French flag analysis of MW intensity inhomogeneity influence on spin rotations.
23-Jul-2009	FORT waist changed to 35 μm
5-Aug-2009	First laser with Axcel laser diode (orange probe).
19-Aug-2009	MZI changed to frequency-based displacement of probe colour fringes (path-length difference set to 1.6 cm).
2-Sep-2008	First SSS tomography with alternative 3 $\pi/2$ pulse sequence.
4-Sep-2009	FORT waist changed to 28 μm
16-Sep-2009	Incorporate DRO in to MW frequency source
30-Sep-2009	Observation of MZI fringe change with temperature in MZI enclosure
1-Oct-2009	Jelmer Jan Renema joins the lab team
1-Oct-2009	Experimental test of composite pulses. Marred by coupling to $m'_F = \pm 1$ levels.
2-Oct-2009	FORT laser chiller pump burns down
7-Oct-2009	Thorough comparison of frequency stability of microwave sources
19-Oct-2009	FORT laser chiller pump replaced
10-Nov-2009	Projection noise limited Ramsey fringe section
27-Nov-2009	Squeezing lifetime measurement
30-Nov-2009	Squeezed atomic clock measurement
19-Dec-2009	arXiv: Entanglement-assisted atomic clock beyond the projection noise limit
20-Dec-2009	Anne Marie Marthe Louchet-Chauvet leaves the lab team
1-Jan-2010	arXiv: Establishing the projection noise in a quantum non-demolition measurement on the caesium clock transition
1-Jun-2010	Daniel Oblak leaves the lab team

Part I

Theory

Probe light pulses

We now set the stage for the great quantum play where diverse actors interact and undergo subtle yet significant changes. The first task is to introduce the main actors namely the optical field and the atomic ensemble, before we can proceed to a description of their interplay. The descriptions of the optical field and the atoms will set out with brief summaries of the main concepts and definitions relating to these so as to provide a coherent point of departure and hopefully rule out any notational ambiguities.

The first party to the interaction is the pulsed laser beam. As such, the optical mode is characterised by a direction of propagation along the wave vector \mathbf{k} and a transverse intensity distribution given by a Gaussian function. This complicates matters slightly for the quantum description where a mode is only localizable within the quantisation volume. However, as will be shown, the gap can be bridged by introduction of a spatial weighing of the field. Thereafter, the path is open for definition of a range of useful variables.

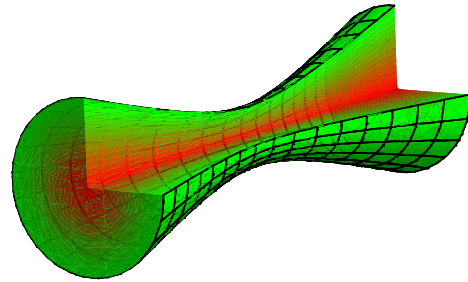


Figure 2.1: Drawing of the probe light beam geometry: A probe beam pulse with transverse Gaussian profile passing through a focal point.

2.1 Photonic operators

One of the hallmarks of quantum optics is the treatment of light quantum mechanically rather than as a classical electromagnetic (EM) field. With the quantisation of the EM field many new and intriguing properties emerge in particular the intrinsic fluctuations related to measurements of the field properties, that will be elaborated in Sec. 2.2. To get the quantum laser-light show on the road we introduce the EM field potential as

$$\hat{A}(\mathbf{r}, t) = \frac{1}{\sqrt{v}} \sum_{\mathbf{k}, s} \sqrt{\frac{\hbar}{2\omega\epsilon_0}} \left[\hat{a}_{\mathbf{k}, s} \boldsymbol{\epsilon}_{\mathbf{k}, s} e^{i(\mathbf{k} \cdot \mathbf{r} - \omega t)} + \hat{a}_{\mathbf{k}, s}^\dagger \boldsymbol{\epsilon}_{\mathbf{k}, s}^* e^{-i(\mathbf{k} \cdot \mathbf{r} - \omega t)} \right].$$

Here $\hat{a}_{\mathbf{k}, s}$ ($\hat{a}_{\mathbf{k}, s}^\dagger$) is the annihilation (creation) operator for a photon in the mode characterised by the wave-vector \mathbf{k} and polarisation $\boldsymbol{\epsilon}_{\mathbf{k}, s}$. The oscillation frequency of the field $\omega = |\mathbf{k}|c$, where c is the speed of light. The sums are over

all allowed wave-vectors k for which there is a further sum over the two possible orthogonal polarisations $s = 1, 2$. The v denotes the quantisation volume, \hbar is Planck's-constant (divided by 2π), and ϵ_0 is the vacuum electric permittivity. The quantum description of light and the notion of photons are inherently connected through the operators $\hat{a}_{k,s}$ and $\hat{a}_{k,s}^\dagger$. When calculating the energy of the EM field one gets $\hat{H} = \hbar\omega(\hat{a}_{k,s}^\dagger\hat{a}_{k,s} + \frac{1}{2})$, where the zero-point energy $\hbar\omega/2$ will be neglected in the ensuing discussion. With the association of $\hbar\omega$ with the single photon energy it is apparent to identify $\hat{n}_{\text{ph},k,s} \equiv \hat{a}_{k,s}^\dagger\hat{a}_{k,s}$ as the photon number operator.

With the main field operators in place we next need to find a way to specify the photonic state. There are a couple of suitable bases for the representation. The basis of eigen-states for \hat{n}_{ph} is called the Fock-basis [Fock28]. Such a *Fock state* is denoted according to the expectation value of $\langle \hat{n}_{\text{ph}} \rangle = n_{\text{ph}}$ so that $\hat{n}_{\text{ph},k,s}|\hat{n}_{\text{ph}}\rangle_{k,s} = n_{\text{ph},k,s}|\hat{n}_{\text{ph}}\rangle_{k,s}$. An alternative basis is spanned by the eigen-states of the photon annihilation operator again labelled by the eigen-value $\hat{a}|\alpha\rangle = \alpha|\alpha\rangle$. It immediately follows that the mean photon number of a such a *coherent state* [Glauber63a, Glauber63b] is ${}_{k,s}\langle \alpha | \hat{n}_{\text{ph},k,s} | \alpha \rangle_{k,s} = |\alpha|^2$, however as will be shown in Sec 2.2 a coherent state has no definite photon number i.e. the outcome of photon detection measurement will fluctuate around the expectation value.

To measure the number of photons in a all modes within some volume v one would detect the photons by some process which annihilates them i.e. what could be described by the operator [Mandel95]

$$\hat{a}(\mathbf{r}, t) = \frac{1}{\sqrt{v}} \sum_{k,s} \hat{a}_{k,s} \boldsymbol{\epsilon}_{k,s} e^{i(\mathbf{k}\cdot\mathbf{r} - \omega t)}$$

We take this as a generalisation of the annihilation operator. The local photon density operator is then $\hat{n}_{\text{ph}}(\mathbf{r}, t) = \hat{a}^\dagger(\mathbf{r}, t)\hat{a}(\mathbf{r}, t)$. Performing the integral of the local photon density over all space it is easily verified that $\int_{R^3} \hat{n}_{\text{ph}}(\mathbf{r}, t) \delta^3 r = \hat{N}_{\text{ph}}$ is fulfilled. The state vector corresponding to $\hat{a}(\mathbf{r}, t)$ and $\hat{n}_{\text{ph}}(\mathbf{r}, t)$ is the direct product of the states of all included modes i.e. $|\cdot\rangle = \prod_{k,s} |\cdot\rangle_{k,s}$.

While the summation over all modes in a local volume is the most correct formal procedure it is however not a particularly feasible formulation of the optical field when examining its spatially inhomogeneous interaction with an atomic ensemble. In our experimental configuration we deal with (pulsed) beams of light that have certain limited spatial intensity distributions. Therefore, we promote an alternative rendition of the photon number density again via the local photon detection operator

$$\hat{a}_{k,s}(\mathbf{r}) = u_{k,s}(\mathbf{r})\hat{a}_{k,s}\boldsymbol{\epsilon}_{k,s} .$$

So that

$$\hat{a}_{k,s}(\mathbf{r}, t) = \hat{a}_{k,s}(\mathbf{r})e^{i(\mathbf{k}\cdot\mathbf{r} - \omega t)} = u_{k,s}(\mathbf{r})\hat{a}_{k,s}\boldsymbol{\epsilon}_{k,s}e^{i(\mathbf{k}\cdot\mathbf{r} - \omega t)} . \quad (2.1)$$

This introduces a time independent spatial intensity distribution of the mode $u_{k,s}(\mathbf{r})$, which must satisfy the normalisation condition $\int_{R^2} |u_{k,s}(\mathbf{r})|^2 d^2 r = 1$ so that $\langle \hat{n}_{\text{at}} \rangle$ corresponds to the number of photons within a cross-sectional slice of the probe beam. To account for more than one mode we simply sum up the modes i.e. $\hat{a}(\mathbf{r}, t) = \sum_k \hat{a}_{k,s}(\mathbf{r}, t)$ and let the total state be the product of the single mode states $|\cdot\rangle = \prod_{k,s} |\cdot\rangle_{k,s}$. The local photon density is still $\hat{n}_{\text{ph},k,s}(\mathbf{r}) = \hat{a}_{k,s}^\dagger(\mathbf{r})\hat{a}_{k,s}(\mathbf{r})$ with the total photon number

$$\hat{N}_{\text{ph},k,s} = \int_{R^3} |u_{k,s}(\mathbf{r})|^2 \hat{n}_{\text{ph},k,s}(\mathbf{r}) \delta^3 r$$

Inspired by this definition we construct the total photon annihilation operator

$$\hat{A}_{k,s} = \int_{R^3} \hat{a}_{k,s}(\mathbf{r}) \delta^3 \mathbf{r} e^{i(\mathbf{k} \cdot \mathbf{r} - \omega t)} = \int_{R^3} u_{k,s}(\mathbf{r}) \hat{a}_{k,s} \delta^3 \mathbf{r} e^{i(\mathbf{k} \cdot \mathbf{r} - \omega t)}, \quad (2.2)$$

from which the total creation operator $\hat{A}_{k,s}^\dagger$ also follows.

The intensity distribution $u_{k,s}(\mathbf{r})$ is as yet unspecified, but since we will use it to describe laser pulses of duration t_p and a Gaussian transverse profile the typical form in radial coordinates is

$$u_{k,s}(\phi, r) = \sqrt{\frac{2}{\pi w_p^2}} e^{-r^2/w_p^2}, \quad (2.3)$$

where w_p is the beam spot size. Under this condition the total photon number for a pulse of duration t_p can be expressed as

$$\hat{N}_{\text{ph},k,s} = c \int_{R^2} \int_{t=0}^{t_p} |u_{k,s}(\mathbf{r})|^2 \hat{n}_{\text{ph},k,s}(\mathbf{r}) \delta^2 \mathbf{r} dt = l_p \hat{n}_{\text{ph}}, \quad (2.4)$$

which is interpreted as the photon density times an effective probe volume $\mathcal{V}_p = \pi \omega_a^2 l_p / 2$, $l_p = ct_p$ being the pulse length. Clearly, the norm-square of the mode function represents the intensity profile of the beam and we define

$$\hat{U}_{k,s}(\mathbf{r}) \equiv |u_{k,s}(\mathbf{r})|^2 \quad (2.5)$$

2.1.1 Schwinger operators

When light is used as a meter it is often convenient to derive a signal from some comparison between two optical modes, be it different polarisation, spatial, or frequency modes. In Sec. 2.3 a number of particular configurations are treated in depth. The state of such a dual mode optical system has a favourable representation in terms of Schwinger angular momentum operators [Schwinger52], whose components are defined in terms of the creation and annihilation operators¹

$$\hat{s}_x \equiv \frac{1}{2} (\hat{a}^\dagger \hat{b} + \hat{b}^\dagger \hat{a}) \quad (2.6a)$$

$$\hat{s}_y \equiv -\frac{i}{2} (\hat{a}^\dagger \hat{b} - \hat{b}^\dagger \hat{a}) \quad (2.6b)$$

$$\hat{s}_z \equiv \frac{1}{2} (\hat{a}^\dagger \hat{a} - \hat{b}^\dagger \hat{b}). \quad (2.6c)$$

In the case of \hat{a} and \hat{b} corresponding to orthogonal polarisation modes, $\hat{\mathbf{s}} = \{\hat{s}_x, \hat{s}_y, \hat{s}_z\}$ is the quantum Stokes vector [Stokes52, Collett70]. In the general case we shall refer to \hat{s}_x , \hat{s}_y , and \hat{s}_z as *Schwinger operators* or *light pseudo-spin*. The z-component measures the photon number difference between the two fields, while the x and y-components parametrise the phase difference between the fields². We supplement the Schwinger operators with the photon number operator $\hat{n}_{\text{ph}} \equiv \hat{n}_{\text{ph},a} + \hat{n}_{\text{ph},b} = \hat{a}^\dagger \hat{a} + \hat{b}^\dagger \hat{b}$. Based on the commutation of \hat{a} and \hat{b} it is simple to determine the commutation relations for $\hat{\mathbf{s}}$ as

$$[\hat{s}_i, \hat{s}_j] = i \epsilon_{ijl} \hat{s}_l, \quad (2.7)$$

¹here we omit the spatial coordinate \mathbf{r} for notational convenience and rather than indexing the two modes by $\{k, s\}$ we let them be denoted by \hat{a} and \hat{b} .

²i.e. for phases ϕ_a and ϕ_b , $\hat{s}_x \propto \cos(\phi_a - \phi_b)$ and $\hat{s}_y \propto \sin(\phi_a - \phi_b)$.

while \hat{n}_{ph} commutes with all the \hat{s} components. Thus, \hat{s} belongs to the special-unitary (SU2) group, indeed behaving as an angular momentum or spin operator.

Lastly, the extension of the Schwinger operators to embrace all space is analogous to eq. (2.2) and may also be accomplished by substituting $\hat{a} \rightarrow \hat{A}$ and $\hat{b} \rightarrow \hat{B}$ etc. in eq. (2.6). Since, e.g. $\hat{s}_z \propto \hat{a}^\dagger \hat{a}$ the integration over space will be weighed by the square norm $|u_{k,s}|^2$. The components of the macroscopic Schwinger operator \hat{S} also comply with the commutations relation of eq. (2.7).

2.2 Quantum shot noise

As for any quantum system the measurement on a photonic state may be subject to a certain quantum uncertainty or as some prefer to phrase it *quantum indeterminacy*. This is associated with the description of quantum states in terms of wave functions which interpret as a sort of probability distribution. Thus outcome of the measurement of a particular observable will vary according to the width of the wave function in the basis of the corresponding operator. Generally a lower bound for the uncertainty product of a set of operators can be inferred from their commutation relation via the Heisenberg uncertainty inequality

$$\langle(\Delta\hat{O}_1)^2\rangle\langle(\Delta\hat{O}_2)^2\rangle \geq \frac{1}{4} \left| \langle [\hat{O}_1, \hat{O}_2] \rangle \right|^2. \quad (2.8)$$

By the variance $\langle(\Delta\hat{O})^2\rangle$ we mean the quantity $\langle\hat{O}^2\rangle - \langle\hat{O}\rangle^2$. Quantum states for which the product of the operator variances on the l.h.s. is equal to the r.h.s. are appropriately named *minimal uncertainty states*.

Using the commutators in eq. (2.7), we find the uncertainty inequality for the Schwinger operators to be

$$\langle(\Delta\hat{S}_i)^2\rangle\langle(\Delta\hat{S}_j)^2\rangle \geq \frac{1}{4} \left| \langle [\hat{S}_i, \hat{S}_j] \rangle \right|^2 = \epsilon_{ijl}^2 \frac{\langle\hat{S}_l\rangle^2}{4}, \quad (2.9)$$

Without any specification of the expectation values of the various components this is a rather weak limit. Fortunately the actual uncertainties are easily calculated for almost any photonic states. For coherent photonic states the uncertainties of the the Schwinger operator components may directly calculated using the fact that the coherent state is an eigen-state of the creation and annihilation operators and the relation $\hat{a}\hat{a}^\dagger = \hat{a}^\dagger\hat{a} + 1$ ³. The result obtained is plainly

$$\langle(\Delta\hat{S}_i)^2\rangle = \frac{1}{4} N_{\text{ph}}. \quad (2.10)$$

Hence, the coherent state is a minimum uncertainty state for the spin components on the l.h.s. if the r.h.s. is equal to $N_{\text{ph}}/16$, which is only the case if the remaining spin component attains the maximal expectation value $\langle\hat{S}_l\rangle = \hat{N}_{\text{ph}}/2$.

The uncertainty relation Eq. (2.9) allows for other (unbalanced) distributions of the uncertainty. Examples of states generating such distributions are squeezed states that fulfil eq. (2.9), but which have smaller uncertainty of one component at the expense of more uncertainty in another. Further, examples and discussion are given in sec. 3.5

³which demonstrates the non-Hermitian nature of the photon counting operator

2.3 Mode configurations

We will now examine particular configurations of the two-mode photonic system expressed in terms of Schwinger operators. For this treatment it is not necessary to keep track of the spatial mode distribution owing to which we will phrase the discussion in terms of the total field operators \hat{A} , \hat{B} , etc. In the next section we examine a Mach-Zehnder interferometer (MZI) setting where the two modes are spatially separated in the MZI arms. In sec. A.6 we study two separate frequency modes propagating along the same geometric path. The two configurations serve the common purpose of being able to measure changes in the differential phase of the two fields, thus relating to the \hat{S}_x and \hat{S}_y Schwinger operator components.

2.3.1 Mach-Zehnder interferometer configuration

We will go through the MZI in two steps; first outlining the behaviour of an ideal MZI and subsequently including imperfection such as losses and mode-mismatch. This procedure may seem a bit cumbersome, however the purpose is first to develop an intuitive understanding of the MZI in the Schwinger operator formalism and only then adding all the relevant effects that result in a more complex and realistic description.

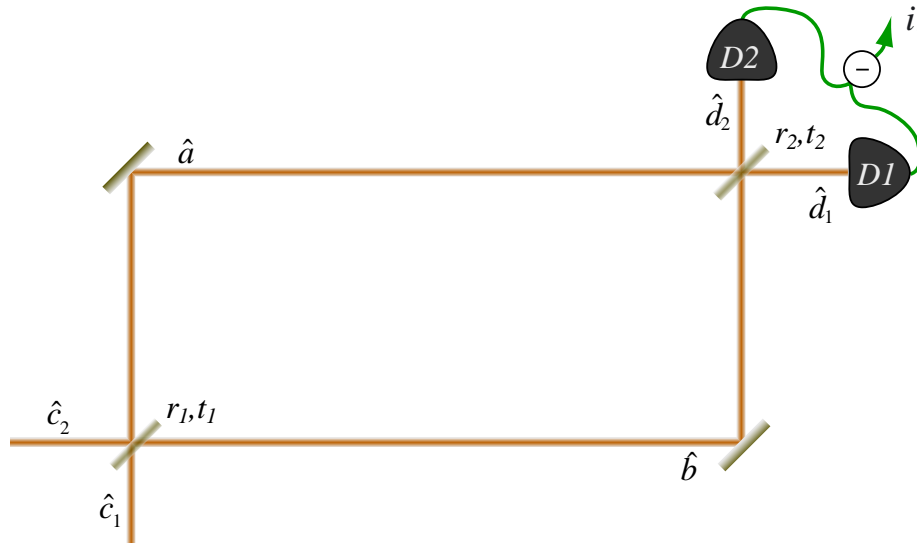


Figure 2.2: Sketch of the MZI configuration.

The MZI configuration is sketched in fig. 2.2. At any given stage of propagation through the MZI we may identify pairs of fields from which we can construct Schwinger operators cf. Eq. (2.6). From the input fields \hat{C}_1 and \hat{C}_2 we get \hat{S}^{in} , from \hat{A} and \hat{B} we get \hat{S} , finally \hat{D}_1 with \hat{D}_2 yield \hat{S}^{out} . As sketched on fig. 2.2 the photo-currents impinging on the two output detectors $D1$ and $D2$ are subtracted from one another generating a difference signal \hat{i}_- that is proportional to \hat{S}_z^{out} .⁴ Obviously the Schwinger operators at different stages are interrelated through the well known transformation of the field operators e.g. at a BS $\hat{A} = t\hat{C}_1 + ir\hat{C}_2$, where the BS reflection r and transmission t must fulfil $r^2 + t^2 = 1$. A thorough derivation of the transformations is presented in Appendix A. In the below we present the essential equations and draw out the most important observations.

⁴In this section we highlight the quantum nature of the photo-current by adding the $\hat{\cdot}$. In later sections we will not be so stringent and indeed when classical noise influences the signal the “quantumness” is but one feature.

It turns out that in the ideal case of a loss-less interferometer with perfectly spatially overlapped modes at the output, the evolution of the Schwinger operator $\hat{\mathbf{S}}$ as it propagate through the MZI can be described by a set of rotations. The effect of a BS can be described by the matrix \mathbf{M}_β which turns out to represent a rotation

$$\hat{\mathbf{S}}' = \mathbf{M}_\beta \hat{\mathbf{S}} \quad , \quad \mathbf{M}_\beta = \begin{pmatrix} 1 & 0 & 0 \\ 0 & r^2 - t^2 & 2rt \\ 0 & -2rt & r^2 - t^2 \end{pmatrix} = \begin{pmatrix} 1 & 0 & 0 \\ 0 & \cos \beta & \sin \beta \\ 0 & -\sin \beta & \cos \beta \end{pmatrix} \quad (2.11)$$

The last equality comes about by defining the angle β

$$\beta = \arctan \left(\frac{2rt}{r^2 - t^2} \right) = \arctan \left(\frac{2r\sqrt{(1-r^2)}}{2r^2 - 1} \right) \quad , \quad (2.12)$$

from which we see that if $r = 1$ or $r = 0$ then $\beta = 0$, but when $r = t = 1/\sqrt{2} \Rightarrow \beta = \pi/2$. That is to say that a 50/50 BS has the effect of rotating $\hat{\mathbf{S}}$ by 90° around the x -axis, effectively interchanging the \hat{S}_y and \hat{S}_z components. For any other beam-splitter the rotation will result in a mixing of the incident \hat{S}_y and \hat{S}_z , but still leaving \hat{S}_x unaffected

Going a step further one may recall that spin components belonging to the SU2 group (spin $\frac{1}{2}$ systems) are generators of rotations [Sakurai94] in the sense that we can write up a unitary operator \hat{U}_β corresponding to \mathbf{M}_β , which transforms the operators in the Heisenberg picture

$$\hat{\mathbf{S}}' = \hat{U}_\beta^\dagger \hat{\mathbf{S}} \hat{U}_\beta = e^{i\beta \hat{S}_x} \hat{\mathbf{S}} e^{-i\beta \hat{S}_x} \quad , \quad (2.13)$$

When phrased in terms of unitary operators it is undemanding to investigate how subsequent transformations commute.

Similarly as for the BS, we can create a transformation matrix for the propagation of two fields with a definite phase relationship, such as the fields \hat{A} and \hat{B} in the two arms of the MZI. The result is

$$\begin{pmatrix} \hat{S}'_x \\ \hat{S}'_y \\ \hat{S}'_z \end{pmatrix} = \begin{pmatrix} \cos \phi & \sin \phi & 0 \\ -\sin \phi & \cos \phi & 0 \\ 0 & 0 & 1 \end{pmatrix} \begin{pmatrix} \hat{S}_x \\ \hat{S}_y \\ \hat{S}_z \end{pmatrix} = \mathbf{M}_\phi \hat{\mathbf{S}} \quad . \quad (2.14)$$

This transformation matrix has the same properties as \mathbf{M}_β and can clearly also be regarded as rotation of $\hat{\mathbf{S}}$ by an angle $\phi = k\Delta l$. However, this time around the z -axis [fig. 2.3c)]. Therefore, the unitary transformation operator is given by

$$\hat{\mathbf{S}}' = \hat{U}_\phi^\dagger \hat{\mathbf{S}} \hat{U}_\phi = e^{i\phi \hat{S}_z} \hat{\mathbf{S}} e^{-i\phi \hat{S}_z} \quad , \quad (2.15)$$

With this in hand we can now model the whole interferometer in the Schwinger operator formalism. we use the notation that β_1 together with r_1 and t_1 are parameters of the first beam-splitter, whilst β_2 , r_2 and t_2 are related to the second beam-splitter and Δl is the path-length difference between the two arms. We can calculate the full interferometer transformation as

$$\hat{\mathbf{S}}^{\text{out}} = \mathbf{M}_{\text{MZI}} \hat{\mathbf{S}}^{\text{in}} = \mathbf{M}_{\beta_2} \mathbf{M}_\phi \mathbf{M}_{\beta_1} \hat{\mathbf{S}}^{\text{in}} \quad , \quad (2.16)$$

Needles to say, the general transformation matrix is rather bulky and not particularly informative. Hence, it will not be written out here, but it is stated in

eq. (A.4). It suffices to state the transformation in the case of a symmetrical interferometer i.e. with 50/50 splitting ratios on both beamsplitters

$$\mathbf{M}_{\text{MZI}}^{(50/50)} = \begin{pmatrix} \cos \phi & 0 & \sin \phi \\ 0 & 1 & 0 \\ \sin \phi & 0 & -\cos \phi \end{pmatrix} \quad (2.17)$$

The detected difference signal is thus given by $\hat{i}_- = 2\epsilon \hat{S}_z^{\text{out}} = -2\epsilon \cos \phi \hat{S}_z^{\text{in}}$ with ϵ the detector's quantum efficiency. Hence, the mean expectation value of the signal is $\langle \hat{i}_- \rangle = \pm \epsilon \cos \phi N_{\text{ph}}$, where the sign depends on whether \hat{C}_2 or \hat{C}_1 is in the vacuum state. As we anticipated, the difference signal provides a measure for the phase difference between the probe and reference MZI fields. Suppose we wish to gauge a small displacement of the phase difference $\phi_0 + \phi_\delta$ and assume we can peg the mean shift $\phi_0 = \pi/2$. It follows that, the phase-displacement can be determined from the signal as $\phi_\delta = \pm \arcsin(\hat{i}_- / (\epsilon N_{\text{ph}})) \approx \pm \hat{i}_- / (\epsilon N_{\text{ph}})$.

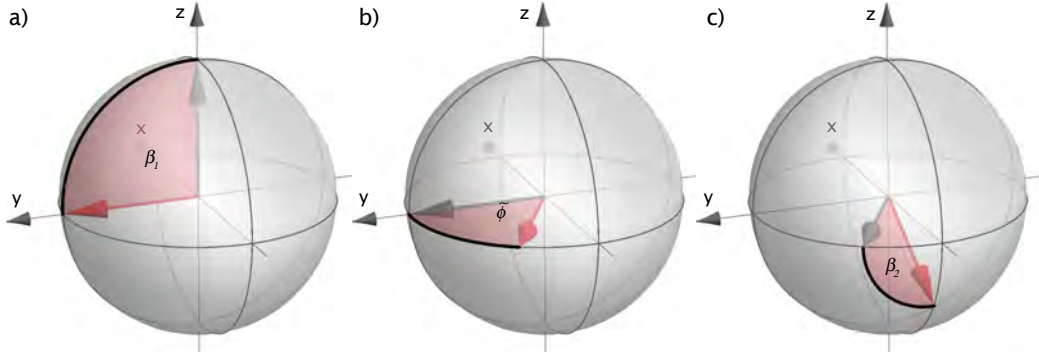


Figure 2.3: Schwinger operator transformation in the MZI. a: $\pi/2$ rotation around x -axis on first BS. b: rotation by ϕ around z -axis during free propagation in MZI. c: $\pi/2$ rotation around x -axis on second BS.

Now to utilise the representation of the MZI as a set of rotations of a vector we will illustrate the evolution of the Schwinger operator. At the input all photons are in one of the input arms, say in \hat{C}_1 , and $\langle \hat{S}^{\text{in}} \rangle$ is oriented along the positive z -axis. Upon passage through the first 50/50 BS the vector is rotated by $\pi/2$ around the x -axis so that $\langle \hat{S} \rangle$ becomes aligned along the y -axis. Next the fields propagate through the interferometer arms acquiring a phase difference ϕ which causes a equivalent rotation around the z -axis with the result that $\langle \hat{S}_x \rangle \propto \sin \phi$ and $\langle \hat{S}_y \rangle \propto \cos \phi$, while $\langle \hat{S}_z \rangle = 0$. The final $\pi/2$ rotation around the x -axis by the output BS maps \hat{S}_y onto \hat{S}_z^{out} , and vice versa, so that $\langle \hat{S}_z^{\text{out}} \rangle \propto \cos \phi$ and $\langle \hat{S}_y^{\text{out}} \rangle = 0$. Hence the output difference photo current $\hat{i}_- = 2\epsilon \hat{S}_z^{\text{out}}$ effectively measures the phase difference accumulated between the fields in the probe and reference arms of the interferometer. Thus any change of physical path-length or refractive index in either of the arms will be detectable as a change in the output signal. Since an atomic sample can affect the refractive index in the probe arm this will provide the way to measure properties of the atomic sample.

An important limitation to the measurement capability of the MZI is the quantum shot noise of the light. As investigated in Sec. 2.2 the shot noise is proportional to the combined number of photons in the two fields and, since we have yet to consider losses, that is simply equal to one fourth of the number of photons entering the input port of the MZI

$$\frac{\langle (\Delta \hat{i}_-)^2 \rangle_{\text{SN}}}{4} = \epsilon^2 \langle (\Delta \hat{S}_z^{\text{out}})^2 \rangle_{\text{SN}} = \epsilon^2 \frac{N_{\text{ph}}}{4}. \quad (2.18)$$

In Appendix A.4.1 the output shot noise is explicitly written in terms of the input fields and Eq. 2.18 is verified. The highest sensitivity for measuring a phase displacement ϕ_δ is achieved by setting $\phi_0 = \pi/2$. The shot noise, on the other hand, is as required independent of the MZI phase ϕ with $\langle(\Delta\phi)^2\rangle_{\text{SN}} = \langle(\Delta\hat{I}_-)^2\rangle/(\epsilon N_{\text{ph}})^2 = N_{\text{ph}}^{-1}$, implying that the phase-resolution of the MZI increases with the photon number. The optimal signal to noise ratio for determining the phase-shift is thus

$$\text{SNR} = \frac{\langle\phi_\delta^2\rangle}{\langle(\Delta\phi)^2\rangle_{\text{SN}}} = N_{\text{ph}}\langle\phi_\delta^2\rangle, \quad (2.19)$$

i.e. increasing linearly with N_{ph} .

Two colour MZI

In most of the theoretical and experimental investigation of the interaction with atoms we will require two sets of modes, which are distinguishable by having different frequencies. This frequency difference we will often refer to as different colours. Hence, at input one we will have the modes $\hat{C}_{1,3}$ and $\hat{C}_{1,4}$, where the 3 and 4 subscript indicates the frequency mode of the field. Since, the modes are separated in frequency the two colours do not interfere at the output and the output Schwinger operator is simply the sum $\hat{S}_z^{\text{out}} = \hat{S}_{z3}^{\text{out}} + \hat{S}_{z4}^{\text{out}}$, which by eq. (2.17) becomes

$$\hat{S}_z^{\text{out}} = -\cos\phi(\hat{S}_{z,3}^{\text{in}} + \hat{S}_{z,4}^{\text{in}}) \quad (2.20)$$

If $\langle\hat{S}_{z,3}^{\text{in}}\rangle/\langle\hat{S}_{z,4}^{\text{in}}\rangle > 0$ the output signal from the two modes will add, but if oppositely the $\langle\hat{S}_{z,3}^{\text{in}}\rangle/\langle\hat{S}_{z,4}^{\text{in}}\rangle < 0$ they will subtract. In the latter case if $\langle\hat{S}_{z,3}^{\text{in}}\rangle = -\langle\hat{S}_{z,4}^{\text{in}}\rangle$ the output fringe will actually be cancelled. This case corresponds to a coherent part of each colour entering different ports, i.e. $\langle\hat{C}_{1,4}^\dagger\hat{C}_{1,4}\rangle = N_{\text{ph}}/2$ and $\langle\hat{C}_{2,3}^\dagger\hat{C}_{2,3}\rangle = N_{\text{ph}}/2$.

It turns out that the fringe cancellation is worth achieving and we will come with a few more suggestions as to how it can be generated. The above equation is only valid if the MZI path-length difference is small, otherwise one would have to write

$$\hat{S}_z^{\text{out}} = -\cos(\omega_3\Delta l/c)\hat{S}_{z,3}^{\text{in}} - \cos(\omega_4\Delta l/c)\hat{S}_{z,4}^{\text{in}} \quad (2.21)$$

$$= -\cos[(\omega_3 + \omega_4)\Delta l/c]\cos[(\omega_3 - \omega_4)\Delta l/c]N_{\text{ph}} \quad (2.22)$$

where for the last equality we set $\langle\hat{S}_{z,3}^{\text{in}}\rangle = \langle\hat{S}_{z,4}^{\text{in}}\rangle$. This reveals that we can cancel the signal for small displacements of the phase if we misalign the MZI by $\Delta l = c\pi/(\omega_3 - \omega_4)$. In that case the last cosine factor suppresses the fringe. The frequency difference between the two colours is in our case around 9.192 GHz, which prescribes the path-length difference to be set to $\Delta l = 16$ mm. As long as the phase or path-length displacements around Δl are small this configuration is equivalent to the 2-input configuration and the output signal behaves as if $\langle\hat{S}_{z,3}^{\text{in}}\rangle = -\langle\hat{S}_{z,4}^{\text{in}}\rangle$. Consequently, we coin the configuration *2-input equivalent*.

Another 2-input equivalent configuration relies on the two colours being in orthogonal polarisation modes. Since, we have only used this method briefly, we will only sketch the idea. The essence is that upon reflection on a mirror s and p-polarised light will acquire different phase-shifts. If we input two orthogonal circular polarisations on a PBS we can ensure that half of the light from each probe goes into each MZI arm. Moreover, the polarisation of the two colours will be the same in both arms, however the optical oscillations will be π out of

phase. The resulting fringes at the output will also be out of phase by π and we have recreated the condition $\langle \hat{S}_{z,3}^{\text{in}} \rangle = -\langle \hat{S}_{z,4}^{\text{in}} \rangle$.

All three 2-input type configurations rely on the modes achieving a phase-shift of π w.r.t. each other. In the first, where the modes are spatially separated at the input, and the second, where the modes are separable by their polarisation, the π phase-shift is supplied by the input BS. In the final we use that the modes can be separated by virtue of their different colour and the π phase is acquired through propagation in the MZI arms.

MZI with imperfections

The analysis of the MZI has so far not taken into account the many imperfections of the setup from losses in the arms to imperfect mode overlap at the output beamsplitter. Equipped with a basic understanding of the MZI description it is, however, time to include these imperfections and thereby approach a more realistic description. Unfortunately, the simple representation of the MZI in terms of rotations on the $\langle \hat{S} \rangle$ is no longer strictly possible as additional fields come in to play.

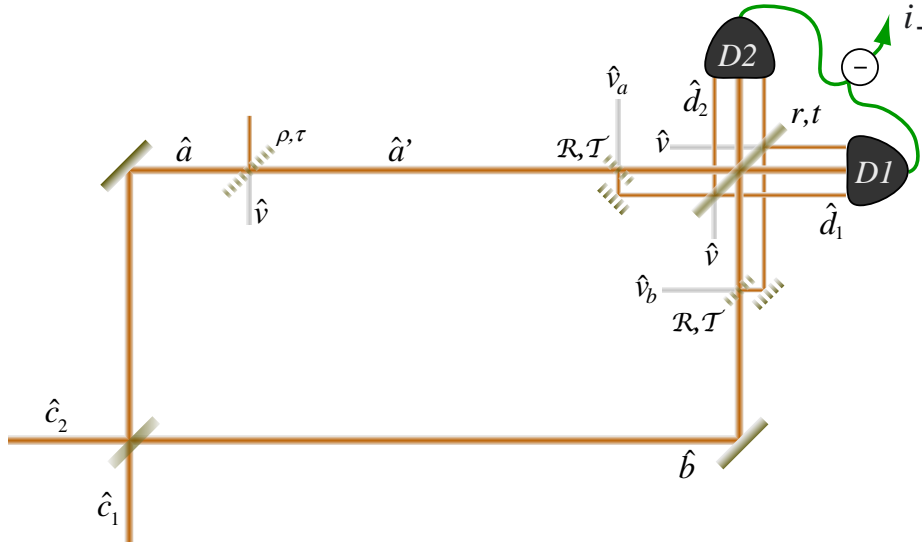


Figure 2.4: Sketch of the MZI configuration with losses and imperfect mode overlap.

Figure 2.4 outlines the amended picture. Following the splitting in the first BS the fields encounter various losses. We restrict our attention to losses in the probe arm only as these are consistently larger than those in the reference arm. The losses are modelled by a beamsplitter with reflection ρ and transmission τ , thus adding a vacuum component to the probe arm field $\hat{A}' = \tau\hat{A} + i\rho\hat{V}$. With the reference arm field unaltered, $\hat{B}' = \hat{B}$, we find the loss transformation of the Schwinger vector to be (Appendix A.3.3)

$$\begin{aligned}\hat{S}'_x &= \tau\hat{S}_x + \rho\hat{S}_y^{vb} \\ \hat{S}'_y &= \tau\hat{S}_y - \rho\hat{S}_x^{vb} \\ \hat{S}'_z &= \tau^2\hat{S}_z + \rho^2\hat{S}_z^{vb} + \rho\tau\hat{S}_y^{va},\end{aligned}\tag{2.23}$$

where we resort to the vacuum admixed operators defined as $\hat{S}_x^{vb} = \frac{1}{2}(\hat{V}^\dagger\hat{B} + \hat{B}^\dagger\hat{V})$, $\hat{S}_y^{vb} = \frac{-i}{2}(\hat{V}^\dagger\hat{B} - \hat{B}^\dagger\hat{V})$, $\hat{S}_z^{vb} = \frac{1}{2}(\hat{V}^\dagger\hat{V} - \hat{B}^\dagger\hat{B})$, and similarly for the combination of \hat{V} and \hat{A} . The effect of the losses on $\langle \hat{S} \rangle$ is depicted on fig. 2.5a), where we assume that the first BS is symmetric such that the incident Schwinger vector

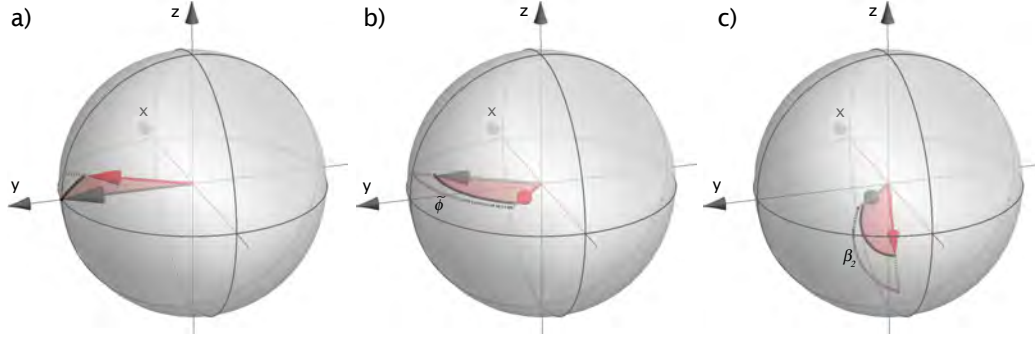


Figure 2.5: Schwinger operator transformation in the MZI. a) . b) rotation by ϕ around z -axis during free propagation in MZI. c) $\pi/2$ rotation around x -axis on second BS.

is representation by fig. 2.3a). As $\langle \hat{S}_x^{vb} \rangle = \langle \hat{S}_y^{vb} \rangle = 0$, the expectation values of \hat{S}_x and \hat{S}_y are simply scaled down by τ i.e. $\langle \hat{S}_x' \rangle = 0$, still, while $\langle \hat{S}_y' \rangle = \tau N_{\text{ph}}/2$. The component $\langle \hat{S}_z \rangle$ attains an extra contribution $\rho^2 \langle \hat{S}_z^{vb} \rangle = -(1 - \tau^2) \langle \hat{B}^\dagger \hat{B} \rangle / 2$. Explicitly writing out the fields one discovers $\langle \hat{S}_z' \rangle = \tau^2 \langle \hat{A}^\dagger \hat{A} - \hat{B}^\dagger \hat{B} \rangle / 2 - (1 - \tau^2) \langle \hat{B}^\dagger \hat{B} \rangle / 2 = (\tau \hat{A}^\dagger \hat{A} + \hat{B}^\dagger \hat{B}) / 2$, which, in fact, is proportional to the photon number difference after the probe arm attenuation.

During free propagation the probe and reference fields pick up a phase difference ϕ resulting in the Schwinger operator illustrated in fig. 2.5b at the input of the final BS. The imperfect mode overlap on the output BS⁵ is modelled as an equal loss \mathcal{R} of each of the incoming fields. The transmitted part of the fields are taken to be perfectly overlapped on the output BS while the lost parts are taken to be overlapped with vacuum fields on the output BS (fig. 2.4). Hence, each output comprises three fields e.g. in one output $\hat{D}_1 = t_2(\mathcal{T}\hat{A}' + i\mathcal{R}\hat{V}_a) + r_2(i\mathcal{T}\hat{B} - \mathcal{R}\hat{V}_b)$, $\hat{D}_1^{(a)} = t_2(i\mathcal{R}\hat{A}' + \mathcal{T}\hat{V}_a)$, and $\hat{D}_1^{(b)} = r_2(-\mathcal{R}\hat{B} + i\mathcal{T}\hat{V}_b)$. Accordingly, three output Schwinger vectors are required to describe the transformation in the imperfectly mode overlapped BS. All the components are written out in eq. (A.3) of Appendix A.3.4. At this point it is adequate to present the expectation values in the symmetric output BS case. In this case, $\langle \hat{S}_x^{\text{out}} \rangle = \mathcal{T}^2 \langle \hat{S}_x \rangle$, $\langle \hat{S}_y^{\text{out}} \rangle = \mathcal{T}^2 \langle \hat{S}_y \rangle$, and $\langle \hat{S}_z^{\text{out}} \rangle = \mathcal{T}^2 \langle \hat{S}_z \rangle$, which is merely the normal BS eq. (2.11) multiplied by \mathcal{T}^2 . Of the additional non-interfering (mode mismatched) output Schwinger operators only the y -components are non-zero in the symmetric BS case. These, however, are not detected and thus of little interest. The main observation is that the z -components of the non-interfering parts have zero expectation values and thus do not add any offset to the signal. In fig. 2.5c) the outcome of the non-perfect mode overlap on a symmetric output BS is illustrated.

The output signal $\hat{i}_- / 2 = \epsilon(\hat{S}_z^{\text{out}} + \hat{S}_z^{\text{out},a} + \hat{S}_z^{\text{out},b})$ can now be traced back to the input fields and for the expectation value we attain

$$\frac{\langle \hat{i}_- \rangle}{2} = \epsilon(\langle \hat{S}_z^{\text{out}} \rangle + \langle \hat{S}_z^{\text{out},a} \rangle + \langle \hat{S}_z^{\text{out},b} \rangle) = -\epsilon \mathcal{T}^2 \tau \cos \phi \langle \hat{S}_z^{\text{in}} \rangle. \quad (2.24)$$

One notes that the signal is more sensitive to mode mismatch than losses in one of the arms. We shall see, the fact that the losses occur in the probe arm actually means that they do not compromise the measurement sensitivity. Again we suppose that we wish to measure a phase-shift ϕ_δ which will be reflected in the output as $\langle \hat{i}_- \rangle = \pm \mathcal{T}^2 \tau \cos(\phi_0 + \phi_\delta) N_{\text{ph}}$. Locking $\phi_0 = \pi/2$ we achieve the

⁵Since at the input BS on incident field is in a coherent mode and the in the vacuum mode these are always perfectly mode matched.

optimal sensitivity to the phase-shift and from the detected signal we may infer $\phi_\delta \approx \pm \hat{i}_- / (\epsilon \mathcal{T}^2 \tau N_{\text{ph}})$.

The signal is to be compared with the shot noise in the detected output difference signal. This now depends on the losses in the probe arm ρ and the amount of the input light split into the probe arm, that is on t_1 . Depending on the fraction of the total photon number lost into undetected modes the output shot-noise will decrease. More precisely the shot-noise is given by

$$\frac{\langle (\Delta \hat{i}_-)^2 \rangle_{\text{SN}}}{4} = \epsilon^2 \langle (\Delta \hat{S}_z^{\text{out}})^2 \rangle_{\text{SN}} = \epsilon^2 (1 - \rho^2 t_1^2) \frac{N_{\text{ph}}}{4}. \quad (2.25)$$

Which is — fortunately — exactly the number of photons surviving to the output.

In phase-shift units, at the maximal sensitivity and specialising to the case of $t_1 = 1/\sqrt{2}$, the shot-noise becomes

$$\langle (\Delta \phi)^2 \rangle_{\text{SN}} \approx \frac{\langle (\Delta \hat{i}_-)^2 \rangle}{(\epsilon \mathcal{T}^2 \tau N_{\text{ph}})^2} = \frac{1 + \tau^2}{2\epsilon^2 \tau^2 \mathcal{T}^4} \frac{1}{N_{\text{ph}}}. \quad (2.26)$$

One may rightfully ponder why the phase-noise scales with the MZI mode overlap, when in eq. (2.25) we affirmed that the shot-noise is proportional to the total number of photons reaching the detectors, a quantity that does not depend on the MZI visibility. The reason is that by translating the noise in to phase-units we assume that all shot-noise has come in the form of phase fluctuations. This is, however, only true if the mode overlap is $\mathcal{T} = 1$. In the case of non-perfect mode overlap some shot-noise will come as intensity noise and by translating in to phase-units we artificially boost the phase fluctuations. As luck would have it, this is of no major concern because irrespective of the form the shot noise has it limits the phase-sensitivity of the MZI. We convey this by the signal to noise ratio which becomes

$$\text{SNR} = \frac{\langle \phi_\delta^2 \rangle}{\langle (\Delta \phi)^2 \rangle_{\text{SN}}} = \frac{2\tau^2 \mathcal{T}^4}{1 + \tau^2} N_{\text{ph}} \langle \phi_\delta^2 \rangle \quad (2.27)$$

This expression however does not truly reveal the implications of probe arm losses. An experimental limitation that will be discussed in great detail subsequently (see sec. 4.1 and sec. 5.2.2) is that there is a limit to the tolerable number of photons in the probe arm due to the destruction of the atomic state they cause. Typically, one can work out an optimal number of photons $N_{\text{ph},a,0}$ for the interaction with the atomic sample. If then, the probe arm losses are inflicted prior to the passage through the atomic sample the losses offer an additional degree of freedom. By increasing the losses it is possible to increase the overall input photon number of the MZI while maintaining the number of photons passing the atomic sample. If for $\tau = 1$ the probe arm photon number is the desired $N_{\text{ph},a,0}$ then the the input photon number is fixed to τ by $\frac{1}{2}\tau^2 N_{\text{ph}} = N_{\text{ph},a,0}$. Including this relation in to eq. (2.27) we can express the shot noise level as

$$\frac{\langle (\Delta \hat{i}_-)^2 \rangle_{\text{SN}}}{4} = \epsilon^2 \langle (\Delta \hat{S}_z^{\text{out}})^2 \rangle_{\text{SN}} = \epsilon^2 \left(1 + \frac{1}{\tau^2}\right) \frac{N_{\text{ph},a,0}}{4} \quad (2.28)$$

Similarly by eq. (2.27) we get for the SNR

$$\text{SNR} = \frac{4\mathcal{T}^4}{1 + \tau^2} N_{\text{ph},a,0} \langle \phi_\delta^2 \rangle, \quad (2.29)$$

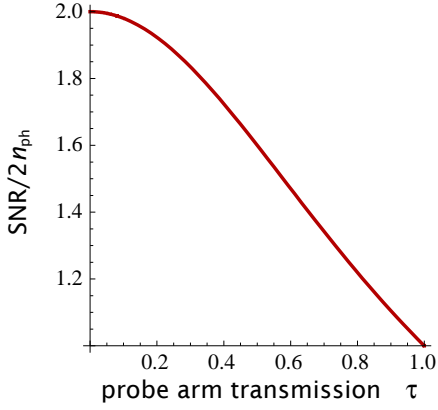


Figure 2.6: Scaling of factor in SNR as function of probe arm transmission.

The factor making up the fraction is plotted on fig. 2.6. This highlights one advantage of attenuating the probe arm that it is possible to achieve up to a factor of two increase in the SNR as compared with the loss-less MZI. Note that to compare with the SNR expression for the symmetric loss-less interferometer eq. (2.19), one has to replace $N_{\text{ph}} = \frac{1}{2}N_{\text{ph},a,0}$ so as to apply the condition of fixed probe arm photon number. Equation eq. (2.29) is equivalent to the familiar result of applying a local oscillator to amplify the quantum properties of a probe beam. Naturally, there will be technical limitations to the possible input probe power, due to classical noise sources (see sec. 6.1) and detector saturation (see sec. 8.2.1). From a practical perspective it is worth noting that for a balanced input BS the probe arm transmission is equal to the power ratio between the probe and reference MZI arms.

Phase fluctuations in output signal We will now look at the phase-noise expression above from a slightly different perspective. As noted above the aim of constructing a MZI is the phase ϕ as precisely as possible. The phase ϕ arises from a difference in the *optical* path-length between the two arms. This can be influenced by e.g. physical displacements of the path-length or changes in the index of refraction in the beam path. The latter is essentially how we will detect the properties of the atomic sample placed in the probe arm (sec. 4). Because of the range of possible perturbations, ϕ will fluctuate around some mean value i.e. we again write $\phi = \phi_0 + \phi_\delta$, where the mean of ϕ_δ is zero. This will naturally add noise to the MZI output signal, which according to eq. (A.9) amounts to

$$\begin{aligned} \langle (\Delta \hat{S}_z^{\text{out}})^2 \rangle &= \langle (\Delta \hat{S}_z^{\text{out}})^2 \rangle_{\text{SN}} + \langle (\Delta \hat{S}_z^{\text{out}})^2 \rangle_{\phi_\delta} \\ &= (1 - \rho^2 t_1^2) \frac{N_{\text{ph}}}{4} + \mathcal{T}^4 \tau^2 \sin^2 \phi \sin^2 \beta_1 \frac{N_{\text{ph}}^2}{4} \langle (\Delta \phi_\delta)^2 \rangle, \end{aligned} \quad (2.30)$$

The mode overlap has a profound influence on the sensitivity to phase fluctuations. The first beamsplitter ratio and the probe arm loss also dampen the phase fluctuations but at the same time the shot noise is reduced by a factor which is of the same order. Finally, the phase-fluctuations propagate most effectively to the output signal when the mean interferometer phase is set to $\phi_0 = \pi/2$ such that $\sin^2 \phi = 1$. If we consider consider the shot-noise to be an unwanted noise which masks our signal in the form of the noise resulting from phase fluctuations the we can write a SNR as

$$\text{SNR} = \frac{\mathcal{T}^4 \tau^2 \sin^2 \beta_1}{1 - \rho^2 t_1^2} \sin^2 \phi N_{\text{ph}} \langle (\Delta \phi_\delta)^2 \rangle, \quad (2.31)$$

which to our great content is the equivalent to eq. (2.29) when we set $t_1 = 1/\sqrt{2}$ and $\phi_0 = \pi/2$ and noting that since per definition $\langle \phi_\delta \rangle = 0$ we have $\langle (\Delta \phi_\delta)^2 \rangle = \langle \phi_\delta^2 \rangle$.

Atomic ensemble

Now enter the other party to the interaction, the atomic ensemble in the form of a dipole trapped cold sample of caesium atoms. The geometry of the sample, illustrated by fig. 3.1, resembles a cucumber¹ with radially symmetric Gaussian density distribution. The actual aspect ratio of the sample is around 10-15. The aim of this section is to find the most useful formulation for the continuous atomic operators for the whole ensemble to be conveniently utilised in the description of the quantum interaction with light pulses. This involves considering the spatial profile of the sample and the probe light and combining the internal atomic operators.

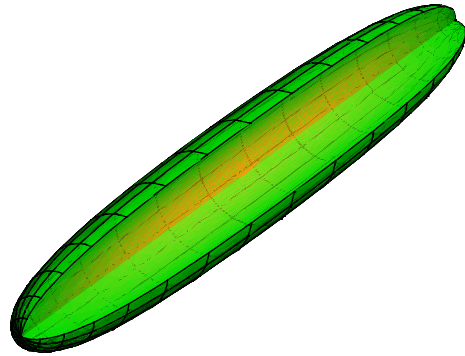


Figure 3.1: Drawing of the atomic ensemble and the light beam geometry.

3.1 Atomic variables

We start out with some geometric considerations, which apply to any operator of the atoms. An operator belonging to a specific atom (k) we denote as $\hat{\delta}^{(k)}$ and \mathbf{r}_k specifies its position. From this one can construct continuous atomic operators [Sørensen08, Hammerer09]

$$\hat{\delta}(\mathbf{r}) = \sum_k \hat{\delta}^{(k)} \delta(\mathbf{r} - \mathbf{r}_k), \quad (3.1)$$

where the sum is over all atoms k in the ensemble. Along these lines, the classical atomic number density is defined as

$$n_{\text{at}}(\mathbf{r}) = \sum_k \delta(\mathbf{r} - \mathbf{r}_k). \quad (3.2)$$

This number density is specified for a specific set of atomic positions. However, the position of a particular atom in the sample is in general random. Hence, we can specify a the number density $\overline{n_{\text{at}}(\mathbf{r})}$ averaged over the random locations of

¹That is one that meets the steepest straightness requirements according to the EU quality standards for cucumbers [EU88]

the atoms and since this is now a continuous distribution we can ascribe some functional dependence $\mathcal{N}(\mathbf{r})$ to it

$$\mathcal{N}(\mathbf{r}) = \overline{n_{\text{at}}(\mathbf{r})} \quad (3.3)$$

Generally there is no practical need to distinguish between $n_{\text{at}}(\mathbf{r})$ and $\overline{n_{\text{at}}(\mathbf{r})}$ and we will not hesitate to substitute $n_{\text{at}}(\mathbf{r})$ for the density distribution $\mathcal{N}(\mathbf{r})$ when this is convenient. To obtain operators for the whole ensemble of atoms it seems natural to integrate the continuous operators over all space i.e.

$$\hat{O}_{\text{tot}} = \int_{R^3} d^3r \hat{o}(\mathbf{r}) = \int_{R^3} d^3r \sum_k \hat{o}^{(k)} \delta(\mathbf{r} - \mathbf{r}_k) = \sum_k \hat{o}^{(k)}. \quad (3.4)$$

The total ensemble operators can also be specify using the number density distribution $\mathcal{N}(\mathbf{r})$. If the operator refers to some internal atomic degree of freedom that is without spatial dependence one can simply pull $\hat{o}r$ out and perform the volume integral over \mathcal{N} .

In our experiment the atomic density distribution may be approximated with a cylindrically symmetric Gaussian distribution (see appendix E.1) that extends a length l along the z -axis

$$\mathcal{N}(\phi, r, z) = \mathcal{N}_0 e^{-2r^2/w_a^2} \mathbf{1}_{[-l_a/2, l_a/2]}(z), \quad (3.5)$$

where w_a is the Gaussian width and l_a the length of the sample and the indicator function $\mathbf{1}_{[-l_a/2, l_a/2]}(z)$ is 1 for $-l_a/2 \ll z \ll l_a/2$ and is 0 elsewhere. As a sample operator we take the single atom identity operator $\hat{\mathcal{I}}_k$ which has expectation value 1 for any and all atoms. The continuous operator where $\hat{n}_{\text{at}}(\mathbf{r}) = \sum_k \hat{\mathcal{I}}_k \delta(\mathbf{r} - \mathbf{r}_k)$ is then logically the operator for the atomic density i.e. $\langle \hat{n}_{\text{at}}(\mathbf{r}) \rangle = \mathcal{N}(\mathbf{r})$. Completing the integral in eq. (3.4) we get

$$N_{\text{tot}} = \int_{R^3} d^3r \langle \hat{n}_{\text{at}}(\mathbf{r}) \rangle = \int_{R^3} d^3r \mathcal{N}_0 e^{-2r^2/w_a^2} \mathbf{1}_{[-l/2, l/2]}(z) = \mathcal{N}_0 \frac{\pi}{2} \omega_a^2 l_a, \quad (3.6)$$

which indeed corresponds to the total number of atoms within a Gaussian distribution of width ω_a and a peak density of \mathcal{N}_0 .

However intuitive the above definition may be, it is not well suited for the experimental conditions. The main issue is that the ensemble operator from eq. (3.4) weighs all atoms equally, whereas in the experiment atoms at different points in space are observed with different weights due to the spatial profile of the probe (fig. 3.2). To account for this one may introduce a mode function $\mathcal{U}_m(\mathbf{r})$ proportional and substitute $\hat{o}(\mathbf{r}) \rightarrow \hat{o}(\mathbf{r})\mathcal{U}_m(\mathbf{r})$, so that an amended definition of the ensemble operator becomes [Sørensen08, Hammerer09]

$$\hat{O}_m = \int_{R^3} d^3r \hat{o}(\mathbf{r}) \mathcal{U}_m(\mathbf{r}). \quad (3.7)$$

which we coin the *mode-restricted operator*. In the case where the the mode m is that of the probe beam we merely refer to it as an *effective atomic operator*. Hereby, the atoms interacting most with the probe, and thus contributing more to the detected probe signal, are also contributing most to the ensemble operator. The virtues of this definition will become more clear when we calculate the effects of the atom-light interaction (see discussion at the end of sec. 4.2). Unfortunately, there is no simple way to expand the total ensemble operator in terms of mode restricted operators. Even though the mode-functions $\mathcal{U}_m(\mathbf{r})$ form a complete set it is unfortunately so that

$$\sum_m \hat{O}_m = \sum_m \int_{R^3} d^3r \hat{o}(\mathbf{r}) \mathcal{U}_m(\mathbf{r}) \neq \hat{O}_{\text{tot}}. \quad (3.8)$$

Only if $\mathcal{N}(\mathbf{r})$ is independent of the transverse coordinates can the last negation be replaced by an equality. When dealing with the interaction of the probe with the atoms this restriction poses some difficulties. Particularly, the atoms will interact with other field modes, and though these will be vacuum modes they couple noise into the atomic variables. We will return to this issue in sec. 4.1. Lastly, though the definition eq. (3.7) is quite natural it is by no means the only imaginable one [Kjærgaard08].

Figure 3.2: Atom and probe geometry - non-exaggerated.

An example that relates to the experimental configuration is of a probe with Gaussian profile in the x and y directions and to a reasonable approximation a constant strength in the z direction (eq. (2.3)). Thus, in cylindrical coordinates the mode function is

$$\mathcal{U}(\phi, r, z) = e^{-2r^2/w_p^2}, \quad (3.9)$$

where, again, w_p is the characteristic width of the probe. Thus, operators receive a weight from 0 to 1. It is not appropriate to normalise $\mathcal{U}(\phi, r, z)$ as is evident in the limit where the probe profile is much broader than the atomic ensemble and all atoms should be weighed by unity. Hence, from eq. (3.7) the corresponding ensemble operator is

$$\begin{aligned} N_{\text{at}} = \langle \hat{N}_{\text{at}} \rangle &= \int_{R^3} d^3r \langle \hat{n}_{\text{at}} \rangle \mathcal{U}(\mathbf{r}) \\ &= \int_0^{2\pi} d\phi \int_0^\infty dr \int_{-\infty}^\infty dz \mathcal{N}_0 r e^{-2r^2(1/w_p^2 + 1/w_a^2)} \mathbf{1}_{[-\frac{l_a}{2}, \frac{l_a}{2}]}(z) \\ &= \mathcal{N}_0 \frac{\pi}{2} w_a^2 l_a \frac{w_p^2}{w_p^2 + w_a^2}. \end{aligned} \quad (3.10)$$

The operator \hat{N}_{at} represents an effective atomic number. If we introduce a the ratio $r_w = w_p/w_a$ it is clear that \hat{N}_{at} equals the atomic density times an effective probed volume of the ensemble $\mathcal{V} = \pi l_a \frac{w_a^2}{2} \frac{r_w^2}{1+r_w^2}$. The total number of atoms in the ensemble is related to the effective atom number simply by $\hat{N}_{\text{at}} = \hat{N}_{\text{tot}} \frac{r_w^2}{1+r_w^2}$.

3.2 The atom

To take the definition a step deeper and specify relevant operators $\hat{o}^{(k)}$ we will investigate the internal degrees of freedom of the atoms, namely the energy levels corresponding to different electronic states. The alkali metal caesium has a single valence electron in the h-shell making it a comparatively simple system to study. We are almost exclusively concerned with the $6^2S_{1/2}$ ground level and the fine-structure level $6^2P_{3/2}$ though we will also touch upon the fine-structure level $6^2P_{1/2}$ (fig. 3.3). The optical transition between the ground state and the $6^2P_{3/2}$ and $6^2P_{1/2}$ levels are called the D1 and D2-lines. Each of these 3 levels are further split by the hyperfine structure according alignment of the electron with the total nuclear spin characterised by the F quantum number. The hyperfine splitting between the levels ranges from ≈ 100 MHz to almost 10 GHz between the two ground levels. Indeed it is the hyperfine ground level pair which makes Cs especially interesting, as the energy splitting between them corresponds to the photon frequency that has been chosen as a universal reference frequency. Hence, all timekeeping relies on the precise measurement of the transition frequency between these "clock levels" of Cs. Application of a magnetic

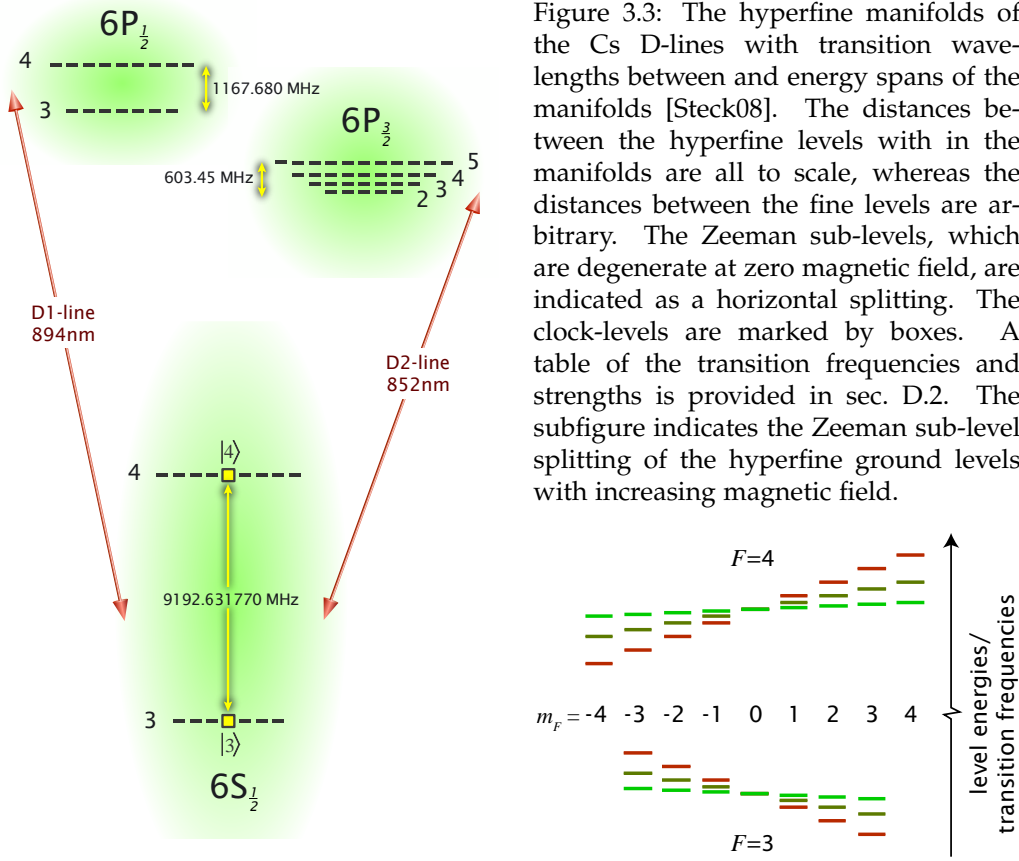


Figure 3.3: The hyperfine manifolds of the Cs D-lines with transition wave-lengths between and energy spans of the manifolds [Steck08]. The distances between the hyperfine levels within the manifolds are all to scale, whereas the distances between the fine levels are arbitrary. The Zeeman sub-levels, which are degenerate at zero magnetic field, are indicated as a horizontal splitting. The clock-levels are marked by boxes. A table of the transition frequencies and strengths is provided in sec. D.2. The subfigure indicates the Zeeman sub-level splitting of the hyperfine ground levels with increasing magnetic field.

field will cause the degeneracy of the Zeeman sub-levels to be lifted as the level energies are shifted by the linear Zeeman effect according to the m_F quantum number [Steck08]

$$\delta_l \omega_{F,m_F} = \mu_B g_F m_F B = \pm 2\pi 350 \frac{\text{kHz}}{\text{Gauss}} m_F B, \quad (3.11)$$

where μ_B is the Bohr magneton, and the Landé hyperfine-structure factors $g_{F=3} = -g_J/8$ and $g_{F=4} = g_J/8$, where g_J is the Landé fine-structure factors. The \pm is due to $g_{F=4} = -g_{F=3}$ which gives rise to the level shifts illustrated in the subfigure of fig. 3.3. With $m_F = 0$ the clock levels are exempt from the linear Zeeman shift, and only experience a quadratic shift and are therefore more resilient to magnetic field fluctuations

$$\delta_q \omega_{\text{clock}} = \delta_q \omega_{4,0} - \delta_q \omega_{3,0} = \frac{\mu_B^2 (g_J - g_I)^2}{2\omega_{\text{hfs}}} B^2 = \pm 2\pi 427.45 \frac{\text{Hz}}{\text{Gauss}^2} B^2 \quad (3.12)$$

The atomic state corresponding to an energy level follows the conventional "bra" $\langle \cdot |$ "ket" $|\cdot \rangle$ notation [Dirac58] with e.g. the lower clock state written as $|F=3, m_F=0\rangle \equiv |3,0\rangle$ where 'k' indexes the atom. When the Zeeman level is apparent from the context the m_F index will sometimes be excluded for notational convenience. The quantum state of an atom is written as linear combination of the basis states (levels) $|\psi\rangle_k = c_i |i\rangle_k + c_j |j\rangle_k + \dots$. The atomic state will, furthermore, be conveniently characterised by the state matrix element $\hat{\rho}_{ij}^{(k)} = |i\rangle_k \langle j|$. The expectation value of the diagonal matrix elements are ${}_k \langle \psi | \hat{\rho}_{ii}^{(k)} | \psi \rangle_k = |c_i|^2$, which are the probabilities that a measurement of the atom will return the atom in the i 'th level. For an ensemble of uncorrelated atoms all in the same state the extension to a continuous *density matrix* operators $\hat{\rho}_{i,j}$ operator follows directly from eq. (3.1). The collective atomic state is then said to be pure. A mixed collective state refers to the case where atoms are in some

statistical mixture of single atom states, i.e., each atom is in the state $|\psi_\alpha\rangle$ with a probability v_α , the density matrix definition is augmented

$$\hat{\rho}_{i,j}(\mathbf{r}) = \sum_\alpha \sum_k v_\alpha \hat{\rho}_{ij}^{(k)} \delta(\mathbf{r} - \mathbf{r}_k). \quad (3.13)$$

The diagonal elements still represent the local-ensemble average probability to measure the atom in the respective levels. The extension to the density operator for the whole ensemble obeys eq. (3.7), with no added remarks.

3.3 Pseudo-spin

In this section we introduce a set of operators that conveniently describe a general system of 2 levels, which in our case will be the clock levels $|3\rangle$ and $|4\rangle$. The four density matrix elements of the two level system in reality only contain three degrees of freedom since $\sum_{i=3,4} \langle i | \hat{\rho}_{ii} | i \rangle = 1$. Thus, it is not surprising that the atomic state is equally well characterised by a set of three operators. To keep the notation simple we suppress the spatial coordinates of the operators. The operators defined in terms of the density matrix elements are

$$\hat{f}_x = \frac{1}{2} (\hat{\rho}_{34} + \hat{\rho}_{43}), \quad (3.14a)$$

$$\hat{f}_y = -\frac{i}{2} (\hat{\rho}_{34} - \hat{\rho}_{43}), \quad (3.14b)$$

$$\hat{f}_z = \frac{1}{2} (\hat{\rho}_{44} - \hat{\rho}_{33}). \quad (3.14c)$$

From these definitions and the fact that we take $\{|3\rangle, |4\rangle\}$ to be an ortho-normal basis for the system, we easily get the commutation relations

$$[\hat{f}_i(\mathbf{r}), \hat{f}_j(\mathbf{r}')] = i\epsilon_{ijl} \hat{f}_l \delta(\mathbf{r} - \mathbf{r}'), \quad (3.15)$$

where ϵ_{ijl} is the Levi-Civita tensor.² The commutation relations show the equivalence of the operators of eq. (3.14) with the Cartesian components of a spin [Feynman57, Itano93]. Thus the vector $\hat{\mathbf{f}} = \hat{f}_x, \hat{f}_y, \hat{f}_z$ is coined a pseudo-spin vector. Additionally, we (re)define the population operator as $\hat{n}_{\text{at}} = \hat{\rho}_{44} + \hat{\rho}_{33}$. A mixed state is equally well represented by the pseudo-spin with the density operator defined according to eq. (3.13). Finally, the collective total ensemble pseudo-spin vector $\hat{\mathbf{F}}$ and population operator \hat{N}_{at} are defined according to eq. (3.7).

3.3.1 Bloch sphere representation

A convenient way to illustrate the atomic state is with the generalised Bloch sphere [Bloch46], which basically is the mapping of the pseudo-spin vector. Why we refer to this as a sphere is not immediately evident, but later in Sec. 15.1 we will argue that under unitary transformations the length of the pseudo-spin vector remains unchanged. However, the individual components can alter, and the pseudo-spin vector will trace out a path on the surface of a sphere. To illustrate this picture we treat a few collective atomic states.

² $\epsilon_{ijl} = 1$ for $(i, j, l) = (x, y, z), (y, z, x), (z, x, y)$, $\epsilon_{ijl} = -1$ for $(i, j, l) = (y, x, z), (z, y, x), (x, z, y)$ and 0 otherwise.

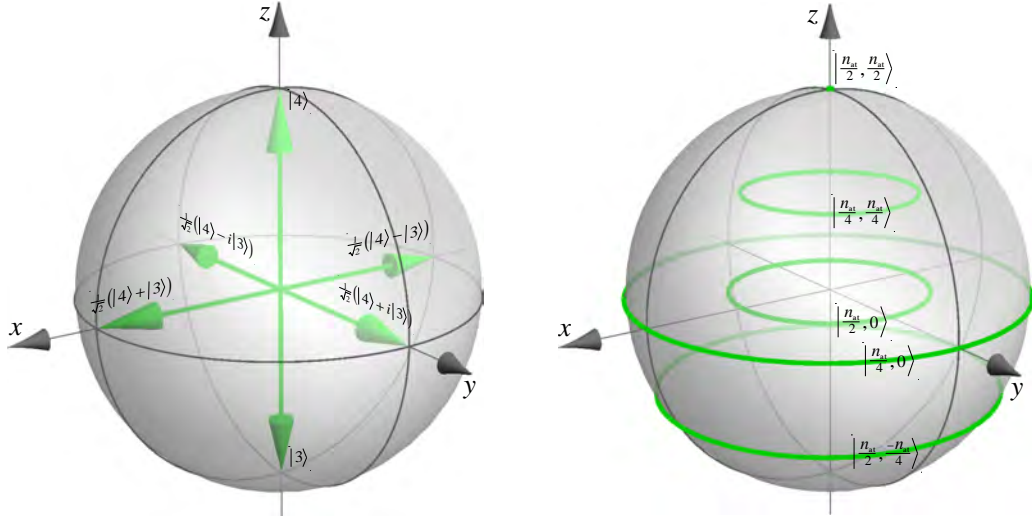


Figure 3.4: Bloch sphere representation of a) single atom or collective coherent states corresponding to pseudo-spin alignment along the axes and b) collective atomic Dicke states corresponding to a couple of illustrative parameter choices.

Coherent states One set of collective states are product states where the ensemble state is simply a product of identical single atom states, i.e., $|\psi\rangle = \prod_k |\psi\rangle_k$. The product states are a subset of the atomic Coherent states, which we will return to below. A general superposition state of $\langle \hat{n}_{at} \rangle = n_{at}$ atoms³ written as $|\psi\rangle_k = \cos \frac{\theta}{2} |4\rangle_k + e^{i\phi} \sin \frac{\theta}{2} |3\rangle_k$, produces the expectation values

$$\langle \hat{f}_x \rangle = \frac{n_{at}}{2} \sin \theta \cos \phi \quad , \quad \langle \hat{f}_y \rangle = \frac{n_{at}}{2} \sin \theta \sin \phi \quad , \quad \langle \hat{f}_z \rangle = \frac{n_{at}}{2} \cos \theta . \quad (3.16)$$

Thus, the product state is conveniently characterised by the two angles ϕ of the projection in the equatorial plane and θ . Alternatively, the state can be denoted by the projection of \hat{f} on the z-axis and the complex phase ϕ in the equatorial plane. These two values can be condensed into a complex number $z \equiv \cot \frac{\theta}{2} e^{i\phi}$ where $\langle \hat{f}_z \rangle = (|z|^2 - 1)/(1 + |z|^2)$ and the state is then labelled $|\frac{1}{2}, z\rangle$. The first index allows for a generalisation to all coherent states written as $|l, z\rangle$, where $l = 0, \dots, n_{at}$ prescribes the length of the vector⁴. In general we avoid writing specific states in the $|l, z\rangle$ form as the significance of z is not particularly conspicuous.⁵ When referring to product states we will usually just specify the single atom state as is done on fig. 3.4a.

Now, a few examples of coherent states with $l = n_{at}/2$ of which some are rendered on fig. 3.4a. Setting $\theta = 0$ (π) gives the state where all atoms are in the upper (lower) clock level $|4\rangle$ ($|3\rangle$) with $\langle \hat{f}_x \rangle = \langle \hat{f}_y \rangle = 0$ and $\langle \hat{f}_z \rangle = n_{at}/2$ ($-n_{at}/2$) i.e. a pseudo-spin vector pointing to the north (south) pole of the Bloch sphere. With $\theta = \pi/2$ we get the state $|4\rangle + e^{i\phi}|3\rangle$ having $\langle \hat{f}_x \rangle = \frac{n_{at}}{2} \cos \phi$, $\langle \hat{f}_y \rangle = \frac{n_{at}}{2} \sin \phi$ and $\langle \hat{f}_z \rangle = 0$ i.e. a vector on the equator of the Bloch Sphere. Finally, if $\phi = 0$ ($\pi/2$) we get \hat{f} aligned in the xz (yz) plane. In contrast to the product states, the statistical mixture of atoms in $|4\rangle$ and $|3\rangle$ with equal probability of $1/2$ produces the expectation values $\langle \hat{f}_x \rangle = \langle \hat{f}_y \rangle = \langle \hat{f}_z \rangle = 0$, which could be represented by a point at the origin of the coordinates system.

³we chose to express $\langle \hat{n}_{at} \rangle$ as n_{at} rather than $\mathcal{N}(r)$ to underline that the representation applies equally well to the the total ensemble operators for which we write $\langle \hat{N}_{at} \rangle = N_{at}$.

⁴The length of the vector refers to the expectation value of \hat{f}^2 , which can take on the values $\langle \hat{f}^2 \rangle = l(l+1)$, again with $l = 0, 1, \dots, n_{at} - 1, n_{at}$.

⁵the value of z is related to the argument of the displacement operator that is applied to the $|l, -l\rangle$ Dicke state to generate the coherent state $|l, z\rangle$.

Dicke states Another relevant set of collective states are the Dicke states [Dicke54] which characterise collective excitation of the local (or total) ensemble. It can be shown that Dicke states are eigen-states of the commuting operators \hat{f}_z and \hat{f}^2 and may thus be labelled with reference to the eigen-values $|l, m\rangle$ where

$$\hat{f}_z|l, m\rangle = m|l, m\rangle \quad , \quad \hat{f}^2|l, m\rangle = l(l+1)|l, m\rangle . \quad (3.17)$$

The value m thus refers to the number of excitations and l is again a measure of the length of the pseudo-spin vector. The two quantum numbers thus fulfil the intuitive condition $|m| \leq l \leq n_{\text{at}}/2$. Dicke states are not eigen-states of the two other pseudo-spin components, which actually have $\langle l, m|\hat{f}_x|l, m\rangle = \langle l, m|\hat{f}_y|l, m\rangle = 0$. A reasonable way to illustrate a Dicke state is thus as a horizontal band on the Bloch-Sphere where the projection on the z-axis is equal to the m quantum number and the radius equal to the l number (fig. 3.4b). In many ways the Dicke states are atomic equivalents to the photon Fock states (Sec. 2.1), in that they both are states of definite excitation and carry no phase information. It is important to realise that not all collective atomic states are Dicke states as for example the collective state of single atom equal super-positions $(|3\rangle + |4\rangle)/\sqrt{2}$.⁶ An immediate consequence is also that not all pure states are Dicke states.

Total ensemble extension When determining the expectation values of the total ensemble pseudo spin it is worth recalling the twist in the definition of these operators in eq. (3.7). For the atomic density and probing weight functions we take the experimentally relevant Gaussian distributions, eqs. (3.5 and 3.9) respectively. For the atomic state we take the product states. From eq. (3.16) we see that the spatial dependence of expectation values are all contained in the atomic number density distribution, whereby the total ensemble expectation values follow directly from eq. (3.10)

$$\langle \hat{F}_i \rangle = \langle \hat{f}_i^{(1)} \rangle \hat{N}_{\text{tot}} \frac{1}{2} \frac{r_w^2}{1 + r_w^2} = \langle \hat{f}_i^{(1)} \rangle N_{\text{at}} . \quad (3.18)$$

Here we have made a small manoeuvre, in which we drag out the dependence on the internal atomic degree of freedom by means of the single-atom pseudo-spin expectation value $\langle \hat{f}_i^{(1)} \rangle$. Hence, the spectrum of this operator is exclusively $\pm \frac{1}{2}$. No surprises in eq. (3.18), $\langle \hat{F}_i \rangle$ corresponds to our definition of the effective atom number. Yet, the below section will highlight the importance of dealing with the extension to total ensemble expectation values in a thorough manner.

Now, we have seen how the expectation values of the pseudo-spin vector components for various atomic states have certain interpretation on the Bloch sphere. Next, we will turn to investigate the uncertainty on these expectation values and thus summon the quantum noise of the atomic states.

3.4 Quantum projection noise

Although the expectation value of the $\langle \hat{f} \rangle$ pseudo-spin is completely determined by the atomic state, this is not to say that one may always exactly predict the outcome of a particular measurement on one of the spin-components. This is of course a direct consequence of the probabilistic nature of quantum mechanics, by which the quantum state describes a certain probability distribution in whatever

⁶e.g. for two atoms $\frac{1}{2}(|3\rangle_k + |4\rangle_k)(|3\rangle_j + |4\rangle_j) = \frac{1}{2}(|3\rangle_k|3\rangle_j + |4\rangle_k|3\rangle_j + |3\rangle_k|4\rangle_j + |4\rangle_k|4\rangle_j)$, which clearly does not correspond to a definite excitation of the atoms.

measurement basis is chosen. The uncertainty is coined *projection noise* as it can be interpreted to arise "from the random projection of the state vector into one of the states compatible with the measurement process" [Itano93]. To quantify the quantum uncertainty of the operator one can specify its variance $\langle(\Delta\hat{o})^2\rangle$, defined as $\langle(\Delta\hat{o})^2\rangle = \langle\hat{o}^2\rangle - \langle\hat{o}\rangle^2$. The well known, uncertainty relation by Heisenberg demands that the variances of two operators \hat{o}_i and \hat{o}_j fulfil

$$\langle(\Delta\hat{o}_i)^2\rangle\langle(\Delta\hat{o}_j)^2\rangle \geq \frac{1}{4} \left| \langle [\hat{o}_i, \hat{o}_j] \rangle \right|^2. \quad (3.19)$$

Heisenberg's relation plays a central role to the main aim of the experiments described in this thesis. Since, eq. (3.19) only prescribes a limit to the certainty one may have on the product of two operators, there is no restriction on how the variances are distributed among these two operators. In a case where one is particularly interested in predicting the measurement outcome of only one operator in the pair it one could attempt to reduce its uncertainty at the expense of an increased uncertainty on the other operator. Naturally, the r.h.s. may be an operator too, and it is crucial to take into account that it may also be affected by the attempts redistribute the uncertainty among the operators on the l.h.s. For the pseudo-spin operators the commutation relations eq. (3.15) show that the uncertainties of the various components are limited by mean values of the others. This leaves ample room for interesting configurations to be discussed below.

We now have a look at the PN of \hat{f} for two realisations of the atomic ensemble that are of relevance to the experiment. In both cases the atoms are in uncorrelated states. In sec. 3.6 we will discuss the very interesting case of correlated atoms. First we take the product state in which the single atom states are in superpositions of the two ground states $e^{i\phi} \sin(\theta/2)|3\rangle + \cos(\theta/2)|4\rangle$. We assume that exchanging two atoms will not change the value of the local operators so long as these refer to internal atomic degrees of freedom. In this case, we can first express the second moment of \hat{f}_i as (c.f. eq. (B.2))

$$\langle \hat{f}_i(\mathbf{r})^2 \rangle = \left\langle \left(\hat{f}_i^{(1)} \right)^2 \right\rangle n_{\text{at}}(\mathbf{r}) + \left\langle \hat{f}_i^{(1)} \hat{f}_i^{(2)} \right\rangle n_{\text{at}}(\mathbf{r}) (n_{\text{at}}(\mathbf{r}) - 1), \quad (3.20)$$

where for uncorrelated states $\langle \hat{f}_i^{(1)} \hat{f}_i^{(2)} \rangle = \langle \hat{f}_i^{(1)} \rangle^2$. Hereby, we have an expression where we base the expectation values on the single atom values and then extend to the continuous picture. We can now calculate the exact values for the pseudo-spins. The expectation values $\langle \hat{f}_i^{(k)} \rangle$ easily follow from eq. (3.16) and for all three components we get $\langle \hat{f}_i^{(k)} \rangle^2 = \frac{1}{4} (\hat{\rho}_{33}^{(k)} + \hat{\rho}_{44}^{(k)})$ and so $\langle (\hat{f}_i^{(k)})^2 \rangle = 1/4$. This finally allows us to extract the variances e.g. for \hat{f}_z we get

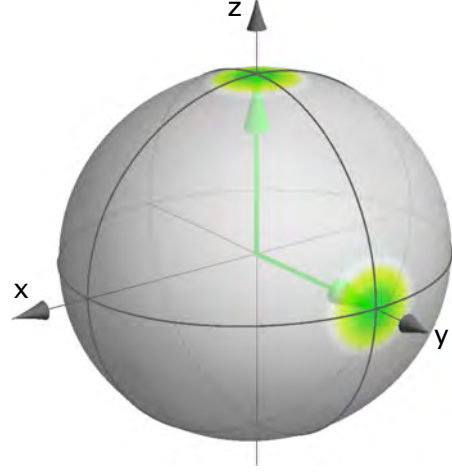
$$\langle (\Delta \hat{f}_z(\mathbf{r}))^2 \rangle = \frac{n_{\text{at}}(\mathbf{r})}{4} \sin^2 \theta. \quad (3.21)$$

Similarly we get for the other components

$$\begin{aligned} \langle (\Delta \hat{f}_x(\mathbf{r}) \hat{f}_x(\mathbf{r}')) \rangle &= \frac{n_{\text{at}}}{4} (1 - \sin^2 \theta \cos^2 \phi) \\ \langle (\Delta \hat{f}_y(\mathbf{r}) \hat{f}_y(\mathbf{r}')) \rangle &= \frac{n_{\text{at}}}{4} (1 - \sin^2 \theta \sin^2 \phi). \end{aligned} \quad (3.22)$$

The uncertainty of the pseudo-spin vector can in an intuitive way be illustrated as a sphere at the tip of and normal to the vector (fig. 3.5). Since the disc does not extend along the direction of the pseudo-spin the quantum uncertainty of the vector's length is zero. This equivalent to conservation of the atom number, which differs from the case of the Schwinger vector for photons whose

Figure 3.5: The Bloch sphere representation of the collective atomic state with projection noise. Sample vectors corresponding to product states are shown where in **a** all atoms are in the upper ground level and in **b** they are in an equal superposition of the two ground levels



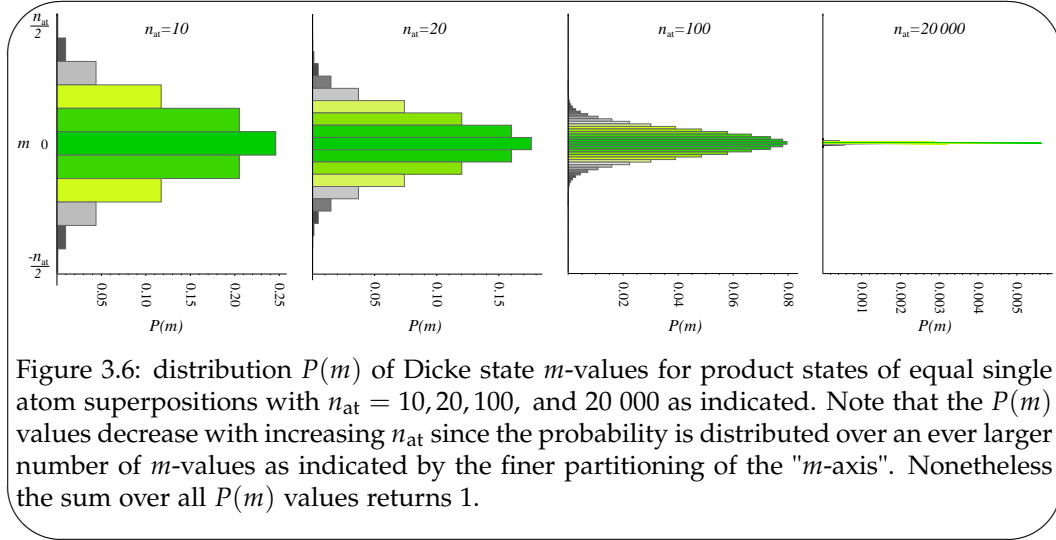
numbers are generally not fixed. Eq. (3.21) further reveals that compared to the spin magnitude ($= n_{\text{at}}/2$) the uncertainty or standard deviation of the spin $\propto \sqrt{n_{\text{at}}}$ grows slower with the number of atoms within the local volume. Hence, more atoms allows the outcome of a measurement of a spin component to be predicted more precisely. Again a parallel may be drawn to the Schwinger operators where in eqs. (2.26 and A.11) we observed that the uncertainty of the phase-difference of the two fields decreases with the photon number. If we focus on the z -component, it evidently has no quantum noise associated with it when the atoms are in either of the ground-levels. For $\theta = \pi/2$ the atoms are in equal superpositions of $|4\rangle$ and $|3\rangle$ and the quantum projection noise reaches its maximal value of $\langle(\Delta\hat{f}_z)^2\rangle = n_{\text{at}}/4$. The states at the equator of the Bloch-sphere are exactly the states that provide the largest sensitivity for spectroscopy and the projection noise has a direct influence of the performance of such measurements.

As a second example we take a symmetric mixed state with half of the atoms in the $|3\rangle$ state and half in the $|4\rangle$ state. The density matrix for this state is diagonal with $\hat{\rho}_{33}^{(k)} = \hat{\rho}_{44}^{(k)} = 1/2$, which renders the expectation values of all the \hat{f} components zero. As for the product state all components $(\hat{f}_i^{(k)})^2$ have expectation value $1/4$, hence from eq. (3.20) all variances are $\langle(\Delta\hat{f}_x)^2\rangle = \langle(\Delta\hat{f}_y)^2\rangle = \langle(\Delta\hat{f}_z)^2\rangle = n_{\text{at}}/4$. We make the important observation that the projection noise of \hat{f}_z is the same for the symmetric superposition product state and the symmetric mixed state.

Projection noise decomposed into distribution of Dicke states: The PN of the coherent states, of which the product states are a subgroup, has a neat relation to their representation in terms of Dicke states. Just as coherent photonic states could be expanded in terms of Fock states, the atomic coherent states have representation in terms of Dicke states. This becomes especially useful since Dicke states being eigenstates of \hat{f}_z have $\langle(\Delta\hat{f}_z)^2\rangle_{DS} = 0$. Restricting our attention to the product states we can write [Mandel95, Itano93]

$$|\tfrac{1}{2}, z\rangle = \frac{1}{(1 + |z|^2)^{\frac{n_{\text{at}}}{2}}} \sum_{m=-\frac{n_{\text{at}}}{2}}^{\frac{n_{\text{at}}}{2}} \binom{n_{\text{at}}}{\frac{n_{\text{at}}}{2} + m}^{\frac{1}{2}} z^{\frac{n_{\text{at}}}{2} + m} |\tfrac{1}{2}, m\rangle \quad (3.23)$$

Further specialising to the state $|\tfrac{1}{2}, e^{i\phi}\rangle$ corresponding to the product state of the equal superposition $|4\rangle + e^{i\phi}|3\rangle$ we write out the expectation value of \hat{f}_z in an



alternative fashion

$$\begin{aligned}
\langle \frac{1}{2}, e^{i\phi} | \hat{f}_z | \frac{1}{2}, e^{i\phi} \rangle &= \sum_{m=-\frac{n_{\text{at}}}{2}}^{\frac{n_{\text{at}}}{2}} \langle \frac{1}{2}, e^{i\phi} | \frac{1}{2}, m \rangle \langle \frac{1}{2}, m | \hat{f}_z | \frac{1}{2}, e^{i\phi} \rangle \\
&= \sum_{m=-\frac{n_{\text{at}}}{2}}^{\frac{n_{\text{at}}}{2}} m \left| \langle \frac{1}{2}, m | \frac{1}{2}, e^{i\phi} \rangle \right|^2 \\
&= \frac{1}{2^{n_{\text{at}}}} \sum_{m=-\frac{n_{\text{at}}}{2}}^{\frac{n_{\text{at}}}{2}} m \binom{n_{\text{at}}}{\frac{n_{\text{at}}}{2} + m},
\end{aligned} \tag{3.24}$$

where we use eq. (3.23) along with the fact that the Dicke states form a complete set. It is only natural to interpret

$$P(m) \equiv \frac{1}{2^{n_{\text{at}}}} \binom{n_{\text{at}}}{\frac{n_{\text{at}}}{2} + m} \tag{3.25}$$

as the probabilities for the measurement of \hat{f}_z on a coherent state to return a projection m corresponding to the Dicke state $|\frac{n_{\text{at}}}{2}, m\rangle$. Thus eq. (3.23) straight-away reveals the distribution of measurement outcomes of a coherent state from which it is possible to determine the width $\langle (\Delta \hat{f}_z)^2 \rangle_{\text{CSS}}$ in terms of m -values. In fig. 3.6 we show samples plots of $P(m)$ for a range of n_{at} values. For $n_{\text{at}} = 10$ there are only 11 allowed values of m over which the measurement results are distributed. As n_{at} increases and the set of m values increases the relative distribution over $P(m)$ narrows, corresponding to a more well-defined mean value \hat{f}_z . The final plot for $n_{\text{at}} = 20\,000$ illustrates the precision required to distinguish the measurement outcomes in a real experimental condition. Eq. (3.24) is a special case of the binomial distribution.⁷ The width of the distribution is $\langle (\Delta P(m))^2 \rangle = \langle (\Delta \hat{f}_z)^2 \rangle = n_{\text{at}}/4$ in agreement with the above findings (eq. (3.21)).

The above recasting of the projection noise may seem unwarranted as it has revealed nothing that wasn't already known. Nonetheless, it will prove very useful for describing how spin squeezing is generated by a QND measurement (sec. 5.1.1).

⁷The general binomial distrib. $\binom{n_{\text{at}}}{\frac{n_{\text{at}}}{2} + m} p^{\frac{n_{\text{at}}}{2} + m} (1-p)^{\frac{n_{\text{at}}}{2} - m}$ reduces to eq. (3.24) for $p = \frac{1}{2}$.

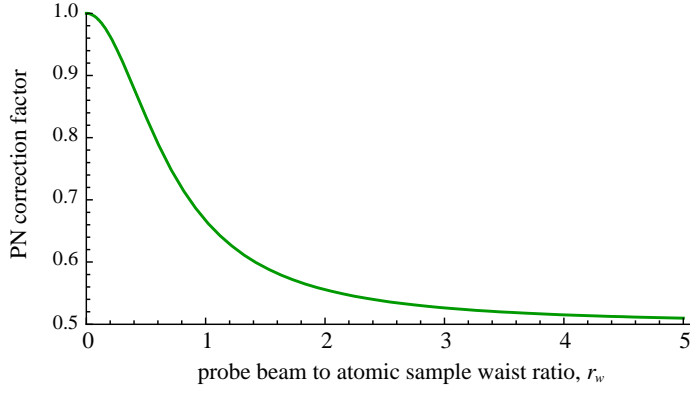


Figure 3.7: Correction factor relating the apparent atom number observed in the pseudo spin projection noise to the effective atom number \hat{N}_{at} corresponding to the pseudo spin expectation values.

Total ensemble projection noise As is custom we revert to eq. (3.7) with eqs. (3.5 and 3.9) defining Gaussian atomic density and probing weight functions respectively. We concentrate on the product states, which have the variances according to eq. (B.3) — the general form of eq. (3.21). Thus,

$$\begin{aligned}
 \langle (\Delta \hat{F}_z)^2 \rangle &= \int_{R^3} \int_{R^3} \langle (\Delta \hat{f}_z(\mathbf{r}) \hat{f}_z(\mathbf{r}')) \rangle \mathcal{U}(\mathbf{r}) \mathcal{U}(\mathbf{r}') d^3r d^3r' \\
 &= \frac{1}{4} \sin^2 \theta \int_{R^3} \mathcal{U}(\mathbf{r})^2 \mathcal{N}(\mathbf{r}) d^3r \\
 &= \frac{N_{\text{tot}}}{4} \sin^2 \theta \frac{1}{2} \frac{r_w^2}{1 + 2r_w^2} \\
 &= \frac{N_{\text{at}}}{4} \sin^2 \theta \frac{1 + r_w^2}{1 + 2r_w^2}.
 \end{aligned} \tag{3.26}$$

And likewise from eq. (B.4) we get

$$\langle (\Delta \hat{F}_x)^2 \rangle = \frac{\hat{N}_{\text{at}}}{4} (1 - \sin^2 \theta \cos^2 \phi) \frac{1 + r_w^2}{1 + 2r_w^2} \tag{3.27}$$

$$\langle (\Delta \hat{F}_y)^2 \rangle = \frac{\hat{N}_{\text{at}}}{4} (1 - \sin^2 \theta \sin^2 \phi) \frac{1 + r_w^2}{1 + 2r_w^2}. \tag{3.28}$$

The projection noise for a coherent atomic state is, thus, characterised by scaling linearly with the effective (or total) atom number, similarly to the shot noise of a coherent state of the light scaling linearly with the probe photon number (eq. (2.10)). This linear scaling is the essential indicator that distinguishes the quantum noise from other classical noise influences. The apparent atom number from the projection noise, however, differs from that inferred from the mean values of the pseudo-spins. The factor connecting the two numbers is plotted in fig. 3.7 as a function of the probe beam to the atomic sample waists. It shows that the projection noise tends to underestimate the atom number by up to a factor of two in the limit of a large probe beam compared to the atomic sample. Only if the sample is much larger than the probe beam, i.e., the atomic density is constant throughout the probing volume, does the projection noise reflect the defined effective atom number \hat{N}_{at} .

3.5 Squeezed states

Squeezing of quantum uncertainties hinges upon the Heisenberg relation only limiting the value of the product of a set of uncertainties. Thus, squeezed states of a set of conjugate operators can be prepared in both optical, atomic or any other quantum system. As it happens, any straight forward preparation of a

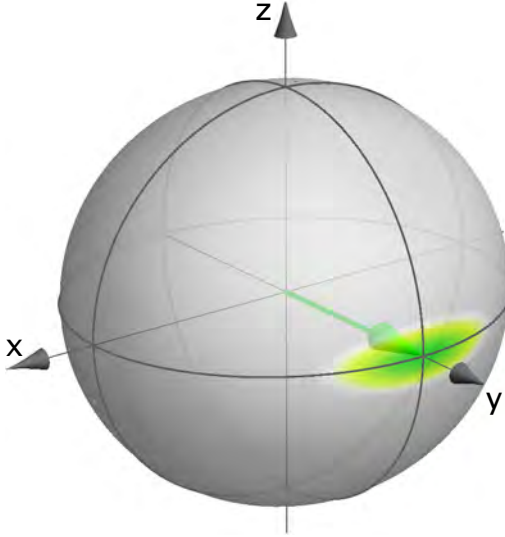


Figure 3.8: Squeezed pseudo-spin state on the Bloch-sphere. In this case $\langle(\Delta\hat{f}_z)^2\rangle$ is squeezed while $\langle(\Delta\hat{f}_x)^2\rangle$ is anti-squeezed.

quantum system tends to produce non-squeezed states in the sense that the uncertainties are in some sense equally distributed between conjugate operators. This is perhaps not surprising, as squeezing equivalates some form of inter particle correlation (see sec. 3.6), which one would not expect to be immediately present. For example coherent atomic and photonic states do not exhibit any squeezing.

3.5.1 Spin squeezed states

As mentioned, one would require that a Squeezed Spin State (SSS) is one that has a reduced noise in some spin component as compared to some standard limiting value of the noise, what is called the SQL. However, there exist several specifications of both terms in this equation, i.e., the squeezed noise and the SQL. The various definitions lead to more or less broad sets of collective quantum states acquiring the label SSS, but as we shall see only one definition ensures that this set is strictly made up of states containing quantum correlation.

Simple definition The natural definition of squeezing comes from the observation of the uncertainty relation

$$\langle(\Delta\hat{f}_i)^2\rangle\langle(\Delta\hat{f}_j)^2\rangle \geq \frac{1}{4}\langle\hat{f}_k\rangle^2. \quad (3.29)$$

One is enticed to define a squeezed state according to this relation as a state where one spin component on the l.h.s. has variance which is smaller than the square root of the r.h.s. i.e. $|\langle\hat{f}_k\rangle|$. The degree of squeezing would be quantified as

$$\zeta_{\text{simp}} = \frac{2\langle(\Delta\hat{f}_j)^2\rangle}{|\langle\hat{f}_k\rangle|} \quad (3.30)$$

However, because the definition is so liberal w.r.t. the choice of components it is possible to get $\zeta_{\text{simp}} < 1$ for a product state of uncorrelated atoms by making a clever choice of pseudo-spin orientation. This is illustrated for $\langle(\Delta\hat{f}_x)^2\rangle$ in a comparison with $|\langle\hat{f}_z\rangle|$ in fig. 3.9 where we plot $|\langle\hat{f}_z\rangle| - \langle(\Delta\hat{f}_x)^2\rangle$ (if this is less than 0 then $\zeta_{\text{simp}} < 1$). By choosing $\phi = 0$ or π we are in a situation where we have squeezing in the sense of eq. (3.30) for all $\theta \neq 0, \pi/2, \pi$. In conclusion a squeezing criterion according to eq. (3.30) is insufficient to prove any atomic correlation and thus inappropriate for our purpose.

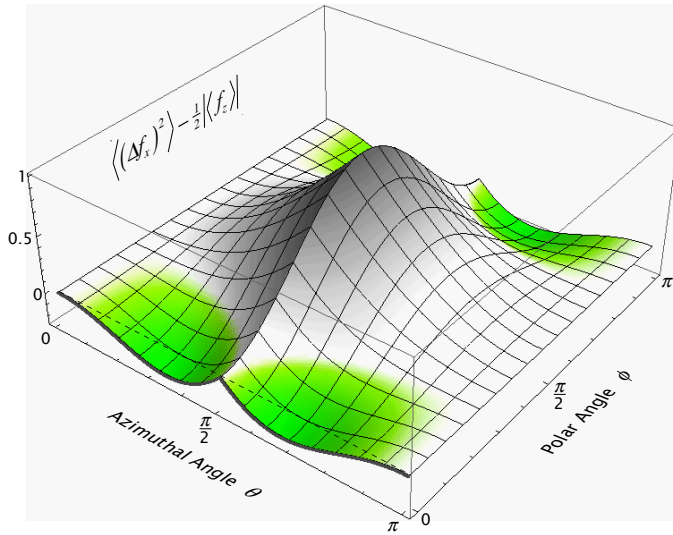


Figure 3.9: Actual uncertainty minus the minimum uncertainty.

Kitagawa and Ueda definition An obvious extension to the definition, which will overcome some ambiguity, is to specify more strictly the spin components that one must verify the squeezing on. Since we know that the quantum uncertainty is represented as a disk perpendicular to the mean spin direction a proper gauging of the projection noise should be done along a direction perpendicular to the mean spin. We denote such a direction by f_{\perp} and the mean spin magnitude is $|\langle\hat{f}\rangle|$. For the product state the variance of the spin along any perpendicular direction is $\langle(\Delta f_{\perp})^2\rangle_{\text{SQL}} = |\langle\hat{f}\rangle|/2$, which in this connection becomes the SQL. A squeezed state may then be said to be one that has a variance less than the SQL along some direction perpendicular to the mean spin and the degree of squeezing is [Kitagawa93]

$$\zeta_{\text{ueda}} = \frac{\langle(\Delta f_{\perp})^2\rangle}{\langle(\Delta f_{\perp})^2\rangle_{\text{SQL}}} = \frac{2\langle(\Delta f_{\perp})^2\rangle}{|\langle\hat{f}\rangle|} \quad (3.31)$$

For any coherent state this definition of squeezing ensures that $\zeta_{\text{ueda}} < 1$ entails atomic correlation, however for mixed states this inference no longer holds.

Wineland et. al definition Eq. (3.31) still falls short of defining a squeezed state in a way that guarantees atomic correlation so we proceed with a third and, thankfully, final approach. Some of the most valuable applications of spin squeezed states are in spectroscopy where one measures the angle of rotation of the pseudo-spin under some external influence or reference. In such an application the main drawback of the projection noise is the uncertainty it produces on the angle of the pseudo-spin and for a squeezed state to be of use it needs to improve on this angular uncertainty.

Consider the situation outlined in fig. 3.10 where a Bloch vector of length $|\langle\hat{f}\rangle|$ has an uncertainty disc of "size" $\langle(\Delta f_{\perp})\rangle$ along all directions perpendicular to the mean spin direction. This yields an uncertainty on the ability to determine the rotation angle $\langle(\Delta\phi)\rangle$, which has the value

$$\langle(\Delta\phi)\rangle = \tan\left(\frac{\langle(\Delta f_{\perp})\rangle}{|\langle\hat{f}\rangle|}\right) \approx \frac{\langle(\Delta f_{\perp})\rangle}{|\langle\hat{f}\rangle|}, \quad (3.32)$$

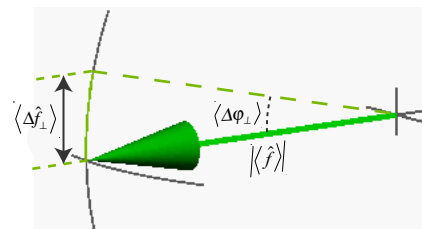


Figure 3.10: illustration of the determinants of the phase sensitivity of the pseudo-spin vector to rotations.

where the approximation holds for large atom numbers. Based on this and eqs. (3.26 and 3.27) we can establish the SQL of the phase noise to be $\langle(\Delta\phi)^2\rangle_{\text{SQL}} = 1/n_{\text{at}}$. Thus we define the parameter ζ_{wineland} for degree of *spectroscopically relevant* quantum noise reduction [Wineland92, Wineland94]

$$\zeta_{\text{wineland}} = \frac{\langle(\Delta\phi)^2\rangle}{\langle(\Delta\phi)^2\rangle_{\text{SQL}}} = \frac{n_{\text{at}}\langle(\Delta f_{\perp})^2\rangle}{\langle\hat{f}\rangle^2} \quad (3.33)$$

Beyond gauging the squeezing in a fashion that is relevant for applications the definition of eq. (3.33) does in fact also ensure that only quantum states that contain quantum correlation actually qualify as SSS [Hald00, Appendix D]. Throughout the remainder of the thesis we will use eq. (3.33) as the definition of the squeezing parameter. Any use of the squeezing parameter ζ will implicitly refer to this definition, unless it specifically stated to be otherwise.

3.6 Entanglement and squeezing

We have been beating around the bush on the matter of squeezing and quantum correlation a.k.a. entanglement. It is also beyond the scope of this thesis to go in depth with the topic but it seems directly relevant to comment on it. As noted a state with below unity squeezing factor by eq. (3.31) is guaranteed to be squeezed in as long as the state is pure. For mixed and pure states we need the factor by eq. (3.33) to be below one in order for atoms to be entangled. This raises questions about the nature of the entanglement especially how many atoms need to be entangled for the pseudo-spin means and variances to attain the values measured. Fortunately, this question has been answered in [Sørensen01b].⁸ The work presents an inequality which any separable, i.e., non-entangled, ensemble state will satisfy. Violation of the inequality implies inter-particle entanglement. The depth of the entanglement is defined by the minimal number of particles that cannot be written as a linear combination of products of N_{at} single particle density matrices. Say the depth is 3 then at least 3 particles are described by a non-separable density matrix, and thus they form a tripartite entangled state.

In order to determine the depth of the entanglement we must supply two measured parameters. Given a measured macroscopic mean spin, which in our case is $\langle\hat{F}_y\rangle$, the first parameter is its ratio with the maximal value it can attain, which is $N_{\text{at}}/2$ because we are dealing with a spin- $\frac{1}{2}$ pseudo-spin. The value of $2\langle\hat{F}_y\rangle/N_{\text{at}}$ is exactly the coherence of the squeezed state and since it is necessary to find the squeezing eq. (3.31)eq:sqwineland it is always measured in the experiments. The second parameter is then the variance of the squeezed spin component again normalised to the maximal spin magnitude, i.e., $2\langle(\Delta\hat{F}_z)^2\rangle/N_{\text{at}}$. In this case $N_{\text{at}}/2$ signifies a normalisation to the coherent state projection noise level making up the SQL. If we take a reasonable example where $2\langle\hat{F}_y\rangle/N_{\text{at}} = 0.8$ and $2\langle(\Delta\hat{F}_z)^2\rangle/N_{\text{at}} = 1/8$ the underlying quantum state exhibits four-partite entanglement [Sørensen01b, fig. 1]. One word of caution, is that the implications of the spatial distribution of the atoms and the probing has yet to be resolved.⁹ Hence, we can use the above estimate of the entanglement depth as a probable estimate, but not as a fact.

Now we have established the measures for squeezed spin states and we have determined how the squeezing relates to particle entanglement, which through

⁸the answer being in a form where an experimentalist, like the author of this account, can plug in numbers and read off a value!

⁹we have a theorist on the case!

the factor $2\langle\hat{F}_y\rangle/N_{\text{at}}$ crucially depended on the coherence of the atomic state. Ideally the atoms are prepared in a fully coherent state hence the decoherence is something that is inflicted upon the state at some point. Later we shall see that the process causing the noise reduction of $\langle(\Delta\hat{F}_z)^2\rangle$ is the same that decoheres the atoms. In the upcoming section we will first investigate how decoherence effects the noise of the atomic state.

3.7 Decoherence and squeezing

Coherence is a key aspect of the “quantumness” of a system that is essentially described by the density matrix. Decoherence can by and large be seen as a result of leakage of information about the density matrix or wave-function. By leakage we mean that part of the wave-function of the atomic ensemble travels beyond the spatial confines of the atomic system initially. The system wave-function can leak as a result of atoms being physically removed from the ensemble or because photons that have interacted and become entangled with the atoms escape detection. Since the photons are entangled with the atoms the combined state is no longer separable and the loss of a photon is equivalent to the leaking of the wave-function. Of course the aim of the probe-atom interaction is that the probe record information about the atomic state and carry this information onwards to an appropriate detection setup. The key point is that the probe-photon is collected on a detector and thus will not cause any decoherence, because the information it carried is salvaged. Decoherence of the atomic state arises from photons scattered by the atoms so that they evade detection. Thus the final atomic state will be an incoherent mixture of states that could have been determined if the lost photons had been detected. If the atoms were initially correlated, then part of the correlation is also lost [Bouchoule02b]. When evaluating the effect of scattering it is thus essential to determine exactly what information is lost. In the treatment of the decoherence caused by the atoms interacting with the probe we will rely heavily on the above principle.

3.7.1 Coherence time

Often decoherence is gauged by the, so called, coherence times. These reflect the characteristic time scales for certain decohering processes. It is conventional to specify two such times, namely T_1 and T_2 , where the former refers to the time of decay of the level population i.e. the diagonal density matrix elements and the latter refers to the decay time of the atomic phase i.e. the off-diagonal density matrix elements. Hence, T_2 is indeed the proper decoherence time. T_1 decay is a result inelastic scattering, either of another atom or a photon. We determine the T_1 time for our atomic sample in sec. 10.2.4. Since decay of the population randomises the atomic phase it follows that T_2 decay can result from both inelastic and elastic scattering of atoms or photons. Thus $T_2 \leq T_1$ must hold. However, T_2 decay need not stem from scattering events. Since, coherence refers to the degree of atomic phase agreement between atoms in an ensemble T_2 decay may also stem from variations in this phase over the spatial extent of the ensemble. Essentially, one ought not call this effect decoherence, but rather dephasing since it is a fully deterministic process. Thereby, it should in principle always be possible to revert the dephasing in what could be called a re-phasing of the ensemble. Scattering events on the other hand are random and it is generally not possible to retrieve the initial state whereby the decoherence would be reverted. The resulting decoherence time after applying various techniques to avoid dephasing is

coined T_2^* . A substantial part of the experimental section is devoted to methods for characterising and circumventing dephasing — see sec. 10.2.4 and 11.2. As a teaser it is noted, that in relation to the QND interaction, decoherence causes a destruction of the system correlation that one would wish to preserve. The decoherence can be due to the interaction itself or the free evolution. However, since decoherence often arises from experimental imperfections¹⁰ they are often not described by the carefully engineered QND Hamiltonian.

3.7.2 Squeezing affected by generic loss and decoherence

Decoherence is important for squeezing in a number of ways which we will discuss here. Firstly when an atom decoheres its correlation with all other atoms is erased; one can say that the atom is reset. Since squeezing is a result of inter-atomic correlation this means that overall the degree of squeezing of the ensemble is reduced. Secondly, the decoherence process is statistical and thus the randomness of the outcome of the decoherence process can add extra noise to the ensemble state. Finally, the decoherence affects the magnitude of the mean spin vector. This is because decohered atoms typically end up in a mixed state which has no mean spin amplitude. The first two effects that affect the noise of the ensemble state will be treated together, whereas the last effect regarding the pseudo-spin magnitude can be treated independently.

Decoherence is modelled as an effect which takes a fraction $e^{-\eta}$ of the atoms into another state than the original one. Here as in the remainder of the theoretical treatment of the decoherence we will assume that η is relatively small, say $\eta < 0.5$, whereby we are allowed to use the approximate expression $e^{-\eta} \approx 1 - \eta$. Thus an initial density matrix $\hat{\rho}$ transforms into $(1 - \eta)\hat{\rho} + \eta\hat{\rho}'$, where the latter term is the density matrix for the decohered atom. We begin with the effect of decoherence on the mean spin $\langle \hat{f} \rangle$ with \hat{f}^* denoting the pseudo-spin following the decoherence. We have the rather obvious equation c.f. eq. (B.5)

$$\langle \hat{f}_i^*(\mathbf{r}) \rangle = (1 - \eta)\langle \hat{f}_i(\mathbf{r}) \rangle + \eta\langle \hat{f}_i'(\mathbf{r}) \rangle, \quad (3.34)$$

where $\hat{f}_i(\mathbf{r})$ refers to the unaffected atoms and $\hat{f}_i'(\mathbf{r})$ refers to the decohered atoms. In many cases the decohered atoms will have $\langle \hat{f}_i'(\mathbf{r}) \rangle = 0$.

Now we turn to the variance of the pseudo-spin components when some of the atoms decohere. The derivations in appendix B.0.3 follow the approaches of [Mølmer03, Echaniz05, Saffman08] and is consistent with the results from [Madsen04]. First we recap eq. (3.20)

$$\langle \hat{f}_i(\mathbf{r}) \rangle = \left\langle \left(\hat{f}_i^{(1)} \right)^2 \right\rangle n_{\text{at}}(\mathbf{r}) + \left\langle \hat{f}_i^{(1)} \hat{f}_i^{(2)} \right\rangle n_{\text{at}}(\mathbf{r}) (n_{\text{at}}(\mathbf{r}) - 1).$$

The term $\langle \hat{f}_i^{(1)} \hat{f}_i^{(2)} \rangle$ contains the information on the inter-atomic correlation. For an uncorrelated state it can be re-written as $\langle \hat{f}_i^{(1)} \rangle^2$ and thus the value of the cross-term is exclusively determined by the mean value of the spin-component. If $\langle \hat{f}_i^{(1)} \rangle = 0$ then the term is zero for any uncorrelated state. Conversely, for a squeezed state the cross-term may be non-zero even if the mean spins is zero, therein lies the inter-atomic correlation (see eq. (B.7)). The expression for the variance of \hat{f}^* contains two terms of the above form, but for the states after the decoherence. Hence, $\langle (\Delta \hat{f}^*)^2 \rangle$ is determined by the effect of the decoherence on

¹⁰background gas scattering, field inhomogeneities, leak light, etc.

the inter-atomic correlation. The formula derived in appendix B.0.3 is

$$\begin{aligned} \langle (\Delta \hat{f}_i^*(\mathbf{r}))^2 \rangle &= (1 - \eta)^2 \langle (\Delta \hat{f}_i(\mathbf{r}))^2 \rangle + \left[\eta(1 - \eta) \langle (\hat{f}_i^{(1)})^2 \rangle + \eta \langle (\hat{f}_i^{(1)'})^2 \rangle \right] n_{\text{at}}(\mathbf{r}) \\ &+ \left[\eta^2 \left(\langle \hat{f}_i^{(1)'} \hat{f}_i^{(2)'} \rangle - \langle \hat{f}_i^{(1)'} \rangle^2 \right) \right. \\ &\quad \left. + 2\eta(1 - \eta) \left(\langle \hat{f}_i^{(1)} \hat{f}_i^{(2)'} \rangle - \langle \hat{f}_i^{(1)} \rangle \langle \hat{f}_i^{(1)'} \rangle \right) \right] n_{\text{at}}(\mathbf{r})^2, \end{aligned} \quad (3.35)$$

Up till this point, we have made no assumptions and the above expression is completely general in that it is valid for any initial and final expectation values of \hat{f}_i and \hat{f}_i^2 . We note a few reductions that will be applied at various stages below. First, as mentioned earlier, the values of $\langle (\hat{f}_i^{(1)})^2 \rangle$ and $\langle (\hat{f}_i^{(1)'})^2 \rangle$ are both equal to $1/4$ in as long as the probing is only sensitive to two atomic levels i.e. we have a spin $\frac{1}{2}$ system. Secondly, if the decohered atoms are uncorrelated $\langle \hat{f}_i^{(1)'} \hat{f}_i^{(2)'} \rangle = \langle \hat{f}_i^{(1)'} \rangle^2$ and $\langle \hat{f}_i^{(1)} \hat{f}_i^{(2)'} \rangle = \langle \hat{f}_i^{(1)} \rangle \langle \hat{f}_i^{(1)'} \rangle$ so that the last terms proportional to $n_{\text{at}}(\mathbf{r})^2$ in eq. (3.35) cancel. Under these, quite lenient, assumptions eq. (3.35) becomes

$$\langle (\Delta \hat{f}_i^*(\mathbf{r}))^2 \rangle = (1 - \eta)^2 \langle (\Delta \hat{f}_i(\mathbf{r}))^2 \rangle + \eta(2 - \eta) \frac{1}{4} n_{\text{at}}(\mathbf{r}) \quad (3.36)$$

If the input state is a coherent state with variance $\langle (\Delta \hat{f}_i(\mathbf{r}))^2 \rangle = n_{\text{at}}(\mathbf{r})/4$ the output variance will be

$$\langle (\Delta \hat{f}_i^*(\mathbf{r})) \rangle = \frac{n_{\text{at}}(\mathbf{r})}{4}. \quad (3.37)$$

It is worth emphasising that the decay of a coherent state does not add any additional noise to the system. This also underlines that if there are no inter atomic correlation the decoherence is immaterial for the variance. The magnitude of the pseudo-spin will of course be reduced according to eq. (3.34) so that the resulting state provides a poorer angular resolution in spectroscopic applications (see eq. (3.32)). In appendix B.0.3 we provide a few examples of types of decay that may aid in understanding the equations.

Atom light interaction

The two preceding chapters have elaborated on two very distinct quantum systems namely a pulse of light in two separate modes and a sample of cold Cs atoms populating the two hyperfine clock levels. In this chapter we will examine how these two systems interact and bring about interesting effects on one another. The treatment will attempt to illustrate how the whole rich system dynamics can be derived from basic principles. Thus, the initial step is to state the applicable Hamiltonian for the combined atom-light system and deduced the evolution of the constituent operators. The final goal is to reformulate the interaction part of the Hamiltonian in terms of the atomic pseudo-spin and photonic angular momentum operators.

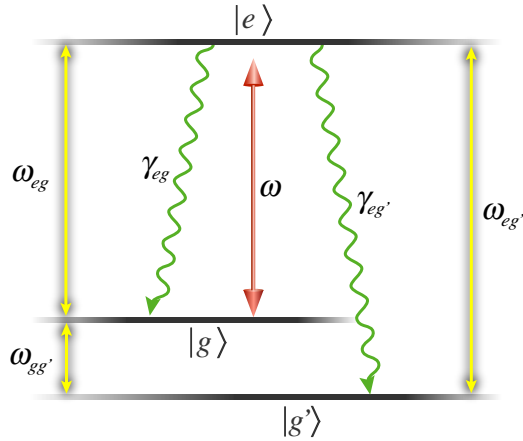


Figure 4.1: Diagram of the a single probe light field interacting with a 3-level atomic system. The probe with optical frequency ω interacts with the dipole moment of the $|g\rangle \rightarrow |e\rangle$ transition at a detuning of Δge , while the detuning from the $|g'\rangle \rightarrow |e\rangle$ is so large that the interaction can be neglected. The excited level can decay spontaneously to either the $|g\rangle$ or $|g'\rangle$ ground-levels with the rates $\gamma_{eg} = r_{eg}\gamma_e$ and $\gamma_{eg'} = r_{eg'}\gamma_e$ given by the respective branching ratios.

When formulating the interaction we will take into account the spatial field and atomic density distribution. To that end, we express the problem in terms of the local photonic and atomic operators and only at the end integrate up the results to arrive at expressions for the whole ensembles. Figure 4.1 outlines the interaction, where we will focus on three atomic levels and a single EM-field. The atomic levels comprise the two hyperfine ground levels $|g\rangle$ and $|g'\rangle$ as well as an excited level $|e\rangle$ belonging to either the $6^2P_{3/2}$ or the $6^2P_{1/2}$ hyperfine manifold. The photon energy $\hbar\omega$ of probe light field is close to the energy spacing $\hbar\omega_{eg}$ between the $|g\rangle$ and $|e\rangle$ levels. The Hamiltonian of this system includes the contributions of the independent/non-interacting field and atoms (See e.g. [Mandel95, Ch. 14]). The former is given by $\hat{\mathcal{H}}_{\text{ph}} = \hbar\omega\hat{a}^\dagger\hat{a}$ and the latter by $\hat{\mathcal{H}}_{\text{at}} = \hbar\omega_{eg'}\hat{\rho}_{ee} + \hbar\omega_{gg'}\hat{\rho}_{gg}$, where we exclude the energy contribution from the $|g'\rangle$ level by re-normalising the energy to be zero for that ground level¹. The

¹According to the diagram in fig. 4.1 the level $|g'\rangle$ indeed has the lowest energy, however even

final term in the Hamiltonian describes the interaction of the electric field of the light with the atomic dipole moment. In the rotating wave approximation this term has the form

$$\hat{\mathcal{H}}_{\text{dip}} = \hbar \left(g_{ge} \hat{a} \hat{\sigma}_{eg} + g_{ge}^* \hat{a}^\dagger \hat{\sigma}_{ge} \right), \quad (4.1)$$

where $g_{ge} = i\omega_{ge} \boldsymbol{\varepsilon} \cdot \hat{\mathbf{d}}_{ge} / \sqrt{2\hbar V \omega \varepsilon_0}$ is the coupling strength expressed in terms of the field polarisation vector $\boldsymbol{\varepsilon}$ and the dipole matrix element $\hat{\mathbf{d}}_{ij}$ (see appendix D.1). The first $\hat{a} \hat{\sigma}_{eg}$ term of eq. (4.1) describes the possibility of a photon to be absorbed by an atom in the ground level $|g\rangle$ thereby exciting it to the $|e\rangle$ level while the second $\hat{a}^\dagger \hat{\sigma}_{ge}$ term corresponds to the inverse process resulting in the generation of a photon and the atom decaying to the ground level $|g\rangle$. The complete system Hamiltonian is then $\hat{\mathcal{H}}_{\text{tot}} = \hat{\mathcal{H}}_{\text{ph}} + \hat{\mathcal{H}}_{\text{at}} + \hat{\mathcal{H}}_{\text{dip}}$.

4.1 Effective Interaction Hamiltonian

The time evolution of the E.M. field and atomic operators is found by Heisenberg's equation $d\hat{o}/dt = (i\hbar)^{-1} [\hat{o}, \hat{\mathcal{H}}_{\text{tot}}]$, which yields the set of Maxwell-Bloch equations

$$\dot{\hat{a}} = -i\omega \hat{a} + i g_g^* \hat{\sigma}_{ge} \quad (4.2a)$$

$$\dot{\hat{\sigma}}_{gg} = r_g \gamma_e \hat{\sigma}_{ee} - i g_g^* \hat{a}^\dagger \hat{\sigma}_{ge} + i g_g \hat{a} \hat{\sigma}_{eg} \quad (4.2b)$$

$$\dot{\hat{\sigma}}_{g'g'} = r_{g'} \gamma_e \hat{\sigma}_{ee} \quad (4.2c)$$

$$\dot{\hat{\sigma}}_{ee} = -\gamma_e \hat{\sigma}_{ee} + i g_g^* \hat{a}^\dagger \hat{\sigma}_{ge} - i g_g \hat{a} \hat{\sigma}_{eg} \quad (4.2d)$$

$$\dot{\hat{\sigma}}_{ge} = \left(-\frac{\gamma_e}{2} - i\omega_{ge}\right) \hat{\sigma}_{ge} - i g_g \hat{a} (\hat{\sigma}_{gg} - \hat{\sigma}_{ee}), \quad (4.2e)$$

with $\hat{\sigma}_{eg}$ immediately available by complex conjugation of the last equation. We have manually added the relevant decay rates to describe the processes of spontaneous emission of photons from the excited level (see fig. 4.1). The branching ratios r_g and $r_{g'}$ are given by the ratio of the Clebsch-Gordan coefficients (listed in sec. D.2) for the two decay channels and must fulfil $r_g + r_{g'} = 1$. The decay of the upper ground-level is sufficiently slow that it is completely negligible compared to all other processes. We proceed by introducing slowly varying operators

$$\tilde{a} = \hat{a} e^{i\omega t}, \quad \tilde{\sigma}_{ge} = \hat{\sigma}_{ge} e^{i\omega t}. \quad (4.3)$$

It is readily seen that this eliminates the fast oscillating term of the field operator eq. (2.1), and likewise the field induced fast oscillations of the atomic dipole are cancelled in $\tilde{\sigma}_{ge}$. Taking the time derivative of the slowly varying operators, $\dot{\tilde{a}} = \hat{a} e^{i\omega t} + i\omega \hat{a} e^{i\omega t}$ and $\dot{\tilde{\sigma}}_{ge} = \hat{\sigma}_{ge} e^{i\omega t} + i\omega \hat{\sigma}_{ge} e^{i\omega t}$, we may rewrite the corresponding Maxwell-Bloch equations

$$\dot{\tilde{a}} = i g_g^* \tilde{\sigma}_{ge} \quad (4.4a)$$

$$\dot{\tilde{\sigma}}_{ge} = \left(-\frac{\gamma_e}{2} - i\Delta_{ge}\right) \tilde{\sigma}_{ge} - i g_g \tilde{a} (\tilde{\sigma}_{gg} - \tilde{\sigma}_{ee}) \quad (4.4b)$$

Next we apply the adiabatic-approximation that the time derivatives of the slowly varying operators are zero. Hence, the dipole matrix element can be expressed as

$$\tilde{\sigma}_{ge} = -\frac{g_g \tilde{a}}{\Delta_{ge} - i\frac{\gamma_e}{2}} (\tilde{\sigma}_{gg} - \tilde{\sigma}_{ee}) \quad (4.5)$$

We are now in a position where we can replace the dipole matrix elements in the dipole interaction Hamiltonian $\hat{\mathcal{H}}_{\text{dip}}$ with expressions that refer only to level

if this is not the case the $|g'\rangle$ energy can be set to zero whereby the frequency $\omega_{gg'}$ just becomes negative.

populations. The key advantage of this is that the populations are measurable. The effective interaction Hamiltonian is

$$\hat{\mathcal{H}}_{\text{int}} = -\hbar \frac{2\hat{a}^\dagger \hat{a} |g_g|^2 \Delta_{ge}}{\Delta_{ge}^2 + (\frac{\gamma_e}{2})^2} (\hat{\rho}_{gg} - \hat{\rho}_{ee}) = -\hbar 2\hat{a}^\dagger \hat{a} \mathcal{K}_{ge} (\hat{\rho}_{gg} - \hat{\rho}_{ee}), \quad (4.6)$$

where we have introduced

$$\mathcal{K}_{ge} = \frac{|g_g|^2 \Delta_{ge}}{\Delta_{ge}^2 + (\frac{\gamma_e}{2})^2}. \quad (4.7)$$

To obtain eq. (4.6) we have neglected the term $\Delta_{ge} - i\gamma_e/2$ in the numerator² as its expectation value is small compared to that of $\hat{a}^\dagger \hat{a}$. Furthermore, since the term commutes with all field operators it does not affect their time evolution.

Finally, the description must be extended to cover the complete level structure of the caesium atom as sketched in fig. 3.3. Firstly, the classification of one ground levels as being on resonance and the other passive is merely dependent on the detuning of the probe. Hence, both levels can be viewed as interacting with the probe. Since the description of the 3-level atom has only considered a single dipole moment it is possible to accommodate interaction with both levels simply by adding another term to the interaction Hamiltonian. Likewise, there are either 2 or 4 excited levels depending on whether we probe the D1 or D2 line respectively. Summing over all possible ground to excited state dipole interaction terms results in the complete picture

$$\hat{\mathcal{H}}_{\text{eff}} = -\hbar \sum_{g=3}^4 \sum_{e=2(3)}^{5(4)} 2\hat{a}^\dagger \hat{a} \mathcal{K}_{ge} (\hat{\rho}_{gg} - \hat{\rho}_{ee}) \quad (4.8)$$

where the summation limits in brackets apply to the D1 line.

We may now adapt an additional approximation pertaining to the choice of detuning. For large Δ ($\gg \gamma_e, n_{\text{ph},a} |g_g|^2$) the transition is far from saturated and the excited state population $\hat{\rho}_{ee}$ will be very small, so much as to be disregarded from the effective interaction Hamiltonian eq. (4.8). Moreover, one can freely rewrite $\hat{\rho}_{44} = \frac{1}{2}(\hat{\rho}_{44} + \hat{\rho}_{33}) + \frac{1}{2}(\hat{\rho}_{44} - \hat{\rho}_{33}) = \frac{1}{2}\hat{n}_{\text{at}} + \hat{f}_z$ and likewise for $\hat{\rho}_{33}$. Similarly, we can introduce a second light field \hat{b} and recast $\hat{a}^\dagger \hat{a} = \frac{1}{2}(\hat{a}^\dagger \hat{a} + \hat{b}^\dagger \hat{b}) + \frac{1}{2}(\hat{a}^\dagger \hat{a} - \hat{b}^\dagger \hat{b}) = \frac{1}{2}\hat{n}_{\text{ph}} + \hat{s}_z$. All combined this allows one to formulate the interaction Hamiltonian as

$$\hat{\mathcal{H}}_{\text{eff}} = -\hbar 2 \left(\frac{\hat{n}_{\text{ph}}}{2} + \hat{s}_z \right) \sum_{e=2(3)}^{5(4)} \left[\mathcal{K}_{3e} \left(\frac{\hat{n}_{\text{at}}}{2} - \hat{f}_z \right) + \mathcal{K}_{4e} \left(\frac{\hat{n}_{\text{at}}}{2} + \hat{f}_z \right) \right], \quad (4.9)$$

whereby only Schwinger and pseudo-spin operators along with the total atom and photon numbers appear.

The Hamiltonian for the interaction of the whole ensemble is found, similarly to eq. (3.7), by integration over all space weighted by the spatial mode function of the field. With a Gaussian mode function (eq. (3.9)) the Hamiltonian becomes

$$\begin{aligned} \hat{H}_{\text{eff}} &= \int_{R^3} \hat{\mathcal{H}}_{\text{eff}}(\mathbf{r}) U(\mathbf{r}) d^3 r \quad (4.10) \\ &= \frac{-4\hbar}{\pi w_p^2} \left(\frac{\hat{n}_{\text{ph}}}{2} + \hat{s}_z \right) \sum_{e=2(3)}^{5(4)} \left[\mathcal{K}_{3e} \left(\frac{\hat{N}_{\text{at}}}{2} - \hat{F}_z \right) + \mathcal{K}_{4e} \left(\frac{\hat{N}_{\text{at}}}{2} + \hat{F}_z \right) \right] \\ &= \frac{-4\hbar}{\pi(w_a^2 + w_p^2)} \left(\frac{\hat{n}_{\text{ph}}}{2} + \hat{s}_z \right) \sum_{e=2(3)}^{5(4)} \left[\mathcal{K}_{3e} \left(\frac{\hat{N}_{\text{tot}}}{2} - \hat{F}_{z,\text{tot}} \right) + \mathcal{K}_{4e} \left(\frac{\hat{N}_{\text{tot}}}{2} + \hat{F}_{z,\text{tot}} \right) \right]. \end{aligned}$$

²arising from the commutator of \hat{a} and \hat{a}^\dagger

The bottom equality only holds for a Gaussian atomic density distribution eq. (3.5). We make a few remarks on the interaction strength, which is set by the factor $1/(w_a^2 + w_p^2)$ and the functions \mathcal{K}_{ge} . The former illustrates that given a certain number of atoms and photons it is advantageous to confine the sample and the probing volume to as small a cross-sectional area as possible. If however, either the sample or the probe width is larger this will tend to determine the interaction strength. Hence there is no advantage from having a narrow dense atomic sample if the probe beam is much wider. The function \mathcal{K}_{ge} is proportional to $1/\Delta_{ge}$ in the limit of large detunings. Thus the interaction falls as the detuning is increased, however in a QND perspective this must be weighed against the destructiveness of the interaction that will be introduced in sec. 4.2. Additionally, the mutual signs and magnitude of \mathcal{K}_{3e} and \mathcal{K}_{4e} appearing in the Hamiltonian can be adjusted so as to make certain terms cancel. This tunability of the interaction will be of crucial importance for implementing the QND measurement in sec. 5.2.

As we shall see the Hamiltonian eq. (4.9) comes very close to fulfilling the criterions for a QND Hamiltonian. Particularly, it is unitary and thus does not predict any losses of any operators. However, this result was only achieved by some deliberate oversight. The losses were manually added as spontaneous decay rates in the Maxwell-Bloch equations eq. (4.2) from which we deduced the time evolution of the dipole matrix elements. However these were then reinserted into the interaction Hamiltonian eq. (4.1), which makes no reference to spontaneous decay, and hence it is hardly surprising that the effective interaction Hamiltonian does not predict any losses. Intuitively, light passing through an optically thick medium will experience a certain degree of absorption along with the above predicted phase-shift. Indeed the connection is demanded by the Kramers-Kronig relation whereby the absorption and dispersion of the field may be formulated as a real and imaginary part of the index of refraction.

4.2 Phase-shift and absorption

The index of refraction is related to the field frequency by $n = |\mathbf{k}|c/\omega$ and the field absorption and phase shift³ are found respectively as $\tilde{\alpha}' = |\mathbf{k}|l_a\Im(n - 1)$ and $\tilde{\phi} = |\mathbf{k}|l_a\Re(n - 1)$. We can relate this to our interaction by working out the time development of the field operators from eq. (4.4b). Inserting the adiabatic solution eq. (4.5) into eq. (4.4b) we get the differential equation

$$\dot{\tilde{a}} = \tilde{a} \frac{-i|g_g|^2}{\Delta_{ge} - i\frac{\gamma_e}{2}} (\hat{\sigma}_{gg} - \hat{\sigma}_{ee}) = \tilde{a} |g_g|^2 \frac{-i\Delta_{ge} + \frac{\gamma_e}{2}}{\Delta_{ge}^2 + (\frac{\gamma_e}{2})^2} (\hat{\sigma}_{gg} - \hat{\sigma}_{ee}) \quad (4.11)$$

Thus if for a moment we assume the populations to be quasi-steady the solution to the field propagation is simply

$$\hat{a}(t) = \tilde{a}(t)e^{-i\omega t} = \hat{a}(0)e^{-i\omega t + |g_g|^2 \frac{-i\Delta_{ge} + \frac{\gamma_e}{2}}{\Delta_{ge}^2 + (\frac{\gamma_e}{2})^2} (\hat{\sigma}_{gg} - \hat{\sigma}_{ee})t} = \hat{a}(0)e^{-i(\omega t + \tilde{\phi}) - \tilde{\alpha}'} \quad (4.12)$$

This describes the field evolution as it is passing through the sample. In the absence of an atomic medium the evolution would purely be $e^{-i\omega t}$. Thus the phase-shift imparted by the medium is

$$\tilde{\phi} = |g_g|^2 \frac{\Delta_{ge}}{\Delta_{ge}^2 + (\frac{\gamma_e}{2})^2} (\hat{\sigma}_{gg} - \hat{\sigma}_{ee})t = \mathcal{K}_{ge}(\hat{\sigma}_{gg} - \hat{\sigma}_{ee})t \quad (4.13)$$

³by phase-shift we mean the displacement of the field oscillation due to the passing through the atomic medium as compared to the oscillations of a freely propagating field.

and the absorption coefficient $\tilde{\alpha}'$ of the field amplitude is then the real part of the exponent in eq. (4.12). Usually, though, we are interested in the absorption of the field intensity i.e. of $\hat{a}^\dagger \hat{a}$ which has the absorption coefficient $\tilde{\alpha} = 2\tilde{\alpha}'$

$$\tilde{\alpha} = 2|g_g|^2 \frac{\frac{\gamma_e}{2}}{\Delta_{ge}^2 + (\frac{\gamma_e}{2})^2} (\hat{\sigma}_{gg} - \hat{\sigma}_{ee})t = \mathcal{L}_{ge}(\hat{\sigma}_{gg} - \hat{\sigma}_{ee})t, \quad (4.14)$$

where we have defined $\mathcal{L}_{ge} = 2|g_g|^2 \frac{\gamma_e}{2} / (\Delta_{ge}^2 + (\frac{\gamma_e}{2})^2)$. The resonant absorption coefficient turns out to have a special importance for the squeezing and we will afford it an individual symbol $\tilde{\alpha}_0 \equiv \tilde{\alpha}(\Delta = 0)$.

On figs. 4.2 and 4.3 we plot the phase-shift and absorption as function of the probe detuning. The plots assume that both ground levels are equally populated

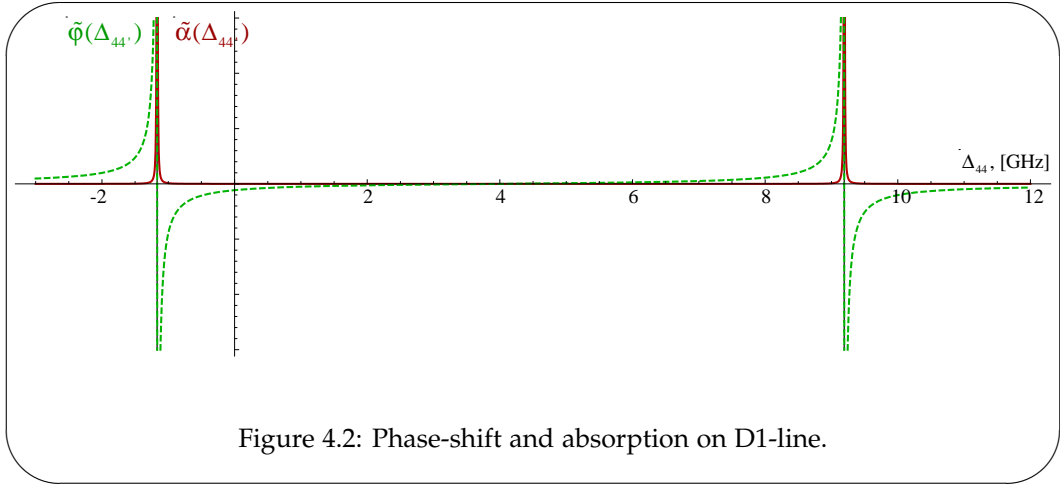


Figure 4.2: Phase-shift and absorption on D1-line.

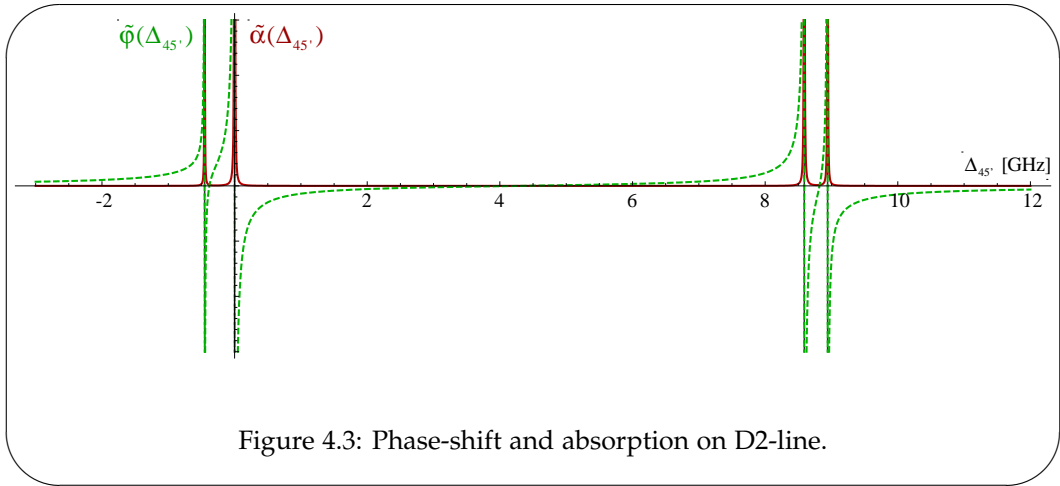


Figure 4.3: Phase-shift and absorption on D2-line.

i.e. $\langle \hat{f}_z \rangle = 0$. It is striking that the absorption is peaked much narrower around the transitions than is the phase-shift. Comparing eqs. (4.13 and 4.14) we see that this behaviour is due to the $1/\Delta$ dependence of the phase shift as opposed to the stronger $1/\Delta^2$ dependence of the absorption. This property of the non-destructive phase-shift vis- $\tilde{\mathcal{A}}$ -vis the destructive absorption is a key ingredient for the feasibility of performing a QND measurement by dispersive probing.

Full ensemble phase-shift and absorption The extension to the phase-shift from the full atomic ensemble starts by specifying the interaction time t in eqs. (4.13 and 4.14). This is the time it takes the probe to pass the atomic sample i.e. $t_{\text{int}} = l_a/c$. Next step is to consider the influence of the radial distribution of the of the probe intensity and atom density. This is achieved by integrating

the phase-shift over the transverse dimensions weighed by the radial intensity distribution of the probe. In other "words"

$$\begin{aligned}
\phi &= \frac{1}{c} \mathcal{K}_{ge} (\hat{\sigma}_{gg}^{(1)} - \hat{\sigma}_{ee}^{(1)}) l_a \int_{\mathbb{R}^2} \mathcal{N}(\mathbf{r}) U(\mathbf{r}) \hat{d}^2 r \\
&= \frac{1}{c} \mathcal{K}_{ge} \frac{\mathcal{N}_0 w_a^2 l_a}{w_p^2 + w_a^2} (\hat{\sigma}_{gg}^{(1)} - \hat{\sigma}_{ee}^{(1)}) \\
&= \frac{3\lambda^2}{2\pi^2} (2J_e + 1) S_{F_g F_e} \frac{\Delta_{ge} \frac{\gamma_e}{2}}{\Delta_{ge}^2 + (\frac{\gamma_e}{2})^2} \frac{1}{w_p^2 + w_a^2} (\hat{N}_{\text{tot},gg} - \hat{N}_{\text{tot},ee}) \quad (4.15) \\
&= \frac{3\lambda^2}{2\pi^2} (2J_e + 1) S_{F_g F_e} \frac{\Delta_{ge} \frac{\gamma_e}{2}}{\Delta_{ge}^2 + (\frac{\gamma_e}{2})^2} \frac{1}{w_p^2} (\hat{N}_{\text{at},gg} - \hat{N}_{\text{at},ee}) .
\end{aligned}$$

To reach the last two lines we have expand the coupling constant according to eq. (D.8). We also assume that the populations $\hat{\sigma}_{ii}$ are independent of the radial coordinate allowing us to take the single atom equivalent out of the integral and integrate over the atomic density distribution. This approximation is not always valid e.g. if the atomic populations are pumped over the duration of the probe pulse as discussed in sec. 4.3. This could be modelled by yet another radial weighing factor on the level population, however, we will mercifully abstain from such measures here. By the same procedure we find the absorption due to the ensemble

$$\begin{aligned}
\alpha &= \frac{3\lambda^2}{\pi^2} (2J_e + 1) S_{F_g F_e} \frac{(\frac{\gamma_e}{2})^2}{\Delta_{ge}^2 + (\frac{\gamma_e}{2})^2} \frac{1}{w_p^2 + w_a^2} (\hat{N}_{\text{tot},gg} - \hat{N}_{\text{tot},ee}) \quad (4.16) \\
&= \frac{3\lambda^2}{\pi^2} (2J_e + 1) S_{F_g F_e} \frac{(\frac{\gamma_e}{2})^2}{\Delta_{ge}^2 + (\frac{\gamma_e}{2})^2} \frac{1}{w_p^2} (\hat{N}_{\text{at},gg} - \hat{N}_{\text{at},ee})
\end{aligned}$$

As noted already when defining the atomic operators in sec. 3.1 the effective atomic operators relate directly to the observed signal either in terms of a phase-shift or absorption of the probe beam. For example the effective atomic number can be derived from the observed phase shift $\hat{N}_{\text{at},gg} \propto w_p^2 \phi$, where the probe waist is easily determined experimentally. On the other hand, when relating the phase-shift or absorption to the total ensemble operators we need to specify an additional geometric factor, the atomic sample waist, which by and large is not known with particularly good precision. Thus the total ensemble operators will be assigned quite arbitrary values depending on ones estimate on the sample size. Using the effective ensemble operators we avoid this ambiguity and also ensure that we only reckon atoms that actually interact with the probe. A shortcoming of this restricted scope is in the case where atomic motion becomes relevant. When atoms move about in the trap, they can move in and out of the "effective probe area" and thus be counted in or out at various times. Furthermore, it can be advantageous to express equations as functions of the total atom (and photon) number when attempting to optimise the experimental parameters. For example, the third line of eq. (4.15) clearly shows that given a certain number of trapped atoms the maximal signal is reached by adjusting the probe beam waist to be no larger than the estimated atomic sample size. This conclusion is not easy to gather from the bottom line, which is phrased in terms of the effective atom number.

4.3 Evolution of the atomic population

The atomic populations were assumed to be constant or at least in a quasi-steady-state. This can be a good approximation for the duration it takes a photon

to pass the sample \sim ps. However, if the probe couples stronger to one ground level than the other the population of the stronger coupled level might diminish during the duration of the whole light pulse \sim μ s. If such level depumping occurs the apparent effect of the level on the light is reduced. To take this effect in to account we consider the evolution of the atomic populations. Inserting eq. (4.5) in to the Maxwell-Bloch equations eq. (4.2b-d)

$$\dot{\hat{\sigma}}_{gg} \approx r_g \gamma_e \hat{\sigma}_{ee} - \frac{|g_g|^2 \hat{a}^\dagger \hat{a} \gamma_e}{\Delta_{ge}^2 + (\frac{\gamma_e}{2})^2} (\hat{\sigma}_{gg} - \hat{\sigma}_{ee}) \quad (4.17a)$$

$$\dot{\hat{\sigma}}_{ee} \approx -\gamma_e \hat{\sigma}_{ee} + \frac{|g_g|^2 \hat{a}^\dagger \hat{a} \gamma_e}{\Delta_{ge}^2 + (\frac{\gamma_e}{2})^2} (\hat{\sigma}_{gg} - \hat{\sigma}_{ee}) \quad (4.17b)$$

$$\dot{\hat{\sigma}}_{g'g'} = r_{g'} \gamma_e \hat{\sigma}_{ee} \quad (4.17c)$$

The approximation “ \approx ” comes from neglecting the term $|g_g|^2 (i\Delta_{ge} + \frac{\gamma_e}{2}) / (\Delta_{ge} + (\frac{\gamma_e}{2})^2)$ which is multiplied with the population inversion.⁴ Eq. (4.17) effectively casts the population evolution as rate equations, in which case we can freely add up the rate-equation terms that correspond to the roles of $|g\rangle$ and $|g'\rangle$ being interchanged. The resulting first order differential equations can be solved by standard methods, but we will not state the rather lengthy analytical expressions here. One assumption needed to solve them is that the photon number is constant $d(\hat{a}^\dagger \hat{a})/dt = 0$. As the photon number is typically at least one order of magnitude larger than the atom number the photon absorption is usually rather small and the approximation is well founded. In fig. 4.4 we plot the level populations as function of the interaction time for a relevant set of experimental parameters. Given the time evolution of the populations it is possible

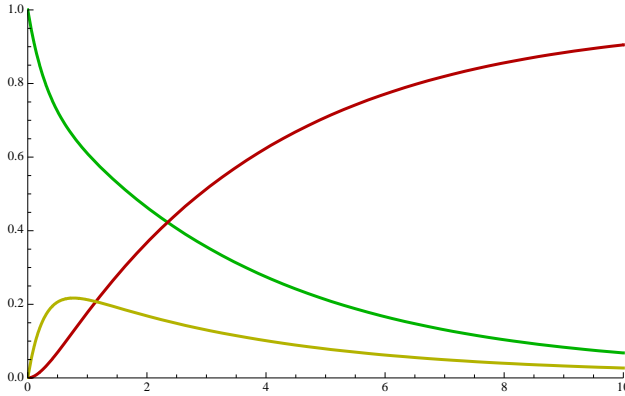


Figure 4.4: Evolution of the atomic level populations during interaction with a single probe.

to compute an averaged population of each level during the probe pulses e.g. $\overline{\hat{\sigma}}_{gg} = \tau^{-1} \int_0^{t_p} \hat{\sigma}_{gg}(t) dt$. This averaged value may then be applied to calculate the phase-shift eq. (4.13) and — hopefully small — absorption eq. (4.14) of the probe light. When expanding to the full ensemble eqs. (4.15 and 4.16) one must consider spatial variations in the population evolution due to varying probe light intensities.

4.3.1 Rate of excitations

Though it's possible to derive the number of atoms scattering probe photons from the solution to the above rate-equations it is desirable to have a more compact expression for this number. To this end, we assume that the excited state

⁴The term arises from the commutator $[\hat{a}^\dagger, \hat{a}]$, and for any appreciable light intensity it is much smaller than the remaining term, which includes $\hat{a}^\dagger \hat{a}$.

population is negligible which requires the probe intensity to be below the saturation intensity of the atoms. With this approximation we can easily solve eq. (4.17a) for the population of the coupled level

$$\hat{\sigma}_{gg}(t) = \hat{\sigma}_{gg}(0) e^{-\frac{|g_g|^2 \hat{n}_{\text{ph},a} \gamma_e}{\Delta_{ge}^2 + (\frac{\gamma_e}{2})^2} t}.$$

The exponent of this solution is what we will coin the excitation rate and denote with an $\tilde{\eta}_g$

$$\tilde{\eta}_g = \frac{|g_g|^2 \hat{n}_{\text{ph},a} \gamma_e}{\Delta_{ge}^2 + (\frac{\gamma_e}{2})^2} t = \frac{1}{2} \mathcal{L}_{ge} \hat{n}_{\text{ph},a} t$$

To get the total excitation rate of the atoms we must account for both ground levels. The total population in the initial state evolves as

$$\hat{n}_{\text{at}}(t) = \hat{\sigma}_{gg}(t) + \hat{\sigma}_{g'g'}(t) = \hat{\sigma}_{gg}(0) e^{-\frac{1}{2} \mathcal{L}_{ge} \hat{n}_{\text{ph},a} t} + \hat{\sigma}_{g'g'}(0) e^{-\frac{1}{2} \mathcal{L}_{g'e} \hat{n}_{\text{ph},a} t}$$

For small values of the exponents, corresponding to a low excitation probability, one may expand the above equation. Furthermore we can chose the expectation values of $\hat{\sigma}_{gg}(0)$ $\hat{\sigma}_{g'g'}(0)$ e.g. to be both equal to $\hat{n}_{\text{at}}/2$. In this case

$$\hat{n}_{\text{at}}(t) = \hat{n}_{\text{at}}(0) e^{-\frac{1}{2} (\mathcal{L}_{ge} + \mathcal{L}_{g'e}) \hat{n}_{\text{ph},a} t} \approx \hat{n}_{\text{at}}(0) \left(1 - \frac{1}{2} (\mathcal{L}_{ge} + \mathcal{L}_{g'e}) \hat{n}_{\text{ph},a} t\right),$$

with a combined excitation rate defined as

$$\tilde{\eta} = \frac{1}{2} (\mathcal{L}_{ge} + \mathcal{L}_{g'e}) \hat{n}_{\text{ph}} t \quad (4.18)$$

For more than a single excited state one simply sums over the contributions from each i.e. $\tilde{\eta} = \frac{1}{2} \sum_{e=2(3)}^{5(4)} (\mathcal{L}_{ge} + \mathcal{L}_{g'e}) \hat{n}_{\text{ph},a} t$. The factor of 1/2 stems from the definition of \mathcal{L}_{ge} .

The excitation probability will be central for the evaluation how non-destructive the QND measurement is and we will show that the noise reduction achieved by the measurement can be expressed as a function of $\tilde{\eta}$ (see sec. 5.2.2).

4.4 Input-output relations

Here we will investigate how the interaction Hamiltonian of eq. (4.9) affects the atomic pseudo-spin and photonic Schwinger operators. To save on page-turning we reprint the Hamiltonian here

$$\hat{\mathcal{H}}_{\text{eff}} = -\hbar 2 \left(\frac{\hat{n}_{\text{ph}}}{2} + \hat{s}_z \right) \sum_{e=2(3)}^{5(4)} \left[\mathcal{K}_{3e} \left(\frac{\hat{n}_{\text{at}}}{2} - \hat{f}_z \right) + \mathcal{K}_{4e} \left(\frac{\hat{n}_{\text{at}}}{2} + \hat{f}_z \right) \right],$$

The operator transformation due to the interaction again found as $d\hat{o}/dt = (i\hbar)^{-1} [\hat{o}, \hat{\mathcal{H}}_{\text{eff}}]$. For the photon operators

$$\begin{aligned} \frac{d\hat{s}_z}{dt} &= 0 \\ \frac{d\hat{s}_x}{dt} &= 2\hat{s}_y \sum_{e=2(3)}^{5(4)} \left[(\mathcal{K}_{4e} + \mathcal{K}_{3e}) \frac{\hat{n}_{\text{at}}}{2} + (\mathcal{K}_{4e} - \mathcal{K}_{3e}) \hat{f}_z \right] \\ \frac{d\hat{s}_y}{dt} &= -2\hat{s}_x \sum_{e=2(3)}^{5(4)} \left[(\mathcal{K}_{4e} + \mathcal{K}_{3e}) \frac{\hat{n}_{\text{at}}}{2} + (\mathcal{K}_{4e} - \mathcal{K}_{3e}) \hat{f}_z \right] \end{aligned} \quad (4.19)$$

and for the atomic operators

$$\begin{aligned}\frac{d\hat{f}_z}{dt} &= 0 \\ \frac{d\hat{f}_x}{dt} &= 2 \left(\frac{\hat{n}_{\text{ph}}}{2} + \hat{s}_z \right) \hat{f}_y \sum_{e=2(3)}^{5(4)} [\mathcal{K}_{4e} - \mathcal{K}_{3e}] \\ \frac{d\hat{f}_y}{dt} &= -2 \left(\frac{\hat{n}_{\text{ph}}}{2} + \hat{s}_z \right) \hat{f}_x \sum_{e=2(3)}^{5(4)} [\mathcal{K}_{4e} - \mathcal{K}_{3e}]\end{aligned}\quad (4.20)$$

The first crucial observation is that the z-components of both vectors do not change by the interaction. This property is worth having in mind when we begin our discussion of non-demolition measurements of quantum observables in the below sec. 5.1. Furthermore the evolution of the x and y components are described by a set of coupled differential equations that refer only to the constant z-component of the opposite system. Hence, the solution to the equations are rotations around the z-axes

$$\hat{\mathbf{s}}^{(out)} = \mathbf{M}_{(\Omega_{\text{ph}}t)} \hat{\mathbf{s}}^{(in)} \quad (4.21)$$

$$\hat{\mathbf{f}}^{(out)} = \mathbf{M}_{(\Omega_{\text{at}}t)} \hat{\mathbf{f}}^{(in)} \quad (4.22)$$

where the rotation matrix is defined as in eq. (2.14)

$$\mathbf{M}_{(\Omega t)} = \begin{pmatrix} \cos \Omega t & \sin \Omega t & 0 \\ -\sin \Omega t & \cos \Omega t & 0 \\ 0 & 0 & 1 \end{pmatrix}. \quad (4.23)$$

and the angular frequencies are defined as

$$\Omega_{\text{ph}} \equiv 2 \sum_{e=2(3)}^{5(4)} \left[(\mathcal{K}_{4e} + \mathcal{K}_{3e}) \frac{\hat{n}_{\text{at}}}{2} + (\mathcal{K}_{4e} - \mathcal{K}_{3e}) \hat{f}_z \right] \quad (4.24)$$

$$\Omega_{\text{at}} \equiv 2 \left(\frac{\hat{n}_{\text{ph}}}{2} + \hat{s}_z \right) \sum_{e=2(3)}^{5(4)} [\mathcal{K}_{4e} - \mathcal{K}_{3e}] \quad (4.25)$$

The two pseudo-spin systems affect one another by exchanging a phase-shift. The phase shift imparted on one vector is for both proportional to a vector component plus the total number of particles of the other system. Hence the interaction exchanges information about the coupled vector components from one system to the other. If we look at the photonic pseudo-spin phase-shift $\tilde{\phi}_{\text{ph}} = \Omega_{\text{ph}} t_a$, with $t_a = l_a/c$ the time it takes the probe to pass the atomic sample, it is effectively proportional to the populations in the two levels with the respective coupling strengths \mathcal{K}_{3e} and \mathcal{K}_{4e} . Hence, this amounts to the usual dispersion of light in a dielectric medium. In exchange the atomic pseudo-spin receives a phase-shift $\tilde{\phi}_{\text{at}} = \Omega_{\text{at}} t_p$ from the probe, where $t_p = l_p/c$ is the duration of the probe pulse. which is the usual light shift caused by the dynamic Stark effect. The effect comes from the electric field component of the light shifting the energy levels of the ground states thus slightly altering the transition frequency ω'_0 . In fig. 5.5 and fig. 5.6 in the below section we plot the the light-shift $\tilde{\phi}_{\text{at}}$ and phase-shift $\tilde{\phi}_{\text{ph}}$ as function of the probe laser detuning. In that section we will discuss more about the different avenues for selecting the probing parameters in light of these complementary shifts.

Finally, we can for small values of $\Omega_{\text{ph}}t$ and $\Omega_{\text{at}}t$ expand the equations to first order

$$\begin{aligned}\hat{s}_z^{(out)} &= \hat{s}_z^{(in)} & \hat{f}_z^{(out)} &= \hat{f}_z^{(in)} \\ \hat{s}_x^{(out)} &= \hat{s}_x^{(in)} + \hat{s}_y^{(in)} \tilde{\phi}_{\text{ph}} & \hat{f}_x^{(out)} &= \hat{f}_x^{(in)} + \hat{f}_y^{(in)} \tilde{\phi}_{\text{at}} \\ \hat{s}_y^{(out)} &= -\hat{s}_y^{(in)} + \hat{s}_x^{(in)} \tilde{\phi}_{\text{ph}} & \hat{f}_y^{(out)} &= -\hat{f}_y^{(in)} + \hat{f}_x^{(in)} \tilde{\phi}_{\text{at}}\end{aligned}\quad (4.26)$$

This will become useful later for the description of the QND measurements.

Full ensemble input-output relations We are now able to express the total ensemble output operators following the interaction. In accordance with eq. (2.4) the photonic operators need to be integrated over the pulse length l_p and over the transverse intensity profile $|u(\mathbf{r})|^2 = U(\mathbf{r})$, assumed to be Gaussian. The simple case of \hat{S}_z becomes

$$\hat{S}_z^{(out)} = \int_{R^2} \int_{z=0}^{l_p} \hat{s}_z^{(in)}(\mathbf{r}) U(\mathbf{r}) d^2r dz = \hat{S}_z^{(in)}, \quad (4.27)$$

For \hat{S}_x the coupling to the atomic pseudo-spin generates a more involved expression

$$\begin{aligned}\hat{S}_x^{(out)} &= \int_{R^2} \int_{z=0}^{l_p} \left(\hat{s}_x^{(in)}(\mathbf{r}) + \hat{s}_y^{(in)}(\mathbf{r}) \Omega_{\text{ph}}(\mathbf{r}) \frac{l_p}{c} \right) U(\mathbf{r}) d^2r dz \\ &= \hat{S}_x^{(in)} + \frac{4}{\pi c} \frac{1}{w_a^2 + w_p^2} \sum_{e=2(3)}^{5(4)} \left[(\mathcal{K}_{4e} + \mathcal{K}_{3e}) \frac{\hat{N}_{\text{tot}}}{2} + (\mathcal{K}_{4e} - \mathcal{K}_{3e}) \hat{F}_{z,\text{tot}} \right] \hat{S}_y^{(in)}(\mathbf{r}) \\ &= \hat{S}_x^{(in)} + \frac{4}{\pi c} \frac{1}{w_p^2} \sum_{e=2(3)}^{5(4)} \left[(\mathcal{K}_{4e} + \mathcal{K}_{3e}) \frac{\hat{N}_{\text{at}}}{2} + (\mathcal{K}_{4e} - \mathcal{K}_{3e}) \hat{F}_z \right] \hat{S}_y^{(in)}(\mathbf{r})\end{aligned}\quad (4.28)$$

A similar expression can be found for $\hat{S}_y^{(out)}$. For the atomic operators we take the weighed integral over the atomic density, assumed to be of the form of eq. (3.9), as prescribed by eq. (3.7)

$$\hat{F}_{z,\text{tot}}^{(out)} = \int_{R^3} \hat{f}_z^{(in)} U(\mathbf{r}) d^3r = \hat{F}_{z,\text{tot}}^{(in)}, \quad (4.29)$$

and for \hat{F}_y

$$\begin{aligned}\hat{F}_{x,\text{tot}}^{(out)} &= \int_{R^3} \left(\hat{f}_x^{(in)} + \hat{f}_y^{(in)} \Omega_{\text{at}}(\mathbf{r}) \frac{l_p}{c} \right) U(\mathbf{r}) d^3r \\ &= \hat{F}_{x,\text{tot}}^{(in)} + \frac{4}{\pi c} \frac{1}{w_a^2 + w_p^2} \sum_{e=2(3)}^{5(4)} [\mathcal{K}_{4e} - \mathcal{K}_{3e}] \hat{F}_{y,\text{tot}}^{(in)} \left(\frac{\hat{N}_{\text{ph}}}{2} + \hat{S}_z \right) \\ \Downarrow \\ \hat{F}_x^{(out)} &= \hat{F}_x^{(in)} + \frac{4}{\pi c} \frac{1}{w_p^2} \sum_{e=2(3)}^{5(4)} [\mathcal{K}_{4e} - \mathcal{K}_{3e}] \hat{F}_y^{(in)} \left(\frac{\hat{N}_{\text{ph}}}{2} + \hat{S}_z \right),\end{aligned}\quad (4.30)$$

Again a similar expression can be found for $\hat{F}_x^{(out)}$.

4.5 Decoherence due to probing

Here we will focus on the decoherence or loss caused by the interaction with the probe beam. The interaction induced decoherence is caused by scattering of photons on atoms. A scattering event involves the excitation of the atom by

absorption of a probe photon and a subsequent decay of the atom in conjunction with the re-emission of a photon [Loudon73]. The excitation follows the coherent interaction of the probe and the atomic sample and is thus included in the description of the interaction in sec. 4.3. On the other hand, the atomic decay and photon emission is a spontaneous process. For this reason, the treatment of the *spontaneous scattering* goes in parallel with the treatment of the interaction. Scattering processes are commonly described by a transition rate or a scattering cross-section. Since, the excitations are already expressed as a rate we will mainly use the former description. Given an excitation rate c.f. eq. (4.18), what remains is to determine the spontaneous decay channels and hence determine the effect on the pseudo-spin moments and correlation. It is particularly important to determine what decay channels result in elastic or inelastic scattering events. By elastic we mean that the atomic state following the excitation and subsequent spontaneous decay is the same as the initial state. What exactly is required for the state to qualify as being *the same* is something we will come back to. Elastic scattering does not require the spontaneously emitted photon to be in the same mode as the exciting photon, however by energy conservation it must have the same frequency and, thus, only the direction of propagation is left undetermined. Inelastic scattering refers to the opposite case where the final atomic state is not the same as the initial state. By the same token, the frequency of the emitted photon will differ from the incident photon by the energy difference between the initial and final atomic states. We note that, elastic scattering is sometimes termed *Raleigh scattering* and inelastic scattering *Raman scattering*.

Due to selection rules for photon light absorption and spontaneous decay we can usually predict the excitation and decay channels. Combining this with the resulting expectation values of the pseudo-spin moments we can compute eq. (3.35). For the moment we use a heuristic picture sketched on fig. 4.5 to

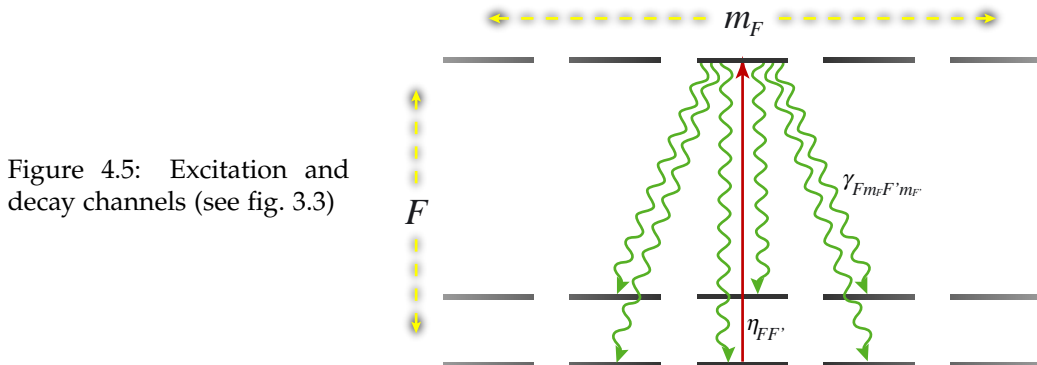


Figure 4.5: Excitation and decay channels (see fig. 3.3)

find the branching ratios of the various decay channels. Each ground level labelled by F and m_F can be excited to a range of excited hyperfine-manifolds F' . The excitation will only go to a specific magnetic sub-level m'_F of each excited hyperfine level determined by the polarisation of the probe light. The fraction of atoms excited through this channel is labelled $\eta_{F,F'}$. From the excited states there is a number of channels through which the atom is allowed decay. The decay rates are labelled by $\gamma_{F' m'_F, F'' m''_F}$ and from each excited level we can determine the branching ratios of the allowed channels as

$$r_{F' m'_F, F'' m''_F} = \gamma_{F' m'_F, F'' m''_F} / \sum_{F^*, m_{F^*}} \gamma_{F' m'_F, F^* m_{F^*}} \quad (4.31)$$

Hence the transition rate from an initial state $|F, m_F\rangle$ to a final state $|F'', m_{F''}\rangle$ is given by $\eta_{FF'} r_{F' m'_F, F'' m''_F}$, which can be computed from the data in tables D.4-D.10. If there are more than one excitation channel by which the atom can reach the

same final state the correct transition rates must be calculated by the Kramers-Heisenberg formula, which includes a sum over the coupling to all intermediate levels $|F', m_{F'}\rangle$. Fortunately, for the experimentally relevant parameters the Kramers-Heisenberg formula yields nearly the same results as what is achieved by summing the transition rates $\eta_{FF'} r_{F' m_{F'}, F'' m_{F''}}$ that share the same excited state $|F', m_{F'}\rangle$.

By summing over the two ground levels, the allowed excited manifolds and the possible magnetic sub-levels in both ground-levels we calculate the effect of the decay on the pseudo-spin components. The mean spin component transforms as

$$\langle \hat{f}_i^*(\mathbf{r}) \rangle = (1 - \eta) \langle \hat{f}_i(\mathbf{r}) \rangle + \sum_{F, F'} \eta_{FF'} \sum_{m_{F'}, m_{F''}} r_{F' m_{F'}, F'' m_{F''}} \langle \hat{f}_i^{(1)''} \rangle n_{\text{at}}(\mathbf{r}), \quad (4.32)$$

where the value of $\langle \hat{f}_i^{(1)''} \rangle$ is fully determined by F'' and $m_{F''}$. We recall that we invoke the first order approximation $e^{-\eta} \approx 1 - \eta$ for small η . One reason for making this approximation is to lighten the notation, but later when we express the spontaneous scattering as a sum of different contribution the 1st order approximation enables us to calculate analytical expressions. For the second moment the expression based on eq. (B.8) is somewhat more cumbersome

$$\begin{aligned} \langle \hat{f}_i^*(\mathbf{r})^2 \rangle &= (1 - \eta)^2 \langle \hat{f}_i(\mathbf{r})^2 \rangle + \eta(1 - \eta) \left\langle \left(\hat{f}_i^{(1)} \right)^2 \right\rangle n_{\text{at}}(\mathbf{r}) \\ &+ \sum_{F, F'} \eta_{FF'} \sum_{m_{F'}, m_{F''}} r_{F' m_{F'}, F'' m_{F''}} \left\langle \left(\hat{f}_i^{(1)''} \right)^2 \right\rangle n_{\text{at}}(\mathbf{r}) \\ &+ \sum_{F, F'} \sum_{F, F'} \eta_{FF'} \eta_{FF'} \sum_{m_{F'}, m_{F''}} \sum_{m_{F'}, m_{F''}} r_{F' m_{F'}, F'' m_{F''}} r_{F m_{F'}, F'' m_{F''}} \left\langle \hat{f}_i^{(1)''} \hat{f}_i^{(2)''} \right\rangle n_{\text{at}}(\mathbf{r})^2 \\ &+ (1 - \eta) \sum_{F, F'} \eta_{FF'} \sum_{m_{F'}, m_{F''}} r_{F' m_{F'}, F'' m_{F''}} \left\langle \hat{f}_i^{(1)} \hat{f}_i^{(2)''} \right\rangle 2n_{\text{at}}(\mathbf{r})^2, \end{aligned} \quad (4.33)$$

In most circumstances we may focus on a limited number of excitation and decay channels since many $\eta_{FF'}$ and $r_{F' m_{F'}, F'' m_{F''}}$ are zero or negligible.

Instead of including all the channels it may be possible to calculate the decay in terms of elastic (Rayleigh) and inelastic (Ramsey) scattering rates. Then the summation above can be reduced to a sum over the hyperfine changing scattering events and the hyperfine conserving events. In the latter case one has to argue that the final \hat{f}_z is the same as the initial because no information is gained about the \hat{f}_z of the individual atoms. For the inelastic events the appropriate terms must be calculated.

4.5.1 Experimental examples

In this section we seek to simplify the expression in eq. (B.16) by specifying particular coupling schemes that resemble the experimental conditions. This will allow us to reduce the number of terms in the equation and make it easier to plug in numbers when we need to get the final result. The first step is, however, to pin down the particular spin component that we want to investigate. We recall that the goal of this grand exercise is to obtain spin squeezing of the pseudo-spin and the only component that has a direct physical meaning is the population difference in the two level system. Thus we will direct our attention to \hat{f}_z . This entails that the pseudo spin be oriented on the equator of the Bloch sphere and the preceding investigation of the projection noise will have prepared the reader

for the fact that we pick an initial state with \hat{f}_y as the only component with non-zero expectation value.

As noted above, we need to distinguish elastic from inelastic scattering and to that end we must define in what cases the atom returns to its initial level. This appears to be a trivial exercise, since the atomic pseudo-spin was defined in the basis of the two clock-levels $|F = 4, m_F = 0\rangle$ and $|F = 3, m_F = 0\rangle$, only real transitions which take the atom to the same hyperfine level and magnetic sub-level will be elastic. Nevertheless, this strict definition does not capture one important feature of the state detection, that the probe can not distinguish between atoms populating different magnetic sub-levels. In other words, the probe laser line-width exceeds the combined magnetic sub-level splitting of a hyperfine level. Thus all sub-levels are coupled to the probe, though the coupling strengths are not the same for all sub-levels. Hence, it is to a certain extent possible to distinguish the sub-levels by their different coupling to the probe, but for the relevant sub-levels which have $|m_F| \leq 1$ the difference in the coupling strengths to linear probe light is only on the order of 1-2% for the mono-chromatic probing of the D-lines and typically 2-4% for the dichromatic probing depending on the detuning. In conclusion the $m_F = 0$ and ± 1 sub-levels remain effectively indistinguishable to the probe despite their differential coupling. Based on the above, we propose the term *quasi-elastic* scattering to describe the real transitions that preserve the hyperfine level of the atom i.e. $|F, m_F = 0\rangle \rightarrow |F, m_F = \{0, \pm 1\}\rangle$.

Effect of quasi-elastic and inelastic scattering

In order for the distinction between (quasi-)elastic and inelastic scattering to be of any use, we must investigate the difference in their effect on the pseudo-spin components initially focusing on \hat{f}_z . Much of this examination hinges on the principle information leakage and especially the fact that a scattering event may not reveal anything about certain atomic operators.

We first sort out the inelastic scattering events. In this case an atom starting in the ground state $|4, 0\rangle$ ($|3, 0\rangle$) ends up in the other hyperfine ground state $|3, \{0, \pm 1\}\rangle$ ($|4, \{0, \pm 1\}\rangle$) and the spontaneously emitted photon has the frequency $\omega_s = \omega + \omega_0$ ($\omega - \omega_0$), where ω is the frequency of the incident photon and ω_0 is the hyperfine splitting of the ground levels. From ω_s it is then possible to infer the excitation and decay channels, which in turn projects the final state on to one of the ground levels. Thus if the initial atomic state was a superposition state $(|4, 0\rangle + i|3, 0\rangle)/\sqrt{2}$ the final state would either $|4, \{0, \pm 1\}\rangle$ or $|3, \{0, \pm 1\}\rangle$ depending on ω_s . Thus, any correlation of the scattering atom with other atoms is lost and the final state is completely uncorrelated with other atoms.

It is important to note that since we deal with collective variables for the atoms and the photons a scattering event cannot be pinned down to a specific atom – there is no straight forward way to tell which atom scattered the photon.⁵ Therefore, the decoherence is effectively distributed over the whole ensemble which is only minimally affected by the single inelastic scattering event. This robustness the decoherence is one of the advantages of systems that are expressed as collective operators.

Now we turn to the case of a photon being scattered elastically off an atom whereby the spontaneously emitted photon will have exactly the same frequency

⁵to determine the position of the scattering atom one would have to detect the spontaneously emitted light e.g. by a CCD camera at the resolution of the inter-atomic separation $\approx 1\mu\text{m}$. If the scattering atom were detected it is likely that this would also reveal ω_s , in which case the information on the projection of \hat{f}_z would not be lost.

as the incoming photon. This holds irrespectively of which transition the incoming photon was actually absorbed on. Hence, even if the scattering event caused the atom to be excited and spontaneously decay, there is no way to tell from the emitted photon which transition was excited. We take a practical example of an atom in a coherent superposition $(|4, m_F\rangle + i|3, m_F\rangle)/\sqrt{2}$ excited by probe photons of frequency ω near resonance with the D1-line.⁶ A probe photon may be absorbed for the atom to make the transition $|4, m_F\rangle \rightarrow |3', m'_F\rangle$ or $|3, m_F\rangle \rightarrow |4', m'_F\rangle$, however since both transitions involve the absorption photon with the same frequency there is no way to determine which excited state the atom is taken to. As a result, the excited state is also a superposition $(|3', m'_F\rangle + i|4', m'_F\rangle)/\sqrt{2}$. By spontaneous emission of a photon with frequency ω the atoms relaxes to the ground levels, but since the photon still does not disclose any knowledge about the decay channel the atom returns to its initial state i.e. the coherent superposition $(|4, m'_F\rangle + e^{i\phi}|3, m'_F\rangle)/\sqrt{2}$, albeit with a random phase ϕ . Since the final and identical states are identical, any correlation of the scattering atom with other atoms is preserved meaning that elastic scattering does not degrade the noise reduction imparted by a QND measurement. In quasi-elastic scattering events where the final state is in the $m'_F = \pm 1$ level, the polarisation of the emitted photon will give away the final magnetic sub-level but not the hyperfine level. Because of this, quasi-elastic scattering does also not perturb \hat{f}_z . For the dichromatic probing the pictures becomes slightly more elaborate as we shall see shortly below.

As argued above the central task is to determine the transition rates for quasi-elastic and inelastic scattering rather than keeping track of the transition rates for all individual real-transition channels. Whether a real-transition is quasi-elastic or inelastic is solely determined by the initial and final hyperfine states i.e. by F and F'' in eqs. (B.15 and B.16). Thus we compress the expressions by summing over all transition rates with shared initial and final hyperfine states

$$\eta_{F, F''} = \sum_{F'} \sum_{m''_F} \eta_{FF'} r_{F'm'_F, F''m''_F} \quad (4.34)$$

We also introduce quasi-elastic and inelastic scattering rates as $\eta_{\text{qel}} = \sum_F \eta_{FF}$ and $\eta_{\text{inel}} = \sum_{F \neq F''} \eta_{FF''}$ respectively. This allows us to simplify eq. (B.15) to

$$\langle \hat{f}_z^*(\mathbf{r}) \rangle = (1 - \eta_{\text{inel}}) \langle \hat{f}_z(\mathbf{r}) \rangle + \sum_{F \neq F''} \langle \hat{f}_z^{(1)''} \rangle n_{\text{at}}(\mathbf{r}), \quad (4.35)$$

which shows that only inelastic scattering affects the \hat{f}_z expectation value. The expectation value $\langle \hat{f}_z(\mathbf{r}) \rangle$ following a QND measurement depends on the measurement outcome c.f. eq. (5.10), wherefore we cannot specify a value for it in the above equation. Of course we can approximate it to be zero as for the initial equal superposition state. We will use this approximation below as we plot the theoretical curves for $\langle \hat{f}_z^*(\mathbf{r}) \rangle$.

From eq. (B.16) together with the above discussion we gain an even larger simplification of the second moment

$$\begin{aligned} \langle \hat{f}_z^*(\mathbf{r})^2 \rangle &= (1 - (1 - \varepsilon)(1 - \eta_{\text{inel}})^2) \frac{n_{\text{at}}(\mathbf{r})}{4} \\ &+ \sum_{F \neq F''} \sum_{F^0 \neq F''^0} \eta_{F, F''} \eta_{F^0 F''^0} \langle \hat{f}_z^{(1)''} \hat{f}_z^{(2)''} \rangle n_{\text{at}}(\mathbf{r})^2, \end{aligned} \quad (4.36)$$

⁶The D2-line behaves similarly, but since it involves four possible excitation channels the treatment is unnecessarily complicated to make a good example.

where ε is a possible noise reduction of the initial state w.r.t. the projection noise level. We neglect contributions from the terms $\eta_{F(F'' \neq F)} \langle \hat{f}_z^{(1)} \hat{f}_z^{(2)''} \rangle$ in that we firstly note that $\hat{f}_z^{(1)}$ and $\hat{f}_z^{(2)''}$ are uncorrelated and in that case we approximate the input state with the initial equal superposition.⁷ Without hesitation we combine eqs. (4.35 and 4.36) to evaluate the variance

$$\langle (\Delta \hat{f}_z^*(\mathbf{r}))^2 \rangle = (1 - (1 - \varepsilon)(1 - \eta_{\text{inel}})^2) \frac{n_{\text{at}}(\mathbf{r})}{4}. \quad (4.37)$$

This result relies on the mutual cancellation of the sum terms in $\langle \hat{f}_z^*(\mathbf{r}) \rangle^2$ and $\langle \hat{f}_z^*(\mathbf{r})^2 \rangle$ ⁸ as can be verified by inserting all possible combinations of F and F'' . It also requires setting the initial \hat{f}_z mean value to zero. This simplification is concurs with the earlier approximation of setting $\eta_{F(F'' \neq F)} \langle \hat{f}_z^{(1)} \hat{f}_z^{(2)''} \rangle = 0$. This restriction does not influence the prediction of the variance, since $\langle \hat{f}_z \rangle$ can always be set to zero by performing a classical rotation (see sec. 10.2.1) around the x -axis by the angle derived from the QND measurement outcome c.f. eq. (5.10).⁹ The implications of eq. (4.37) agree well with what we anticipated. Firstly, only the inelastic scattering causes a degradation of the noise reduction. Secondly, for input states with $\varepsilon \leq 1$ the noise never exceeds the SQL and in the case of $\varepsilon = 1$ the scattering has no effect. Hence, scattering on a product state does not increase the noise as we already saw in eq. (B.11). All that remains is to get some values for η_{qel} and η_{inel} . These depend on the atomic level structure and the probe detuning and intensity. In the next sections we will illustrate the cases of the D1-line and D2-line, respectively. To that end, we plot the branching of excitations resulting in quasi-elastic and inelastic scattering, the output $\langle \hat{f}_z^* \rangle$, and the output variance $\langle (\Delta \hat{f}_z^*)^2 \rangle$.

Cs D1-line with one probe

On the D1-line the probe couples each hyperfine ground state to only one excited level as opposed to two for the D2-line. From each excited state there are five decay channels three of which return the atom to the same hyperfine while two take it to another hyperfine ground level. From the decay rates and coupling constants we compute the quasi-elastic and inelastic decay rates and plot these normalised to the total excitation rate as a function of the probe detuning. For the

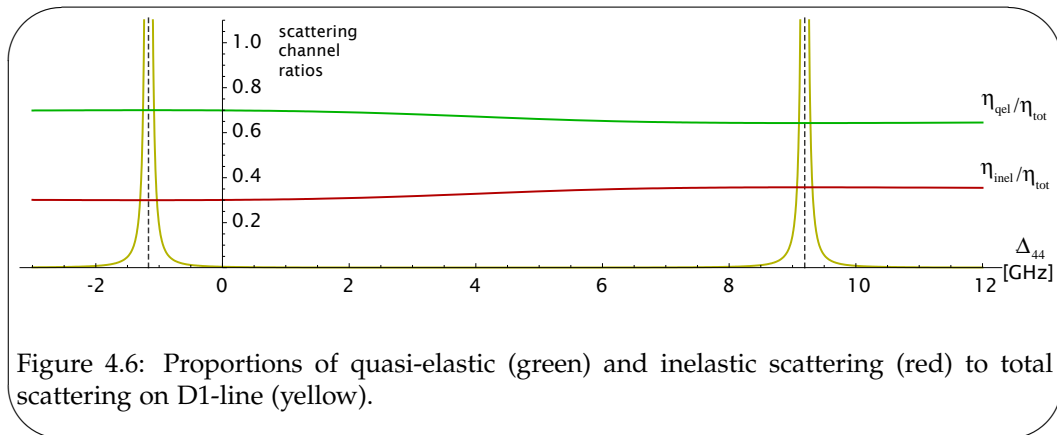


Figure 4.6: Proportions of quasi-elastic (green) and inelastic scattering (red) to total scattering on D1-line (yellow).

probe on resonance with either the $|4, m_F\rangle \rightarrow |3', m'_F\rangle$ or $|3, m_F\rangle \rightarrow |4', m'_F\rangle$ the

⁷then we get $\langle \hat{f}_z^{(1)} \hat{f}_z^{(2)''} \rangle \propto (\frac{1}{2} - \frac{1}{2})(\pm \frac{1}{2}) = 0$

⁸by which we mean $\sum_{F \neq F''} \sum_{F^0 \neq F''} \eta_{F, F''} \eta_{F^0, F''} \langle \hat{f}_z^{(1)''} \hat{f}_z^{(2)''} \rangle - (\sum_{F \neq F''} \langle \hat{f}_z^{(1)''} \rangle n_{\text{at}}(\mathbf{r}))^2$

⁹The author strongly believes that if the excluded terms were instead retained they would cancel each other, anyway.

ratio $\eta_{\text{qel}}/\eta_{\text{inel}}$ is given almost exclusively by the branching ratio of the respective excited level i.e. $7/3(= 2.33)$ and $9/5(= 1.8)$, respectively. Since, these are not vastly different the ratio does not vary much for probe detunings over the entire D1-line. In the limit of $|\Delta| \gg \omega_0$ the ratio $\eta_{\text{qel}}/\eta_{\text{inel}} \rightarrow 66/31 \approx 2$ which is the average of the ratio of the elastic to inelastic decay probabilities for the whole D1-line.

In sec. 5.2.2 we accentuate that the QND measurement strength was proportional to the total excitation rate η , which for constant photon number is strongly peaked around the transition frequencies. As, we wish to examine the influence of scattering on the pseudo-spin under constant "QND conditions" the below curves of $\langle \hat{f}_z^* \rangle$ and $\langle (\Delta \hat{f}_z^*)^2 \rangle$ are plotted with the photon number varied so as to hold η constant. To moderately exaggerate the curves we hold $\eta = 1$. First,

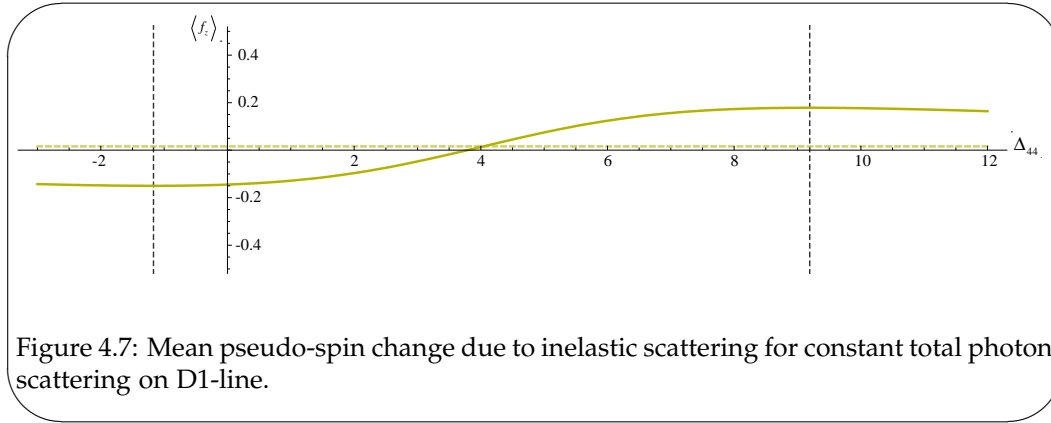


Figure 4.7: Mean pseudo-spin change due to inelastic scattering for constant total photon scattering on D1-line.

we examine the change in the pseudo-spin z-component, which can be seen as optical pumping by the probe. Thus, $\langle \hat{f}_z^* \rangle$ depends on the ratio of inelastic scattering from the two ground levels. When the probe is near resonant with the $|4, m_F\rangle \rightarrow |3', m'_F\rangle$ transition the excitation predominantly occurs on this transition and thus the inelastic scattering tends to depopulate the $F = 4$ ground level causing $\langle \hat{f}_z^* \rangle < 0$. Near resonance with the $|3, m_F\rangle \rightarrow |4', m'_F\rangle$ transition the probe induces the opposite effect. Achieving, $\langle \hat{f}_z^* \rangle = 0$ is only possible when the probe is detuned about halfway between the two allowed transitions. For large detunings the pseudo-spin change is proportional to the ratio of the inelastic scattering rates from the two excited states $\eta_{\text{inel},34}/\eta_{\text{inel},43} = 5/3$.

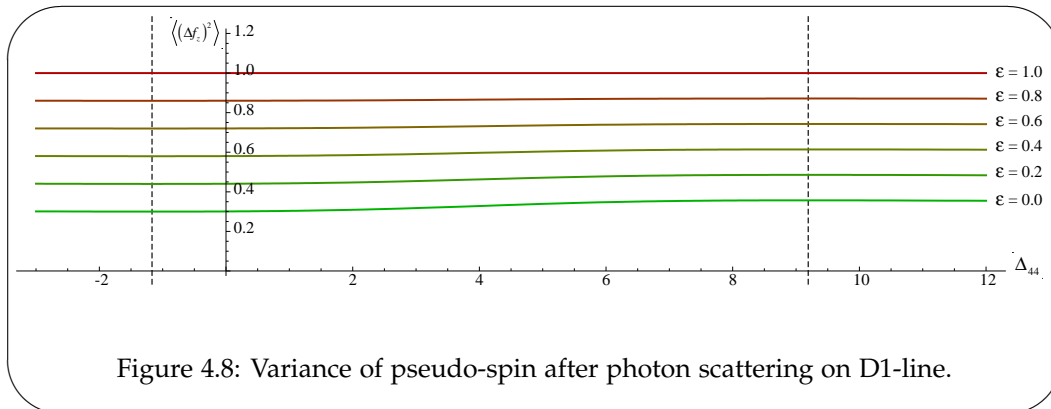


Figure 4.8: Variance of pseudo-spin after photon scattering on D1-line.

Next we look at the variance following decoherence of an input state with various degrees of QND-measurement induced noise-reduction ϵ . Since, we fix η one can imagine the different ϵ to arise from different optical densities of the atomic sample. We observe that the lower the input noise the larger is the noise increase due to scattering. For input noise at the SQL decoherence has no effect.

The noise increase is slightly lower at the $4 \rightarrow 3'$ transition than the $3 \rightarrow 4'$ due to the more favourable ratio of $\eta_{\text{qel}}/\eta_{\text{inel}}$ (fig. 4.6).

Cs D2-line with one probe

To take a positive stance this is a very rich system. The probe can excite an atom from either ground state to two excited levels and from each of these there are either 3 or 5 decay channels producing a total sum of 16 decay channels. Of particular interest, will be the quasi-cycling transitions $4 \rightarrow 5'$ and $3 \rightarrow 2'$ on which an excited atom can only decay back to the same hyperfine ground level. On the D2-line, the ratios of quasi-elastic and inelastic scattering to the total scat-

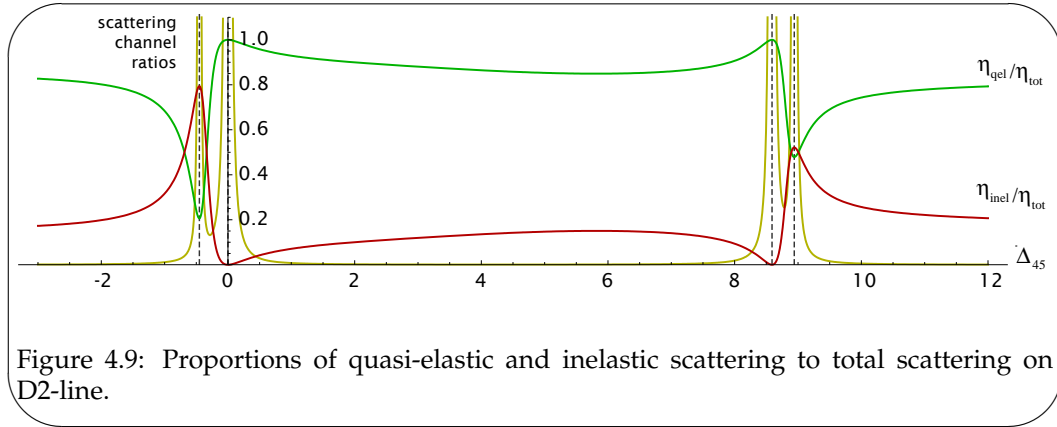


Figure 4.9: Proportions of quasi-elastic and inelastic scattering to total scattering on D2-line.

tering rate exhibit some very sharp features as compared with the D1-line case. The most noteworthy feature is that at two detunings we get $\eta_{\text{qel}}/\eta \approx 1$ and thus $\eta_{\text{inel}}/\eta \approx 0$. These detunings correspond to the probe being on resonance with the quasi-cycling transitions, which consequently are the dominant excitation channels. Hence, for probe frequencies in the vicinity of the quasi-cycling transitions we obtain a favourable ratio $\eta_{\text{qel}}/\eta_{\text{inel}} \gg 1$. Oppositely, near the two remaining transitions the inelastic scattering rate predominates. For $|\Delta| \gg \omega_0$ the ratio $\eta_{\text{qel}}/\eta_{\text{inel}} \rightarrow 7497/1889 \approx 4$, which is somewhat better than that of the D1-line.

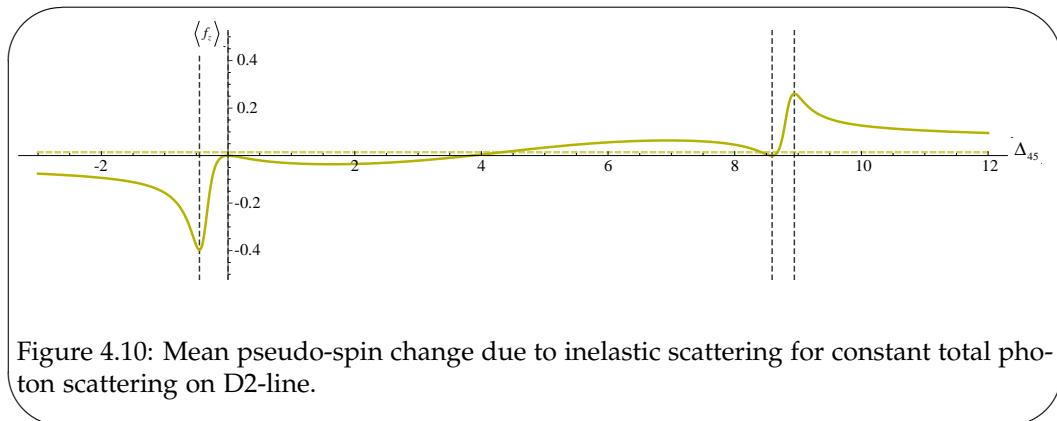
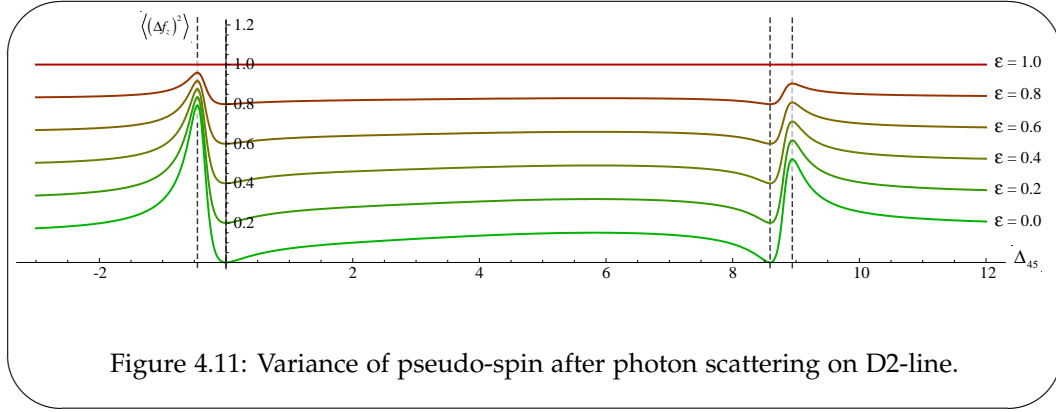


Figure 4.10: Mean pseudo-spin change due to inelastic scattering for constant total photon scattering on D2-line.

The lively detuning dependence of the scattering rates carries over to the pseudo-spin expectation values. Since on the quasi-cycling transitions the scattering is almost exclusively quasi-elastic, $\langle \hat{f}_z \rangle$ does not experience any change and thus remains at 0. As for the D1-line $\langle \hat{f}_z^* \rangle = 0$ is also achieved for a probe detuning about half way between the hyperfine ground-levels where inelastic scattering rates from each ground level are equal. The largest $\langle \hat{f}_z^* \rangle$ change happens when the probe is resonant with the two non-quasi-cycling transitions. In the limit of large detunings $\langle \hat{f}_z^* \rangle \rightarrow \eta_{\text{inel},34}/\eta_{\text{inel},43} = 66/91$.



Finally, we plot the curves for $\langle(\Delta f_z^*)^2\rangle$ for the probe frequency tuned over the D2-line. Because, for probe frequencies on resonance with the quasi-cycling transition, almost all scattering is elastic the variance does not experience any increase. In contrast, probe frequencies near the two other transitions cause a great deal of noise increase and thus degradation of the QND-measurement. Besides, these special frequencies near the transitions, the probing on the D2-line causes a noise increase that overall is smaller than that of the D1-line. This is a direct consequence of the larger $\eta_{\text{qel}}/\eta_{\text{inel}}$ ratio for the D2-line as a whole.

Now we have investigated how squeezing and atomic correlation are affected by decoherence, and even before that we developed the scales by which we measure the degree of squeezing. Yet, we have not seen how correlation and squeezing might at all appear in the atomic ensemble. This short coming will be thoroughly amended by the following sections. This can be taken as an encouragement or a threat depending on ones disposition.

QND measurements and squeezing

5.1 QND measurements

Up till this point we have loosely used the term QND, implicitly assuming some common understanding of what it means. Obviously, QND implies that a target system is measured by *some amount* of interaction and that this does not in *some sense* disturb the quantum state of the target system. On the other hand, any interaction will leave the quantum state affected in some way, so it is essential that we specify exactly in *what sense* the interaction must be non-destructive in order to be awarded the distinction of QND. Before stating any definition let us attempt to motivate it by an example.

A, by now, standard example is that of the position \hat{x} and momentum \hat{p} of a target system comprising a single particle. The expectation values and variances of these operators can both be deduced from the particle's wave-function. They fulfil the, so called, canonical commutation relation $[\hat{x}, \hat{p}] = i\hbar$. Thus, the uncertainty product is limited by a constant value $\langle(\Delta\hat{x})^2\rangle\langle(\Delta\hat{p})^2\rangle \geq \hbar^2/4$. The time evolution of the particle is described by $\hat{x} = (i\hbar)^{-1} [\hat{x}, \hat{\mathcal{H}}_{\text{free}}] = \hat{p}/m$. If there is no external influence on the particle \hat{p} is a constant of motion¹ and we are allowed to write $\hat{x}(t) = \hat{x}_0 + \hat{p}t/m$. Now we apply a QND interaction which measures one of the observables and thereby determine its value with some precision, resulting in a reduction of its variance. Say, one chooses \hat{x} as the target variable and measure it without destroying the particle. The variance of \hat{x} is then reduced by ε so that $\langle(\Delta\hat{x}'_0)^2\rangle = \varepsilon\langle(\Delta\hat{x}_0)^2\rangle$, then from the uncertainty relation the variance of the momentum is at least $\langle(\Delta\hat{p}')^2\rangle \geq \langle(\Delta\hat{p}_0)^2\rangle/\varepsilon$. This is all fine, but a problem arises if we look at the position after some time $\langle(\Delta\hat{x}'(t))^2\rangle \geq \varepsilon\langle(\Delta(\hat{x}'_0 + \hat{p}_0t/m))^2\rangle = \varepsilon\langle(\Delta\hat{x}_0)^2\rangle + \langle(\Delta\hat{p}_0)^2\rangle t/(\varepsilon m) \geq \varepsilon\langle(\Delta\hat{x}_0)^2\rangle + \hbar^2 t/(4\varepsilon m\langle(\Delta\hat{x}_0)^2\rangle)$. This shows that even though we initially pinned down the particles position this information quickly becomes useless because the particle moves and it even does so more unpredictably than before the measurement. The time it takes for the variance of a particle's position after a QND measurement to exceed that of the non-measured particle is $t = \varepsilon 4m\langle(\Delta x_0)^2\rangle^2/\hbar^2$, which naturally depends on the initial variance $\langle(\Delta x_0)^2\rangle^2$ and in relation to this the time is proportional to the noise reduction i.e. the smaller ε the shorter the time until the position measurement is scrambled by the particle's movement. If on the other hand we had measured \hat{p} and recorded some value we would reduce

¹Expressed otherwise $[\hat{p}, \hat{\mathcal{H}}_{\text{free}}] = [\hat{p}, \hat{p}^2/2m] = 0$

its variance $\hat{p}' = \varepsilon\hat{p}$. Even if the particle's position becomes more uncertain this would not influence \hat{p} and thus not compromise the credibility of the measured value. The key here is that \hat{p} is a constant of motion, which means that it commutes with the Hamiltonian for the free evolution or non-interacting system. In this example we have not specified how to measure the system, but in general this is done by an indirect measurement [Neumann32] where the target system interacts with a quantum meter system, which thence acquires some information about the target variable. By a subsequent classical measurement of the meter system the recorded information about the meter variable can be harnessed.

Inspired by the above example we can construct requirements for a measurement to be QND. A sufficient though not strictly necessary requirement for a variable of a target \hat{o}_T and a meter \hat{o}_M system to comprise a QND interaction is that the target variable commute with the time evolution operator of the combined system $\hat{U}_{M+T}(t)$. This is clearly satisfied if the following two conditions are simultaneously met

- The target variable commutes with the interaction Hamiltonian

$$[\hat{o}_T, \hat{\mathcal{H}}_{\text{int}}] = 0 \quad (5.1)$$

- The target variable commutes with the free evolution Hamiltonian

$$[\hat{o}_T, \hat{\mathcal{H}}_0] = 0 \quad (5.2)$$

The simplest form of interaction Hamiltonian fulfilling eq. (5.1) and coupling the system and meter variables is of the form

$$\hat{\mathcal{H}}_{\text{QND}} = \mathcal{K}\hat{o}_M\hat{o}_T \quad (5.3)$$

where \mathcal{K} is the characteristic coupling constant of the interaction. The above conditions are surely appropriate to gauge whether or not an interaction deserves to be designated as QND, but it does not question what the effect of the interaction should be on the meter nor establish any figures of merit for the QND interaction. Indeed, the easiest approach to meet them is to identify a variable that is a constant of motion and then do nothing. This evidently is not in the spirit of what QND is meant to describe. As a result, one must include some measures for the usefulness of the measurement in establishing some knowledge about the target system. A possible set of measures has been suggested [Holland90, Poizat94] as

Measurement efficiency – The degree of correlation between the meter and the value of the target variable prior to the interaction

Degree of non-demolition – The degree of correlation between the value of the target variable before and after the interaction

Quantum state preparation ability – The degree of correlation between the meter and the value of the target variable after the interaction

The commutation based QND criteria eqs. (5.1 and 5.2) are mainly concerned with the second measure i.e. ensuring that the interaction does not cause excessive disturbance of the target system. The first measure obviously rules out the *do nothing* approach since that will not enable any prediction of the target variable. The third measure is to a large extent a merger of the preceding two. It seeks to establish the extent to which the information gained by detection of

the meter variable reveal the value of target variable after the interaction. Hence a fully destructive measurement would not contradict the first measure, but because it violates the second the it also fails to fulfil the third measure. The idea of spin squeezing by QND measurement is very much an embodiment of the the third measure, in that an SSS, having a reduced variance of the target variable, is also closer to being in a well-defined eigen-state of the target variable.

5.1.1 Squeezing by QND measurements

The requirements for a QND measurement are to a large extent similar to those for creating a squeezed state.² By performing a QND of the target operator one partially projects the state on to an eigen-state of the operator that is compatible with the measurement outcome. An eigen-state by nature yields a uniquely specified value when measured in the basis of the same operator, thus it is intuitively clear that a partial projection will result in a more certain prediction of a subsequent measurement outcome. This reduction of the quantum measurement uncertainty is exactly the essence of a squeezed state (sec. 3.5). It turns out that a complete projection is not really interesting in squeezing circles since the resulting complete randomisation of the conjugate variable inevitably disturbs the system beyond the point where it is useful for applications.

We will illustrate the effect of the Generic QND interaction eq. (5.3) on the coupled system using basic concepts from *classical* probability theory of conditional probability distributions. Actually, the conditioning is not due to the QND Hamiltonian itself, but due to the subsequent measurement of the light system revealing some value. To link this discussion to the variables discussed in other chapters we let the QND Hamiltonian be of the form $\hbar\mathcal{K}\hat{s}_z\hat{f}_z$ where it couples atomic and photonic pseudo-spins. We further specialise to the case where the spin is aligned along one of the components — we pick \hat{f}_y . We will not demand that $\langle\hat{f}_z\rangle$ and $\langle\hat{f}_x\rangle$ are exactly zero, however the preceding assumption dictates that they be rather small compared to n_{at} . We make a similar requirement for the photon pseudo-spin whereby we get

$$\hat{s}_z^{(\text{out})} = \hat{s}_z^{(\text{in})}, \quad \hat{s}_x^{(\text{out})} = \hat{s}_x^{(\text{in})} + \mathcal{K}\hat{s}_y\hat{f}_z^{(\text{in})}t_a \quad (5.4)$$

$$\hat{f}_z^{(\text{out})} = \hat{f}_z^{(\text{in})}, \quad \hat{f}_x^{(\text{out})} = \hat{f}_x^{(\text{in})} + \mathcal{K}\hat{f}_y\hat{s}_z^{(\text{in})}t_p \quad (5.5)$$

Since \hat{f}_y and \hat{s}_y are large we take them to be equal to their mean values $f_y \equiv \langle\hat{f}_y\rangle = n_{\text{at}}/2$ and $s_y \equiv \langle\hat{s}_y\rangle = n_{\text{ph}}/2$. As required for a QND measurement \hat{f}_z is unchanged. At this point, it is advantageous to complicate the description slightly. The above equations are asymmetric as they contain either $t_a = l_a/c$ and $t_p = l_p/c$, that under normal circumstances are not the same. A straightforward solution is to multiply the top equation by l_p and the bottom one by l_a and introduce the operators $\hat{f}_i \equiv \hat{f}_i l_a$ and $\hat{s}_i \equiv \hat{s}_i l_p$ so that

$$\hat{s}_z^{(\text{out})} = \hat{s}_z^{(\text{in})}, \quad \hat{s}_x^{(\text{out})} = \hat{s}_x^{(\text{in})} + \frac{\mathcal{K}}{c}\hat{s}_y\hat{f}_z^{(\text{in})} \quad (5.6)$$

$$\hat{f}_z^{(\text{out})} = \hat{f}_z^{(\text{in})}, \quad \hat{f}_x^{(\text{out})} = \hat{f}_x^{(\text{in})} + \frac{\mathcal{K}}{c}\hat{f}_y\hat{s}_z^{(\text{in})}. \quad (5.7)$$

The operators \hat{f}_i and \hat{s}_i represent the column atom and photon number respectively. Now all equations are made up of the product of the atomic and photonic operators multiplied by their respective spatial extent along the z-axis. How,

²which is not the same as saying that the creation of a squeezed state requires QND measurements.

then, do these expressions bestow us any advantages? Firstly, our measurements are not continuous, but pulsed. The signal acquired from the measurement is that of the whole duration of the probe pulse.³ It, thus, makes perfect sense to include the whole column photon density of the probe pulse. We may still leave out the transverse probe intensity distribution as concentrate on the local transverse intensity as it would be possible to block all but a small part of the probe beam and detect only this. As for the atomic operators, the probe interacts with all atoms at the corresponding x, y along the z -axis. From the detected probe signal there is no way to deduce how atoms at different z -coordinates contributed to the signal.⁴ Therefore, it only makes sense to consider the entire column density of the atoms in the sample. Since, \hat{f}_i and \hat{s}_i describe column density operators we must also treat the variances accordingly e.g. $\langle(\Delta\hat{f}_i)^2\rangle = \langle(\Delta\hat{f}_i)^2\rangle_{l_a}$ and *not* $\langle(\Delta\hat{f}_i)^2\rangle_{l_a}^2$. If this is not convincing we refer to the derivation of eq. (3.26) as well as the rigorous explanation in sec. B.

We need to decide which \hat{s} component to measure. It makes little sense to measure \hat{s}_z since it is also constant, thus we measure $\hat{s}_x^{(out)}$ which yields some value x_s . Now we can compute the moments of the atomic pseudo-spins conditioned upon the measurement of \hat{s}_x . These are given by [Hammerer09]

$$\begin{aligned} \langle\hat{f}_i^{(out)}\rangle|_{\{\hat{s}_x^{(out)}=x_s\}} &= \langle\hat{f}_i^{(out)}\rangle - \frac{\langle\hat{f}_i^{(out)}\hat{s}_x^{(out)}\rangle}{\langle(\hat{s}_x^{(out)})^2\rangle} x_s \\ \langle(\Delta\hat{f}_i^{(out)})^2\rangle|_{\{\hat{s}_x^{(out)}=x_s\}} &= \langle(\Delta\hat{f}_i^{(out)})^2\rangle - \frac{\langle\hat{f}_i^{(out)}\hat{s}_x^{(out)}\rangle^2}{\langle(\hat{s}_x^{(out)})^2\rangle}, \end{aligned}$$

where $|_{\{\hat{s}_x^{(out)}=x_s\}}$ denotes that the preceding expression is conditioned upon the measurement outcome of \hat{s}_x . The mean values and variances are thus computed by inserting the output terms of eq. (5.6). The term $\langle(\hat{s}_x^{(out)})^2\rangle$ appears in all the expressions and we find it to be

$$\langle(\hat{s}_x^{(out)})^2\rangle = \frac{n_{ph}}{4} + \frac{\mathcal{K}^2 (n_{ph})^2 n_{at}}{c^2 \cdot 4 \cdot 4} = (1 + \kappa^2) \frac{n_{ph}}{4},$$

where we introduced the compound coupling constant $\kappa^2 = \mathcal{K}^2 n_{ph} n_{at} / (4c^2)$. If we take $\langle\hat{s}_x^{(in)}\rangle = 0$ ⁵ then the noise in the detected meter variable is $\langle(\Delta\hat{s}_x^{(out)})^2\rangle = (1 + \kappa^2) \frac{n_{ph}}{4}$, where the first term is the shot noise and the second term comes from the phase-fluctuations introduced by the projection noise of the atomic target variable. The SNR of the measurement, understood as the projection noise imprint divided by the shot noise (see sec. 2.3), becomes

$$SNR = \kappa^2, \quad (5.8)$$

which means that the compound coupling constant can be found by observing the ratio of the projection noise imprint to shot noise in the detected output signal. This gives us a simple and direct access to the coupling constant.

³we do in fact have some temporal resolution of the recorded probe signal and the total pulse signal is only reached after digitally integrating up the signal. Thus, one could imagine dividing a pulse into segments and considering these as individual pulses. Nevertheless, the detector bandwidth always sets a lower limit to the temporal resolution and it makes no sense to talk about a signal on a time-scale shorter than this. The bottom line is that for our description it is practical though not strictly required to integrate over the whole pulse duration.

⁴this principle is strictly true

⁵we earlier already required it to be small

Based on the above, we first compute the conditioned mean values of the atomic pseudo-spin components

$$\langle \hat{f}_x^{(out)} \rangle |_{\{\hat{s}_x^{(out)}=x_s\}} = \langle \hat{f}_x^{(in)} \rangle + \kappa \sqrt{\frac{n_{at}}{n_{ph}}} \langle \hat{s}_z^{(in)} \rangle \quad (5.9)$$

$$\langle \hat{f}_z^{(out)} \rangle |_{\{\hat{s}_x^{(out)}=x_s\}} = \langle \hat{f}_z^{(in)} \rangle - \frac{\kappa}{1 + \kappa^2} \sqrt{\frac{n_{at}}{n_{ph}}} x_s \quad (5.10)$$

The mean value of \hat{f}_x is affected solely by the interaction itself and not by the measurement result. Thus if for the generic QND interaction we have $\langle \hat{s}_z \rangle = 0$ then the mean of \hat{f}_x does not change. In sec. 5.2 we will elaborate on how to ensure that the interaction leaves \hat{f}_x unaffected. The z -component's expectation value is on the contrary unaffected by the interaction itself but *does* change based upon the measurement result. This was expected since the detected meter variable carries information about the value of \hat{s}_z , the result should also influence our prediction of its mean value. Next step is to deduce the variances conditioned on the measurement result.

$$\begin{aligned} \langle (\Delta \hat{f}_x^{(out)})^2 \rangle |_{\{\hat{s}_x^{(out)}=x_s\}} &= \langle (\Delta \hat{f}_x^{(in)})^2 \rangle + \kappa^2 \frac{n_{at}}{n_{ph}} \langle (\Delta \hat{s}_z^{(in)})^2 \rangle \\ &= (1 + \kappa^2) \frac{n_{at}}{4} \end{aligned} \quad (5.11)$$

$$\begin{aligned} \langle (\Delta \hat{f}_z^{(out)})^2 \rangle |_{\{\hat{s}_x^{(out)}=x_s\}} &= \frac{\langle (\Delta \hat{f}_z^{(in)})^2 \rangle + \kappa^2 \left(\langle (\Delta \hat{f}_z^{(in)})^2 \rangle - \frac{n_{at}}{4} \right)}{1 + \kappa^2} \\ &= \frac{1}{1 + \kappa^2} \frac{n_{at}}{4} \end{aligned} \quad (5.12)$$

To reach the final simple form, we have taken $\langle (\Delta \hat{s}_z^{(in)})^2 \rangle = n_{ph}/4$ as well as $\langle (\Delta \hat{f}_x^{(in)})^2 \rangle = \langle (\Delta \hat{f}_z^{(in)})^2 \rangle = n_{at}/4$, in agreement with the initial assumption about the pseudo-spin y -orientations. The above set of equations confirms that the generic QND interaction followed by destructive detection of the meter system does produce a target system state which has a reduced uncertainty of the target variable as compared to the SQL. In return the noise in the conjugate target variable is above the SQL. It is equally interesting that the post-detection uncertainty product remains at $\langle (\Delta \hat{f}_x^{(out)})^2 \rangle \langle (\Delta \hat{f}_z^{(out)})^2 \rangle |_{\{\hat{s}_x^{(out)}=x_s\}} = (n_{at})^2/16$ ratifying that the target system continues to be in a minimal uncertainty state. A profound observation is that the additional back-action noise on \hat{f}_x arises from the actual QND interaction, whereas the noise reduction of \hat{f}_z only comes about when the conditional term from the measurement is included. This is similar to what was found for the expectation values and underlines that generation of a SSS requires both an interaction to entangle the target with the meter as well as a subsequent precise detection of the meter variable. These roughly correspond to the. In essence the strong coupling and quantum noise-limited detection are two independent experimental objectives for a setup. A third practical objective relates to the non-demolition character, that is closely tied to the strong coupling requirement.

In sec. 5.2.1 we give a supplementary derivation of the QND measurement induced noise reduction, that is based on the full probability distribution of the coupled operators. A third approach on the derivation due to [Zoller03], that involves the Schrödinger picture evolution of the wave-function caused by the QND interaction and the tracing out of photonic system caused by the measurement. Though it may appear as an overkill to provide this range of distinct

derivations of the same result, there are, nevertheless, two clear aims of this. Firstly, it varies from person to person, which derivation is found to be the most enlightening. Hence, the ample supply of derivations should be seen as a way to cater to readers' individual preferences. Secondly, the form of the noise reduction eq. (5.12) is often stated and applied, yet there seems to have been some confusion as to its origin and validation. Hence, this is a deliberate attempt to collect thorough treatments of a number of approaches to disclose this form.

Experimental context Experimentally the verification of QND measurements discussed in the previous section are somewhat linked to proving squeezing. As the meter measurement outcome is correlated with the expectation value of the squeezed target variable so any subsequent meter measurement of the target value will be correlated with the initial *squeezing* measurement outcome. What limits this correlation of the subsequent meter measurement outcomes is the noise of the meter itself. For the *squeezing* measurement the fact that the QND interaction has to partially leave intact the target state limits how precise the measurement can be. Essentially, this is because high precision is a result of stronger coupling which entails greater destruction of the target state. For subsequent *squeezing verification* measurements there is no restriction on the target state destruction and one can thus increase the measurement precision whereby the relative correlation of this measurement with the squeezing measurement is strengthened. These considerations form the basis of the data analysis described in sec. 12.2.1.

5.2 Atom light interaction and QND measurement squeezing

We have yet to substantiate our claim that we actually realise a QND interaction let alone are able to squeeze anything with the atom-light interaction described in chapt. 4. By the end of this section we hope to have convinced all but the most sceptical readers that we are in fact able, at least in theory, to do both. To achieve this we will investigate our interaction Hamiltonian in light of the QND criteria of the above section and in parallel trace out the rationale behind our choice of QND target and meter variables.

When one compares the generic QND Hamiltonian eq. (5.3) with the interaction Hamiltonian that was derived eq. (4.9) there are clearly similarities though the latter contains some extra terms. For obvious reasons the stationary atomic ensemble is the target system and the travelling probe beam makes up the meter system. As for the choice of target variables we first put our attention on the population terms \hat{n}_{ph} and \hat{n}_{at} . These do commute with the interaction Hamiltonian, however, they have very large mean values, which would make a precise measurement of fluctuations around their mean values at the level of the quantum noise very difficult. Since they are also highly susceptible to classical sources of noise the population variables are not suitable as QND variables. The remaining variables in the Hamiltonian contains the z-components of the photonic and atomic pseudo-spins, where the latter is our candidate for QND target variable. During free evolution \hat{f}_z is in principle a constant of motion, but collisions and inhomogeneities will cause it to decay with some characteristic time (see discussion in sec. 3.7.1). Depending on the quantum states of the ensemble and the probe \hat{s}_z and \hat{f}_z can attain large or small mean values. Hence, to be able to relate the interaction described by the Hamiltonian eq. (4.9) to a QND measure-

ment we must be specific about the initial quantum states. Since, we wish to measure minute fluctuations of \hat{f}_z it is desirable that the initial atomic state has $\langle \hat{f}_z \rangle = 0$, which is for example fulfilled for the product state of equal superpositions $(|4\rangle + i|3\rangle)/\sqrt{2}$ (see eq. (3.16)). We have made an, in principle arbitrary, choice of the phase of the product state that results in $\langle \hat{f}_x \rangle = 0$ and $\langle \hat{f}_y \rangle = n_{\text{at}}/2$. Because of the large mean value of \hat{f}_y we make the replacement $\hat{f}_y \rightarrow \hat{n}_{\text{at}}/2$. For the probe we will only require that $\langle \hat{s}_x \rangle = 0$, which is fulfilled if e.g. \hat{s} is comprised of the output of a BS with one input in a coherent state and the other in a vacuum state (see eq. (2.11) or fig. 2.3). Though we *don't* demand that $\langle \hat{s}_z \rangle = 0$ we will add the condition that \hat{s}_y is large and may be replaced by $\hat{s}_y \rightarrow \pm n_{\text{ph}}/2$ — the sign is deliberately, and for a good reason, left unspecified. With these initial properties at hand we re-cap the linearly expanded input output relations eqs. (4.26 and ??) leaving out the macroscopic y -components

$$\hat{s}_z^{(out)} = \hat{s}_z^{(in)}, \quad \hat{s}_x^{(out)} = \hat{s}_x^{(in)} + \hat{s}_y \tilde{\phi}_{\text{ph}} \quad (5.13)$$

$$\hat{f}_z^{(out)} = \hat{f}_z^{(in)}, \quad \hat{f}_x^{(out)} = \hat{f}_x^{(in)} + \hat{f}_y \tilde{\phi}_{\text{at}} \quad (5.14)$$

where $\tilde{\phi}_{\text{ph}} \propto \hat{f}_z$ and $\tilde{\phi}_{\text{at}} \propto \hat{s}_z$ c.f. eq. (4.24). As a QND target variable \hat{f}_z fulfils the non-demolition criterion in that the output value is correlated with the input value. Though eq. (5.14) suggests that this correlation is perfect it is actually limited by decoherence due to photon absorption as discussed in sec. 4.5. We see that \hat{s}_x is correlated with the target variable, thus, qualifying as a meter variable. The measurement efficiency criterion hinges on the coupling strength, which in turn depends on a whole range of experimental parameters discussed in later chapters. Hence, conditioned on the measurement strength and the degree of photon scattering, the interaction and subsequent detection meet the criterion of being able to engineer the quantum state of \hat{f}_z . As a final note on the meter variable, we must verify that we indeed have a means of measuring it. As photo-detectors only "count" photons and not fields it is in fact not possible to measure \hat{s}_x directly. Fortunately, all the investigated probe configurations circumvent this catch either by transformation of \hat{s}_x into \hat{s}_z at the output BS in the MZI (sec. 2.3.1) or by lock-in detection of the field-sum in the SBI (sec. A.6). Hence, it is sufficient to be able to encode the information about \hat{f}_z in \hat{s}_x . All together, the atom-light interaction measures up to the QND criteria, but how this actually results in a SSS being generated is the topic of the next section.

5.2.1 QND measurement as projection on Dicke-state basis

We will now view the QND measurement from an angle, which might appeal to some for being more intuitive than the treatment in sec. 5.1.1. This treatment is by and large the same as in [Windpassinger09b]. We make use of the fact that we actually know the initial atomic and photonic distributions and not only their mean values and variances. Moreover, we explicitly utilise that the light meter variable records the value of \hat{f}_z and if this were done with infinite strength and without noise, the QND measurement would project the atomic state onto an eigen-state of \hat{f}_z i.e. a Dicke-state as described in sec. 3.3.1. The starting point is a measurement outcome x_s of \hat{s}_z (\hat{s}_x) at the MZI (SBI) output corresponding to \hat{s}_x interacting with the atomic ensemble. Because of the shot noise of light we cannot determine exactly the \hat{f}_z value corresponding to this measurement. Still, we know that the shot-noise of \hat{s}_x has a Gaussian distribution in the Fock-basis i.e. not accounting for the interaction or the measurement (See appendix A.2)

$$\mathcal{P}(\hat{s}_x = \frac{n}{2}) = |\langle n_{\text{ph}}, \frac{n}{2} | \hat{s}_x | \frac{nl_p}{2}, n_{\text{ph}} \rangle| = \frac{2}{\pi n_{\text{ph}}} e^{-\frac{((\hat{s}_x) - \frac{n}{2})^2}{2n_{\text{ph}}}}.$$

We assume that MZI or SBI is adjusted so that in the absence of atoms we would have $\langle \hat{s}_x \rangle = 0$. With atoms present the value changes according to eq. (5.13) and $\hat{s}_x^{(out)} = \hat{s}_x^{(in)} + \frac{\mathcal{K}}{c} \hat{s}_y \hat{f}_z$. Presuming that the atoms are in a Dicke-state with $\langle \hat{f}_z \rangle = m$ the resulting $\langle \hat{s}_x \rangle = \frac{\mathcal{K}}{c} \hat{s}_y m$. Thus the distribution of \hat{s}_x conditioned on the atoms being in the Dicke-state $|\frac{n_{at}}{2}, m\rangle$ becomes

$$\mathcal{P}(\hat{s}_x^{(out)} = \frac{n}{2})|_{\{\hat{f}_z=m\}} = |\langle n_{ph}, \frac{n}{2} | \hat{s}_x^{(out)} | \frac{n}{2}, n_{ph} \rangle| |_{\{\frac{n_{at}}{2}, m\}} = \frac{2}{\pi n_{ph}} e^{-\frac{(\frac{\mathcal{K}}{c} \hat{s}_y m - \frac{n}{2})^2}{2n_{ph}}}$$

On the other hand we found in sec. 3.3.1 that a product state of equal superpositions can be written in the basis of Dicke-states according to eq. (3.24), which in the limit of large atom numbers can be approximated by the Gaussian distribution

$$\mathcal{P}(\hat{f}_z = m) = |\langle \frac{n_{at}}{2}, 0 | \frac{n_{at}}{2}, m \rangle|^2 = \frac{2}{\pi n_{at}} e^{-\frac{((\hat{f}_z)-m)^2}{2n_{at}}},$$

where for an exact equal superposition $\langle \hat{f}_z \rangle = 0$. In an experiment we let the meter variable interact with the target variable whereupon we detect the meter and based on the result want to predict the value of the target variable to better than the SQL. Thus we wish to learn about the distribution of \hat{f}_z values, e.g. in the Dicke-state basis, given a certain measurement result. In other words we seek the distribution $\mathcal{P}(\hat{f}_z = m)|_{\{\hat{s}_x^{(out)} = \frac{n}{2}\}}$. With Bayes' rule (see e.g.) and the above distributions at hand we are actually able to express this as

$$\mathcal{P}(\hat{f}_z = m)|_{\{\hat{s}_x^{(out)} = \frac{n}{2}\}} = \frac{\mathcal{P}(\hat{s}_x^{(out)} = \frac{n}{2})|_{\{\hat{f}_z=m\}} \mathcal{P}(\hat{f}_z = m)}{\mathcal{P}(\hat{s}_x^{(out)} = \frac{n}{2})}$$

The probability that $\hat{s}_x^{(out)}$ obtains a certain value is not immediately known but we can use that $\mathcal{P}(\hat{s}_x^{(out)} = \frac{n}{2}) = \int_{-\infty}^{\infty} \mathcal{P}(\hat{s}_x^{(out)} = \frac{n}{2})|_{\{\hat{f}_z=m\}} \mathcal{P}(\hat{f}_z = m) dm$. In other words the probability of measuring a certain output $\hat{s}_x^{(out)}$ is the same as the probability to measure a certain $\hat{s}_x^{(out)}$ given a certain Dicke state multiplied by the likelihood to have that Dicke state and then integrating over all Dicke states. Performing the integration yields

$$\mathcal{P}(\hat{s}_x^{(out)}) = \frac{1}{2\pi(\kappa \frac{n_{at}}{4} + \frac{n_{ph}}{4})} e^{-\frac{\frac{n^2}{4}}{2(\kappa \frac{n_{at}}{4} + \frac{n_{ph}}{4})}}.$$

with the coupling constant now defined as

$$\kappa = \frac{\mathcal{K}}{c} \hat{s}_y \sqrt{\frac{n_{at}}{n_{ph}}} = \pm \frac{1}{2} \frac{\mathcal{K}}{c} \sqrt{n_{at} n_{ph}}. \quad (5.15)$$

The sign depends on the expectation value $\langle \hat{s}_y \rangle = \pm n_{ph}/2$, and except for a factor 1/4 this agrees with the definition given in the above sec. 5.2. With this in hand we derive an expression for the probability of the atomic state to be in a Dicke state given a particular measurement outcome

$$\begin{aligned} \mathcal{P}(\hat{f}_z = m)|_{\{\hat{s}_x^{(out)} = \frac{n}{2}\}} &= \frac{\mathcal{P}(\hat{s}_x^{(out)} = \frac{n}{2})|_{\{\hat{f}_z=m\}} \mathcal{P}(\hat{f}_z = m)}{\int_{-\infty}^{\infty} \mathcal{P}(\hat{s}_x^{(out)} = \frac{n}{2})|_{\{\hat{f}_z=m\}} \mathcal{P}(\hat{f}_z = m) dm} \\ &= \frac{2(1 + \kappa^2)}{\pi n_{at}} e^{-\frac{\left(m - \sqrt{\frac{n_{at}}{n_{ph}}} \frac{\kappa}{1 + \kappa^2} \frac{n}{2}\right)^2}{2 \frac{n_{at}}{4} \frac{1}{1 + \kappa^2}}}. \end{aligned} \quad (5.16)$$

The final distribution still has a Gaussian functional dependence, however with different mean value and variance than the original one. As compared to the initial zero mean value, eq. (5.16) has the mean at $\langle \hat{f}_z \rangle |_{\{\hat{s}_x^{(out)} = \frac{n}{2}\}} = \sqrt{\frac{n_{\text{at}}}{n_{\text{ph}}}} \frac{\kappa}{1+\kappa^2} \frac{n}{2}$ i.e. it is shifted towards a value which corresponds better with the measurement. The variance on the other hand becomes $\langle (\Delta \hat{f}_z)^2 \rangle |_{\{\hat{s}_x^{(out)} = \frac{n}{2}\}} = \frac{n_{\text{at}}}{4} \frac{1}{1+\kappa^2}$, which is smaller than the uncorrelated spin state variance of $n_{\text{at}}/4$ by the factor $\varepsilon = 1/(1+\kappa^2)$. Note that since the variance depends on $\kappa^2 \propto \hat{s}_y^2$ it does not depend on the sign of $\langle \hat{s}_y \rangle$. To our luck, this result is exactly equivalent to eqs. (5.10 and 5.12), which were found by slightly different — and probably simpler — means. Nevertheless, the representation in this section has the advantage that it is possible to visualise the QND squeezing process. On fig. 5.1 we plot the numerator of

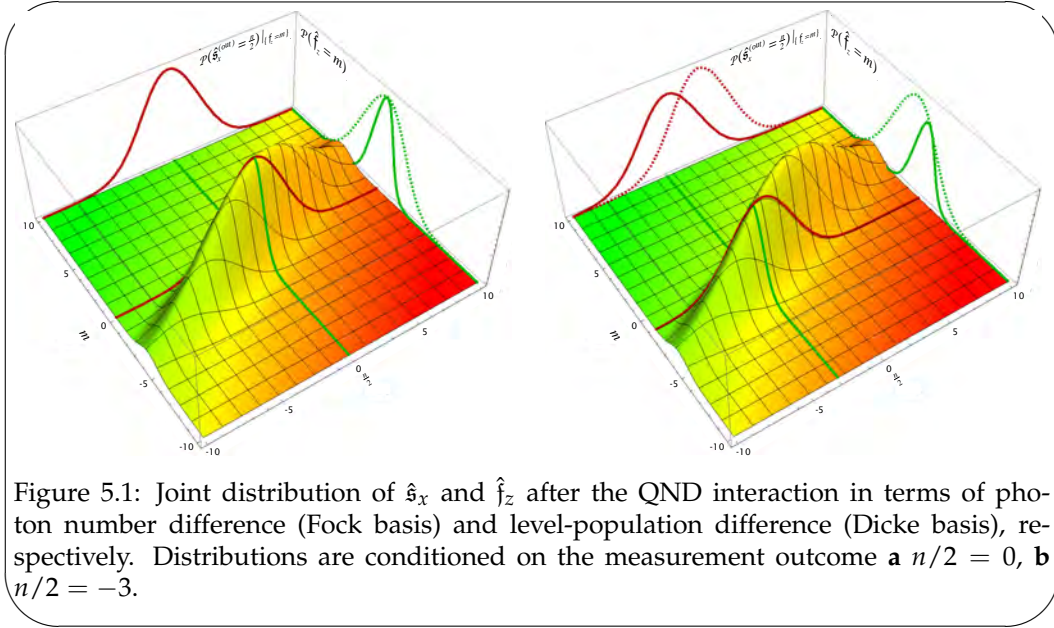
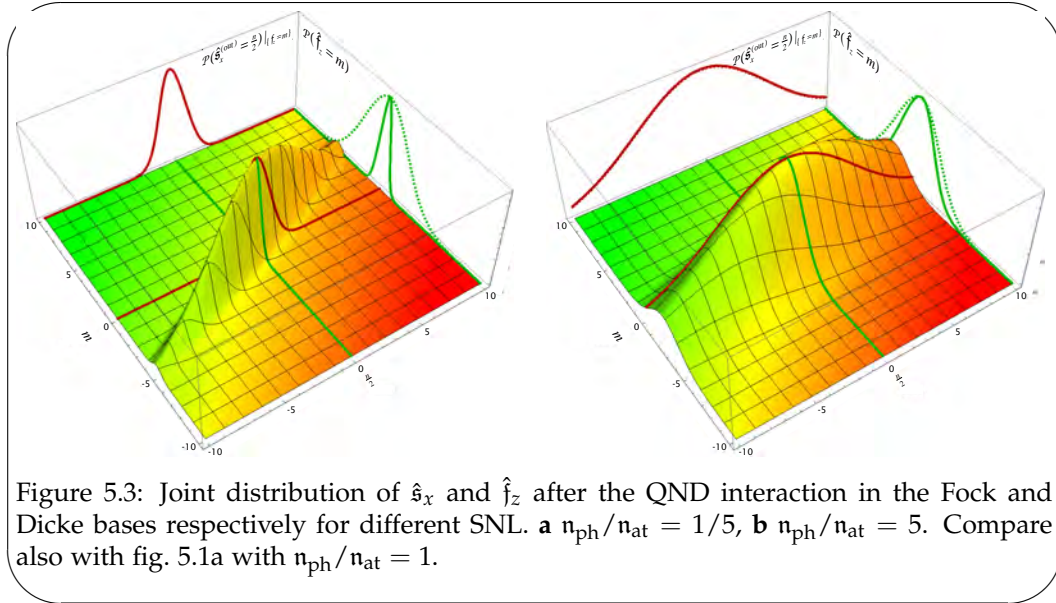
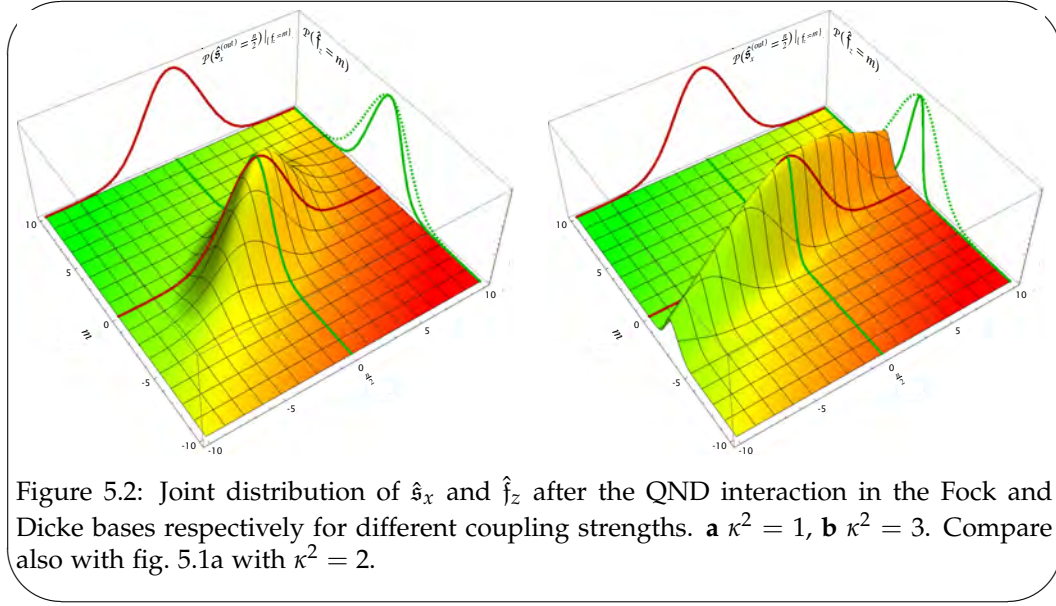


Figure 5.1: Joint distribution of \hat{s}_x and \hat{f}_z after the QND interaction in terms of photon number difference (Fock basis) and level-population difference (Dicke basis), respectively. Distributions are conditioned on the measurement outcome **a** $n/2 = 0$, **b** $n/2 = -3$.

eq. (5.16) i.e. $\mathcal{P}(\hat{s}_x^{(out)} = \frac{n}{2}) |_{\{\hat{f}_z = m\}} \mathcal{P}(\hat{f}_z = m)$.⁶ This plot is the joint probability distribution of \hat{s}_x and \hat{f}_z after their interaction but before the measurement. The green dashed curve represents the distribution of $\hat{f}_z^{(in)}$ and the red dashed line is the distribution of $\hat{s}_x^{(in)}$. A measurement corresponds to taking a slice at a measured value x_s of \hat{s}_x as indicated by the green line overlaid the surface plot. The resulting distribution along the \hat{f}_z -axis is then the resulting un-normalised conditional probability of \hat{f}_z in the Dicke state basis. For $\kappa^2 > 0$ this distribution (green curve on fig. 5.1) will be narrower than the initial coherent state \hat{f}_z -distribution (dashed green line on fig. 5.1). This is in essence what makes up a SSS. The Red curve would be the distribution of $\hat{s}_x^{(out)}$ for a subsequent measurement on a perfectly projected atomic state i.e. following a measurement with $\kappa^2 \gg 1$. Fig. 5.1a and b illustrate the change in mean-value of the $\hat{f}_z^{(out)}$ depending on the \hat{s}_x measurement outcome. The width of the distribution is, however, independent of the outcome. The width of the atomic distribution conditioned on the measurement is determined by three factors. Trivially, the projection noise of the initial distribution is the first of these. Secondly, the interaction strength κ^2 governs the strength with which the atomic state is recorded and thus also to what degree the measurement outcome conditions the atomic state. This is illustrated by fig. 5.2 together with fig. 5.1a, where the difference between the dashed and the full green line increases the larger κ^2 is. Finally, the ratio of the projection to

⁶the fully normalised conditional distribution eq. (5.16) would not be overly instructive as it would fail to illustrate that some measurement outcomes are more likely than others. A plot of



the shot noise determines how precise the probe is at measuring the atomic state and thus again the degree that the measurement conditions the atomic state. On fig. 5.3 along with fig. 5.1a this is seen as an increased noise reduction of $\hat{f}_z^{(out)}$. Hence, the degree of noise reduction is dictated by the combined influence of the coupling \mathcal{K} and the projection noise to shot noise ratio. These, factors determine the SNR defined in eqs. (2.19 and 2.29).

5.2.2 Relation between coupling strength and real transitions

Here we will introduce an illuminating relation between the QND coupling strength κ^2 , the excitation probability η , and the absorption coefficient α . In the preceding section we expressed the coupling strength as c.f. eq. (5.15)

$$\kappa^2 = \frac{1}{4} \frac{\mathcal{K}^2}{c^2} n_{at} n_{ph} = \frac{1}{4} \mathcal{K}^2 n_{at} t_a n_{ph} t_p .$$

Here we wish to get a simple picture of the factors determining the squeezing so we will not specify the levels involved in \mathcal{K} . In the same vein we take the eq. (5.16) would just have an infinite width along the $n/2$ axis.

spontaneous excitation rate to be

$$\tilde{\eta} = \frac{1}{2} \mathcal{L} \hat{n}_{\text{ph},a} t = \frac{1}{4} \mathcal{L} \hat{n}_{\text{ph}} t$$

where in the rightmost equality we have assumed that only half of the photons interact with the atomic sample as is the case for a symmetric MZI. In the case of the asymmetric MZI and SBI this does not hold, however we shall write out the exact expressions in the following sections and reserve this space for a simplified illustration. Substituting $\tilde{\eta}$ into the equation for κ^2 we get

$$\kappa^2 = \frac{\mathcal{K}^2}{\mathcal{L}} n_{\text{at}t_a} \tilde{\eta} \approx \frac{1}{2} \frac{|g|^2}{\gamma_e/2} n_{\text{at}t_a} \tilde{\eta}. \quad (5.17)$$

The approximation comes from writing out \mathcal{K} and \mathcal{L} explicitly and cancelling terms. It is not completely clear, which coupling constant $|g|^2$ is referred to here, but from eq. (5.27) it will be clear that it is the sum of all transition strengths $|g|^2 = \sum_{e=2(3)}^{5(4)} (|g_{3e}|^2 + |g_{4e}|^2)$. If the probe is far detuned $\Delta \gg \gamma_e$ then the whole thing reduced to $\approx \frac{1}{2}$. The last simplification proceeds from eq. (4.14) for the absorption coefficient. On resonance this condenses to

$$\tilde{\alpha}_0 \equiv \tilde{\alpha}(\Delta = 0) = 4 \frac{|g|^2}{\gamma_e} \hat{n}_{\text{at}t_a},$$

which is the far-detuned equivalent resonant optical depth of the atomic sample⁷. Inserting expression for the $\tilde{\alpha}_0$ into eq. (5.17) yields the simple relation

$$\kappa^2 \approx \frac{1}{4} \tilde{\alpha}_0 \tilde{\eta}. \quad (5.18)$$

Because this formula relates the interaction strength to two easily comprehended quantities it proves to very useful for getting an intuitive understanding of the limiting factors in the QND spin-squeezing process. It highlights that the achievable noise-reduction depends on one quantity, $\tilde{\alpha}_0$, which is entirely a property of the atomic sample and another, $\tilde{\eta}$, which depends on the intensity, detuning, and geometry of the probe beam. Admittedly, $\tilde{\eta}$ does covertly depend on the atoms via the choice of transitions and their coupling strengths.

Eq. (5.18) leads to two observations. Firstly, a large optical depth of the sample is essential if one wishes to achieve a large degree of spins squeezing. The noise reduction can be increased simply increasing the excitations $\tilde{\eta}$, but since these produce decoherence of the output state, this will not necessarily increase the squeezing as it is defined in eq. (3.33). Hence, there is a limit on the size off $\tilde{\eta}$ and only an increase of $\tilde{\alpha}_0$ will help. Secondly, as a contradiction in terms, it is not possible to create a spin-squeezed state by a QND measurement unless it partly demolishes the atomic state. That is, $\tilde{\eta} = 0 \Rightarrow \kappa^2 = 0$. Fortunately, if we recall the discussion of sec. 4.5.1, not all excitations necessarily add noise to the output state. Thus, the unavoidability of $\tilde{\eta}$ is not always as bad as it initially appears.

Assuming the optimal case where the decoherence does not add any noise to the output state of the QND measurement we get the squeezing parameter as

$$\xi_{\text{wineland}} = \frac{\langle (\Delta \hat{f}_z^{(out)})^2 \rangle}{(1 - \eta)^2 \langle (\Delta \hat{f}_z^{(in)})^2 \rangle} = \frac{1}{(1 - \eta)^2} \frac{1}{1 + \frac{1}{4} \tilde{\alpha}_0 \tilde{\eta}} \quad (5.19)$$

⁷far off resonance the detuning dependence of all levels are equal and they all couple equally but weighed by their coupling strength. Hence the optical depth appears as if it was caused by a single transition with coupling strength equal to the sum of all hyperfine coupling strengths, i.e., $|g|^2$

where we take $e^{-\eta} \approx 1 - \eta$. The minimal ξ_{wineland} can easily be found from the r.h.s. and we get the optimal η_{opt} yielding the maximal squeezing $\xi_{\text{wineland}}^{(\text{opt})}$ to be

$$\eta_{\text{opt}} = \frac{-8 + \tilde{\alpha}_0}{3\tilde{\alpha}_0} \quad , \quad \xi_{\text{wineland}}^{(\text{opt})} = \frac{27\tilde{\alpha}_0^2}{(4 + \tilde{\alpha}_0)^3} \quad (5.20)$$

It is rather interesting that in the limit of $\tilde{\alpha}_0 \rightarrow \infty$ this prescribes an optimal $\tilde{\eta} = 1/3$, which is independent of the optical depth. It is also clear that the optical depth needs to be $\tilde{\alpha}_0 > 8$ before any squeezing can be achieved. Finally, the optimal squeezing value for large $\tilde{\alpha}_0$ will tend towards $3^3/\tilde{\alpha}_0$ [Saffman09]. In fig. 5.4 the optimal values are plotted as function of $\tilde{\alpha}_0$.

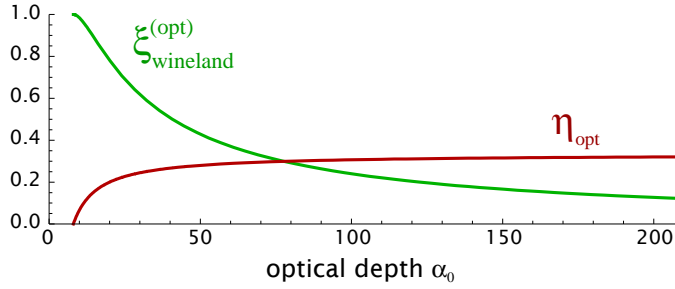


Figure 5.4: Optimal decoherence and squeezing parameter for simplified relation $\kappa^2 = \frac{1}{4}\tilde{\alpha}_0\tilde{\eta}$ between coupling constant κ^2 , optical depth $\tilde{\alpha}_0$, and decoherence $\tilde{\eta}$.

In the following sections we will return to the local ensemble operator picture and discuss the QND measurement in the configurations outlined in sec. 2.3. This will lead to three spin squeezing scenarios, two of which will be subject to investigation in the experimental part of this dissertation.

5.3 QND and squeezing in experimental probing configurations

The procedure of the next three sections will be as follows: First we specify the states of the atoms and the light just before the interaction in order to deduce the values of the pseudo-spin operators. Next step is to analyse the interaction given the specific input operator values and finally we will transform the probe operators to the stage where the probe is detected. Based on this we can find the correlation of the measured photonic meter variable with the atomic target variable and using the intrinsic noise in the measured signal we can deduce the SNR of that particular configuration. Unlike, the simplified analysis of the squeezing in the previous sections we will here include all imperfections that affect the quality of the measurement.

5.3.1 Monochromatic MZI

The monochromatic MZI experimental configuration refers to the case where a single probe beam enters the interferometer at one of the outputs $\langle \hat{c}_1^\dagger \hat{c}_1 \rangle = n_{\text{ph}}$ while the other input contains the vacuum field $\langle \hat{c}_2^\dagger \hat{c}_2 \rangle = 0$ (see fig. 5.5). After the input BS we thus have $\langle \hat{s}_y \rangle = n_{\text{ph}}/2$ and $\langle \hat{s}_x \rangle = \langle \hat{s}_z \rangle = 0$. Losses in the probe arm would cause $\langle \hat{s}'_y \rangle = \tau n_{\text{ph}}/2$, $\langle \hat{s}'_z \rangle = (\tau^2 - 1)n_{\text{ph}}/2$ and $\langle \hat{s}'_x \rangle = 0$ as described in sec. 2.3.1. Given these input states we get the following interaction rotation

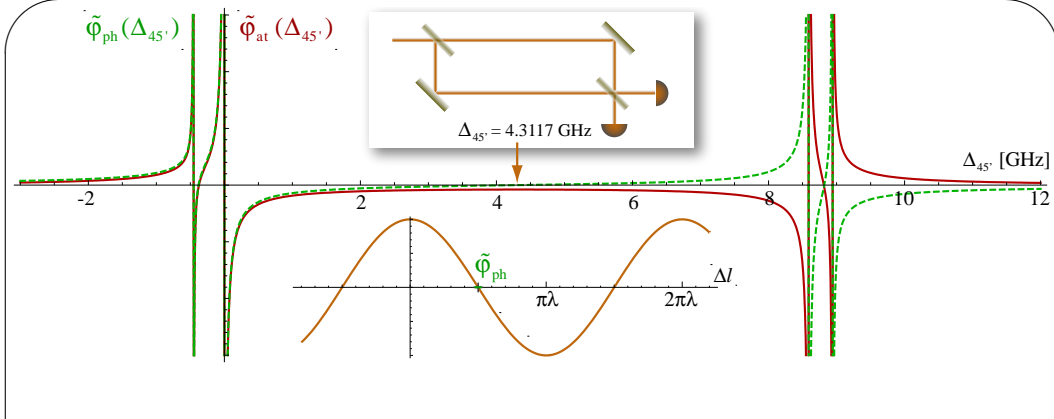


Figure 5.5: Phase-shift (green dashed curve) and light-shift (red curve) as function of probe detuning on D2-line. For atomic state with $\langle \hat{f}_z \rangle = 0$ the phase-shift vanishes at $\text{det } 45' = 4.3117$ GHz, however the light-shift is not zero. Upper insert: monochromatic MZI sketch. Lower insert: Interference fringe in difference output signal as function of MZI path-length. For $\text{det } 45' = 4.3117$ GHz the output signal is unaffected by the atoms and only projection noise causes fluctuations around zero.

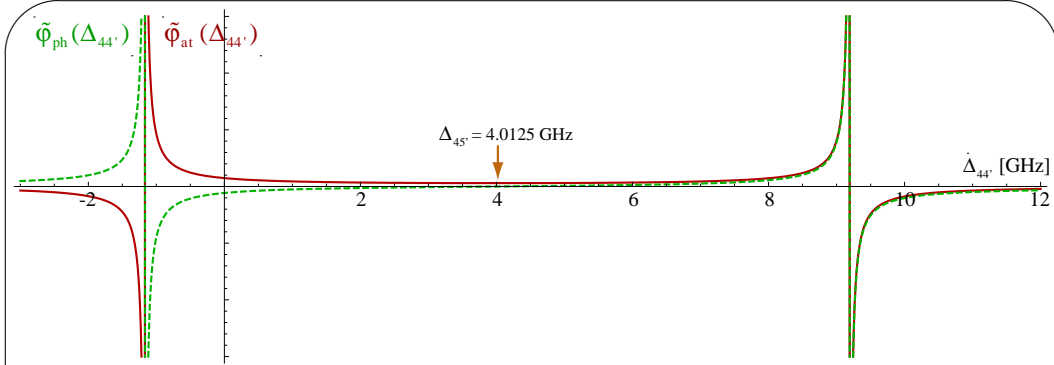


Figure 5.6: Phase-shift (green dashed curve) and light-shift (red curve) as function of probe detuning on D1-line. For atomic state with $\langle \hat{f}_z \rangle = 0$ the phase-shift vanishes at $\text{det } 44' = 4.0125$ GHz, however the light-shift is not zero.

angles

$$\tilde{\phi}_{\text{ph}} = \frac{2}{c} \sum_{e=2(3)}^{5(4)} \left[(\mathcal{K}_{4e} + \mathcal{K}_{3e}) \frac{\hat{n}_{\text{at}}}{2} + (\mathcal{K}_{4e} - \mathcal{K}_{3e}) \hat{f}_z \right] l_a \quad (5.21)$$

$$\tilde{\phi}_{\text{at}} = \frac{2}{c} \left(\frac{\hat{n}_{\text{ph}}}{2} + \hat{s}_z \right) l_p \sum_{e=2(3)}^{5(4)} [\mathcal{K}_{4e} - \mathcal{K}_{3e}] \quad (5.22)$$

In order for $\tilde{\phi}_{\text{ph}}$ to be sensitive to \hat{f}_z but not n_{at} we must have $\mathcal{K}_1 = \sum_e \mathcal{K}_{4e} = -\sum_e \mathcal{K}_{3e}$. From the form of the coupling constants and the involved resonant coupling constants listed in appendix D.2 we find a probe detuning Δ_0 where this is fulfilled. The detuning corresponds to the point on the curve where fig. ?? where the net phase-shift is zero. Obviously, this is the point where the probe is equally sensitive to populations in both ground levels, and if these are equally populated the phase shifts should rightfully be zero. With this setting of the

probe detuning the input output relations become

$$\hat{s}_z^{(out)} = \hat{s}_z^{(in)} \quad , \quad \hat{s}_x^{(out)} = \hat{s}_x^{(in)} + \tau^2 \frac{\hat{n}_{ph}}{2} 4 \frac{\mathcal{K}_1}{c} \hat{f}_z \quad (5.23)$$

$$\hat{f}_z^{(out)} = \hat{f}_z^{(in)} \quad , \quad \hat{f}_x^{(out)} = \hat{f}_x^{(in)} + \frac{\hat{n}_{at}}{2} 4 \frac{\mathcal{K}_1}{c} \left(\frac{\hat{n}_{ph}}{2} + \hat{s}_z \right) \quad , \quad (5.24)$$

where we again summon the column photon and atom operators. Exclusively considering the transformation of the meter variable \hat{s}_x this correctly records the value of the target variable \hat{s}_z , which is a constant of the interaction. Thus we expect \hat{s}_z to be squeezed by a measurement of \hat{s}_y . On the other hand we observe that \hat{f}_x receives a non-zero light shift from the \hat{n}_{ph} term as well as from the \hat{s}_z term if there are losses $\tau < 1$. This is not really desired because this coupling may risk feeding of excess noise into the target system or in other words though \hat{s}_z is squeezed \hat{s}_x can become excessively anti-squeezed. From the form of $\tilde{\phi}_{ph}$ and $\tilde{\phi}_{at}$ it is clear that the light shift is unavoidable in the single probe MZI configuration.

Atomic noise in output signal There are two approaches to calculate the noise in the detected output MZI output. Either we can use the input output relations to calculate the noise of the output operator eq. (5.23) and then apply the appropriate adjustments to account for the mode mismatch of the output. Alternatively, we can use the eq. (A.9) and then compute and insert $\langle (\Delta\tilde{\phi}_{at})^2 \rangle$ from eq. (5.21). Whichever way we chose to do it, the result we get for the monochromatic MZI is

$$\begin{aligned} \langle (\Delta\hat{s}_z^{out})^2 \rangle &= \langle (\Delta\hat{s}_z^{out})^2 \rangle_{SN} + \langle (\Delta\hat{s}_z^{out})^2 \rangle_{\tilde{\phi}_{at}} \\ &= (1 - \rho^2 t_1^2) \frac{n_{ph}}{4} + \mathcal{T}^4 \tau^2 \sin^2 \tilde{\phi} \sin^2 \beta_1 \frac{n_{ph}^2}{4} 16 \frac{\mathcal{K}_1^2}{c^2} \langle (\Delta\hat{f}_z)^2 \rangle \\ &= \frac{n_{ph}}{4} \left[(1 - \rho^2 t_1^2) + \mathcal{T}^4 \tau^2 \sin^2 \tilde{\phi} \sin^2 \beta_1 \frac{n_{ph}}{4} 4 \frac{\mathcal{K}_1^2}{c^2} \frac{n_{at}}{4} \right] \quad , \quad (5.25) \end{aligned}$$

Here a central formula makes its first appearance; the output noise expressed as a sum of a shot noise and a projection noise term. A crucial property of the terms contributing to the noise is their scaling with the particle numbers. The shot noise, of course, scales linearly with the photon number and is independent of atom number. The projection noise term sales linearly with n_{at} but quadratically with n_{ph} . This whether experimentally observed noise in the signal is shot noise, projection noise, or something else. One just has to vary either n_{ph} or n_{at} and observe the effect on the noise. Only requirement is that we have an independent way to determine n_{ph} and n_{at} .

By use of eq. (5.25) we calculate the SNR as the ratio of projection noise term to the shot noise term (see eq. (2.31))

$$SNR = \frac{\frac{1}{4} \mathcal{T}^4 \tau^2 \sin^2 \tilde{\phi} \sin^2 \beta_1 \frac{\mathcal{K}_1^2}{c^2} n_{ph} n_{at}}{1 - \rho^2 t_1^2} = \kappa_1^2 \quad , \quad (5.26)$$

Which is maximal for $\tilde{\phi} = \beta_1 = \pi/2$ and $\mathcal{T} = \tau = 1$. As pointed out in eq. (5.8) the SNR is equivalent to the coupling strength relevant for the squeezing, which the reason for the last equality in eq. (5.26). The noise of the output pseudo-spin z-component is then $\langle (\Delta\hat{f}_z^{out})^2 \rangle = n_{at} / (4(1 + \kappa_1^2))$

In the below sections we will find equivalent expressions to eq. (5.25) for the output noise in the other experimental configurations.

Squeezing and decoherence In sec. 5.2.2 we found a simple relation between a simplified coupling constant and a simplified spontaneous scattering rate (see eq. (5.17)). If we now include the more complete coupling constant that is a sum over all coupled transitions and likewise for the spontaneous scattering, keeping in mind that $\tilde{\eta} \propto n_{\text{ph},a} = t_1^2 \tau^2 n_{\text{ph}}$, we get

$$\begin{aligned} \kappa_1^2 &= \frac{\mathcal{T}^4 \sin^2 \tilde{\phi} \sin^2 \beta_1}{4t_1^2(1 - \rho^2 t_1^2)} \sum_e \frac{(\mathcal{K}_{4e} + \mathcal{K}_{3e})^2}{(\mathcal{L}_{4e} + \mathcal{L}_{3e})} n_{\text{at}t_a} \tilde{\eta} \\ &= \frac{\mathcal{T}^4 r_1^2 \sin^2 \tilde{\phi}}{(1 - \rho^2 t_1^2)} r_{\text{Di}} \frac{|g|^2}{\gamma_e/2} n_{\text{at}t_a} \tilde{\eta}. \end{aligned} \quad (5.27)$$

If we first take the part pertaining to the MZI we note that a number of factors will benefit the SNR. Firstly, high visibility/mode overlap $\mathcal{T} \approx 1$ is crucial since it scales with the fourth power. Secondly, losses in the probe arm $\rho > 0$ (before the atoms!) such that $(1 - \rho^2 t_1^2)$ is small. This signifies the fact that we can increase the total power n_{ph} at the MZI input and thus the fringe amplitude without increasing $\tilde{\eta}$ if we just attenuate the probe beam before the atoms. If the $n_{\text{ph},4}$ is kept constant the fringe height, will still increase by increasing n_{ph} . Thirdly, the same effect as losses in the probe arm comes from increasing the reflection of the MZI input BS so that less light passes in the probe arm. When we go to configurations where light enters both inputs to the MZI, this is not a feasible method, since t_1 and r_1 are interchanged for the two inputs.

Advancing, now to the atomic part we will for the sake of the analysis assume a balanced MZI without imperfections, whereby the factor before the sum reduces to $1/2$. In eq. (5.27) we have introduced $r_{\text{D1}} = 0.67$ and $r_{\text{D2}} = 1.33$ and the coupling constant $|g|^2 = \sum_e (|g_{4e}|^2 + |g_{3e}|^2)$. With this at hand we can state a similar expression for the SNR as in eq. (5.18) and thereby deduce a formula for the noise reduction

$$\frac{\langle (\Delta \hat{f}_z^{\text{(out)}})^2 \rangle}{\langle (\Delta \hat{f}_z^{\text{(in)}})^2 \rangle} = \begin{cases} 1 - (1 - 0.14\tilde{\eta})^2 \left(1 - \frac{1}{1 + \frac{1}{4}r_{\text{D2}}\tilde{\eta} \tilde{\alpha}_0} \right) + \frac{\tilde{\eta}(1 - \tilde{\eta})}{5323}, & \text{(D2)} \\ 1 - (1 - 0.33\tilde{\eta})^2 \left(1 - \frac{1}{1 + \frac{1}{4}r_{\text{D1}}\tilde{\eta} \tilde{\alpha}_0} \right) + \frac{\tilde{\eta}(1 - \tilde{\eta})}{4891}, & \text{(D1)} \end{cases} \quad (5.28)$$

where we include the noise added to the state by the inelastic scattering (the rightmost term). The D2 line is clearly preferable not only because of the stronger coupling giving a large QND noise reduction, but also because the inelastic scattering causes less added noise, albeit the latter is only slightly different for the two lines. As a numerical example, an optical depth of $\tilde{\alpha}_0 = 50$ and $\eta = 0.2$ gives on the D2(D1) line 0.27(0.45) for the above, which again gives a squeezing of $\xi_{\text{wineland}} = 0.42(0.70)$.

In all this, we have silently taken over the approximation of sec. 3.7.2 that the noise reduction and the decoherence can be treated as if they operate in sequence: First the state is squeezed, then spontaneous scattering adds noise, and finally we make the comparison to corrected projection noise level $\langle (\Delta \hat{f}_z^{\text{(in)}})^2 \rangle / (1 - e^{-\eta})^2$ c.f. eq. (3.33).

5.3.2 Dichromatic 1 and 2-input MZI

The monochromatic MZI setup has two major drawbacks; the detuning Δ_0 is pegged by the condition that the coupling to both ground-levels must have the

same magnitude; there is no way to avoid the light shift on the atomic pseudospin x -component. If one allows for a second probe we can adjust the detunings of these and we will show that it is also possible to cancel the light shift. What's more it turns out that to a good approximation the decoherence effect of atomic excitations is greatly reduced. The frequency of the probes will be adjusted such that they predominantly couple to a single ground states and are labelled accordingly. As before one probe enters the input $\langle \hat{c}_{1,4}^\dagger \hat{c}_{1,4} \rangle = n_{\text{ph}4}$ while the other input contains the vacuum field $\langle \hat{c}_{2,4}^\dagger \hat{c}_{2,4} \rangle = 0$ (see fig. 2.2). Hence we get $\langle \hat{s}_{z,4} \rangle = n_{\text{ph}4}/2$ at the MZI input. The second probe can be chosen to enter either the same or the opposite MZI input port i.e. either $\langle \hat{c}_{1,3}^\dagger \hat{c}_{1,3} \rangle = n_{\text{ph}3}$ or $\langle \hat{c}_{2,3}^\dagger \hat{c}_{2,3} \rangle = n_{\text{ph}3}$ resulting in either $\langle \hat{s}_{z,3} \rangle = n_{\text{ph}3}/2$ or $\langle \hat{s}_{z,3} \rangle = -n_{\text{ph}3}/2$, respectively. We will hereafter refer to the former case as the 1-input configuration and the latter as the 2-input configuration. Upon the transformation on the first MZI beamsplitter we have then have $\langle \hat{s}_{y,4} \rangle = n_{\text{ph}4}/2$ and $\langle \hat{s}_{y,3} \rangle = \pm n_{\text{ph}3}/2$, with a plus for the 1-input and a minus for the 2-input configuration. For the interaction we assume that the probe detunings are arranged such that they couple much stronger to one ground-level than the other. We thus neglect the contributions to the interaction angles that refer to the weakly coupled ground-level and thus write

$$\begin{aligned} \tilde{\phi}_{\text{ph}4} &= \frac{2}{c} \sum_{e=3(3)}^{5(4)} \left[\mathcal{K}_{4e} \frac{\hat{n}_{\text{at}}}{2} + \mathcal{K}_{4e} \hat{f}_z \right] l_a, & \tilde{\phi}_{\text{ph}3} &= \frac{2}{c} \sum_{e=2(3)}^{4(4)} \left[\mathcal{K}_{3e} \frac{\hat{n}_{\text{at}}}{2} - \mathcal{K}_{3e} \hat{f}_z \right] l_a \\ \tilde{\phi}_{\text{at}4} &= \frac{2}{c} \left(\frac{\hat{n}_{\text{ph}4}}{2} + \hat{s}_{z,4} \right) \sum_{e=3(3)}^{5(4)} \mathcal{K}_{4e} l_p, & \tilde{\phi}_{\text{at}3} &= -\frac{2}{c} \left(\frac{\hat{n}_{\text{ph}3}}{2} + \hat{s}_{z,3} \right) \sum_{e=2(3)}^{4(4)} \mathcal{K}_{3e} l_p \end{aligned}$$

where $\tilde{\phi}_{\text{ph}4}$ ($\tilde{\phi}_{\text{ph}3}$) refers to the phase-shift of probe P_4 (P_3) and $\tilde{\phi}_{\text{at}4}$ ($\tilde{\phi}_{\text{at}3}$) is the light shift of the atoms caused by P_4 (P_3). Before we can start to engineer the coupling we need to look at the combined effect off/on the two probe beams. Obviously, the light shifts just add up to a combined light shift $\tilde{\phi}_{\text{at}4+3} = \tilde{\phi}_{\text{at}4} + \tilde{\phi}_{\text{at}3}$ ⁸. As for the probes, we detect the sum of the two fields thus the combined input output relations become

$$\begin{aligned} \hat{s}_{z,3+4}^{(\text{out})} &= \hat{s}_{z,4}^{(\text{in})} + \hat{s}_{z,3}^{(\text{in})} = \hat{s}_{z,3+4}^{(\text{in})} \\ \hat{s}_{x,3+4}^{(\text{out})} &= \hat{s}_{x,4}^{(\text{in})} + \hat{s}_{x,3}^{(\text{in})} + \tau^2 \frac{\hat{n}_{\text{ph}4}}{2} \tilde{\phi}_{\text{ph}4} \pm \tau^2 \frac{\hat{n}_{\text{ph}3}}{2} \tilde{\phi}_{\text{ph}3} \\ &= \hat{s}_{x,4+3}^{(\text{in})} + \frac{\tau^2}{c} \sum_{e=2(3)}^{5(4)} \left(\frac{\hat{n}_{\text{at}}}{2} \left[\frac{\hat{n}_{\text{ph}4}}{2} \mathcal{K}_{4e} \pm \frac{\hat{n}_{\text{ph}3}}{2} \mathcal{K}_{3e} \right] + \hat{f}_z \left[\frac{\hat{n}_{\text{ph}4}}{2} \mathcal{K}_{4e} \mp \frac{\hat{n}_{\text{ph}3}}{2} \mathcal{K}_{3e} \right] \right) \end{aligned} \quad (5.29)$$

$$\begin{aligned} \hat{f}_z^{(\text{out})} &= \hat{f}_z^{(\text{in})} \\ \hat{f}_x^{(\text{out})} &= \hat{f}_x^{(\text{in})} + \frac{\hat{n}_{\text{at}}}{2} (\tilde{\phi}_{\text{at}4} + \tilde{\phi}_{\text{at}3}) \\ &= \hat{f}_x^{(\text{in})} + \frac{\hat{n}_{\text{at}}}{2} \frac{2}{c} \sum_{e=2(3)}^{4(4)} \left(\frac{\hat{n}_{\text{ph}4}}{2} \mathcal{K}_{4e} - \frac{\hat{n}_{\text{ph}3}}{2} \mathcal{K}_{3e} + \hat{s}_{z,4} \mathcal{K}_{4e} - \hat{s}_{z,3} \mathcal{K}_{3e} \right) \end{aligned} \quad (5.30)$$

Where we simplify the notation by introducing the sum probe operators $\hat{s}_{z,4+3}$ and $\hat{s}_{x,4+3}$ (see footnote on page 82). Now we can begin to make some qualified choices for the coupling strengths so as to achieve a QND measurement. Due to the \pm and \mp in eq. (5.29) we need to treat the 1-input and 2-input cases separately

⁸As a general notational principle we let the the sum of operators of each probe be denoted by the subscript $4+3$ e.g. $\hat{n}_{\text{ph}4+3} = \hat{n}_{\text{ph}4} + \hat{n}_{\text{ph}3}$. Likewise the difference between operators of each probe are denoted by the subscript $4-3$ e.g. $\hat{n}_{\text{ph}4-3} = \hat{n}_{\text{ph}4} - \hat{n}_{\text{ph}3}$

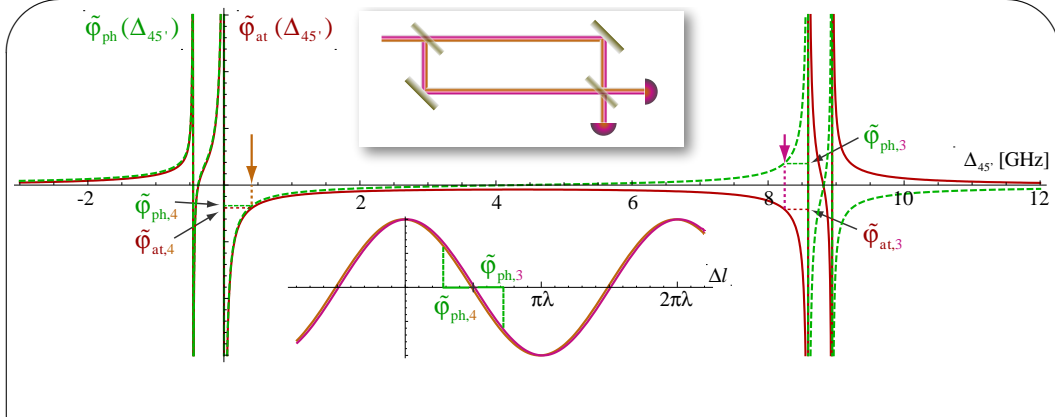


Figure 5.7: Phase-shift (green dashed curve) and light-shift (red curve) as function of probe detuning on D2-line. In the 1-input dichromatic configuration (upper insert) the probe detunings are chosen such that for $\langle \hat{f}_z \rangle = 0$ the phase-shifts of each probe are equal in magnitude but with opposite signs. Sample detunings are marked by orange (P_4) and purple (P_3) arrows. In this case the combined signal of the probes remains zero (lower insert). However, the light shifts from each probe add up.

Dichromatic 1-input MZI In this case it is the upper sign in eq. (5.29) that applies. Thus, for $\hat{s}_{x,3+4}^{(out)}$ to be sensitive to \hat{f}_z and not \hat{n}_{at} we must demand that $\mathcal{K}_{21} \equiv \sum_{e=3(3)}^{5(4)} \mathcal{K}_{4e} = -\frac{n_{ph,3}}{n_{ph,4}} \sum_{e=2(3)}^{4(4)} \mathcal{K}_{3e}$. To simplify matters we take the input photon numbers to be equal for the two beams whereby the requirement becomes $\mathcal{K}_{21} \equiv \sum_{e=3(3)}^{5(4)} \mathcal{K}_{4e} = -\sum_{e=2(3)}^{4(4)} \mathcal{K}_{3e}$. This is not strictly necessary at this point, but sec. 6.1 will uncover that this is actually a wise to impose this condition.

$$\hat{s}_{z,3+4}^{(out)} = \hat{s}_{z,3+4}^{(in)} \quad (5.31)$$

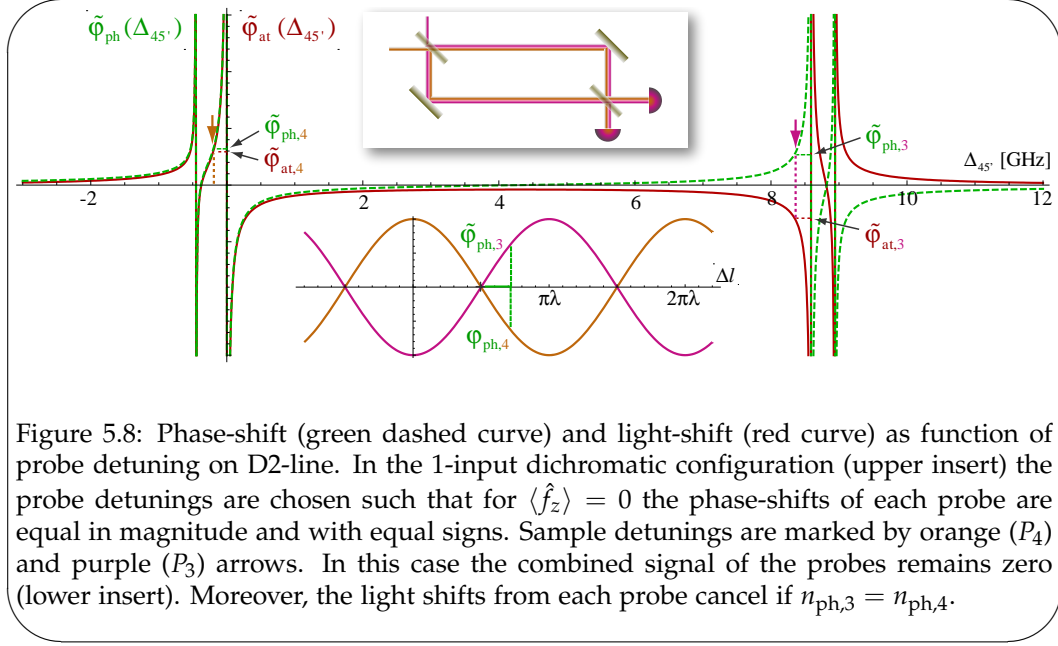
$$\hat{s}_{x,3+4}^{(out)} = \hat{s}_{x,4+3}^{(in)} + \tau^2 \frac{\mathcal{K}_{21}}{c} \left(\frac{\hat{n}_{at}}{2} \frac{\hat{n}_{ph,4-3}}{2} + \hat{f}_z \frac{\hat{n}_{ph,4+3}}{2} \right)$$

$$\hat{f}_z^{(out)} = \hat{f}_z^{(in)} \quad (5.32)$$

$$\hat{f}_x^{(out)} = \hat{f}_x^{(in)} + \frac{\hat{n}_{at}}{2} \frac{\mathcal{K}_{21}}{c} \left(\frac{\hat{n}_{ph,4+3}}{2} + \hat{s}_{z,4+3} \right)$$

Since $\langle \hat{n}_{ph,4-3} \rangle = 0$ eq. (5.31) predicts the coveted recording of \hat{f}_z onto \hat{s}_x . Nevertheless, the terms $\hat{n}_{ph,4-3} \hat{n}_{at}/2$ does appear unlike for the monochromatic configuration eq. (5.23) where the choice of coupling constants eliminated this term. This will also cause an extra term the noise in the \hat{s}_x output. With respect to the atomic operators we see that the light shift is proportional to the combined pseudo-spin z-component $\langle \hat{s}_{z,4+3} \rangle = (\tau^2 - 1)n_{ph}/2$ and photon number $\langle \hat{n}_{ph,4+3} \rangle > 0$. Hence, the light shift has a nonzero value, which is not ideal for the same reasons as mentioned for the monochromatic configuration. As output noise is independent of the signs between the output operator terms we compute the output noise after first treating the 2-input configuration.

Dichromatic 2-input MZI By inputting the probes through different input ports of the interferometer we can harness the full potential of the dichromatic probe setup. For this configuration the lower signs in eq. (5.29) apply and in order to record \hat{f}_z we must now demand $\mathcal{K}_{21} \equiv \sum_{e=3(3)}^{5(4)} \mathcal{K}_{4e} = \sum_{e=2(3)}^{4(4)} \mathcal{K}_{3e}$, still assuming equal photon numbers $\langle \hat{n}_{ph,4} \rangle = \langle \hat{n}_{ph,3} \rangle$. Plugging this into eqs. (5.29 and 5.30)



arrive at

$$\hat{\mathbf{s}}_{z,3+4}^{(out)} = \hat{\mathbf{s}}_{z,3+4}^{(in)} \quad (5.33)$$

$$\hat{\mathbf{s}}_{x,3+4}^{(out)} = \hat{\mathbf{s}}_{x,4+3}^{(in)} + \tau^2 \frac{\mathcal{K}_{22}}{c} \left(\frac{\hat{\mathbf{n}}_{\text{at}}}{2} \frac{\hat{\mathbf{n}}_{\text{ph},4-3}}{2} + \hat{\mathbf{j}}_z \frac{\hat{\mathbf{n}}_{\text{ph},4+3}}{2} \right)$$

$$\hat{\mathbf{j}}_z^{(out)} = \hat{\mathbf{j}}_z^{(in)} \quad (5.34)$$

$$\hat{\mathbf{j}}_x^{(out)} = \hat{\mathbf{j}}_x^{(in)} + \frac{\hat{\mathbf{n}}_{\text{at}}}{2} 2 \frac{\mathcal{K}_{22}}{c} \left(\frac{\hat{\mathbf{n}}_{\text{ph},4-3}}{2} + \hat{\mathbf{s}}_{z,4-3} \right)$$

This is naturally very similar to what we got in the 1-input configuration, with the only difference in the $\hat{\mathbf{j}}_x$ output. The small, but significant difference is that the light shift is now proportional to $\hat{\mathbf{n}}_{\text{ph},4-3}$ and $\hat{\mathbf{s}}_{z,4-3}$ both having zero mean value. Thus there is no mean⁹ light-shift of the atomic pseudo-spin. By all means, $\hat{\mathbf{j}}_x$ now records information about $\hat{\mathbf{s}}_{z,4-3}$ and no longer about the sum of $\hat{\mathbf{s}}_{z,4+3}$, however, this is just the back-action term whose origin we care little about. Altogether, the 2-input configuration seems to be superior. This will be further backed by observations on the classical noise behaviour of the setup in sec. 6.1. On the downside the 2-input configuration is also the most demanding to implement in practice.

Atomic noise in output signal We now investigate the output noise in the dichromatic MZI. These calculations will be valid for both the 1 and 2-input configurations.

$$\begin{aligned} \langle (\Delta \hat{\mathbf{s}}_z^{out})^2 \rangle &= \langle (\Delta \hat{\mathbf{s}}_z^{out})^2 \rangle_{\text{SN}} + \langle (\Delta \hat{\mathbf{s}}_z^{out})^2 \rangle_{\tilde{\varphi}_{\text{at}}} \quad (5.35) \\ &= (1 - \rho^2 t_1^2) \frac{\mathbf{n}_{\text{ph},4+3}}{4} \\ &\quad + \mathcal{T}^4 \tau^2 \sin^2 \tilde{\varphi} \sin^2 \beta_1 4 \frac{\mathcal{K}_{2i}^2}{c^2} \left(\frac{(\mathbf{n}_{\text{at}})^2}{4} \frac{\langle (\Delta \hat{\mathbf{n}}_{\text{ph},4-3})^2 \rangle}{4} + \langle (\Delta \hat{\mathbf{j}}_z)^2 \rangle \frac{(\hat{\mathbf{n}}_{\text{ph},4+3})^2}{4} \right) \\ &= \frac{\mathbf{n}_{\text{ph},4+3}}{4} \left[(1 - \rho^2 t_1^2) + \mathcal{T}^4 \tau^2 \sin^2 \tilde{\varphi} \sin^2 \beta_1 4 \frac{\mathcal{K}_{2i}^2}{c^2} \frac{\mathbf{n}_{\text{at}}}{4} \mathbf{n}_{\text{ph},4+3} \left(\frac{\mathbf{n}_{\text{at}}}{\mathbf{n}_{\text{ph},4+3}} + 1 \right) \right], \end{aligned}$$

⁹here *mean* takes on a double meaning...

This expression is qualitatively the same as eq. (5.25) for the monochromatic MZI, except for the term $n_{\text{at}}/(n_{\text{ph},4+3})$ stemming from $\langle(\Delta\hat{n}_{\text{ph},4-3})^2\rangle$. This term is interpreted as coming from the shot noise of the photon number of two probe beams. Though the mean value $\langle\hat{n}_{\text{ph},4-3}\rangle = 0$, as required, this relies on the combined phase-shift of the two probes to cancel and is thus sensitive to variations in the relative intensity between the probes. Hence, shot noise fluctuations in the photon number will translate into different fluctuations in the signal from each probe and the difference will fluctuate around zero. Fortunately, this term is proportional to ratio $n_{\text{at}}/(n_{\text{ph},4+3})$, which under usual experimental conditions is $\approx 1/100$.¹⁰ Although this means that the term can usually be neglected we must keep in mind that we cannot tolerate too low photon numbers. If we want to reach a certain coupling constant this in return means that we the probe detunings should not be too low. We get the SNR

$$\text{SNR} = \frac{\mathcal{T}^4 \tau^2 \sin^2 \tilde{\phi} \sin^2 \beta_1 4 \frac{\mathcal{K}_{2i}^2}{c^2} \frac{n_{\text{at}}}{4} n_{\text{ph},4+3}}{1 - \rho^2 t_1^2} = \kappa_2^2, \quad (5.36)$$

which very much resembles eq. (5.26) except for \mathcal{K}_{2i} .

Squeezing and decoherence Here we will follow the procedure in sec. 5.2.2 of relating the coupling strength to the optical depth and the spontaneous scattering rate. We note in the same treatment for the mono-chromatic probing scheme that the simple relation in eq. (5.17) should be amended slightly. In the dichromatic probing scheme the frequencies of the two probe colours are not fixed to an absolute value, but only mutually dependent. It turns out that the correction to the simple relation in eq. (5.17) can be significant if the probes are put near a transition. We can generally write the transition strength for the probes as

$$\kappa_{2\mp}^2 = \frac{1}{2} \sum_e \frac{(\mathcal{K}_{4e} \mp \mathcal{K}_{3e})^2}{(\mathcal{L}_{4e} + \mathcal{L}_{3e})} n_{\text{at}} t_a \tilde{\eta} = \frac{1}{2} r_{\text{Di}\mp}(\Delta) \frac{|g_-|^2}{\gamma_e/2} n_{\text{at}} t_a \tilde{\eta}. \quad (5.37)$$

Here $\tilde{\eta}$ is the combined spontaneous scattering due to both probe colours. Since we add the coupling strengths of the probes it is implicit in this equation that the probes couple with equal strength. The \mp refers to the the 1-input (-) and the 2-input (+) configuration, respectively. We plot the fraction for the D2-line in fig. 5.10 where green goes for the 1-input and red for the 2-input MZI and likewise for the D1-line in fig. 5.9 How to interpret these curves? Well, we will

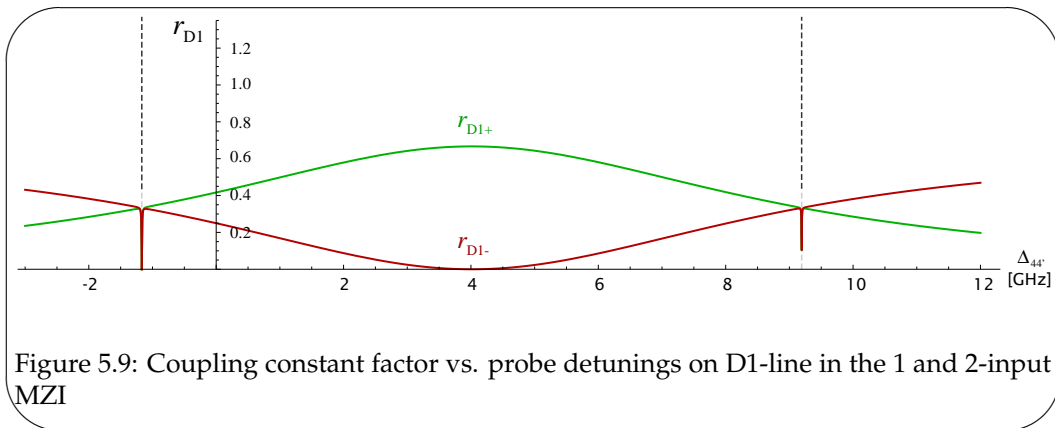


Figure 5.9: Coupling constant factor vs. probe detunings on D1-line in the 1 and 2-input MZI

give it a try, though admittedly the arguments are very intricate for someone not very familiar with the experiment. First of all we notice that right on resonance the ratio goes to zero. This is clear because the \mathcal{K}_{ge} changes sign and at

¹⁰if we take the whole atomic ensemble and probe pulse.

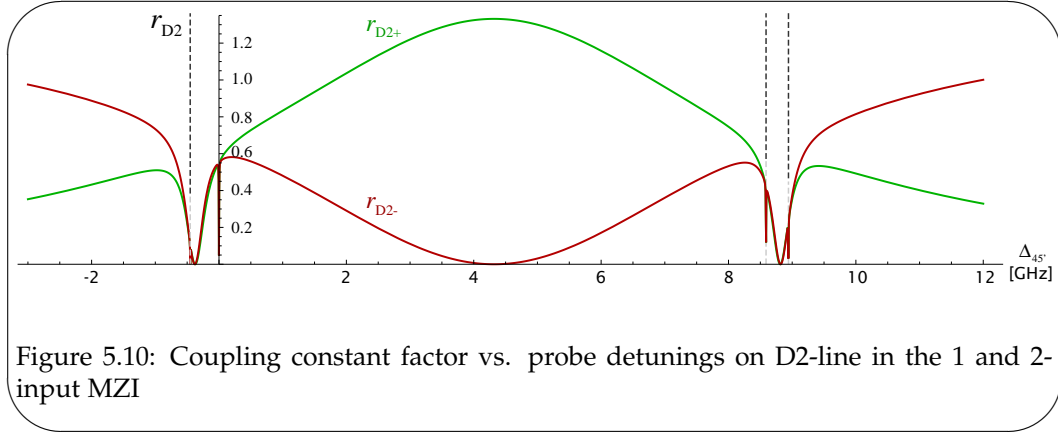


Figure 5.10: Coupling constant factor vs. probe detunings on D2-line in the 1 and 2-input MZI

the same time \mathcal{L}_{ge} becomes very large. Thus we completely lose sensitivity to the ground level coupling to that transition. For the D2-line we see that there is a broad region around the hyperfine excited state transition pairs where the coupling strength is also suppressed by the factor. This is because in between the transitions to the hyperfine transitions the probe receives opposite phase shifts due to the two transitions. E.g. a probe detuned red to $|4\rangle \rightarrow |5'\rangle$ but blue to $|4\rangle \rightarrow |3'\rangle$ will be phase-shifted in one direction by the former and the opposite by the latter. Finally, we see that for the 1-input configuration (green curves) the factor is maximal in between the transitions at the point where we set the monochromatic probe. This is because at this point each of the dichromatic probes detect population fluctuations from both ground states. I.e. they basically act as two monochromatic probes. Hence it is no shame that the coupling strength is lower near the transitions because we are actually utilising twice the number of photons, i.e., $n_{\text{ph}} \equiv n_{\text{ph},3} + n_{\text{ph},4}$. When going red or blue detuned from both transitions we see that the coupling starts to drop, hence we must stay close to the transitions and with a slight preference for the probes being in between ground level transitions. In the 2-input case the picture is reversed since right in between the ground level hyperfine transitions the two probes would see the opposite effect of population changes and thus the signal from the projection noise would cancel. In this case it is better to be red detuned to the lower or blue detuned to the upper, however just sticking close to the transitions will suffice.

Because the probe detunings are not pinned down we cannot state a formula for the noise reduction and squeezing. This was possible in the simple relation eq. (5.19), which makes no reference to the probe detuning, and for the monochromatic the set detuning allowed us to calculate eq. (5.28). Instead we will plot the noise reduction and squeezing as a function of the probe detuning. Note that the detuning refers to one of the probes, where the other probe's detuning follows from the condition that the magnitude of the coupling strengths be equal. We omit the plots of the D1-line, since, it they add no understanding beyond what we can learn from the D2-lines. Furthermore our experiments are all performed on the D2-line. In all graphs we set the optical depth to be $\tilde{\alpha}_0 = 40$.

The noise reduction fig. 5.11 and fig. 5.12 depend highly on the probe frequency. The projection noise level $\langle (\Delta \hat{f}_z)^2 \rangle^{(in)}$ is marked by the green line where $\tilde{\eta} = 0$. Near the non-cycling transitions where the inelastic scattering dominates the $\langle (\Delta \hat{f}_z)^2 \rangle^{(out)}$ is initially decreased by having a small $\tilde{\eta}$, but quickly starts growing again as $\tilde{\eta}$ is increased further. Hence, the optimal η is rather low. Near the cycling transitions where quasi-elastic decay channels dominate the noise reduction keeps improving as $\tilde{\eta}$ is increased, and the optimal $e^{-\eta}$ rather very large. Again this signifies that the spontaneous decay process adds very little noise to the output \hat{f}_z variance. The behaviour of the noise reduction in between the ground

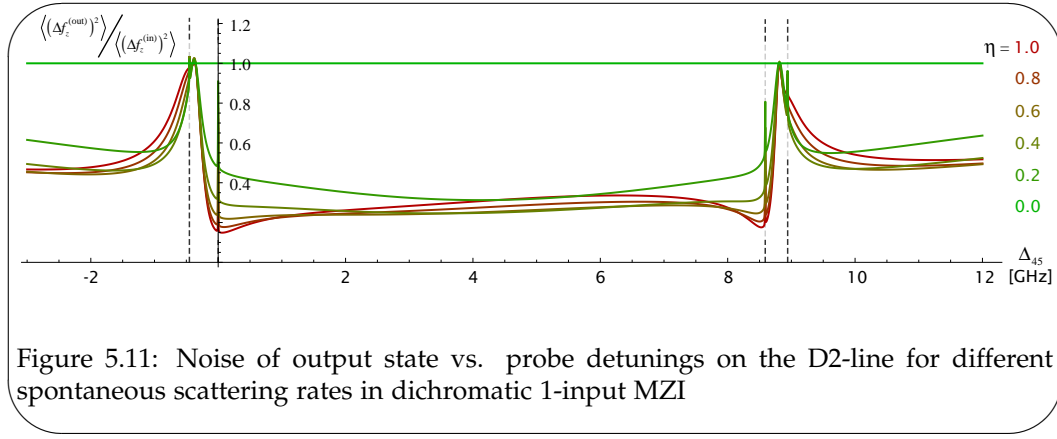


Figure 5.11: Noise of output state vs. probe detunings on the D2-line for different spontaneous scattering rates in dichromatic 1-input MZI

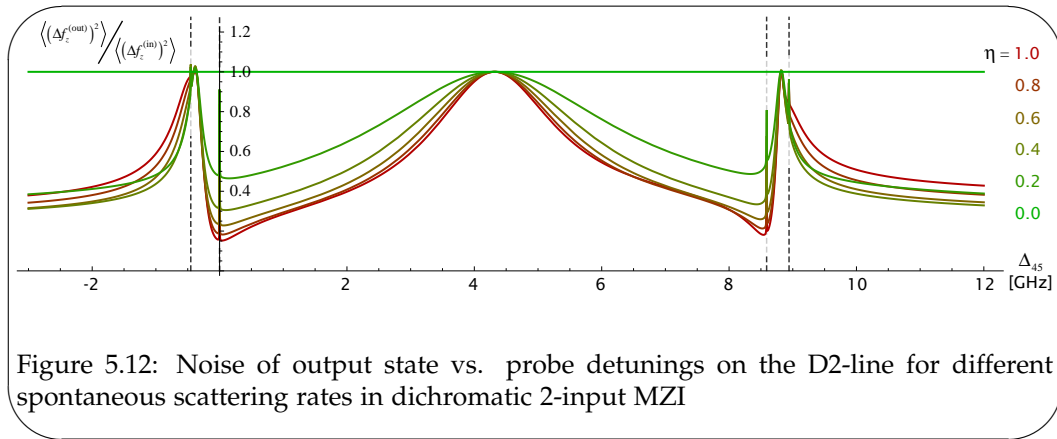


Figure 5.12: Noise of output state vs. probe detunings on the D2-line for different spontaneous scattering rates in dichromatic 2-input MZI

state transitions and for very large detunings reflect the coupling constants plotted in fig. 5.10. When the coupling constants are low in either the 1 or 2-input configuration the noise reduction is also absent.

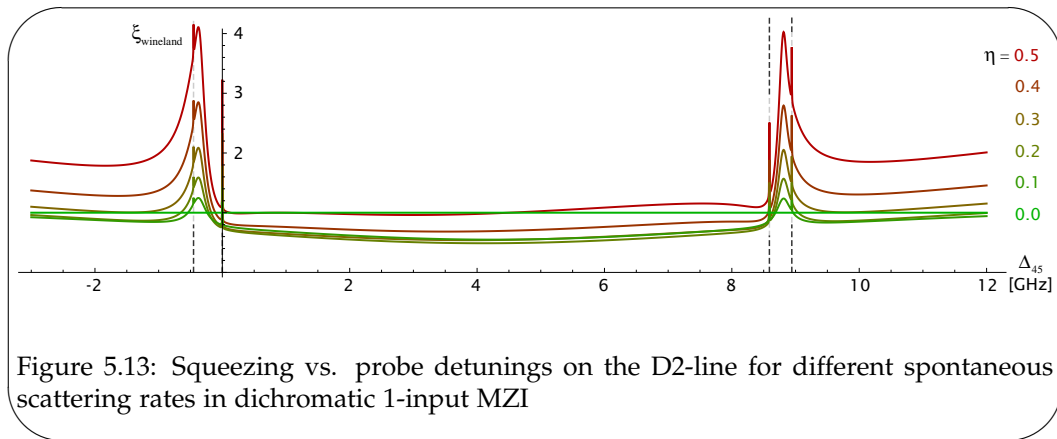


Figure 5.13: Squeezing vs. probe detunings on the D2-line for different spontaneous scattering rates in dichromatic 1-input MZI

For the squeezing (see fig. 5.13 and fig. 5.14) the decoherence of the spin-vector sets further limit to the desirable amount of spontaneous decay. Hence, the detunings for which the noise reduction was low will result in the squeezing factor ξ_{wineland} being large (small is good!). On the non cycling transition the optimal spontaneous decay rate is low, around 0.1. Near the cycling transition the optimal values is around 0.2-0.3. The latter is fairly close to the $\eta_{\text{opt}} = 1/3$ for the idealised case from sec. 5.2.2.

As a final remark, in eq. (5.37) we omitted the part related solely to the MZI. For an unbalanced MZI with losses one factor $1/2$ must be replaced by the pre-factor in eq. (5.27). In the 2-input configuration it becomes exceedingly complicated if one does not assume equal splitting at the MZI input, i.e., $t_1 = r_1 = 1/\sqrt{2}$.

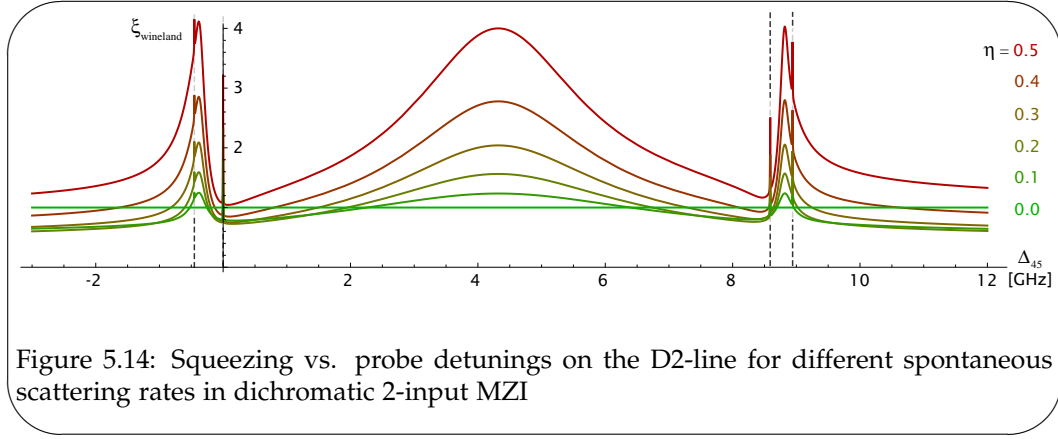


Figure 5.14: Squeezing vs. probe detunings on the D2-line for different spontaneous scattering rates in dichromatic 2-input MZI

When evaluating the noise reduction and excitations for the entire ensemble we must keep in mind that $\tilde{\alpha}_0$ and $\tilde{\eta}$ vary over the transverse dimension of the interaction region. In the next section we will point to this issue.

5.4 Full ensemble squeezing

The derivations so far have been phrased in terms of the local ensemble operators. Since the coupling constant κ^2 , which governs the noise reduction, is proportional to the atomic and photon densities it too will be spatially dependent. Moreover, the photon absorption is logically larger where the photon density is high, hence making the decoherence spatially dependent. All together, the noise reduction and squeezing will vary over the width of the sample according to the particle densities. The effective noise reduction and squeezing are thus only found by integrating the local noise over the ensemble dimensions. we believe that these geometric considerations are not unimportant, although they also should not cause any conclusions made so far to be changed drastically.¹¹ Unfortunately, we have not yet developed the treatment completely. Some sketches and ideas on the point can be found in sec. C, while here we take a short-cut.

Let us first examine the basic approach of finding a total ensemble coupling strength and a resulting estimate of the noise reduction. Here we simply define the coupling constant as the transverse spatial integral over the ensemble using the mode function of the probe

$$\kappa_{\text{uni}}^2 = \int_{R^2} \frac{\mathcal{K}^2}{c^2} \mathcal{N}(\mathbf{r}) U(\mathbf{r}) l_a \hat{n}_{\text{ph}} l_p d^3 r = \mathcal{K}^2 N_{\text{at}} N_{\text{ph}}, \quad (5.38)$$

from which we get an effective uniform noise reduction $\varepsilon_{\text{uni}} = 1/(1 + \kappa_{\text{uni}}^2)$. Using eq. (3.26) the reduced projection noise of the ensemble after the QND measurement is

$$\langle (\Delta \hat{F}_z^{\text{(out)}})^2 \rangle = \varepsilon_{\text{uni}} \langle (\Delta \hat{F}_z^{\text{(in)}})^2 \rangle = \frac{1}{1 + \kappa_{\text{uni}}^2} \frac{N_{\text{at}}}{4} \frac{1 + r_w^2}{1 + 2r_w^2} \quad (5.39)$$

The above approach effectively simplifies the treatment to a one-dimensional case where the squeezing and decoherence are uniform over the whole ensemble, in which case the density distribution of the atoms is also irrelevant.

A full understanding of the geometric intricacies of the coupling is as yet beyond the comprehension of this text's author. There have been serious theoretical investigations most comprehensively in [Raymer81, Sørensen08], but with many of the important points of the latter conveyed in [Hammerer09].

¹¹a careful statement

Noise sensitivity

Following the mostly theoretical considerations on the QND measurement in terms of the achievable SNR it is now time to start bridging to the experimental part of the thesis by treating slightly more empirical aspects of the system. This entails considering so called *classical noise* that is not rooted in the quantum uncertainty of the states. Among the classical sources are for example laser frequency and intensity noise, acoustic noise. Before looking at these sources in detail we will clarify the significance of additional "non-quantum" noise in the quest for creating squeezed spin states. Intuitively, the ability of the QND measurement result to inform us about the quantum state of the atoms is reduced when the measurement becomes less precise. Thus all noise will tend to wash out the entanglement of the measured \hat{S}_z with \hat{F}_z and thus reduce the spin-squeezing achieved by the measurement. In eqs. (5.8 and 5.26) we already explicated that the ratio of atomic to shot noise is a measure of the coupling strength in the QND measurement and thus sets the limit for the achievable spin squeezing c.f. eq. (5.12) or eq. (5.16). That, the SNR was equated with \mathcal{K}_d^2 was only due to us not yet accounting for any other noise influences in the measurement. However, when classical noise disturbs the QND measurement we will have $SNR < \mathcal{K}_d^2$ and thus the squeezing will drop. In the following sections we will express the output signal in terms the MZI output difference current $i_- = 2\hat{S}_z^{out}$.¹ We then amend eqs. (5.25 and 5.35) by

$$\langle(\Delta i_-)^2\rangle = \langle(\Delta i_-)^2\rangle_{\text{SN}} + \langle(\Delta i_-)^2\rangle_{\hat{\phi}_{\text{at}}} + \langle(\Delta i_-)^2\rangle_{\text{classical}}$$

where $\langle(\Delta i_-)^2\rangle_{\text{classical}}$ is a compound of several contributions, which we will now describe one by one after a couple of definitions. A more fundamental account of classical noise sources pertaining to an MZI can be found in [Oblak04].

6.1 Classical interferometer noise

As an overall approximation we do not consider second order effects. In other words, we neglect the fact that noise from one source will give rise to varying noise from another source. As long as the noise contributions are small (less than a few percent) this is a safe assumption. An exception to this, is that we will need to discuss some second order effects in the section about atomic noise ??.

¹In this sense it would be more appropriate to write \hat{i}_- rather than i_- , but here we need to compromise with the operator notation. The reason is that we will investigate influences on the signal which are both quantum and classical origin such as shot noise and acoustic fluctuations. To accommodate both we suppress the $\hat{\cdot}$.

To find the noise contributions we *linearise* $i_-(t)$ around its mean value classically defined as $\langle i \rangle = \lim_{t' \rightarrow \infty} \frac{1}{t'} \int_0^{t'} i(t) dt$ or for quantum fluctuations as the expectation value $\langle i \rangle \propto \langle n_{\text{ph}} \rangle$. The photocurrent is thus expressed as $i_-(t) = \langle i \rangle + \delta i_-(t)$ where by definition $\langle \delta i(t) \rangle = 0$. Often we possess knowledge of the spectral distribution of the fluctuations. To exploit this we write $\delta i_-(t)$ in terms of its Fourier decomposition

$$\delta i_-(t) = \frac{1}{2\pi} \int_{-\infty}^{\infty} \delta i_-(\omega) e^{i-\omega t} d\omega \quad (6.1)$$

with the Fourier components $\delta i_-(\omega)$.² From the spectrum we can always compute the variance by employing Parseval's

$$\langle (\Delta i_-(t))^2 \rangle = \int_{-\infty}^{\infty} \langle |(\Delta i_-(\omega))^2| \rangle \frac{d\omega}{2\pi} = \int_{-\infty}^{\infty} W_{i_-}(\omega) d\omega, \quad (6.2)$$

we have defined the spectral power density of fluctuations in $i(t)$ as $W_{i_-}(\omega) = \langle |(\Delta i_-(\omega))^2| \rangle / 2\pi$. To account for the limited frequency response of the detection system we introduce the transfer function $g(\omega)$, which is normalised to 1 at the frequency of maximum responsivity. We define the detection bandwidth ω_{BW} as $\omega_{BW} = \int_0^{\infty} |g(\omega)|^2 d\omega$. In sec. 8.2.2 we shall see that the pulsed detection naturally imposes a detection transfer function $\mathcal{M}_{\text{int}}(\omega)$. Taking the detection limitation into account, the proper expression for the photo current variance becomes

$$\langle (\Delta i_-(t))^2 \rangle = \int_{-\infty}^{\infty} |g(\omega)|^2 W_{i_-}(\omega) d\omega. \quad (6.3)$$

The framework is now ready for the treatment of the individual noise sources in the interferometer signal. As a teaser we can take a look at the shot noise. Since it is *white noise*, i.e., it has a constant spectral power density, we can pull W_{i_-} out of the integral whereby

$$\langle (\Delta i_-(t))^2 \rangle_{\text{SN}} = W_{i_-} \int_{-\infty}^{\infty} |g(\omega)|^2 d\omega = 2B\epsilon (1 - \rho^2 t_1^2) \frac{N_{\text{ph}}}{4} \quad (6.4)$$

where ϵ denotes the detector's quantum efficiency, ρ the probe arm losses, and t_1 the reflection of the MZI input BS c.f. eq. (2.25). We introduce a visualisation of the shot-noise in fig. 6.1. Since the shot noise is independent of the fringe

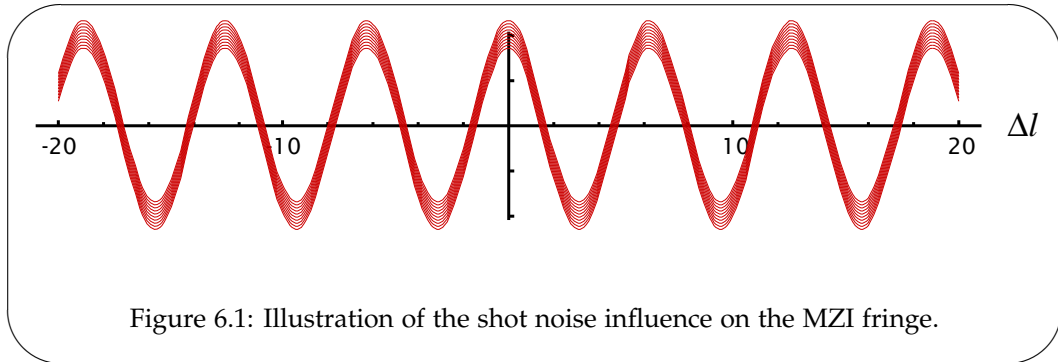


Figure 6.1: Illustration of the shot noise influence on the MZI fringe.

phase it does not appear very action-packed, but shown as a point of reference for subsequent noise illustrations. What regards the atomic quantum projection noise, we have no a priori insight in its spectral power density. Hence we will assume that it is also constant over our detection bandwidth, and as a result eqs. (5.8 and 5.26) is not altered. Now we move on to classical noise sources.

²Note that even though we use the same symbol $\delta i(\cdot)$ for the photo current fluctuation and its Fourier components, the two functions are not the same. The two functions can only be distinguished by the dependent variable in the brackets, i.e., (t) or (ω) . When we don't write any variable δi we implicitly mean $\delta i(t)$.

6.1.1 Laser intensity noise

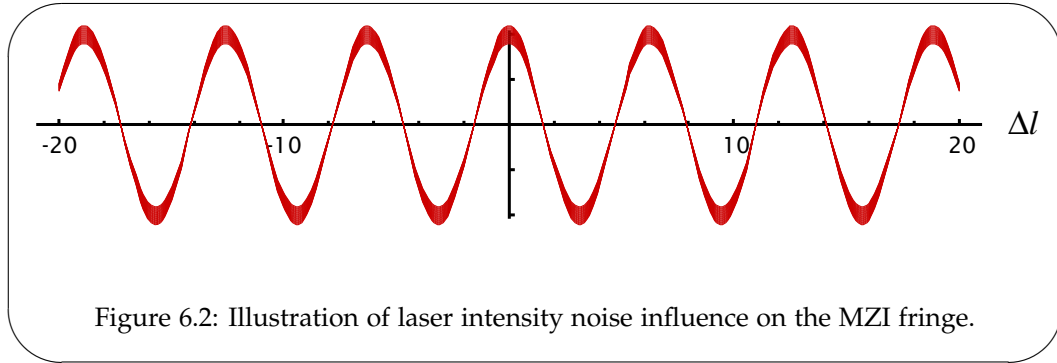
To gauge the effect of classical fluctuations we turn to the classical MZI output signal eq. (2.24), which is equivalent to

$$i_- = -2\epsilon T^2 \tau \cos \tilde{\phi} N_{\text{ph}}/t_p \quad (6.5)$$

Thereupon we deduce the effect of classical fluctuations of the laser intensity, i.e., of N_{ph} ,

$$\langle (\Delta i_-)^2 \rangle_I = \left(2\epsilon T^2 \tau \cos \tilde{\phi} \frac{N_{\text{ph}}}{t_p} \right)^2 \int_{-\infty}^{\infty} |g(\omega)| W_A(\omega) d\omega \quad (6.6)$$

The crux of this expression is that the classical intensity noise scales with the square of the photon number and it depends as \cos^2 on the MZI phase. The former attribute enables us to distinguish classical noise from shot noise, and the latter means that we can suppress laser intensity noise by adjusting the MZI path-length difference so that $\tilde{\phi} = (n + 1/2)\pi$. We refer to this setting as the *balanced* position of the MZI. In pictorial representation (fig. 6.2) the intensity



noise is identified as a fluctuating fringe amplitude. So we conclude, that in the balanced setting the power, including its fluctuations, is the same in both MZI outputs, hence subtracting the signals in the two outputs also eliminates the fluctuations. On 112 we measure the probe lasers' intensity noise spectrum.

6.1.2 Laser frequency/phase noise

The MZI fringe phase in the absence of atoms³ can be expressed as $\tilde{\phi} = \omega \Delta l$, where Δl is the path-length difference between the probe and reference arms. Variation of the MZI phase are written as $\delta \tilde{\phi} = \delta \omega \Delta l / c + \omega / c \delta(\Delta l)$. The former is the effect of laser frequency noise whereas the latter is rooted in acoustic noise, which we shall discuss in the next section. In light of laser frequency noise we can write the output signal as

$$i_- = -2\epsilon T^2 \tau \cos(\tilde{\phi} + \delta \omega \Delta l / c) N_{\text{ph}}/t_p \quad (6.7)$$

where we could also have written $\tilde{\phi}$ in terms of the nominal frequency $\tilde{\phi} = \omega \Delta l / c$.⁴ For small $\delta \tilde{\phi}$ we can expand the cosine to first order $\cos \tilde{\phi} + \delta \omega \Delta l / c \sin \tilde{\phi}$,

³this remark allows us to neglect the index of refraction, which for the remaining elements ought to be constant.

⁴this expression only holds for spectral components of the noise that are well below $2\pi c / \Delta l$, which in our case will be no less than $2\pi 15$ GHz. Higher components will be uncorrelated at the MZI output BS due to the relative time delay between the fields in the two arms arising from MZI path-length difference. This is a result of the laser phase noise only being visible when there is interference.

by which

$$\langle (\Delta i_-(t))^2 \rangle_{\delta\omega} = (2\epsilon T^2 \tau \frac{\Delta l}{c} \frac{N_{\text{ph}}}{t_p} \sin \tilde{\phi})^2 \int_{-\infty}^{\infty} |g(\omega')| W_{\delta\omega}(\omega') d\omega', \quad (6.8)$$

This expression has three highlights. Firstly, the noise arising from laser phase noise will scale quadratically with the N_{ph} — the hallmark of classical noise. Secondly, it vanishes when the sine is zero i.e. when $\tilde{\phi} = n\pi$. This is exactly opposite to the laser intensity noise, and for this reason it is not possible to cancel both intensity and frequency noise by adjusting $\tilde{\phi}$. In any case, setting $\tilde{\phi} = n\pi$ would leave us insensitive to small phase-displacements e.g. by the atoms. We are rescued by the $(\Delta l/c)$ factor, which tells us that the frequency noise can be suppressed by aligning the MZI close to zero path-length position, what is called the *white-light* position. In sec. 8.4.1 we describe the procedure for aligning the MZI to white-light. A graphical representation of the frequency noise (see

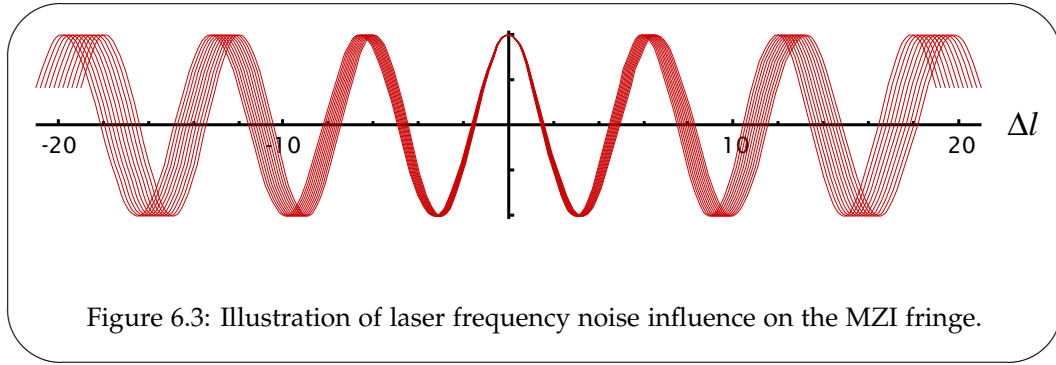


Figure 6.3: Illustration of laser frequency noise influence on the MZI fringe.

fig. 6.3) illustrates how the fluctuations changes the period of the interference fringes causing the whole fringe pattern to stretch like an accordion around the white-light position.

In eq. (6.8) we naturally used the frequency noise power spectrum $W_{\delta\omega}$. As it is sometimes simpler to detect the laser-phase noise we give the relation between the frequency and phase noise spectra [Petermann91]

$$W_{\delta\omega}(\omega') = \frac{(\omega'/2)^2}{\sin^2(\omega'\Delta l/(2c))} W_{\delta\phi}(\omega'). \quad (6.9)$$

emphasising that ϕ in this equation refers to the phase of laser field and *not* that of the MZI. In sec. 8.1.2 we measure the frequency spectrum and in sec. 8.1.3 the phase-noise spectrum for two separate locking schemes for the probe laser frequencies.

Laser diodes are known to have a large frequency noise in the output, which is true even in the case of grating stabilisation. For most low frequencies the spectral density will be larger than that of the quantum Shawlow-Townes limit, growing as $1/\omega$ towards zero frequency [Petermann91, Telle93].

6.1.3 Acoustic noise

The acoustic noise is probably the most unpredictable of all the noise sources in the experiment. In general any effect that perturbs the path-length difference is what we will call acoustic noise. The sources can be anything from vibrations or sounds created by pieces of equipment, air fluxes around the interferometer, or loud lab staff members.

Box 6.1: Examples of laser phase noise affecting MZI output

It is appropriate to study a couple of special cases of frequency noise distributions. As always we first take a white noise distribution $W_{\delta\omega}(\omega') = \Delta\omega$ so that when we remember to account for the detection bandwidth

$$\langle(\Delta i_-(t)_{\delta\omega})^2\rangle = (e\eta T\langle N_{\text{ph}}\rangle\Delta t \sin\tilde{\phi}/t_p)^2 2B\Delta\omega.$$

The quantity $\Delta\omega$ can be referred to as the line-width of the laser [Petermann91].

Another example is where the frequency noise is dominated by a component at one particular frequency ω_μ . The corresponding spectral density is $W_{\delta\omega}(\omega') = \mu^2\delta(\omega - \omega_\mu)$ where $\delta(\omega - \omega_\mu)$ is Dirac's Delta function and μ is called the modulation depth. Since we neglect noise at other frequencies we will not have to account for the bandwidth as long as the modulation frequency ω_μ lies within the bandwidth. Hence we have

$$\langle(\Delta i_-(t))_{\phi}^2\rangle = (e\eta T\langle N_{\text{ph}}\rangle\mu\Delta t \sin\tilde{\phi}/t_p)^2.$$

Experimentally it is easy to apply a harmonic oscillation to the laser frequency, e.g. by modulating the laser current or the cavity grating. Monitoring and minimising the MZI noise induced by the applied laser frequency modulation provides one practical way of finding the white light position [Oblak04, Oblak05].

Since path-length variations affect the MZI phase we go back to the expression just above eq. (6.7) stating that $\delta\tilde{\phi} = \delta\omega\Delta l/c + \omega/c\delta(\Delta l)$. Hence, for the acoustic noise we have

$$i_- = -2\epsilon\mathcal{T}^2\tau \cos(\tilde{\phi} + \omega/c\delta(\Delta l))N_{\text{ph}}/t_p \quad (6.10)$$

and exactly as the procedure in the previous section we expand the cosine to arrive at

$$\langle(\Delta i_-(t))^2\rangle_{\Delta(\delta l)} = (2\epsilon\mathcal{T}^2\tau\omega\frac{N_{\text{ph}}}{t_p} \sin\tilde{\phi})^2 \int_{-\infty}^{\infty} |g(\omega')|W_{\Delta(\delta l)}(\omega')d\omega'. \quad (6.11)$$

Besides the, by now, trivial quadratic dependence on N_{ph} , we see that the noise scales with the light frequency squared. This is expected since the smaller ω is, the longer is the spatial periodicity of the fringe. However, this information is of no use since ω is a fixed experimental parameter. Moreover, the balanced position is where the output signal is most vulnerable to acoustic noise, as is easy to see from the portrayal in fig. 6.4. It is difficult to determine the exact

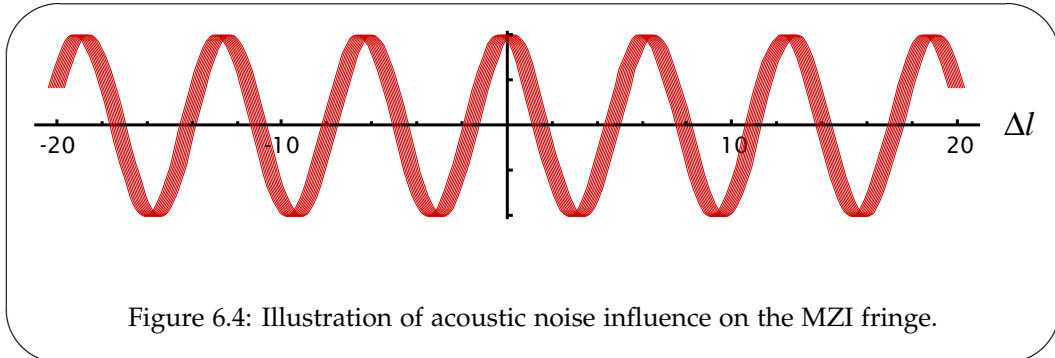


Figure 6.4: Illustration of acoustic noise influence on the MZI fringe.

spectral power density of the acoustic fluctuations $W_{\Delta l}(\omega')$ except by measuring the effect on the MZI. We are left with two complementary ways to reduce the

acoustic noise. The first is to actively hold the path-length difference by way of various locking methods (see sec. 8.6). The other, which we will put forward below, relies on the clever arrangement of the modes of two probe beam.

Acoustic noise cancellation

We saw in sec. 2.3.1 three different configurations where two probes are arranged in the MZI such that their fringes are π out of phase. Because one of these configurations requires the two probes to have different frequencies and we concluded in sec. 5.3.2 that a dichromatic probe would benefit the QND measurement, we consider here the two-colour probe case. We assumed an equal number of photons in the two colours, and if now we stipulate that the fringe amplitudes be equal, as well, we get the combined signal to be

$$i_- \propto \cos \left[\tilde{\phi} + \cos \left[\frac{\omega_3}{c} \delta(\Delta l) \right] \right] + \cos \left[(-\tilde{\phi} + \cos \left[\frac{\omega_4}{c} \delta(\Delta l) \right]) \right]$$

expanding this to first order we see that

$$\langle (\Delta i_-(t))^2 \rangle_{\Delta(\delta l)} \propto \left[\sin \tilde{\phi} \left(\cos \left[\frac{\omega_3}{c} \delta(\Delta l) \right] - \cos \left[\frac{\omega_4}{c} \delta(\Delta l) \right] \right) \right]^2.$$

This reveals that the acoustic noise influence is reduced by $2(\omega_3 - \omega_4)/(\omega_3 + \omega_4) \approx 2.5 \cdot 10^{-5}$ compared to that in the single probe fringe case. It is essential that the acoustic fluctuations $\delta(\Delta l)$ are shared between the two probes. This requires their spatial modes to be fairly well overlapped. In this case we say that the fluctuations are *common mode*. How much the noise cancellation means in real life we will show in sec. 8.7.

6.2 Classical noise in atomic state measurement

The noise considered above was due to the MZI alone, and we could characterise them as the noise of the passive detection system. When measuring the atomic sample we aim to see the influence of the projection noise of the prepared atomic state. The projection noise imprint on the MZI output noise was given by eqs. (5.25 and 5.35). However, imperfections in the way we prepare or detect the atomic state can also add noise to the atomic phase imprint. This we will call classical atomic noise and as for the classical MZI noise it will scale quadratically, not with the photon number, but with the atom number. To derive the influence of the various sources we need focus on the part of the output signal resulting from the atoms. Leaving out correction factors due to sample and probe geometry,⁵ the atomic signal in the output current is given by

$$i_- \propto \epsilon T^2 \tau \sin \tilde{\phi} \sin \beta_1 4 \frac{\mathcal{K}_2}{c} \left(\frac{\hat{N}_{\text{at}}}{2} \frac{\hat{N}_{\text{ph},4-3}}{2} + \hat{F}_z \frac{\hat{N}_{\text{ph},4+3}}{2} \right), \quad (6.12)$$

which can be derived from the eq. (5.23) for a monochromatic probe and eq. (5.31) or eq. (5.33) for the dichromatic probe. In the above we state the expression for the dichromatic probe, since it is easily reduced to the monochromatic probe case.

⁵in the final expression these would anyhow cancel.

6.2.1 Atom number fluctuations

The atomic population \hat{N}_{at} in the sample will fluctuate between each preparation of the ensemble. We let N_{at} signify the mean atomic number and δN_{at} deviations from the mean. Fluctuations in the atomic population can enter the atomic signal through either of the two terms in the brackets of eq. (6.12). The first term relies on $N_{\text{ph},4-3} \neq 0$, i.e., misbalancing of the probe powers,⁶ while the other relies on $\langle \hat{F}_z \rangle \neq 0$, i.e., the initial state not being an exact equal superposition state. If we take the balancing of both values to be off by some fraction so that $N_{\text{ph},4-3} = \vartheta_{\text{ph}} N_{\text{ph},4+3}$ and $\langle \hat{F}_z \rangle = \vartheta_{\text{at}} (N_{\text{at}} + \delta N_{\text{at}})$ we can specify the influence of atom number fluctuations as

$$\langle (\Delta i_-)^2 \rangle_{\delta N_{\text{at}}} \propto \left(\epsilon \mathcal{T}^2 \tau \sin \tilde{\phi} \sin \beta_1 4 \frac{\mathcal{K}_2}{c} \frac{\hat{N}_{\text{ph},4+3}}{2} \right)^2 \left(\frac{\vartheta_{\text{ph}}}{2} + \vartheta_{\text{at}} \right)^2 \langle (\Delta \delta N_{\text{at}})^2 \rangle,$$

We want to compare the classical noise with the quantum projection noise eq. (5.35). When we neglect the small $N_{\text{at}}/N_{\text{ph},4+3}$ term we get the ratio of the two noise contributions.

$$\frac{\langle (\Delta i_-)^2 \rangle_{\delta N_{\text{at}}}}{\langle (\Delta i_-)^2 \rangle_{\text{PN}}} = \frac{\left(\frac{\vartheta_{\text{ph}}}{2} + \vartheta_{\text{at}} \right)^2 4 \langle (\Delta \delta N_{\text{at}})^2 \rangle}{\frac{N_{\text{at}}}{1}},$$

Realistically we can only hold the atom number from shot to shot within a 10% margin, so if we presume $\langle (\Delta \delta N_{\text{at}})^2 \rangle = N_{\text{at}}/10$ we can determine the requirements on the balancing. As minimum we want the above ratio to be below unity, in which case we demand

$$\frac{\vartheta_{\text{ph}}}{2} + \vartheta_{\text{at}} < \frac{5}{\sqrt{N_{\text{at}}}} \quad (6.13)$$

The inequality must be fulfilled up to the highest atom numbers, which routinely reach a few 10^5 . Taking a moderately more demanding estimate of 10^6 we must be able to balance $\vartheta_{\text{ph}}/2 + \vartheta_{\text{at}}$ to better than 0.5%. This is fairly demanding, especially w.r.t keeping the balancing constant over a measurement run lasting days. To keep the probe power balancing within range we had to implement methods to actively stabilise them (see sec. 8.6.3). For the state preparation the prime task is to precisely make the superposition state equal (see fig. 12.1). Eq. (6.13) indicates that we can compensate an offset of one of the balancing parameters with the other. This constitutes a significant easing of the absolute balancing requirement of $N_{\text{at}}/N_{\text{ph},4-3}$ and $\langle \hat{F}_z \rangle$ individually.

6.2.2 Coupling strength fluctuations

The final noise influence comes indirectly from the probe laser frequency noise, which causes a fluctuating coupling constant. To uncover the connection we must go back to eq. (4.7) for the coupling strength. In this section we aim not at producing exact measures but at giving qualitative estimates. In line with this, we approximate the detuning dependence⁷ by $1/\Delta_{ge}$ where $\Delta_{ge} = \omega - \omega_{ge}$ is the probe's detuning from the nearest transition $|g\rangle \rightarrow |e\rangle$. As in sec. 6.1.2 we let

⁶this is a result of implicitly assuming the same visibility of both probe colours. If this was not assumed the condition would be that the fringe amplitudes must be equal.

⁷which in full is $\mathcal{K}_{ge} = \frac{|g_s|^2 \Delta_{ge}}{\Delta_{ge}^2 + (\frac{\gamma_e}{2})^2}$

the frequency noise be modelled by a $\omega = \langle \omega \rangle + \delta\omega$. The resulting noise in the coupling constant will be

$$\begin{aligned}\delta\mathcal{K}_{ge} &\propto \delta\left(\frac{1}{\Delta_{ge}}\right) = \delta\left(\frac{1}{\omega - \omega_{ge}}\right) \\ &= -\mathcal{K}_{ge}\frac{\delta\omega}{\Delta_{ge}}\end{aligned}\quad (6.14)$$

Based on this it is straight forward to calculate the ratio of classical atomic noise to the quantum projection noise

$$\frac{\langle(\Delta i_-)^2\rangle_{\delta\mathcal{K}_1}}{\langle(\Delta i_-)^2\rangle_{\text{PN}}} = \left(\frac{\delta\omega}{\Delta_{ge}}\right)^2 N_{\text{at}}$$

As earlier we must at least demand that this ratio be no larger than one, which means that

$$\frac{\delta\omega}{\Delta_{ge}} < \frac{1}{\sqrt{N_{\text{at}}}}\quad (6.15)$$

In words the fractional noise of the detuning should be less than $1/\sqrt{N_{\text{at}}}$, which would typically be no smaller than 10^{-3} . We get a clue for the optimal choice of detuning by the fact that the inequality is harder to fulfil for small detunings. Thus if the laser frequency noise is visible one should tune the probe further off resonance.

The above equation only reveals the stability requirement for a single probe laser and is thus only directly applicable to the monochromatic MZI. For the dichromatic probe it is not the individual coupling constants that matter but, depending on the input configuration, their sum or difference. In sec. 5.3.2 we determined that we must choose the probe detunings such that $\mathcal{K}_2 \equiv \mathcal{K}_4 = \mp\mathcal{K}_3$, where we only account for the coupling on the nearest resonance. Throughout this section the upper sign applies to the 1-input configuration and the lower sign to the 2-input configuration. Holding $\mathcal{K}_4 + \mathcal{K}_3 = 0$ requires stabilising the sum frequency while $\mathcal{K}_4 - \mathcal{K}_3 = 0$ requires stabilising the difference frequency, which experimentally is more expedient. We will come back to the practical realisation below, but first we formalise the requirements.

Based on eq. (5.29) we can similar to above find the variation in the output current due to probe frequency fluctuations

$$\begin{aligned}\delta i_- &\propto \frac{N_{\text{at}}}{2} N_{\text{ph}} \left(-\mathcal{K}_4 \frac{\delta\omega_4}{\Delta_4} \mp \mathcal{K}_3 \frac{\delta\omega_3}{\Delta_3} \right) + \hat{F}_z N_{\text{ph}} \left(-\mathcal{K}_4 \frac{\delta\omega_4}{\Delta_4} \pm \mathcal{K}_3 \frac{\delta\omega_3}{\Delta_3} \right) \\ &N_{\text{ph}} \mathcal{K}_2 \left[\frac{N_{\text{at}}}{2} \left(-\frac{\delta\omega_4}{\Delta_4} + \frac{\delta\omega_3}{\Delta_3} \right) + \hat{F}_z \left(-\frac{\delta\omega_4}{\Delta_4} - \frac{\delta\omega_3}{\Delta_3} \right) \right]\end{aligned}$$

The requirement $\mathcal{K}_4 = -\mathcal{K}_3$ for the 1-input MZI requires $\Delta_4/\Delta_3 < 0$, i.e. the detunings have opposite signs. In contrast, the 2-input MZI $\mathcal{K}_4 = \mathcal{K}_3$ necessitates $\Delta_4/\Delta_3 > 0$, i.e. the detunings have the same sign. If we approximately say that the detunings have the same magnitude $|\Delta| = |\Delta_4| \approx |\Delta_3|$ we can reach further simplify the expression for the photo-current variation

$$\delta i_- \propto N_{\text{ph}} \mathcal{K}_2 \frac{1}{|\Delta|} \left[\frac{N_{\text{at}}}{2} (-\delta\omega_4 \mp \delta\omega_3) + \hat{F}_z (-\delta\omega_4 \pm \delta\omega_3) \right]$$

The latter term in the brackets has zero mean because $\langle \hat{F}_z \rangle = 0$. This term only contributes through fluctuating coupling strength to the projection noise $\langle(\Delta \hat{F}_z)^2\rangle$, but this will always be dominated by the former term. If we keep

only the former term we get a simple formula for the probe frequency induced classical atomic noise to the quantum projection noise

$$\frac{\langle(\Delta i_-)^2\rangle_{\delta\mathcal{K}_2}}{\langle(\Delta i_-)^2\rangle_{\text{PN}}} = \frac{\langle(\Delta(\delta\omega_4 \pm \delta\omega_3))^2\rangle}{|\Delta|^2} N_{\text{at}}$$

Again demanding the ratio to be below one we get the condition

$$\frac{\langle(\Delta i_-)^2\rangle_{\delta\mathcal{K}_2}}{\langle(\Delta i_-)^2\rangle_{\text{PN}}} = \frac{\langle(\Delta(\delta\omega_4))^2\rangle + \langle(\Delta(\delta\omega_3))^2\rangle \pm 2\langle(\Delta(\delta\omega_3 \delta\omega_4))\rangle}{|\Delta|^2} < \frac{1}{N_{\text{at}}} \quad (6.16)$$

where we have factorised the variance. If the two laser frequencies are statistically independent the covariance $\langle(\Delta(\delta\omega_3 \delta\omega_4))\rangle$ vanishes and we are left with a twice as strict condition as eq. (6.15). If the two laser frequencies are correlated it makes a *big* difference whether we set the coupling constants to accommodate the 1-input or 2-input configuration. For the 1-input MZI the correlation add to the noise while in the 2-input MZI they reduce the noise.

Is it at all relevant to consider frequency correlation?... Yes. On the slow to medium time-scale the probe lasers experience the same thermal and mechanical perturbations and may share some electronic influences in case of shared supplies for drivers and locking circuits etc. These external influences are likely to correlate or anti-correlate the laser frequencies. Of course this give no apparent clue to which MZI input configuration we should advocate. A much clearer preference can be made for different laser frequency locking schemes. If the locking of the two probes is independent no or only random correlation is anticipated (see sec. 8.1.2). If however the two probe frequencies are locked to one another (see sec. 8.1.3) or derived from the same laser source [Buchkremer00] the correlation can be considerable and in that case the 2-input MZI is by all means favourable.

Part II

Experiment

Overview of setup

There are a number of reasons why a career in experimental physics is not suited for all. One, that is commonly overlooked, is the deliberate effort of senior experimentalists to create an experimental setup that is so complex and messy that no one without access to their unique insight can possibly figure out how to operate the setup. Nevertheless, with the risk of endangering the positions of colleagues, this chapter constitutes an honest attempt to unveil the many hidden mysteries of our setup.

From a practical point of view the setup can be structured into a number of vaguely distinct parts. First is the MOT setup comprising optical elements and vacuum parts that are mainly controlled by the LabView programme CAMOT via DAC/ADC computer interface cards. The optical pumping is incorporated into this part as the beams are derived from the MOT lasers. Closely related is the second setup with the high power VersaDisk laser for the Far Off-Resonant Trap (FORT). The microwave elements for state preparation and manipulating the pseudo-spin make up the third part. Fourth is the QND probe and interferometer setup – including a locking laser – that are chiefly handled by the DIO-64 LabView programme via the DIO-64 computer interface card. The DSO and data processing is also viewed as belonging to the fourth part. None of the parts can really be viewed independently but the division serves as a rough tool to provide some structure for the uninitiated.

7.1 Layout, instrumentation and control system

More and more tweaks and degrees of freedom have been added to the setup in order to exterminate the vast number of bugs, which have materialised in an all too regular pace. In parallel with the progression of the experiment the degree of automation has steadily grown so as to simplify the increasingly complex and time consuming measurements. Not surprisingly, the result is a rather modular experimental setup littered with small units that each make a small, but indispensable, contribution to the overall functionality.

Figure 7.2 on the following pages outlines the interconnections between the various elements of the setup. Evidently, the diagram is by no means easy to overview and it is presented here mainly to gain a grand overview and to be a point of reference when the various subparts are introduced in later sections. The computer based control system is the central element, which oversees and interlinks the whole setup. Most of the computer control is executed by one computer ("Godzilla") fitted with three analogue input/output (ADC/DAC) cards

from National Instruments ¹ and a single digital output card from ViewPoint Systems ². The operation of ADC/DAC cards is handled by the LabView programme CAMOT (see sec. 9.1 for a screen-shot and a thorough introduction to the software). The cards are synchronised by exchanging the *analogue output start* trigger and the *analogue output update* triggers over the inter-card Real Time System Integration (RTSI) bus. The update frequency is set to 1 kHz giving output a 1 ms temporal resolution, which is suitable for controlling the MOT and the shutters.

Previously the 1 MHz counter signals from the the ADC/DAC were used as sources for generating fast pulse trains of the probe lasers. However, this method is very restrictive allowing only for evenly spaced trains of pulses of equal duration. To allow for more versatile pulse configurations we procured a FPGA-based 64 channel digital output card with 50 ns time resolution controlled by the *dio-64* Labview programme shown in fig. 7.1. Whereas the ADC/DAC cards require the output values for all channels to be specified for each update trigger the DIO64 can be programmed with time-stamps and values only for the event that the output on a channel changes. Hence, the data transfer load from the PC to the on-board FIFO memory is significantly reduced and it is possible to generate complex output patterns at a fast rate. Since the FIFO memory size of 512 bits is too small to hold all time-stamps and associated channel updates for a whole experimental cycle it is not possible to loop over the FIFO. Instead time-stamps and values must be input to the FIFO memory at regular intervals [Windpassinger08a]. To ensure synchronisation with the CAMOT programme the output of the DIO64 is triggered by the output from one of the DAC/ADC cards.



Figure 7.1: Screen-shot of DIO64 pulse timing program. Main lesson from this figure is that we need to set *a lot* of values.

¹Product names: PCI-MIO16E-4, PCI-6713, and PCI-6711.

²Product name: PCI-DIO64.

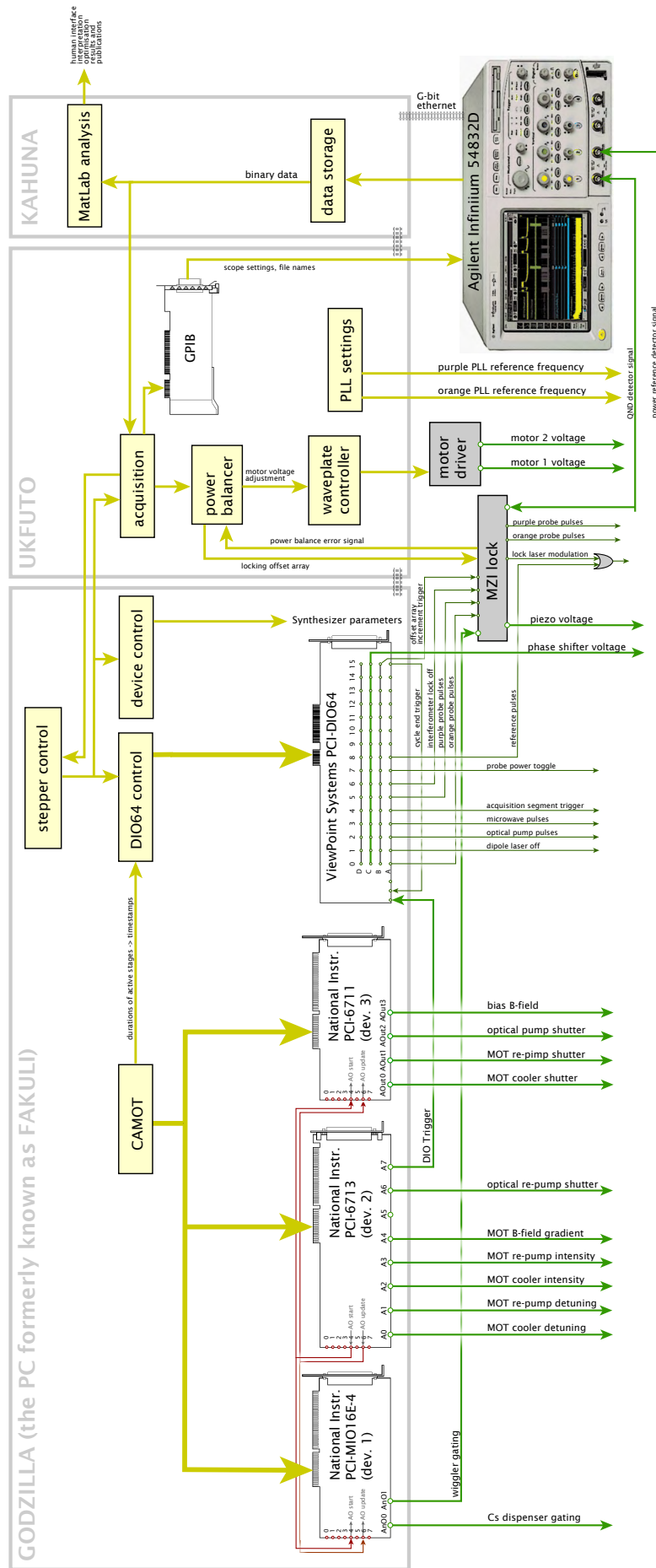


Figure 7.2: Layout of the control system.

MZI performance

8.1 Probe laser layout

Before describing the MZI as such we take a glance at the setup for generating the MZI probe and locking laser fields. Following a rundown of the probe lasers themselves, we describe two general versions of the probe-laser setup characterised by the lasers' frequencies being locked by either absorption-saturation spectroscopy or beat-note locking. Naturally, the actual experimental setup evolved from one to the other version through a number of steps and certain experiments were performed with each probe laser locked by a separate method.

8.1.1 Frequency locked grating stabilised diode lasers

Our probe lasers are based on a general design which has proven to work in several labs and commercially [Ricci95]. The specific design was developed by Jörg H. Müller and has been optimised gradually. The design and alignment of the laser is described in detail in [Petrov06] and here we just outline a few features. The laser is based on an AR-coated ridge-waveguide laser-diode from EagleYard (formerly Ferdinand Braun Institute).¹ The laser cavity is bounded by the back face of the laser diode at one end and a diffraction grating at the other. The frequency of the light that is reflected from the grating back in to the cavity mode depends on the grating line separation and its angle w.r.t the cavity axis. Thus, the grating angle is used to tune the laser frequency. This is of course only possible as long as the frequency of the reflected order lies within the diode's gain profile. The direct reflection off the grating is the laser output. The laser frequency can be further fine-tuned by the diode current and temperature. When locking the laser we stabilise the frequency by feedback to the laser current for fast fluctuations and to a piezo-actuator attached to the grating for slow fluctuations.

Background light The properties of the laser output depend heavily on the specific diode used. The EagleYard diodes from a single batch are fairly consistent in terms of gain-profile and output power. However, different batches can come with quite different specifications. A problem we encountered with the batch used for most of the measurements presented here, was that the D2-line

¹due to short lifetime that we we experienced for the EagleYard diodes, we have recently changed to use non AR-coated diodes from Axcel Photonics.

frequency of 852 nm was on the very edge of the gain profile. Firstly, this complicated the laser alignment and forced us to use rather high drive currents. More seriously, we found that the diode produced a broad incoherent background of light spread out over 20 nm towards the centre of the gain profile (see fig. 8.1).

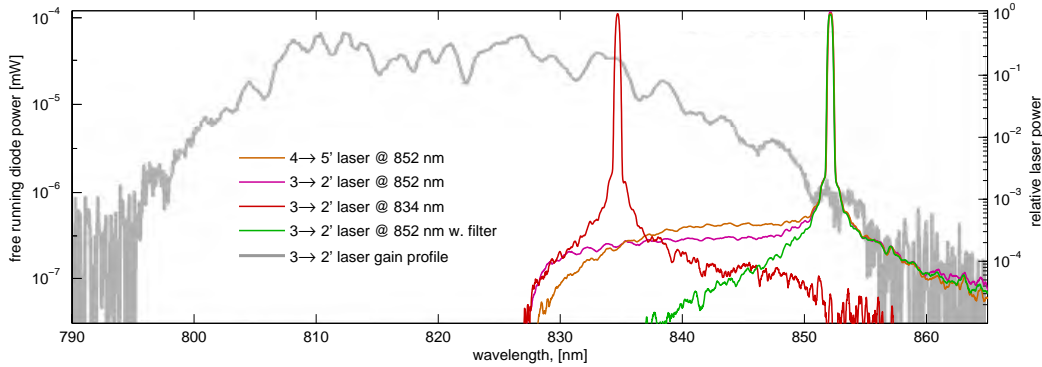


Figure 8.1: Output power frequency spectrum probe of lasers tuned to different lasing frequencies. The spectrum is measured in the reflection off a 1200 lines/mm diffraction grating. Orange and purple lines: When tuned to 852 nm both probe laser diodes produce a significant amount of background light with broad spectrum towards the centre of the gain profile. Red line: Lasing at 834 nm where the gain is maximal the background vanishes. Green line: Lasing at 852 nm with a 860 nm band-pass filter at a small angle the background light is greatly attenuated. Grey line: laser diode output when not lasing – adapted from EagleYard data-sheet

Side modes Some times random circumstances seem to collude in disrupting ones experiment. One such instance relates to the modes of the probe laser cavity. The length of the laser cavity is typically around $l_{\text{cav}} = 3.5$ cm, which results in a free-spectral-range of $c/(2l_{\text{cav}}) \approx 4.3$ GHz. Only one carrier mode is lasing strongly, but other side modes will compete with it and contain a small fraction of the overall laser power. The trouble comes from the fact that in the dichromatic MZI configuration the frequency difference between the probe lasers is around 8.5 GHz i.e. two free spectral ranges. Thus, when the two probe lasers are mixed a side-mode of each laser will interfere with carrier mode of the other laser. The result is interference intensity modulation in the combined signal at relatively low frequencies 100-1000 kHz. On fig. 8.2 the interference is

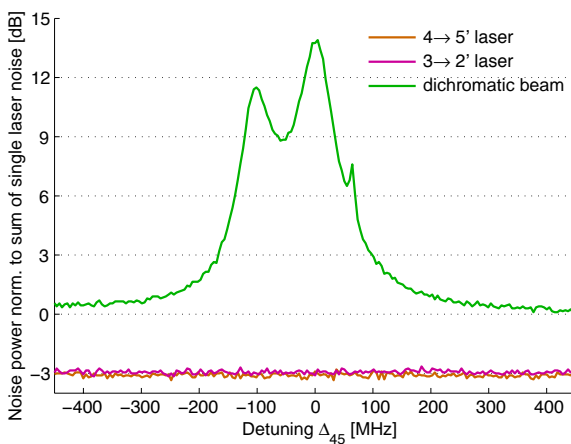


Figure 8.2: Intensity noise spectrum of individual probe lasers (orange and purple lines) and dichromatic beam (green line) normalised to the sum noise of the individual lasers. The noise is recorded on a spectrum analyser (SA) as the $4 \rightarrow 5'$ laser frequency is scanned over ≈ 1 GHz centred at $\Delta_{45'} = 0$. The SA is set in 0-span mode at 500 kHz with video BW 100 kHz of and resolution BW 1 MHz.

manifested as an excess noise in the intensity of the combined dichromatic laser beam when the detuning of one laser is tuned. Two distinct noise peaks are visible corresponding to the side-modes of one and the other laser respectively. Since in this measurement the $3 \rightarrow 2$ laser detuning is fixed to $\Delta_{32} = -86$ MHz

and $\Delta_{32} = \Delta_{45} + 8589.2$ MHz we infer that twice the free spectral range of the lasers is ≈ 8.5 GHz and ≈ 8.4 GHz corresponding to cavity lengths $l_{\text{cav}} = 3.53$ cm and $l_{\text{cav}} = 3.57$ cm respectively.

The issue of side modes was manifested in unpredictable changes to the MZI shot-noise performance (see sec. 8.7), seemingly changing from day to day. In fact we did not realise the issue for a long time as most of the measurements were performed with $\Delta_{45} \geq 100$ MHz where the side-mode interference noise is minimal. However, when we needed to lock the laser to $\Delta_{45} \approx -100$ MHz (see table 12.2) we were no longer able to reach the shot-noise limited performance of the MZI. Fig. 8.2 clearly explains what went wrong. We mend the problem by changing the position of the diffraction grating, thus shortening the cavity length to 2.5 cm. The resulting free spectral range of 6 GHz no longer causes any side-modes to be resonant with any probe laser carriers.

8.1.2 Absorption saturation locking

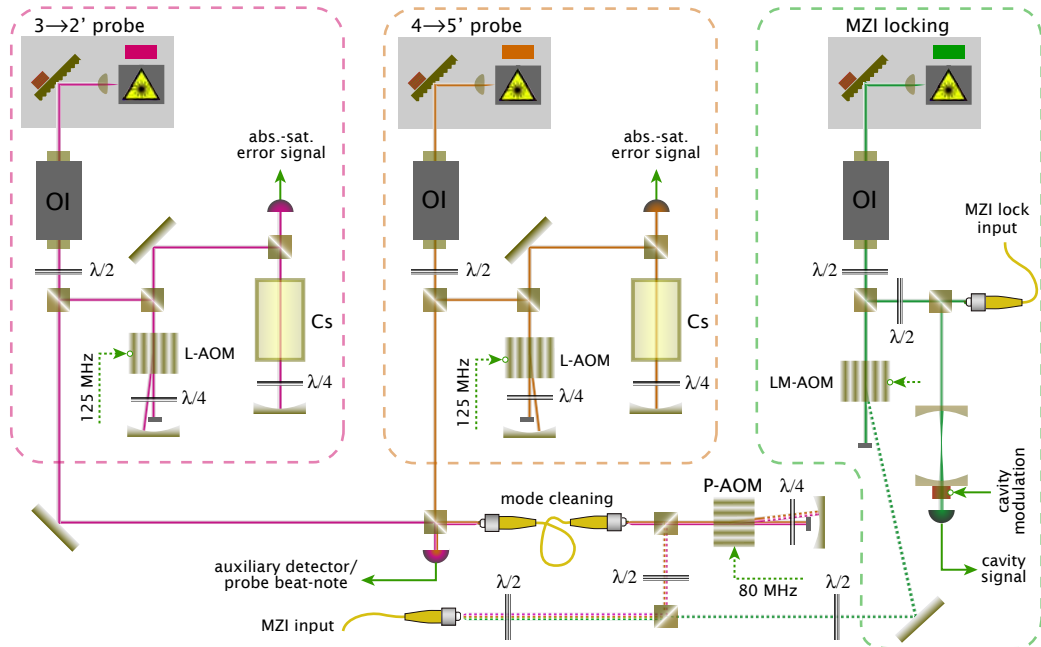
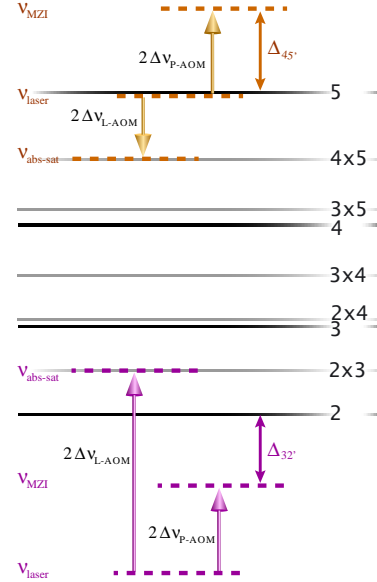


Figure 8.3: Probe laser layout for absorption saturation locking and 1-input MZI.

The setup is sketched on fig. 8.3. The probe lasers are independently locked by absorption saturation spectroscopy using a Pound-Drever-Hall locking scheme pioneered in [Bjorklund80, Hall81, Bjorklund83, Drever83] and also elaborated in [MacAdam92, Schmidt94]. For the implementation in our experiment refer to [Petrov06]. In the sketched setup we generate 4 MHz sidebands for the locking by modulating the AOM (L-AOM) drive frequencies in the lock branches of the setup. Hereby, we avoid inducing sidebands in the lasers themselves and thus in the probe beams that enter the MZI. Introducing the sidebands via modulation of the laser currents has a serious effect on the amount of classical noise in a detector signal, as is documented in [Windpassinger08a]. We shall point out that for the trap characterisations presented in sec. 9.2.1 -9.2.3 the lasers were directly locked to the absorption saturation signal with the 4 MHz modulation applied to the laser drive currents. On fig. 8.4 we illustrate the three different frequencies associated with each probe laser. The L-AOM shifts are chosen so as

Figure 8.4: Probe detunings/frequencies at various points in the absorption saturation locking scheme illustrated in fig. 8.3. The pulsing AOM shift is $2\delta\nu_{P-AOM} = 160$ MHz throughout all experiments. The $4 \rightarrow 5'$ probe laser is locked to the $4 \rightarrow (4 \times 5)'$ cross-over and the MZI probe detuning is thus $\Delta_{45'} = 2\delta\nu_{L-AOM} + (160 - 125)$ MHz. For many experiments we chose $2\delta\nu_{L-AOM} = 125$ so that the MZI probe detuning was 160 MHz while the probe laser was on resonance, i.e. $\Delta_{45'} = 0$. The $3 \rightarrow 2'$ probe laser is locked to the $3 \rightarrow (2 \times 3)'$ cross-over and the MZI probe detuning is thus $\Delta_{32'} = -2\delta\nu_{L-AOM} + (160 + 75)$ MHz. To match the $\Delta_{45'} = 160$ MHz probe we must chose $2\delta\nu_{L-AOM} = 370$ so that the MZI probe detuning was 135 MHz



to generate a the desired probe frequency when accounting for the shift of the probe pulsing AOM (see fig. 8.4 caption for examples).

The two probe laser beams are overlapped on a PBS and coupled into a single-mode fibre so as to ensure perfect spatial mode overlap. After the fibre the dichromatic probe beam takes two passes through the final AOM (P-AOM) which generates the probe pulses. A very important note on the AOM is that we ensure that the AOM is driven by the RF power, which gives the optimal diffraction efficiency. At this power the optical power in the diffracted order is not sensitive to intensity noise in the RF source. We have seen that the RF intensity noise significantly increases the noise in the probe powers if we drive the AOM in a range where it responds more linearly to drive power changes. As the last step, the probe can be overlapped with the locking beam and all modes are then coupled into the fibre-link to the MZI input.

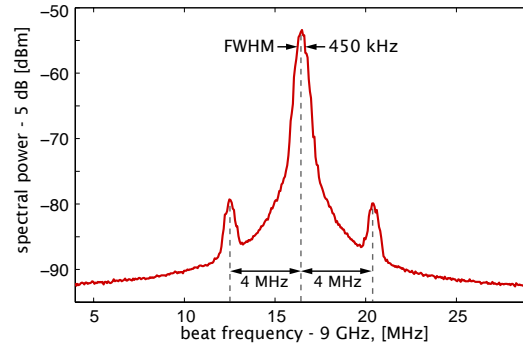
The locking laser is not frequency stabilised but by monitoring the laser in a scanned Fabry-Perot cavity we ensure that the laser operates in a single frequency mode. For the DC locking scheme the locking laser is simply coupled in to a fibre link which takes the beam to the back-input of the MZI (see sec. 8.6.1). For the AC-locking the lock-modulation AOM (LM-AOM) creates the intensity modulation of the locking beam, which is mixed with the probe on a PBS before entering the fibre-link to the MZI input.

Power spectrum of probe beat signal

To gauge the frequency stability of the probe lasers we measure the linewidth of the beat-note signal achieved by mode-matching two independently absorption saturation locked probe lasers on a detector. We take the detector output to a spectrum analyser (SA) and obtain a power spectrum of the beat-signal (fig. 8.5). For the data presented here we utilised the two MOT master lasers, which are identical in construction and locked by the same method as the probe lasers.² The 4 MHz sidebands are due to the current-modulation of the lasers for the locking. Since for the probe laser we apply the modulation to the AOMs in the locking branch, these sidebands are absent in the beat-signal. The FWHM of the

²This is not an attempt to cover up anything, but merely due to the oversight that we did not properly record data for the probe-lasers before changing to the beat-note locking scheme described in sec. 8.1.3.

Figure 8.5: Power spectrum of beat-note signal of two lasers independently locked by absorption saturation spectroscopy (see fig. 8.3). Trace acquired on Infiniium SA with 100 kHz resolution BW, 1 MHz video BW and 5 dB of attenuation on input. The line-width of the beat-note is around 450 kHz.



beat-note is approximately 450 kHz and assuming that the lasers have the same linewidth this yields individual linewidths of $\sqrt{2} \cdot 450 \text{ kHz} \approx 650 \text{ kHz}$ i.e. below 1 MHz.

8.1.3 Beat-note locking

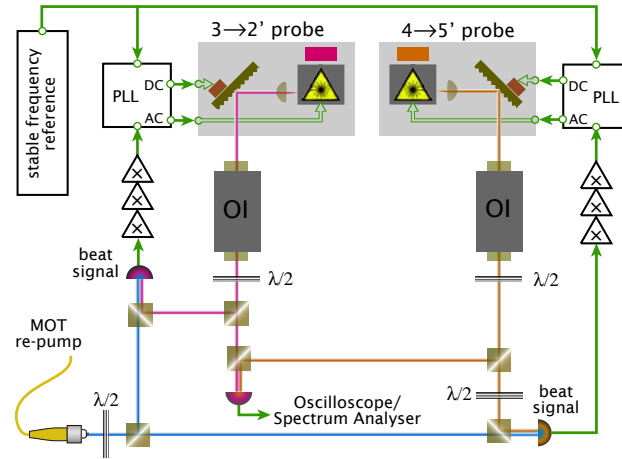
In the absorption saturation frequency locking scheme it is rather cumbersome to change the probe frequencies by more than about 10 MHz, because the AOMs have a limited bandwidth $\sim 20 \text{ MHz}$. Furthermore the beam paths are changed slightly and the locking scheme must be realigned for every significant change in frequency. To make the probe laser setup more versatile we employ a beat-note locking scheme developed in [Appel07, Appel08] similar to schemes described in [Santarelli94, Schünemann99]. In simple terms the lock relies on the beat-notes generated when lasers of two different frequencies, say ω_p and ω_l , are mixed into the same mode. The beat-notes will occur at $\omega_p \pm \omega_l$. For lasers operating on the Cs D2-lines the difference frequency ω_{l-p} is in the range of *Mhz-Ghz* depending on which hyperfine levels they address. If the dichromatic beam is detected the photo-current will only display the difference frequency beat-note as the PHz oscillations of the sum frequency are way beyond the detector bandwidth. This electronic beat-note may subsequently be mixed with a reference frequency oscillator signal and the resulting side-bands/beat-notes are used to lock the frequency difference of the lasers to that of the reference oscillator. The feedback to the lasers has both a DC (0-100 Hz) and an AC component (100 Hz-1 MHz). The DC component is fed to the piezo stack supporting the diffraction grating. The AC component is set to modulate the laser drive current, which has a modulation bandwidth of $\approx 1 \text{ MHz}$.

Ideally, a truly versatile lock should be able to stabilise two lasers in the whole frequency range, however with the analogue techniques utilised in [Santarelli94, Schünemann99, Oblak04, Petrov06] this is challenging. Resorting to digital signal processing proves to overcome the challenge and with the locking system built for our setup we are able to lock the frequency difference of two lasers from 1 MHz to 12 GHz [Appel08].

Lock performance

We test the lock stability with the setup sketched in fig. 8.6. We use the MOT master re-pump laser as the reference optical frequency that we admix the two probe lasers and detect on fast-photo diodes. The detector beat-signals are amplified and fed to the PLL, where they are scaled by some set factors and compared to the same reference frequency. The scaling can be different for the two PLLs, so that the lasers can be locked to different frequencies. We also detect the

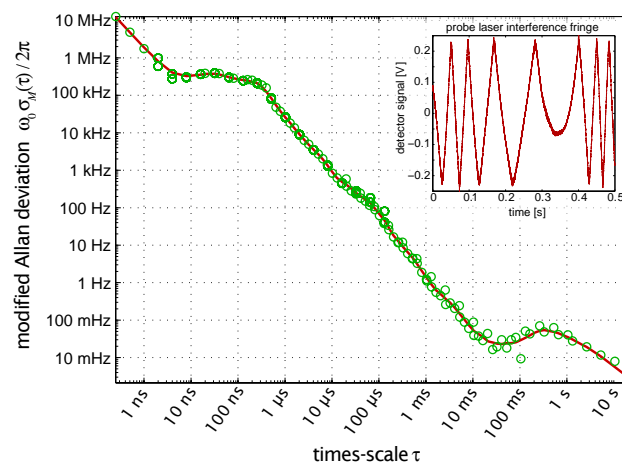
Figure 8.6: Beat-note locking scheme and test setup.



beat-note of the two lasers with each other and send the signal to a spectrum analyser or oscilloscope, depending on the measurement.

Frequency stability First we wish to determine the frequency stability of the locked lasers. This is done by locking the two probe lasers to the same frequency whereby their mutual beat-note will be at DC (0 Hz). Thus, the magnitude of the beat signal depends on the phase-offset between the lasers at the mixing PBS. Essentially, the beat note detection constitutes an interferometer albeit with two different but mutually phase-locked sources. Thus, by tapping a mirror in one of the beam paths one can generate an interference fringe in the mixed signal (see insert in fig. 8.7). A measurement of the laser phase-stability is done by adjusting the beat signal to about 50% of the interference fringe and then just recording the signal over some duration of time. Phase-fluctuations in the laser frequencies will be manifested as intensity fluctuations in the beat signal. Normalising the measured signal to the fringe amplitude directly yields the phase-fluctuations between the lasers. We quantify the noise in terms of the modified Allan-variance [Allan81]. Briefly the Allan variance quantifies the frequency stability of an oscillating signal source on different time-scales. The modified Allan variance is particularly useful for unambiguously determining the type of noise influencing the stability of an oscillator signal. For definitions and a brief summary of the properties of the Allan variance refer to appendix F. Here we will merely focus on the magnitude of the noise on the relevant time-scales for our experiments.

Figure 8.7: Green circles: Modified Allan deviation of beat-note phase of two lasers locked to the same frequency using common optical and RF frequency references (see fig. 8.6). Red line: smoothed data. Raw traces corresponding to six time-scale ranges were recorded on Infiniium DSO with appropriate sampling rates. Insert: Interference of beat-signal when changing the path-length of one laser. The fringe amplitude is used to convert amplitude fluctuations in to phase fluctuations.

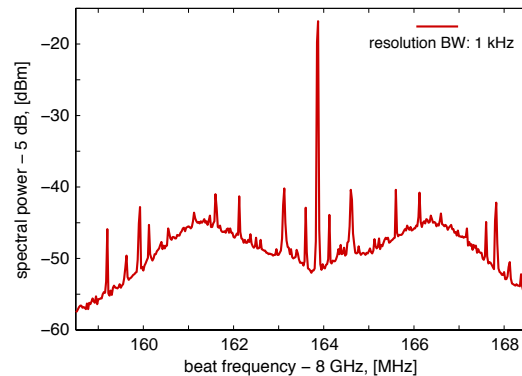


On fig. 8.7 we plot the modified Allan deviation, i.e. the square-root of the variance, for sample times from around 1 ns to 10 s. As discussed in appendix F we multiply the variance with the nominal beat frequency in order to get the deviation in frequency units. The different slopes are a result of different dominating noise sources, and on time-scales from around 100 ns to 10 ms the the laser-noise is dominated by white-phase noise [Appel08]. Since increasing the integration time of the phase signal obviously averages out the phase fluctuations, the Allan deviation will thus be monotonously decreasing over this range (see also eq. (F.4)). The time relevant for our experiment ranges from 1-100 μs where the modified Allan deviation is at 0.1-10 kHz. This is a significant improvement over the absorption saturation locking scheme. The laser frequency noise is important for the fluctuations it induces in the coupling of the probes to the atoms (see sec. 6.2.2).

Lastly, we note that for the measurement we use about 1 mW of power per probe so that the photon-flux is around $4 \cdot 10^9 \mu\text{s}^{-1}$, wherefore the shot-noise will be negligible. We also verify that laser intensity noise is not of importance in this measurement.

Power spectrum of probe beat signal So that we can compare with the power spectrum of the beat-signal of the lasers locked by absorption saturation spectroscopy (fig. 8.5) we present a similar plot for the beat-note locked lasers. For this measurement the two probe lasers are again locked to the MOT master re-pump but the PLL scaling factors are set so that the laser frequencies differ by 20 MHz. The power spectrum of the beat signal can now be recorded away from DC, as shown on fig. 8.8. We find that the line-width of the spectrum ≈ 1 kHz,

Figure 8.8: Power spectrum of beat-note signal of two lasers locked 8.16 GHz apart using the same optical and RF references but with different PLL frequency scaling factors (see fig. 8.6). Trace acquired on Infiniium SA with 1 kHz resolution BW, 10 kHz video BW and 5 dB of attenuation on input. The beat-note FWHM is 1.1 kHz, which is a result of the resolution BW.

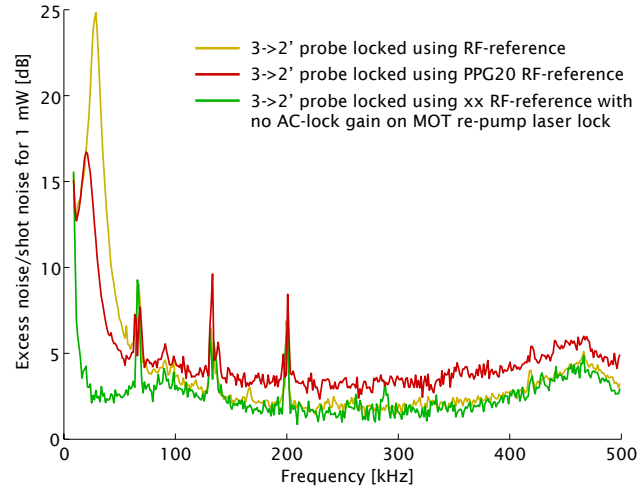


which is limited by the set resolution bandwidth of the scope. Thus, we are unable to resolve the actual width of the beat-note. In any case, the line-width is drastically smaller than that recorded in fig. 8.5. The shoulder on the spectrum is due to the locking bandwidth and gain settings. We recap, that the narrow linewidth refers to the laser frequency difference, whereas the absolute laser frequencies will have a significantly larger linewidth set by that of the MOT master re-pump. As we noted in sec. 6.2.2 for certain probing configurations it is precisely the difference frequency that counts.

Probe intensity noise induced by the lock Typically, the intensity noise spectrum of laser diodes has a $1/\omega$ behaviour at low frequencies. In the MHz range the fluctuations remain at a fairly constant level and can be compared to white noise, but still at a level above the shot noise level [Petermann91, Telle93]. Another feature of the characterisation setup (fig. 8.6) is that a noisy RF-frequency reference may add noise to the absolute probe laser frequencies without it being

visible in their beat signal. The PLL interprets the RF-reference frequency fluctuations as laser frequency fluctuations and thus attempts to correct for them with feedback to the lasers. Since the feedback is applied to both lasers their frequency difference is unaffected, however, the AC-feedback to the laser currents inevitably also causes perturbation of the laser intensities. To gauge this effect we successively block the two probe lasers before the mixing PBS and obtain power spectrums of the intensities (fig. 8.9). We obtain spectra for a number of different

Figure 8.9: Power spectrum of the intensity noise of a probe laser for different reference frequency sources and settings. We use 1 mW of laser power and normalise the noise to the corresponding shot-noise level. Yellow line: 10 MHz RF-reference derived from Infiniium DSO. Red line: 20 MHz RF-reference derived from PPG20 unit. Green line: 10 MHz RF-reference derived from Infiniium DSO and with AC gain on MOT re-pump locking turned off.



lock parameters and by varying the probe intensities we extract the shot-noise and classical intensity noise (the procedure is thoroughly explained in sec. 8.7). Hence, we normalise the observed noise to the shot noise. Using a 10 MHz RF-reference from the Infiniium digital oscilloscope the intensity noise spectrum (yellow line) has a very large peak at 25 Hz and a broad peak at around 480 Hz. Changing the RF-reference to a home-built 20 MHz Programmable Phase Generator (PPG20) (red line) the 25 Hz peak remains and additionally about 2 dB of noise is added to the entire spectrum above 100 Hz. Evidently, the PPG20 based source has significant frequency noise, thereby compromising the intensity stability of the laser. Finally, we revert to the 10 MHz scope RF-reference and lower the AC-gain on the MOT re-pumper absorption saturation locking, causing the 25 Hz peak to vanish. It turns out that the AC-lock of the MOT re-pumper induces oscillations in the re-pump frequency and the beat-note lock, in an attempt to correct for this, transfers the modulation to the probe-lasers. Following these measurements we initially kept the AC-gain of the MOT re-pumper low, but finally we adjusted the locking parameters and got rid of the modulation altogether.

In the setup used for the actual squeezing experiments the two probe lasers are locked to each other and not to a common reference laser. In this configuration noise in the RF-source directly translates into noise in the beat frequency of the two probes. We have confirmed that the probe beat-signal is not significantly increased by noise in the RF-reference, and that the intensity noise is comparable to that shown in fig. 8.9.

Application to probe laser setup

The way we employ the beat-note lock to our setup is outlined in fig. 8.10. We need one laser for absolute frequency reference and pick the MOT re-pump master laser, which is locked by absorption saturation spectroscopy. We then first lock the $3 \rightarrow 2'$ probe since its frequency is already close to that of the MOT

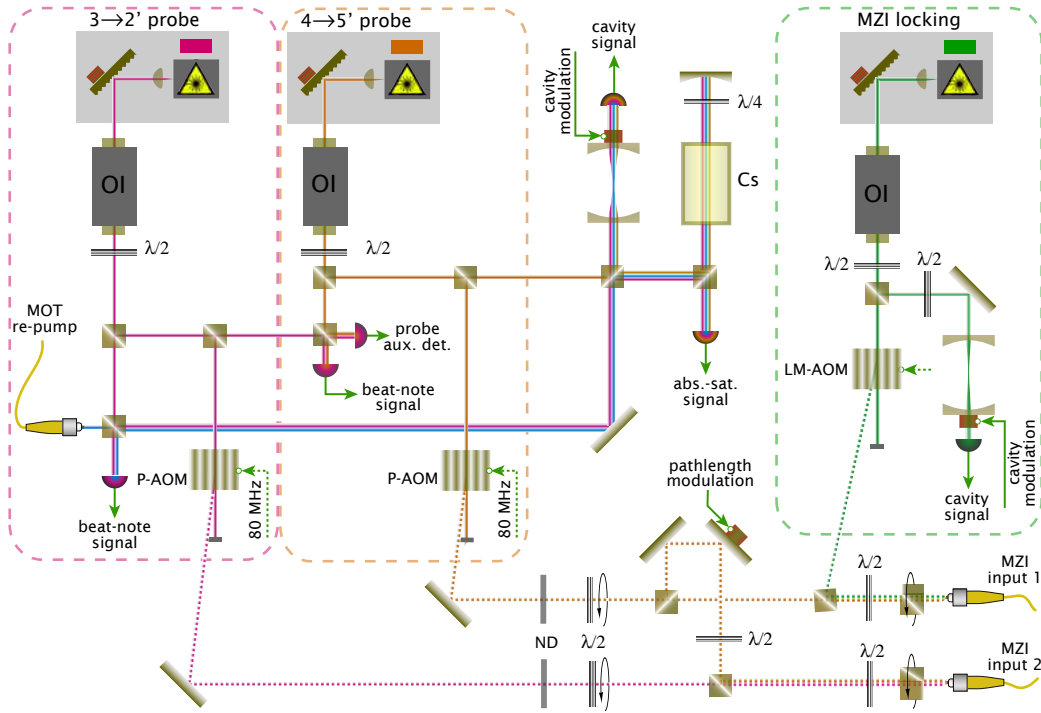
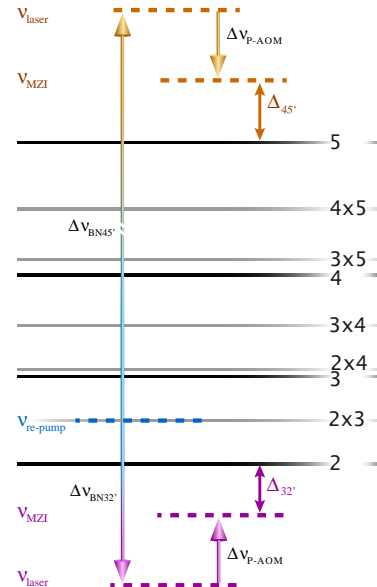


Figure 8.10: Probe laser layout for beat-note locking and 1 or 2-input MZI. To simplify the figure we omit explicitly drawing the lock feedback loop (refer to fig. 8.6) and focus on the optical fields.

re-pumper. Instead of also locking the $4 \rightarrow 5'$ probe laser to the MOT re-pumper we lock it to the $3 \rightarrow 2'$ probe laser. This ensures that the frequency difference of the two probes is locked as tightly as possible — something that will be of importance for the QND measurement (see sec. 6.2.2). Since the probes couple to different ground levels the beat-note frequency is 8-10 GHz. A sketch of and formulas for the involved frequencies is given in fig. 8.11.

Figure 8.11: Probe detunings/frequencies at various points in the beat note locking scheme illustrated in fig. 8.10. MOT re-pump master laser providing the optical reference frequency, is locked by absorption saturation spectroscopy to the $3 \rightarrow (2 \times 3)'$ cross-over. Accounting for the probe pulsing AOM shift $\delta v_{P-AOM} = 80$ MHz the final probe detuning is $\Delta_{32'} = 75.6$ MHz + 80 MHz + v_{bn3} . For $v_{bn3} = 241.6$ MHz one gets $\Delta_{32'} = 86$ MHz. The final detuning of the $4 \rightarrow 5'$ probe, again accounting for the pulse-generating AOM, becomes $\Delta_{45'} = 8664$ MHz - 80 MHz - v_{bn3} - v_{bn4} . For $v_{bn4} = 8243$ MHz one gets $\Delta_{45'} = 100$ MHz.



We regularly monitor the intensity noise of the probe lasers on an auxiliary probe detector and all three lasers involved in the locking can be monitored in a Fabry-Perot cavity or in an absorption saturation spectroscopy setup. Engaging the beat-note locks and slowly scanning the frequency of the MOT master re-pump laser, the absorption saturation spectroscopy allows us to verify that all lasers

are locked correctly.

Following the P-AOMs the probe beams are attenuated and a set of $\lambda/2$ -plates on motorised rotation stages in combination with PBSs allow for adjustment of the probe powers. Another set of $\lambda/2$ -plates align the probe polarisations to the PM-axis of the fibres that carry the probes over to the two MZI input ports. Since wave-plates tend to pollute the beam polarisation we insert high-quality PBS cubes³ aligned to the fibre PM-axes as the final elements before the fibres. The MZI locking laser is intensity modulated by the LM-AOM and mixed with the $4 \rightarrow 5'$ probe that goes to the input port 1 of the MZI. For mode matching of the two MZI input port we enable the $4 \rightarrow 5'$ probe to be coupled in to both fibre-links and thus enter the MZI from both inputs (see sec. 8.4.2).

8.2 Pulsed acquisition

Efficient and noise-less acquisition of the information contained in the probe pulses is an absolutely crucial element of the experiment. The first step is the conversion and amplification of the photon signal into an electronic signal in a photo-detector. Next step is the digital recording and storage of the electronic signal on a computer for further analysis. In this section we treat the two steps successively, starting with the photo-detection.

8.2.1 Pulsed photo-detector

To distinguish this detector from subordinate ones we coin it the *QND-detector*. The experiment has seen several version of the QND-detector, though all have been developed from the blueprint described in [Hansen01]. The first QND-detector (QND1-detector) was used in for the measurements described in [Oblak04, Oblak05, Petrov06, Petrov07]. For the experiments documented in [Windpassinger08a, Windpassinger08c, Windpassinger08b, Oblak08, Appel09, Windpassinger09b] the second generation (QND2) detector was used. In sec. 8.2.2 we describe the gain and electronic noise of the detectors and it will be clear why the QND2 detector replaced the QND1 detector.

8.2.2 Digitisation and storage

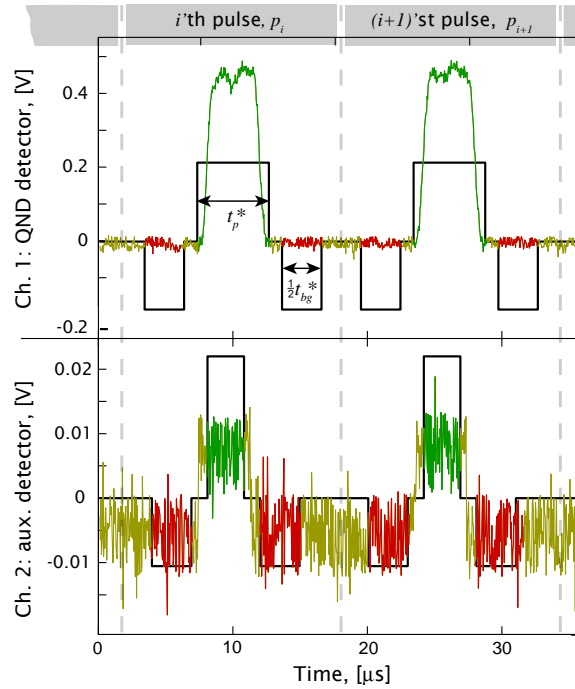
Once converted into an electronic signal the next task is to record the pulse so that the data can be stored on a computer for further processing. For the measurements documented in [Oblak04, Oblak05, Petrov06, Petrov07] we used an analogue integration circuit based on a commercial sample-and-hold chip⁴ to first integrate the detector signal over the duration of the pulses. This involved supplying the integrator with a gating-pulse so that only the actual pulse signal was integrated. The integrator output voltage was read out by a NI ADC computer interface card and stored on the hard drive of the computer. Though this method did not seem to compromise the detector signal it also proved to be rather inflexible, in that we did not have access to other, possibly interesting, sections of the signal that lie outside the actual probe pulse. Thus the acquisition was redesigned to be based on the Infiniium 54832D Digital Storage Oscilloscope (DSO). The detector signal is directly input to the DSO which records data from

³from Bernhard-Halle Nachf.

⁴Burr-Brown IVC102

selected time-segments in its memory and then stores it in a binary-format⁵ on a hard-drive. The DSO is controlled via an ethernet link by the LabView programme handling the acquisition. There has been two versions of this program. We will focus on the second generation version named *scope program*. The DSO is set to *segment mode* where it acquires a preset number of segments in its memory before writing to the file. The sample rate, span, voltage-scale, output file-name etc. is likewise set by the LabView interface. The actual trigger signals for the acquisition and the segments are programmed in the DIO64-control LabView programme and supplied by the PCI-DIO64 card (see fig. 7.2).

Figure 8.12: Raw detector traces recorded on DSO and integration matrices. Pulse integral found by multiplying integration matrix values with the DSO traces and summing up all samples corresponding to a pulse. a) QND detector usually hooked up to channel 1 on DSO. Pulse integration window chosen so that the whole pulse is covered. b) Reference detector for probe power determination usually input on DSO channel 2. Integration window chosen narrower than pulse so as to determine only the pulse height. Background windows chosen to be as close to yet clear of the pulse. The integral of the integration matrix is zero, i.e. the area in the pulse window and the two background windows are equal.



The binary data-files are processed in a couple of steps in MatLab using a selection of code-scripts⁶. Each binary file contains data about all segments acquired on a single channel, and on fig. 8.12 we plot a section of traces from two channels contained in a single segment. We next need to sum up over all samples that were taken during a probe-pulse. This is done by defining windows of lengths t_p^* around the pulses and constructing a matching integration matrix depicted as a black line in fig. 8.12. One integration matrix simply takes the value $1/t_p^*$ for all sample points inside the window and 0 outside it i.e.

$$M_{\text{int}}(t) = \frac{1}{t_p^*} \mathbf{1}_{\left[-\frac{t_p^*}{2}, \frac{t_p^*}{2}\right]} \quad (8.1)$$

When multiplied with and summed over the data it returns the integral over the pulse. An added feature is that we can define background windows in some range of samples close to the pulse-window

$$M_{\text{int}}(t) = \frac{1}{t_p^*} \left(\mathbf{1}_{\left[-\frac{t_p^*}{2}, \frac{t_p^*}{2}\right]} \right) - \frac{1}{t_{\text{bg}}^*} \left(\mathbf{1}_{\left[-\frac{t_{\text{bg}}^* + t_p^*}{2} - t_{\text{del}}, -\frac{t_p^*}{2} - t_{\text{del}}\right]} + \mathbf{1}_{\left[\frac{t_p^*}{2} + t_{\text{del}}, \frac{t_{\text{bg}}^* + t_p^*}{2} + t_{\text{del}}\right]} \right) \quad (8.2)$$

which is shown in fig. 8.12. By assigning the value $1/t_{\text{bg}}^*$ to all matrix elements inside the background window we automatically subtract any detector offset.

⁵file extension ".bin"

⁶file extension ".m"

When this is done over all pulses of each segment, all segments of each experimental cycle, and all channels we store the data in a four dimensional array and write this to a MatLab data file⁷. In many cases we actually define a number of integration windows corresponding to different probe or reference pulses (see sec. 12.4.1). In these cases we store the different pulse integral under different variable names in the MatLab data-files. Further analysis of the data stored in the MatLab data-files is performed by dedicated Matlab scripts.

Pulse bandwidth The pulsed detection allows us to detect signals only on certain time-scales. This may be expressed through a decomposition of the signal into its Fourier components whereby it is simpler to see that e.g. a 1 μ s pulse will easily sense a signal component at 1 Hz whereas a 1 MHz component will average out over the pulse. To formalise these statements we calculate the Fourier spectrum of the pulse or rather the integration matrix⁸, which defines the detection time. The spectrum is only approximately equal to the detection transfer function $g(\omega)$ (see sec. 6.1), which also accounts for the frequency response of other elements i.e. the detector, cables, DSO, etc. For the matrix eq. (8.1) the Fourier components are

$$\mathcal{M}_{\text{int}}(\omega) = \frac{\sin\left[\frac{t_p^*}{2}\omega\right]}{\frac{t_p^*}{2}\omega}, \quad (8.3)$$

which shows that by using the integration matrix of eq. (8.1) the value of the integrated pulse area is sensitive to frequency components in the detected signal up to a bandwidth frequency of $\omega_{BW} \sim 2\pi/t_p^*$ (see red curve in fig. 8.13). The

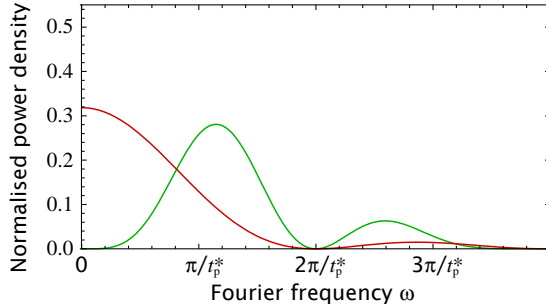


Figure 8.13: Pulse detection power spectrum $|\mathcal{M}_{\text{int}}(\omega)|^2$ for symmetric integration windows. The red curve corresponds to eq. (8.3), while the green curve corresponds to eq. (8.4) with no spacing between pulse and background window $t_{\text{del}}^* = 0$ and the same total duration of the two integration windows $t_p^* = t_{\text{bg}}^*$.

signal is ergo sensitive to DC components in the signal. As we commonly see a more or less pronounced offset of the detector baseline [Windpassinger08a] the DC sensitivity is disadvantageous. As stated above, this is circumvented by constructing a background-subtraction windows as in eq. (8.2). The Fourier spectrum of this integration matrix is

$$\mathcal{M}_{\text{int}}(\omega) = \frac{\sin\left[\frac{t_p^*}{2}\omega\right]}{\frac{t_p^*}{2}\omega} + \frac{\sin\left[\left(\frac{t_p^*}{2} + t_{\text{del}}^*\right)\omega\right] - \sin\left[\left(\frac{t_p^* + t_{\text{bg}}^*}{2} + t_{\text{del}}^*\right)\omega\right]}{\frac{t_{\text{bg}}^*}{2}\omega}, \quad (8.4)$$

which is plotted as the green curve in fig. 8.13. The plot shows the special case where there is no separation between the pulse and background windows $t_{\text{del}}^* = 0$ and the two have the same duration $t_p^* = t_{\text{bg}}^*$, so that eq. (8.4) simplifies to $\mathcal{M}_{\text{int}}(\omega) = 2 \sin[t_p^*/2 \omega] / (t_p^*/2 \omega) - 2 \sin[t_p^* \omega] / (t_{\text{bg}}^* \omega)$. The important things to notice are that the pulse integral is no longer sensitive to DC-components of the detector signal and the peak sensitivity is at the frequency $\sim \pi/t_p^*$. In

⁷file extension ".mat"

⁸defined as $\mathcal{M}_{\text{int}}(\omega) = \int_0^\infty e^{-i\omega t} \mathcal{M}_{\text{int}}(t) dt$.

fig. 8.14 we show how the spectrum of eq. (8.4) changes as $t_{\text{del}}^* \neq 0$ and $t_{\text{bg}}^* \leq t_p^*$. A common setting for the experiment would be $t_{\text{del}}^* \approx t_p^*/10$ and $t_{\text{bg}}^* \approx t_p^*/2$

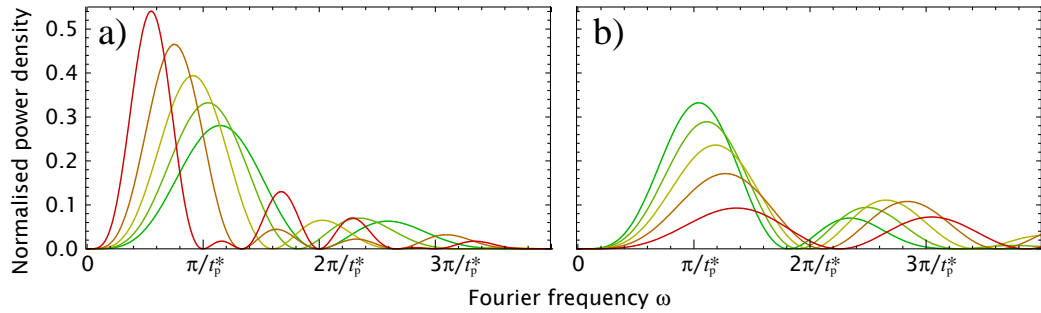


Figure 8.14: Pulse detection power spectrum $|\mathcal{M}_{\text{int}}(\omega)|^2$ for non-symmetric integration windows, meaning that there can be a delay $t_{\text{del}}^* \neq 0$ between pulse and background window and the total duration of the two windows may differ $t_p^* \neq t_{\text{bg}}^*$. Specifically in a) we vary t_{del}^* and in b) we vary t_{bg}^* .

corresponding to orange curve in fig. 8.14 (see figure legend).

In the following discussion on electronic noise, light noise, and later atomic noise it is important to keep in mind that the noise from each source may have different intrinsic noise spectra and that the overlap of these spectra with the detection bandwidth should be considered. Electronic noise for example can be assumed to have a fairly flat spectrum and spectral response of the detection is exactly as in eq. (8.4). Shot noise from the light is only present during the actual pulse signal and thus has a bandwidth more resembling eq. (8.3). Other classical noise sources in the light will influence the signal in yet another way.

Electronic noise

Large portions of the analysis presented in this dissertation concerns the determination of the noise level of the integrated pulse signals. To get off to a slow start, we will investigate the electronic noise of the detector and the DSO. Determining the electronic noise we block all optical beams and define pulse windows corresponding to typical probe-pulse settings. The electronic noise of the different QND-detector versions is summarised in table 8.1

detector version	detector gain	electronic noise	$P_{3\text{dB}}$	$n_{3\text{dB}}$
QND1	9 V/ μW	$7 \cdot 10^{-6} \text{ V}^2$	1.5 μW	$6 \cdot 10^5 \mu\text{s}^{-1} \cdot t_p$
QND2	32 V/ μW	$1.12 \cdot 10^{-6} \text{ V}^2$	0.02 μW	$8 \cdot 10^4 \mu\text{s}^{-1} \cdot t_p$

Table 8.1: QND detector gain and noise characteristics. The electronic noise level is the variance of the detector voltage on the 1 M Ω terminated DSO input. The $P_{3\text{dB}}$ value states the optical power resulting in a shot-noise level equal to the electronic noise. Likewise the ($n_{3\text{dB}}$) value states the number of photons in a 1 μs pulse required for the shot-noise level to equal the electronic noise level.

Since the noise is almost perfectly white, the level is very close to constant for all time-scales i.e. size of the integration window. We see that the QND2 detector has about 75 times lower electronic noise than the first version. This improvement has been one of the essential factors allowing us to proceed with the experiment. For the data presented in this thesis the old detector was used for all of the sample characterisation measurements and some of the optical pumping

efficiency and microwave Rabi oscillation measurements. However, all characterisations of the coherence times, light-atom interaction, and QND measurements employed the QND2 detector. A more thorough description and characterisation of the detector is found in [Windpassinger08a, Windpassinger09a]

digitisation noise For a short period of time one cause of confusion was that the electronic noise estimate appeared to have grown much larger than normal. At that point we had needed to set the DSO voltage scale quite large so as to accommodate rather large signal fluctuations/decays. We then would use the background data to estimate the electronic-noise. As the voltage value has a fixed bit-depth the coarseness of the digitisation increases with the voltage scale. It turned out that the large voltage scale meant that the electronic noise was barely resolvable and thus the background signal appeared to jump in discrete steps. This again resulted in an apparent increased electronic noise level. We have established that the voltage span should not exceed 200 mV/div for the electronic noise not to be artificially amplified by too coarse digitisation. The blow-up of the noise from 200 mV/div to 500 mV/div is extremely sharp and related to the DSO internally switching to a different set of electronics.⁹

In order to fit the signal on the scope without amplifying the electronic noise we have some times attenuated the detector signal by a factor of 4-5 with a simple voltage divider so as to avoid going to the 500 mV/div. At other times we have used different DSO channels to record different parts of the data. We have verified that neither of these procedures add noise to the output signal. When we use low probe powers we do not have trouble fitting the signal (including fluctuations) on the 200 mV DSO scale.

Notation for different signal values

We end the section on pulsed acquisition with a table of the various representations of the detector signal. Not all entries have been defined yet. Even so we put the table here as a reference in later sections.

8.3 MZI layout

The Mach-Zehnder interferometer is a key element in the experimental setup. It has been subjected to numerous revisions since the first incarnation with optical fibres [Oblak04, Oblak05]. The current free-space realisation is situated on an elevated aluminium optical breadboard so that the laser beam heights match that of the vacuum components viz. the quartz glass-cell containing the atomic sample. The whole MZI setup including the vacuum parts and MOT optics are enclosed in a box which is lined with a special sound absorbing *magic fleece*¹⁰ that serves to reduce acoustic disturbances of the MZI. Though several optical elements have been exchanged and added a number of core elements have retained their position. We will describe the basic MZI make-up of these core components (Fig. 8.15) before discussing the variations to the setup.

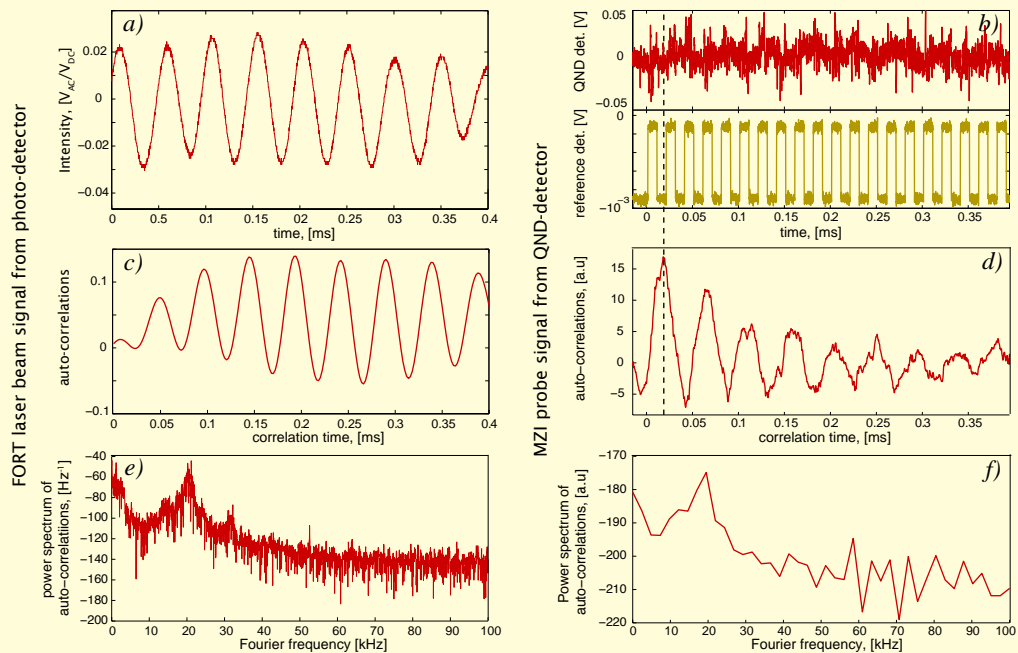
The various laser beams are carried to the MZI from the main optical breadboard by polarisation maintaining (PM) fibres. Initially oval-cladding fibres from Thorlabs were used, but due to poor PM properties, causing large drifts in the probe

⁹we clearly hear some relays in the DSO switching when we go from the 200 mV/div to the 500 mV/div scale.

¹⁰this is used in luxury cars to reduce engine and tyre noise in the passenger cabin.

Box 8.1: FORT laser intensity noise

Because of reflections on optical elements some amount of FORT laser light will scatter into the probe-beam path and thus into the QND detector. As discussed in sec. 9.1.2 we have inserted an ever increasing number of dichroic mirrors in the probe beam to filter away the scattered FORT light. In the below figure we show the raw detector output in the absence of probe light just before installing yet another dichroic mirror. One can clearly see an oscillating behaviour, which also shows up in the power spectrum of the data. A comparison with the intensity noise spectrum of the FORT laser convinced us that the scattered FORT laser light entered the QND detector. Thus, the addition of another dichroic mirror. The FORT laser light increased the detector background noise level by 3 to 4 times above the electronic noise level. Moreover, the period of the relaxation oscillations that contaminate the probe signal are on exactly the time-scale of the probe pulse separation. As a result, we at some point observed that consecutive probe pulses were anti-correlated, because the pulse separation happened to be exactly half a relaxation oscillation period.



Box 8.2: Contamination of QND detector signal by FORT laser classical intensity noise. Figures to the left correspond to the photo-detector signal measuring the FORT laser intensity while those to the right correspond to the QND detector. a) Raw detector signal of FORT intensity clearly showing oscillations. b) QND and reference detector signals (see sec. 8.3) during a pulse sequence with no atoms in the trap. The plotted QND signal is that of two subsequent cycles' raw data-traces subtracted (see sec. 12.2.2) and thus is completely dominated by noise — no DC level. The reference detector signal is averaged over 500 cycles. c) Auto-correlation and e) Power spectrum of FORT intensity revealing a 20 kHz modulation corresponding to relaxation oscillations of the laser cavity. d) Auto correlation of a particular time-sample (indicated by a dashed line) with the remaining time-samples averaged over 500 cycles. The chosen sample contains no photons and for white electronic and probe shot-noise should not be correlated with other time samples. The modulation indicates contamination of the electronic noise. f) Power-spectrum of QND signal auto-correlation that evidently resembles that of the FORT intensity.

	Description	Relation to other properties
t_p	Probe pulse duration	-
t_p^*	Probe pulse integration window time-width	QND-detector: $\approx t_p + 1 \mu s$
t_{bg}^*	Background/baseline integration window time-width	-
\hat{N}_{ph-}	Photon number (difference) incident on diode(s)	QND-detector: $\hat{N}_{ph-} = 2S_z^{(out)}$, (eq. (2.24))
i_-	Photo-current from detector diodes	$i_- = \epsilon \hat{N}_{ph-} / t_p$ (eq. (2.24))
q_-	Photo-charge from detector diodes	$q_- = t_p i_- = \epsilon \hat{N}_{ph-}$
a	Detector output signal	$a = \mathcal{G} i_-$
p	Pulse integral of detector signal	$p \sim t_p^* a \approx \mathcal{G} q_-$
ϕ	Phase-shift of fringe on QND-detector	$\phi = p / \mathcal{A}_p = p / (\mathcal{G} \mathcal{A} \bar{p})$ (eq. (8.5))

Table 8.2: Symbols, Descriptions, and mutual relationship of different signal representations.

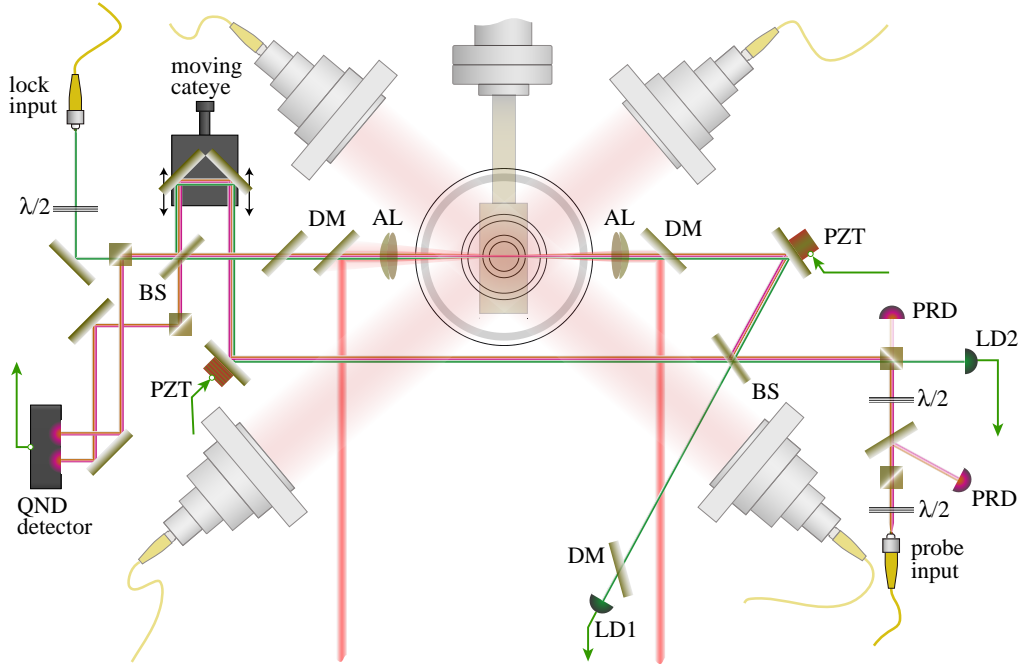


Figure 8.15: Basic layout of 1-input MZI.

power in to the MZI, they have been replaced by panda-fibres, also from Thorlabs. The probe and lock beams are coupled into free space through Thorlabs F220FC-B $f = 11$ mm aspheric lens collimators. Adding an $f = 750$ mm lens yields collimated beams with a spot size of 1 mm. In the basic configuration of the MZI the input probe beam is s-polarised w.r.t. the input BS. In later configurations the input probe polarisation may be slightly tilted or even circular, however by polarising optical elements we ensure that the probe in the MOT cell is always s-polarised i.e. vertically linearly polarised.

The input non-polarising BS, used in the MZI as the input BS and in some of the experiments also as the output BS, would ideally have equal reflection and transmission i.e. $r^2 = t^2 = 0.5$. Needless to say, any real optical element is not

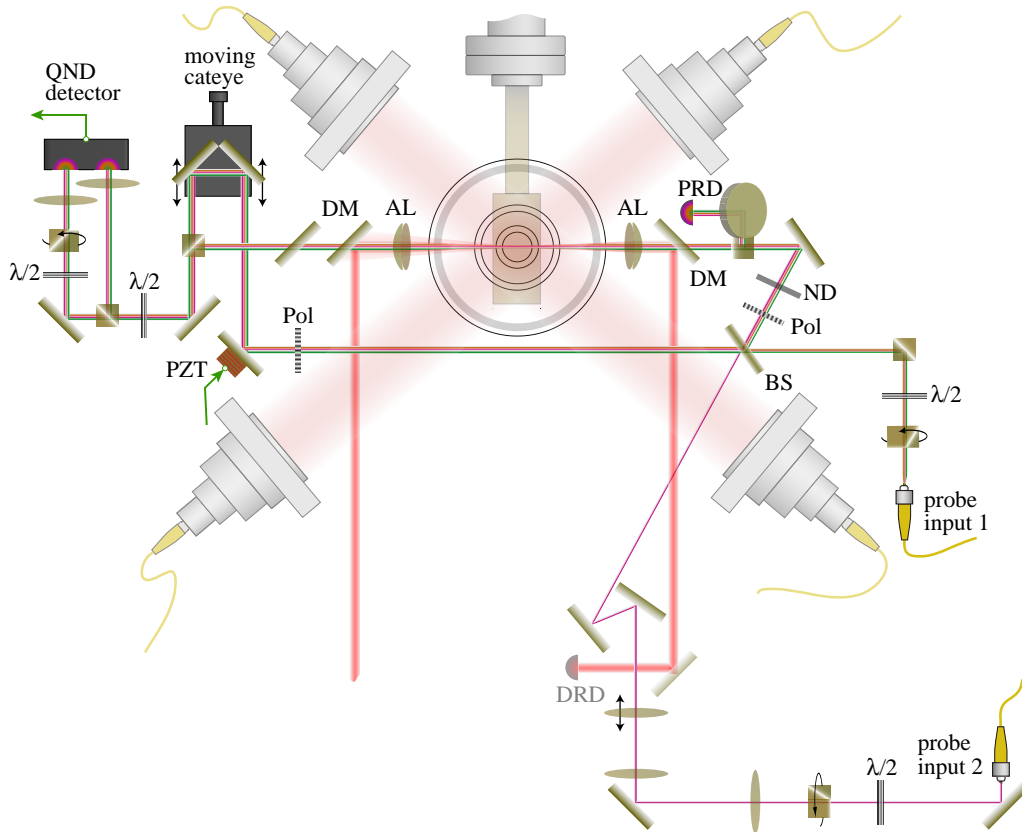


Figure 8.16: Basic layout of 2-input MZI.

ideal and the BS from Eksma is no exemption. As expected the measured r^2 and t^2 values shows a large dependence on the incident angle for both s-polarised and p-polarised input beams. At the intended 45° angle of incidence the reflection and transmission are, however, not equal for any of the polarisations. In the setup the angle is around 40° , which for the s-polarised light utilised yields $r^2 \approx 0.6$ and $t^2 \approx 0.4$. Since, for the initial MZI setup the reflected input went into the probe arm the intensity misbalance was to a large extent rebalanced at the output BS by the losses in the probe arm from the lenses and quartz-cell walls. In the 2-input setup this unequal splitting was problematic and eventually had to be undone by inducing additional polarisation dependent losses in both interferometer arms.

8.4 Alignment

The MZI alignment consists of two to three steps depending on the configuration: overlapping the reference and probe arm modes on the output BS (mode-matching MZI), adjusting the optical path-lengths of the probe and reference arms to be equal (white light alignment), and in the 2-input configuration the two input modes must be overlapped on the input BS (mode-matching inputs).

The MZI mode-matching is simply done by measuring the visibility of the interference fringe in one of the outputs. This was done either using a CW probe signal on a standard detector or using a pulsed signal on the QND detector. The former has the advantage of tolerating a larger probe intensity thus enabling a visual inspection of the beams during the process. The latter allows simultaneous detection of different light sources (e.g. probe from different inputs

and the locking laser) if these are temporally separated into different pulses (see fig. 8.17). Typically, we achieve a visibility of 96% with an all time maximum of 98%. When we measure this "optimal" visibility V_{is0} we make sure to have equal intensities in the probe and reference arms. In the case where the probe arm is attenuated the actual visibility during a measurement will be smaller by

$$V_{is} = \frac{2\sqrt{P_p P_r}}{P_p + P_r} V_{is0}$$

where P_p and P_r refer to the power in the probe and reference arms respectively.

The visibility of the MZI should change only due to misalignment of the probe and reference arm mode overlap on the output BS. Naively, one would not expect this to change much in a rigid construction as our MZI setup. Nevertheless, it turns out that over the duration of a long experimental run the visibility can vary by as much as 10%, though more commonly it is a few percent. The cause of this change, is apparently the thermal expansion/contraction of the MZI setup in particular the base-plate. We have tested this inference by placing a heat source (a 100 W lamp) inside the MZI enclosure while simultaneously detecting the air temperature and fringe amplitude. As the temperature increased the fringe amplitude was seen to drop and switching off the heat source we saw the fringe amplitude rise again, though not returning completely to the initial value. During the regular experimental operation the sources heating the MZI enclosure are chiefly the FORT laser light dumping and the MOT trapping coils. The visibility drift does not pose a serious problem and we have not made further efforts to stabilise the temperature around the setup.

8.4.1 White light positioning

Before describing the procedure let us ponder the question of "why white-light?" Whereas, not all questions have an answer, this one has two. First, reason is the immunity of the MZI to classical laser frequency noise as was discussed in sec. 6.1.2. Though, this is of course a valid point, we need to consider the order of magnitude of the laser noise and thus the influence on the MZI. Our diode lasers all have a bandwidth of less than $\delta\omega = 2\pi$ MHz (see sec. 8.1). The resulting classical phase-noise is then $\delta\tilde{\phi}_\omega = \frac{2}{3}\pi 10^{-2}\Delta l$. We require this to be less than the shot-noise, which depends on the probe power. As we typically use 10^7 photons we can set the benchmark of $\delta\tilde{\phi}_{sn} = \frac{1}{3}10^{-3}$. Invoking the condition $\delta\tilde{\phi}_\omega < \delta\tilde{\phi}_{sn}$ results in the requirement $\Delta l < 1.5$ cm. In other words for classical frequency noise suppression the white light alignment need not be particularly precise.

The second reason relates to the ability to tune the probe frequencies. Aligning the MZI to the white-light position means that we are free to tune the laser frequencies without changing the signal balancing i.e. the fringe zero crossing remains fixed at the offset phase ϕ_0 (≈ 0). This is particularly important when two probe lasers are used simultaneously. For the phase-offset between two probe lasers separated by 9.2 GHz to be negligible, that is less than the precision set by the shot-noise, we must demand that $\Delta l < 1.5 \mu\text{m}$. Though, a small detectable discrepancy in the offset of the two probe fringes is acceptable the requirement is a good indicator for the degree of white-light alignment we need to achieve. Finally, we note that the locking laser is detuned by more than 10 nm equivalent to 4 THz. In this case the condition $\Delta l < 3.5$ nm becomes unduly small. However, since the locking offset is adjustable we need not be concerned with the locking fringe offset. I conclude aligning the MZI to within a few

μm of the white light position gives us freedom to tune and use multiple probe lasers and ensures a more than adequate suppression of classical laser frequency noise.

We developed a number of procedures for the white-light alignment two of which were described in [Oblak04]. Here we focus our attention on the approaches that are used currently. The equalisation of the probe and reference arm path-lengths of course starts out with a ruler. Once a rough equalisation, taking in to account the added optical path-length through glass elements, has been done we replace the probe-laser input with a weak broadband light source¹¹. The MZI output is detected on a sensitive detector while the length of the probe arm is adjusted until an interference signal appears. From the spectral width of the white-light source a interference region of around $\pi\lambda_0^2/\delta\lambda = 60 \mu\text{m}$ is expected.¹² With some care it is also possible to observe the interference pattern of the white light source on a camera. This is advantageous when the mode overlap at the output is not optimal, which is easily the case after changing the probe arm length.

For greater precision in the white light alignment we use the pulsed detection of weak laser pulses of two different wavelengths. By spatially separating the pulses from each laser one can simultaneously observe the interference fringes of both beams (fig. 8.17). If the two lasers have frequencies corresponding to the

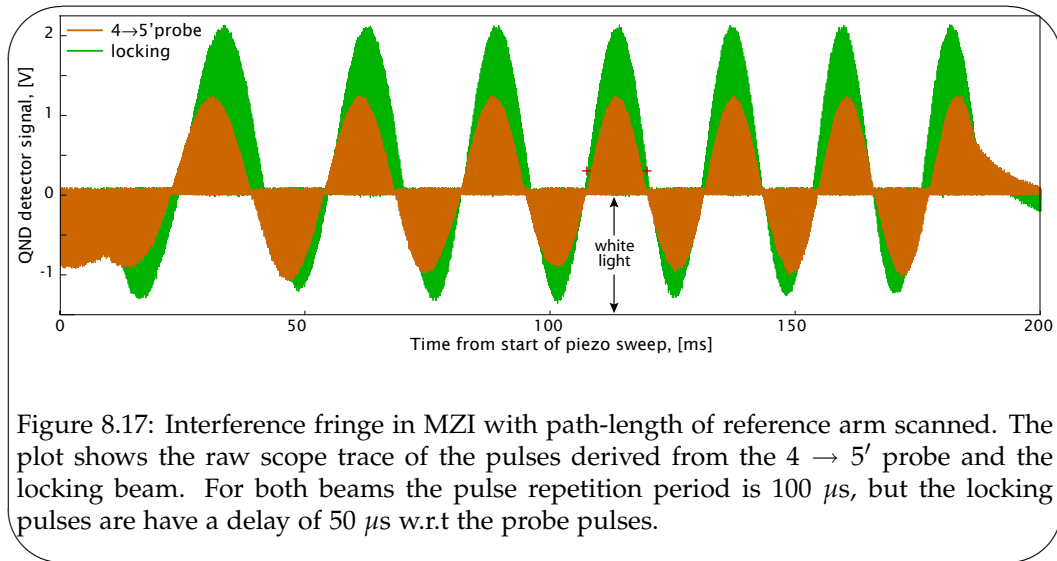


Figure 8.17: Interference fringe in MZI with path-length of reference arm scanned. The plot shows the raw scope trace of the pulses derived from the $4 \rightarrow 5'$ probe and the locking beam. For both beams the pulse repetition period is $100 \mu\text{s}$, but the locking pulses are have a delay of $50 \mu\text{s}$ w.r.t the probe pulses.

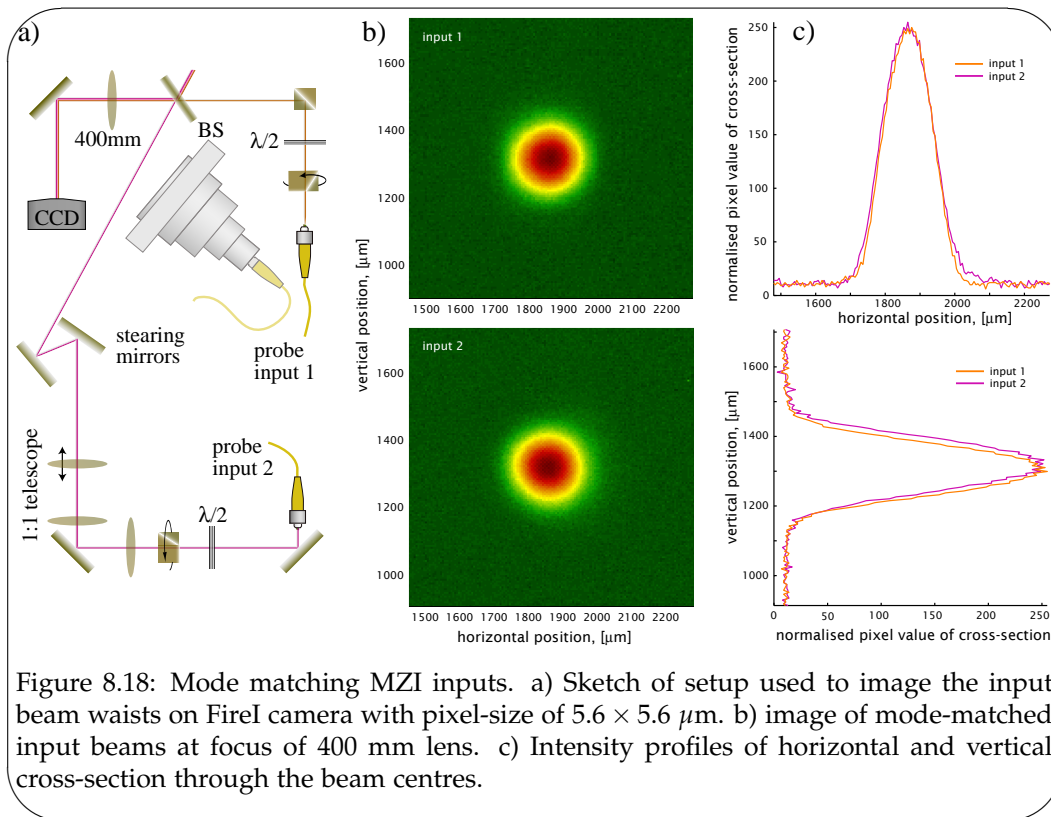
probes that we use in the dichromatic MZI i.e. $\lambda_0 \approx 852 \text{ nm}$ separated by $\delta\nu \approx 9 \text{ GHz} \Rightarrow \delta\lambda \approx 0.024 \text{ nm}$, their interference fringes will be out of phase when the path-length difference is $\Delta l = 1.6 \text{ cm}$. This is of course not more precise than the previous method, but it reveals that a rough adjustment of the path length could also be performed by observing the fringe displacement of the probe lasers. If instead one laser is at 852 nm and another is at 835 nm then the two will come out of phase when $\Delta l = 134 \mu\text{m}$. It is possible to determine whether the fringes are out of phase by only a few degrees, say 5° , which allows one to locate the white light position to within $\pm 2 \mu\text{m}$, corresponding to only 2 fringes. Fig. 8.17 shows the recorded fringes of the the two probe lasers ($\lambda = 852 \text{ nm}$) and the locking laser ($\lambda = 830 - 40 \text{ nm}$). One can clearly pick out exactly which fringe corresponds to the white light position.

¹¹FOD fibre coupled LED. Centre wavelength $\lambda_0 = 850 \text{ nm}$, spectral FWHM $\delta\lambda = 35 \text{ nm}$, output power -17 dBm in multimode fibre coupled (-30 dBm in single-mode fibre coupled)

¹²Simplified expression differs from the exact $\pi(\lambda_0 + \delta\lambda)(\lambda_0 - \delta\lambda)/\delta\lambda$ by only 4%.

8.4.2 Mode overlap in 2-input configuration

The task very much resembles that of aligning the probe and reference arms of the interferometer. The main difference is that the two modes to be overlapped originate from two different fibre outputs. Even when using fibre-patchcords manufactured from the same piece of raw fibre and identical fibre collimators the output modes are far from the same. The solution is to add a 1:1 telescope in one of the input arms so that the beam size and divergence can be matched to that of the other input (fig. 8.18a). We gauge the overlap in two ways. The



first and more qualitative is to image the two inputs after the input BS on a camera (see fig. 8.18a). We insert a 400 mm focal length lens to ensure that the two inputs have both the same spot size and divergence. If the beams from both inputs are derived from the same laser it is possible to observe and maximise the interference in their overlap. This provides a very precise way to adjust the modes to one another, and the resulting individual spot images are shown in fig. 8.18b. The cross sections of the spot images can be plotted and compared as is done in fig. 8.18c. The overlap is clearly very good. The second way to measure the overlap is to detect the interference on a detector and deduce the fringe visibility. Typically we measure $V_{is} = 0.97 - 0.98$, which is about as good as one can expect. As we shall see in sec. 11.2.3. Fig. 8.19 shows the fringes ensuing from a good alignment of the MZI arm modes and two MZI input modes. As compared to fig. 8.17 we now include both probe colours (purple and orange traces) along with the locking pulses (green traces). As a small interactive feature, we invite the reader to pin-point the white-light position.

8.5 Fringe calibration

The fringe calibration measurement establishes the factor between the power reference detector voltage and the amplitude of the MZI interference fringes

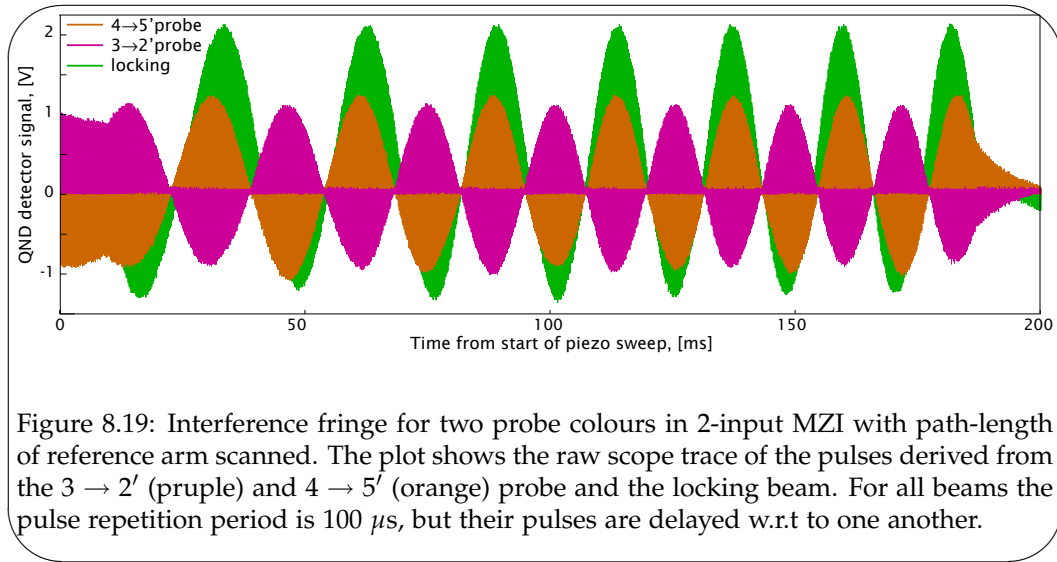


Figure 8.19: Interference fringe for two probe colours in 2-input MZI with path-length of reference arm scanned. The plot shows the raw scope trace of the pulses derived from the $3 \rightarrow 2'$ (pruple) and $4 \rightarrow 5'$ (orange) probe and the locking beam. For all beams the pulse repetition period is $100 \mu\text{s}$, but their pulses are delayed w.r.t to one another.

as detected by the QND detector. The aim is that the factor is the same for both probe colours, but this is not always possible due to differences in the fringe visibility of the probe fringe.¹³ Hence, we always acquire a separate calibration for each probe colour. Ideally, when the fringe visibility is close to unity the QND fringe amplitude (in integrated pulse-signal units) is $\mathcal{A}_p = \mathcal{G}_{QND} \epsilon_{QND} \sqrt{N_{\text{ph},a} N_{\text{ph},b}}$, where \mathcal{G}_{QND} and ϵ_{QND} are the gain and quantum efficiency of the QND detector while $N_{\text{ph},a}$ and $N_{\text{ph},b}$ are the photons in the probe and reference arms, respectively. The signal on the power reference detector is similarly $\bar{p} = \mathcal{G}_{\text{pow}} \epsilon_{\text{pow}} K N_{\text{ph},a}$, where K is the ratio between the photons impinging on the power reference detector and the photons in the probe arm passing through the atoms. Finally, the sought after ratio can be expressed as

$$\mathcal{G}_A \equiv \mathcal{A}_p / \bar{p} = \frac{\mathcal{G}_{QND} \epsilon_{QND}}{K \mathcal{G}_{\text{pow}} \epsilon_{\text{pow}}} \sqrt{\frac{N_{\text{ph},b}}{N_{\text{ph},a}}} \quad (8.5)$$

Usually, we will not be concerned with the above equation and just rely on the experimental determination of \mathcal{G}_A . With \mathcal{G}_A in hand we are able to convert QND detector probe pulse integrals into phase-shifts as $\phi = p / \mathcal{A}_p = p / (\mathcal{G}_A \bar{p})$. This of course assumes that $p = 0$ corresponds to $\phi = 0$.

8.6 Locking MZI path-length

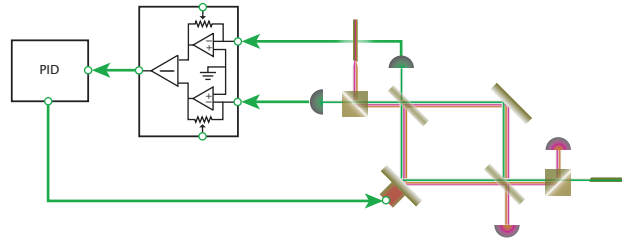
Once the interferometer is aligned to a certain position yielding a certain probe power difference between the outputs, it is necessary to lock the path-length difference so that the probe signal remains at a constant level. To be able to detect the atomic noise we require a stability of the path-length that corresponds to less than 0.5% change of a fringe equivalent to 5 nm. This can obviously only be achieved with some form of active stabilisation. To that end we deduce an error signal from an auxiliary laser, a so called *locking laser*, which propagates through the MZI in parallel with the probe pulses. As path-length variations affect the probe and locking laser alike the error signal for the MZI locking is simply the detected fringe of the locking laser. It is, however, required that the locking laser is unaffected by the atomic ensemble and therefore its frequency is chosen to be more than 10 nm from the D2 lines. We have implemented

¹³this has only been a problem when the probes enter different inputs. In this case it can be caused by the unequal splitting at the MZI input BS or differences in the polarisation purity.

two variations of the locking initially with a counter-propagating CW beam and subsequently with a co-propagating modulated laser.

8.6.1 Counter propagating CW laser

Figure 8.20: Locking scheme with counter-propagating off-resonant CW locking laser



The most straight forward method to apply the locking laser is to let it propagate through the interferometer in the opposite direction of the probes. By having the lock beam p-polarised it is possible to separate it from the s-polarised probes with PBSs in one of the input and output arms (see fig. 8.20).¹⁴ The optical power of the lock laser on the MZI input side are detected by a S1337-66BR Si photodiode from Hamamatsu and the photo-signals are subtracted with adjustable gain for each detector so as to permit a tuneable locking offset. The difference voltage is passed on to a PLL box with adjustable gain settings. An output error signal is fed through a high-voltage amplifier to a piezo-actuator supporting one of the mirrors in the MZI probe arm.

Though this locking configuration enabled us to measure shot noise limited operation of the MZI [Oblak05] it proved unable to stabilise the MZI sufficiently on long time-scales. The principal cause of this instability is that the lock and probe beams enter the interferometer at opposite ends of the MZI. This means that if the alignment of e.g. the probe beam from the input-fibre changes slightly the other will not follow and thus the phase between the probe and lock fringes will drift. Hence, the probe fringe offset phase tended to drift causing large swings in the output signal at the end making it hard to keep the QND detector signal from saturating. Another constant difficulty was the disturbance of the lock signal by the co-propagating FORT laser light even if it was only that leaking through two dichroic mirrors. On a less fundamental level, the components in terms of the photo-diodes, the initial amplification, the PLL lock, and piezo actuator were severely limited in terms of their bandwidth. At some point, we decided to opt for a new lock that would overcome most of these difficulties.

8.6.2 Co propagating modulated laser

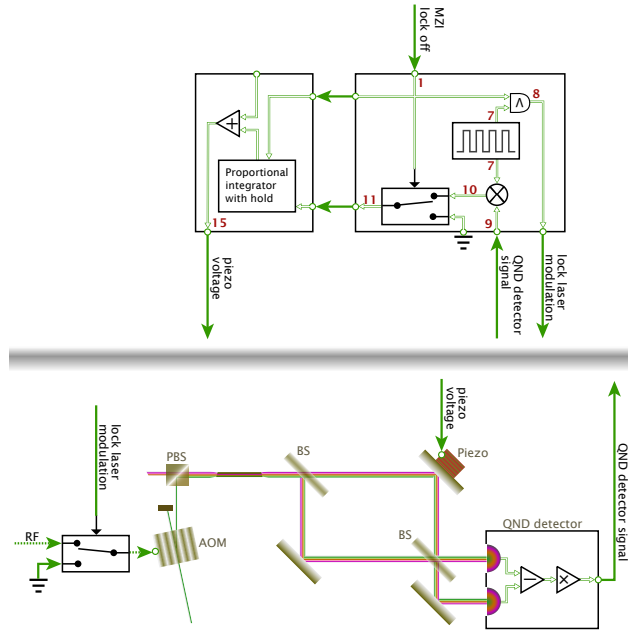
An ideal lock for the MZI should trace out the same path as the probe beams, i.e. the two should co-propagate in the same mode. Since we do not wish the locking light to be present in the probe signal it is necessary somehow to separate the two. Such separation could be done on basis of the beams having orthogonal polarisations or by temporally segregating the beams in pulses. The polarisation approach suffers from the inevitable contamination of the the probe beam by leaking lock light.¹⁵ Moreover slight polarisation drifts at the inputs would translate into power fluctuations that would cause the locking point of

¹⁴In principle it would be possible to have the CW lock laser co-propagating as well, but this would require a near perfect separation of the probe and lock beams on the PBS.

¹⁵the polarisation cannot be kept purely linear after passage through the numerous elements in the MZI arms.

one fringe to drift w.r.t the other. To keep the probe and locking beams temporally separated also presents a number of problems. As the first, the time that we can keep the lock off is limited to very short time and thus we are limited in the timing of the probe pulses. Secondly, the scheme implies detecting the probe and locking laser on the same photo-detector. The QND detector does, however, not maintain a DC level, which means that it would have no way of detecting the drift of a DC locking laser — the QND detector output would always be pulled to zero [Windpassinger08a, Windpassinger09a]. To circumvent the problem with the QND detector we opted for a AC-modulated lock laser. The diagram of this locking is shown in fig. 8.21, with numbered elements. The

Figure 8.21: Locking scheme with co-propagating off-resonant modulated locking laser. The 100 kHz lock beam modulation is done by an AOM in single-pass and it is mixed with the probe beam on a PBS before entering the fibre-link to the MZI setup. The QND detector signal is divided so that one part goes to the DSO for data acquisition while the other part goes to the locking setup (9). In the locking device the signal is demodulated (10) — by a lock-in with the local oscillator for the AOM modulation — and a DC error signal is forwarded to a PID. There is an option (1) to dump the demodulated error signal and instead input a ground signal to the PID (11). In this case the lock-laser is also gated off (8). This is relevant in cases where the error signal contains probe pulses, which because of their intensity would kick the lock if not blocked. There is an option of adding an offset to the PID feedback signal before it goes to the piezo in the MZI (15). Refer to fig. 8.22 for signal properties at the different numbered stages in the diagram.

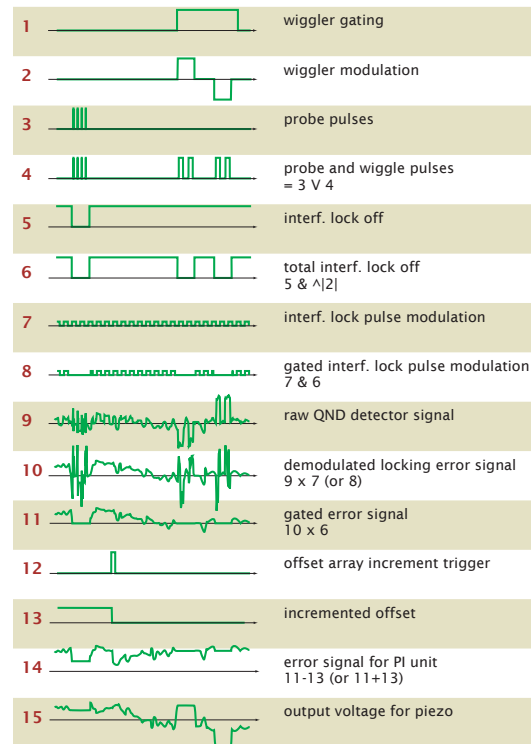


locking light is switched on and off with a 100 kHz frequency and the error signal from the QND detector is then demodulated to obtain a DC error signal, which via a PID generates a feedback to the MZI piezo. The locking light is gated off around probe pulses so that the probe phase-shift measurement will not be disturbed. The electronic signals at the different points in the diagram are sketched in fig. 8.22. During the periods where the locking is switched off the piezo output is frozen and we rely on the passive stability of the MZI to suppress fluctuations. In sec. 8.7 we will characterise the MZI noise performance, but some hints are already available from the theoretical considerations in sec. 6.1. From this we anticipate the 2-input MZI configuration to have superior passive stability because of its immunity to path-length variations. This however requires the fringes of both colours to have exactly the same amplitude. By ingenuity, it turns out that this demand can be turned in to a tool.

8.6.3 Power stabilisation and path-length wiggling

The power stability of the probe lasers proved to be a serious problem, especially when using a dichromatic probe, where the signal strengths must be kept equal over a long time. If the relative power of the probes changes, the phase-shift

Figure 8.22: Signal properties in MZI AC-locking circuits sketched in fig. 8.21 and fig. 8.24. Numeric labels correspond to the labels in the figures (with the reservation that in fig. 8.21 not all signals appear). The signals shown are constructed renderings of the signals as they are known to look like. Real records of signals (2), (11), (3), and (9) are in that order plotted in fig. 8.25.



arising from an equal atomic superposition state will no longer be zero. If this offset is constantly some small value it would not be an issue for concern as it could be compensated by a slight adjustment of probe detunings. The problem is precisely that the powers drift, so that the initially balanced atomic phase-shift signal will end up being larger than the saturation voltage on the QND detector. We also do not have any way to measure the probe powers in the MZI with the precision required to implement any form of feed-back. The solution to fix the relative probe powers is to be derived from fig. 8.23. Our attention is on the

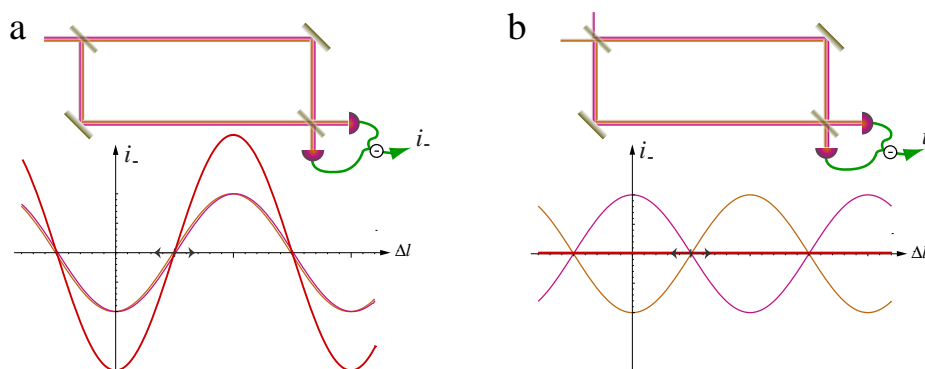


Figure 8.23: Comparing the sum output signal in the 1 and 2-input MZI. a) In the 1-input configuration the two probe fringes (orange and purple) interfere constructively and their combined signal (red) has double the fringe amplitude. b) In the 2-input configuration the two fringes interfere destructively and the combined signal is constantly zero. Thus, small wiggles of the MZI path-length difference (indicated by grey arrows) will result in a change of the combined signal in the 1-input MZI but will be camouflaged in the 2-input MZI.

2-input configuration fig. 8.23b, where due to the π phase-difference of the two probes' output signals their sum signal will always be zero. This gives rise to the immunity to acoustic vibrations in the MZI setup. However, if the probe powers are not equal — assuming that the fringe visibilities *are* equal for both colours — any path-length excursions *will* give rise to a change in the combined probe signal. We decided to use this property and deliberately offset the MZI

the action of turning these $\lambda/2$ plate will change the probe powers going to the MZI fibre-link. The power-balancer feedback is applied to the $3 \rightarrow 2$ probe laser wave-plate, while the $4 \rightarrow 5$ probe laser is used as reference.¹⁶ In the *power-balancer* script one can set the sign and magnitude of the gain used to adjust the $\lambda/2$ plate.

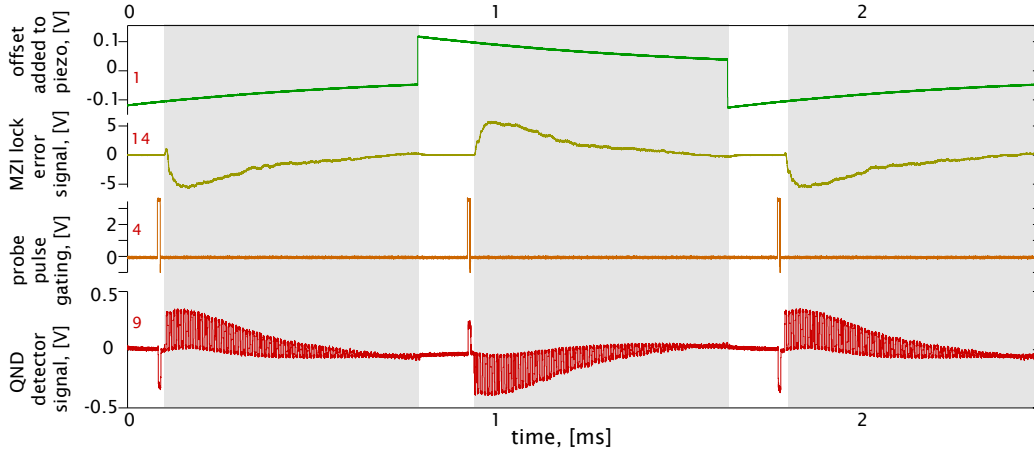


Figure 8.25: Probe power balancing by MZI path-length wiggling. The red numbers refer to the location of the signals in fig. 8.24 Green curve: the piezo offset voltage modulated by a square function. Due to a high-pass filter the offset slowly decreases. Yellow curve: The error signal which is grounded for a while as the probe pulses are fired. Orange curve: the gating signal for the probe pulse AOM. Red curve: Raw QND detector signal. Initially, no light impinges on the detector until a dichromatic probe pulse is fired. After the probe pulse the locking-pulses are turned on again and the error signal is no longer grounded. Thus the PID tries to null the error signal, which effectively means applying a voltage to counteract the offset voltage added for the wiggling. After ≈ 1 ms the offset changes sign and the sequence is repeated starting with the probe pulse. If the powers in the probe colours is not balanced the QND detector signal will be different for this pulse compared with the first.

8.6.4 Lock-point offset

As one final element we allow for the MZI locking point to be offset. That is we set the PID to level the error signal not to zero but to some externally input offset voltage. In fig. 8.24 we set the offset voltage V_{os} at (13) and added to the error signal (14) so that the PID effectively adjusts the piezo so as to level the error signal (11) to $-V_{os}$. The offset voltages are determined by the values stored in a shift register inside the wiggler unit. The elements of this shift register are programmed over a USB bus and are incremented by an external offset increment trigger. By this method we can quickly step the MZI path-length – and thus the MZI fringe phase – by forcing the locking point to different values. The speed at which the offset can be adjusted is set by the piezo. At the moment the offset stepping may seem rather futile but in sec. 12.4.3 it turns out to be a central last improvement towards the successful spin-squeezing experiment.

We have now done our utmost to make the locking of the MZI as comprehensive and versatile as possible. This elaborate amalgamation of elements did not come about by sheer foresight, but has been developed on a need to solve-a-problem basis. Therefore, when we now turn to characterise the MZI performance and

¹⁶it is sufficient to adjust only on probe power as the main objective is to stabilise the probe powers relative to one another.

later use it for QND measurements on the atomic sample, we will present results from various stages of the optimisation process.

8.7 Quantum and classical noise characteristics

The noise of the MZI determines the noise floor for our QND measurement; the lower the noise of the “MZI measurement device” the higher the SNR of the QND measurement. The ultimate goal for the SNR is that it be limited only by the unavoidable quantum shot noise of the probe light (see chapt. 6). The aim of this section is thus to investigate how successful we have been at suppressing all classical noise sources that were described in sec. 6.1. We separate this treatment in to sections on the 1 and 2-input MZI configurations.

Before, describing the measurements we consider how we arrive at an experimentally determined shot noise level and how we can compare this to the anticipated level. For both we need to know the calibration of the MZI fringe and power reference detector so that from the measured signals we can compute the MZI phase variances. The experimental shot-noise is given by the relations in sec. 8.5

$$\langle(\Delta\tilde{\phi})^2\rangle_{\text{SN}}^{(\text{exp})} = \frac{\langle(\Delta p_-)^2\rangle}{\mathcal{A}_p^2} \quad (8.6)$$

where the superscript signifies that it is based on the experimental determination of the signal fluctuations. On the other hand we get from eqs. (2.27 and 2.28) that in theory the output signal fluctuations due to shot noise should be $\langle(\Delta p_-)^2\rangle = \mathcal{G}_{\text{QND}}\epsilon_{\text{QND}}(1 + \tau^{-2})N_{\text{ph},a}$. Combining this with the expression for the fringe amplitude $\mathcal{A}_p = \mathcal{G}_{\text{QND}}\epsilon_{\text{QND}}N_{\text{ph}}^{(a)}/\tau$ we can arrive at a “theoretical” prediction for the shot noise

$$\langle(\Delta\tilde{\phi})^2\rangle_{\text{SN}}^{(\text{theo})} = \frac{1 + \tau^2}{4T^4 N_{\text{ph},a}} \quad (8.7)$$

Where $N_{\text{ph},a}$ in this case is deduced from the calibration of the power reference detector. In the below sections we will use these two estimates to verify that the measured shot noise is at the right level. Instead of using $\langle(\Delta\tilde{\phi})^2\rangle_{\text{SN}}$ directly we multiply the phase-noise by the photon number so as that the shot-noise can be plotted against the $N_{\text{ph},a}$ in the same units.

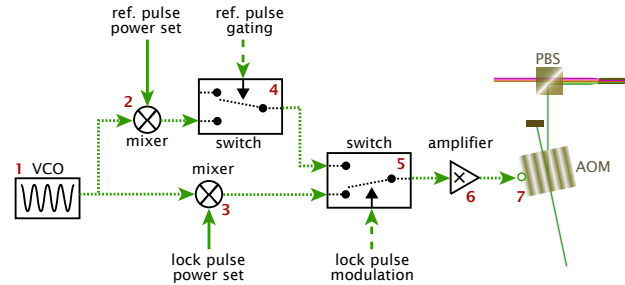
8.7.1 1-input configuration

In the 1-input MZI (see fig. 8.15) the output signal is maximally sensitive to acoustic/vibrational noise of the MZI setup and we rely heavily on the MZI lock to compensate this classical noise. For the counter-propagating locking scheme it is possible to have the lock engaged constantly during the QND measurements. However, as hinted earlier, the performance of this lock was sub-optimal due to the locking detector and feedback electronics as well as to the propagation of the probe and locking beams in slightly different spatial modes (see sec. 8.6.1). Since, this locking scheme was only used for some of the characterisation measurements and not for any of the presented QND measurements we will not detail the noise characteristics of the MZI with this locking configuration. An elaborate account of the noise properties is found [Oblak04], where the conclusion is that the MZI can be kept shot-noise limited up to $\sim 10^8$ photons for pulses separated by $< 10 \mu\text{s}$ and up to $\sim 10^7$ photons for pulses separated by $100 \mu\text{s}$. This is not quite as good as we want and thus the locking was changed to the co-propagating modulated laser scheme.

The main disadvantage of the co-propagating locking laser scheme is that the lock must be disengaged during the probing leaving the MZI to drift freely. This limits the allowable duration of the QND measurements sequence. Before, characterising the 1-input setup with the co-propagating locking laser, we discuss a method for compensating the MZI drift during the lock-off period. After the discussion we can then analyse the 1-input MZI both with and without this compensation.

Reference pulses One way to ensure a stable phase-reference for the probe measurements using the 1-input MZI is to track the MZI phase. This can best be done by observing the MZI fringe phase of an auxiliary laser beam traversing the MZI alongside the probe beam. A requirements for this auxiliary *reference* is that is not on simultaneously with the probe-pulses and that its fringe is not shifted by the atomic sample. Since, tracking the MZI baseline is essentially what

Figure 8.26: Setup for generating reference pulses from locking laser beam. This is an extension to the setup in fig. 8.21. The 80 MHz VCO (1) signal is divided in two arms, one for reference pulses and one for locking pulses/modulation. In each arm the amplitude is controlled by mixing (2,3) with a DC set voltage and switched on-and-off (4,5) for pulse generation.



The combined signal is amplified (6) to 2 W and input to the locking beam AOM (7). We note that the MZI-lock off signal (see fig. 8.21 and fig. 8.24), which is set to zero in the vicinity of the probe pulses, ensures that the signal at (5) in the above figure ensues from the reference pulse arm (4). Since, the reference pulses are put as close as possible to the probe pulses, this also ensures that locking modulation does happen during the reference pulses.

the locking pulses do, we derive the reference pulses from the locking laser as shown on fig. 8.26. The sceptic might ask why we do not use the locking pulses themselves and this question actually has two answers. Firstly, the modulation of the locking-pulse is un-synchronised with the probe-pulse generation. Thus we can not control the arrival of a locking pulse w.r.t to the probe pulses. Secondly, the intensity of the locking modulation is kept very low so as not to saturate the QND detector. Thus the individual locking pulses are far to weak to serve as MZI phase-reference for the probe pulses and moreover their relative shot-noise content is much higher. Hence, we need to control the power of the reference pulses independently from the locking pulses. More precisely, we require the reference pulses to be as intense as possible in order to suppress their shot-noise fluctuations. In other words we want the reference pulse noise to be dominated by classical fluctuations because only these fluctuations can be correlated with probe pulse fluctuations. The reference signal amplitude is only limited by the saturation of the QND detector.

To test the 1-input MZI performance we acquire pulse trains without any atoms in the probe arm. Sample traces of the raw data from the QND and power reference detectors are shown on fig. 8.27. Each QND probe pulse $p_{\text{qnd},i}^j$ (tinted green) is followed by an intense reference pulse (tinted red), which we label $p_{\text{ref},i}^j$. Here j indexes the pulse train and i the pulse's position in that train. Initially, we disregard the reference pulses and just extract the noise of the uncompensated probe pulses. We compute the variance between pulses within the same train or

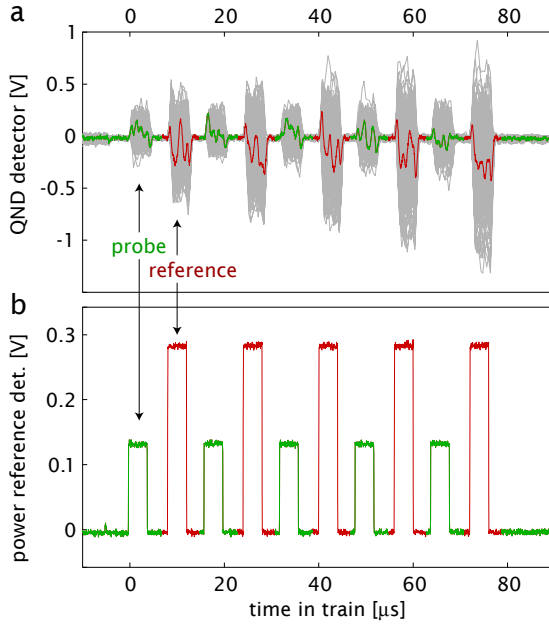


Figure 8.27: Raw detector traces of probe pulses (tinted green) with reference pulses (tinted red). The QND detector signal plot a) shows a single sample trace, with the entire 200 train measurement set at the given probe power shown as stacked grey traces. The power reference signal plot a) shows the average over the 200 trains for the given probe power, which in this case is at the maximal measured value. The slightly increased noise of the QND detector signal right at the start of the trace is caused by the locking laser modulation, which is switched off $5 \mu\text{s}$ before the first probe pulse.

between pulses in subsequent trains, that is

$$\langle (\Delta p_{i i', \Delta j})^2 \rangle = \frac{1}{2} \langle (p_i^j - p_{i'}^{j+\Delta j})^2 \rangle \quad (8.8)$$

where the expectation value is to be understood as the mean over all pulse trains acquired, i.e., the index j . The factor of $1/2$ is due to the subtraction of two pulses from one another. Since the indices correspond to pulses separated by a certain time, the variances will reflect the noise on the time-scale of the pulse separation c.f. sec. 8.2.2. For the measurement data shown in fig. 8.27 probe pulses are $4 \mu\text{s}$ long and within a train they are separated by $16 \mu\text{s}$, whilst the trains containing 5 pulses are separated by $100 \mu\text{s}$. To learn about the sources of light noise we vary the power of the probes using the wave-plates before the optical fibre-links (see fig. 8.10). At each set power we acquire about 200 trains so as to compute the variance plotted in fig. 8.28a. The objective is to deter-

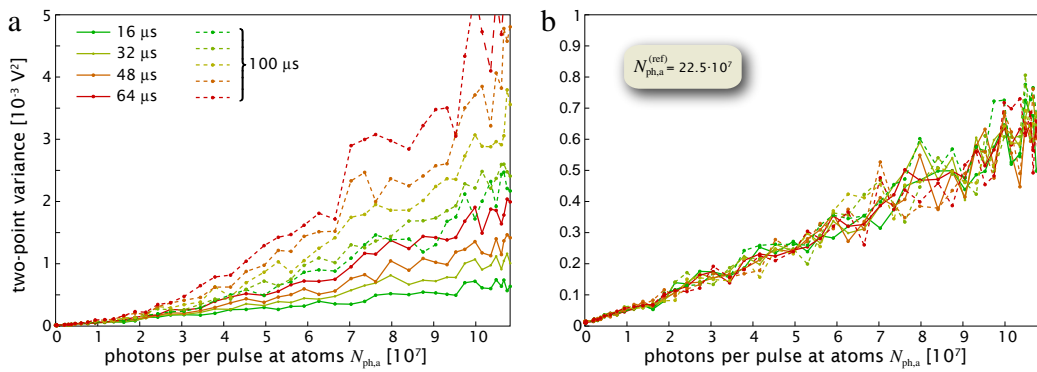


Figure 8.28: Shot noise in 1-input MZI without a) and with b) reference pulses. In both cases we plot $\langle (\Delta p_{1 i', \Delta j=0})^2 \rangle$ as full lines with $i' = 2$ in green, $i' = 5$ in red, and $i' = 3, 4$ in intermediate hues. We plot $\langle (\Delta p_{i i', \Delta j=1})^2 \rangle$ as dashed lines with $i' = 1$ in green, $i' = 5$ in red, and $i' = 2, 3, 4$ in intermediate hues. The corresponding time scales are given by the figure legend. For this data the MZI fringe amplitude was not measured and the noise in phase units cannot be computed. Thus the absolute value of the noise cannot be verified.

mine to what extent the variances scale linearly with the probe photon number as this is the signature of the quantum shot-noise. Classical noise on the other

hand will induce a quadratic scaling of the noise (see sec. 6.1). In fig. 8.28a the variance of the pulse differences increases rapidly with the temporal separation of the pulses, and only the variance of the neighbouring pulse difference $\langle(\Delta p_{12,\Delta j=0})^2\rangle$ shows a proportionally large linear scaling. This is backed up by the fit shown in fig. 8.29, which we will elaborate on farther below. That the variance $\langle(\Delta p_{1i',\Delta j=0})^2\rangle$ increases with i' is also clearly visible from the stacked grey raw-data traces in fig. 8.27. This indicates that the added classical noise mainly stems from acoustic fluctuations, which cause the MZI phase to drift as the MZI lock is switched off during the probe pulse train. The same explanation predicts the increase of $\langle(\Delta p_{ii,\Delta j=1})^2\rangle$ with i in fig. 8.28a i.e. the farther the delay of the pulse w.r.t. time the lock is disengaged to more it's value will fluctuate. We also find that $\langle(\Delta p_{ii,\Delta j})^2\rangle$ for a given i is roughly constant for all $\Delta j > 0$, e.g. $\langle(\Delta p_{11,\Delta j=1})^2\rangle \approx \langle(\Delta p_{11,\Delta j=150})^2\rangle$. This further establishes that the main cause of classical (acoustic) noise perturbing the MZI is due to the switching off of the MZI lock during the probing.

We can correct the drift of the probe pulses by use of the reference pulses. As introduced above, the idea is that the reference pulse signal is affected in the same way by acoustic fluctuations as the probe pulse signal, and by subtracting a weighed proportion of the reference pulse signal these fluctuations can be traced out of the probe pulse signal. As noted, not all fluctuations of the probe and reference pulses need be correlated. Examples of such are shot noise, classical probe laser noise, or acoustic noise with characteristic time scales less than the probe and reference pulse separation. Hence, we compute the compensated pulse value

$$p_{\text{qnd},i}^j - \zeta_{\text{ref}} p_{\text{ref},i}^j \rightarrow p_{\text{qnd},i}^j, \quad (8.9)$$

where the correlation factor ζ_{ref} is given by

$$\zeta_{\text{ref}} = \frac{\langle(\Delta p_{\text{qnd},i}^j p_{\text{ref},i}^j)\rangle}{\langle(\Delta p_{\text{qnd},i}^j - p_{\text{ref},i}^j)^2\rangle}, \quad (8.10)$$

The size of the correlation ζ_{ref} varies considerably depending chiefly on the probe to reference pulse power ratio but also to some extent on the MZI *noise-of-the-day*. For a measurement dominated by classical fluctuations of the interferometer ζ_{ref} will be large whereas a shot-noise limited interferometer would give $\zeta_{\text{ref}} \approx 0$. For this measurement, the reference pulse power is twice as large as the highest probe power value (this is the situation shown in fig. 8.27).

We find the variances of the pulse differences as directed by eq. (8.8) and plot these on fig. 8.28b. The variances for any pulse pair difference are all equal and the scaling is very close to being linear. How close is given by the coefficients of the polynomial in fig. 8.29. To reduce the data scatter we fit to the average $\langle(\Delta p_{1i',\Delta j=0})^2\rangle$ over $i' = 2, 3, 4, 5$. The variance is dominated by the linear scaling and the residual quadratic scaling is partly due to insufficient suppression of the reference pulse shot-noise as the probe to reference power ratio becomes $\lesssim 1$. At the highest measured probe photon number $15 \cdot 10^7$ the classical noise amounts to about 20% of the total quantum shot-noise level. The grey points show the uncompensated neighbouring pulse difference variance $\langle(\Delta p_{12,\Delta j=0})^2\rangle$, which clearly is *as* shot-noise limited as the reference pulse corrected probe pulse variance.

Though the reference pulse compensation of the acoustic noise seems to deliver the sought after stability, the discussion of the QND measurements in sec. 12.4.2

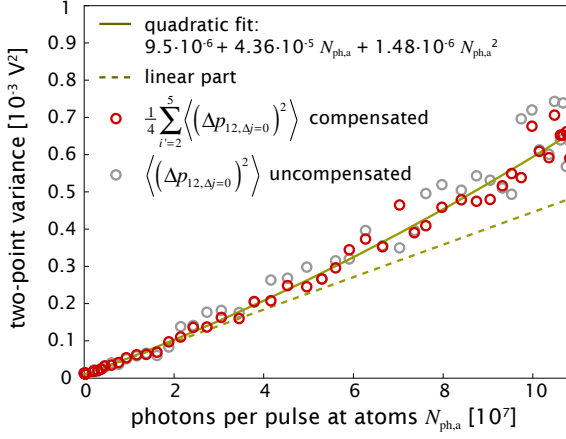


Figure 8.29: Shot noise scaling with photon number in 1-input MZI with reference pulses. A second order polynomial (yellow line) is fitted to the noise of the mean difference of pulses within a train, i.e., to $\frac{1}{4} \sum_{i'=2}^5 \langle (\Delta p_{1i', \Delta j=0})^2 \rangle$ (red circles). The linear part of the fit (yellow dashed line) corresponds to the shot noise. Grey circles mark the variances of the uncompensated neighbouring pulse difference $\langle (\Delta p_{12, \Delta j=0})^2 \rangle$, i.e., the green line in fig. 8.28a.

unveils that the presence of the reference pulses becomes an obstacle for the freedom to choose probe powers and detunings in order to minimise other classical noise sources. Hence, we turn to a MZI configuration where the reference pulses are unnecessary.

8.7.2 2-input configuration

In the 2-input MZI the combined probe signal should to 1st order be unaffected by acoustic/vibrational perturbations of the MZI and we anticipate no longer to need the reference pulse compensation. To characterise the noise we again acquire pulse trains without any atoms in the probe arm. However, the pulse trains used differ somewhat from those described in the preceding section. The individual pulses in the train are 4-10 μs long and separated by some 10-20 μs , while the trains are now spaced by 2-4 s. In sec. 12.2.2 we shall illustrate how such trains are an integral part of the QND measurement sequence, but for now the above information will suffice. The fact that we deduce the shot-noise performance from the same data as used for the QND measurement analysis is exactly why we choose to present it in this way.

To evaluate how much of the detected noise is shot-noise and how much stems from other sources we must vary the photon number and observe the scaling of the noise. Experimentally, we change the number of photons by merging more and more neighbouring pulses in the trains. As a consequence we see different spectral components of the noise for the different total photon numbers (see sec. 8.2.2). For the white shot-noise the pulse merging poses no problems, but it might make it more tricky to deduce the source of some classical noise. Now we compute the variance between pulses within the same train or between pulses in subsequent trains. That is, if i is the index of the pulse position within the train and j is the index of the train then we calculate

$$\langle (\Delta p_{ii'}(K_i))^2 \rangle = \frac{1}{K_h} \frac{1}{K_i} \left\langle \sum_{h=0}^{K_h/2} \left(\sum_{i=1}^{K_i} (p_{h+i}^j - p_{h+K_i+i}^j) \right)^2 \right\rangle \quad (8.11a)$$

$$\langle (\Delta p_{jj'}(K_i))^2 \rangle = \frac{1}{2K_h} \frac{1}{K_i} \left\langle \sum_{h=0}^{K_h} \left(\sum_{i=1}^{K_i} (p_{h+i}^j - p_{h+i}^{j+1}) \right)^2 \right\rangle \quad (8.11b)$$

where the expectation values $\langle \cdot \rangle$ are to be understood as the mean over all pulse trains acquired, i.e., the index j . The sum over all displacements h within the train ensures maximal utility from the acquired data. K_h gives the number of

pulses within a train. The grouping K_i becomes the parameter which determines the photon number. For the variance $\langle(\Delta p_{ii'}(K_i))^2\rangle$ between pulses within a train $K_i < K_h/2$, while for the variance $\langle(\Delta p_{jj'}(K_i))^2\rangle$ between trains $K_i < K_h$.

The above procedure is in principle also possible for the 1-input MZI data with reference pulses, however in practice the problem is that the reference pulse power is set at the highest possible value, where the QND detector tends to saturate after the first couple of pulses. Hence, combining pulses in the train, comes at the expense of a large amount of data being discarded due to detector saturating. For that reason we refrain from the method of combining pulses in the 1-input MZI and instead make independent measurement runs for different probe laser intensities (see sec. 8.7.1).

Returning to the 2-input configuration we expect a significant reduction of the classical light noise, especially on the time-scale between pulse trains. The data points in fig. 8.30 confirm this prediction. Within the pulse train the scaling of

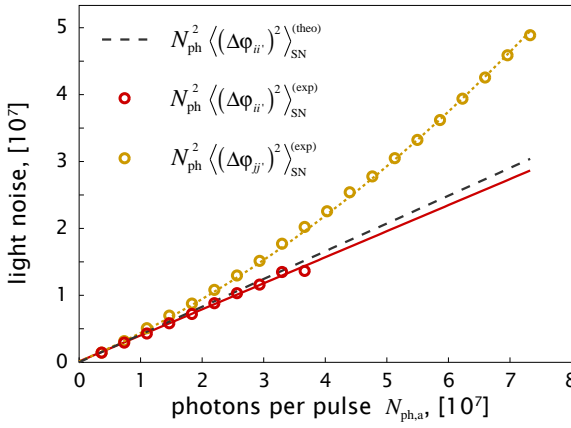


Figure 8.30: Shot noise scaling with photon number in 2-input MZI. Red and orange circles is the variance of the difference between pulses within a train (eq. (8.11a)) and in subsequent trains (eq. (8.11b)) respectively. The translation into phase-units is done by eq. (8.6). The dashed grey line is the shot-noise level predicted by the photon number detected by the power reference detector c.f. eq. (8.7). The probe to reference arm power ratio is $\sim 1:12$ and $N_{ph,a} = 0.37 \cdot 10^7$ for a single probe pulse

the light-noise (red circles) is now perfectly linear and coincides beautifully with the theoretical prediction (grey dashed line). In between the pulse trains the light noise (orange circles) stays very close to the SNL up till $4 \cdot 10^7$ photons. Within the range of $N_{ph,a}$ shown on the graph, the shot-noise is the dominating noise, hence we say that the MZI is shot noise limited.

We also verify the light noise in the 2-input equivalent version of the MZI where we misbalance the arms to have about 1.6 cm path-length difference. This is shown on fig. 8.31. Again more or less the same conclusions can be drawn as for

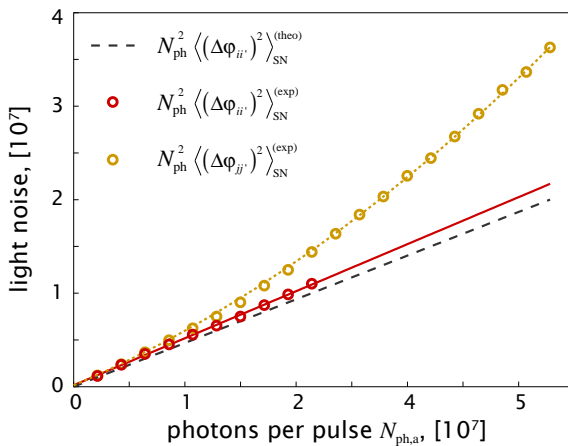


Figure 8.31: Shot noise scaling with photon number in 2-input equivalent MZI (path-length separation). Red and orange circles is the variance of the difference between pulses within a train (eq. (8.11a)) and in subsequent trains (eq. (8.11b)) respectively. The translation into phase-units is done by eq. (8.6). The dashed grey line is the shot-noise level predicted by the photon number detected by the power reference detector c.f. eq. (8.7). The probe to reference arm power ratio is $\sim 1:10$ and $N_{ph,a} = 0.21 \cdot 10^7$.

the "true" 2-input MZI. The two curves actually look conspicuously similar. We take this as an indication that the two configurations, at least on time-scales up to a couple of seconds, behave the same.

The fact that we record the shot noise only on two specific time-scales is not really a deficiency, since the two time-scales are exactly the ones relevant for the QND measurement. We have established now that at least with the proper stabilisation the MZI in both the 1-input and 2-input configurations is as sensitive as to be limited by the shot-noise of the probe light. This of course is only true up to a certain probe power, but it turns out that the powers needed for the QND measurement are well within the range where the MZI is shot-noise limited.

Sample preparation and characterisation

9.1 Atom trapping setup and control

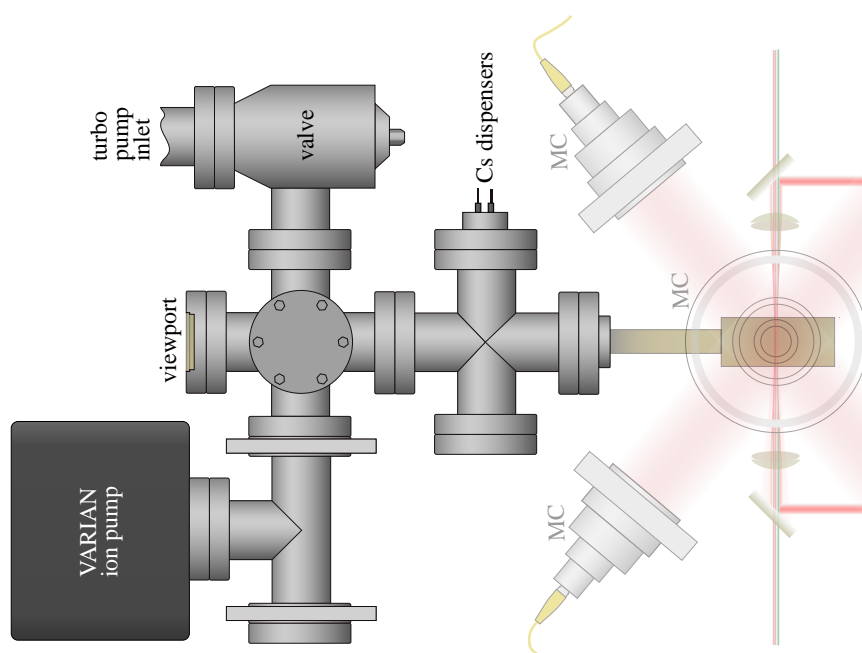


Figure 9.1: Vacuum setup.

vacuum setup The vacuum setup is sketched in fig. 9.1. At the heart of it all is a quartz-cell from Hellma with dimensions $5 \times 5 \times 15$ cm and glass thickness of 0.5 mm. The cell is AR-coated on the external faces but un-coated on the inside. The cell is attached to a cross-piece via a glass-metal transition. The Cs-dispensers from SAES Getters¹ are attached to one of the branches and protrude into the centre of the cross. The vacuum is maintained by a Varian StarCell ion-pump. Since we have no vacuum-gauge attached permanently to the setup the ion-pump current is the main measure of the pressure. However, due to age and exposure to Cs the pump current is dominated by leakage through Cs deposits in the pump, that do, however, not affect the pumping efficiency [gam06]. Thus, the FORT lifetime is the only indicator of the vacuum quality. The setup can

¹CS/NF/16/50 FT10+10

be attached to a Varian turbo-pump via a vacuum-valve. The turbo-pump has a vacuum gauge mounted to it and while connected to the setup it reads a pressure of $1.4 \cdot 10^{-9}$ Torr.

computer interface As discussed in sec. 7.1 the experimental sequence is automated through a PC. Whereas sec. 7.1 focused on the setup of the hardware, we will here introduce the software which controls the sample trapping and a number of other functions discussed in later sections. Fig. 9.2 shows a screenshot of the main programme for operating the sample preparation. The front



Figure 9.2: Screen-shot of a reasonably recent and representative version of the LabView programme CAMOT, which controls the National Instruments PCI cards and numerous other PC output busses.

panel consists of columns of values which are set in stages on the relevant DAC output channels as sketched on fig. 7.2. On the very top is a row of green markers, which sets a boolean on/off for that stage. If the program encounters an off-stage, it will return to the first column and make another cycle. The first row with numerical values determines the duration of the stage and the row underneath sets a transition time during which the values of two subsequent stages are linearly interpolated. The remaining rows set all the parameters for the MOT loading. As not all of these have been introduced we will not explain them all here. Furthermore, the labels should make the identification quite intuitive.

9.1.1 Magneto-optical trap

The first stage in preparing the atomic ensemble is the MOT. The main ingredients for the MOT are a six laser beams, two magnetic coils in an anti-Helmholz configuration and a set of compensating coils in a Helmholtz configuration. The laser beams contain two frequencies, one for cooling and the other for re-pumping, and both are generated in a similar fashion. A diagram of the MOT laser setup and the frequencies at different stages is shown on fig. 9.3. The master lasers are frequency locked by means of absorption saturation spectroscopy. The master lasers double-pass in AOMs allowing for tuning of the frequency input to the injection locked slave lasers. The slave laser beams pass

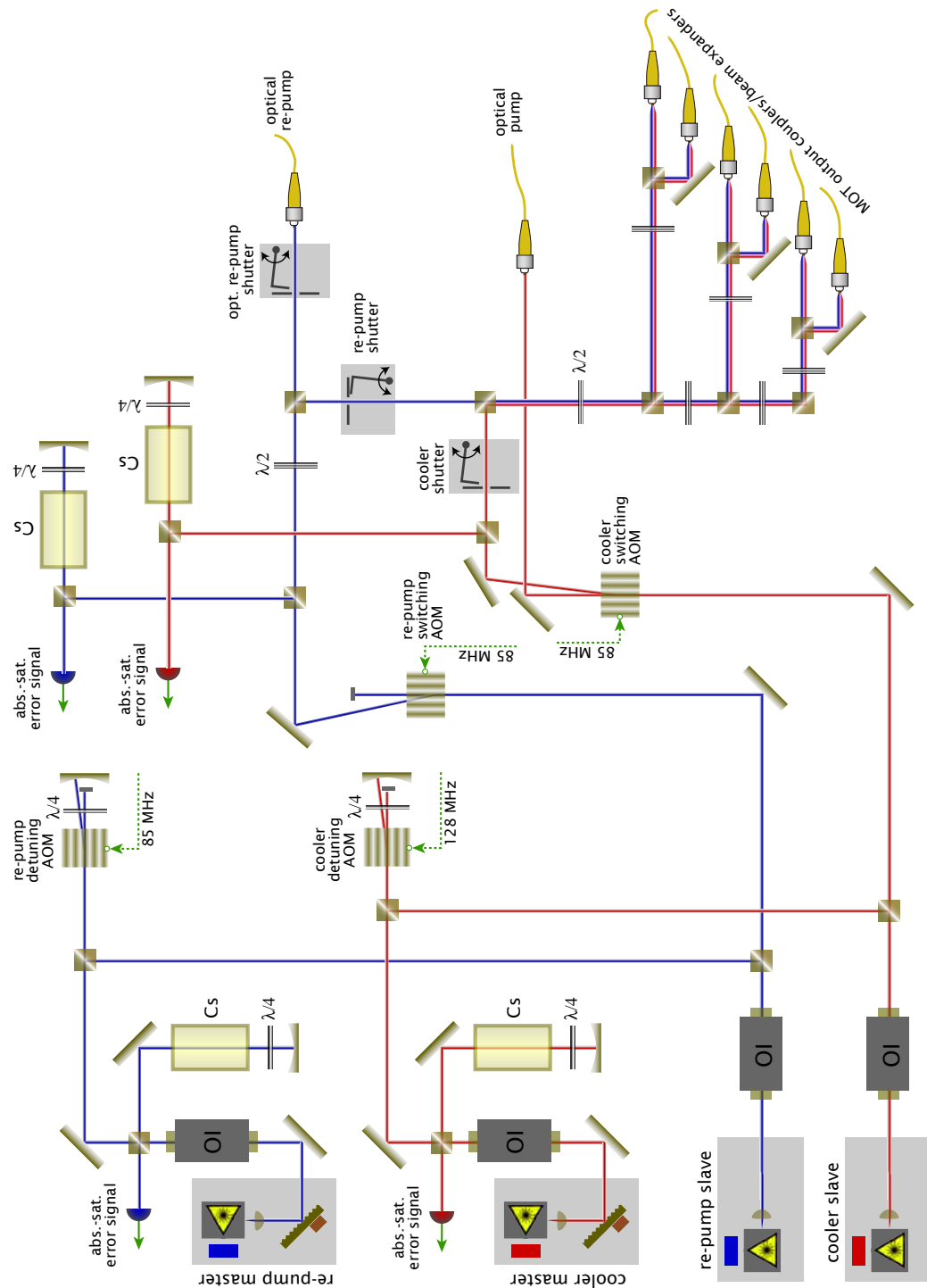


Figure 9.3: MOT laser setup. Details given in the body text.

another pair of AOMs, which are used for switching the beams on or off. This switch is not perfect and in order to block the beams completely we installed home-made shutters, which close in a few ms [Windpassinger08a]. The cooler and re-pump slave beams are mixed on a BS and subsequently distributed over 7 optical fibre inputs, 6 of which go to the vacuum and MZI setup, which is outlined on fig. 9.4. Not shown on the outline are the three pairs of Helmholtz compensating coils which surround the whole trapping and MZI setup.

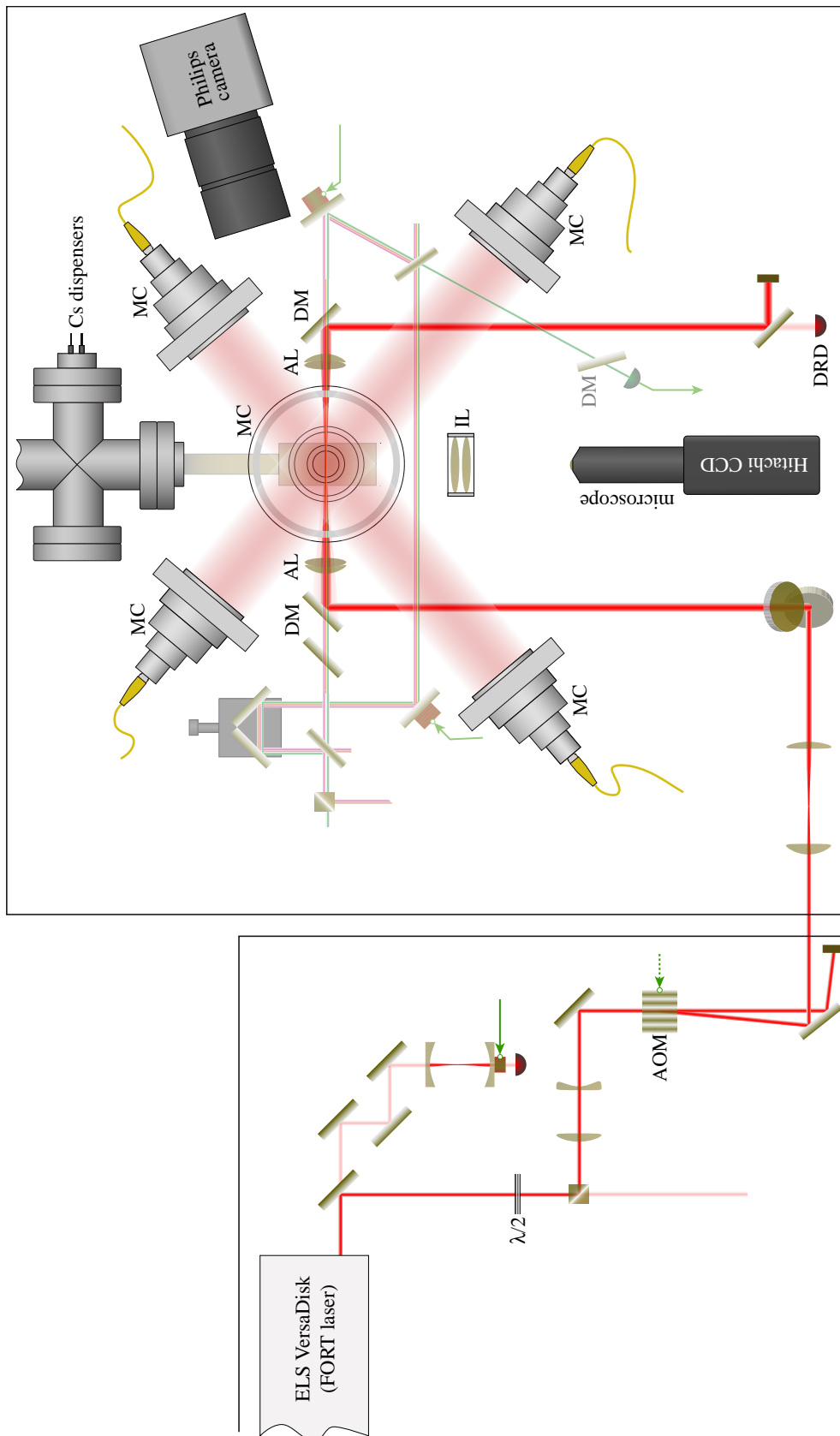


Figure 9.4: Trapping setup of combined MOT and FORT. Mot Collimators (MC), Imaging Lenses (IL), Achromat Lenses (AL), Dichroic Mirrors (DM), Acousto-Optical Modulator (AOM), FORT laser Reference Detector (DRD).

9.1.2 Far Off Resonant Trap

Back of envelope trapping principles

After cooling and spatially concentrating the atoms in the MOT we transfer them into a conservative trap formed by an off resonant focused laser beam [Chu86]. If the laser frequency is red detuned w.r.t. the dominant transitions from the ground levels, the AC-Stark shift (a.k.a. light shift) of the levels will cause atoms to experience a potential through in the electric field of the laser beam. For a focused Gaussian beam the potential has the form [Grimm00, Petrov06]

$$V(r, z) = V_0 \frac{w_t^2}{w(z)^2} e^{2r^2/w(z)^2} \quad (9.1)$$

where w_t is the trapping beam waist, and the spot-size $w(z) = w_t \sqrt{1 + z^2/z_r^2}$ is a function of the Raleigh-range $z_r = \pi w_t^2/\lambda_t$ which in turn depends on the wavelength λ_t . The potential minimum for a linearly polarised and Far Off-Resonant Trapping (FORT) beam is given by [Grimm00]

$$V_0 = \frac{P}{8\pi^3 c w_t^2} \left(\frac{\gamma_{D1} \lambda_{D1}^3}{\Delta_{D1}} + 2 \frac{\gamma_{D2} \lambda_{D2}^3}{\Delta_{D2}} \right) \approx \frac{P \gamma_D \lambda_D^3}{8\pi^3 c w_t^2} \left(\frac{1}{\Delta_{D1}} + \frac{2}{\Delta_{D2}} \right) \quad (9.2)$$

where γ_{D1} is the decay rate of the $P_{3/2}$ excited state, λ_{D1} is the D1-line transition wavelength coupling it to the $S_{1/2}$ ground level, and Δ_{D1} is the detuning to the trapping laser i.e. $\Delta_{D1} = 2\pi c(1/\lambda_t - 1/\lambda_{D1})$ (see table D.2 for values). Similarly for the D2-line. For the last equality we have used that $(\gamma_{D1} \lambda_{D1}^3)/(\gamma_{D2} \lambda_{D2}^3) = 1.02 \approx 1$ to take the product as a common factor. For a red detuned laser the potential is thus negative i.e. confining the atoms. Eq. (9.1) can also be derived from the above studied QND interaction by appropriate approximations for the far detuned limit of eq. (4.21). The QND property of that interaction was linked to the light-shift scaling as Δ^{-1} and the excitation rate scaling as Δ^{-2} . This same property, is precisely what makes it feasible to trap atoms using the light shift of a laser beam, in that excitations can be made negligible by detuning far enough. Inserting the values from table D.2 in to eq. (9.2) the potential depth for the Gaussian $\lambda_t = 1032$ nm laser utilised in our setup was calculated to be

$$V_0 = \frac{P k_B}{w_t^2} 0.173 \frac{\text{K } \mu\text{m}^2}{\text{W}} \quad (9.3)$$

where k_B is Boltzmann's constant and it is understood that the trapping beam waist be entered in μm and the beam power in Watts. Standard parameters for the FORT power $P = 3.5\text{W}$ and the trap waist $w_t = 40 \mu\text{m}$ give a potential depth of $380 \mu\text{K}$.

Though the trapping beam detuning is 6700 times larger than the ground level hyperfine splitting ω_0 there will be a small difference in the light-shift and thus the potential depth for the two ground levels. This *differential light shift* can be expressed as

$$\begin{aligned} \Delta V_0 = V_{0, F_s=3} - V_{0, F_s=4} &= \frac{3P \gamma_D \lambda_D^3}{8\pi^3 c w_t^2} \left(\frac{1}{\Delta_{D, \text{eff}}} - \frac{1}{\Delta_{D, \text{eff}} + \omega_0} \right) \\ &= V_0 \frac{\omega_0}{\Delta_{D, \text{eff}} + \omega_0}, \end{aligned} \quad (9.4)$$

where the effective D-line detuning is defined as

$$\frac{1}{\Delta_{D, \text{eff}}} = \frac{1}{3} \left(\frac{1}{\Delta_{D1}} + \frac{2}{\Delta_{D2}} \right) \quad (9.5)$$

Again, inserting the atomic constants and the trapping laser wavelength 1032 nm we get

$$\Delta V_0 = \frac{Pk_b}{w_t^2} 28.9 \frac{\mu\text{K}}{\text{W}} \quad (9.6)$$

$$= \frac{P\hbar}{w_t^2} 2\pi 601 \frac{\text{Hz}}{\text{W}} \quad (9.7)$$

Typical values for the FORT power $P = 3.5\text{W}$ and the trap waist $w_t = 40 \mu\text{m}$ give a differential light-shift of $\Delta V_0 = k_b 0.063 \mu\text{K}/\text{W} = \hbar 2\pi 1300 \text{Hz}/\text{W}$. In terms of trapping, the potential difference for the two levels is negligible, however the effect that the ground level energies are shifted w.r.t. each other is clearly visible when performing microwave spectroscopy on transitions between the ground levels. We describe the hypothesised influence in sec. 10.2.1 and in sec. 10.2.3 show empirical evidence thereof.

For small radial and axial excursion the potential eq. (9.1) is approximately harmonic with characteristic trap frequencies

$$\omega_{\perp} = \sqrt{\frac{4V_0}{m_{Cs}w_t^2}}, \quad \omega_{\parallel} = \sqrt{\frac{2V_0}{m_{Cs}z_r^2}} = \frac{\lambda_t}{\sqrt{2}\pi w_t} \omega_{\perp} \quad (9.8)$$

for the transverse and axial directions respectively. In secs. 9.2.2 and 11.2.1 we experimentally determine the radial trap frequency.

Experimental setup

The setup for the FORT trapping is sketched on fig. 9.4. The FORT beam generated by a ELS VersaDisk laser has a wavelength of 1032 nm and a specified power of 40 W though we never managed to output more than about 10 W. The cavity mirrors and filters are cleaned regularly with solvents to remove dirt-coatings. The laser can be made to lase in a single frequency mode by tuning the internal etalon. However, mode jumps tend to occur at intervals of some minutes at best and in the worst case constantly. To improve on the mode stability an active feed-back to the piezo mounted etalon has been implemented. This works on a quite simple principle. We monitor the frequency mode of the FORT laser by injecting the leak-light through the first mirror in to a simple Fabry-Perot cavity, that we lock on resonance. If the FORT laser jumps to a different single frequency mode the cavity will just re-lock to a new displacement. If however, the FORT laser begins to lase on multiple frequencies the cavity peak will decrease. Via the data acquisition programme this triggers the etalon angle to be offset by a small amount whereupon the peak height in the Fabry-Perot is rechecked. This continues until the cavity can be locked to a resonance with a height above the set threshold value. In every experimental cycle we actually proactively check if it is worth displacing the etalon, by offsetting it slightly to both sides. If the Fabry-Perot signal decreases for one of the etalon offsets the etalon is adjusted to the opposite direction.

We measured the relative intensity noise (RIN) of the laser by impinging the beam on a detector and performing a Fourier transform. The RIN is at a base level of -120 dB/Hz, which is significantly higher than the specified value of -150 dB/Hz². The noise peak at around 21 kHz is caused by relaxation oscillations that unexpectedly showed up in measurements of the MZI noise (see box 8.1).

²According to ELS this "over-specification" is due to a erroneous method used in their measurement.

At first the laser was situated on the same table as the MZI setup, however we found that the cooling water flow for the laser caused excessive acoustic noise in the MZI signal. Consequently, the laser was moved to a separate table, with the risk of compromising the pointing stability of the beam w.r.t. the MZI. Attempts, were made to transport the FORT laser beam from the laser table to the MZI table through optical fibres. Because of poor coupling efficiencies or transverse mode contamination these attempts were unsuccessful. Fortunately, we never saw any adverse affects of having the laser on a separate table.

From the laser, the beam is reflected on a mirror. The residual transmission through the initial mirror is input into the above described Fabry-Perot cavity. The reflected beam goes through a $\lambda/2$ -plate and into a PBS, whereby it is possible to attenuate the beam for alignment purposes. A telescope adjusts the spot-size before the beam passes through an AOM from IntraAction, which serves as an optical switch. A second telescope has been installed so as to fine tune the beam collimation and adjust the spot size (see fig. 9.5). The beam is elevated up

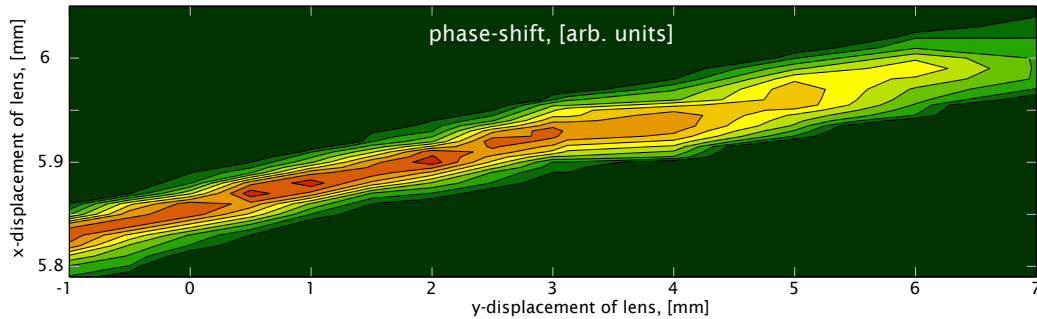


Figure 9.5: Alignment of FORT beam waist. Using the 50 mm lens mounted on the xyz-translation stage we step the FORT beam waist and sweep it in the transverse direction to gauge the maximal achievable phase-shift. The maximum phase-shift not occurring at a fixed x-displacement is a result of a slight misalignment of the translation stage. Due to the numerous lenses that follow it is not straightforward quantitatively to relate the lens y-displacement with a corresponding z-displacement of the FORT waist. We observe that the signal is not particularly sensitive to the lens' y-position.

to the MZI base-plate by a periscope consisting of two mirrors, which are also used for overlapping the FORT with the probe beam. The overlap with the MZI beams is done on a custom coated dichroic mirror from VLOC, which for 45° AOI reflects 99.99% at 1030 nm while it transmits 98% at 852 nm. The beam is focused to a waist of around 40-60 μm by a 100 mm Thorlabs achromatic-lens. At the output an identical achromat re-collimates the beam and a second dichroic mirror reflects the FORT beam out of the MZI. The beam is finally put to a beam-dump or incident on a thermal power detector. In the former case a small part of the beam is directed to a reference detector for gauging the power. The total losses in the beam-path from the AOM to the dump amounts to about 30%.

Power Stabilisation We actively stabilise the FORT laser power by detecting the leak light through one of the periscope mirrors and in a feedback loop adjust the RF power of the FORT beam AOM. The stabilisation levels out the typical 10% power drifts of the laser over the course of a day, but also smoothes the intensity noise. Improving the feedback loop to achieve a maximal noise suppression of 25 dB with ~ 40 kHz bandwidth we actually see an extension to the trap lifetime (see sec. 9.2.1).

FORT imaging As a supplement to the MZI detection of the sample we have installed a CCD imaging system which consists of a 1:1 image displacement lens-pair a microscope objective and a Hitachi CCD camera (see fig. 9.4). The FORT is viewed from the end face of the vacuum cell and an example of a fluorescence image of the sample is shown on fig. 9.6. For more details on the imaging setup

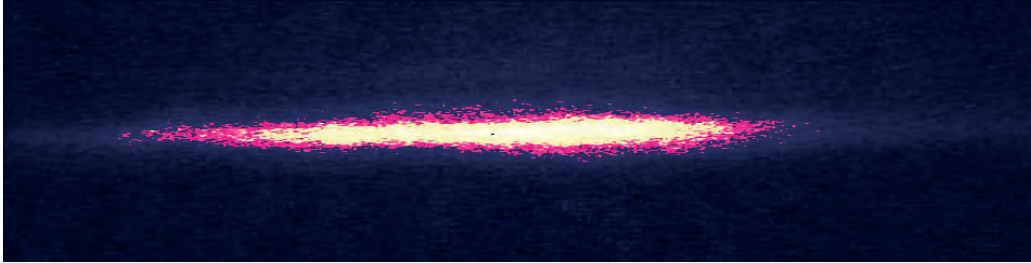


Figure 9.6: CCD camera fluorescence image of FORT with fake-colours representing intensity. The image width and height correspond to $991 \mu\text{m}$ and $374 \mu\text{m}$ respectively (648×243 pixels). To expose the cloud the MOT cooling detuned by ≈ -16 MHz and the MOT re-pump are switched on for 1 ms and simultaneously the camera is triggered to charge the CCD. The FORT laser scatters almost no light into the camera and is kept on during the exposure. Due to heating by the MOT lasers the sample size in the image is somewhat larger than the actual undisturbed sample size.

refer to [Petrov06]. The possibility of imaging the MOT and the FORT has proven particularly valuable for rough alignment of the probe and FORT laser beams. The first observations and optimisations of our FORT were indeed done using the camera.

FORT transverse mode The mode of the FORT beam has been a source of some unpleasant surprises. When the setup was first aligned we ensured that the beam was collimated when hitting the achromat before the vacuum cell. Probably, due to subsequent alignment of the laser cavity the beam was found at a later time not to be collimated any longer and in order to amend this we inserted extra lenses in the beam-path. Unfortunately, we did not notice the fault for some time since we were able to measure decent atomic phase-shifts with the MZI. Hence, we believe it is the cause of some deviating experimental trap characteristics in sec. 9.2.2 and sec. 9.2.3. Furthermore, more recently we discovered that the beam mode depended heavily on the power in the beam. At the maximum powers it even developed a toroidal shape. This we found was due thermal lensing in the AOM, and by re-collimating the beam in the AOM the effect disappeared. Since, this was also linked to the beam collimation going bad it is not clear how long this effect had been present. Since, most data seems consistent with predictions we assume that the transverse mode of the FORT had mostly been in "good shape".

influence on MZI The trapping beam propagates in the opposite direction of the MZI probe beam in order to minimise the amount of trapping light on the QND detectors. Nevertheless, some trapping light makes it into the QND detector mainly from reflections on the (un-coated) vacuum cell walls (see box 8.1). To block the reflected trapping light we insert additional dichroic mirrors in the probe beam and in front of the MZI lock-beam detectors when using the CW locking configuration (see fig. 9.4). Moreover, one can often move the reflections away from the QND detector by slightly adjusting the FORT laser path.

A more indirect influence the FORT laser comes from the heat deposited in the optical elements. When the FORT laser intensity is changed the resulting temperature change affects the optical path length of the MZI probe arm. This is visible as shift in the MZI phase over a time-scale of 50 ms. Hence, if the FORT laser is switched off only shortly this thermal effect can be neglected.

9.2 Non-destructive trap characterisation

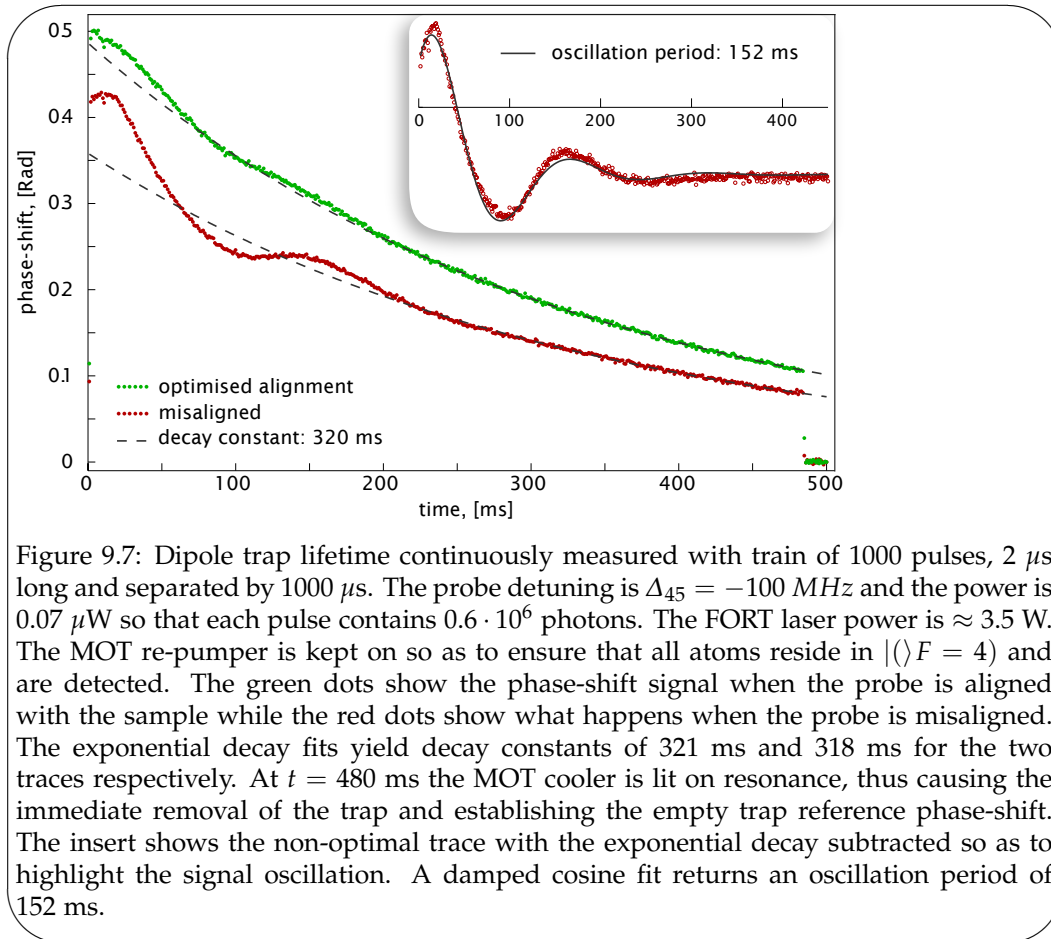
We are now set to make use of the MZI to detect the trapped atoms and thus characterise the trap properties. The characterisation is still only of classical properties, i.e., not relying on a specific quantum state of the atoms and the QND character of the probing. Nevertheless, we have an advantage from the probing being near the $4 \rightarrow 5'$ and/or $3 \rightarrow 2'$ transitions, so that there is little reshuffling between the hyperfine ground levels. In this sense the probing is classically non-destructive. The non-destructive measurements of the trap properties have previously been treated thoroughly in the thesis work by Plamen G. Petrov [Petrov06] and in a publication [Petrov07]. As a consequence, we will only present a short overview of the trap properties here, however, using the opportunity to introduce a method of numerical simulation of the atomic motion, that will be used in subsequent sections.

When characterising the trap we found it preferable to probe on the $4 \rightarrow 5'$ transition rather than on $3 \rightarrow 2'$ transition. The reason is that the spontaneous decay from $3 \rightarrow 2'$ tends to pump the atoms into the $|F = 3, m_F = \pm 3\rangle$ dark state. Consequently, the phase-shift when probing the $3 \rightarrow 2'$ transition rapidly decreases to zero. No similar dark state exists for the $4 \rightarrow 5'$ transition, which is why it is favoured. We note that for the QND measurements because the atoms are prepared in $|F = 3, m_F = 0\rangle$ and the excitation rate is sufficiently slow the dark state is not significantly populated.

9.2.1 Loading and lifetime

The FORT loading and decay are governed by the MOT parameters and the background pressure. Various loading procedures yield different loading times as described in great detail in [Petrov07, Petrov06]. We typically need a couple of seconds of MOT trapping to load the maximal number of atoms into the FORT. For all parameters optimised and a very large MOT we achieve a signal of more than half the fringe height, which equates to a phase-shift of $\pi/6$ rad. More commonly the phase-shift is in the range $0 - \pi/10$ rad i.e. the detector signal corresponds to $1/3$ of the fringe amplitude. The phase-shift is found to depend more or less linearly on the trapping power.

Since the background pressure is not very low the lifetime of the trap is limited. The decay of the FORT is easily monitored by weakly probing the sample at intervals (fig. 9.7). An exponential fit to an optimally probed sample (grey dashed line and green dots) yields a e^{-1} decay constant of around 320 ms. When the probe is slightly misaligned with the sample one sees slow fluctuations of the signal, which are due to the longitudinal motion of the sample. We elaborate on these in sec. 9.2.2, but note that they suggest that the sample is slightly off centre w.r.t the trapping-laser waist. With an optimal stabilisation of the FORT laser power we have seen the lifetime increase up to 450 ms.



Optical depth

The principle of the optical depth measurements is very simple: shine a laser pulse through the atomic ensemble and compare the output intensity $I(\Delta)$ with that of a reference pulse generated while there are no atoms in the trap. A few things need to be noted, though. Firstly, the probe intensity must be well below the saturation intensity. Secondly, the absorption can be very difficult to determine precisely for samples of large optical depth, hence it is advantageous to measure the absorption near but not on resonance and then extrapolate to derive the resonant optical depth. Thirdly, any extrapolation will rely on correctly estimating the FORT laser light shift of the probe transition. This will introduce some uncertainty. To measure the absorption we block the MZI reference arm as well as one detector input. Using the sensitive QND detector has the advantage of making it possible to use very low probe intensity that does not exceed the saturation intensity. In fig. 9.8 we present the measurements of the

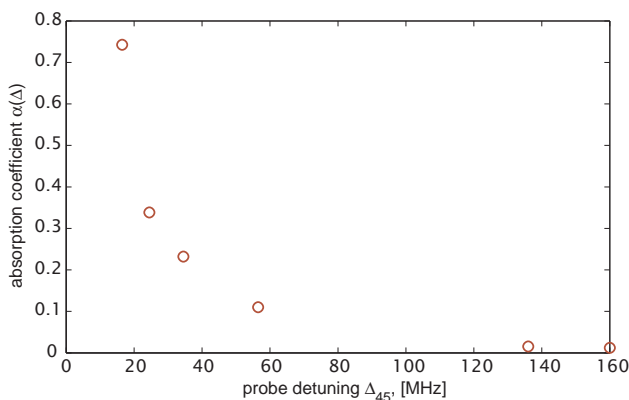


Figure 9.8: Directly measured probe beam attenuation as a function of probe detuning $\Delta_{45'}$. From this we compute the optical depths at the different detunings.

optical depth as $\tilde{\alpha} = -\log(I(\Delta)/I_0)$ c.f. eq. (4.12), where I_0 is the transmitted intensity without the atomic sample. The theoretical dependence of $\tilde{\alpha}$ follows from eq. (4.14), which allows us to deduce the resonant optical depth $\tilde{\alpha}_{45',0}$ corresponding to each of the measurements. As mentioned above the FORT laser light shift influences the detuning and thus the estimate of $\tilde{\alpha}_{45',0}$. If we assume a 20-MHz shift as evaluated in sec. 9.3.1, we can with some uncertainty arrive at $\tilde{\alpha}_{45',0} = 15 - 30$. We have deliberately added the 45' subscript to specify that it is the optical depth for the $4 \rightarrow 5'$ resonance. This is distinct from the effective far-detuned resonant optical depth $\tilde{\alpha}_0$. By the transition strengths we can relate $\tilde{\alpha}_0 = 2.4 \cdot \tilde{\alpha}_{45',0} = 35 - 70$. From the phase-shift measurement we deduce $\tilde{\phi}_{\text{ph},0} =$, which by virtue of eqs. (4.13 and 4.14) corresponds to $\tilde{\alpha}_{45',0} = 30$. Though this is not exactly a textbook example of experimental agreement it confirms the ballpark estimate of the resonant optical depth.

One explanation for the large variation in the $\tilde{\alpha}_0$ estimates is that at the time that the measurements were taken the tuning of the probe-laser frequency was still performed with an AOM. This method of tuning results in the overall probe power changing as the coupling to the fibre-link goes on-and-off. Hence, tuning this way is cumbersome when we wish to measure the sample in time for the overall atom number to remain constant. To avoid power fluctuations the probe frequency was instead changed by locking it to different peaks in the absorption-saturation error signal. In hindsight, this gives an error on the probe frequency as the exact locking point depends on the shape and offset of the locking signal. Thus we believe an uncertainty in frequency axis of up to a natural line-width 5.2 MHz is possible.

9.2.2 Trap frequency

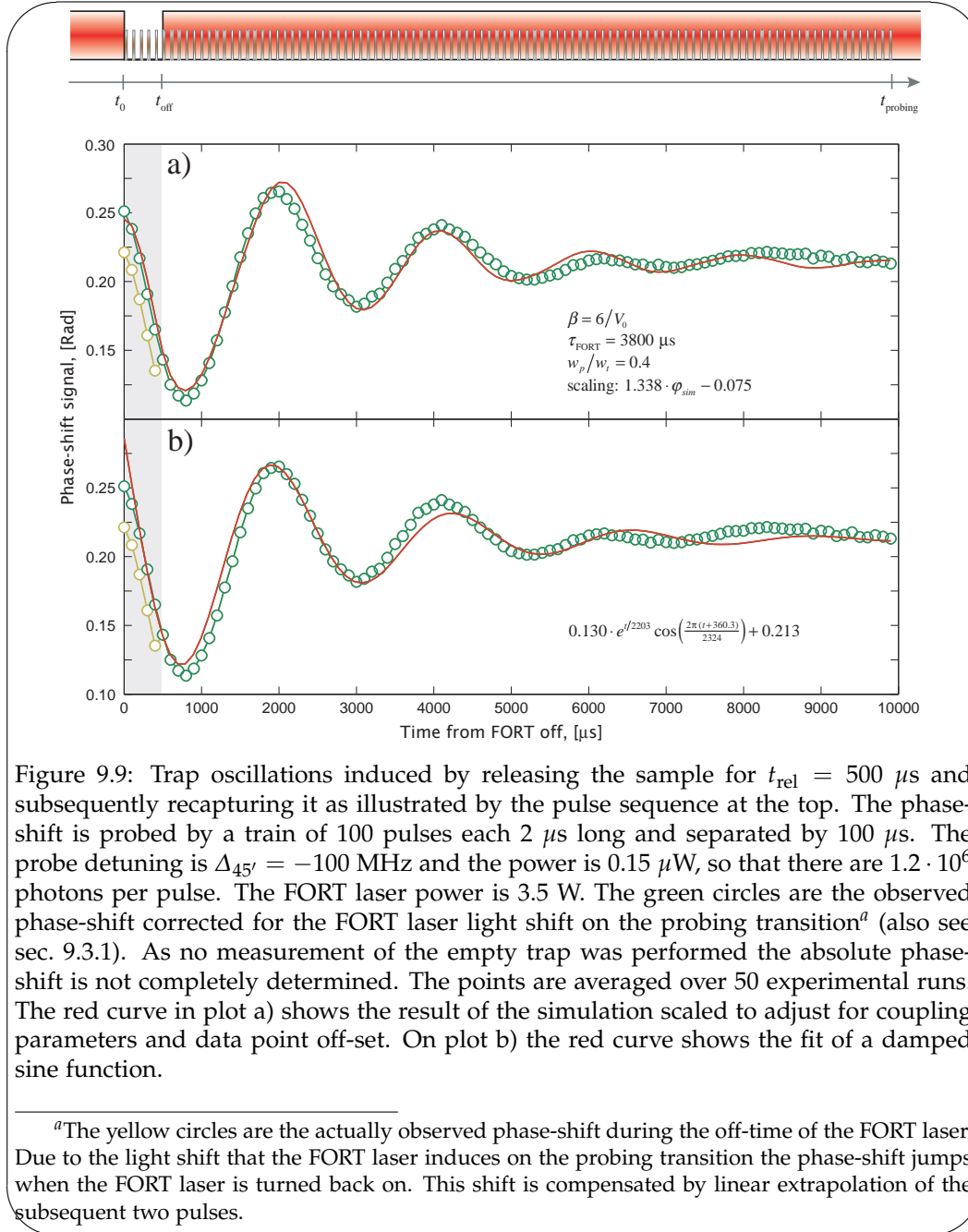
The characteristic frequency of atomic oscillation determines the relevant time-scale for atomic motion in the trap. The trap frequency is directly related to the degree of confinement, c.f. eq. (9.8), and is thus substantially different from the transverse and longitudinal dimensions of the trap. Here we will concentrate on the radial oscillations, but at the end of the section we take up the observation of axial oscillations in fig. 9.7. We developed two methods for determining the radial trap frequency. In this section we will investigate one, while the other will surface in the below treatment of the differential light shift imprinted on the sample by the probe (see sec. 11.2.1). The trap frequency stated in eq. (9.8) relies on the trap potential being approximately harmonic. However, a significant portion of the atoms will experience the anharmonic regions of the Gaussian trapping potential, causing damping of any collective motional effects. To model the atomic motion in an anharmonic potential we employ computer simulations of random ensembles of atoms as described in detail in appendix E. For each of the N_{tot} atoms in the ensemble we pick random initial positions $\mathbf{r}_k(t_0)$ and momenta $\mathbf{p}_k(t_0)$ with appropriately chosen distributions. We then propagate these in time so that we for atoms determine $\mathbf{r}_k(t)$ and $\mathbf{p}_k(t)$. The equations of motion may be solved with different potentials at various stages of the evolution e.g. allowing us to model changes in trap power. When probing the phase-shift of the atoms we must numerically calculate

$$\tilde{\phi}_{\text{ph}} = \tilde{\phi}_{\text{ph},0} \sum_{k=1}^{N_{\text{tot}}} U(\mathbf{r}_k(t)) \quad (9.9)$$

where $\tilde{\phi}_{\text{ph},0} = \frac{3\lambda^2}{2\pi^3} (2J_e + 1) S_{F_g F_e} \frac{\Delta_{ge} \frac{\gamma_e}{2}}{\Delta_{ge}^2 + (\frac{\gamma_e}{2})^2} (\hat{\sigma}_{gg}^{(1)} - \hat{\sigma}_{ee}^{(1)})$ is the phase-shift imparted on the probe by a single atom c.f. eq. (4.15). This way one can simply deduce the

time dependent phase-shift from the ensemble. In later sections we will again use the numerical simulation to track effects of atomic motion (see sec. 9.2.3 and 11.2.1).

The atomic ensemble is initially at rest in the FORT — all collective motion has been damped — and the probe phase-shift will not show any signature of the trap frequency. Thus, it is necessary to induce some form of collective motion of the trap, such that the atomic density in the probe volume is modulated. In fig. 9.9 we illustrate how this is most easily done by reducing or completely switching off the FORT laser, whereby the ensemble will start to expand and drop under the influence of gravity. After a short time the FORT laser power is



turned up and the force acting on the expanding ensemble will induce breathing oscillations, where the cross-sectional area of the ensemble grows and contracts. If the atoms have dropped significantly due to gravity there will also be sloshing oscillations where the ensemble moves up and down in the potential. For an atomic temperature of say $T = 15$ (50) μK with a resulting characteristic velocity of $v_{\text{rms}} = \sqrt{k_B T / m_{\text{Cs}}} = 0.0306$ (0.0559) $\mu\text{m} / \mu\text{s}$ [Metcalf99] the cloud expands

roughly 15 (28) μm during the $t_{\text{off}} = 500\mu\text{s}$ the trap is switched off. This is to be compared with the $\frac{1}{2}gt_{\text{off}}^2 = 1.2\mu\text{m}$ that an atom initially at rest drops during the same time. Consequently, the breathing motion will be vastly dominant. The density modulation of the atomic sample is clearly recognised in the phase-shift signal and is modelled reasonably well by the simulation (fig. 9.9). The oscillation frequency in the experimental data appears to increase slightly as the atoms are damped. The simulation does not quite manage to trace this behaviour. This irregularity may be due to axial oscillations of the atoms or the non-unity beam quality factor³. The simulation returns an optimal value (see sec. E.2) for the harmonic oscillation frequency ω_{FORT} , which according to eq. (9.8) together with eq. (9.2) should scale with the square root of the FORT trapping power. On fig. 9.10 (green points) we plot ω_{\perp} extracted for measure-

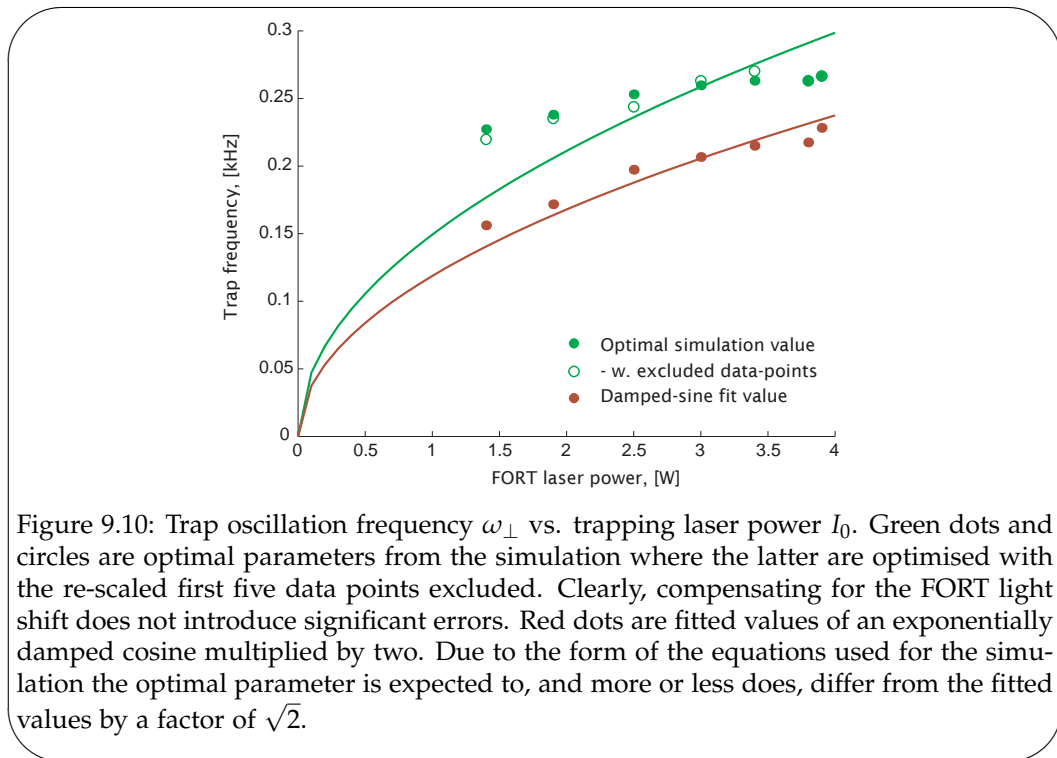


Figure 9.10: Trap oscillation frequency ω_{\perp} vs. trapping laser power I_0 . Green dots and circles are optimal parameters from the simulation where the latter are optimised with the re-scaled first five data points excluded. Clearly, compensating for the FORT light shift does not introduce significant errors. Red dots are fitted values of an exponentially damped cosine multiplied by two. Due to the form of the equations used for the simulation the optimal parameter is expected to, and more or less does, differ from the fitted values by a factor of $\sqrt{2}$.

ment at different I_0 . Though the trap frequency does drop with lower powers the scaling is not exactly as $\sqrt{I_0}$. As a comparison we fit the data with an exponentially damped sine function (fig. 9.9b) and plot twice the fitted frequency as red dots on fig. 9.10. These points fit more convincingly with the square-root of FORT power. For typical trapping powers we thus expect a trap frequency around 200 Hz. By eq. (9.8) we get a theoretical prediction of $\omega_{\perp} = 2\pi 1220$ Hz. We will refrain from using any exclamations to describe the agreement with the experiment and rather attempt to uncover some clues in the other simulation parameters. First, we will bring up the longitudinal oscillations visible on fig. 9.7. We assume that the oscillations are due to sloshing rather than breathing because the trap is loaded slightly off-centre. Thus the period of 152 ms translates directly to a frequency of $\omega_{\parallel} = 2\pi 6.5$ Hz. In comparison the theoretical value using eq. (9.8) is $\omega_{\parallel} = 2\pi 7.03$ Hz. At last a matching set! How, it is possible for ω_{\parallel} to be as anticipated while ω_{\perp} turns out very fishy, we will try to uncover below.

The simulation optimisation additionally yields a value of 0.4 for the probe to trapping beam waist ratio. With a FORT laser waist size of 40 μm and a probe

³the quality factor M^2 is a measure for the radial symmetry of the beam. We measured $M^2 = 1.34$ indicating a slightly oval beam.

waist of $27 \mu\text{m}$ the experimental value is 0.62. We presume that the error is mainly due to imperfect estimate of the trapping laser size. Hence, if alternatively we put our faith in the simulation, the trapping waist ought to be $27\mu\text{m}/0.4 = 68 \mu\text{m}$ instead. The resulting theoretical trap frequency would then be 420-kHz, which is closer but still off by a factor of 2. Finally, the optimal value for $\beta = 1/(k_B T)$ gives us an estimate of the sample temperature. In the subsequent section we elaborate on the temperature measurement.

9.2.3 Temperature

The temperature of the atoms has a profound effect on a whole range of ensemble parameters and therefore also appears in the context of several measurements. The most direct way to independently determine the temperature is to release the trap from the confines of the FORT and measure the rate of expansion. The expansion can be gauged from CCD camera images of the trap or as done here from the phase-shift imparted on the probe beam (fig. 9.11). The data is normalised to the initial phase-shift and the offset is set so that the phase-shift goes towards zero. To model the observed phase-shift we may construct

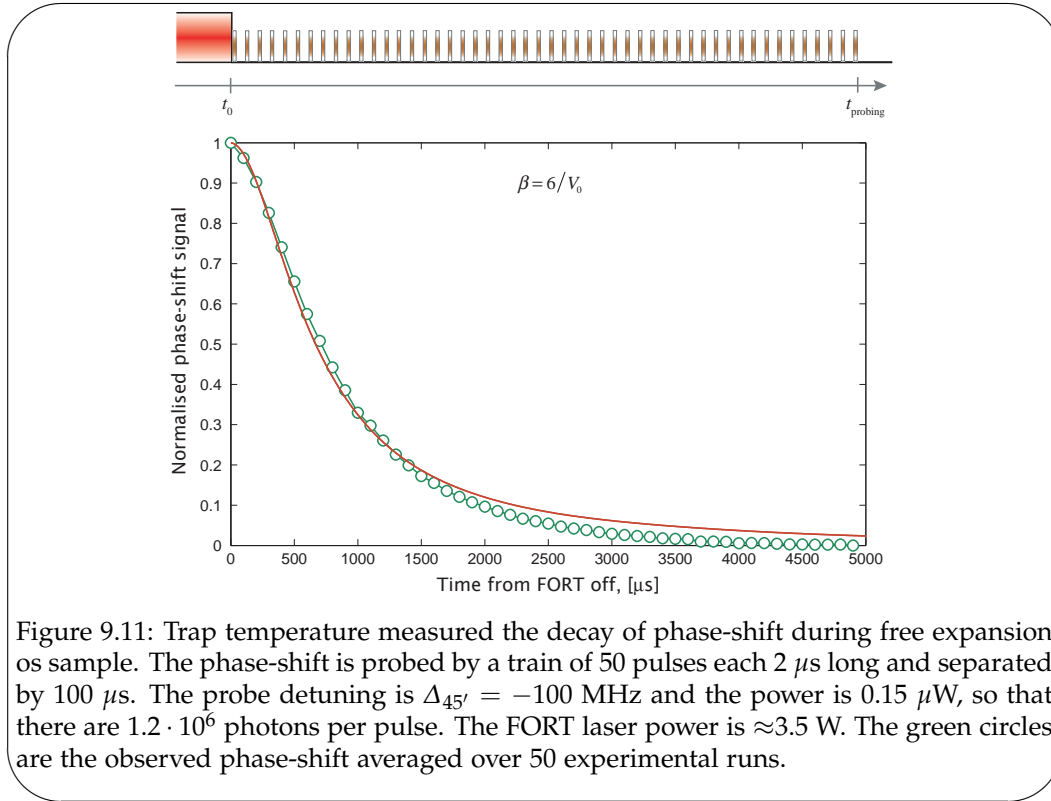


Figure 9.11: Trap temperature measured the decay of phase-shift during free expansion os sample. The phase-shift is probed by a train of 50 pulses each $2 \mu\text{s}$ long and separated by $100 \mu\text{s}$. The probe detuning is $\Delta_{45'} = -100 \text{ MHz}$ and the power is $0.15 \mu\text{W}$, so that there are $1.2 \cdot 10^6$ photons per pulse. The FORT laser power is $\approx 3.5 \text{ W}$. The green circles are the observed phase-shift averaged over 50 experimental runs.

a simple analytical model as done in [Petrov06, Petrov07] but here we employ our ensemble simulation. The red curve on fig. 9.11 shows the simulation curve that closest matches the data and it corresponds to a value of $\beta = 6/V_0$. After $\approx 3000 \mu\text{s}$ the phase-shift is nearly at zero, whereas the simulation predicts a small residual phase-shift. This discrepancy arises from the effect of gravity, which is not included in the simulation. For a $40 \mu\text{m}$ trapping beam waist and a power of 3.5 W we get from eq. (9.3) that $V_0 = k_B 380 \mu\text{K}$, and thus the estimated trap temperature is $T = 380/6 \mu\text{K} \approx 60 \mu\text{K}$. We note that $\beta = 6/V_0$ was also the optimal found in the trap-oscillation measurements. The main uncertainty on the temperature estimate stems from the measurement of the trapping waist. To investigate this point a bit deeper, we use eq. (E.6) to relate β to the sample size. In the limit of $\beta \gg V_0$ the effective Gaussian size of the sample is

$w_a = w_t / \sqrt{\beta V_0} = w_t / \sqrt{6}$. Thus for a trapping waist of $w_t = 40 \mu\text{m}$ we predict the sample to have $w_a = 16 \mu\text{m}$. This appears to be rather small sample size. Alternatively we can try to rely on the probe to trapping size beam estimate, which in the temperature simulation is 0.1. This is again different from the estimate of 0.4 in the preceding section. Let us give both a try in order to sort out the confusion. From the $w_p/w_t = 0.1$ we get $w_t = 270 \mu\text{m}$ and $w_a = 110 \mu\text{m}$ whereas from $w_p/w_t = 0.4$ we get $w_t = 68 \mu\text{m}$ and $w_a = 28 \mu\text{m}$. We also note that $w_t = 270 \mu\text{m}$ gives a radial oscillation frequency of $\omega_{\perp} = 2\pi 170 \text{ Hz}$, which is significantly closer to the observed frequency. Thus the value of w_p/w_t is likely to be somewhere between 0.1 and 0.4 and the trap size is a whole lot bigger than the $40 \mu\text{m}$ stated in [Petrov06] and [Petrov07]. Since, in sec. 9.1.2 we also found that the initial collimation of the FORT beam had been poor, we believe that the discrepancy in trap size is due to the trapping beam waist not coinciding with the MOT position. In other words the FORT is loaded off-centre where the trapping beam is wider. This conclusion is supported by the fact that after re-collimation measurements of ω_{\perp} by an alternative method yields frequencies much closer to those anticipated for a $40 \mu\text{m}$ waist trapping beam (see sec. 11.2.1). The axial trap frequency ought not to be affected by the off-centre loading as the Raleigh-range is unaffected i.e. $w_t(z=0)$ is actually determined correctly.

9.3 Effects from FORT

The whole point of preparing the atomic sample in a FORT is that the atoms being held in a conservative potential are not significantly disturbed. This is of course not the same as saying that some of the atomic properties of interest will not be perturbed by the trapping potential. Mainly, the very effect that traps the atoms, the AC-Stark shift, is also the one perturbing the parameters that we measure. In subsequent sections, we will treat several ramifications of this perturbation in various experimental investigations (see sec. 10.2.4 and sec. 10.2.3). Here, we will look at the AC-Stark shift on the probe transitions.

9.3.1 Light-shift and dephasing

The resonance frequencies of the D-lines will be shifted according to the AC-stark/light shift on the ground and excited fine-states. In sec. 9.1.2 we already found the light shift of the ground-states causing these to be trapped by the FORT laser. The excited states experience an equivalent shift, which in the absence of other excited levels would be equal in magnitude but with opposite sign of the ground state shift. However, the host of higher excited levels reduces the excited state shift. The ground state trap depth for 3.5 W FORT power is equivalent to the frequency shift $V_0 = k_B \cdot 380 \text{ K} = \hbar \cdot 2\pi \cdot 7.92 \text{ MHz}$ where we assume a trapping beam waist of $40 \mu\text{m}$.⁴ Thus we expect the D-line transitions to shift by roughly twice this frequency i.e. $\delta\nu_{LS} \lesssim 16 \text{ MHz}$.

We experimentally determine the light-shift of the D2-line in two ways, which we will outline below. First, method is to sweep the frequency of the probe laser and simultaneously record the absorption-saturation error signal and MZI phase-shift of a weak probe (fig. 9.12a). The transition frequencies do not occur at the same time in the sweeps because of the frequency shifts added by the

⁴since this agrees with the value of the axial oscillation frequency (p. 151) and the radial oscillation frequency found in sec. 11.2.1

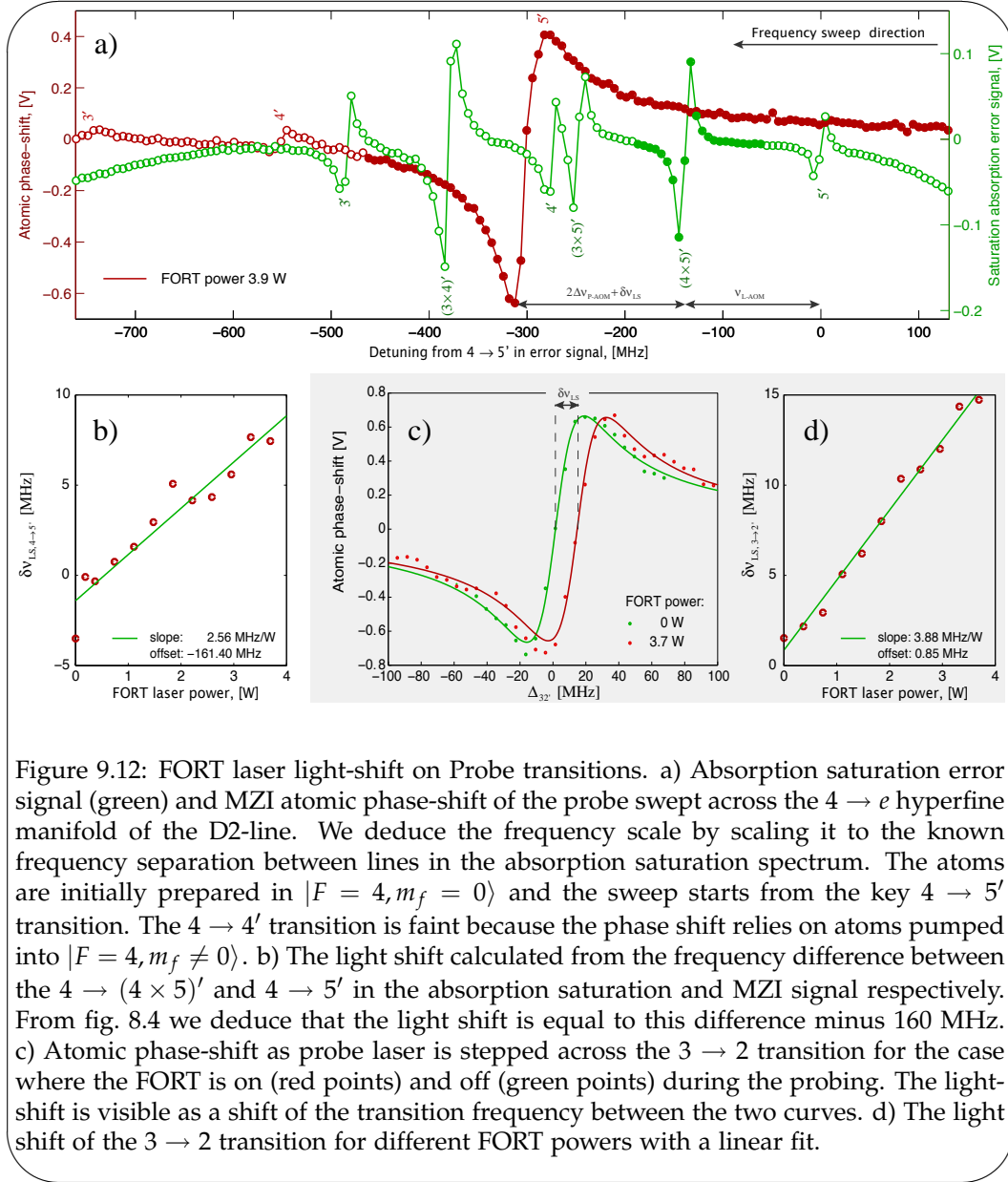


Figure 9.12: FORT laser light-shift on Probe transitions. a) Absorption saturation error signal (green) and MZI atomic phase-shift of the probe swept across the $4 \rightarrow e$ hyperfine manifold of the D2-line. We deduce the frequency scale by scaling it to the known frequency separation between lines in the absorption saturation spectrum. The atoms are initially prepared in $|F = 4, m_f = 0\rangle$ and the sweep starts from the key $4 \rightarrow 5'$ transition. The $4 \rightarrow 4'$ transition is faint because the phase shift relies on atoms pumped into $|F = 4, m_f \neq 0\rangle$. b) The light shift calculated from the frequency difference between the $4 \rightarrow (4 \times 5)'$ and $4 \rightarrow 5'$ in the absorption saturation and MZI signal respectively. From fig. 8.4 we deduce that the light shift is equal to this difference minus 160 MHz. c) Atomic phase-shift as probe laser is stepped across the $3 \rightarrow 2$ transition for the case where the FORT is on (red points) and off (green points) during the probing. The light-shift is visible as a shift of the transition frequency between the two curves. d) The light shift of the $3 \rightarrow 2$ transition for different FORT powers with a linear fit.

absorption saturation AOM Δv_{L-AOM} and the pulsing AOM $\Delta v_{P,AOM}$ c.f. fig. 8.3. However, by comparing the position of prominent transitions in both sweeps and accounting for the known shifts of the AOM's we can deduce the additional frequency shift due to the FORT. We choose to compare the $4 \rightarrow (4 \times 5)'$ line in the error signal with the $4 \rightarrow 5'$ line in the MZI signal at different FORT powers and plot their difference in fig. 9.12b). The linear fit indicates a mean light-shift of 2.56 MHz/W.

In principle the same procedure should be applicable to the $3 \rightarrow e$ transitions, however, it turned out not to be possible to sweep the frequency across the $3 \rightarrow 2'$ line because the atoms quickly shelved into the $|F = 3, m_F = \pm 3\rangle$ dark state thus no longer giving rise to any atomic phase-shift in the MZI. As an alternative method we used the versatility of the beat-note locking method (see sec. 8.1.3 and fig. 8.10) to precisely step the locking point of the probe laser so as to acquire the atomic phase-shift signal across the transition piece wise (fig. 9.12c). Thus determining the transition frequency for different FORT trapping powers we extract the light-shift and fit the linear dependence 3.88 MHz/W (fig. 9.12c). This value is somewhat larger than that achieved by the sweep method. We believe that the method of stepping the lock point is more reliable. Mainly the reason

is that the absorption saturation signal, used to determine the both frequency scale and the frequency shift, is not completely regular and even a small error on the order of a natural line-width would cause a grave mistake in the light-shift estimate. In conclusion we subscribe to the FORT light shift estimate of 3.88 MHz/W so that at maximum 3.5 W of FORT laser power the light shift is about 13.5 MHz. We note that this estimate conforms to the theoretical estimate of $\delta\nu_{LS} \lesssim 16$ MHz.

State preparation and characterisation

The state preparation consists of two stages namely an optical pumping sequence followed by a microwave pulse. To increase the state purity the two are actually combined in what we call a blow away sequence described in sec. 10.2.3. The two state preparation elements are implemented in the MZI/trapping setup as shown on fig. 10.1. We will use this figure as reference in the following more detailed discussions on the two stages.

10.1 Optical pumping

10.1.1 Principles and theory

When the atoms are loaded into the FORT they will be distributed more or less randomly among the Zeeman sub-levels of the ground states. The goal of the optical pumping is to localise all atoms in a single $|F, m_F\rangle$ state — preferably $|F, 0\rangle$. Fortunately, the importance of optical pumping for atomic clock operation has spurred a wide selection of studies on the topic [Arditi78, Clercq84, Avila87, Audoin92, Jau04]. Nearly all schemes rely on the inhibition of transitions which have $F' - F = 0$ and $m'_F = m_F = 0$, as for example $|3, 0\rangle \rightarrow |3', 0'\rangle$ or $|4, 0\rangle \rightarrow |4', 0'\rangle$ on the D2-line. If a pumping laser resonant with either of these transitions is applied to the atomic sample it will excite atoms in all m_F levels but the $m_F = 0$ level and thus by spontaneous decay and several excitations the population of the hyperfine level will end up in the $m_F = 0$ level. Naturally, atoms may decay to the hyperfine level not coupled by the pumping laser, so a re-pump laser is required to return these to the pumped hyperfine level. Several, combinations of pump and re-pump configurations are possible and we pick a linearly polarised optical pump on the $|4, m_F\rangle \rightarrow |4', m'_F\rangle$ transition and a linearly polarised re-pumper on the $|3\rangle \rightarrow |4'\rangle$ transition (see fig. 10.2) that is among those yielding the highest efficiency [Avila87]. In this configuration the $|4, 0\rangle$ is not coupled by the optical pump laser and thus the atomic population in this level will steadily increase by spontaneous decay from the $|4', \pm 1\rangle$ excited states. In the ideal limit this scheme should allow for up to $\approx 80\%$ of the atomic population to be pumped into the $|4, 0\rangle$ level. The reason for this and other schemes not reaching 100% efficiency is mainly due to coupling of the pump laser to other hyperfine excited states. The effect has been coined *leakage* [Avila87] and an example is the $|4, m_F\rangle \rightarrow |4', m'_F\rangle$ optical pump laser which

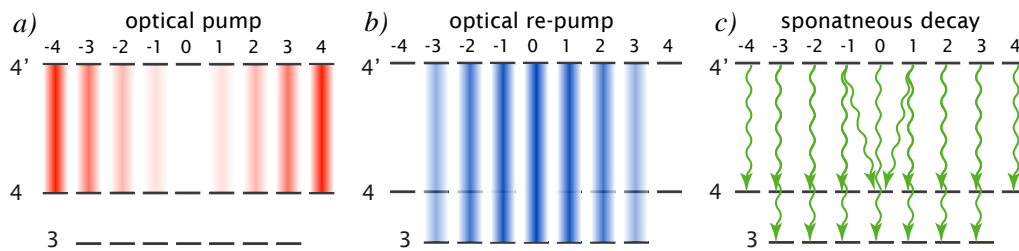
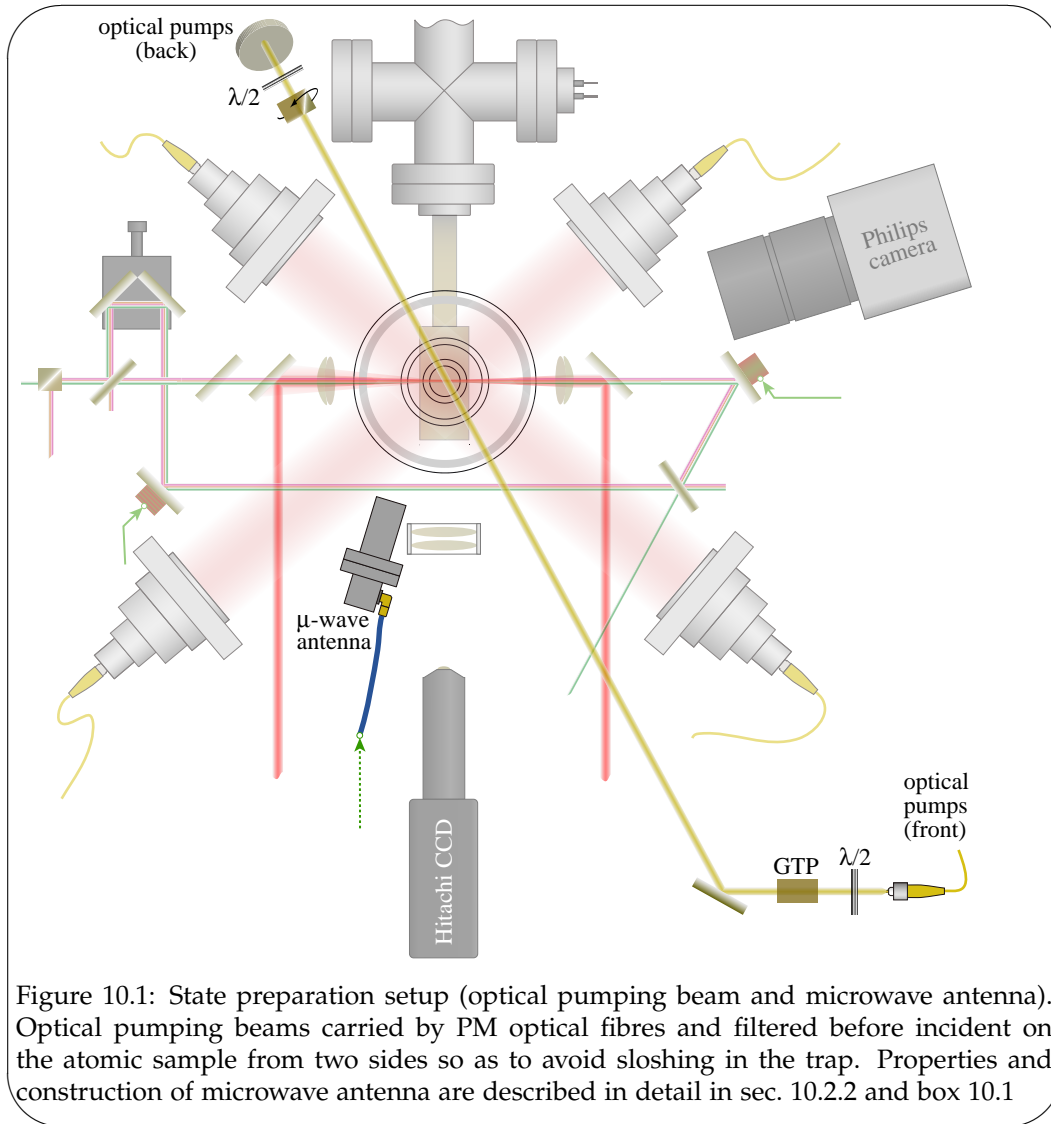


Figure 10.2: Principle of optical pumping scheme. a) The strength that optical pump on the $|4, m_F\rangle \rightarrow |4', m_F'\rangle$ transition couples to the different m_F levels (see table D.9) is indicated by the opacity of the lines connecting the levels. b) The optical re-pumper with transition strengths indicated (see table D.7). c) Selected spontaneous decay channels highlighting that the $|4, 0\rangle$ level is populated only by spontaneous decay of elliptically polarised photons from the $|4', \pm 1\rangle$ levels

also couples to the $F' = 5$ excited state. Thus transitions on $|4, 0\rangle \rightarrow |5', 0'\rangle$ will tend to degrade the optical pumping.

We have also implemented an optical pumping laser on $|4, 0\rangle \rightarrow |4', 0'\rangle$ on the D1-line as discussed in more detail in [Windpassinger08a]. Since the $P_{1/2}$ hyperfine splitting is somewhat larger than that of the $P_{3/2}$ we expect the leakage to be correspondingly smaller. Indeed we observed an increase in pumping efficiency to 87%. This was, however, not deemed to be significant enough to merit the

introduction of yet another (potentially troublesome) laser.

10.1.2 Optical pumping setup

The optical pump beams have been derived from a range laser sources. Initially, we split off part of the probe laser light and further shifted the frequencies by AOMs so as to come on resonance with the desired transitions. This was done while the probe lasers were locked in the rather inflexible absorption saturation setup (see sec. 8.1.2). However, with the probe lasers locked by the beat-note detection (see sec. 8.1.3), maintaining the optical pump laser frequencies on resonance would interfere with the objective of being able to tune the probe frequencies. Thus we turned to tapping the optical pumping beams from the MOT slave lasers (see fig. 10.3), with the added advantage of gaining in optical pump intensity.

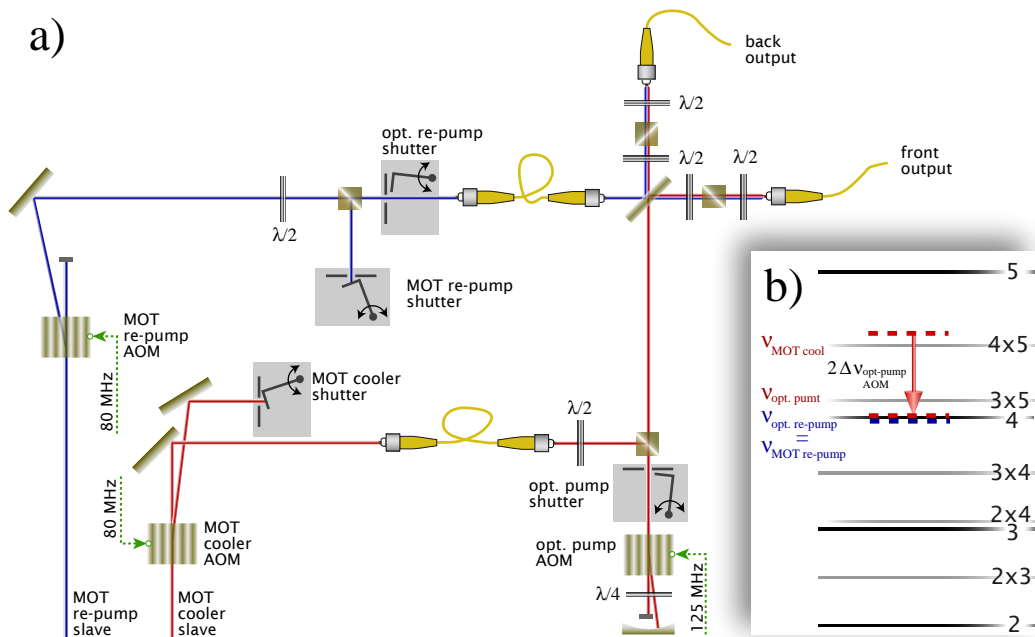


Figure 10.3: a) Optical pumping setup based on MOT slave lasers and b) diagram of beam frequencies and shifts. The optical pump beam comes from the 0th order of the MOT cooler, which is ≈ 90 MHz red detuned from the $4 \rightarrow 5'$ transition. Since optical pumping is done when the MOT is off, we have all 100+ mW of cooler power available for the optical pumping. The beam is passed through a fibre, double-passed through an AOM to shift the frequency by $\approx 2 \cdot 80$ MHz on to resonance with the $4 \rightarrow 4'$ transition. Following a mechanical shutter the optical pump beam is overlapped with the optical re-pump beam on a (non-polarising) BS and both outputs are coupled into PM-fibres. The optical re-pump is similarly derived from the 1st order of the MOT re-pumper and via a fibre-link injected through an AOM before being coupled in to the fibre link to the MZI setup. fig. 10.4 for the time sequence of switching of the various AOMs and shutters.

As illustrated on fig. 10.3 the 0th order from the MOT cooler switching AOM and the 1st order from MOT re-pumper switching AOM are used for the optical pumping on the $|4\rangle \rightarrow |4'\rangle$ and optical re-pumping on $|3\rangle \rightarrow |4'\rangle$ transitions, respectively (See fig. 10.3 caption for details). On fig. 10.4 we sketch the time sequence for the many AOMs and shutters, with the resulting optical pumping pulses on the sample shown at the bottom. The spot-size of the optical pump beam is ≈ 1.5 mm. For the optical pump beams derived from the probe lasers we typically get 0.5-1.5 mW incident on the atoms. The resulting peak intensity of 14-42 mW/cm² is an order of magnitude above the saturation intensity for

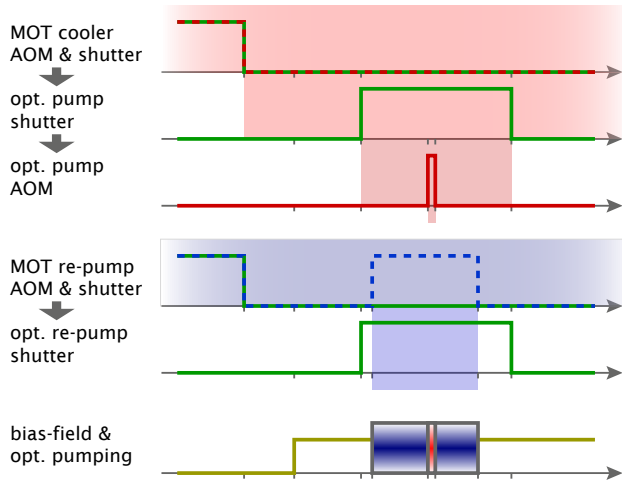


Figure 10.4: Optical pumping sequence. The top three diagrams show the timing and effect of the elements in the path of the MOT cooler that is used as the optical pump light. The 0th order of the MOT cooler AOM is incident on the opt. pump shutter. When the shutter is open the opt. pump AOM generates the short pumping pulse. The 1st order of the MOT re-pump is used as optical re-pump, but to block it from the MOT collimators the MOT re-pump shutter is switched closed. When the opt.

optical re-pump shutter is open the optical re-pump light goes to the sample. The re-pump light is kept on for a while after the optical pump pulse in order to ensure all atoms are in $F = 4$. This will be important for the blow-away described in sec. 10.2.3.

the transition (see table D.2). In the case where the optical pump beams are derived from the MOT slave lasers the incident power is even 5-10 mW, which corresponds to a peak intensity of 140-280 mW/cm².

On the MZI/trapping setup the two optical pumping beams are cleaned by high-quality polarisation splitting elements and sent counter propagating in to the vacuum cell where they hit the trapped atoms (see fig. 10.1). Besides the mixing of the optical pump and re-pump automatically generating two beams, there is another reason for having optical pumping beams incident on the trap from opposite directions. This is illustrated on fig. 10.5 where we show the atomic

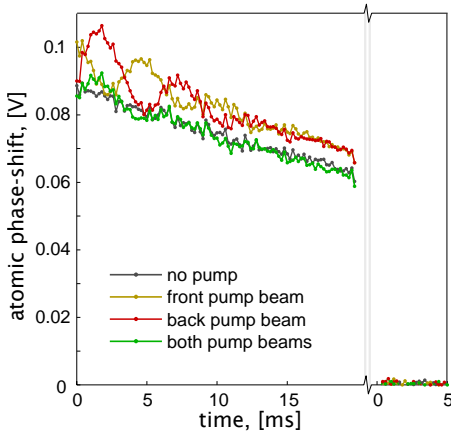


Figure 10.5: Sloshing atomic sample after optical pumping. All traces show phase-shift of atoms in $|4\rangle$ right after an optical pumping stage and at a later time when atoms have been removed from the trap. Grey trace: No optical pumping applied and the sample slowly decays. Yellow and red traces: Optical pumping applied from front or back fibre output, respectively. This causes the sample to oscillate at the trap frequency ≈ 0.2 kHz (see fig. 9.10 and discussion in sec. 9.2.2). Green trace: Optical pumping applied from both fibre outputs so that the oscillations are significantly damped.

phase-shift following optical pumping with either one or two beams incident on the trap. When only one beam is used we clearly see that the optical pumping photons give a momentum kick to the atomic sample. Though this effect is not devastating it is neither particularly attractive, and as evidenced by fig. 10.5 it is easy to avoid by using two pumping beams.¹

¹Retro-reflecting a single optical pump beam is not feasible, due to high loss of intensity at the angle of incidence on the quartz-cell. At 62° only 82% of the power is transmitted through the air-quartz surface. Experimentally we measured the transmission through the whole cell to be 0.5, implying a transmission of 0.82 and 0.86 for the un-coated inner surface and AR-coated outer surface of the cell, respectively.

10.1.3 Efficiency and dependence on parameters

In this section we will investigate to which extent the optical pumping is influenced by a number of parameters. Since the optical fields are unable to resolve the Zeeman sub-levels we rely on the microwave interaction described in sec. 10.2.1 to gauge the distribution among the different m_F levels. Since, we have not yet treated the microwave interaction we will merely state that it allows us selectively to move the population of a single $|F, m_F\rangle$ level to an m_F level of the other ground state $F' \neq F$. For more details we refer to sec. 10.2.3.

Optical pumping time

The optical pumping time hinges on the pump intensity together with and the spontaneous decay rate. For the Cs D2-line the lifetime of the excited state is below one μs and we expect the pumping time to be on the order of tens of μs , in as long as the pump intensity is above the saturation intensity for the pumping transition. Theoretical models [Avila87] also predict the equilibrium pumping efficiency to be reached after some 10 μs . Our experimental investigation of the pumping efficiency shows that the pumping time is close to 150 μs (see fig. 10.6). It is not clear why even with very large optical pumping powers we do not reach

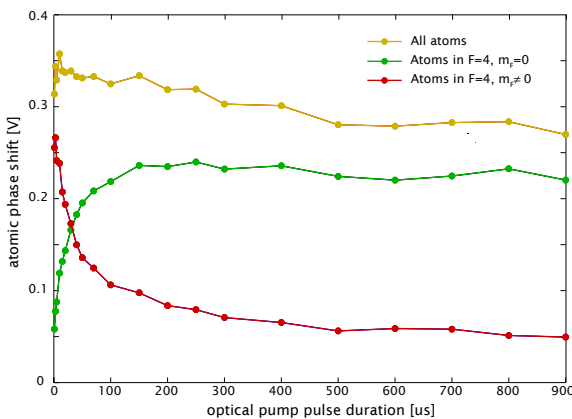


Figure 10.6: Optical pumping efficiency vs. pumping time. The population in $|4, 0\rangle$ (green) is deduced by observing the change in phase-shift of the $4 \rightarrow 5'$ probe when the $|4, 0\rangle$ atoms are moved to $|3, 0\rangle$ by the microwave interaction. The total number of atoms (yellow) is determined from the phase-shift of the $4 \rightarrow 5'$ probe when next the atoms are re-pumped into $|4, m_F\rangle$. The atoms not in $|4, 0\rangle$ after optical pumping (red) is simply derived from the difference of the previous two populations.

an equilibrium pumping efficiency faster, but we believe it may be related to radiation trapping of the spontaneously emitted resonant photons. Since some of these photons are circularly polarised they would couple the $|4, 0\rangle$ state and thus disrupt the pumping. On the other hand, any pumping time below 1 ms is perfectly acceptable for our purposes. We note the positive fact that the pumping efficiency seems to reach the theoretical optimum of 81% [Avila87]. As, the optical pumping also causes some amount of loss of atoms (c.f. the yellow curve on fig. 10.6) we find an optimal pumping time 150-200 μs , where the absolute number of atoms in $|4, 0\rangle$ is the largest. At that point the pumping efficiency is 75-80%.

Optical pump laser detuning

Ideally the optical pump laser should be on resonance with the pumping transitions. Going away from resonance causes the coupling strength to decrease and thus the pumping time to increase. At the same time 'leakage' to other excited levels will grow. Both effects cause the optical pumping efficiency to drop. For pumping intensities above saturation we, however, expect the efficiency only

to decrease slowly with increasing detuning. Experimentally, we step the optical pump laser detuning by setting different values for the MOT slave laser frequency in the CAMOT programme, and for each setting we determine the optical pumping efficiency and the total number of atoms remaining in the trap after the optical pumping (see fig. 10.7a). The number of atoms pumped in to

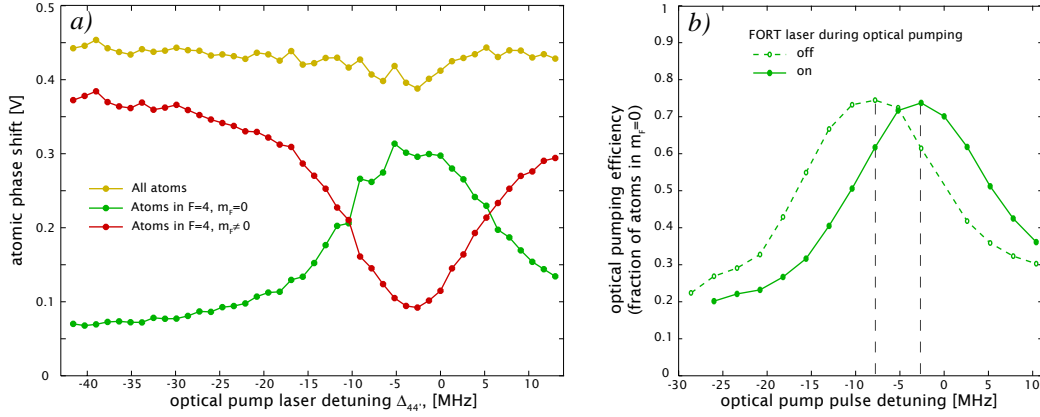


Figure 10.7: Optical pumping efficiency vs. optical pump laser detuning. a) The populations in $|4, 0\rangle$ (green), $|4, m_F \neq 0\rangle$ (red), and the total number of atoms (yellow) are measured in the same fashion as that described in the fig. 10.6 caption. The curves are used for finding the optimal optical pumping detuning. The data is somewhat noisy, because all are proportional to the total number of atoms which fluctuates from loading cycle to loading cycle. b) The shift in optimal pumping frequency due to the FORT trapping laser.

$|4, 0\rangle$ is more or less constant over 5 MHz around the optimal detuning. The reason for the optimal detuning not being 0 is likely caused by a calibration error of the MOT slave detuning and by the FORT laser light shift (see paragraph below). We also note that the total atom number drops slightly around the optimal detuning. By subtracting the atoms in $|4, 0\rangle$ from the total number we also determine the fraction of atoms in other magnetic sub-levels, i.e. $m_F \neq 0$.

As noted the FORT laser shifts the $F = 4 \rightarrow F' = 4$ transition frequency and thus the optimal detuning for the optical pumping. Switching the FORT off during the optical pumping and performing the frequency scan as above, we can determine the non-shifted optimal detuning. As seen on fig. 10.7b) the average light-shift is around -5 MHz. In this case the FORT laser power was some 4-5 W. Furthermore, there appears to be a slight increase in the optical pumping efficiency when the FORT is off. This is because the inhomogeneous broadening of the line due to the spatial intensity distribution of the FORT beam is removed. Thus, when atoms at different radial positions in the trap have the same resonance frequency, the optical pump frequency can be adjusted to zero detuning for all atoms.

Optical pump polarisation

The pumping scheme relies on the optical pumping laser to be π polarised, and as the magnetic bias-field defines the quantisation axis parallel to the probe light polarisation this translates into the pump light also being linearly polarised parallel to the probe light. Since, the probe polarisation is perpendicular to the MZI plane it is always possible to set the optical pump polarisation parallel. We determine the sensitivity of the pumping to the polarisation by rotating the polarising cubes that filter the pump light before the atoms. On fig. 10.8 the results from

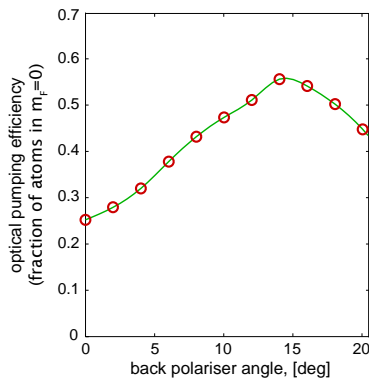


Figure 10.8: Optical pumping efficiency vs. optical pumping beam polarisations from back-output. The polarisation is rotated by simultaneously turning the wave-plate and polariser after the fibre output. Note, that the optical pumping efficiency was not optimal due to insufficient pumping power, which again was caused by loss of coupling into the fibre-link to the MZI. [21/7/06]

the back input — i.e. front input is blocked — show that pumping efficiency does not change significantly in a range of $\pm 2^\circ$ from the optimal setting of the polariser. Thus, we conclude that it is fairly easy to set the polariser. Similar results apply to the front polariser.

Magnetic bias-field-strength

The magnetic bias-field defines the quantisation axis along the probe polarisation and lifts the degeneracy of the magnetic sub-levels c.f. eq. (3.11). If the bias field is too weak one would expect the optical pumping to be rather inefficient because of the level degeneracy. We use the top-and-bottom pair of the Helmholtz configured compensation coils to generate the bias-field. Using a simple transistor circuit we can switch the compensation coil to have a current that compensates the external fields or a current that adds a large bias-field component along the quantisation-axis. We denote the latter the bias-current. The switching between the two states is handled by the CAMOT programme. To ensure that the applied bias field is of a sufficient magnitude we measure the optical pumping efficiency at different magnetic bias field strengths i.e. at different bias-currents (see fig. 10.9). We normally use around 600 mA bias-

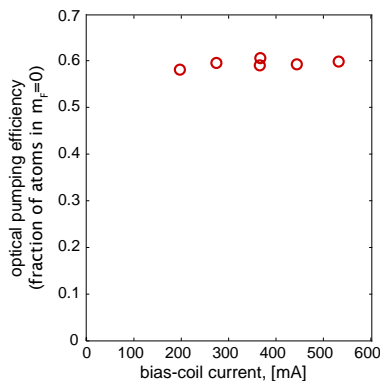


Figure 10.9: Optical pumping efficiency vs. magnetic bias field strength, which is proportional to the current in the top-and-bottom compensating coils. The optical pumping efficiency is constant over all the measured coil currents. As for the absolute values in fig. 10.8, the optical pumping efficiency was not optimal due to insufficient pumping power.

current, which appears to be ample for good optical pumping. Though, lower currents of say 200 mA would suffice for the optical pumping it is desirable for the microwave-interaction described in sec. 10.2 to have a large separation of the magnetic sub-levels.

10.2 Microwave interaction

Following the optical pumping, atoms are prepared in the $m_F = 0$ level of the $F = 4$ hyperfine manifold. The final step is to prepare all atoms in the same coherent superposition of the two clock-levels, so that we achieve the desired

ensemble product state $\frac{1}{2^{N_{at}}} \prod_{N_{at}} (|3,0\rangle + |4,0\rangle)$. Clearly, the final state preparation step will rely on the coherent interaction of the two levels and some driving force, which in our case is a near resonant EM-field. In the next section we will derive the equations that prescribe the coherent interaction before describing the experimental realisation and experiments in the subsequent sections.

10.2.1 Principles and theory

As a point of departure we take what we already studied in chapt. 4 about the interaction of an EM-field with an atom. We simplify the treatment by focusing on only the two ground levels. Since, for all practical purposes, their natural lifetime is infinite we may for the time being assume complete absence of decays. Thus, from eqs. (4.2 and 4.4) we take only the equations describing the levels directly coupled by the field and erase all decay terms.² Combining these we can write up the following

$$\begin{aligned} \dot{\tilde{\sigma}}_{34} + \dot{\tilde{\sigma}}_{43} &= -i\Delta_0(\tilde{\sigma}_{34} - \tilde{\sigma}_{43}) - \Im(\chi)(\hat{\sigma}_{44} - \hat{\sigma}_{33}) \\ -i(\dot{\tilde{\sigma}}_{34} - \dot{\tilde{\sigma}}_{43}) &= -\Delta_0(\tilde{\sigma}_{34} + \tilde{\sigma}_{43}) + \Re(\chi)(\hat{\sigma}_{44} - \hat{\sigma}_{33}) \\ \dot{\hat{\sigma}}_{44} - \dot{\hat{\sigma}}_{33} &= i\Re(\chi)(\tilde{\sigma}_{34} - \tilde{\sigma}_{43}) + \Im(\chi)(\tilde{\sigma}_{34} + \tilde{\sigma}_{43}) \end{aligned} \quad (10.1)$$

In these equations we have substituted the operator-coupling strength product with the classical Rabi-frequency χ . This substitution is merely a generalisation, which also allows us to specify a different interaction than that of the electric-dipole Hamiltonian eq. (4.1). Indeed, the hyperfine ground levels are coupled through their magnetic moment interacting with a harmonically varying magnetic field $\hat{\mathbf{B}}(t) = \hat{\mathbf{B}}_0 e^{-i\omega_0 t}$. The microwave interaction Hamiltonian is

$$\hat{\mathcal{H}}_{\mu w} = -\hat{\boldsymbol{\mu}} \cdot \hat{\mathbf{B}}, \quad (10.2)$$

The magnetic field will usually be the magnetic part of an EM-field, which is perpendicular to the EM-field polarisation defined from the electric field part. The Rabi-frequency is identified as $\chi = 2\langle \hat{\boldsymbol{\mu}} \cdot \hat{\mathbf{B}}_0 \rangle / \hbar$. Firstly, it is simplified in that we only consider expectation values. This simplification is justified as the number of photons used is too large for quantum effects to matter. For example 1 W of power at the clock-frequency $\omega_0 \approx 9$ GHz corresponds to $1.5 \cdot 10^{17}$ microwave photons per μs and thus a mere $2.5 \cdot 10^{-9}$ relative photon shot-noise. As for the vector product we apply the strong static magnetic bias field to quantise the system along the z -axis and we also align \mathbf{B}_0 along the z -axis. Thus, if we decompose the magnetic moment into its spherical components in the z -basis, $\boldsymbol{\mu} = \{\mu_{-1}, \mu_0, \mu_1\}$, what remains is $\boldsymbol{\mu} \cdot \mathbf{B}_0 = \mu_0 B_0$. This implies that only $\Delta m_F = 0$ transitions occur. Unlike, for the electric-dipole transitions we do not list the theoretical χ since we will anyhow be able to directly measure the Rabi frequency.

We also note, that the problem has been termed in slowly varying operators, which equates to observing the evolution in a frame rotating with the frequency of the EM-field. Eq. (10.1) are written so that the relationship to the atomic pseudo-spin $\hat{\mathbf{f}}$ defined in eq. (3.14) is immediately visible. The equations actually describe the evolution of the pseudo-spin components and can be expressed as

$$\frac{d}{dt} \hat{\mathbf{f}} = \hat{\mathbf{f}} \times \boldsymbol{\Omega}, \quad \boldsymbol{\Omega} = \begin{pmatrix} \Re(\chi) \\ \Im(\chi) \\ \Delta_0 \end{pmatrix} \quad (10.3)$$

²that is we disregard the equations that refer to the passive ground state g' and assign the ground-level index g to the lower clock level $|3,0\rangle$ while the excited-level index e is assigned to the upper clock level $|4,0\rangle$

This is the familiar result that the action of an EM-field on a two level atomic system can be expressed as a torque-axis vector acting on the corresponding atomic pseudo-spin [Milonni88]. Eq. (10.3) shows that the change of $\hat{\mathbf{f}}$ is only in the direction of $\boldsymbol{\Omega} \times \hat{\mathbf{f}}$, which is always perpendicular to $\hat{\mathbf{f}}$ as well as $\boldsymbol{\Omega}$. Thus the pseudo-spin is rotated around $\boldsymbol{\Omega}$ and the length of $\hat{\mathbf{f}}$ is unchanged. Moreover, since $\boldsymbol{\Omega} \times \hat{\mathbf{f}} = |\boldsymbol{\Omega}| |\hat{\mathbf{f}}| \sin \theta$, where θ is the angle between the $\boldsymbol{\Omega}$ and $\hat{\mathbf{f}}$, the rotation is not accelerated. The constant rotation frequency is proportional to the magnitude of the torque-axis vector $\Omega = |\boldsymbol{\Omega}| = \sqrt{\Delta_0^2 + \Re(\chi)^2 + \Im(\chi)^2} = \sqrt{\Delta_0^2 + |\chi|^2}$, which one calls the *generalised Rabi frequency*. All together, it is no surprise that the solution to eq. (10.3) can be expressed as a rotation matrix

$$\mathbf{M}_{\mu w}(t, |\chi|, \Delta_0) = \begin{pmatrix} \frac{\Delta_0^2 \cos(\Omega t) + |\chi|^2}{\Omega^2} & \frac{\Delta_0 \sin(\Omega t)}{\Omega} & -\frac{|\chi| \Delta_0 (\cos(\Omega t) - 1)}{\Omega^2} \\ -\frac{\Delta_0 \sin(\Omega t)}{\Omega} & \cos(\Omega t) & \frac{|\chi| \sin(\Omega t)}{\Omega} \\ -\frac{|\chi| \Delta_0 (\cos(\Omega t) - 1)}{\Omega^2} & -\frac{|\chi| \sin(\Omega t)}{\Omega} & \frac{|\chi|^2 \cos(\Omega t) + \Delta_0^2}{\Omega^2} \end{pmatrix} \quad (10.4)$$

so that

$$\hat{\mathbf{f}}(t) = \mathbf{M}_{\mu w}(t, |\chi|, \Delta_0) \hat{\mathbf{f}}(0) \quad (10.5)$$

Since the microwave field is (or is supposed to be) homogeneous over the atomic sample the extension to effective or total ensemble expectation values is straightforward, $\hat{\mathbf{F}}(t) = \mathbf{M}_{\mu w}(t, |\chi|, \Delta_0) \hat{\mathbf{F}}(0)$. At the point, where we start to consider light-shift of the energy levels due to FORT and/or probe light the extension is no longer as simple (see sec. 10.2.1 and sec. 11.1). The above rotation matrix actually presumes a real Rabi frequency. Fortunately, incorporating the a complex phase is simple. From eq. (10.3) we learned that $|\boldsymbol{\Omega}|$ determined the axis of rotation of $\hat{\mathbf{f}}$ and writing $\chi = |\chi| e^{i\theta_\chi}$ we see that θ_χ sets the angle of the rotation in the equatorial plane. This simply converts in to a transformation of $\hat{\mathbf{f}}$ by the matrix

$$\mathbf{M}_{\mu w}(\theta_\chi) = \begin{pmatrix} \cos(\theta_\chi) & \sin(\theta_\chi) & 0 \\ -\sin(\theta_\chi) & \cos(\theta_\chi) & 0 \\ 0 & 0 & 1 \end{pmatrix}. \quad (10.6)$$

For a complex Rabi frequency we can thus compute action on the pseudo-spin as

$$\mathbf{M}_{\mu w}(t, \chi, \Delta_0) = \mathbf{M}_{\mu w}(t, |\chi|, \Delta_0) \mathbf{M}_{\mu w}(\theta_\chi) \quad (10.7)$$

The choice of complex phase of χ is linked to the phase of the electromagnetic field w.r.t. to the phase of the atomic state. For an atom in one of the ground levels the phase relationship between the two levels is irrelevant (as is also reflected by eq. (10.6)). Thus it is only when the atom is put in a superposition state that the phase takes on any meaning. The phase of the atomic superposition is determined by the phase of the microwave field w.r.t the initial state of all atoms in the lower ground level. Since, the initial atomic phase is arbitrary we may as well choose it so that $\Im(\chi) = 0$. Subsequently, we may wish the phase of the microwave field to differ from the initial phase, whereby the pseudo-spin rotates around a different angle. This is phase-change is achieved either by directly shifting the phase of the field (see sec. 10.2.2) or by letting the atomic state accumulate the phase $\phi_{\Delta_0} = \tau \Delta_0$ during a free evolution time τ . This is the essence of Ramsey spectroscopy discussed below.

Rabi oscillations

A few illustrations of the \hat{f} evolution are instructive. The microwave interaction is applied after the optical pumping has aligned the pseudo-spin along the z -axis. If, thus, we let the initial pseudo-spin be aligned to have $\langle \hat{f}_z \rangle = -n_{\text{at}}/2^3$ and we assume a real Rabi-frequency ($\Im(\chi) = 0$) the pseudo-spin will evolve as

$$\begin{aligned}\langle \hat{f}_x(t) \rangle &= \frac{n_{\text{at}} \chi \Delta_0 (\cos(\Omega t) - 1)}{2 \Omega^2} \\ \langle \hat{f}_y(t) \rangle &= \frac{n_{\text{at}} \chi \sin(\Omega t)}{2 \Omega} \\ \langle \hat{f}_z(t) \rangle &= -\frac{n_{\text{at}} \chi^2 \cos(\Omega t) + \Delta_0^2}{2 \Omega^2}\end{aligned}\quad (10.8)$$

The evolution is also depicted on fig. 10.10. The special case of resonant coupling

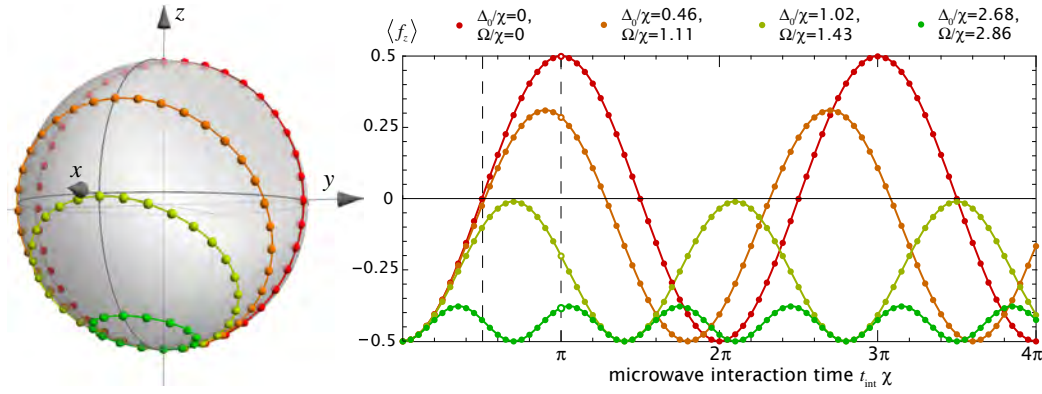


Figure 10.10: Pseudo-spin vector rotations on the Bloch-sphere due to interaction with microwaves for different detunings. The Bloch-vector, initially aligned to the south-pole of the Bloch-sphere, rotates in circles around the torque-axis vector resulting in Rabi-oscillations of the atomic populations as shown by the plot of $\langle \hat{f}_z(t) \rangle$. Only if the microwave field is resonant ($\Delta_0 = 0$) do the Rabi-oscillations result in complete population transfer at the time $t_{\text{int}} = \pi/\chi$. The change in z -projection for constant pulse length and varying detunings leads to the curves shown on fig. 10.24)

($\Delta_0 = 0$) is of particular interest since according to eq. (10.8) the pseudo-spin trajectory follows the yz -meridian. Consequently, at the time $t_{\text{int}} = \tau_{\pi/2} = (\frac{1}{2} + n)\pi/\chi$ the atomic population has been put in an equal coherent-superposition of the two ground levels and at $t_{\text{int}} = \tau_{\pi} = (1 + 2n)\pi/\chi$ it has been completely transferred to the other ground-level. Pulsed microwave fields with these durations are coined $\pi/2$ and π -pulses. Most importantly, our objective of preparing the equal coherent superposition state is met by the $\pi/2$ pulse.

For some of the measurements it is useful to write up the evolution of the population in a single hyperfine level. If atoms are initially in the $F = 3$ level the population in the other ground level is

$$n_{\text{at},4} = \langle \hat{f}_z(t) \rangle + \frac{n_{\text{at}}}{2} = n_{\text{at}} \frac{\chi^2 \sin^2(\frac{1}{2}\Omega t)}{\Omega^2}$$

³due to the state purification (blow-away) sequence described in sec. 10.2.3 this is indeed the initial state of the atoms.

Ramsey spectroscopy

Ramsey spectroscopy is a work-horse in precision measurements of frequencies. The main requirement for the Ramsey method is that the system (atomic state and microwave field) behaves coherently during the whole spectroscopy experiment. Conversely, the degradation of the Ramsey spectroscopy can be used to estimate the time-scale that coherence is maintained i.e. what is referred to as the decoherence time (see sec. 10.2.4). First, we explain what Ramsey spectroscopy is about.

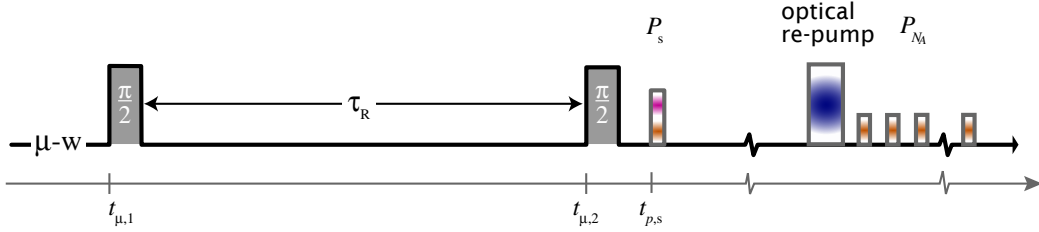


Figure 10.11: Ramsey spectroscopy experimental sequence. In most cases $\tau_{\text{int}} \ll \tau_R$.

The basic Ramsey method sketched on fig. 10.11 embodies the atomic sample interacting with the microwave field during two interaction periods that each last τ_{int} and are separated by a non-interaction time τ_R . We assume that by optical

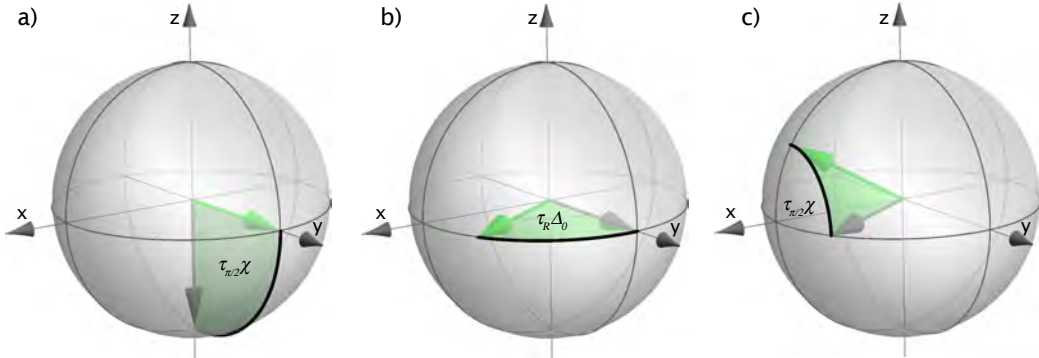


Figure 10.12: Bloch vector rotations in a Ramsey sequence.

pumping the atomic pseudo-spin has been aligned along to the south-pole of Bloch-sphere and the interaction time is set so that the first microwave pulse performs a $\pi/2$ rotation of $\langle \hat{f}_z \rangle$ to the Bloch-sphere equator (see fig. 10.12a).⁴ During τ_R the microwave field is absent and the atomic state evolves freely, which according to eq. (10.4) is prescribed by the matrix

$$\mathbf{M}_{\mu w}(\tau_R, 0, \Delta_0) = \begin{pmatrix} \cos(\Delta_0 \tau_R) & \sin(\Delta_0 \tau_R) & 0 \\ -\sin(\Delta_0 \tau_R) & \cos(\Delta_0 \tau_R) & 0 \\ 0 & 0 & 1 \end{pmatrix}, \quad (10.9)$$

which merely describes a rotation of $\langle \hat{f} \rangle$ around the z-axis (see fig. 10.12b). Following the application of the second $\pi/2$ pulse we get a complete Ramsey rota-

⁴it may seem contradicting that the microwave-pulses constitute $\pi/2$ pulses even when $\Delta_0 \neq 0$ in contrast to the requirement we set earlier. However, the offset of $\langle \hat{f}_z \rangle$ from the equator after the $\pi/2$ pulse scales as $\cos(\Delta_0 \tau_{\text{int}})$, which to zeroth order in $\Delta_0 \approx 0$ is just 1. Thus, the offset error on the $\pi/2$ pulse is small. If $|\Delta_0| \gg 0$ the basic microwave pulses will not make a full $\pi/2$ rotation causing the contrast of the Ramsey spectroscopy to be reduced.

tion matrix

$$\overline{\mathbf{M}}_{\mathbf{R}}(\tau_{\mathbf{R}}, \chi, \Delta_0) = \mathbf{M}_{\mu\omega}(\tau_{\pi/2}, \chi, \Delta_0) \mathbf{M}_{\mu\omega}(\tau_{\mathbf{R}}, 0, \Delta_0) \mathbf{M}_{\mu\omega}(\tau_{\pi/2}, \chi, \Delta_0), \quad (10.10)$$

which we generously avoid writing out in full. We may add one twist to the Ramsey fringes by allowing the atomic coherence to decay during the Ramsey interrogation time. For the moment, we will just phenomenologically add an exponential decay to eq. (10.9), but in sec. 10.2.1 we are going to partially justify this. We write

$$\mathbf{M}_{\mu\omega}(\tau_{\mathbf{R}}, 0, \Delta_0, T_2) = \begin{pmatrix} e^{-\frac{\tau_{\mathbf{R}}}{T_2}} \cos(\Delta_0 \tau_{\mathbf{R}}) & e^{-\frac{\tau_{\mathbf{R}}}{T_2}} \sin(\Delta_0 \tau_{\mathbf{R}}) & 0 \\ -e^{-\frac{\tau_{\mathbf{R}}}{T_2}} \sin(\Delta_0 \tau_{\mathbf{R}}) & e^{-\frac{\tau_{\mathbf{R}}}{T_2}} \cos(\Delta_0 \tau_{\mathbf{R}}) & 0 \\ 0 & 0 & 1 \end{pmatrix}, \quad (10.11)$$

where T_2 is the dephasing time (see sec. 3.7.1 or sec. 10.2.1). We note that, dephasing of the atomic state has no effect on the level populations and thus $\langle \hat{f}_z \rangle$, hence the 1 in eq. (10.11).

Now, to take up our favourite initial state $\langle \hat{f}(0) \rangle = -n_{\text{at}}/2 \mathbf{z}$ as an example and as before set $\Im(\chi) = 0$ then after the first $\pi/2$ pulse $\langle \hat{f}_x(\tau_{\text{int}}) \rangle = 0$ and $\langle \hat{f}_y(\tau_{\text{int}}) \rangle = n_{\text{at}}/2$. The atomic state after the free evolution is $\langle \hat{f}_x(t_{\mu,2}) \rangle = n_{\text{at}}/2 e^{-\frac{\tau_{\mathbf{R}}}{T_2}} \sin(\Delta_0 \tau_{\mathbf{R}})$, $\langle \hat{f}_y(t_{\mu,2}) \rangle = n_{\text{at}}/2 e^{-\frac{\tau_{\mathbf{R}}}{T_2}} \cos(\Delta_0 \tau_{\mathbf{R}})$, and $\langle \hat{f}_z(t_{\mu,2}) \rangle = 0$. The application of the second $\pi/2$ pulse, thus creates the final pseudo-spin state

$$\langle \hat{f}(t_{\mu,2} + \tau_{\text{int}}) \rangle = e^{-\frac{\tau_{\mathbf{R}}}{T_2}} \frac{n_{\text{at}}}{2} \begin{pmatrix} \sin(\Delta_0 \tau_{\mathbf{R}}) \\ 0 \\ \cos(\Delta_0 \tau_{\mathbf{R}}) \end{pmatrix}. \quad (10.12)$$

as illustrated on fig. 10.12c for $T_2 = \infty$. Hereby, the phase accumulated between the microwave field and the atomic state during the Ramsey-interrogation time is related to the projection of the pseudo-spin z-component. This is a crucial point, as \hat{f}_z the population number difference of the clock-levels is directly measurable. In fig. 10.13 we plot $\langle \hat{f}_z(t_{\mu,2} + \tau_{\text{int}}) \rangle$ as function of the microwave detunings

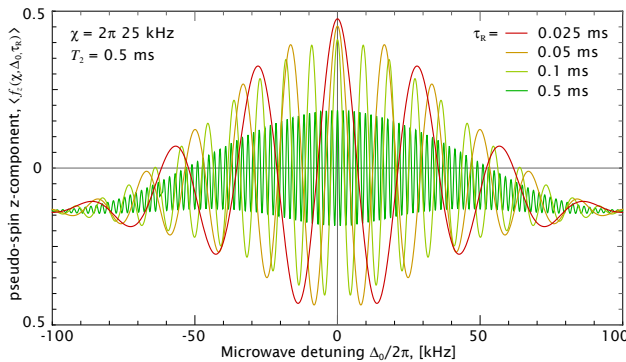


Figure 10.13: Pseudo-spin z-component in frequency domain Ramsey spectroscopy. We take $|\chi| = 2\pi \cdot 25 \text{ kHz}$, $T_2 = 0.5 \text{ ms}$ and $\tau_{\mathbf{R}} = 0.025, 0.05, 0.1, 0.5 \text{ ms}$. The parameter values are somewhat deliberately chosen in order to recreate fig. 10.26

Δ_0 for a set of interrogation times. The plot incorporates the loss of efficiency of the $\pi/2$ pulses and thus shows the non-approximated version of eq. (10.12). Clearly, the Ramsey fringes can also be achieved as function of the interrogation time by keeping a constant detuning. To distinguish the two Ramsey experiments we name the former *frequency domain* and the latter *time domain* Ramsey spectroscopy.

Again, as reference for the experimental data where we detect only one hyperfine level population, we write out the population in the $F = 4$ level assuming the same initial conditions as for eq. (10.12)

$$n_{\text{at},4}(t_{\mu,2} + \tau_{\text{int}}) = \langle \hat{f}_z(t_{\mu,2} + \tau_{\text{int}}) \rangle + \frac{n_{\text{at}}}{2} = n_{\text{at}} \cos^2\left(\frac{1}{2}\Delta_0 \tau_{\mathbf{R}}\right), \quad (10.13)$$

where, to keep the equation simple, we have neglected the decay due to decoherence.

The angle of $\langle \hat{f} \rangle$ w.r.t the z -axis, $\phi_z = \Delta_0 \tau_R$ provides a measure for the deviation of the microwave frequency w.r.t. the universal atomic transition frequency. Moreover, the angle is proportional to the Ramsey-interrogation time τ_R and by making this large the sensitivity of ϕ to the Δ_0 is increased. In the Bloch-sphere picture this is because the longer time the pseudo-spin precesses freely on the equator the smaller rotation frequencies one is able to detect. Altogether, Ramsey spectroscopy is a powerful method for clock experiments where an oscillator frequency is locked to an atomic transition frequency. The limit to the interrogation time τ_R and thus to the precision of the measurement is ultimately set by the time that it is possible to maintain the sample and the coherence of the atomic state. Degrading of the atomic state causes a reduction in the amplitude of the Ramsey fringes, which thereby offer a way to gauge the state degradation/decoherence.

Ramsey spin-echo spectroscopy

The coherence time of the Ramsey method can nearly always be extended by compensating some of the decoherence mechanism. In order to understand this we must recap the various forms of atomic state decoherence. In sec. 3.7.1 we noted that decoherence can be separated in to a contribution from temporally constant and spatially inhomogeneous dephasing of the atomic state and a contribution from temporally random phase-perturbations. Since the latter occurs as a random process there is no way to reverse it, however the former is in principle and in practice reversible. The distinction between reversible dephasing and irreversible dephasing/decoherence will be important. The practical way of reverting the dephasing is called Hahn-echo or spin-echo and uses that it is possible to induce an effective time inversion of the pseudo-spin evolution by application of a microwave π -pulse [Hahn50]. In this way, spatial inhomogeneity of the atomic state phase accumulated during some period is re-phased in an period of equal duration following the spin-echo (π) pulse [Kaplan02, Andersen04, Kuhr05]. In fig. 10.14 we present the experimental sequence for the Ramsey spin-echo

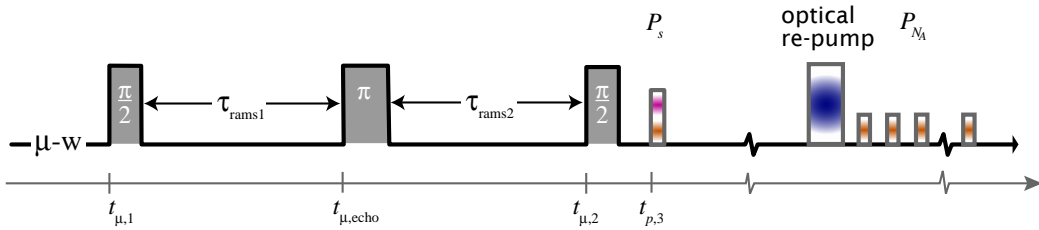


Figure 10.14: Ramsey spin-echo spectroscopy experimental sequence.

method, which differs from the pure Ramsey sequence (see fig. 10.11) only by the addition of a spin-echo pulse in between the two Ramsey $\pi/2$ -pulses. Starting from the expression of the pseudo-spin after a free evolution time (just above eq. (10.12)) we can write the pseudo-spin state right after the spin-echo π pulse

$$\langle \hat{f} \rangle(t_{\mu,echo} + t_{\pi}) = \begin{pmatrix} \frac{n_{at}}{2} \sin(\Delta_0 \tau_{R,1}) \\ \frac{n_{at}}{2} \cos(\pi) \cos(\Delta_0 \tau_{R,1}) \\ \sin(\pi) \ 0 \end{pmatrix} = \frac{n_{at}}{2} \begin{pmatrix} -\sin(-\Delta_0 \tau_{R,1}) \\ -\cos(-\Delta_0 \tau_{R,1}) \\ 0 \end{pmatrix} \quad (10.14)$$

The effect of the π -pulse can be described as a transposition (reflection in the $z \times \hat{f} - z$ plane) of the pseudo-spin and inversion of the preceding interrogation time (see fig. 10.15c). As the pseudo-spin keeps evolving freely during the second Ramsey interrogation time $\tau_{R,2}$ it accumulates an additional phase so that the final pseudo-spin phase is $\Delta_0(\tau_{R,2} - \tau_{R,1})$ and the state after the second $\pi/2$ pulse becomes

$$\langle \hat{f}(t_{\mu,2} + \tau_{\pi/2}) \rangle = \frac{n_{\text{at}}}{2} \begin{pmatrix} -\sin[\Delta_0(\tau_{R,2} - \tau_{R,1})] \\ 0 \\ -\cos[\Delta_0(\tau_{R,2} - \tau_{R,1})] \end{pmatrix}. \quad (10.15)$$

This reveals that if $\tau_{R,2} = \tau_{R,1}$ the pseudo-spin is put back to its original state before the first $\pi/2$ pulse. Other than this, $\langle \hat{f}_z \rangle$ after the Ramsey spin-echo sequence will trace out a Ramsey fringe pattern with a period $\Delta_0/2\pi$ in a time-domain measurement and a period $(\tau_{R,2} - \tau_{R,1})$ in a frequency-domain measurement. Manifestly, the frequency-domain Ramsey spin-echo measurement is not particularly useful for precise frequency measurement unless $\tau_{R,2}$ and $\tau_{R,1}$ are vastly different.

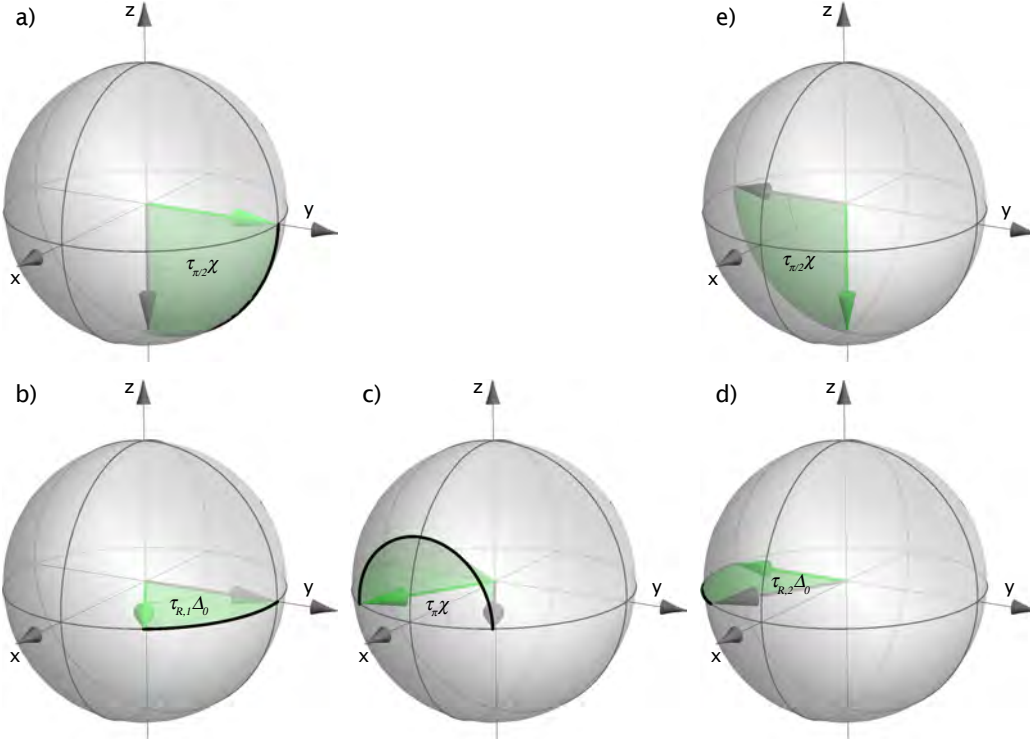


Figure 10.15: Bloch vector rotations in a Ramsey sequence with Hahn-echo pulse.

In terms of the population in the $F = 4$ level assuming the same initial conditions as for eq. (10.15) we get

$$n_{\text{at},4}(t_{\mu,2} + \tau_{\pi/2}) = \langle \hat{f}_z(t_{\mu,2} + \tau_{\pi/2}) \rangle + \frac{n_{\text{at}}}{2} = n_{\text{at}} \sin^2 \left(\frac{1}{2} \Delta_0 \tau_R \right) \quad (10.16)$$

The merits of the spin-echo scheme is uncovered when incorporating some spatial distribution of the accumulated phase, which can be due to inhomogeneous light shift from the trapping or probe laser. The former was expressed as shift of resonance frequency in eq. (9.4) while the latter was framed as a phase-shift

to the pseudo-spin in eq. (4.24). Naturally, the two formulations are equivalent and allow us some freedom of expressing the issue at hand. Since the FORT light-shift is present throughout the evolution of the atomic state while the sample is trapped, it is simpler to let the inhomogeneity enter as an offset to the microwave detuning. Hereby, we express the phase-perturbation as a spatially dependent detuning deviation with the total phase accruing to $\tilde{\phi}_{\text{at}}(\mathbf{r}) = (\Delta_0 + \delta_{\Delta}(\mathbf{r}))\tau_{\text{R}}$. Suppose $\Delta_0\tau_{\text{R}} = m\pi$ and $\delta_{\Delta}(\mathbf{r})\tau_{\text{R}} \ll \pi$, we can express the final $\langle \hat{f}_z(t_{\mu,2} + \tau_{\pi/2}) \rangle \approx \frac{1}{2}n_{\text{at}}(1 - m\delta_{\Delta}(\mathbf{r})\tau_{\text{R}})$. Integrating over the spatial extent of the sample we get

$$\begin{aligned} \langle \hat{F}_z^{(tot)}(t_{\mu,2} + \tau_{\pi/2}) \rangle &= \int_{R^3} \tilde{d}^3r \mathcal{N}(\mathbf{r})(1 - m\delta_{\Delta}(\mathbf{r})\tau_{\text{R}}) \\ &= \frac{N_{\text{tot}}}{2} \left(1 - \int_{R^3} \tilde{d}^3r \frac{\mathcal{N}(\mathbf{r})m\delta_{\Delta}(\mathbf{r})\tau_{\text{R}}}{N_{\text{tot}}} \right) \end{aligned} \quad (10.17)$$

Below and in sec. 11.1 we will make an attempt at specifying the distribution of $\delta_{\Delta}(\mathbf{r})$, however, at present it suffices to note that the inhomogeneous spread of the pseudo-spin phase causes a reduction of the Ramsey fringe amplitude. For the Ramsey spin-echo sequence we found that it was equivalent to the Ramsey sequence except for the change of sign of the final state and replacement of $\tau_{\text{R}} \rightarrow (\tau_{\text{R},2} - \tau_{\text{R},1})$. We then deduce the total ensemble pseudo-spin to be

$$\langle \hat{F}_z^{(tot)}(t_{\mu,2} + \tau_{\pi/2}) \rangle = -\frac{N_{\text{tot}}}{2} \left(1 + \int_{R^3} \tilde{d}^3r \frac{\mathcal{N}(\mathbf{r})m\delta_{\Delta}(\mathbf{r})(\tau_{\text{R},2} - \tau_{\text{R},1})}{N_{\text{tot}}} \right), \quad (10.18)$$

where the integral over the phase inhomogeneity goes to zero when $\tau_{\text{R},2} = \tau_{\text{R},1}$, which we will refer to as a symmetric spin-echo sequence. In sum, the Ramsey spin echo sequence causes a re-phasing of the spatially inhomogeneous phase that would otherwise reduce the Ramsey fringe amplitude.

To get an analytical expression for the Ramsey (spin-echo) signal we refer to the treatment made in [Kuhr05], where the thesis is that inhomogeneous dephasing ensues from the differential light shift from FORT trapping laser. Since, we know the cross-section of the FORT potential to be Gaussian the first impulse would be to incorporate this distribution of $\delta_{\Delta}(\mathbf{r})$ in to eqs. (10.17 and 10.18), however the atomic density distribution $\mathcal{N}(\mathbf{r})$ is also determined by the trapping potential along with the sample temperature c.f. sec. E.1. Thus, the approach of [Kuhr05] is rather to term the problem in atomic energy distributions. This analysis results in equations for $\langle \hat{F}_z^{(tot)} \rangle$ in a Ramsey experiment

$$\langle \hat{F}_z^{(tot)}(t_{\mu,2} + \tau_{\pi/2}) \rangle = -\frac{1}{2}\alpha(\tau_{\text{R}}, T'_2) \cos [(\Delta_0 + \overline{\delta_{\Delta}})\tau_{\text{R}} + \kappa(\tau_{\text{R}}, T'_2)] \quad (10.19)$$

where $\overline{\delta_{\Delta}}$ is the average light-shift and

$$\begin{aligned} \alpha(\tau_{\text{R}}, T'_2) &= \left[1 + 0.95 \left(\frac{\tau_{\text{R}}}{T'_2} \right) \right]^{-3/2} \\ \kappa(\tau_{\text{R}}, T'_2) &= -3 \arctan \left(0.97 \frac{\tau_{\text{R}}}{T'_2} \right) \end{aligned}$$

are the Ramsey fringe amplitude and a conspicuous supplementary phase. In this description the Ramsey amplitude $\alpha(\tau_{\text{R}}, T'_2)$ does not exactly decay exponentially with τ_{R} , thus the time T'_2 constant is deliberately chosen to resemble an exponential decay time in that $\alpha(T'_2, T'_2)/\alpha(0, T'_2) = 1/e$. The phase $\kappa(\tau_{\text{R}}, T'_2)$ is an artefact of the atomic density being biased towards the central and flatter part of the trapping potential. Additionally, the reversible dephasing can be predicted from the sample temperature [Kuhr05]

$$T'_2 = 0.97 \frac{2\hbar\Delta_{\text{D,eff}}}{\omega_0 k_{\text{B}} T} \quad (10.20)$$

where the effective detuning $\Delta_{D,\text{eff}}$ was defined in eq. (9.5). Our take is to use the expression in reverse and estimate the sample temperature from the measured T_2' time.

In as long as irreversible dephasing is negligible, the corresponding equations for the Ramsey spin-echo sequence are attained by simple substitution of $\tau_R \rightarrow (\tau_{R,2} - \tau_{R,1})$. When irreversible dephasing starts to play a role, the fringe amplitude should include an exponential decay factor

$$\alpha(\tau_{R,1}, \tau_{R,2}, T_2', T_2^*) = e^{-(\tau_{R,1} + \tau_{R,2})/T_2^*} \left[1 + 0.95 \left(\frac{\tau_R}{T_2'} \right) \right]^{-3/2} \quad (10.21)$$

The description here concerns the total ensemble evolution and thus does not take into account that the ensemble is probed inhomogeneously according to the probe beam intensity distribution. This flaw is not sufficient ground to disavow eqs. (10.19 and 10.21), merely something to keep in mind should there be a discrepancy between theory and data. In sec. 11.1 we amend the expression for the light-shift by avoiding the reference to the energy distribution of the atoms. Nevertheless, we chose to harness the treatment of [Kuhr05] so as to bridge our results with those in the literature. This concludes the theoretical overview of the microwave interaction and we proceed with a description of the microwave setup.

10.2.2 Microwave Setup

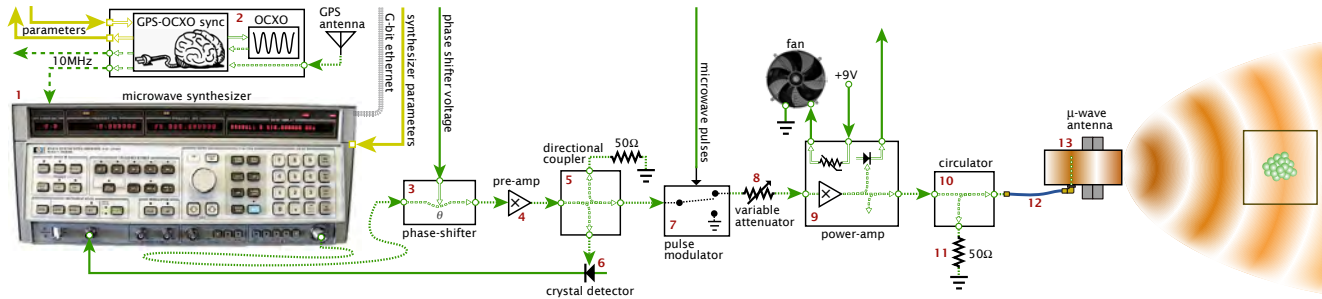


Figure 10.16: Layout of the microwave setup. **1** Source, microwave synthesiser HP8341B (see sec. 10.2.2). **2** Morion MV87-A50I-500MHz-G oven controlled oscillator. **3** phase-shifter MCE/KDI PQ-1867 (optional). **4** microwave amplifier Narda DBS-0411N630 either as stand-alone or pre-amplifier. **5** Directional coupler 780-30-9.700 to split off power for **6** HP33330B Shottky diode power detector used as reference to stabilise synthesiser output power. Microwave pulse generator as either **7** pulse modulator HP11720A or **7*** SPDT switch AMC SWN-RRA-2DRH-COMDEV (not shown). **8** Variable attenuator HP8496B (optional) mainly used during characterisations of setup. **9** microwave power amplifier Kuhne KU PA 922 XL-226 (optional). **10** Circulator ATM ATc8-12.4 mounted with **11** 50 Ω resistor ATM TO516 as protection of amplifier from antenna reflections. **12** Low loss cable ATM CF-300-30-SM-SMR connecting the amplifier with **13** SMA to wave-guide adaptor. For details refer to Tab. G.1

The microwave setup (fig. 10.16) consists of 4 main elements, a frequency source, a switch, an amplifier, and an antenna. The amplification may occur in a single stage or in two stages with a pre-amplifier and a power amplifier (on fig. 10.16 the latter configuration is sketched). Additional elements such as a phase-shifter, a directional coupler for feedback, an attenuator, and and a protective circulator add functionality. In the below sections we will discuss and characterise aspects related to the different elements.

Antenna design In order to generate microwave radiation that couples to the atomic sample we must construct an antenna. There are various forms of antenna designs that each fit a specific application. In our case we need the radiation to have only a short range, but have well defined polarisation. For this purpose a horn antenna is well suited. However, we found that our self made antennae were very inefficient at coupling the microwave power from the cable to free space. Finally, we decided to use a commercial wave-guide coupler with one end-face open. The construction of the antenna is detailed in Box 10.1. The small dimensions of the wave-guide has the added advantage that it can be put very close to the vacuum cell and thus irradiate the atoms with high power. In

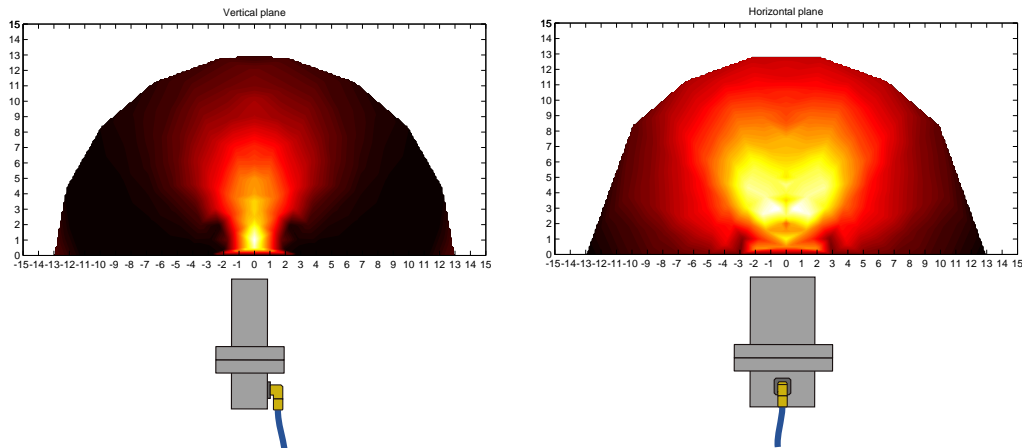


Figure 10.17: Microwave antenna radiation pattern. The microwave radiation power was measured at different positions. The measurements were only done to one side of the antenna and the two sided intensity plot is generated by mirroring the data around the antenna axis. We wish to induce magnetic-dipole transitions with the microwave field. Thus, the radiation should have its magnetic component parallel to the quantisation axis of the atoms given by the magnetic bias field along the z -axis of the setup. Since, the electric field component is given by the direction of the diode inside the wave-guide, the wave-guide must be oriented with the diode in the plane of the MZI as illustrated on fig. 10.1. Therefore, fig. 10.17a) shows the radiation in the (horizontal) MZI plane and fig. 10.17b) shows that along the (vertical) z -axis.

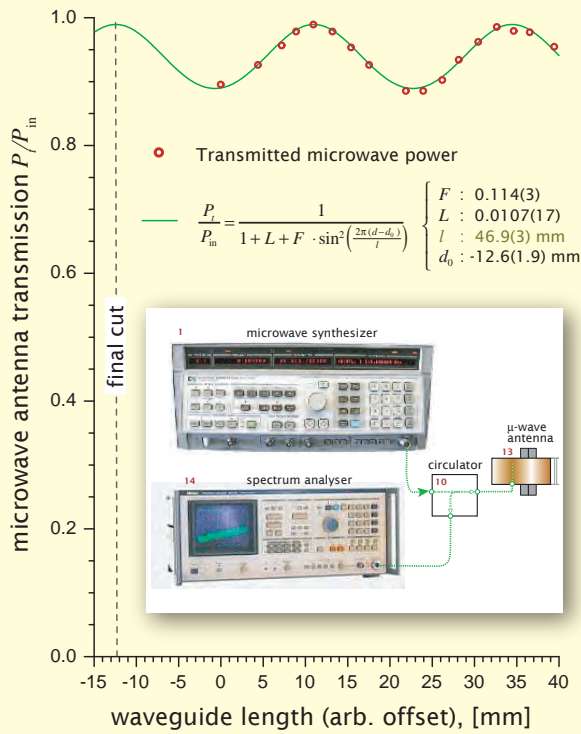
fig. 10.17 we show the measured radiation pattern of the antenna. The location of the atomic sample can be envisioned from the position of the antenna in the MZI setup on fig. 10.1.

Microwave pulses We need to precisely control the interaction time of the microwave radiation with the atoms. Since, in our setup the atomic sample is stationary and the microwave radiation is not spatially localised inside a wave-guide, as is typically the case in clock-experiments [Vanier89, Audoin01], the only way to control the interaction time is by pulsing the microwave radiation. To that end we have employed a range of switching devices. Initially, we made use of the built-in modulation capability of the synthesiser, however, the output amplitude of the resulting pulses turned out to vary significantly (5-10%) over the duration of the pulse. As a consequence, we acquired an independent pulse modulation unit (HP11720A) with 80 dB isolation and 6 dB insertion loss (IL). The high IL limited the achievable microwave output power, and in order to boost the power we procured a low loss switch from AMC with 50 dB isolation and only ≈ 0.8 dB IL. Unfortunately, the AMC switch broke after about one year of operation⁵ and we reemployed the HP modulator. Rather, than investing in a

⁵i.e. just past the warranty period!

Box 10.1: Construction of "sawn-off" wave-guide antenna

In order to get the best efficiency of the free-space coupling, the wave-guide length should correspond to an odd half number of wavelengths. To achieve this we simply measure the power reflected from the antenna. By use of a circulator we ensure that the reflected power does not return to the synthesizer/amplifiers, but is dumped in a termination resistor or a spectrum analyser.



Box 10.2: Open-ended wave-guide transmission to free-space as function of the wave-guide antenna length. Inset shows the setup for measuring the power reflected by the antenna P_r . To establish the input power P_{in} we simply connect the synthesiser directly to the spectrum analyser input. The transmission $(P_{in} - P_r)/P_{in}$ as a function of the wave-guide length (red points) corresponds to that of a poor cavity and a fit to the theoretical model [Milonni88] (green line) yields a microwave wavelength of 46.9 mm in the wave-guide. The wave-guide dimensions set the cut-off frequency of the (lowest) TE-01 mode at $\nu_{01} = c/(2a) = 6.58$ GHz, where $a = 22.8$ cm is the transverse wave-guide size. From this we can predict the frequency of the microwave radiation in the wave-guide $\nu_c = \sqrt{\nu_0^2 - \nu_{01}^2} = 6.41$ GHz [Jackson99]. This in turn

gives a predicted wavelength of $\lambda_c = c/\nu_c = 46.73$ cm, which agrees well with the value extracted from the fit to the measured data.

The figure shows the reflected power at 9.192 GHz measured on a spectrum analyser. Each measurement point corresponds to a different wave-guide length as achieved by milling off short sections of the end face. Since the minimal reflection indicates the best free-space coupling we stop shortening the wave-guide at -12.6 cm on the length-scale of the figure.

new switch we decided to purchase a second high-power amplifier (22 dB gain, max. output power 41 dBm) from Kuhne. Since the HP modulator doesn't stand more than 20 dBm the power amplifier is placed after the switch. The main gain of the low IL switch and power amplifier reconfiguration is the shortening of the Rabi oscillation period, which we generally desire to be short and especially so in cases where trap dynamics are important (see sec. 11.2.2).

phase-shifter When we treated the microwave interaction we saw that the microwave field induces a rotation of the pseudo-spin around a vector in the equatorial plane of the Bloch-sphere. By eq. (10.6) the azimuthal angle of the rotation vector is determined by the phase of the microwave field. It is possible to change the phase of the synthesiser by changing the phase of the 10 MHz reference sig-

nal, however it takes a little less than 10 ms before the synthesiser output adjusts to a phase-shift of π . This is much too long. In order to change the microwave phase rapidly we acquired a phase-shifter, which depending on an applied bias voltage displaces the phase of its output w.r.t the input. We use the simple test setup drawn in fig. 10.18a to characterise the phase-shift dependence on the bias voltage. This basically constitutes an interferometric measurement in which the

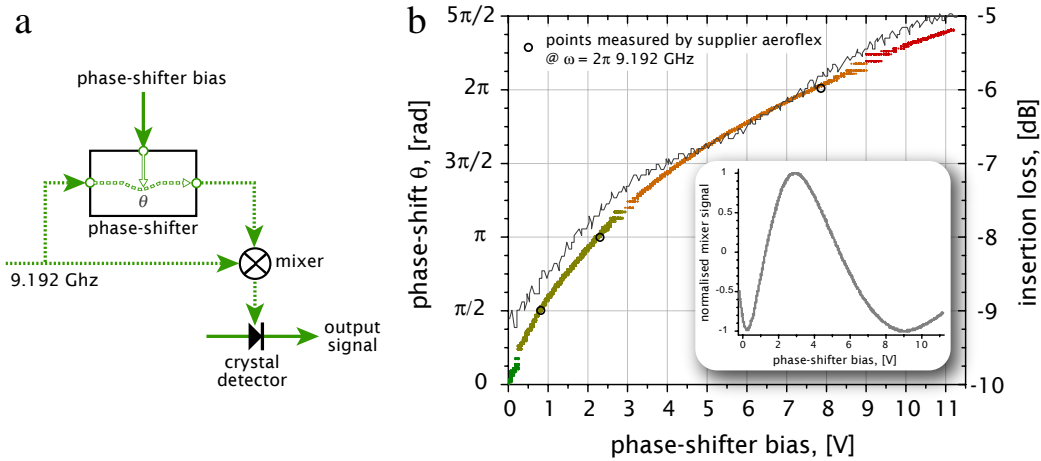


Figure 10.18: Phase shift of output of microwave phase-shifter vs. applied bias voltage. a) test setup for measuring phase-shift. b) output signal normalised to the maximal signal amplitude v/v_0 in insert. In main plot the $n\pi + \arccos(v/v_0)$. The colours correspond to different integer multiples of π that are added to make a smooth plot. The grey line is the insertion loss of the phase-shifter, which has been taken into account for the phase-shift measurement.

output detector voltage will be $v = v_0 \cos(\delta\theta)$. The phase-difference is set by the cable length difference from the point where the signal is split until the mixer, plus the additional phase-shift from the phase-shifter. The insert of fig. 10.18b shows the signal we observe. If we define $\delta\theta = 0$ for 0 V bias we can determine $\delta\theta = \arccos(v/v_0)$. Thus, we get the phase-shift dependence on the bias voltage shown in fig. 10.18b. The phase-shifter bias voltage is set by the DIO card via the *DIO-64* LabView program. The DIO can only set TTL values on its outputs, so in order to set a particular voltage we use 12 DIO outputs and convert the logical values by a 12-bit DAQ to an analogue voltage. The *DIO-64* program can in turn be set to receive values from the *stepping* LabView programme and thereby the phase-shift can be automatically stepped through a parameter range so as to e.g. observe a full Ramsey-fringe. The phase-shifter has been used for the characterisation of the dephasing and decoherence e.g. in sec. 11.2.3 and sec. 11.3. For the later measurements with squeezing and clock sequences we used a new setup described in the below section.

One unfortunate property of the phase-shifter is that besides shifting the phase it also induces losses, which are dependent on the bias voltage. In fig. 10.18 we plot the measured insertion loss (grey line) and see that it varies from about $P_{\text{out}}/P_{\text{in}} = 0.87$ attenuation at 0 phase-shift to $P_{\text{out}}/P_{\text{in}} = 0.70$ at $5\pi/2$ phase-shift. These phase-shift dependent losses are not particularly welcome as they will change the interaction parameters with the atoms, i.e. the Rabi frequency and thus τ_π . To prevent the losses in changing the microwave power at the atoms, we make sure that the microwave source provides enough power that the NARDA amplifier output is saturated. In this case changes in the amplifier input power will translate into minor variations at the output. Secondly, we actively stabilise the power as close as possible to the atoms (see sec. 10.2.2 below).

Revamped microwave source

In cases where the microwave frequency needs to be kept very stable over long periods we found that the synthesiser did not suffice. This point will be elaborated in sec. 10.2.2 where we characterise the frequency stability of different sources. Hence we constructed ⁶ an alternative frequency source which we will outline now.

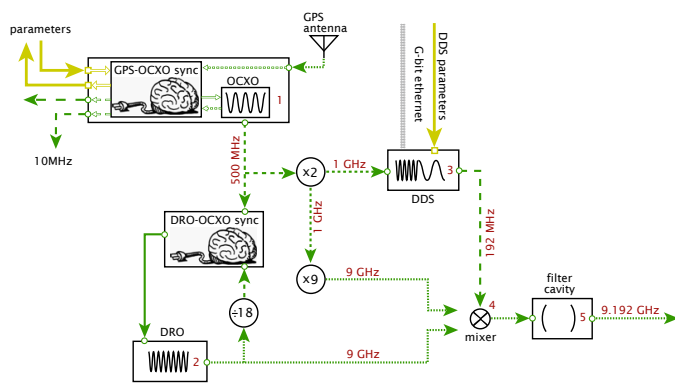


Figure 10.19: Schematic of new microwave source. 1 Morion MV87-A50I-500MHz-G oven controlled oscillator. 2 Analog Devices AD9910 Direct Digital Synthesiser 3 Poseidon Scientific Instruments DROO-9.000-FR Dielectric Resonator Oscillator 4 Mini-Circuits ZMX-10G+ frequency mixer 5 Lorch Microwave 5CF7-9200/50-S cavity filter.

Besides the elements drawn on the figure the setup contains a number of amplifiers and filters. The frequency multiplication and division is for the most part also done stepwise so as to generate the final values indicated. The output signal at 9.192 GHz is passed to the Narda pre-amplifier and the signal passes the same components as in the old setup from fig. 10.16. For details of the schematic we refer to the body text.

The source is made in a modular design so that we can build the complete source as a chain (see fig. 10.19). The first stage is, as with the synthesiser based source, a GPS receiver that generates a 10 MHz reference signal. The GPS signal ensures the absolute calibration of the later stages and in this respect keeps the frequency deviations low on the long time-scale. The 10 MHz signal is passed to an Oven Controlled Crystal Oscillator (OCXO) from Morion. The OCXO outputs a 500 MHz signal which is specified to have a high phase stability up to around 10-20 kHz.⁷

At this point we have two options. One is to multiply the OCXO first by a factor of two up to 1 GHz and then up to 9 GHz with a chain of frequency multipliers. The other option is not to use the OCXO signal directly, but as reference to which we lock another 9 GHz source. This other source is a Dielectric Resonance Oscillator from Poseidon Scientific Instruments (PSI) outputting a 9 GHz signal. This is specified to have a very low phase noise in the MHz range, whereas in the kHz and Hz range it is more noisy than the OCXO.⁸ Thus we have the option of locking the DRO by mixing its signal down to the 500 MHz of the OCXO and via frequency comparison tune the DRO via its VCO control input. Since we have 500 MHz and 9 GHz signals derived from both the OCXO and the DRO we can compare their noise with either of the two frequency signals.

We still need to bridge the last 192 MHz from 9 GHz to the Cs clock transition. This is done by a key element of the setup, a Direct Digital Synthesiser (DDS), which derives an output frequency by sampling a 1 GHz reference signal. The DDS from Analog Devices, that we use, delivers output frequencies up to 400 MHz with < 0.23 MHz resolution, and less than -125 dB phase-noise

⁶the chief responsibility for the implementation was taken by Jürgen Appel.

⁷at 10 kHz the phase-noise is stated to be -140 dB/Hz below the carrier. above 10 kHz the phase noise is not specified

⁸above 1 MHz the phase noise is specified to be at ~ -160 dB below the carrier. At 10 kHz the same figure is -112 dB while for the OCXO it is -140 .

w.r.t. the carrier. The 1 GHz reference signal is taken from the first frequency multiplication of the OCXO output. The 192 MHz signal from the DDS is mixed with the 9 GHz signal, derived from either the DRO or the OXCO directly, resulting in a 9 GHz carrier signal with sidebands at 9 ± 0.192 GHz. The upper sideband is resonant with the Cs clock transition, while the other sideband and the carrier are so far detuned that they have no influence on the atoms. However, the carrier and lower sideband are unwanted since they would saturate the amplifiers and thus limit the power in the upper sideband. Hence the signal is filtered in a wave-guide cavity designed to pass frequencies of 9.2 ± 0.05 GHz with 3 dB insertion loss. The attenuation at the carrier frequency is -63 dB and similar at the lower sideband.

The great advantage of the DDR is the flexibility of choosing both the amplitude and frequency/phase of the output. The DDR generates its output by running through a pre-stored signal sequence. Thus we can modify the pulse shape and phase precisely as we need them. The DDR can hold up to eight signal profiles and it can switch between them in a few ns. This allows us to switch the microwave pulses on and off by using the DDR instead of the HP pulse modulator. When the DDR output is set to zero the 9.192 GHz sideband is absent and all the microwave power is absorbed in the filter cavity. Hence to generate a microwave pulse we open the HP pulse-modulator and simply modulate the amplitude of the DDR output. Because of the limited number of profiles that can be stored on the DDR we only switch the demanding pulses, i.e., those that require a phase-change or complicated amplitude envelope. For the more regular pulses, such as those used in the optical pumping blow-away and state preparation, we keep the DDR amplitude in DC mode and switch the pulses in the standard way with the HP pulse-modulator.

Microwave power stability

We will discuss our observations of instability in the microwave output power along with the measures taken to stabilise the power. In the synthesiser based configuration, the predominant cause of slow fluctuations in the output power is thermal and spatial changes in the cables carrying the microwave signal. Our placement of the microwave synthesiser in an enclosed cooling cabinet⁹ and the ensuing long cable path only accentuates this source of power fluctuations. In

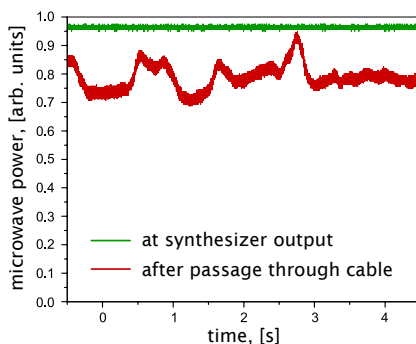


Figure 10.20: Microwave power drifts in cables. Green curve is power measured at synthesiser output. Red curve is power measured after long stretch of cable while twisting it.

fig. 10.20 we illustrate the difference in the power stability at the synthesiser output and following a lengthy stretch of cable. We amended the setup by implementing a feedback loop. The synthesiser output is by default levelled to an internal calibrated detector, but it is also possible to level it to an external voltage signal. Thus, we split off one tenth of the power just before the switch and detect it with a HP33330B Shottky diode detector. The synthesiser output is then

⁹this placement was chosen in order to keep the noise level in the lab at a tolerable level.

levelled to the detector voltage, with a feedback bandwidth of 80 kHz mainly determined by the synthesiser input. The levelling mode and value are set along with the synthesiser frequency in the LabView programme *instrumentstepper.vi* through a GPIB or ethernet interface.

Another measure that ensures more higher power stability of the output is to drive the amplifiers into moderate saturation. When this is done, modest fluctuations in the amplifier input power will be suppressed in the amplifier output. To state some numbers, the synthesiser output power is around -4 dBm (~ 0.4 mW) of which about 80%, i.e. -5 dBm, reaches the Narda amplifier input. The amplification is 43.5 dB, but the output power is limited to 31.5 dBm (1.4 W). When only the Narda amplifier is used we utilise the AMC switch and loose no more than 1 dB so that including losses in cables we estimate 30 dBm (1 W) to reach the antenna. In the two stage amplification setup the Kuhne input power is limited to 25 dBm. Using the HP8496B variable attenuator for the switching exactly induces a 6 dB loss which reduces the input to 25.5 dBm. With 22 dB gain and 41 dBm maximal output power the Kuhne amplifier is also saturated and we estimate around 40 dBm (10 W) power for the antenna.

A second major perturbation on the microwave radiation power is caused by the environment of the MZI/trapping setup, specifically the thin aluminium sheets to which the acoustic damping fleece is mounted. These make up an enclosure of the whole setup that turns out to act as a giant and very imperfect microwave cavity. Any changes to the physical location of one the sheets visibly alters the interaction of microwave with the sample. Presumably, the perturbation is not only in the absolute microwave power but also in the polarisation of the field. Thus a simple measurement of the field amplitude would not reveal the full extent of the effect. We tried to fix the problem by use of microwave absorption material. Unfortunately and indeed very surprisingly, the absorber proved to generate such quantities of fine dust to be incompatible with an optical setup. In conclusion, the MZI/trapping enclosure should not be touched after the microwave parameters (power, pulse length, frequency) have been set and when the sheets are removed/reinserted these parameters must be re-calibrated.

With the above measures and precautions the microwave power was sufficiently stable to perform the vast majority of the measurements. Since, in the new microwave setup, we shape the some of the pulses with the DDS we do not have a constant power before the HP pulse modulator and therefore cannot generate any feedback. On the other hand, the new microwave sources are located much closer to the setup and thus cable losses play a lesser role. Still, we observe slow drifts of the microwave power. These drifts are very likely caused by the thermally induced changes in the efficiency of the power amplifier. We chose to monitor the pulse power measured by the internal detector of the Kuhne power amplifier. The microwave pulse powers are stored on a DSO channel and an average microwave pulse power is computed using an appropriate integration window as described in sec. 8.2.2. In a very recent move the measured microwave power is used for a feed back to the amplitude of the DDS.

Microwave frequency stability

Stabilising the microwave frequency is a somewhat demanding task and as our measurements have steadily increased in complexity we have had to perfect the frequency precision and accuracy¹⁰. First we discuss the accuracy.

¹⁰in clock terminology accuracy of an oscillator is the closeness of its mean frequency to the reference frequency and the precision is the standard deviation of the oscillator frequency around

Accuracy of microwave frequency source Performing spectroscopy of the Cs clock transition we realised that the calibration of the synthesiser frequency was off by ≈ 30 kHz corresponding to $3 \cdot 10^{-6}$ relative off-set (see fig. 10.22-10.27). To improve on the accuracy we employed the GPS based frequency reference, where we locked a 10 MHz Oven-Controlled Crystal Oscillator (OXCO) to the signal from a GPS-antenna (see fig. 10.16). First we used the 10 MHz reference for a spectrum analyser and acquired the spectrum of the synthesiser output. We found that due to expected ageing of the internal time-base the un-referenced synthesiser frequency was off by 30.841 kHz. With the 10 MHz GPS reference fed to the synthesiser we get good correspondence between the set and tabulated clock-frequency (≈ 0.5 kHz $\equiv 5 \cdot 10^{-8}$ relative offset). At this point, we believe, the accuracy is limited by the perturbations of the clock-transition in the sample.

Precision of microwave frequency source At first we relied solely on the synthesiser and saw no effect on the state preparation from the imprecision of the microwave radiation. Only, when using several subsequent pulses as needed for Ramsey spectroscopy and state tomography (see sec. 12.6) we observed excess noise due to the synthesiser's frequency instability.

To characterise the phase-noise of an oscillator one should ideally look at the phase coherence of the same oscillator signal at different points in time. However, to do so one would need to split the signal and then mix the split parts after travelling through delay lines of different lengths. A slightly less ambitious strategy to determine the source's stability is by comparing it with another source. Unless, one source has significantly higher precision the comparison will, however, not be able to completely characterise either source. One could first compare a pair of essentially identical sources and thereafter deduce the precision of other sources. Since we do not have to identical sources (at least not at the right frequency) we must compare. We characterise the sources by the Allan variance in basically the same way as was done for two probe lasers in fig. 8.7. The Allan deviations for different combinations of sources at 9 GHz are shown in fig. 10.21. The data below 100 ns is at the limits of the amplifier

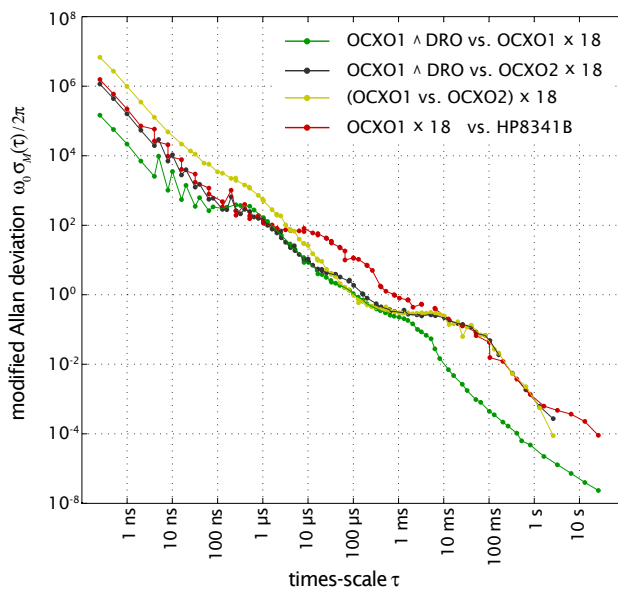


Figure 10.21: Allan deviations for beat signal between different microwave sources as indicated by the legend. OXCO1 and OXCO1 refer to two identical units that output 500 MHz signal. The $\times 18$ refers to the frequency multiplication chain of the OXCO up to 9 GHz. The OXCO \wedge DRO label symbolises the DRO locked to the OXCO. Finally, HP8341B suggests a signal derived from the synthesiser. The beat signals were detected on the DSOO with different time-spans for different time-scale ranges. The acquired traces were then post-processed in a Matlab script.

and detector bandwidths and should not be taken too seriously. The red curve compares the OXCO (multiplied up to 9 GHz) with the HP8341B synthesiser, the mean frequency.

and we see that the noise is consistently higher than all the other combinations. We conclude that this is due to the phase noise of synthesiser, which in the experimentally most relevant range from $1 \mu\text{s}$ - 1ms shows about one order of magnitude more noise than the rest. The yellow curve compares the 500 MHz signals from two identical OXCO sources and the calculated Allan deviation is then scaled to allow comparison. For the most part the noise of this combination is as good as that which contains a DRO. Only in the range below $10 \mu\text{s}$ does it seem that the OXCO noise is slightly higher than that from the comparison of the OXCO (multiplied up to 9 GHz) and the DRO. This indicates that on short time-scales the DRO is superior, as was expected from the data-sheets. On time scales longer than $10 \mu\text{s}$ the DRO is locked to the other OXCO and we expect the noise to be the same as for the direct comparison of the OXCOs. Finally, we compare the frequency multiplied OXCO signal with that from the DRO locked to the same OXCO. On short time-scales there is no difference between the previous comparison, since the DRO is effectively free running, i.e., the lock to the OCXO is slower than $10 \mu\text{s}$. On intermediate time-scales the DRO is locked to the OCXO, and the signal shows the same level of noise as when two different OXCOs are used. On long time-scales all signals are locked to the GPS, but evidently the lock is not so very strong, as the signal derived from the same OCXO still has the lowest noise.

In sum the new source(s) show a much better phase stability than the synthesiser especially in the range of times relevant for our measurements. Moreover, the bandwidth of the DRO-OCXO lock seems to be set reasonably appropriate.

10.2.3 Rabi, Ramsey, and spin echo sequences

Having described the theory of microwave interaction between hyperfine ground levels and presented the experimental setup, we are now in a position to display the experimental observations on the final state preparation step. Already at this stage, the experiments will begin to reveal some of the great advantages of our MZI based probing, in particular its ability to extract information about the atomic state without destroying the state. The degree of state destruction caused by the probing will be the main topic in chapt. 11.3 and we shall not dwell in it here. However, in sec. 10.2.4 we will try and grasp the rate of state disruption, i.e. decoherence, caused by other effects. Before we get to that, we must calibrate the microwave interaction starting with the tuning of the microwave source to the atomic transition frequency. We recap that the probes detect the phase-shift from all atoms in a particular hyperfine ground level irrespective of their magnetic sub-level. Thus, the probes cannot themselves detect the distribution of atoms in the different sub-levels. What they can detect is, however, the effect on the overall hyperfine level population that the microwaves have by interacting with a particular sub-level.

We follow the experimental cycles illustrated by fig. 10.11 and fig. 10.14, where following optical pumping and optionally a state purification we perform a Rabi or Ramsey type microwave pulse sequence and measure the phase-shift with either single or two colour probe pulses. To normalise the measurement to the total atom number we may re-pump all atoms to the $F = 4$ level and again measure the phase-shift (also shown in fig. 10.11 and fig. 10.14). Finally, to establish the MZI phase offset we make one measurement with no atoms in the FORT once every loading cycle. When using the single colour probe we effectively gauge the population in one hyperfine level while the two colour probe is equivalent to a direct measurement of the pseudo-spin z -component.

Since, for historical and practical reasons we use both one and two colours for different measurements we just bear in mind to use the appropriate equations in sec. 10.2.1.

Determining transition frequency

The task of tuning the microwave frequency on resonance with the clock transition should be a standard task, but for a number of reasons it required several months of perfection before we could nail it down with confidence. The first difficulty arose when no apparent effect was visible at the expected microwave transition frequency of $\omega_0 = 9192.631770$ GHz. Thus to locate the resonance frequency we turned to a sweep of the microwave frequency over a certain range centred at ω_0 . The red curve in fig. 10.22 gives a good idea of our observations, where we see the population of one hyperfine level being depleted as the microwave radiation crosses the transition frequency. Making exact predictions as

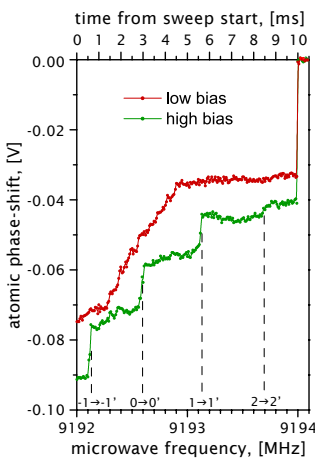


Figure 10.22: Atomic phase-shift from $F = 4$ during sweep of microwave field frequency. We use the synthesiser as source with only the Narda amplifier (see fig. 10.16). The sweep over 2 MHz from 9192-9194 MHz lasts 10 ms. For a low magnetic bias field (red curve) the $F = 4$ level is depleted almost continuously over a 600 kHz range centred on ~ 9192.6 MHz. For a high bias magnetic field (green curve) the linear Zeeman shift splits the transition frequencies for the different $|F, m_F\rangle \rightarrow |F', m'_F\rangle$ transitions. Since, the microwaves magnetic field is polarised along the direction of the bias-field (z-axis) π transitions i.e. $m'_F = m_F$ dominate and according to eq. (3.11) $|(w_{4,m_F} - w_{3,m_F}) - (w_{4,m_F\pm 1} - w_{3,m_F\pm 1})| = 2\pi \cdot 700.1 \frac{\text{kHz}}{\text{Gauss}} |B|$. The measured frequency splitting is 567 kHz, which is analogous to 809 mGauss bias

to what one should observe is, however, difficult as it requires prior knowledge of the microwave field intensity, background magnetic field, etc. Nevertheless, assuming that the width of the population depletion range is due to Zeeman splitting of the magnetic sub-levels, we are able roughly estimate clock-transition frequency corresponding to the the centre of the range at $\omega_{\mu w} = 9191.600$ MHz, i.e. ≈ 30 kHz off from the tabulated value. As pointed out in sec. 10.2.2 we later found this to correspond almost precisely with the synthesiser calibration offset. With this first estimate at hand, we could narrow the scan and try to calibrate and see some effect of optical pumping (see sec. 10.1.3), which in turn enabled us to pick out the clock-transition more easily. Crucial to optical pumping is a bias field strong enough to overshadow stray background magnetic fields, and additionally the sub-level splitting brought about by the bias field neatly isolates the clock-transition from adjacent sub-level transitions (green curve in fig. 10.22). By observing the frequency separation of the transitions we infer the Zeeman splitting and thus compute the bias field strength using eq. (3.11) (see fig. 10.22 caption). Similarly, when turning the bias field off, the width of the population depletion range is a measure of the total splitting of the hyperfine level due to background magnetic fields. Based on this relation we adjust the magnetic field compensation coils to minimise the background field around the atoms - the procedure is described in detail in sec. H.0.1.

Rabi oscillation measurements

With an optically pumped ensemble and a good estimate of the clock-transition frequency the ensuing goal was to observe Rabi-oscillations of the population in $m_F = 0$. In fig. 10.23 (green curve) we indeed see that the $F = 4$ hyperfine

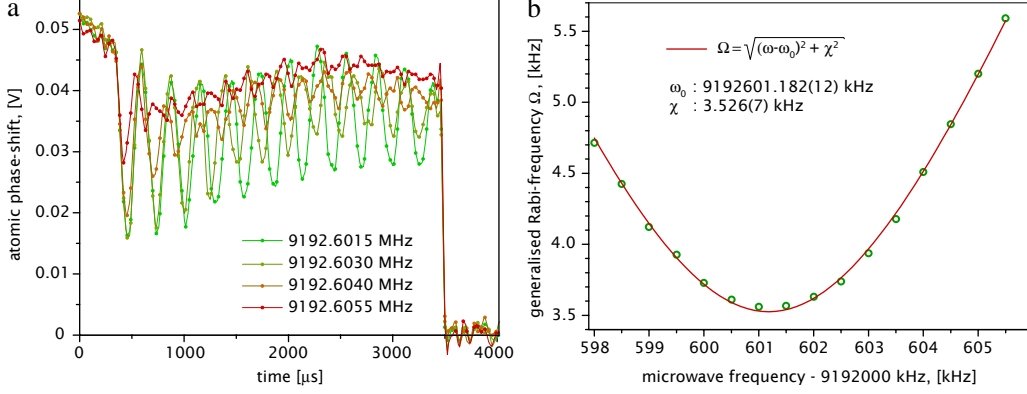


Figure 10.23: Rabi oscillation amplitude and frequency vs. microwave frequency. We use the synthesiser as source, with only the Narda amplifier and a the HP switch (see fig. 10.16). a) Example traces of Rabi oscillations observed in the $F = 4$ atomic phase-shift for different microwave drive frequencies $\omega_{\mu W}$. The microwave field is applied after $300 \mu s$ and in order to find the reference phase-shift the atomic sample is destroyed by resonant MOT cooling light after $3500 \mu s$. b) Plot of the Rabi oscillation frequency derived from a simple sine fit to the $F = 4$ phase-shift observed in a). The fit to $\Omega = \sqrt{(\omega_{\mu W} - \omega_0)^2 + \chi^2}$ gives a clock transition frequency of $\omega_0 = 2\pi \cdot 9192.601182$ MHz.

population oscillates during the time that the microwave field is present. The oscillations do not remove all atoms from $|F = 4\rangle$, since only atoms successfully pumped in to the $m_F = 0$ level interact with the microwaves. Thus the ratio of the Rabi-oscillation amplitude to the initial phase-shift from all atoms in the hyperfine level gives the fraction of atoms which are optically pumped. This fraction was used as a measure of the optical pumping efficiency in sec. 10.1.3. We expect the Rabi-oscillation amplitude and frequency to depend on the microwave frequency $\omega_{\mu W}$ according to eq. (10.8). From fig. 10.23a we confirm that the Rabi oscillation amplitude decreases as $\omega_{\mu W}$ is turned farther from the atomic resonance. At the same time, the Rabi oscillation frequency increases, and a plot of the Rabi oscillation frequency Ω vs. microwave frequency $\omega_{\mu W}$ is neatly fitted by a $\Omega = \sqrt{(\omega_{\mu W} - \omega_0)^2 + \chi^2}$ (see fig. 10.23b). The fitted resonance frequency $\omega_0 = 2\pi \cdot 9192.601182$ MHz agrees well with the initial estimate. The resonant Rabi frequency χ of $2\pi \cdot 3.5$ kHz, corresponding to a π -pulse duration of $t_\pi = 142 \mu s$, is rather slow. This prompted us to boost the microwave power by getting a switch with lower losses and later a second power amplifier (see sec. 10.2.2). Mostly we do not fine tune the $\omega_{\mu W}$ by observing Rabi oscillation amplitude or frequency, but instead rely on Ramsey spectroscopy discussed below.

We show one further characterisation of the Rabi oscillation, firstly because it is really neat, secondly because it confirms an assumption made in the theory of the microwave interaction, and finally because it will serve as a reference to explain an observation made below in sec. 12.6. By optical pumping and purification (see next section) the atoms are initially prepared in $F = 3, m_F = 0$ and for a given Rabi frequency χ we apply a π pulse ($t_\pi = 2\pi/\chi$) and observe the population transfer to $F = 4, m_F = 0$. On resonance, the whole population is

transferred but for detunings $\Delta_0 \neq 0$ the π pulse will only transfer a fraction of the atoms — this is evident from fig. 10.10. We usually say that the π pulse efficiency is reduced. On fig. 10.24 we plot the fractional population transfer as

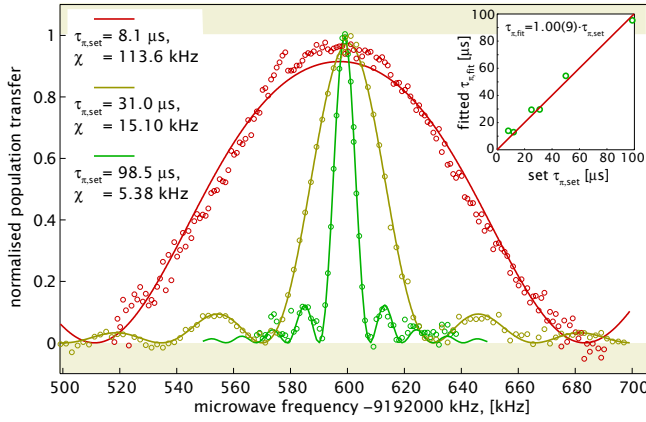


Figure 10.24: Rabi spectroscopy of microwave transition. We use the synthesiser as source, with the Narda amplifier, the HP switch and for the 8.1, 12, 25, and 50 μs π -pulse traces additionally the Kuhne power amplifier (see fig. 10.16). We vary the microwave field power by changing the synthesiser output power and then adjust the duration of the pulse so that on resonance it makes up a π -pulse.

With all atoms starting in $F = 3, m_F = 0$, we detune the microwave field and observe the normalised population transfer to $F = 4, m_F = 0$, which will be on the form $n_{\text{at},4}/n_{\text{at}} = \chi^2(\sin^2(\frac{1}{2}\Omega t_\pi))/\Omega^2$ c.f. eq. (10.8). We fit the data to this with χ , t_π , and ω_0 as free parameters curve. In the insert we plot the fitted $t_{\pi, \text{fit}}$ against the set $t_{\pi, \text{set}}$ and from a linear fit get a nice 1:1 correspondence.

a function of $\omega_{\mu\text{W}}$ for a few Rabi frequencies. The data is fitted with a slightly modified eq. (10.8) where the pulse duration t_π , the Rabi frequency χ and resonance frequency ω_0 are fitting parameters. As a check of consistency we see that there is a one-to-one correspondence between the set and fitted π -pulse durations (see inset in fig. 10.24).

The fact that the data fits with eq. (10.8) for all of the chosen Rabi frequencies bolsters the assumption in sec. 10.2.1 that decays do not play a role on any of the chosen time-scales. In other words the coherence time is (and better be) safely above the maximal $t_\pi \approx 100 \mu\text{s}$. The shape of the population transfer can be seen as measure of the frequency spectrum of the microwave pulse as seen by the atoms. In this sense, even an off-resonant atom will interact with the microwaves with some strength. The duration of the microwave pulse sets the width of the atomic frequency response $\sim 1/t_\pi$. This very much resembles the Fourier spectrum of the pulse as written in eq. (8.1) and shown on fig. 8.13 for the probe pulses. Hence we refer to this result as the microwave pulses being Fourier limited, though strictly the two concepts differ.¹¹ To restate what we said above, this also means that we do not resolve the natural line-width of the transition as it is much smaller than $1/t_\pi$. In sec. 12.6 we shall see that the width of the spectral response causes other transitions than the desired one to be addressed.

State purification (blow-away)

We make a short interjection on how to improve the ratio of the atomic population in the $m_F = 0$ level to that of the whole hyperfine level. As stated in sec. 10.1 there is no way to optically pump the entire population in to the $m_F = 0$ -level. Therefore, we need to selectively expel the atoms in $m_F \neq 0$. The procedure for

¹¹in the Fourier decomposition the minima occur at $\omega = n 2\pi/t_\pi$ whereas in the Rabi spectroscopy they appear at $|\omega_{\mu\text{W}} - \omega_0| = \sqrt{n(n+1/2)} 2\pi/t_\pi$, which differ by the factor $\sqrt{1+1/(2n)}$. For $n = 1$ this factor is $\sqrt{3}/2 = 0.86$, while for large n it becomes insignificant.

this is sketched in fig. 10.25. After the optical pumping the atomic population

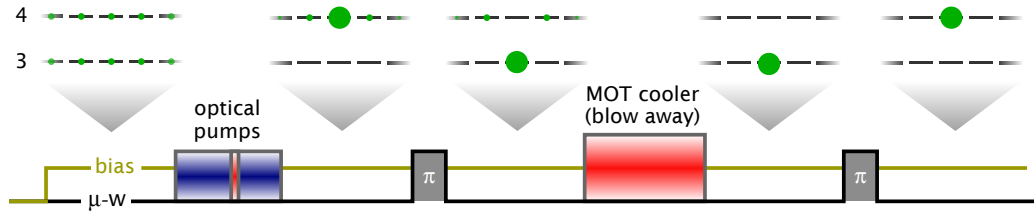


Figure 10.25: Optical pumping and state-purification by blow-away. The top part shows the distribution of the atomic population among the sub-levels of the hyperfine ground states while the lower part sketches the time sequence of the method. The optical pumping concentrates the evenly distributed population into the $|4,0\rangle$ level with some residual population in the nearby $|4, \neq 0\rangle$ levels, but no population in any $|3, m_F\rangle$ levels. A microwave π -pulse transfers the $|4,0\rangle$ population to $|3,0\rangle$, and subsequently a pulse of MOT cooler light on resonance with the $4 \rightarrow 5'$ cycling transition expels the $|4, \neq 0\rangle$ atoms from the FORT, and only the $|3,0\rangle$ population remains in the sample. If desired, a final π -pulse may transfer the atoms back to $|4,0\rangle$.

is distributed in a single hyperfine level — say $F = 4$ — with the bulk-part in the $m_F = 0$ level. With a microwave π -pulse we can selectively move the $m_F = 0$ population to the $F = 3$ hyperfine level, whereafter MOT cooling light on resonance heats $F = 4$ atoms out of the FORT — a process we have coined *blow-away*. Since the cooler is on the $F = 4 \rightarrow F' = 5$ cycling transition there is only a small probability for an atom to relax to the $F = 3$ ground level before it is expelled from the trap. The atoms remaining in the trap are now ideally all in the $F = 3, m_F = 0$ state. Experimentally, we can pump $> 99\%$ of the population into $m_F = 0$. In some cases even a small contamination of $m_F \neq 0$ atoms is disrupting, and in that case the blow-away sequence can be repeated a couple of times.

Ramsey spectroscopy

Next stage of the rocket is to investigate the Ramsey spectroscopy, focusing on frequency domain measurements. That is to say, we pick a Ramsey interrogation time τ_R and then vary the microwave frequency $\omega_{\mu w}$ to observe Ramsey fringes as given by eq. (10.12). On fig. 10.26a we show the Ramsey fringes for a number of τ_R . We use the fact that the overlap of the fringes for different τ_R only occurs at $\omega_{\mu w} = \omega_0$ as yet another way to locate the clock-frequency. The narrowing of the oscillation period for large τ_R manifests the increased sensitivity of the Ramsey fringe to the microwave detuning. We mark that the Ramsey fringe amplitude is not unity in all cases. There are two causes for this, the first one being atomic state decoherence, which explains why the amplitude (even on resonance) drops the larger τ_R (see theoretical curve in fig. 10.13). In sec. 10.2.4 we quantify this observation. Secondly, for large detunings the $\pi/2$ pulse efficiency drops considerably and it is no longer possible to transfer the population from one hyperfine state to the other. We notice a more surprising dependence of the resonance frequency ω_0 on Ramsey interrogation time (see fig. 10.26b). In fig. 10.26c we plot the resonance frequency as function of τ_R . We believe the shift of ω_0 to be related to the light-shift of the clock transition by the FORT, which consequently we set out to characterise.

FORT light shift of clock-transition Usually, we leave the FORT trapping laser on during the Ramsey sequence as we would otherwise lose atoms from the

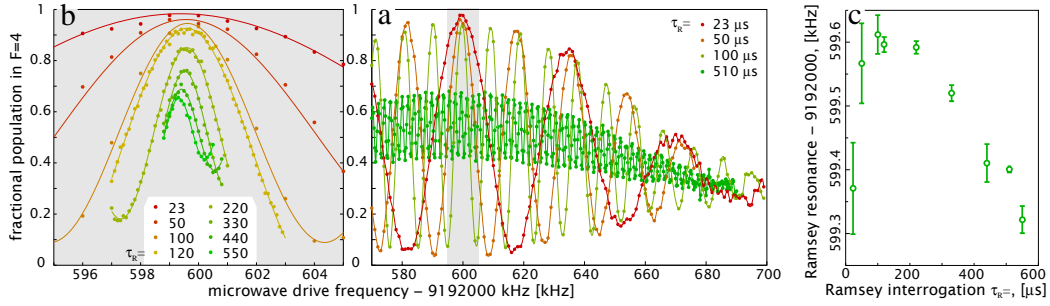


Figure 10.26: Ramsey fringes in frequency domain for different interrogation times. We use the synthesiser as source, with the Narda pre-amplifier, the HP switch and the Kuhne power amplifier (see fig. 10.16) giving a $\pi/2$ pulse duration $\tau_{\pi/2} = 4.15 \mu\text{s} \Leftrightarrow \chi = 2\pi 60 \text{ kHz}$. a) A wide frequency scan of the Ramsey fringes thus resembling fringes obtained from atomic microwave clock experiments [Vanier89]. b) A narrow frequency scan enables precise determination of ω_0 , however we note that ω_0 drifts slightly due to inhomogeneous FORT light-shift in combination with atomic motion. The lines show the fit of eq. (10.12) to the data (only data in a 40 kHz range around ω_0 is used for the fit). c) A plot of the fitted transition frequency ω_0 vs. the interrogation time τ_R highlights the drift of ω_0 .

trap. The longer τ_R the fewer atoms would remain and the worse the SNR of the fringe. For the sake of investigating the FORT laser differential light shift of the two hyperfine ground states we can naturally anyhow switch off the FORT laser during the Ramsey sequence. In fig. 10.27 we compare the Ramsey fringe with the FORT on and off. From the difference of the resonance frequency we extract

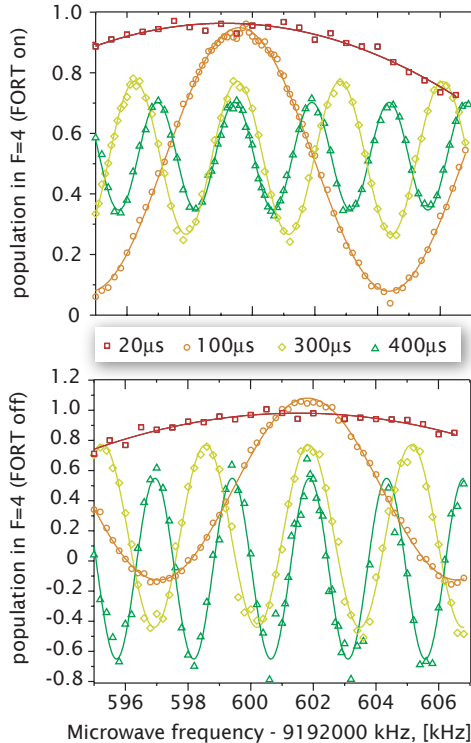


Figure 10.27: FORT light-shift of Ramsey fringe phase. We use the synthesiser as source, with the Narda pre-amplifier, the HP switch and the Kuhne power amplifier (see fig. 10.16). We perform frequency domain Ramsey spectroscopy for four different interrogation times either with the FORT laser on or off during the interrogation. The shift of resonance frequency equals the FORT light-shift $\delta\omega_{Is,FORT} = 2 \text{ kHz}$. In the upper plot (FORT on) the reduction of Ramsey fringe amplitude is due to decoherence. For the lower plot (FORT off) the reduction in amplitude is additionally affected by the loss of atoms during the off-time of the trap. Though, this is to some extent compensated by the normalisation to the remaining total atom number, the small population and thus size of the atomic phase-shift, means that the points scatter significantly more and some offsets in the signal cause the fringes to shift below zero atomic phase-shift.

the FORT light-shift of $\delta\omega_{Is,FORT} = 2 \text{ kHz}$. This shift is more or less insignificant compared to the spectral response for the π pulses fig. 10.24 but for any Ramsey type measurement it must be accounted for. There is little point in quantifying the shift e.g. in terms of FORT power, because $\delta\omega_{Is,FORT}$ heavily depends on the exact FORT and the probe modes. Thus, even if some approximate relationship between $\delta\omega_{Is,FORT}$ and the FORT power was established, an experimental determination of ω_0 would still be required. Alas, the location of the exact transition

frequency by the Ramsey method is a standard calibration step each time a measurement run is started. Because, of the ease of implementation and analysis we prefer the Ramsey method over the Rabi oscillation method for determining ω_0 .

We take the opportunity to elaborate on sec. 10.2.2 and establish the accuracy of the atomic frequency measurement in the absence of trap light-shift. The Ramsey fringes with the FORT off prescribe a Ramsey frequency of 9192601.8 kHz, and adding the known off-set of 30.841 kHz we arrive at a clock-frequency of 9192632.6 kHz. The discrepancy with the defined value is 0.87 kHz. Some of this is explained by the quadratic Zeeman shift, which for an 800 mGauss bias field (see fig. 10.22) amounts to only 0.27 kHz c.f. eq. (3.12). The remaining discrepancy of 0.6 kHz is probably due to imperfect estimation of the resonance frequency in the fit – having the trap off during the Ramsey interrogation causes a big loss in contrast of the fringe.

We return to the shifting light shift observed in fig. 10.26b+c. With some good will, a similar effect may be seen on fig. 10.27a while being absent on fig. 10.27b. We attribute the changing shift to the movement of the atoms within the FORT. We recall that the FORT light shift is inhomogeneous. For short τ_R compared to the trap oscillation period, the atoms do not have time to move significantly inside the FORT potential and the atoms probed have been in the same position in the FORT the whole time. For longer τ_R the atoms will have moved about and sampled regions of different $\delta\omega_{Is,FORT}$. The apparent increase of $\delta\omega_{Is,FORT}$ with time indicates that the transverse mode of the probe is not perfectly aligned to the FORT mode¹² or the atomic sample is slightly displaced from the FORT waist and thus moves longitudinally. The time-scale of the light-shift drift on fig. 10.26c agrees well with the transverse oscillation period of ≈ 0.5 ms found in sec. 11.2.1¹³. We rest the case for the FORT light shift here, but take it as a warm-up for sec. 11.1 where we shall be confronted with a clear effect of the *probe* light-shift coupled with atomic motion.

10.2.4 Relationship with coherence measurements

The microwave interaction is essential for the state preparation, but as seen in the preceding sections also reveals a great deal of information about the atomic state. In the following sections we will use the Rabi and Ramsey oscillation measurements to characterise the time-scales that the sample maintains certain characteristics from sub-level population to state coherence.

Sub-level population lifetime - T_1 time

The atoms optically pumped to $F = 4, m_F = 0$ may decay to other m_F levels in either hyperfine level or to the $m_F = 0$ of the $F = 3$ level. Since the former does not interact resonantly with the microwaves and the latter is out of phase by π on the Bloch-sphere, both cause a reduction of the Rabi oscillation amplitude. Hence, the lifetime of the $m_F = 0$ magnetic sub-level population — the T_1 time — is found by measuring the decrease of Rabi oscillation amplitude as the microwave is applied with increasing delay. On fig. 10.28a we show a few examples of the Rabi oscillations for different delays between the optical pumping and the microwave field application. The decay of the initial offset (total population of all $F = 4$ sub-levels) and the decay of the Rabi fringe amplitude (population of

¹²If the probe beam is well mode matched with the FORT the probe always detects the atoms in the centre of the trap where the FORT intensity and thus $\delta\omega_{Is,FORT}$ is large. Hence, total ensemble

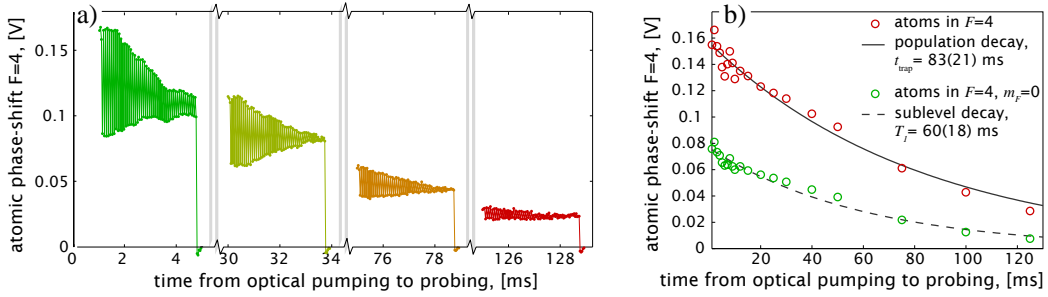


Figure 10.28: T_1 time for decay of sub-level population measured as decay of Rabi fringe amplitude. We use the synthesiser as source, with the Narda pre-amplifier, and the HP switch (see fig. 10.16) giving a Rabi frequency of $\chi = 2\pi 13.3$ kHz. a) Sample traces of Rabi oscillations in the $F = 4$ population observed at different delays w.r.t to the end of the optical pumping stage. The probing is done with a train of 100 pulses of $1.5 \mu\text{s}$ duration and spaced by $37.7 \mu\text{s}$. After the first 3 probe pulses the microwave field is turned on continuously so that the measurement is thus done on the state during its evolution. The probe pulse separation is adjusted so that probing occurs when the $m_F = 0$ atoms pass the upper or lower hyperfine levels where the probe light shift has no effect (see box 11.1). The decay of the individual Rabi oscillation traces is due to scattering of probe photons. b) Population in $|4, m_F\rangle$ (red circles) measured as the average phase-shift of the first two probe pulses and fit yielding a 83 ms lifetime. Population in $|4, 0\rangle$ measured as the difference between the first 3 top and bottom phase-shifts of the Rabi oscillations. The T_1 lifetime is fitted to 60 ms.

$F = 4, m_F = 0$) are plotted on fig. 10.28b. The exponential decay fits show a hyperfine level population decay time of 83 ms and a T_1 time of 60 ms. Since, the decay to another hyperfine level necessarily also changes the sub-level the T_1 time should indeed be the smaller of the two. The fact that it is not much smaller indicates that most of the T_1 losses are due to hyperfine changing events such as background gas collisions. The trap lifetime was found to be somewhat longer $T_{\text{FORT}} = 300$ ms, indicating that not all hyperfine changing events cause the atom to be expelled from the FORT. Thus, the hyperfine population decay is very likely aided by leak light from the probes, MOT, and/or optical pumping. This hypothesis is backed by the fact that the T_1 time improved when we inserted RF-switches to the pulsing AOM input and shutters in to all the relevant beam paths.

Dephasing time - T_2 times

To extract the T_2 coherence time we analyse the decay of the Ramsey fringe amplitudes in fig. 10.26. These are plotted as a function of τ_{R} in fig. 10.29 and fitted to an exponential decay. Since, the state is only sensitive to decoherence while in the superposition state, the interrogation time is the relevant time factor and we infer $T_2 = 0.4$ ms. The conjecture in sec. 3.7.1 that $T_2 < T_1$ surely holds. Assuming irreversible decay is much slower ($T_2' \ll T_2^* \Leftarrow T_2 \approx T_2'$) we use eq. (10.20) to estimate the sample temperature of $T = 220 \mu\text{K}$, which is on the high end compared with the $\sim 60 \mu$ we got in sec. 9.2.3. The discrepancy may be due to leaking probe light.

The T_2 is a measure of both reversible and irreversible state dephasing. As said in sec. 10.2.1 we can eliminate the effect of reversible dephasing by means of a spin-

light-shift should decrease as atoms probe regions of the FORT with lower $\delta\omega_{Is, \text{FORT}}$.

¹³for the reasons explained in sec. 9.2.2 we put more faith in the radial trap frequency estimated in sec. 11.2.1 than that found in sec. 9.2.2.

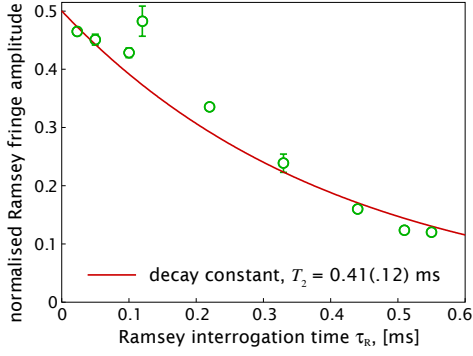


Figure 10.29: T_2 time measured as decay of Ramsey fringe amplitude with increasing interrogation time τ_R . We use the synthesiser as source, with the Narda pre-amplifier, the HP switch and the Kuhne power amplifier (see fig. 10.16). The plot is based on the data and fits shown in fig. 10.26a+b. The exponential decay fit gives $T_2 = 0.41$ ms.

echo pulse in the Ramsey sequence. We perform the spin-echo measurement in the time domain and pick a suitable microwave detuning, which allows us to see at least a couple of full oscillations within the T_2 decay time. Changing, the interrogation time $\tau_{R,1}$ we are able to observe the changing amplitude of the Ramsey spin-echo fringe centred on $\tau_{\mu,2} = 2\tau_{R,1} + \tau_\pi$ (see fig. 10.30). We fit the

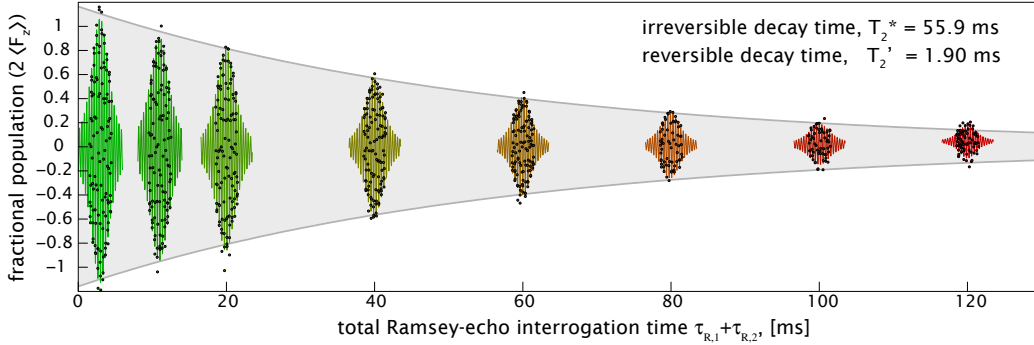


Figure 10.30: T_2' (reversible dephasing) and T_2^* (irreversible dephasing) times measured as decay of Ramsey spin-echo fringe amplitudes. We use the synthesiser as source, with the Narda pre-amplifier, the HP switch and the Kuhne power amplifier (see fig. 10.16). The microwave detuning is set to $\Delta_0 = 3$ kHz. For 8 different $\tau_{R,1}$ we probe the $F = 4$ population over a scan of $\tau_{R,2}$ over $\tau_{R,1} \pm 1$ ms. We fit the Ramsey spin-echo fringe with $A_0 \alpha(\tau_R, T_2') (1 - \cos[(\Delta_0 + \delta_\Delta)\tau_R + \kappa(\tau_R, T_2')])$ c.f. eq. (10.19). From these fits we extract the $T_2' = 1.90$ ms. A_0 is a fitting parameter that accounts for irreversible dephasing and fitting A_0 to an exponential decay, c.f. eq. (10.21), we get $T_2^* = 55.9$ ms. The exponential T_2^* decay is indicated by the grey envelope.

Ramsey echo-fringes with eq. (10.19) and thus get an estimate of a number of parameters. The decay of the envelope of each individual Ramsey spin-echo fringe is caused by the reversible dephasing, for which the average over all the fitted fringes is $T_2' = 1.9$ ms. The value of the peak amplitude is related to the time-scale of irreversible dephasing fitting these to an exponential decay c.f. eq. (10.21) we estimate $T_2^* = 55.9$ ms. This value is not far below T_1 time of 60 ms, whereby we may conclude that irreversible decoherence is caused by the same process that induces population decay. We also note that the total dephasing time $T_2 = (1/T_2' + 1/T_2^*)^{-1} = 1.84$ ms is in acceptable agreement with the estimate of $T_2 = 0.41$ ms from the pure Ramsey method. Again the sample temperature is estimated from eq. (10.20) to be $T = 59 \mu\text{K}$, which is in perfect agreement with $\sim 60 \mu$ from sec. 9.2.3. We note that the T_2' and thus the temperature is the same for all the fringes and thus does not seem to change with loading time. We believe that the variations in the measured temperatures from experiment to experiment is partly due to “mood swings” of our cooling laser, but probably even more due to different cooling efficiencies for large and small initial MOTs [Drewsen94]. This is, however, not a proposition we have

investigated in detail.

To conclude the treatment of decoherence/dephasing times we have established that T_1 decay and irreversible T_2 decay are of little importance on time-scales below 1 ms. If we require less than 1% (2%) irreversible dephasing we must perform all measurements within ~ 0.5 ms (~ 1 ms). Reversible dephasing is relevant even on short time-scales, but we show that we can efficiently compensate them by spin-echo techniques. Without these, the benchmark of 1% (2%) T_2' dephasing would entail all measurements to be performed within ~ 10 μ s (~ 20 μ s), something that is not realistic. The short T_2' time is a consequence of the FORT trapping and in presents a technical limitation to the usability of the QND measurements characterised in the next chapter. On the other hand, the principle of the QND measurements is not rocked by the FORT dephasing. The dephasing could of course be eliminated by turning of the FORT during the measurement, but this would seriously limit the trap life-time and not add anything to the achievable interrogation time/frequency sensitivity. A better approach would be to pick the FORT wavelength and polarisation so that it shifts both ground states by an equal amount [Katori99, McKeever03, Targat06, Ludlow06, Choi07, Ludlow08, Flambaum08, Rosenbusch09]¹⁴ At this wavelength, coined the *magic wavelength*, and/or polarisation setting the clock transition is not light-shifted and thus also the inhomogeneous and reversible dephasing would disappear. In both [Choi07, Flambaum08, Rosenbusch09] that deal specifically with the problem of cancelling the differential light shift in the hyperfine ground levels of Cs the conclusion seems to be that for the $0 \rightarrow 0'$ transition there exists no setting that will eliminate the differential light-shift. For other clock-like transitions i.e. on the form $|3, m_F = \alpha\rangle \rightarrow |4', m'_F = -\alpha\rangle$ [Flambaum08] demonstrates that when applying a magnetic field (as we already do) nearly perpendicular to the k-vector of a circularly polarised FORT beam it is possible to cancel the light shift of that transition. On the other hand in [Schleier-Smith08] they claim to have done exactly what we want, namely eliminating the differential light shift on the $0 \rightarrow 0'$ clock-transition, albeit in Rb. With all this confusion the most fruitful course of action would probably be to simply try out changing the FORT polarisation and observing the resulting light-shift on the Ramsey fringes.

¹⁴Most of these papers actually deal with the concept of magic wavelength w.r.t the ground and excited levels i.e. where these two levels are shifted by the same amount. This is relevant for optical clocks.

Atomic interaction and characterisation

At last we have reached the point where we study the interaction of the probe light with the atomic sample. For us to be able to interpret the results of the QND interaction faithfully we must first understand the interplay between the light and the atoms and amend a number of defects that would disturb the QND measurements. The defects are predominantly related to the light shift term in the interaction Hamiltonian eq. (4.9). We also seek to characterise the intrinsic side-effect of the probing, namely the decoherence caused by real excitations. As these degrade the non-demolition nature of our measurement and limit the achievable spin-squeezing it is important that we are able to measure the decoherence very precisely. Especially, we must be able to distinguish decoherence from the dephasing caused by the light-shift. To that end we make use of the fact that dephasing by the probe, as it is due to spatial inhomogeneity, is in principle reversible by spin-echo techniques. The reversibility is, unluckily, limited by the atomic motion and we are prompted to find ways to eliminate the light-shift all-together.

Before diving in to the imperfections of the interaction we take the chance in fig. 11.1 to present what the dispersive interaction does enable us to measure *even* with the influence of the light-shift. By using very low probe powers $0.2 \mu\text{W}$

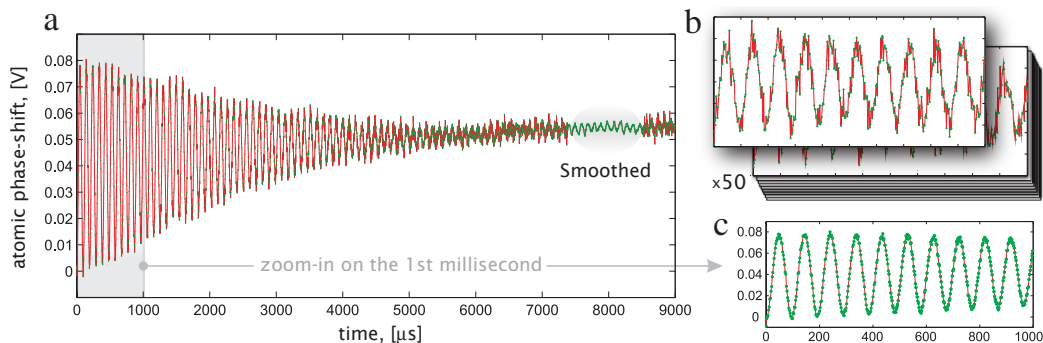


Figure 11.1: Long time non-destructive observation of Rabi oscillations, using $1 \mu\text{s}$ pulse of $0.2 \mu\text{W}$ ($N_{\text{ph}} = \sim 10^5$) with $2.3 \mu\text{s}$ repetition period. a) Average over 50 experimental cycles. b) Single cycle data for the first ms. c) Averaged data for the first ms.

and short pulse-lengths $\approx 1 \mu\text{s}$ we were able to probe the Rabi oscillating atomic state for several ms with almost 4000 pulses. The pulse repetition period is $2.3 \mu\text{s}$

so that the each Rabi cycle is probed nearly 50 times. Even without averaging over experimental cycles the Rabi oscillations are clear during the first couple of ms and would enable the determination of the Rabi frequency. This result is the central result of [Windpassinger08c].

11.1 Probe light shift observations

We begin our treatment with a short recap of the probe light-shift in order also to introduce a few relevant parameters. We learnt in eq. (4.23) that the probe light-shift induces a rotation of the pseudo-spin around the z -axis

$$\mathbf{M}_{\phi_{\text{ls}}} = \mathbf{M}_{\mu w}(t_p, 0, \Omega_{\text{at}}) = \begin{pmatrix} \cos \phi_{\text{ls}} & \sin \phi_{\text{ls}} & 0 \\ -\sin \phi_{\text{ls}} & \cos \phi_{\text{ls}} & 0 \\ 0 & 0 & 1 \end{pmatrix}. \quad (11.1)$$

The middle expression illustrates the before mentioned equivalence of the light-shift to a microwave detuning eq. (10.11). By eq. (4.24) or equivalently eq. (5.21) the phase-shift assuming $\langle \hat{s}_z \rangle = 0$ is

$$\phi_{\text{ls}}(\mathbf{r}) \equiv \langle \tilde{\phi}_{\text{at}}(\mathbf{r}) \rangle = n_{\text{ph}} t_p 2\mathcal{K}_1(\mathbf{r}) = \phi_{\text{ls},0} e^{-2r^2/w_p^2} \quad (11.2)$$

where $\phi_{\text{ls},0} = 2I_0 t_p \mathcal{K}_1$ is the maximal light shift (which is in the probe centre), $\mathcal{K}_1 = \sum_{e=2(3)}^{5(4)} [\mathcal{K}_{4e} - \mathcal{K}_{3e}]$ is the atomic-coupling constant, I_0 is the peak probe intensity, and t_p is the pulse length. The above expression underlines the spatial dependence of the light-shift magnitude. For the present, we considering monochromatic probe light, but the extension to dichromatic light follows easily by substituting \mathcal{K}_1 by either \mathcal{K}_{21} or \mathcal{K}_{22} (see sec. 5.3.2).

If the probe-light shift were the same over the whole atomic ensemble it would be a nuisance perhaps affecting the classical noise infused in to the equatorial pseudo-spin components, but it would not make up a fundamental problem. As it happens, the probe dimensions are similar to those of the sample and the light-shift will be anything but homogeneous. Using eqs. (3.7 and 3.10) we get the effective ensemble pseudo-spin as

$$\begin{aligned} \langle \hat{\mathbf{F}} \rangle &= \int_{\mathbb{R}^3} \left[\mathbf{M}_{\phi_{\text{ls}}} \langle \hat{\mathbf{f}}^{(1)}(0) \rangle \right] n_{\text{at}}(\mathbf{r}) \mathcal{U}(\mathbf{r}) d^3r \\ &= 2\pi l_a \int_0^\infty \left[\mathbf{M}_{\phi_{\text{ls}}} \langle \hat{\mathbf{f}}^{(1)}(0) \rangle \right] \mathcal{N}_0 e^{-2r^2/w_a^2} e^{-2r^2/w_p^2} r dr \\ &= \frac{\pi l_a \mathcal{N}_0 w_p^2}{2\phi_{\text{ls},0}^{(1+r_w)}} \int_0^{\phi_{\text{ls},0}} \left[\mathbf{M}_{\phi_{\text{ls}}} \langle \hat{\mathbf{f}}^{(1)}(0) \rangle \right] \phi_{\text{ls}}^{r_w^2} d\phi_{\text{ls}} \end{aligned} \quad (11.3)$$

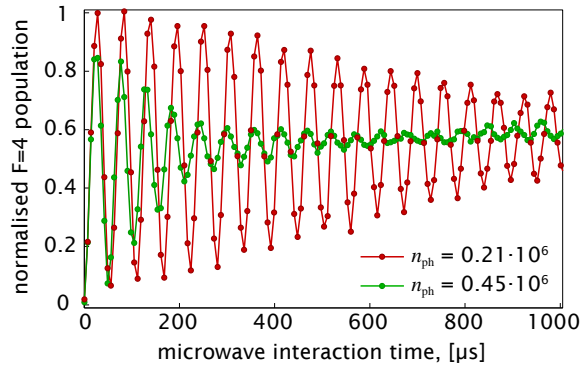
where we conveniently express the initial spatially independent pseudo-spin state in terms of the single atom operator $\hat{\mathbf{f}}^{(1)}$ (refer to sec. B) and incorporate the probe to sample waist ratio r_w . Eq. (11.3) reveals the fortunate circumstance that it suffices to integrate over light-shifts instead of the radial coordinate. The expression states that the light-shift transformation must be integrated with a weighing factor $\phi_{\text{ls}}^{r_w^2}$ over all shifts from zero to the maximal shift $\phi_{\text{ls},0}$. For a large probe waist compared to that of the sample, $r_w \gg 1$, the light-shift values close to $\phi_{\text{ls},0}$ receive a strong weight, in that all atoms are located in the centre of the probe-beam. In the opposite case, $r_w \ll 1$, the probe samples the centre of the sample and atoms within a region of similar density experience from zero to the maximal light-shift. Thus, the weighing is almost constant for all ϕ_{ls} . The case of

$r_w = 1$, gives a linear dependence of the weighing. Altogether, depending on the distribution of light-shifts the magnitude of the effective ensemble pseudo-spin will be reduced. As we shall see in the upcoming sections, this dephasing of the atomic state reduces the contrast and thus the useful application of any sort of coherent evolution of the atomic state e.g. as in Rabi oscillations or Ramsey fringes. We now consider the specific measurement sequences in detail.

11.1.1 Rabi oscillations

First we look at the effect of the probe light shift on the evolution of the Rabi oscillations. In a chronological perspective, the perturbation of the Rabi oscillating atomic state when we tried to observe it gave us the first indication of the rather serious effect that the light-shift has on our system (see fig. 11.2). Here we

Figure 11.2: Probe light-shift perturbation of Rabi oscillations. Rabi frequency $|\chi| = 2\pi 17$ kHz. Traces made from 50 averages using 145 pulses of $0.5 \mu\text{s}$ duration separated by $7 \mu\text{s}$. A two-fold increase of the probe power has a dramatic effect on the state evolution not explainable by spontaneous emission. Moreover, the high probe power trace shows evidence of a revival of the oscillations, not compatible with irreversible decoherence.



discuss a very typical scenario where we prepare the collective atomic state in the $|3, 0\rangle$ level, turn on a continuous microwave field and observe the population in $|4, m_F\rangle$ at some intervals (see fig. 11.3). In essence we monitor the state during its evolution under the influence of the microwaves, however, in the following we will split the effect of the microwaves and the probing as if they appear interchangeably. This, is not a serious limitation in as long as one effect happens on a very short time-scale compared to that of the other. In our case the probe pulses are a few micro-seconds long, which is much shorter than the typical Rabi period of around $50 \mu\text{s}$.

Theoretical evolution

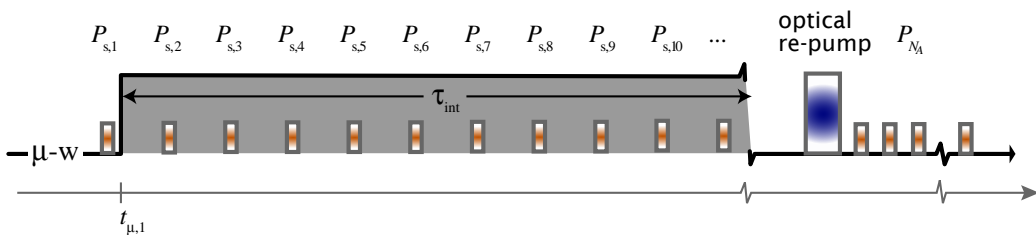


Figure 11.3: Sequence for Rabi oscillations of atomic state driven by continuous microwave field and perturbed by monochromatic probe pulse train.

To merge the light-shift effect with the atomic evolution in a microwave field we take the rotation matrix in eq. (10.4) and simplify to the case of a resonant

microwave field

$$\mathbf{M}_{\mu w}(\tau_{\mu w}, |\chi|, 0) = \begin{pmatrix} 1 & 0 & 0 \\ 0 & \cos(|\chi|\tau_{\mu w}) & \sin(|\chi|\tau_{\mu w}) \\ 0 & -\sin(|\chi|\tau_{\mu w}) & \cos(|\chi|\tau_{\mu w}) \end{pmatrix}. \quad (11.4)$$

We will always commence the microwave interaction when the pseudo-spin $\hat{\mathbf{f}}(0)$ is aligned to one of the poles of the Bloch-sphere, whereby, as asserted in sec. 10.2.1, we can overlook the complex phase of the Rabi frequency χ . The combined effect on the pseudo-spin of a microwave pulse of duration $\tau_{\mu w}$ followed by a probe pulse of duration t_p is summarised by

$$\hat{\mathbf{f}}(t_f) = [\mathbf{M}_{\phi_{ls}} \mathbf{M}_{\mu w}(\tau_{\mu w}, |\chi|, 0)] \hat{\mathbf{f}}(0) \quad (11.5)$$

where t_f is the time that the probe-pulse ends and t_p is related to ϕ_{ls} by eq. (11.2). A number of k subsequent microwave and probe pulses will result in the combined matrix

$$\overline{\mathbf{M}}_{\mu w, p}(\tau_{\mu w}, |\chi|, \phi_{ls}, k) = [\mathbf{M}_{\phi_{ls}} \mathbf{M}_{\mu w}(\tau_{\mu w}, |\chi|, 0)]^{\otimes k} \quad (11.6)$$

When depicted on the Bloch-sphere the pseudo-spin evolution consists of series of alternating rotations around the x -axis and the z -axis as shown on fig. 11.4a. When plotting $\langle \hat{f}_z \rangle$ we see a clear resemblance with the Rabi oscillations for an

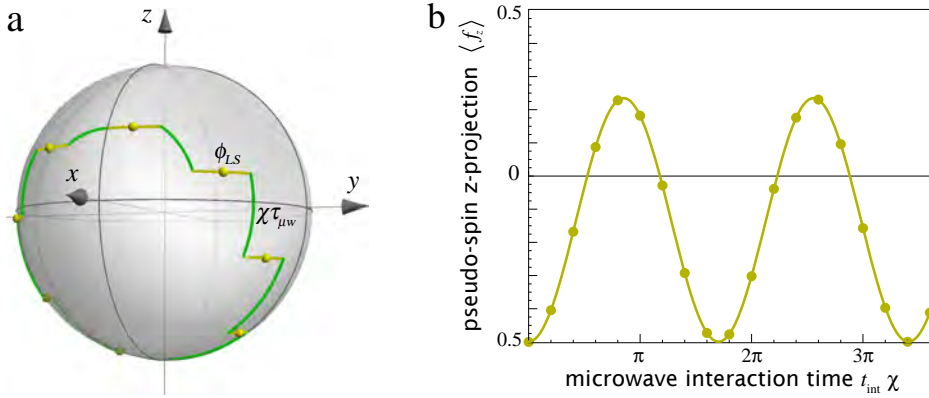


Figure 11.4: Theoretical pseudo-spin evolution during probed Rabi oscillations. a) On the Bloch-sphere, the resonant microwave-field drives Rabi-oscillations (green segments), which are interrupted/perturbed by the light-shift of the probe pulses. The probe $\langle \hat{f}_z \rangle$ measurement outcome are indicated as yellow dots on the Bloch-sphere and plotted on b) as a function of time.

off-resonant microwave field (compare fig. 11.4b and fig. 10.10b). As we show in Box 11.1 the evolution described by $\overline{\mathbf{M}}_{\mu w, p}(\tau_{\mu w}, |\chi|, \phi_{ls}, 1)$ and the microwave $\overline{\mathbf{M}}_{\mu w}(\tau_{\mu w}, |\chi|, \Delta_0)$ (see eq. (10.4)) are, indeed, to first order the same.

So far, the norm of $\langle \hat{\mathbf{f}} \rangle$ is preserved, but this changes as we consider the whole atomic ensemble where atoms located at different radial positions within the probe beam experience different light-shifts. In a measurement we observe the effective ensemble operator \hat{F}_z . Thus, we need to compute the evolution of the effective ensemble pseudo-spin, and by the same method as applied in eq. (11.3)

$$\begin{aligned} \langle \hat{\mathbf{F}}(t_f^{(k)}) \rangle &= \int_{R^3} \left[\overline{\mathbf{M}}_{\mu w, p}(\tau_{\mu w}, |\chi|, \phi_{ls}, k) \langle \hat{\mathbf{f}}^{(1)}(0) \rangle \right] n_{at}(\mathbf{r}) \mathcal{U}(\mathbf{r}) d^3 r \\ &= \frac{\pi l_a \mathcal{N}_0 \omega_p^2}{2\phi_{ls,0}^{(1+r_w)}} \int_0^{\phi_{ls,0}} \left[\overline{\mathbf{M}}_{\mu w, p}(\tau_{\mu w}, |\chi|, \phi_{ls}, k) \langle \hat{\mathbf{f}}^{(1)}(0) \rangle \right] \phi_{ls}^{r_w} d\phi_{ls} \quad (11.8) \end{aligned}$$

Box 11.1: Equivalence between microwave detuning and average light-shift

Looking at fig. 11.4 we surmise that for two probe pulse sequences, where one has half the probe power but twice the repetition period, the pseudo-spin evolution will be the same. What matters is the average probe power over the whole repetition period. This spurs the definition of an effective light-shift average detuning

$$\bar{\Delta}_{\text{ls}} \equiv \frac{\phi_{\text{ls}}}{\tau_{\mu\text{w}}} = \Omega_{\text{at}} \frac{t_p}{\tau_{\mu\text{w}}} \quad (11.7)$$

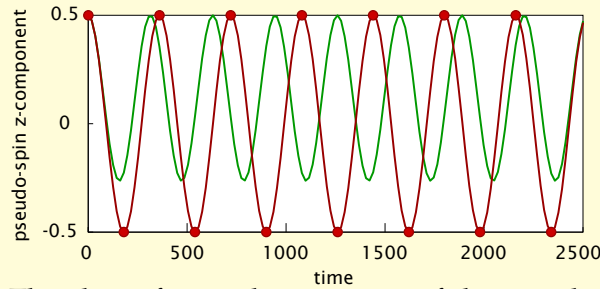
Substituting $\bar{\Delta}_{\text{ls}} \tau_{\mu\text{w}}$ for ϕ_{ls} in the microwave-probe evolution matrix and making a polynomial expansion of the sine and cosine factors to first non-zero order we get

$$\begin{aligned} & \bar{\mathbf{M}}_{\mu\text{w},p}(\tau_{\mu\text{w}}, |\chi|, \bar{\Delta}_{\text{ls}}, 1) \\ & \approx \begin{pmatrix} 1 - (\bar{\Delta}_{\text{ls}} \tau_{\mu\text{w}})^2 & \bar{\Delta}_{\text{ls}} \tau_{\mu\text{w}} [1 - (|\chi| \tau_{\mu\text{w}})^2] & \bar{\Delta}_{\text{ls}} |\chi| \tau_{\mu\text{w}}^2 \\ -\bar{\Delta}_{\text{ls}} \tau_{\mu\text{w}} & [1 - (\bar{\Delta}_{\text{ls}} \tau_{\mu\text{w}})^2] [1 - (|\chi| \tau_{\mu\text{w}})^2] & [1 - (\bar{\Delta}_{\text{ls}} \tau_{\mu\text{w}})^2] |\chi| \tau_{\mu\text{w}} \\ 0 & -|\chi| \tau_{\mu\text{w}} & 1 - (|\chi| \tau_{\mu\text{w}})^2 \end{pmatrix} \end{aligned}$$

This expression is to be compared with the off-resonant microwave evolution matrix eq. (10.4), which after polynomial expansion reads

$$\begin{aligned} & \bar{\mathbf{M}}_{\mu\text{w},p}(\tau_{\mu\text{w}}, |\chi|, \Delta_0) \\ & \approx \begin{pmatrix} 1 - (\Delta_0 \tau_{\mu\text{w}})^2 & \Delta_0 \tau_{\mu\text{w}} & \Delta_0 |\chi| \tau_{\mu\text{w}}^2 \\ -\Delta_0 \tau_{\mu\text{w}} & 1 - (\Delta_0 \tau_{\mu\text{w}})^2 - (|\chi| \tau_{\mu\text{w}})^2 & |\chi| \tau_{\mu\text{w}} \\ \Delta_0 |\chi| \tau_{\mu\text{w}}^2 & -|\chi| \tau_{\mu\text{w}} & 1 - (|\chi| \tau_{\mu\text{w}})^2 \end{pmatrix} \end{aligned}$$

To first order in $|\chi|$ and $\Delta_0 \leftrightarrow \bar{\Delta}_{\text{ls}}$ the matrices now agree. Additionally, several elements agree even to second order. In sum, it is not surprising that the microwave-probe evolution closely mimics the Rabi oscillations.



Evolution of $\langle \hat{f}_z \rangle$ described by (red) $\bar{\mathbf{M}}_{\mu\text{w},p}(\tau_{\mu\text{w}}, |\chi|, \bar{\Delta}_{\text{ls}}, k)$ when probing only as $\langle \hat{f}_z \rangle$ passes the Bloch-vector poles and (green) $\bar{\mathbf{M}}_{\mu\text{w},p}(\tau_{\mu\text{w}}, |\chi|, \bar{\Delta}_{\text{ls}})$ corresponding to the influence of microwave field detuned by $\bar{\Delta}_{\text{ls}}$.

The above figure shows a case of the two descriptions being vastly different. Using a resonant microwave field and probing only at integer increments of τ_{π} when the pseudo-spin vector passes the Bloch-sphere poles means that the evolution of $\langle \hat{f}_z \rangle$ is unaffected by the probe light-shift. In particular the Rabi frequency remains the same. If we set a light-shift of $\phi_{\text{ls}} = 100^\circ = 5\pi/9$ and we get $\bar{\Delta}_{\text{ls}} = 5\pi/(9\tau_{\pi})$ and for the off-resonant an generalised Rabi frequency of $\Omega = \sqrt{106}\pi/(9\tau_{\pi}) \approx 8\pi/7$, wherefore the off-resonant Rabi oscillations re-phase with the pole-probed oscillations after 8 periods.

This prescribes a rather complex evolution of the pseudo-spin, with change in the oscillation frequency and the possibility of revivals of the oscillation amplitude. Fortunately, the evolution is determined by only two free parameters, the maximal light-shift $\phi_{ls,0}$ and the probe beam to atomic sample waist ratio $r_w = w_p^2/w_a^2$, which are easily implemented as fitting parameters to experimental data.

Experimental observations

We now come to the point where we see if the theoretical models are able to explain the observed data. The results shown here are covered in the paper [Windpassinger08b]. In fig. 11.5a we plot the measured $F = 4$ population

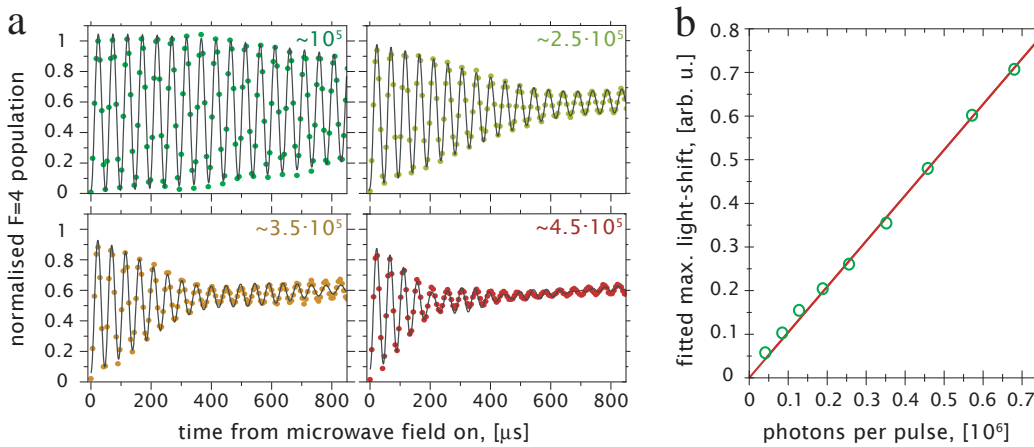


Figure 11.5: Probe light shift perturbation of Rabi oscillations. The unperturbed Rabi frequency is $|\chi| = 2\pi 17$ kHz. a) Rabi oscillation of the $F = 4$ population for different $4 \rightarrow 5'$ probe powers. The 145 probe pulses are $0.5 \mu s$ long, separated by $7 \mu s$ and the traces are averages of 50 experimental runs. The combined effect of the microwave field and the probe light-shift is fitted by eq. (11.8) (grey curves). b) the fitted $\phi_{ls,0}$ vs. the photon-number per pulse as deduced from the power reference detector signal.

normalised to the total number of atoms as function of the time the atoms have interacted with a resonant microwave field. For the different probe-powers used in the four traces the state evolution changes significantly as expected. To fit the data we slightly modify the theoretical expression in eq. (11.8) to account for irreversible, homogeneous dephasing mainly caused by spontaneous scattering of probe photons. Since, we probe with a monochromatic probe, spontaneous photon scattering will tend to bias the Rabi-oscillations towards the $F = 4$ level as the atoms decay in to $|4, m_F \neq \pm 1\rangle$ sub-levels. As these atoms no longer couple to the microwave radiation they remain and are detected in the $F = 4$ manifold. The best fits, shown as grey curves in fig. 11.5a, are very satisfactory. The fitted probe to sample waist ratio is $r_w = 0.8$, which is entirely reasonable. On fig. 11.5b The maximal light-shift value is plotted against the photon-number per pulse. The scaling of the light-shift is clearly linear, as anticipated. We will not elaborate further on the light-shift influence on the Rabi oscillation, as this is not really directly applicable to the effect that we would see in a QND measurement. Instead, we turn to a new section...

11.1.2 Ramsey fringes

The perturbation of the Rabi fringes do not yield a particularly intuitive measure for the exact magnitude and inhomogeneity of the probe light shift. Resorting to Ramsey spectroscopy in the frequency domain provides a much clearer relation between observable parameters and the characteristics of the light shift. To be specific, the offset of the resonance frequency is exactly equal to the light-shift and the decrease of Ramsey fringe amplitude is proportional to the light-shift inhomogeneity. The treatment found here is to a large extent corresponding to that of [Windpassinger08b].

Theoretical evolution

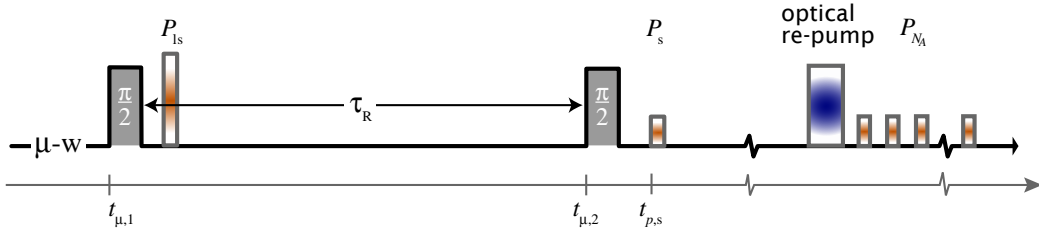


Figure 11.6: Ramsey spectroscopy experimental sequence with monochromatic probe pulse light-shift.

We consider the Ramsey sequence depicted in fig. 11.6 where a probe pulse is fired right after the first $\pi/2$ pulse. As before, we start with expressing the transformation matrix for the present case. The only difference between this and the Ramsey sequence in eq. (10.10) is the addition of a light-shift matrix eq. (11.1) so that

$$\overline{\mathbf{M}}_{\text{R,ls}}(\tau_{\text{R}}, \chi, \Delta_0, \phi_{\text{ls}}) = \mathbf{M}_{\mu\text{w}, \frac{\pi}{2}} \mathbf{M}_{\mu\text{w}}(\tau_{\text{R}}, 0, \Delta_0) \mathbf{M}_{\phi_{\text{ls}}} \mathbf{M}_{\mu\text{w}, \frac{\pi}{2}}$$

where we use the short-hand notation $\mathbf{M}_{\mu\text{w}, \frac{\pi}{2}} \equiv \mathbf{M}_{\mu\text{w}}(\tau_{\frac{\pi}{2}}, \chi, 0)$ and neglect any effect of the microwave being off resonant during the $\pi/2$ pulses (i.e. $|\chi| \gg \Delta_0$). Applying the transformation to the initial pseudo-spin at the Bloch-sphere south pole, $\langle \hat{f}(0) \rangle = -n_{\text{at}}/2 \mathbf{z}$, we compute the output value

$$\langle \hat{f}(t_{\text{p,s}}) \rangle = \overline{\mathbf{M}}_{\text{R,ls}}(\tau_{\text{R}}, \chi, \Delta_0, \phi_{\text{ls}}) \left[-\frac{n_{\text{at}}}{2} \mathbf{z} \right] = \frac{n_{\text{at}}}{2} \begin{pmatrix} \sin(\phi_{\text{ls}} - \Delta_0 \tau_{\text{R}}) \\ 0 \\ \cos(\phi_{\text{ls}} - \Delta_0 \tau_{\text{R}}) \end{pmatrix},$$

To relate this to effective ensemble observable we proceed exactly as in eq. (11.8) only with the matrix for the Ramsey sequence instead of that for the Rabi oscillations

$$\langle \hat{\mathbf{F}}(t_{\text{f}}) \rangle = \frac{\pi l_a \mathcal{N}_0 \omega_p^2}{2 \phi_{\text{ls},0}^{(1+r_w)}} \int_0^{\phi_{\text{ls},0}} \left[\overline{\mathbf{M}}_{\text{R,ls}}(\tau_{\text{R}}, \chi, \Delta_0, \phi_{\text{ls}}) \langle \hat{f}(0) \rangle \right] \phi_{\text{ls}}^{r_w} d\phi_{\text{ls}} \quad (11.9)$$

The essence of the above equation was already introduced in eq. (10.17), but now we have an expression with physical parameters to which we can fit our data.

Experimental observations

To confirm our model we obtain frequency domain Ramsey fringes as prescribed by fig. 11.6, varying the light-shift probe pulse power. A similar experiment with

a homogeneous light-shift was documented in [Featonby98]¹. Sample fringes are shown in fig. 11.7a, and by fitting a cosine to the data we obtain the Ramsey fringe amplitude and the light-shift as the cosine frequency offset. Thus

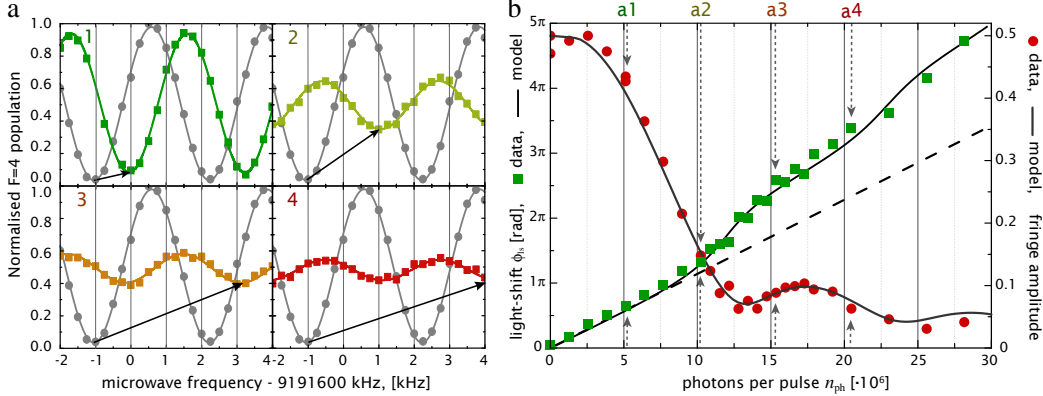


Figure 11.7: Probe light shift influence on Ramsey fringes. in a) we plot sample Ramsey fringes for different probe powers/photon numbers in the light shifting pulse (green, yellow, orange, and red squares). For the a_k 'th figure ($k = 1, 2, 3, 4$) the photon number is $n_{\text{ph}}(k) = k \cdot 5.12 \cdot 10^6$. The solid lines of corresponding colours are cosine fits to the data. The grey circles and accompanying fit shown in all sample traces is the reference Ramsey fringe with no light-shifting probe pulse. The arrows indicate the light-shift phase and fringe amplitude reduction. In b) we plot the the Ramsey fringe amplitude (red circles) and light-shift phase (green squares), given by the cosine fits, as function of the photon number in the light-shifting pulse. The solid lines relay the model predictions for optimised parameters $r_w = 0.6$. The dashed line illustrates the light-shift phase if it were homogeneous over the sample as in [Featonby98].

we are able to plot both the light-shift phase and the Ramsey fringe amplitude as a function of the probe-power on fig. 11.7b. The interesting news is that both parameters follow non-trivial curves, which actually have fairly intuitive explanations. If first we take the light-shift, it makes a jump approximately as it reaches 2π and 4π . A 2π light shift means that the atomic pseudo-spin has made a full rotation around the equator of the Bloch-sphere. What then happens as the mean light-shift reaches 2π is that the atoms with the largest light shift come in phase with atoms that have received the least light-shift. This phase-overlap will cause an increase in the Ramsey amplitude, which also acts to give an apparent jump in the light-shift. Both effects are easily distinguishable in the experimental data.

We use the model given by eq. (11.9) to plot curves to both the Ramsey fringe light-shift and amplitude, using the light-shift per photon and the sample to probe beam waist ratio r_w as free parameters. The model curves on fig. 11.7b confirm the experimental data remarkably well.

11.2 Light shift cancellation

The first step to solving a problem is to know it. The preceding sections relate to the first step and we now move on to the solution to the problem of the probe light-shift dephasing of the pseudo-spin. We suggest and characterise two possible solutions. The first relies on compensating the light shift by applying it twice but with different signs as enabled by a spin-echo pulse. The second approach relies on the mutual cancellation of the light-shift from the two colours

¹in that experiment the light-shift was induced in a MOT by a large diameter beam.

in a dichromatic probe beam. Both, approaches have limitations, but we find that for one they are more fundamental than for the other.

11.2.1 Ramsey spin-echo re-phasing method

We learnt from eq. (10.14) that the effect of the spin-echo pulse could be described as inverting or changing the sign of all phase accumulated prior to the echo pulse, this irrespective of it being due to a the microwave detuning or the probe induced light shift². In line with this, we decided to try out a pulse

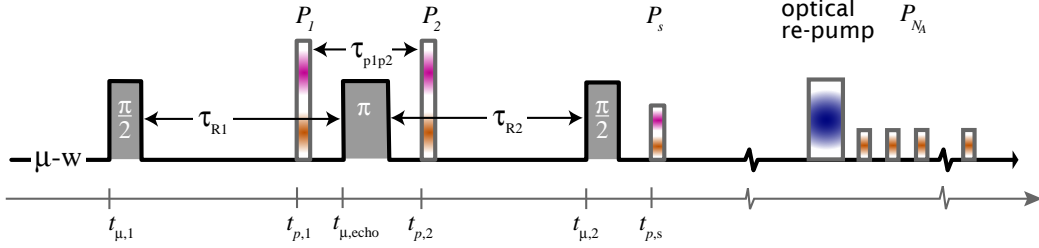


Figure 11.8: Re-phasing of probe induced light-shift using Ramsey spin-echo technique.

sequence sketched in fig. 11.8 where the light-shift induced by a probe pulse before the spin-echo pulse is exactly compensated by a second probe pulse after the spin-echo pulse. This sequence is easily constructed out of our repository of transformation matrices

$$\begin{aligned} \overline{\mathbf{M}}_{R\pi,ls}(\tau_{R1}, \tau_{R2}, \chi, \Delta_0, \phi_{ls,1}, \phi_{ls,2}) \\ = \mathbf{M}_{\mu w, \frac{\pi}{2}} \mathbf{M}_{\mu w}(\tau_{R2}, 0, \Delta_0) \mathbf{M}_{\phi_{ls,2}} \mathbf{M}_{\mu w, \pi} \mathbf{M}_{\phi_{ls,1}} \mathbf{M}_{\mu w}(\tau_{R1}, 0, \Delta_0) \mathbf{M}_{\mu w, \frac{\pi}{2}} \end{aligned}$$

Applied to our pet post-optical pumping pseudo-spin $\langle \hat{f}(0) \rangle = -n_{at}/2 \mathbf{z}$ we arrive at

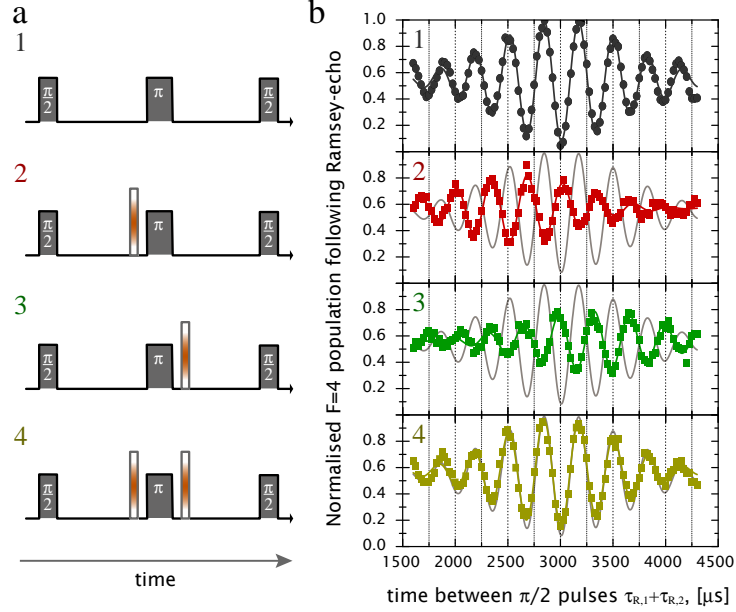
$$\begin{aligned} \langle \hat{f}(t_{p,s}) \rangle &= \overline{\mathbf{M}}_{R\pi,ls}(\tau_{R1}, \tau_{R2}, \chi, \Delta_0, \phi_{ls,1}, \phi_{ls,2}) \left[-\frac{n_{at}}{2} \mathbf{z} \right] \\ &= \frac{n_{at}}{2} \begin{pmatrix} \sin [(\phi_{ls,2} - \phi_{ls,1}) - \Delta_0(\tau_{R,2} - \tau_{R,1})] \\ 0 \\ \cos [(\phi_{ls,2} - \phi_{ls,1}) - \Delta_0(\tau_{R,2} - \tau_{R,1})] \end{pmatrix} \end{aligned}$$

Just as choosing the Ramsey interrogation times equal, $\tau_{R,1} = \tau_{R,2}$, applying two probe pulse with the same light-shift, $\phi_{ls,1} = \phi_{ls,2}$, will cause the pseudo-spin not to acquire any phase. Furthermore, it implies that the magnitude of the light-shift is unimportant as long as it is the same for both pulses. Hence, inhomogeneity in the light-shift will not dephase the final pseudo-spin.

We test our method by comparing the Ramsey spin-echo fringe for different positions of the light-shifting pulse w.r.t. the spin-echo pulse (see fig. 11.9 also featured in [Windpassinger08b]). From eq. (??) we expect that applying a single probe pulse either before or after the spin-echo will cause the fringe to shift in opposite directions. This is indeed what we observe in fig. 11.9b2+3). The result of the re-phasing shown on the bottom plot is that the light-shift is completely compensated to within the resolution of the measurement and the dephasing is substantially reduced compared to the single pulse traces. The latter statement

²again, the two are in principle equivalent.

Figure 11.9: Probe light shift and re-phasing in Ramsey spin-echo sequence. a) Sketch of the pulse-sequence with emphasis on the position of the light-shifting probe pulse. The Ramsey interrogation time is $\tau_{R1} = 1500 \mu\text{s}$, and the Rabi-frequency is $|\chi| = 24.1 \text{ kHz}$ and the microwave detuning is $\Delta_0 \approx 3 \text{ kHz}$. We use only the $4 \rightarrow 5'$ probe for the light-shifting pulses that are $t_p = 4 \mu\text{s}$ long, separated by $50 \mu\text{s}$ (when there are two), and each contain $n_{\text{ph}} \approx 10 \cdot 10^6$.



b) Ramsey spin-echo fringe data points for the different sequences (averaged over 4 data sets). Data points are fitted (solid curves) to eq. (10.19) with fringe amplitude and phase-offset as free parameters. a+b1) Reference sequence and fringe with no light-shift pulse (the reference fringe fit is redrawn as a grey curve on all subsequent plots). a+b2) probe-pulse before spin-echo pulse resulting in fringe phase to be light-shifted negatively and amplitude reduced by dephasing. a+b3) probe-pulse after spin-echo pulse resulting in fringe phase to be light-shifted positively and amplitude reduced by dephasing. a+b4) probe-pulses before *and* after spin-echo pulse so that there is no light-shift of the fringe phase and amplitude reduced only slightly due to spontaneous scattering and imperfections of the re-phasing.

should be seen in light of the photon-number in the two-pulse trace being twice that of the single pulse traces. There is still a small amount of fringe amplitude reduction, which is ascribed to spontaneous photon scattering and imperfect re-phasing. The ability to measure the irreversible decoherence due to spontaneous photon scattering is a key factor for estimating the spin-squeezing c.f. eqs. (3.33, 3.34, and 5.18) and exactly why the ability to *re-phase the dephasing* is so important. Imperfections in the re-phasing will limit our ability to establish the spontaneous scattering rate and thus wrongfully estimate the parameters for the spin-squeezing measurements. In the following section we reveal the source of this imperfection, which at the end will limit the applicability of the spin-echo re-phasing method.

11.2.2 Light-shift re-phasing in light of atomic motion

The mutual cancellation of the light-shifts of the probe-pulses P_1 and P_2 relied on the light shifts being equal for each atom at the time that the probe-pulses are applied. The implicit assumption is that the atoms are stationary, however, the earlier characterisation of the FORT trap frequency should convince even the sceptic that, despite being cold, the atoms in the sample do move about. Whether, this is of any concern for the re-phasing is a matter of time-scales. For the atomic motion the characteristic time is given by the trap oscillation period $\approx 2 \text{ ms}$, whereas the typical QND and squeezing measurements will be performed within $100 \mu\text{s}$. However, atoms need not perform a full oscillation to, depending on the probe beam size, experience a huge change in the probing

conditions. In only a quarter of the oscillation period $\approx 0.5 \mu\text{s}$ atoms at the trap centre will move to the maximal radial distance allowed by their energy viz. temperature. The results related to the re-phasing in light of atomic motion correspond to a somewhat elaborated version of [Oblak08].

Initially, observations of the sort in fig. 11.11 prompted us to characterise the effect of trap dynamics on the reversibility of the probe light-shift by the re-phasing method. To get an understanding of what was happening we acquired Ramsey spin-echo fringes for various separations τ_{p1p2} of the probe light-shift re-phasing pulses. The sequence, drawn on fig. 11.10a) along with the experi-

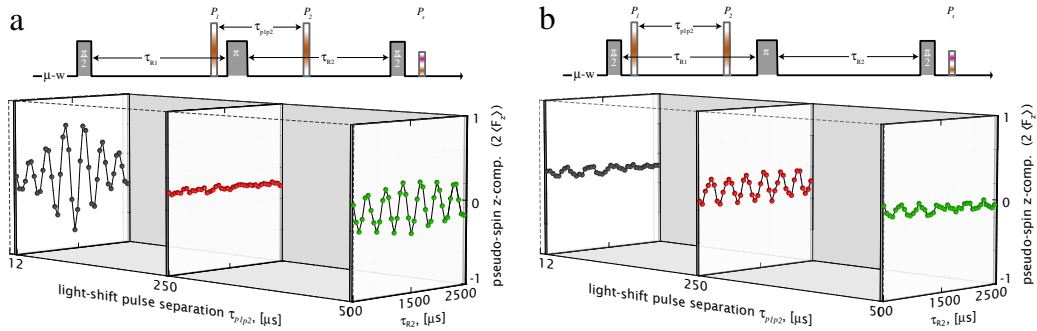
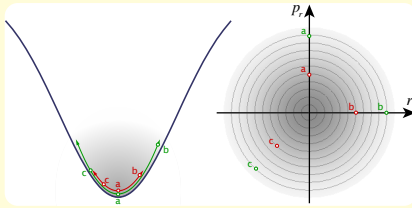


Figure 11.10: Ramsey spin-echo sequences and fringes for different light-shift re-phasing pulse configurations and separations. a) light-shift pulses placed one before and one after the spin-echo pulse at separations of 12, 250, and 500 μs . b) both light-shift pulses placed before the spin-echo pulse at 12, 250, and 500 μs separations. The behaviour of the fringes is explained in the body text.

mental data, reveals some striking effects. Firstly, if the light-shifting pulses are applied right before and after the echo pulse with 12 μs separation the atoms have hardly moved and the re-phasing works very well (as already illustrated by fig. 11.9). If τ_{p1p2} is increased the re-phasing efficiency rapidly decreases and at a separation of 250 μs , corresponding to roughly a quarter of the trap period, no Ramsey fringe is visible. The fringes are washed out, because the atoms imprinted with a light shift from the first pulse have been replaced by another subset of atoms that receive the “opposite” light-shift of the second pulse, whereby no re-phasing occurs. Increasing the light-shift pulse delay to half a trap period results in a miraculous revival of the Ramsey fringe. At this time the atoms will have the same radial distance as during the first light-shifting pulse, hence the the two light shift imprints again cancel each other. The above arguments presuppose that atoms move in a harmonic potential, which is of course not exactly the case. We expect the anharmonicity to be the cause of the imperfect revival of the Ramsey fringe. The re-phasing in light of the trap dynamics has a neat visualisation in a phase-space representation of the atomic position and momentum variables. We refer to Box 11.2.

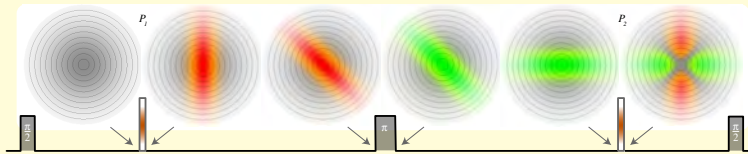
Fig. 11.10b) shows a very gratifying though not particularly useful measurement sequence. Based on the observation in Fig. 11.10a) we were inspired to look if imprinting the same light shift twice but allowing the atoms to maximally exchange, i.e. evolve during a quarter of a trap period, would undo some amount of the dephasing. The notion is that if the light shift is distributed more evenly over all atoms they will be more in phase than if the light-shift were applied twice to exactly the same subset of the atoms. Thus we apply both light-shifting pulses before the spin-echo pulse and vary their time separation. The resulting fringes recorded at $\tau_{p1p2} \approx 0, 1/4,$ and $1/2$ trap period separation confirm our suspicion. Again, we refer to Box 11.2 for a pictorial illustration of the principles at play.

Box 11.2: Phase-imprints and atomic motion in phase-space

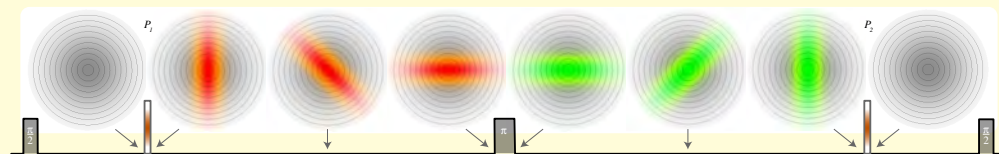


The phase-imprints and degree of re-phasing can be visualised in the momentum-position phase-space of the atoms. On the sketch we draw atoms at various points in phase-space and relate them to their physical position and trajectories in the trap. The phase-space density is represented by the darkness of

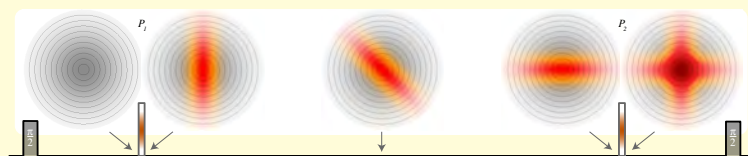
plot. For now, we disregard angular motion as it is not essential for the discussion. The light shift is imprinted on atoms as a function of r , which is the horizontal phase-space axis. We represent the light-shift by a reddish tint of the phase-space distribution. As the ensemble evolves the light-shift imprint rotates counter-clock-wise in phase-space. Applying a spin-echo pulse effectively inverts the light-shift imprint, thus we give it a greenish tint. The second light-shift imprint adds another reddish tint and depending on the evolution in phase-space of the first imprint the two either add constructively, destructively, or somewhere in between. The Ramsey spin-echo fringe is largest the more uniform the atomic phase is over the ensemble. Thus the fringe is largest when the phase-imprints add destructively and smallest when they add constructively.



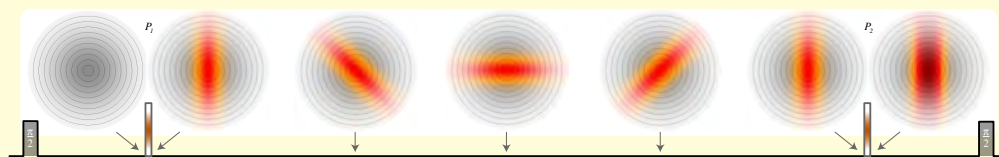
Light shift pulses before and after spin-echo and separated by $1/4$ trap period add destructively but out of phase causing a large phase gradient over the ensemble. Thus the fringe amplitude is small.



Light shift pulses before and after spin-echo and separated by $1/2$ trap period add destructively in phase causing a uniform phase over the ensemble. Thus the fringe amplitude is large.



Light shift pulses without spin-echo and separated by $1/4$ trap period add constructively but out of phase causing a distribution of the light-shift phase over the ensemble. Thus the fringe amplitude is not completely washed out.



Light shift pulses without spin-echo and separated by $1/2$ trap period add constructively in phase causing huge phase gradient over the ensemble. Thus the fringe amplitude is very small.

phase-imprint for trap-oscillation

In light of the above described revivals of the Ramsey spin-echo fringes, an obvious digression is to use the light-shift imprints to extract the trap-frequency. To that end, we need not record the full fringe, merely the value at $\tau_{R2} = \tau_{R1}$ equal to the maximal fringe amplitude. Varying τ_{p1p2} we then measure the variation in the Ramsey fringe amplitude (see fig. 11.11a). We pick the probe power so that the dephasing is significant but never complete, in which case it turns out that the curves can be closely fit by a damped cosine (see fig. 11.11a legend). Acquiring curves for different FORT trapping powers and fitting a damped harmonic we can plot the revival frequency against the FORT laser power on fig. 11.11b). In accordance with the discussion above the trap frequency is equal to half the

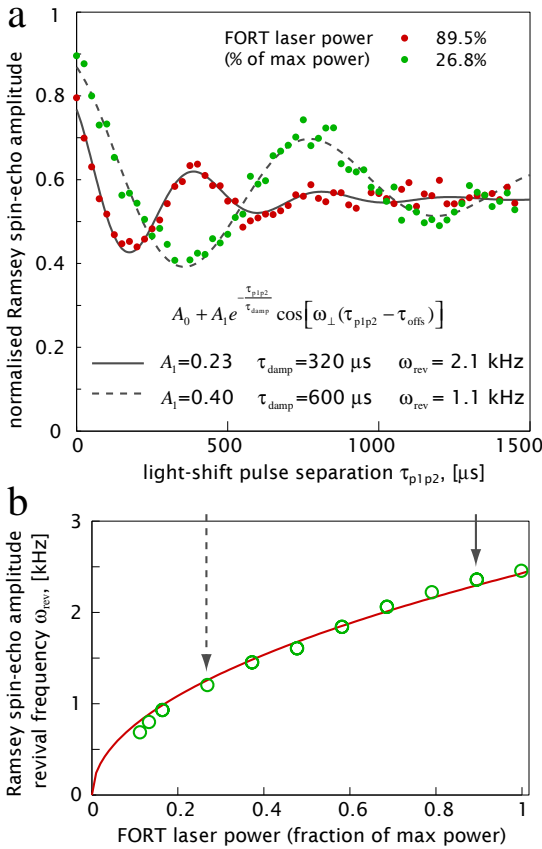


Figure 11.11: Light-shift re-phasing for determining trap-oscillation frequency. a) Ramsey spin-echo amplitude vs. light-shift pulse separation for different relative FORT trapping powers (red and green points). For both the light-shift pulses and the final state detection the $3 \rightarrow 2'$ probe is used. In the Ramsey spin-echo sequence $\tau_{R1} = 1500 \mu\text{s}$ and we peg $\tau_{R2} = \tau_{R1}$ in order to measure the fringe amplitude given by $n_{\text{at},3}$. The revival frequencies of the observed Ramsey amplitude oscillations are extracted by fitting exponentially damped cosines (grey lines). b) The revival frequencies vs. relative FORT trapping power. The revival frequency corresponds to twice the characteristic trap oscillation frequency ω_{\perp} . A square-root fit (red curve) to the revival frequency yields near perfect agreement.

revival frequency. To our great satisfaction a square-root dependence is a good fit to the revival frequency, thus confirming the relation to the trap frequency (see eq. (9.8)). The trap frequencies predicted from fig. 11.11b) are in the range 0.3 – 1.2 kHz, which is markedly larger than the measured values of 0.1 – 0.2 from fig. 9.10. However, for a FORT laser waist size of $40 \mu\text{m}$ and typical trapping powers 4 W we noted in sec. 9.2.2 that we indeed expect $\omega_{\perp} \approx 2\pi \cdot 1.2 \text{ kHz}$ (see p. 151). An interesting remark to the damping time is that it seems to increase with increased trap period. If the damping is due to anharmonicity of the trapping potential, this is also what one would expect, since the dephasing is proportional to the rate that atoms move in to the anharmonious (outer) parts of the trap. For lower trap frequencies this happens at a slower rate, thus the lower damping.

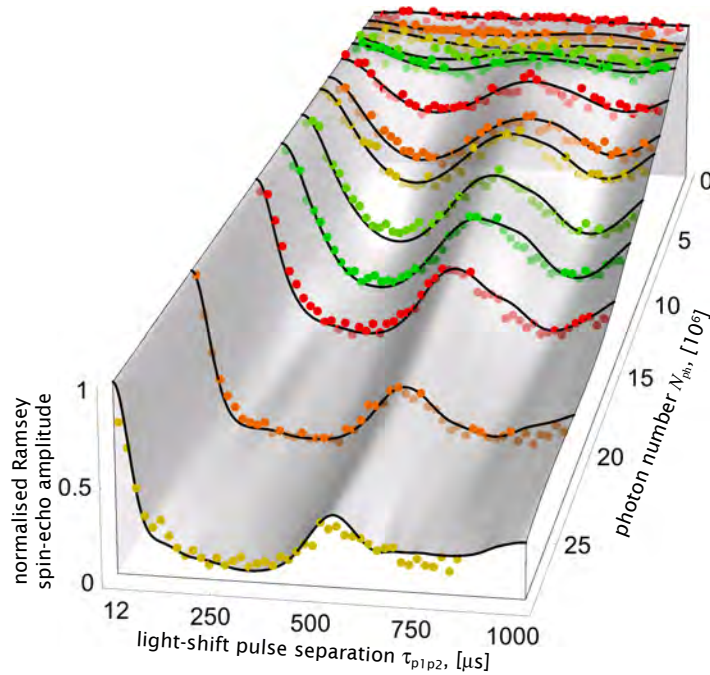
As pointed out in [Oblak08], a highlight of this method of determining the trap frequency is that we are able to determine it without perturbing any external degrees of freedom of the atoms. Effectively, the probe pulses via the imprinted light-shift tag each atom and the second probe pulse by imprinting another light shift tags the atoms in a way that later can be measured. In contrast the method

in sec. 9.2.2 required us to induce collective motion that was measured from the resulting atomic density modulation.

phase-imprint simulations

The method of fitting a damped harmonic function to the Ramsey spin-echo fringe amplitude works fine for moderate photon-numbers, which do not cause complete dephasing of atoms as for the data in fig. 11.11a). For larger probe intensities the fringe amplitude is zero over a whole range of pulse separations, such as around $\tau_{p1p2} = 250 \mu\text{s}$ in fig. 11.10a), and is consequently no longer approximate to a cosine. In order to recreate the fringe amplitudes for completely general experimental settings we are impelled to use simulations of the atomic evolution. These, were introduced in sec. 9.2.2 and described in sec. E. We assume that the FORT and probe laser beams are Gaussian and maximally mode overlapped, i.e. their radial centres overlap, and neglect the axial trap dynamics. The variable parameters for the simulation are the ensemble temperature, trap frequency, probe to FORT laser beam ratio, and the peak light-shift at the probe-beam centre. For a suitable range of the parameters we generate simulated data of the Ramsey fringe amplitude versus the light-shifting pulse separation. Calculating the squared error between the experimental and simulated data we can pin down the optimal combination of simulation parameters. In fig. 11.12 we plot the experimental Ramsey fringe amplitude (circles) together with the those corresponding to the optimal simulation parameters (black lines) for a suitable range of probe-powers. The qualitative correspondence between the experiment and simulations is outstanding, and certainly underlines our understanding of the dephasing mechanism.

Figure 11.12: Ramsey spin-echo amplitude vs. light-shift pulse separation for different light-shift pulse photon numbers. The measurement principle is identical to that described in fig. 11.11 except the FORT trapping power being constant and the light-shifting probe power being varied. The data is compared by simulation based on sec. E.3, by which we extract the optimal simulation parameters that yield the best agreement with the data (grey curves). The optimised maximal light-shift is plotted vs. the probe power in fig. 11.13.



It is very pertinent to inspect the optimal simulation parameters. For trap temperature the optimal value lies around $\beta = 2/V_0$ which given a FORT beam waist of $w_t = 40 \mu\text{m}$ ³ entails a atomic sample radius of $w_a = w_t / \sqrt{\beta V_0} = 28 \mu\text{m}$. On

³estimated from the spot-size of the collimated beam together with the focal length of the achromats.

the other hand the optimal ratio of probe to FORT beam waists is $w_p/w_t = 0.7-0.8$ and given a $w_p = 27 \mu\text{m}$ this predicts $w_t = 34-39 \mu\text{m}$ in good agreement with the anticipated value. The optimisation yields a radial trap oscillation frequency of $\Omega_{\perp} = 1.1-1.2 \text{ kHz}$, which in a FORT potential of $40 \mu\text{m}$ width accords with 3.36 W of FORT laser power (see eqs. (9.3 and 9.8)), perfectly in line with that measured on a power detector. Finally, the maximal light-shift phase should be proportional to the probe power measured on the reference detector. On

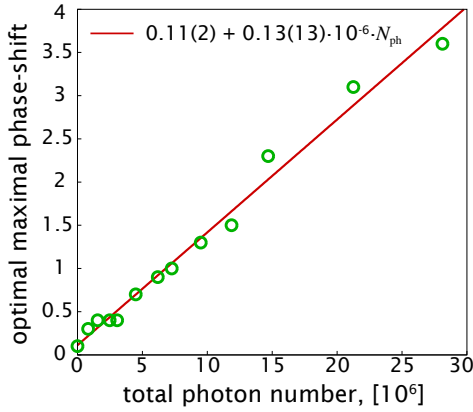


Figure 11.13: Optimal simulation light-shift phase versus probe power from fig. 11.12. The fit (red line) shows a nice linear relation.

fig. 11.13 we plot the optimal light-shift parameter against the probe power and the two are clearly linearly proportional.

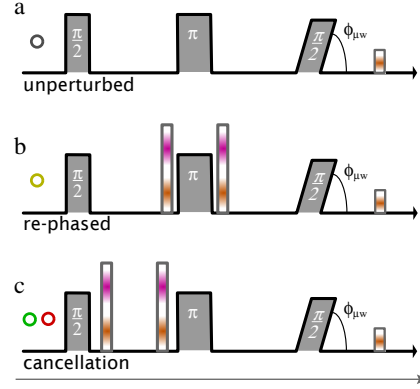
11.2.3 2-input method and equivalents

It is time to harness some of the great advantages of the dichromatic probing scheme. One of these, highlighted in sec. 5.3.2, was the possibility of having each probe contribute with a light-shift of equal magnitude but opposite sign so that their combined light-shift is zero. In the picture of box 11.2 this corresponds to the simultaneous imprint of a light-shift of each sign. This required the two probe detunings to have same sign, i.e. either both red or both blue detuned. Since in that case the phase-shift of the probes due to the atomic sample have the same sign we need to configure the MZI so that the fringes of the two probes are π rad out of phase, whereby the imprints of the two ground level populations in the detected output signal would still have opposite signs. We discovered three different configuration that cause a π rad shift between the probes (see also sec. 2.3.1): firstly the the probes may enter a different input port of the MZI (phase-displacement due to spatial splitting of input); secondly the probes may enter the same input port but be orthogonally circularly polarised and split on a PBS at the MZI input (phase-displacement due to polarisation splitting of input), and thirdly the probes enter the same input and the MZI probe and reference arm may have a path-length difference of $\approx 1.5 \text{ cm}$ (phase-displacement due to frequency splitting of input).

In the below we will characterise how well the light-shift cancellation by the dichromatic probe works. To get from one of the above configurations to the other it is necessary to restructure the MZI. Hence, we are not able to successively compare their efficiency at light-shift cancellation. On the other hand, the polarisation split input only causes the optical oscillation of the probes in the MZI arms to be the out-of-phase and neither this nor the mutual path-length displacement of the MZI arms has any influence on the light-shift from the probes on the atoms. Thus, the essential characteristics relate to the ability to tune the correct frequency of the probes and align them to the same spatial mode. We expect the latter to be trivial when the probes enter the same spatial input but

somewhat difficult when the input are spatially separated. Hence, we take as a starting point the 2-input configuration, which we first characterise in a Ramsey type sequence. Subsequently we couple the probes through the same input fibre⁴ and after characterising this we compare with the previous configuration. Needless, to say the 1-input configuration in this form cannot be used for a QND measurement since the imprints of the ground-levels on the output signal add up. However, this is de-coupled from the ability to cancel the light-shift, and we also make sure to detect the final state in the Ramsey sequence with only one probe (see fig. 11.14).

Figure 11.14: Ramsey spin-echo sequence for characterising dichromatic probe light-shift cancellation (coloured circles refer to data in fig. 11.15 and fig. 11.16). a/grey, Unperturbed reference measurement; and b/yellow, spin-echo re-phasing of probe light-shift irrespective of dichromatic probe cancellation. c/red and green, the actual characterisation of the light-shift by the dichromatic probe. The microwave radiation is on resonance and the interrogation times are fixed $\tau_{R2} = \tau_{R1}$. To obtain Ramsey fringes we vary the phase of the microwave field by use of the phase-shifter.



To characterise the light-shift cancellation we use a Ramsey spin-echo measurement where two dichromatic probe-pulses are fired in quick succession before the spin-echo microwave pulse (see fig. 11.14c). We use a spin-echo type measurement to remove other inhomogeneous dephasing and because it allows us to perform a re-phasing measurement (where the two probe pulses surround the spin-echo pulse), which we use as a minimal light-shift dephasing benchmark. In fig. 11.15a the Ramsey spin-echo fringe with the re-phasing is plotted in yellow

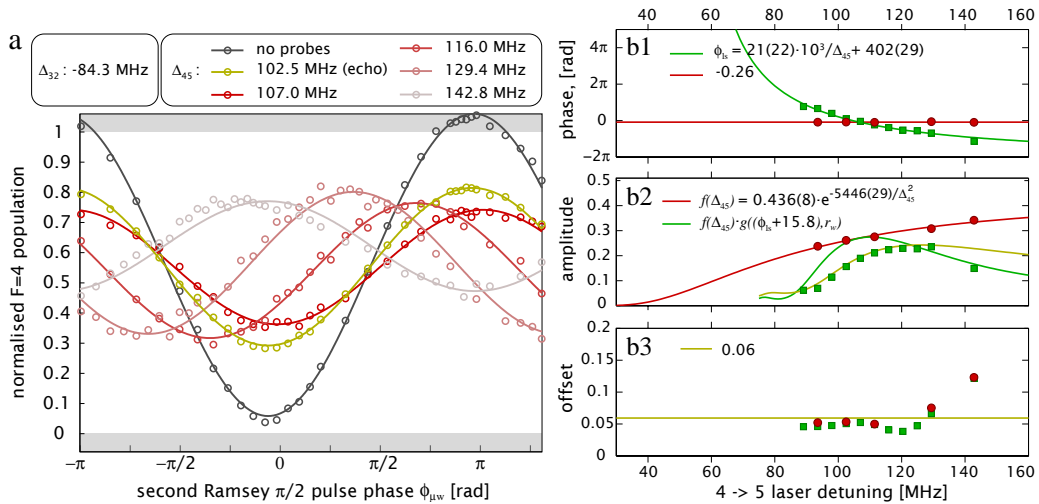


Figure 11.15: a) Ramsey fringes in 2-input configuration for different detunings of 4 \rightarrow 5' probe with 3 \rightarrow 2' probe detuned by $\Delta_{32}' = -84.3$ MHz. Grey curve, no light reference; Yellow curve, spin-echo re-phasing reference; Red curves, different 4 \rightarrow 5' probe detunings. b) Fitted Ramsey fringe parameters as function of Δ_{45}' . b1) Fringe phase-shift in sequence with re-phasing echo (red) and without (green). b2) Fringe amplitude with (red) and without (green) re-phasing

low and the reduction in amplitude w.r.t. to the grey fringe, without perturbing probe-pulses, is due to spontaneous scattering events. We note that the yellow

⁴without changing the input polarisation and displacing the MZI arms.

fringe, which we will refer to as the *re-phased fringe*, is in phase with the grey fringe, which we refer to as the *unperturbed fringe*.

With both probe pulses before the echo pulse we peg the detuning of the $3 \rightarrow 2'$ probe and vary the $4 \rightarrow 5'$ probe detuning to record the light-shift *cancellation fringes*. We see that the phase and amplitude of the cancellation fringes (data in shades of red) change depending on Δ_{45} , indicating different degrees of light-shift cancellation, and at a certain Δ_{45} the fringe is in phase with the unperturbed fringe, i.e. the mean light-shift is cancelled. In fig. 11.15b1 we plot the fitted phase of the cancellation fringe against Δ_{45} for a large set of measurements and inspired by eqs. (11.2 and 4.7) we fit the phase with a $1/\Delta_{45}$ function with convincing result. The phase of the re-phased fringes is assumed to be constant and accordingly we plot the mean phase value. In fig. 11.15b2 we also plot the fitted fringe amplitude of both the re-phasing and the cancellation fringes. Unfortunately, the amplitude of the cancellation fringe where the mean light shift is cancelled is below the amplitude of the re-phased fringe, revealing that some amount of inhomogeneous light-shift remains. We are convinced that this is due to imperfect mode-matching of the probes from the two inputs. By tweaking the alignment of one of the inputs we have confirmed that the cancellation is extremely sensitive to mode-mismatching of the inputs. The re-phased fringe amplitude is reduced by spontaneous scattering of the probe and is neatly fitted to a $a \cdot e^{-b/\Delta_{45}}$ function c.f. sec. 4.3.1. To model the amplitude of the cancellation fringes we make use of the findings in sec. 11.1.2. There we expressed the Ramsey fringe amplitude and the mean light shift as a function of the probe to sample ratio and the maximal phase shift. Hence, we can interpolate the mean light shift, e.g. as plotted in fig. 11.7, and the fringe amplitude curves and relate them to each other. Using the mean light shift from the fit in fig. 11.15b1, subtracting the small offset deduced from re-phased fringe and scaling the amplitude down by the spontaneous scattering (red curve), we can plot the predicted cancellation fringe amplitude (green curve). Since, the maximal cancellation fringe amplitude does not coincide with the cancellation of the mean light-shift the curve obviously does not predict the data very well. By allowing an offset to the mean light-shift phase and a scaling of the fringe amplitude it is possible to fit a curve (yellow) to the data, however, this is not particularly useful. Finally, we plot the fringe amplitude offset, which ought to be constant at 0.5. The reason for it being slightly larger is due to pumping to $m_F \neq 0$ levels by the probe pulses. As expected this should increase for $\Delta_{45} \rightarrow 0$. The offset at large detuning is a technical artefact, connected to the choice of probing the final state by the $4 \rightarrow 5'$ probe. As Δ_{45} is increased the detector output signal decreases and becomes more susceptible to off-set errors in the detector baseline.

Now we compare with the cancellation achievable for probes entering the MZI through same spatial input mode with the detunings set for the 2-input MZI configuration. As above, we record an unperturbed fringe and a number of re-phased fringes one of each show on fig. 11.16. The phase of the cancellation fringes again shifts according to the $4 \rightarrow 5'$ probe detuning and for the greenest fringe on fig. 11.16 the mean light-shift is approximately cancelled. Fortunately it appears that the cancellation fringe amplitude is also maximal and as large as that of the re-phased fringe for the same detuning. We extract the average re-phased fringe phase and fit the cancellation fringe by a $1/\Delta_{45}$ dependence. Using these together with a fit of the spontaneous scattering, we again generate a curve for the predicted cancellation fringe amplitude. With quite some contentment we conclude that the prediction fits the recorded data very well. One can spot the slight revival of the amplitude at $\Delta_{45} = 50\text{-}60\text{MHz}$ that corresponds to the revival at 2π phase-shift in fig. 11.7. We emphasise that there are no free parameters,

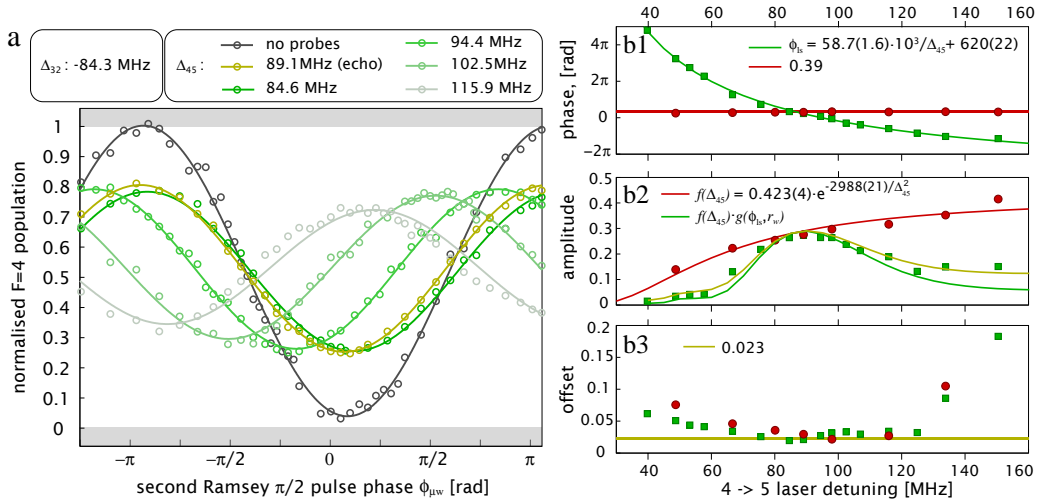


Figure 11.16: a) Ramsey fringes in 1-input configuration for different detunings of $4 \rightarrow 5'$ probe with $3 \rightarrow 2'$ probe detuned by $\Delta_{32'} = -84.3$ MHz. Grey curve, no light reference; Yellow curve, spin-echo re-phasing reference; Green curves, different $4 \rightarrow 5'$ probe detunings. b) Fitted Ramsey fringe parameters as function of $\Delta_{45'}$. b1) Fringe phase-shift in sequence with re-phasing echo (red) and without (green). b2) Fringe amplitude with (red) and without (green) re-phasing echo. b3) Fringe voltage offset.

except for the choice of r_w . In the plot we pick $r_w = 0.75$ according to the re-phasing simulations in sec. 11.2.2 in place of the $r_w = 0.6$ that was optimal for the light-shift dephasing curves in sec. 11.1.2, simply because the former gives better correspondence between the prediction and the data.

Finally, in fig. 11.17 and fig. 11.18 we plot a neat 3-dimensional representation of the light-shift re-phasing/cancellation data for the probes at different or the same inputs of the MZI, respectively. To conclude the treatment of the dichro-

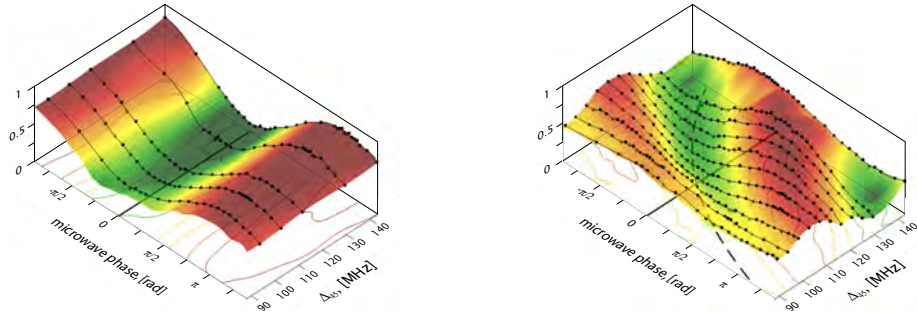


Figure 11.17: Surface plot of Ramsey fringes showing the dichromatic probe cancellation of light-shift as function of the $4 \rightarrow 5'$ probe detuning in the configuration where the probe colours enter through *different* MZI input ports. The fitted parameters in fig. 11.15b are based on the fringes in this figure of which a subset are presented in fig. 11.15a.

matic probe cancellation of the light-shift, we have demonstrated that we are able to cancel the mean light-shift in either the configuration using two or one inputs for the probes. Completely cancelling the inhomogeneous light-shift, thus recovering the Ramsey fringe to the level limited by spontaneous scattering, is only possible when the probes enter the same MZI input, in which case they are spatially mode-matched in an optical fibre. Though, we try our very best we are simply not able to outperform the quality of the mode-matching by the coupling through a fibre.

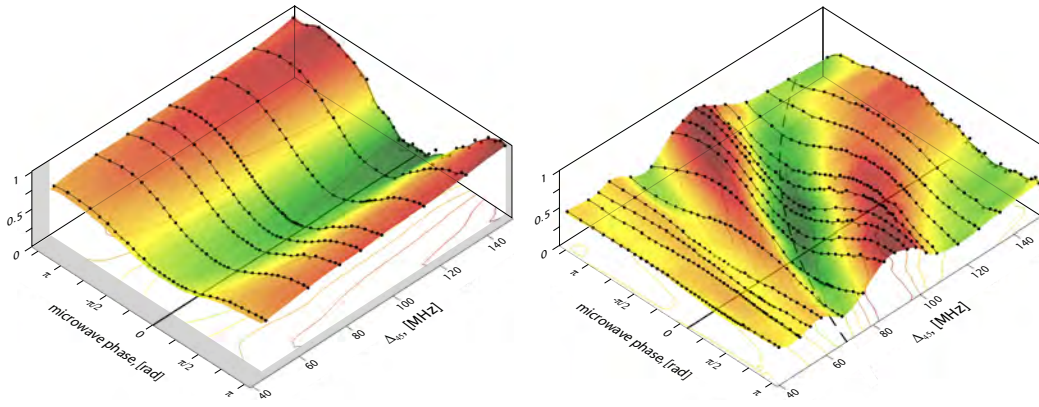


Figure 11.18: Surface plot of Ramsey fringes showing the dichromatic probe cancellation of light-shift as function of the $4 \rightarrow 5'$ probe detuning in the configuration where the probe colours enter through *the same* MZI input port. The fitted parameters in fig. 11.16b are based on the fringes in this figure of which a subset are presented in fig. 11.16a.

11.3 Spontaneous scattering decoherence

In the preceding section we have focused on the light-shift imparted by the probe, while sidelining spontaneous scattering as an *add-on* effect. The attention given to the light-shift is merely due to the elaborate measures needed to eliminate it. In a grander perspective spontaneous scattering is really the central effect and unlike the light-shift it cannot be eliminated, at least not without simultaneously stamping out the interaction strength. Thus the *raison d'être* of this section is to measure how large the spontaneous scattering rate η is as a function of relevant parameters. As the η depends only on the number of photons $N_{\text{ph}}^{(a)}$ that impinge on the atomic sample, we state this photon-number in the present section.⁵

The spontaneous scattering rate is most faithfully measured in a Ramsey sequence as the reduction of the fringe amplitude due to probe pulse fired during the interrogation time. Fig. 11.16 illustrates how we can bypass the light-shift, either by re-phasing method or advantageously by the dichromatic probe cancellation, in order to get the fringe reduction exclusively due to spontaneous scattering.⁶ In fig. 11.19 we present the Ramsey fringes using the re-phasing method recorded at different probe-powers. The surface-plot gives a good intuitive impression of how spontaneous scattering washes out the atomic coherence and consequently also the Ramsey fringe contrast. We fit the Ramsey fringes (black lines) and plot the fitted fringe amplitudes in fig. 11.20. The Ramsey fringe amplitude ought to decay exponentially as function of the photon number used, however, an exponential decay does not seem to agree perfectly with the fitted amplitudes. The yellow dashed line is not a fit, but only a guide-to-the-eye exponential decay, which is offset by $20 \cdot 10^6$ along the x-axis. The deviation from a purely exponential decay is due to the atomic motion between the re-phasing pulses. Part of the reason, for presenting the above data is exactly to highlight the various difficulties of estimating the spontaneous scattering rate using the re-phasing method. This again is relevant, because a substantial amount of the spin-squeezing experiments in the next chapter were performed using the 1-

⁵earlier we have denoted photon operators in the probe by \hat{a} , thus we use $N_{\text{ph}}^{(a)}$ for the probe-arm photon number.

⁶In truth, the application of the squeezed spin-state resulting from the QND measurement would involve a Ramsey sequence, and thus measuring the fringe contrast, the ratio of the amplitude to the noise in the signal, is immediately *the* relevant parameter.

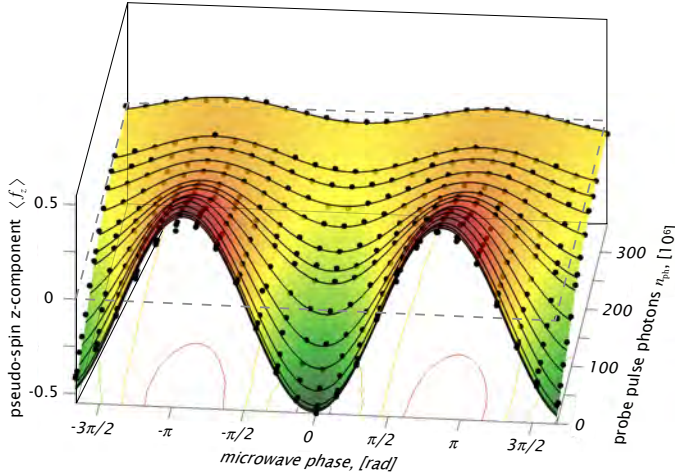


Figure 11.19: Ramsey spin-echo fringes for different probe powers. The probe and microwave pulse parameters are given in the insert of fig. 11.20. We phase-shift the second Ramsey $\pi/2$ pulse to trace out the fringes. We emphasise that the we state $N_{\text{ph}}^{(a)}$ the photon number in the probe arm i.e. passing through the atomic sample. For this measurement this number is about 60% of the total input photon number.

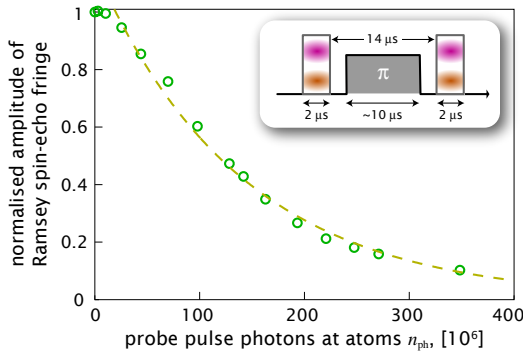


Figure 11.20: Estimating spontaneous scattering rate inferred from the Ramsey spin-echo fringe amplitude as function of the probe power. The photon number is varied by changing the pulse power, and it is equally distributed with half of the photons in each probe colour. The probe detunings are $\Delta_{45} = 320$ MHz and $\Delta_{32} = -298.8$ MHz. The decay is not completely exponential (yellow dashed line) because atomic motion slightly spoils the re-phasing.

input MZI configuration, where the light shifts of the two probes add up. The fact that functional dependence of the spontaneous scattering $1 - e^{-\eta}$ deviates from an exponential does not result in wrong estimates of the decoherence in the spin-squeezing measurement, because we always measure $1 - e^{-\eta}$ for the specific photon-number used in the spin-squeezing measurement. However, it does mean that *the fringe reduction measured in the Ramsey spin-echo re-phasing measurement gives an upper bound to the spontaneous scattering decoherence.*

In a move to underline the above statement we show the amplitude of the Ramsey spin-echo fringe varying the probe detuning for a range of re-phasing separations τ_{p1p2} (see fig. 11.21). By and large, this is a replication of the red data-points

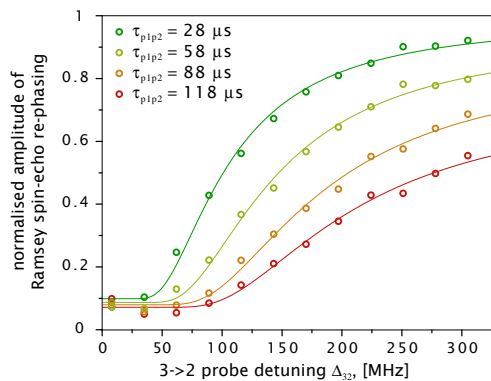


Figure 11.21: Estimating spontaneous scattering rate inferred from the Ramsey spin-echo fringe amplitude as function of the probe detuning. We use only the $3 \rightarrow 2'$ probe in two $2 \mu\text{s}$ pulses, one before and one after spin-echo pulse. The larger the separation of the probe-pulses the poorer the re-phasing works and the higher the estimated decoherence. Solid curves represent fits to

shown on fig. 11.15b2 and fig. 11.16b2 and indeed the points in fig. 11.21 can be fitted with a similar model. The key point we wish to make is that the shorter the separation of the probe pulses around the spin-echo pulse the lower the es-

timated decoherence level will be. The best estimate is thus achieved by making the separation as short as possible. The key to this requirement is to perform the spin-echo π pulse fast, which is why we acquired a power-amplifier for the micro-waves.⁷

Not relying on the light-shift re-phasing by switching to the 2-input MZI (or an equivalent) configuration should tighten the bound from our estimate of to the actual spontaneous scattering decoherence of the state. We have not quantitatively studied this conjecture, but we do see that the measured decoherence as function of the probe power is very convincingly fitted by an exponential decay (compare fig. 11.22 with fig. 11.20).⁸ Based on a series of measurements

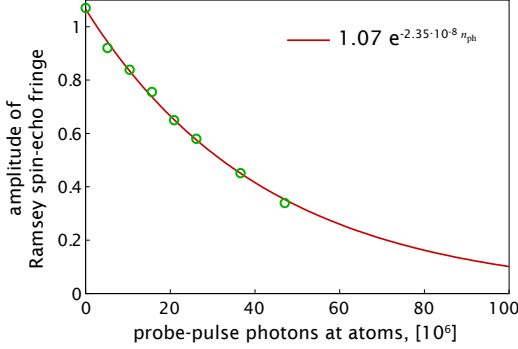


Figure 11.22: Estimating spontaneous scattering rate inferred from the Ramsey spin-echo fringe amplitude as function of the probe power. The fringe amplitude is normalised to the phase-shift from the atom-number measurement. The photon number is varied by changing the pulse length, and it is equally distributed with half of the photons in each probe colour. The probe detunings are $\Delta_{45} = -100$ MHz and $\Delta_{32} = -87.6$ MHz.

performed over the range of a half a year we arrive at the following very approximate relation for the spontaneous scattering rate

$$\eta \approx 1.8 \cdot 10^{-4} N_{\text{ph}}^{(a)} \left(\frac{3}{7} \frac{1}{\Delta_{32}^2} + \frac{5}{9} \frac{1}{\Delta_{45}^2} \right), \quad (11.10)$$

which is only valid when $\Delta_{32}, \Delta_{45} \gg \gamma_e = 5.2$ MHz. The fractions multiplying the detuning dependence are proportional to the transition-strengths of the $|F, 0\rangle \rightarrow |F', 0'\rangle$ probe transitions c.f. table D.5 and D.10.

⁷the shorter $\tau_\pi \sim 10 \mu\text{s}$ in fig. 11.20 compared with the $\tau_\pi \sim 25 \mu\text{s}$ in fig. 11.21 is a direct consequence of the Kuhne amplifier being installed.

⁸We note that the fringe-amplitude in fig. 11.22 exceeds unity when no probe-photons are present. This is due to the normalisation of the fringe to the signal in the atom number measurement. Since the atom number is measured some time after the Ramsey experiment and following re-pumping to the $F = 4$ state some atoms will be lost, with the result that the Ramsey fringe is normalised to a slightly too low signal. Hence, the above unity value, which does, however, not affect the estimate of η . Usually, we normalise the fringes to the amplitude of the $N_{\text{ph}}^{(a)} = 0$ fringe, whereby the error is removed. Taught by fig. 11.22, we keep in mind that whenever using the atom number measurement to gauge the N_{at} at an earlier time, we need to extrapolate the measured N_{at} to that point in time (see sec. 12.1.1).

QND measurements and squeezing

Much like Moses we have now arrived at the promised land, but rather than indulging in a feast of milk and honey we shall outline our experimental demonstrations of QND measurements and spin squeezing. We will venture in to a rugged noise landscape and our principal task will be to map the different kinds of noise so that ultimately we may tell one from the other. In earlier sections (sec. 8.2.2 and 8.7) we have already characterised the topography of the electronic, classical and quantum noise of the probe and detection system. What remains is to chart the atomic fluctuations that via the interaction with the probe appear in the detected signal. Our anticipation is to detect the signature of the quantum uncertainty of the atomic state in terms of atomic projection noise. As outlined in the Introduction the detection of the projection noise is the most demanding task in the path towards the goal of demonstrating spin-squeezing. We remind ourselves that the other main tasks towards the goal are to gauge the degree of quantum-state demolition by the QND measurement¹ and the detection of correlation between subsequent measurements of the atomic state. The former task has already been taken care of in sec. 11.3 of the previous chapter while the latter, as the highlight of this chapter, will be treated in parallel with the establishment of the projection noise level.

12.1 General procedures

To ease the understanding of the chapter we first establish the usual procedures, which we follow when commencing a measurement run. We will not mention here the various calibrations and alignments that are performed only at long intervals. Instead we focus on the calibrations required prior to a measurement run

- align MZI to optimise visibility (sec. 8.4)
- balance power in MZI outputs for probe and reference arms separately.
- engage MZI lock and adjust offset to balanced position for probes.
- determine the clock transition resonance frequency (sec. 10.2.3)

¹almost a contradiction in terms — masked by the use of an acronym.

- determine the $\pi/2$ pulse duration (fig. 12.1)
- balance powers in each probe colour — if applicable locking their relative power.
- adjust probe detuning of one colour for equal coupling strength

As the MZI visibility drifts due mainly to thermal expansion/contraction of the MZI base-plate the fringe visibility should be checked once every so often. It is necessary to determine the clock frequency regularly because depending on the FORT laser power it experiences a slightly different light-shift. Since the local microwave power and thus the Rabi-frequency is affected by the physical environment of the setup the $\pi/2$ -pulse calibration should be done every time the MZI shielding is opened. It is important that we set $\tau_{\pi/2}$ precisely as it determines how close we prepare the atoms in an *equal* superposition state. Fig. 12.1 illustrates the procedure we use for finding $\tau_{\pi/2}$.

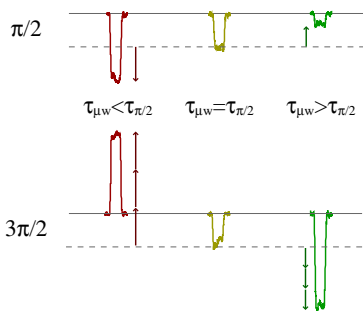


Figure 12.1: Determining the $\pi/2$ pulse duration. we use the fact that all pulses with duration that are an odd integer multiples of $\tau_{\pi/2}$ will create an equal superposition state. Thus we compare the atomic phase-shift when doing a single $\pi/2$ pulse and e.g. three $\pi/2$ pulses adjusting $\tau_{\pi/2}$ until both result in the same QND detector signal. The traces illustrate the pulse signals for microwave pulse durations that are either shorter than (red), equal to (yellow), or longer than (green) $\tau_{\pi/2}$.

After taking some or all of the above courses of action, we are set to start a measurement run. This should comprise the following measurements

- fringe calibration (sec. 8.5)
- atom number decay measurement (sec. 12.1.1)
- decoherence measurement (sec. 11.3)
- QND squeezing measurement or similar (sec. 12.1.1)

The fringe calibration as described in sec. 8.5 enables us to translate the integrated pulse signals in to phase-shifts of the MZI fringe using the power reference detector signal. The MZI phase-shift, unlike the detector voltage, is an absolute physical quantity to which we can compare theoretical predictions. The measurement of the atom number decay will enable us to compensate for the loss of atoms from the time of the QND measurement till the atom number measurement. This will be elaborated in sec. 12.1.1. The decoherence estimate obtained by the procedure in sec. 11.3 allows us to compute the squeezing parameter ξ according to the criteria given in sec. 3.5.1. Finally, the squeezing measurements puts us in a position where we can publish papers and on account of that secure our future career.

12.1.1 General QND measurement sequence

The QND measurement sequence sketched on fig. 12.2 very much follows the order of the previous chapters. The first step is to prepare the cold atomic sample

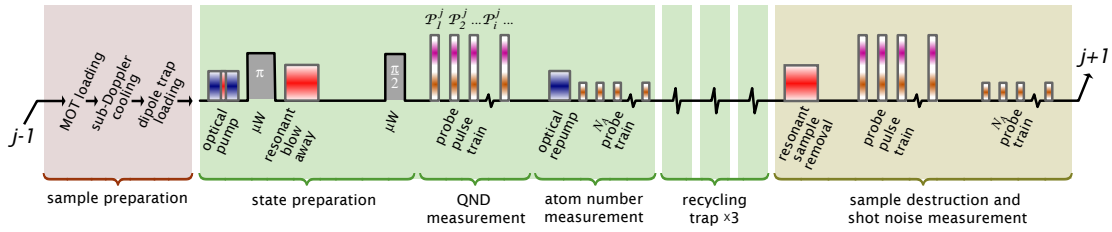


Figure 12.2: Experimental sequence for the QND measurement. The elements of the sequence are explained in the body text.

in the FORT as described in chapt. 9. This step defines a trap-loading cycle. After preparing the sample we prepare its quantum state by optical pumping and interaction with microwave field as covered in sec. 10. We then perform the actual QND measurement and acquire a train of pulse data values. After each QND pulse train we re-pump the atoms to the $F = 4$ hyperfine level and acquire an atom-number measurement pulse train. Since, the time-scale for the state preparation is considerably shorter than for the sample preparation (10-20 ms vs. 1-2 s) we optimise the data acquisition rate by recycling the sample a number of times (a 3 time recycling measurement is shown in fig. 12.3). For this we repeat the tasks collected in the green shaded area of fig. 12.2, i.e. the state-preparation, QND and atom-number measurement, and so within each trap-cycle acquire a number of data segments. Finally, we discard all atoms using resonant MOT cooling light and in what we coin the *empty MZI* we acquire one or more segments of QND and atom number measurements, which we use for gauging the shot-noise and tracing the drift of the interferometer. The whole cycle-sequence is repeated an unspeakable number of times with the aim of collecting enough data that we can produce statistically significant predictions.

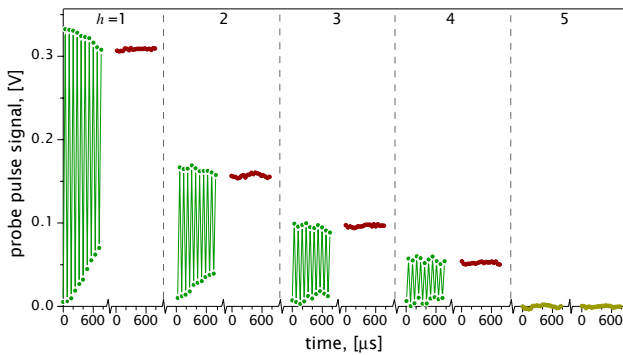


Figure 12.3: Recycling the atomic sample. Signal from 4 \rightarrow 5' probe showing Rabi-oscillations (green) — so as to illustrate that a coherent state has been prepared — and the atom number measurement following optical re-pumping (red). The two measurement types are repeated four times with steadily decreasing atom-numbers due to the limited efficiency of the optical pumping and decay of the sample.

As the last, an empty MZI shot-noise/MZI baseline measurement is taken (yellow). Here the same optical power is used in all probe pulses, but for the actual QND measurement the probing of the coherent superposition will employ much higher probe powers than the atom number measurement. We note that due to the sample decay, the initial amplitude of the Rabi oscillations tend to surpass the signal from the atom number measurement.

Varying the atom number We will be concerned with the noise properties of the QND measurement as a function of different parameters most notably the photon and atom numbers. To vary the former we may increase the probe power, pulse length or group pulses together as described in sec. 12.2.2. As for the atom-number we can vary this by several means. The segmented acquisition shown on fig. 12.3 already produces QND measurements for several atom number values. The inevitable variation of the initially trapped number of atoms also serves to

vary the parameter. In particular, the number varies with the changing background Cs pressure as the Cs dispensers are off or turned on. We do not change any other trapping parameters that affect the sample size, such as the FORT laser intensity, MOT cooler intensity and detuning, or optical pumping power, as this will affect the sample geometry, temperature or initial state in a way that would change the properties of the QND measurement. Nevertheless, as mentioned in sec. 10.2.4 the size of the MOT may influence the temperature of the atomic sample in the FORT and thus the dimensions of the sample. It would be difficult to account for such an effect and we assume that it can be neglected.

Correcting for atom number decay

The slight drop in the atom-number from the Rabi-oscillations to the atom number measurement in fig. 12.3 is due either to the natural decay of the sample size or a small inefficiency of the re-pumping process. Whatever the reason, the drop should be taken into account when we use the atom number measurement to estimate N_{at} at the time of the QND measurement. This correction is relevant when we want to make comparisons of the absolute magnitude of the projection noise as compared with the size of the mean atomic phase-shift. Thus in each measurement run with incorporate a measurement where we perform optical pumping and re-pumping as in the QND measurement sequence, but only measure the atom number at the different measurement times. When thus get a factor $C_{\phi,h}$ by which we multiply the phase-shift of the atom number measurement of the h 'th segment. The determination of $C_{\phi,h}$ can be combined with a spontaneous scattering measurement where an atom-number measurement at the time of the QND measurement is extracted from the amplitude of the reference Ramsey spin-echo fringe (e.g. the value at the origin of fig. 11.22, that as argued is above unity exactly because of the error in the atom number estimate.).

12.2 Analysis methods

When presented with a bulk of useful information it is crucial to handle it in a productive fashion. Failure to do so will at best lead to nothing and at worst cause numerous setbacks. If we accept this wisdom, it seems only fair to devote ample space for discussing our methods of data analysis. In doing so, we take up the baton from sec. 8.2.2 where we discussed how the measurement traces were stored as integrated pulse values on a PC (it may be useful to refer to table 8.2). In this section we will explain the initial steps to extract fruitful information out of these stored data values. Throughout the treatment, it is understood that we are endowed with a large set of measurements so that we are able to compute meaningful estimates of the statistical distribution of the data, predominantly in terms of variances and covariances. From a conceptual point of view it is important to bear in mind that all our measurement data allows us, is to estimate the distributions of the stochastic processes that influence the stored data values. When based on the data we claim a certain variance $\langle(\Delta p)^2\rangle$ it is in fact only our best estimate of the underlying variance $\langle(\Delta P(x))^2\rangle$, where $P(x)$ is the stochastic function of some parameter vector x responsible for the measured pulse values. This best estimate is naturally defined as

$$\langle p \rangle = \frac{1}{K} \sum_{j=1}^K p_j, \quad \langle(\Delta p)^2\rangle = \frac{1}{K-1} \sum_{j=1}^K (p_j - \langle p \rangle)^2$$

where we have included the mean-value as well. The p_j are individual measurement results and K is the size of the data set. In this case the bra-ket $\langle \cdot \rangle$ has the meaning of a sum over the data-set. This again is distinct from the quantum expectation value or ensemble average, which $\langle \cdot \rangle$ was set to represent in the Theory. There the bra-ket revealed the underlying statistics of the quantum state of the system/ensemble. To summarise, though the distinction exists between estimated and actual quantum and/or classical statistical properties of the measurements we will not convey it in our notation, in that we write our empirical variance as just $\langle (\Delta \cdot)^2 \rangle$.

12.2.1 Correlation

As a result of the discussion at the end of sec. 5.1.1 we understand that a key exercise in the data analysis is to extract the correlation between measurements. This is how we can claim squeezing of the measured atomic state, but it will also be a crucial element of several "data correction" steps in the analysis. The question of correlation boils down to the situation where, given two measurement results p_1 and p_2 which both have zero mean we must find the value ζ that minimises

$$\langle (\Delta(p_2 - \zeta p_1))^2 \rangle = \langle (\Delta p_2)^2 \rangle + \zeta^2 \langle (\Delta p_1)^2 \rangle - 2\zeta \langle (\Delta p_2 p_1) \rangle \quad (12.1)$$

where we recall that $\langle (\Delta p_2 p_1) \rangle = \langle (p_1 - \langle p_1 \rangle)(p_2 - \langle p_2 \rangle) \rangle$ is the covariance. The above expression is minimal for

$$\zeta = \frac{\langle (\Delta p_2 p_1) \rangle}{\langle (\Delta p_1)^2 \rangle}, \quad (12.2)$$

which is of course just the correlation coefficient of the two measurements. The fact that it is the first-pulse variance that appears in the numerator, underlines that in the formulation we implicitly presumed to be interested in the correlation of the first pulse with the second and not vice-versa. To rephrase, we determined that we want to deduce how much information the first pulse has on the value of the second pulse. This is indeed the relevant question to ask in the QND measurement. Quite often, though, we find the variances of both pulses to be equal. Given a sequence of measurements p_1, p_2, \dots, p_k eq. (12.2) hints that we would benefit greatly from computing the covariance matrix

$$\mathbf{C} = \begin{pmatrix} \langle (\Delta p_1)^2 \rangle & \langle (\Delta p_1 p_2) \rangle & \dots & \langle (\Delta p_1 p_k) \rangle \\ \langle (\Delta p_2 p_1) \rangle & \langle (\Delta p_2)^2 \rangle & \dots & \langle (\Delta p_2 p_k) \rangle \\ \vdots & \vdots & \ddots & \vdots \\ \langle (\Delta p_k p_1) \rangle & \langle (\Delta p_k p_2) \rangle & \dots & \langle (\Delta p_k)^2 \rangle \end{pmatrix} \quad (12.3)$$

whereby the correlation coefficient between two pulses may be defined as $\zeta_{\alpha\beta} = C_{\alpha\beta}/C_{\alpha\alpha}$. The covariance matrix has the important property that it is symmetric, i.e. $\mathbf{C}^T = \mathbf{C}$, in that clearly $\langle (\Delta p_1 p_2) \rangle = \langle (\Delta p_2 p_1) \rangle$.²

²this has a number of interesting consequences namely that the covariance matrix can be diagonalised by $\mathbf{D} = \mathbf{E}^{-1}\mathbf{C}\mathbf{E}$, where \mathbf{D} is the diagonal matrix and \mathbf{E} is an orthogonal matrix. Furthermore, the diagonal elements of \mathbf{D} are the eigenvalues of \mathbf{C} and \mathbf{E} is made up of the corresponding eigenvectors, which can be proven to be real and orthogonal [Fraleigh95].

Correlated and uncorrelated signal components

We now take further steps to develop a framework for understanding our measurement results. Given two pulse values p_1^j and p_2^j we can, generally, split each of them into a part c^j that is shared or correlated between the two and parts u_1^j and u_2^j , which are different or uncorrelated. Hence we write $p_1^j = c^j + u_1^j$ and $p_2^j = c^j + u_2^j$. The fact that c^j is correlated among the pulses and u_i^j not, dictates that c^j and u_i^j are uncorrelated and we can simply derive the variances and covariance between the two pulses over many realisations (j)

$$\langle(\Delta p_1)^2\rangle = \langle(\Delta c)^2\rangle + \langle(\Delta u_1)^2\rangle \quad (12.4a)$$

$$\langle(\Delta p_2)^2\rangle = \langle(\Delta c)^2\rangle + \langle(\Delta u_2)^2\rangle \quad (12.4b)$$

$$\langle(\Delta p_1 p_2)\rangle = \langle(\Delta c)^2\rangle \quad (12.4c)$$

whereby the correlation factor eq. (12.2) can be written as $\zeta = \langle(\Delta c)^2\rangle / [\langle(\Delta c)^2\rangle + \langle(\Delta u_1)^2\rangle]$. Applying our new insight to eq. (12.1) we get to the expression

$$\begin{aligned} \langle(\Delta p_2 - \zeta p_1)^2\rangle &= (1 - \zeta)\langle(\Delta c)^2\rangle + \langle(\Delta u_2)^2\rangle \\ &= \langle(\Delta c)^2\rangle + \langle(\Delta u_2)^2\rangle - \frac{\langle(\Delta c)^2\rangle^2}{\langle(\Delta c)^2\rangle + \langle(\Delta u_1)^2\rangle}. \end{aligned} \quad (12.5)$$

In fig. 12.4 we have plotted (red curve) the above variance as a function of

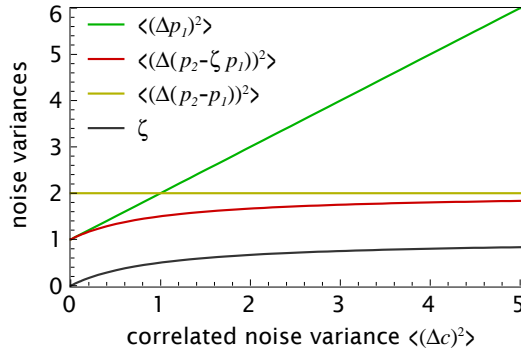


Figure 12.4: Predictions for the variances of various pulse combinations and the correlation factor. Green - is correlated noise. Red - Optimally reduced noise of second pulse using the first pulse. Yellow - noise of pulse difference. Grey - correlation factor ζ . Ideally, the classical noise is due to atomic projection noise in which case the x-axis would be equivalent to N_{at} .

$\langle(\Delta c)^2\rangle$ for an uncorrelated noise variance $\langle(\Delta u)^2\rangle \equiv \langle(\Delta u_1)^2\rangle = \langle(\Delta u_2)^2\rangle = 1$. If we take the limit of $\zeta = 0$, i.e., no correlation, then it is not surprising that we get $\langle(\Delta(p_2 - \zeta p_1))^2\rangle = \langle(\Delta u_2)^2\rangle$. In the interesting limit of perfectly correlated pulses $\langle(\Delta c)^2\rangle \gg \langle(\Delta u)^2\rangle \Rightarrow \zeta \approx 1$ it is a bit trickier to see that $\langle(\Delta p_2 - \zeta p_1)^2\rangle = \langle(\Delta u_2)^2\rangle + \zeta^2 \langle(\Delta u_1)^2\rangle$.³ This also makes sense, in that we can never reduce the variance below the level of the uncorrelated noise, which we have no way of predicting. The yellow curve show the result of subtracting the two pulses without taking ζ in to account

$$\langle(\Delta p_2 - p_1)^2\rangle = \langle(\Delta u_2)^2\rangle + \langle(\Delta u_1)^2\rangle \quad (12.6)$$

This tells us that just subtracting the two pulses we remove all the correlated noise and end up with twice the level of the uncorrelated noise, one half from the p_1 and the other half from p_2 .

Scaling with atom and photon number

Drawing on all the predictions we have made in the theory for the types of fluctuations influencing the signal, we should be in a good position to assign certain

³For $\zeta \rightarrow 1$ the factor $1 - \zeta$ in eq. (12.5) goes to 0, but $\zeta \rightarrow 1$ also implies $\langle(\Delta c)^2\rangle \rightarrow \infty$ and we are left to determine $0 \cdot \infty$.

sources to the noise depending on it being correlated or uncorrelated. Furthermore, the scaling with the atom and photon number will reveal something about the origin of the noise. As a good approximation we assume all noise sources to be statistically independent and we will write the correlated and uncorrelated noise in terms of its scaling with the atom number

$$\langle(\Delta c)^2\rangle = \langle(\Delta c^{(0)})^2\rangle + \langle(\Delta c^{(1)})^2\rangle + \langle(\Delta c^{(2)})^2\rangle \quad (12.7a)$$

$$\langle(\Delta u)^2\rangle = \langle(\Delta u^{(0)})^2\rangle + \langle(\Delta u^{(1)})^2\rangle + \langle(\Delta u^{(2)})^2\rangle \quad (12.7b)$$

so that $\langle(\Delta c^{(0)})^2\rangle \propto N_{\text{at}}^0$, $\langle(\Delta c^{(1)})^2\rangle \propto N_{\text{at}}^1$, $\langle(\Delta c^{(2)})^2\rangle \propto N_{\text{at}}^2$, and likewise for the uncorrelated noise terms. Any higher order terms are unphysical and — with the risk of making a tautology — don't show up in the experimental data. As a reference when we analyse our data we list the noise terms and their possible sources

$\langle(\Delta c^{(0)})^2\rangle$ All noise with no dependence on the number of atoms stems from fluctuations of the detection system. Signal components that are correlated between pulses within a train but not between different experimental realisations are rooted in slow drifts of the MZI. This could be due to drifts in the probe powers (see sec. 6.1.1) and acoustic noise of the MZI (see sec. 6.1.3).

$\langle(\Delta u^{(0)})^2\rangle$ Ideally the only source of signal components that are uncorrelated between two pulses within a segment is the quantum shot-noise of the probe (see eq. (2.25)). Additionally they can be caused by fast frequency fluctuations of the probes (see sec. 6.1.2) and high frequency acoustic noise in the MZI (see sec. 6.1.3).

$\langle(\Delta c^{(1)})^2\rangle$ Correlated signal components scaling linearly with the atom number are a signature of quantum projection noise (see eqs. (5.25 and 5.35)).

$\langle(\Delta u^{(1)})^2\rangle$ If the atomic state has not been modified in between the two probe pulses there is no sensible explanation for uncorrelated noise scaling as N_{at} . Classical noise necessarily scales quadratically in N_{at} . If the atomic state has been modified, e.g. by rotation of the pseudo-spin so that the probes detect two different initial spin components, this could also be a sign of projection noise (see sec. 12.6).

$\langle(\Delta c^{(2)})^2\rangle$ Correlated classical atomic noise will be induced by slow drifts of the probe powers, total atom numbers and the state preparation (see sec. 6.2.1). The latter effectively means drifts in the microwave power.

$\langle(\Delta u^{(2)})^2\rangle$ Uncorrelated classical atomic noise can be caused by fast fluctuations of the probe frequencies (see sec. 6.2.2). The probe power drifts, mainly caused by thermal drifts in relation to the fibres, should not appear on short time-scales except RF-intensity noise transferred by the pulsing AOMs (see sec. 8.1.2).

When based on a set of data we have calculated the variances and covariances we can fit them with 2nd order polynomials (quadratic fits) where according to eq. (12.4) the coefficients of the three terms in the polynomial should be related

$$\begin{aligned} \langle(\Delta p_i)^2\rangle &= \langle(\Delta c)^2\rangle + \langle(\Delta u)^2\rangle \\ &= [a_c^{(0)} + a_u^{(0)}] + [a_c^{(1)} + a_u^{(1)}]N_{\text{at}} + [a_c^{(2)} + a_u^{(2)}]N_{\text{at}}^2 \end{aligned} \quad (12.8a)$$

$$\begin{aligned} \langle(\Delta p_i p_j)\rangle &= \langle(\Delta c)^2\rangle \\ &= a_c^{(0)} + a_c^{(1)}N_{\text{at}} + a_c^{(2)}N_{\text{at}}^2. \end{aligned} \quad (12.8b)$$

This approach will be a key tool for analysing the extracted noise.

Gauging the noise reduction In the best case scenario the signal variance is composed of only shot noise ($\langle(\Delta u^{(0)})^2\rangle$) and atomic projection noise ($\langle(\Delta c^{(1)})^2\rangle$). In this case any noise reduction by eq. (12.5) can truly be ascribed to squeezing of the atomic projection noise. Yet, it is more than likely that other sources of noise also add variance to the signal. The most care must be taken when the variance has a contribution from light noise that is correlated between the pulse. In this case the correlation factor $\zeta_0 \neq 0$ even when no atoms are present. This is acceptable, but the problem arises when atoms add correlated atomic noise, thereby increasing ζ . When ζ grows with the number of atoms we not only subtract more and more correlated atomic noise, but also the correlated part of the light-noise. If the light-noise is dominated by the non-shot-noise contribution, one is given the impression that the noise reduction grows considerably, though essentially a large part of the reduction is unrelated to the squeezing of the projection noise. If the added noise is classical atomic noise which is correlated between the pulses the noise reduction is only affected slightly and as a crucial point it can only cause $\langle(\Delta(p_2 - \zeta p_1))^2\rangle$ to increase. Thus it does not create any conceptual misunderstandings. What regards uncorrelated noise influences, these, again, can only add to $\langle(\Delta(p_2 - \zeta p_1))^2\rangle$. The bottom line is that correlated classical light-noise must be kept low and when quantifying the squeezing we should compare the level of $\langle(\Delta(p_2 - \zeta p_1))^2\rangle$ at the given atom number with that when no atoms in the trap, i.e.

$$\frac{\langle(\Delta[p_2(N_{\text{at}}) - \zeta_{N_{\text{at}}} p_1(N_{\text{at}})])^2\rangle - \langle(\Delta[p_2(0) - \zeta_0 p_1(0)])^2\rangle}{\langle(\Delta p_2(N_{\text{at}}))^2\rangle - \langle(\Delta p_2(0))^2\rangle} \quad (12.9)$$

Linking different noise components with real numbers

We will use the symbols c and u a bit loosely to refer to either the actual probe signals or after the signals have been converted to phase-shifts. The exact meaning should be conveyed by the context of the analysis. Say that we have found the variances for the phase shift signal and have identified the part $\langle(\Delta c^{(1)})^2\rangle$ scaling linearly with N_{at} . Since, we equate this contribution with the projection noise we can express it together with the mean atomic phase-shift by

$$\langle(\Delta c^{(1)})^2\rangle = \langle(\Delta\phi_{\text{qnd},1,2})^2\rangle_{\text{PN}} = \frac{\langle(\Delta p_{1,2})^2\rangle_{\text{PN}}}{\left(\frac{1}{K_h} \mathcal{G}_A \sum_i^{K_h} \bar{p}_{\text{qnd},i}^j\right)^2} = \bar{\mathcal{G}}^2 \frac{1 + r_w^2}{1 + 2r_w^2} N_{\text{at}}$$

$$\langle\phi_{\text{ph}}\rangle = \frac{\langle p_{\text{at}}\rangle}{\frac{1}{K_h} \mathcal{G}_A \sum_i^{K_h} \bar{p}_{\text{at},i}^j} = \bar{\mathcal{G}} N_{\text{at}}$$

where $\bar{\mathcal{G}}$ is a common proportionality factor which in the expression for the variance is multiplied by the geometric factor from eq. (3.26). The factor $\bar{\mathcal{G}} = \frac{4}{c} \mathcal{K}_1$ We will use the above to estimate of the projection noise from the atomic phase shift through the reformulation

$$\langle(\Delta\phi_{\text{qnd},1,2})^2\rangle_{\text{PN}} = \bar{\mathcal{G}} \frac{1 + r_w^2}{1 + 2r_w^2} \langle\phi_{\text{ph}}\rangle \quad (12.10)$$

There is a neat trick for calculating the effective atom number without troubling ones mind to compute $\bar{\mathcal{G}}$. We simply divide the square of the phase-shift with

the noise so that the factors cancel and we are left with

$$N_{\text{at}} = \frac{1 + r_w^2}{1 + 2r_w^2} \frac{\langle \phi_{\text{ph}} \rangle^2}{\langle (\Delta c^{(1)})^2 \rangle} \quad (12.11)$$

To compute the atom number this way one needs to analyse the noise to find the projection noise $\langle (\Delta \phi_{\text{qnd},1,2})^2 \rangle_{\text{PN}}$, and one must know the gain \mathcal{GA} as well as the probe pulse powers measured on the power reference detector. To get the numbers exact we must also estimate the sample to probe beam waist ratio r_w , however for an order of magnitude estimate of N_{at} one can safely ignore the geometric factor replacing it by $1/2$.

In sec. 8.7 we already discussed that extracting the photon number is related to the uncorrelated light noise part of the noise. Therefore, we will quickly move on to the very involved pulse labelling conventions.

12.2.2 Data organisation and correction

Understanding the steps of the analysis (unfortunately) requires some insight in to how we organise our data. In line with the pulse labelling of fig. 12.2 we index the integrated pulse signals as p_i^j , where j denotes the cycle number and i the position in the pulse train. Some confusion arises from the fact that we repeat the QND and atom number measurements for a number of times as we recycle the atomic sample and take repeated projection-noise measurements. We accommodate this feature by allowing a double sub-index as in $p_{i,h}^j$. We term j the *cycle index*, h the *segment index*, and i the *pulse index*. When possible we restrict the number of indices to a minimum.

We already see in fig. 12.2 that we employ light pulses of different power depending on whether we perform a QND measurement or an atom number measurement. Later we will even have a few more pulse "types" join the zoo. It will be to our advantage to distinguish between the different pulse types, which can only be done by adding yet another label. As a start, we write QND measurement pulses as $p_{\text{qnd},i,h}^j$ and N_{at} measurement pulses as $p_{\text{at},i,h}^j$.

Having now created, stored and named our data we need to rear it for some productive outcome.

two-point pulses As a general procedure the next step is that we subtract the QND probe pulses from two consecutive experimental cycles making the substitution

$$\frac{1}{2}(p_{\text{qnd},i,h}^j - p_{\text{qnd},i,h}^{j+1}) \longrightarrow p_{\text{qnd},i,h}^j \quad (12.12)$$

We keep the same symbol for the modified pulse, but when wishing to underline this step we refer to the substituted pulse as the two-point pulse. The reason for doing the substitution is to cancel slow drifts (> 2 s) of the MZI and probe power balancing. This procedure is normally acceptable since in determining the projection noise one is interested in the fluctuations of $p_{\text{qnd},i,h}^j$ rather than the mean values. On the other hand, this procedure is problematic for certain applications as we will discuss in sec. 12.6. We must also keep in mind that this procedure effectively doubles the level of *all* variances, hence the factor of $1/2$ in the equation. We find the corresponding N_{at} probe pulse value by averaging over two consecutive cycles

$$\frac{1}{2}(p_{\text{at},i,h}^j + p_{\text{at},i,h}^{j+1}) \longrightarrow p_{\text{at},i,h}^j \quad (12.13)$$

Here we take the average value, because the very point of the atom number measurement is to measure the absolute phase-shift of the MZI phase due to the atoms (this is exactly what eq. (12.12) erases)

“Empty” MZI baseline subtraction We take another step to minimise drifts of the MZI. This involves subtracting the mean QND-pulse values over the shot-noise measurement segment h_{SN} , where the MZI is empty i.e. there are no atoms in the sample. We define the MZI baseline as

$$p_{\text{BL}}^j = \sum_{h=h_{\text{SN}}} \sum_{i=1}^{K_h} p_{\text{qnd},i,h}^j \quad (12.14)$$

where K_h is the number of pulses in the shot-noise measurement segment. Next we find the degree of correlation between the above baseline and the baseline in each QND measurement segment defined as above but with a particular h .

$$\zeta_{\text{BL},h} = \frac{\langle (\Delta(p_{\text{qnd},h}^j p_{\text{BL}}^j)) \rangle}{\langle (\Delta p_{\text{BL}}^j)^2 \rangle} \quad (12.15)$$

which finally allows us to remove the appropriate amount of baseline from each QND measurement pulse

$$p_{\text{qnd},i,h}^j - \zeta_{\text{BL},h} p_{\text{BL}}^j \longrightarrow p_{\text{qnd},i,h}^j \quad (12.16)$$

The aim of eq. (12.16) is again to compensate for drifts of the MZI baseline. By going to the two-point pulses we cancelled drifts on the cycle time-scale, and now the baseline-subtraction will cancel drifts on the ~ 100 ms time-scale⁴. In other words we remove noise that is correlated over ~ 100 ms but not over ~ 3 s. We subtract the mean pulse value over all available shot-noise pulses in order to minimise the amount of shot-noise that we add to the QND pulses. This leads to one note of caution, that the amount of correlated noise removed by the procedure should be less than the amount of shot noise added. For the atom number pulses we subtract the signal in the empty interferometer measurement from the pulse values measured in the four realisations of the atomic measurement. Again we subtract the MZI offset and thus ensure the atomic probe signal p_{at}^j to be proportional to N_{at} .

Converting to phase-shift We want to convert the integrated detector signals into a meaningful physical quantity, namely the phase-shift of the MZI fringe. The transformation of the pulse signals into phase-shifts is prescribed by

$$\phi_{\text{qnd},i}^j = \frac{p_{\text{qnd},i}^j}{\frac{1}{K_h} \mathcal{G}_{\mathcal{A}} \sum_i^{K_h} \bar{p}_{\text{qnd},i}^j} \quad , \quad \phi_{\text{ph},h}^j = \frac{\sum_i^{K_h} p_{\text{at},i}^j}{\mathcal{G}_{\mathcal{A}} \sum_i^{K_h} \bar{p}_{\text{at},i}^j} \quad (12.17)$$

for the QND and atomic phase-shift measurements respectively. K_h is the number of pulses per segment and $\mathcal{G}_{\mathcal{A}}$ relates the reference power signal to the fringe amplitude on the QND detector c.f. sec. 8.5. Within a segment the atom-number should be pretty constant, which is why for the atom-number estimate we take the average value within a segment. To relate the atomic phase shift to the value it would have had at the time of the QND measurement we use the compensation factor from sec. 12.1.1 and substitute $\mathcal{C}_{\phi,h} \phi_{\text{ph},h}^j \rightarrow \phi_{\text{ph},h}^j$. As a note, we use the “ph” subscript for the atomic-phase shift $\phi_{\text{ph},h}^j$ to be consistent with the theoretical treatment where in sec. 4.4 we assigned $\tilde{\phi}_{\text{ph}}$ to the phase-shift of the probe and $\tilde{\phi}_{\text{at}}$ to the phase-shift of the atomic state.

⁴on average the duration from the QND measurements to the shot-noise measurement

Combining pulses A final pulse operation is to create composite pulses by combining subsequent probe pulses within a segment

$$\tilde{\phi}_{\text{qnd},i,h}^j = \sum_{i'=g \cdot (i-1)+1}^{g \cdot i} \phi_{\text{qnd},i',h}^j \quad (12.18)$$

This provides an easy way to vary the effective probe photon number and thus the interaction strength in order to explore the optimal experimental parameters. However, it is important to keep in mind that combining several pulses modifies the detection bandwidth of the measurement. Hence, the increase of effective pulse duration may also impact the measurement's sensitivity to classical noise sources.

Sorting and binning We now need to make use of the expected behaviour of the noise in our data, so that we can intelligently sort it and find the statistical properties over appropriate subsets of the data. This intelligent choice of course depends on which parameters we chose to vary in a given measurement run, but for the moment we focus on the situation where it is only the number of atoms that is (deliberately) varied (see sec. 12.1.1).⁵ Therefore, the probe phase-shifts $\tilde{\phi}_{\text{qnd},i,h}^j$ are sorted according to the corresponding atom number given by the value of $\phi_{\text{ph},h}^j$. As we sort the phase-shifts we may finally toss out the segment index h and just expand the sorted cycle dimension j . To determine the statistical properties for different atom numbers we compute $\langle (\Delta\tilde{\phi}_{\text{qnd},i})^2 \rangle$ and $\langle (\Delta\tilde{\phi}_{\text{qnd},i} \tilde{\phi}_{\text{qnd},j}) \rangle$ over a subset of K_j data points in ascending bins according to $\phi_{\text{ph},h}^j$. We shall refer to K_j as the *bin-size*. We treat the empty-interferometer segments like all the other and naturally they all have $N_{\text{at}} \approx 0$. When we bin the data we stack all the $N_{\text{at}} \approx 0$ traces into a single bin, which consequently can contain more data points than K_j . As a final remark, it does not matter whether we first combine pulses, as described in the preceding paragraph, or first sort and bin pulses, because the atom number is calculated as a mean over all atom-number measurement pulses.

12.2.3 Conditioning data

Conditioning and discarding portions of the experimental data is always a contentious issue, but with very few exceptions it is an important and necessary task [Ravetz05]. Rather than sweeping it under the rug we shall be open about this step. The crucial stipulation is that data is evaluated and discarded with criteria that do not directly reflect the quantity that is considered the final outcome. In our case, this means that we should be very careful to condition data based on the value of the QND measurement phase-shift. Corresponding to every QND measurement phase-shift we do, luckily, have at our disposal a number of supplementary measurements that disclose most of the information relevant for determining irregular operation of the experimental apparatus.

DSO range saturation When the QND or power reference detector signals exceed the set y-ranges the DSO simply stores a not-a-number *NaN* value in the recorded file. When the traces are integrated the NaN value will carry over to the calculated pulse integral. Thus we start the data conditioning by sorting out all the NaN values and then discarding all data in the same segment.

⁵When sorting we mix pulses acquired at vastly different times and it is crucial that all long term drifts of the pulse values are compensated by the preceding measures.

Probe powers The probe powers are recorded on the power reference detector either in terms of the combined power or if programmed in the control program we can choose to monitor the individual powers (see e.g. fig. 12.8ai). We condition the probe powers by demanding that the average within a segment should not deviate from the corresponding mean over the 100 neighbouring cycles by more than a fixed number, typically 2-3 standard deviations. This discards all cycles where the probe laser mode has jumped in one or more segments. In the case where the probe laser settles to a new stable mode the procedure will fail to remove the points. The procedure will also fail if the whole measurement is marred by an unstable laser such that the standard deviation is very large. In both cases we put our faith in the presiding *human interface* to step in and condition the data instead.

Atom numbers The conditioning on the atom numbers works in almost the same way as the probe power filtering. The averaged atom number over the segment is compared with the mean over a set of 100 neighbouring values and if the current value deviates from the mean by more than 2-3 standard deviations all data in the cycle is discarded.

FORT laser mode With the Fabry-Perot described in sec. 9.1.2 we continuously monitor if the FORT laser is lasing on a single frequency. In the acquisition program we store the resonance peak amplitude of the Fabry-Perot and if this falls below a set threshold all data from the corresponding measurement cycle is discarded. This monitoring was not implemented during the first QND measurements, but only from the measurements described in sec. 12.4.3 and onwards.

MZI signal balancing We can measure how balanced the MZI is i.e. how far the individual probe colour fringes are offset from zero. In the 1-input MZI we can test how far the mean of the QND measurement pulses are off-set from zero. In the 2-input MZI the dichromatic probe pulses will always be balanced and the test can only be performed if the QND pulse train contains pulses of the individual probe colours as in fig. 12.8a. In both the 1 and 2-input MZI the balancing can be shifted by sudden changes in the probe powers or frequencies. Likewise, jumps in the number or collective state of atoms will misbalance the MZI.⁶ The data is conditioned on being balanced to better than a certain threshold fraction of the fringe amplitude — typically 2.5%.

Excessive noise Now we risk being evicted from Eden. Since the measurement noise is precisely the quantity we are interested in we must be very careful about what limits we impose on it. Necessarily, we impose a very generous limit of a particular two-point norm not being larger than six standard deviations as computed over all two-point data values. The probability of a *real* data point exceeding this value is $e^{-6^2} \approx 2 \cdot 10^{-16}$. Thus it seems fair to assume that all data failing this test are truly contaminated by some experimental glitch not detected by any of the above. Such glitches could be the probe laser frequency jumping with the result that the atomic phase-shift changes drastically, but still so that the QND detector signal remains within the range of the DSO channel. When the

⁶why the individual probe colours of the 2-input MZI should be balanced even in the presence of atoms will be explained in sec. 12.4.3.

MZI is aligned to white light such frequency jumps will not cause a significant change in the baseline of that probe.

Buffering If something causes a data point to be discarded it is not unlikely that the same *something* has influenced the experiment right before and after the discarded data was acquired. This may have been too small a disturbance of the data values to be caught by the above conditions, but to be sure we also remove all data in the cycles before and after a discarded cycle.

Manual exclusion When we have observed some parts of the experiment performing badly, e.g. probe or MOT lasers out of lock or multi-moding, for a period we often manually exclude the corresponding data points because we know they are polluted.

12.3 State destruction

We reserve a few lines to remind ourselves that the spontaneous scattering has a number of consequences for the squeezed spin-state envisaged as the outcome of a QND measurement. Firstly, spontaneous scattering of an equal coherent superposition product-state reduces the pseudo-spin magnitude, thus reducing the output state's usefulness for improving the resolution in spectroscopic measurements. This is captured by the spin squeezing criterion of eq. (3.33). Secondly, spontaneous scattering, being a random process, may add statistical noise to the final pseudo-spin state, thus counter-acting the noise reduction from the QND measurement. This effect can, however, be almost eliminated by intelligent choice of the probe detunings as hypothesised in sec. 4.5.1.

12.4 Spin squeezing experiments - approaches and results

The focus of this part will revolve around how high a SNR we can achieve in the measurement. By virtue of its name, the SNR depends on two factors, firstly the amount of signal which equates to the achievable coupling strength. The coupling is closely linked to the atomic density and the probe detunings and powers. On the other hand, these parameters also affect the other inherent part of the SNR, namely the noise contributions that limit the measurement's sensitivity. In the Introduction we enrolled some more or less distinct approaches to the task of stabilising the MZI detection. One was to do everything to make the inherent stability of the MZI so that the detection system becomes noise-less. An alternative is to construct a system which is immune to particular limiting sources of noise. Hence, the MZI may be noisy in several regards, but without affecting the actual QND measurement. The final approach, is to trace any fluctuations, instead of removing them, and then compensate for them in the data analysis. In the following chapter we treat the last of these approaches, which chronologically was the second that we tried out. By this we admit that we had hoped the setup to be sufficiently well constructed so as to achieve full inherent stability. Alas, life is a learning experience.

12.4.1 One-input MZI with reference pulses

In sec. 8.7.1 we established that the 1-input MZI could be made to operate shot-noise limited if the QND probe pulses were compensated for MZI phase drifts by use of a train of reference pulses. Thus, for the 1-input MZI QND measurement we apply the pulse sequence shown on fig. 12.5. Each QND probe pulse (tinted

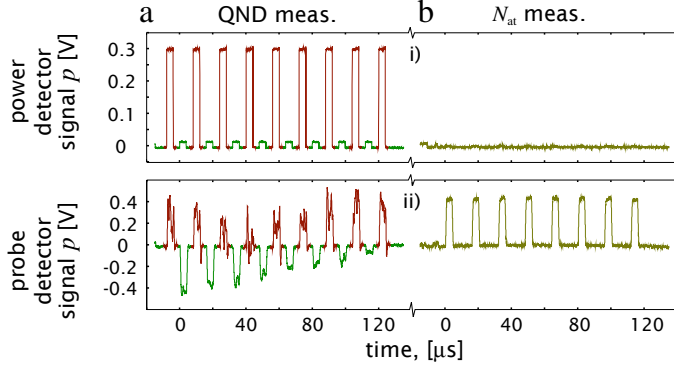


Figure 12.5: Raw detector signals for 1-input MZI configuration with reference pulses. a) QND measurement pulses train reflected in i) power reference detector and ii) QND detector. Time slices surrounding probe pulses are in green while those around reference pulses are in red. b) atom-number measurement pulse train signal on the two detectors.

green) is surrounded by a set of intense reference pulses (tinted red), which we label $p_{\text{ref},i,h}^j$. Using two instead of a single reference pulse for the compensation should result in a better compensation. Before the transformation of the probe pulses in to two-point pulses sec. 12.2.2 we correct the probe pulses by use of the reference pulses. As noted, shot noise, classical probe laser noise, and fast acoustic noise are not correlated with reference pulses. Hence, to achieve the optimal compensation we subtract only a fraction of the reference pulse value

$$p_{\text{qnd},i,h}^j - \zeta_{\text{ref}} \frac{1}{2} (p_{\text{ref},i,h}^j + p_{\text{ref},i+1,h}^j) \rightarrow p_{\text{qnd},i,h}^j, \quad (12.19)$$

where the correlation factor

$$\zeta_{\text{ref}} = \frac{\langle (\Delta p_{\text{qnd},i,h}^j - \frac{1}{2} (p_{\text{ref},i,h}^j + p_{\text{ref},i+1,h}^j)) \rangle}{\langle (\Delta p_{\text{qnd},i,h}^j - \frac{1}{2} (p_{\text{ref},i,h}^j + p_{\text{ref},i+1,h}^j))^2 \rangle}, \quad (12.20)$$

is computed by taking the average value of the reference pulses flanking each probe pulse. One caveat is that each reference pulse — except the first and last ones — is used to compensate two neighbouring probe pulses, thus possibly giving rise to a small amount of correlation between neighbouring compensated probe pulses. We remind, that a measurement dominated by classical fluctuations of the MZI results in a large ζ_{ref} whereas a shot-noise limited MZI yields $\zeta_{\text{ref}} \approx 0$. Following the reference pulse correction we proceed with all the steps described in sec. 12.2.2. We are in principle able to combine pulses in the train, however doing so comes at the expense of a large amount of data being discarded as the detector saturates. After a few reference pulses just a small fluctuation can drive the QND detector in to saturation. Hence, we make independent measurement runs for different probe laser intensities.

As we sort and bin the QND measurement pulse trains according to atom number, we construct the covariance matrix between the different pulses in the train, over all the pulse trains within a bin. In fig. 12.6 we plot selected variances as function of the bin's mean atom number. The variance of the first and second pulses (green open and filled circles respectively) are almost equal indicating no change in noise due to the probing. A second order polynomial fit (green

Δ_{32}	Δ_{45}	t_p	t_{rep}	$N_{\text{ph},a}$	$N_{\text{pha}}/N_{\text{phb}}$	$\tau_{\pi/2}$	$1 - e^{-\eta}$	$N_{\text{ph,ref},a}$
MHz	MHz	μs	μs	–	–	μs	–	–
135	-160	4	16	$1.15 \cdot 10^7$	0.65	43*	0.35	$41 \cdot 10^7$

Table 12.1: Experimental parameters and probe settings for 1-input MZI measurement with reference pulses. The photon number and decoherence correspond to a single probe pulse. *During this measurement the low insertion loss switch from AMC had just broken, but we could still use it to switch one output off, though with half the power constantly lost to the other output.

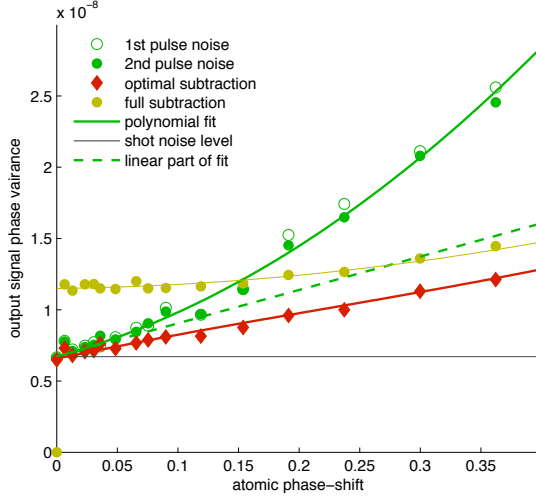


Figure 12.6: Plot of variances for different pulses and combinations in 1-input MZI. The variance of the first and second pulses (green open and filled circles respectively) is fitted to a polynomial and the linear part is plotted as green dashed line.

line) to the atomic noise shows a comparable influence of quadratical classical and linear quantum projection noise (green dashed line). The light noise (grey line) is given by the variance of the $N_{\text{at}} = 0$ bin. The variance of the difference of pulse 1 and 2 (yellow points) is a little bit lower than twice the light-noise. Since $\langle(\Delta\tilde{\phi}_{\text{qnd},2} - \tilde{\phi}_{\text{qnd},1})^2\rangle$ only reflects uncorrelated noise, this means that in the light noise there is some correlated component added to the shot noise. Additionally, the increase of $\langle(\Delta\tilde{\phi}_{\text{qnd},2} - \tilde{\phi}_{\text{qnd},1})^2\rangle$ with larger N_{at} is another mark of uncorrelated classical atomic noise. The SNR, i.e., the ratio of projection to light noise, nearly reaches 3/2. All this, means that the reduced noise points $\langle(\Delta(\tilde{\phi}_{\text{qnd},2} - \zeta\tilde{\phi}_{\text{qnd},1}))^2\rangle$ (red diamonds) do fall below the believed projection noise level, but not significantly. The fact that we *can* lower the noise shows that much of the classical atomic noise is correlated between subsequent pulses.

To get a better grasp of the noise sources we fit the average variance $(\langle(\Delta\tilde{\phi}_{\text{qnd},1})^2\rangle + \langle(\Delta\tilde{\phi}_{\text{qnd},2})^2\rangle)/2$ and the covariance $\langle(\Delta\tilde{\phi}_{\text{qnd},1}\tilde{\phi}_{\text{qnd},2})^2\rangle$ with interdependent coefficients as explained in sec. 12.2.1. In fig. 12.7 we plot the average pulse variance (green circles) along with the squeezed variances $\langle(\Delta(\tilde{\phi}_{\text{qnd},2} - \zeta\tilde{\phi}_{\text{qnd},1}))^2\rangle$ (red diamonds). The fits confirm that most of the classical atomic noise is correlated between the pulses (yellow area). Thus, according to eq. (12.5) it will not disturb the noise reduction much. We also see a small amount of uncorrelated classical atomic noise (orange area). Therefore the classical atomic noise stems mainly from slow drifts, e.g. of the relative probe powers or frequencies. As expected, the light noise contains a component, which is correlated between the pulses, though most of the light noise is still uncorrelated shot-noise, meaning that we have not added much shot-noise by the reference pulse correction. As for the noise reduction, we already mentioned that $\langle(\Delta(\tilde{\phi}_{\text{qnd},2} - \zeta\tilde{\phi}_{\text{qnd},1}))^2\rangle$ falls below the projection noise level, here by 1.8 dB. When taking the decoherence into account, this reduction is no longer effective. The squeezing w.r.t. the "Kitagawa criterion" eq. (3.31) is basically $\xi_{\text{ueda}} = 0$, while according to the "Wineland

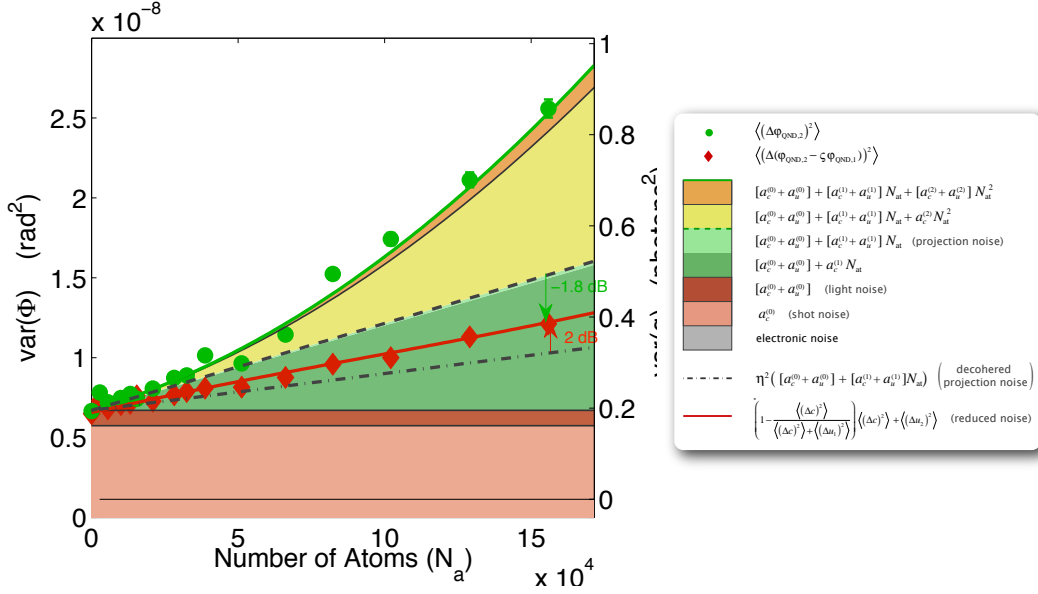


Figure 12.7: Plot of correlated and uncorrelated pulse variances with different atom-number scaling in 1-input MZI. The atom number is calculated from the mean bin phase-shift $\langle \tilde{\phi}_{\text{ph}} \rangle$ c.f. eq. (12.10).

criterion” the reduced noise is anti-squeezed by $\xi_{\text{wineland}} = 1.5$ (2 dB). In sum, the QND measurement does reduce the uncertainty of \hat{F}_z to below the projection noise level, but the amount of spontaneous scattering means that reduced noise is still larger than the noise of the coherent part of the final state. As a consolation, the measured reduced variances agree well with that expected (red curve) from the amounts of correlated and uncorrelated noise c.f. eq. (12.5). This agreement demonstrates that we perform our statistical data analysis properly and consistently.

One explanation for the cause of the correlated classical atomic noise is that it is an indirect effect of the atomic phase-shift. If without atoms the probe signal is balanced, the atoms will shift the fringe so that the signal becomes unbalanced. Since the signals from each probe is opposite this does not affect their combined signals and we had presumed this to be a sufficient condition. However, we recall from sec. 6.1.1 that an unbalanced probe signal allows classical laser intensity noise to affect the output signal. Since the intensity noise of the two probe colours is not correlated it will contaminate the combined signal as soon as the probe signals individually become unbalanced. The larger N_{at} the larger the misbalancing and thus the larger the feed-through of classical laser intensity noise. To generate signal fluctuations corresponding to a phase variance of 10^{-7} at a phase-shift of 0.3 rad we only need about 0.1% intensity noise in both probe lasers. For low frequencies this level of intensity noise is not unreasonable. As indicated by fig. 8.9 in the relevant 10-100 kHz range corresponding to the typical duration of a pulse train the intensity noise is rather low, in agreement with the near absence of uncorrelated atomic noise in fig. 12.7. It is worth remembering that fig. 12.7 did not account for the intensity noise that the pulsing AOM — despite our best efforts — may add to the probe. To round off, it is quite a subtle how pure noise in the MZI in this way masks as atomic noise. In the 2-input configuration it turns out there is a way to overcome this dummy classical atomic noise.

12.4.2 One input MZI — what now?

Another, cause of the classical atomic noise may be classical probe laser frequency noise. The influence of frequency noise can be reduced by increasing the probe detunings c.f. eq. (6.14). Hence, we decided to perform another series of measurements at double the probe detunings, i.e., $\Delta_{45'} = -320$ MHz and $\Delta_{32'} = -198.8$ MHz. To maintain the SNR of the QND measurement the increase of detuning must be accompanied by a quadrupling of the probe powers (see eq. (5.18)).⁷ As most considerations are unchanged, we do not make a detailed account of that measurement, but draw out the main lessons from it. First of all, we did see reduction, roughly by one half, of the classical atomic noise, indicating that part of it is indeed rooted in probe frequency drifts and fluctuations. Nevertheless, a significant amount of classical atomic noise remained and on top of that the light noise was increased considerably above the shot noise level. The reason for this is twofold. Firstly all classical noise scales quadratically (see sec. 6.1) with the power and eventually can come to dominate the linearly scaling shot-noise. To understand the second cause we must recall that the reference pulses only pay off in is as long as subtracting them does not add too much of their own shot noise. The requirement for the reference pulse power to be higher than the probe power becomes difficult to meet when the latter is increased and the former is limited by the QND detector saturation. For the optimal probe power the reference power could only be set 3-5 times higher. Hence the shot-noise level of the compensated probe pulses was increased by about 15-30%. A curious detail is that since each reference pulse is shared for two probe pulses, some of the added light-noise will turn up as noise that is correlated between subsequent pulses.

The above measurements had come within a hair's breath of demonstrating spin squeezing but to improve the results we needed to root out the remaining classical noise. When increasing the powers proved unfeasible we decided to reconfigure the MZI to the 2-input version. Except for the actual task of re-building parts of the setup the 2-input MZI seemed to offer many advantages. The acoustic noise would be suppressed (see sec. 6.1.3) and we would not need the added trouble of having reference pulses. The probe laser frequencies could be locked tightly by the beat-note locking (see sec. 8.1.3) so that their difference frequency, which is crucial in the 2-input configuration, would be very stable. Additionally, the correlated classical atomic noise caused by the drifts of the relative probe powers could be minimised by use of the precise relative power measurement ingrained in the path-length wiggling method (see sec. 8.6.3). Finally, the light-shift of the atomic state could be cancelled, so that the re-phasing procedure would no longer be required (see sec. 11.2.1). This was a pertinent issue, because all attempts to insert a spin-echo pulse in between two probe pulses resulted in extreme growth of classical atomic noise, which made any projection noise completely undetectable.⁸ Much of this effect was due to the microwave pulses seeding noise in the QND detector electronics — a displacement of the detector baseline was quite clear. Later experiment also revealed a notable intensity noise in the microwave power (see sec. 12.6). The case seemed clear..

⁷the reason is that the coupling strength roughly scales with the decoherence $\eta \propto N_{\text{ph}}\Delta^{-2}$. Hence, doubling Δ must be accompanied by a four-fold increase of N_{ph} .

⁸it is not trivial exercise to find the space for a π pulse in between two probe pulses when that is also where a reference pulse should be located.

12.4.3 Two-input MZI

The setup for the 2-input MZI is sketched in fig. 8.16. In the 2-input MZI configuration the rejection of common mode acoustic noise should eliminate the need for reference pulses to trace the interferometer baseline. We thus rely on the empty-MZI trace to correct drifts of the probe pulse phase as described in sec. 12.2.2. The raw QND and power reference detector signals are shown in fig. 12.8. In the QND measurement pulse train the actual QND pulses are tinted

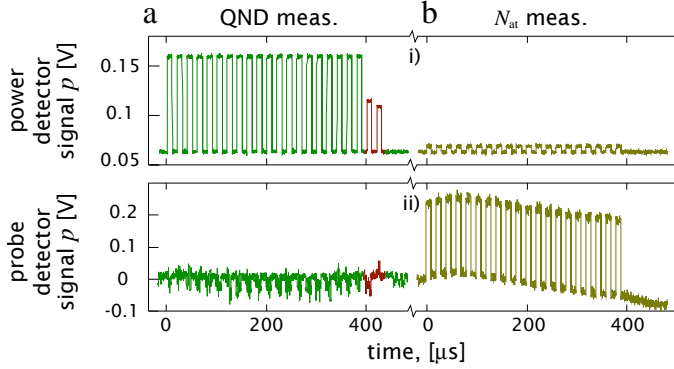
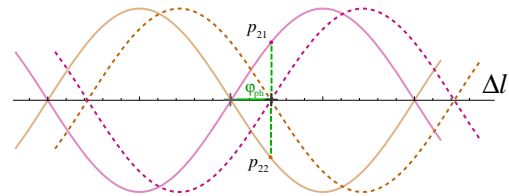


Figure 12.8: raw QND and power reference detector signal for 2-input MZI configuration.

green while the purpose of the two red tinted pulses are to balance the individual probe signals. In the analysis of the 1-input MZI results we noted that the misbalancing of the individual probes would allow classical laser intensity noise to mask as classical atomic noise. Thus, to avoid classical amplitude noise we wish both probes *individually* to be in the balanced position during the QND measurement. Since in the 2-input case the mean atomic phase-shifts have the same signs for both colours it is possible to offset the MZI locking point to cancel this mean shift. Notice that this would not be achievable in the 1-input configuration where the atoms shift the two probes by opposite mean phases. To determine the offset locking point we make use of the additional pulse pair ($p_{21,h}^j$ and $p_{22,h}^j$) at the end of the probe train, marked red in figure 12.8a. Each of these pulses contain only one probe colour and for a given atomic phase-shift will result in the signal indicated on fig. 12.9. The locking point is found by demanding that

Figure 12.9: Phase offset in to balance probe signals in 2-input MZI. For an MZI balanced without atoms the atoms shift both probe fringes by $\tilde{\phi}_{ph}$, which results in the individual signals $p_{21,h}^j$ and $p_{22,h}^j$ of equal magnitudes but opposite signs. Displacing the MZI fringe by $-\tilde{\phi}_{ph}$ by adjusting the Δl causes the probe signals to be re-balanced, i.e., $p_{21,h}^j = p_{22,h}^j = 0$.



the signal difference between them be zero i.e. $p_{21,h}^j - p_{22,h}^j = 0$, as is the case in figure 12.8aii. Thus this difference serves as an error signal, which is fed forward to adjust the MZI offset in the subsequent experimental cycle. An important note is that within a cycle the offset during all atom number measurements is fixed to the value set for the pulse train recording the empty MZI noise at the end of the cycle. Hence, it is only during the QND probe pulses that the phase is offset. The offset values for each segment are transferred to the locking unit fig. 8.24 shift-register, which is incremented by a trigger pulse right after each pulse train has ended (sketched in fig. 8.22 trace 12 and 13).

Measurement settings The probe settings are given by table 12.2.

Δ_{32}	Δ_{45}	t_p	t_{rep}	$N_{ph,a}$	N_{pha}/N_{phb}	$\tau_{\pi/2}$	$1 - e^{-\eta}$
MHz	MHz	μs	μs	–	–	μs	–
-85	-160	10	20	$0.37 \cdot 10^7$	12	4.1	0.054

Table 12.2: Probe settings for 2-input MZI measurement. The photon number and decoherence correspond to a single probe pulse.

Now that we can use all probe pulses in the trains without having to discard data, we start the analysis by computing the correlation matrix between all the pulses (c.f. note below eq. (12.3)) and visualise it in fig. 12.10. The correlation

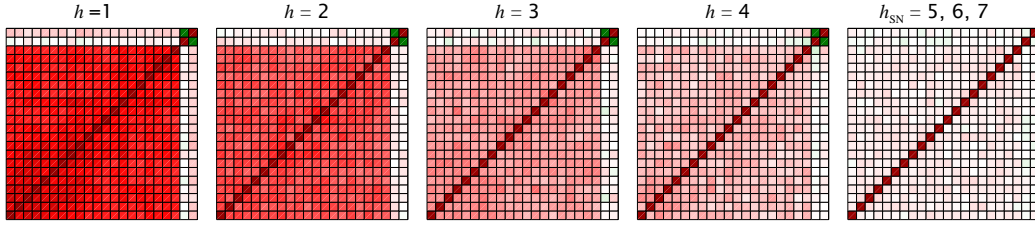


Figure 12.10: Correlation matrix for pulses within each segment. The diagonal elements are by nature 1 while the off-diagonal elements give the correlation factor ζ between the pulses. Red indicates positive values while green indicates negative values and white corresponds to 0.

is computed for the pulses after going to two-point values, subtracting the baseline, and conditioning, but before combining and sorting according to N_{at} (see sec. 12.2.2 and sec. 12.2.3). The diagonal elements are all 1 while the off-diagonal elements reveal the correlation between pulses. Focusing on the first 20 pulses, for which a dichromatic probe was used, we see clear correlation. The high N_{at} segments yield the strongest correlation. A slight amount of correlation is also visible in the shot-noise segment, indicating some remaining drifts in the MZI. Since this correlation is much smaller than that of the atomic noise, we can reaffirm that the 2-input interferometer in the balanced position operates at the shot noise limit up to the time scale of the experimental cycles $\approx 2s$. As we expect, the two offset detecting pulses $p_{21,h}$ and $p_{22,h}$ are strongly anti-correlated. This is because any acoustic noise in the MZI affects the two pulses oppositely. For the dichromatic pulses the 2-input configuration removes their susceptibility to acoustic noise altogether. The fact that $p_{21,h}$ and $p_{22,h}$ are completely uncorrelated with the other pulses, shows that the two last pulses are dominated by acoustic MZI noise. In the 2-input MZI the baseline subtraction has only a small noise reducing effect and it is possible to leave it out. This again indicates that the MZI baseline only drifts on slow time-scales above a few seconds where. These slow fluctuations are removed by the two point procedure of subtracting pulses in subsequent cycles.

From this point on we will analyse the data *after* sorting and binning according to atom number. Hence, all information on the segments is erased and the different QND measurement pulse trains are ordered according value from the corresponding atom number measurement. For pulse trains falling within a bin⁹ we construct the covariance matrix between the different pulses in the train, and plot selected variances as function of the mean bin atom number fig. 12.11. For

⁹in fig. 12.10 the matrix was calculated for pulses in the same segments.

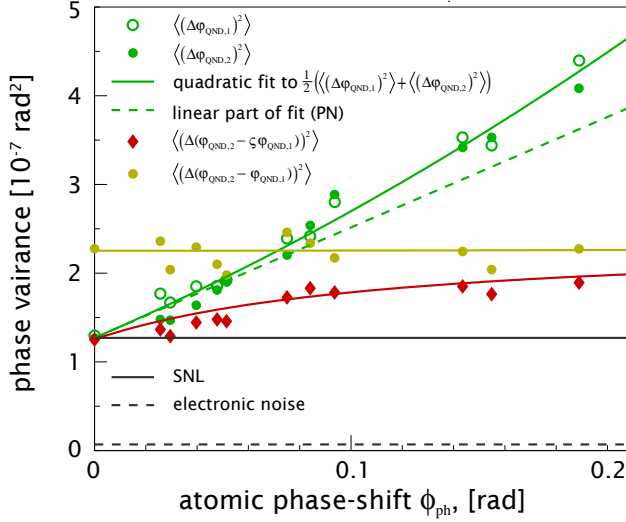


Figure 12.11: Plot of variances for different pulses and combinations in 2-input MZI. The variance of the first and second pulses (green open and filled circles respectively) is fitted to a polynomial and the linear part is plotted as green dashed line.

the variances shown we have specified 11 bins and combined 4 pulses in $\tilde{\phi}_{\text{qnd},i'}$ for a reason that will become clear shortly. The variance of the first and second pulses (green open and filled circles respectively) are almost equal indicating no change in noise due to the probing. The polynomial fit (green line) returns a large linear component (green dashed line), which means that classical atomic noise is relatively small. The light noise (grey line) is given by the variance of the $N_{\text{at}} = 0$ bin. As for the 1-input MZI, $\langle(\Delta\tilde{\phi}_{\text{qnd},2} - \tilde{\phi}_{\text{qnd},1})^2\rangle$ (yellow points) is slightly lower than twice the light-noise, which therefore must contain a small correlated part. The SNR, i.e., the ratio of projection to light noise, goes up to almost 2. Achieving this SNR despite the fact that we reach a smaller atomic phase-shift than in the 1-input MZI, is mostly a result of the unequal power in the probe and reference arms. For this measurement the power ratio is 12, so that shot-noise from the reference arm is suppressed by a factor of 1/12. The combination of all these factors results in a noteworthy reduction of $\langle(\Delta(\tilde{\phi}_{\text{qnd},2} - \zeta\tilde{\phi}_{\text{qnd},1}))^2\rangle$ (red diamonds) w.r.t. the projection noise level. We will quantify the statement following the next figure.

We now account for the covariances and make interdependent quadratic fits to the variances and covariances (see eq. (12.8)). In fig. 12.12 we again plot the av-

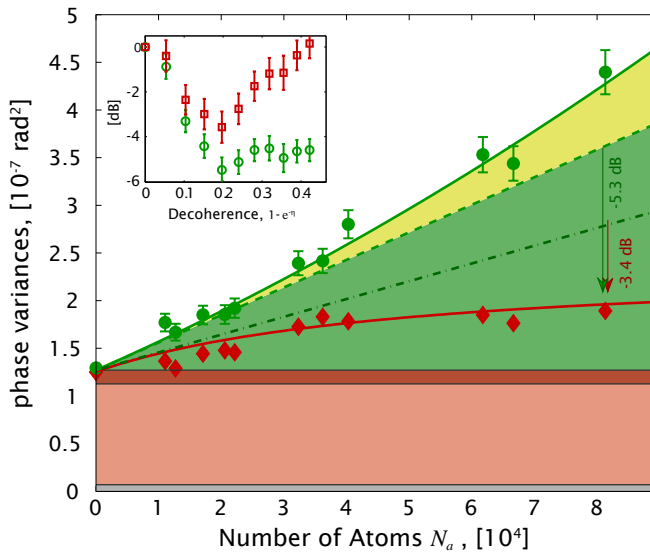


Figure 12.12: Plot of correlated and uncorrelated pulse variances with different atom-number scaling in 2-input MZI. The atom number is calculated from the mean bin phase-shift $\langle\tilde{\phi}_{\text{ph}}\rangle$ c.f. eq. (12.10).

erage variance of the 2 first pulses ($\langle(\Delta\tilde{\phi}_{\text{qnd},1})^2\rangle + \langle(\Delta\tilde{\phi}_{\text{qnd},2})^2\rangle$)/2 (green circles) along with the squeezed variances $\langle(\Delta(\tilde{\phi}_{\text{qnd},2} - \zeta\tilde{\phi}_{\text{qnd},1}))^2\rangle$ (red diamonds). We see that the remaining classical atomic noise (yellow area) is correlated between

the pulses and thus does not affect the noise reduction, c.f. eq. (12.5), nor cause $\langle(\Delta(\tilde{\phi}_{\text{qnd},2} - \tilde{\phi}_{\text{qnd},1}))^2\rangle$ to increase with N_{at} c.f. eq. (12.6). There is no indication of uncorrelated classical atomic noise, whereby we conclude that only slow drifts, e.g. of the relative probe powers, matter. This seems to indicate that the MZI offset adjustment has indeed helped to remove the effect of laser intensity noise caused by the signal misbalancing for large N_{at} . It is hard to determine exactly which sources of noise were subdued to get the improvement, since the 2-input configuration effectively suppresses a whole range. We believe, that inhibition of classical frequency noise in the coupling to the atoms, balancing of the probe signals during the QND measurement, and immunity to acoustic noise have all played a role in eliminating the classical atomic noise in the measurement. The fits also confirm that part of the light noise is correlated between the pulses, though the major part is still uncorrelated shot-noise. We shall not forget the *pièce de résistance*, which is the “squeezed noise” points. The variance $\langle(\Delta(\tilde{\phi}_{\text{qnd},2} - \zeta\tilde{\phi}_{\text{qnd},1}))^2\rangle$ of the bin with the highest atom number is reduced to 0.29 of the projection noise level, i.e., a 5.3 dB reduction.¹⁰ The decoherence was measured at $1 - e^{-\eta} = 0.80 \pm 0.02$, so that we can claim $\zeta_{\text{ueda}} = 0.36 \pm 0.015$ (-4.4 dB) and $\zeta_{\text{wineland}} = 0.46 \pm 0.03$ (-3.4 dB). This result formed the centerpiece of [Appel09]. The red curve is a plot of the level of the reduced noise based on eq. (12.5). Again, the agreement of the curve with the data points merely shows that we perform our statistical data analysis properly and consistently. In continuation of the discussion on the relation between squeezing and inter-particle entanglement in sec. 3.6 we can estimate by [Sørensen01b] that we have achieved four-particle entanglement.

We decided to combine 4 probe pulses for the plots above. The insert of fig. 12.12 illustrates this choice. The green points show the noise reduction and the red the squeezing ζ_{wineland} as a function the number of pulses combined. The more pulses are combined the higher the number of photons in the combined pulse and the higher the measurements signal to noise. Effectively the larger number of photons reduces the shot-noise fluctuations of the MZI phase and therefore increases the sensitivity of the detection. One would expect the noise reduction to increase but in fig. 12.12 it seems to level off after 5-6 pulses are combined. The increase in N_{ph} also intensifies the spontaneous scattering whereby the projection noise level of the coherent part of the finals state fall. In fig. 12.12 this means that the slope of the dashed grey line goes down and eventually the line will pass below the reduced noise points. This feature is apparent from the squeezing for different pulse combinations. When the decoherence grows beyond about 20% the squeezing starts to degrade. For the probe powers and detunings used in this experiment it seems that combining 4 pulses gives the largest squeezing. The state decoherence of 0.2 is lower than the 0.33 predicted in the limit of high optical depth (see eq. (5.20)). To make a more accurate comparison we use the relation between the coupling constant κ^2 , decoherence η , and optical depth $\tilde{\alpha}_0$ given by eq. (5.37). Moreover we shall use the derivations in sec. 4.5.1 to account for the noise increase due to the non-elastically scattered photons. This allows us to plot the expected squeezing as a function of the decoherence for the probe detunings used in the experiment. In fig. 12.13 we plot curves for different optical depths along with the experimentally measured squeezing. All things considered, the qualitative agreement is rather good and we would give an estimate of the optical depth between $\tilde{\alpha}_0 = 60$ -90. This is not too far off the previous estimates. The squeezing seems to reduce quicker after the first

¹⁰To root out any confusion what we calculate is $\frac{\langle(\Delta(\tilde{\phi}_{\text{qnd},2} - \zeta\tilde{\phi}_{\text{qnd},1}))^2\rangle - [(\Delta c^{(0)})^2 + (\Delta u^{(0)})^2]}{\langle(\Delta c^{(1)})^2\rangle}$. In the figure this means we take the ratio of the distance between the light noise (top of red area) to the squeezed noise point to the size of the projection noise (height of the green area).

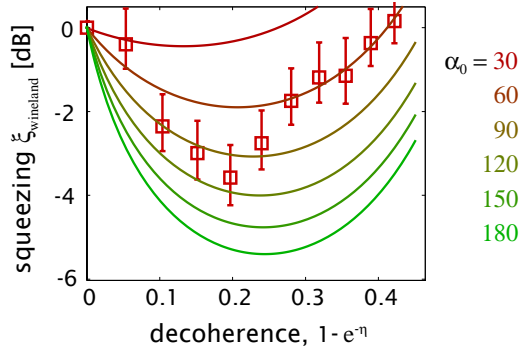


Figure 12.13: Experimental squeezing vs. decoherence. The data points are the same as in the insert of fig. 12.12 and the theoretical curves are plotted for different optical depths $\tilde{\alpha}_0$

four pulses. This is likely due to the influence of classical noise sources, which seem to increase as more pulses are combined, thereby increasing the effective duration of the combined pulse.

Data consistency check – atom number comparison One important check of the results is to see how well the measured pulse variances conform with what one would expect. In the case of the projection noise we can calculate it independently from the measured mean phase-shift. In fig. 12.14 we reproduce the pulse variance $(\langle(\Delta\tilde{\phi}_{\text{qnd},1})^2\rangle + \langle(\Delta\tilde{\phi}_{\text{qnd},2})^2\rangle)/2$ along with the quadratic fit and the linear part. The yellow line represents the atomic noise expected from the mean

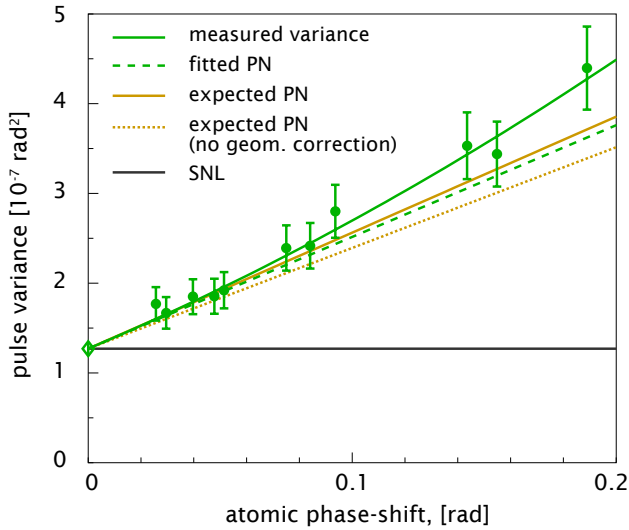


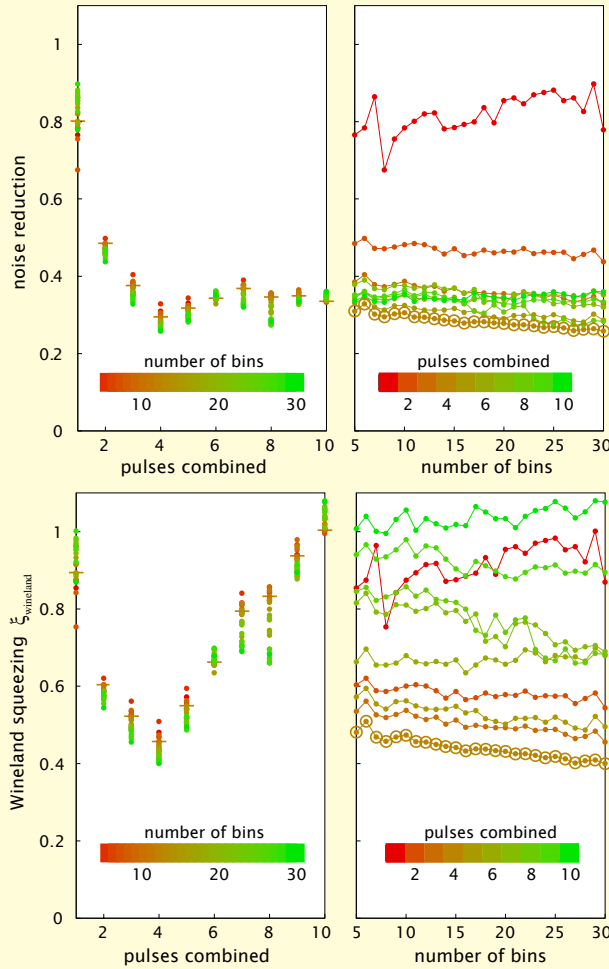
Figure 12.14: Plot of shot-noise and projection noise derived from pulse variances and phase-shift.

phase shift taking the geometric correction factor in to account, while the dotted line is without the correction. It suffices to say that the projection noise level observed experimentally agrees very well with that predicted from the phase-shift. This reinforces the claim that the atomic noise scaling linear with N_{at} is indeed the quantum projection noise.

Effect of spontaneous scattering on correlations In sec. 4.5.1 we accentuated that the dichromatic probing on the two quasi-cycling transitions was very beneficial to the aim of squeezing the pseudo-spin. We have still to elaborate on this prediction in the experimental data. The data shows several clear interrelated signs of it. Firstly, the scaling of the variance and covariance do not produce any uncorrelated noise scaling linear with N_{at} . In other words the quasi-elastic spontaneous scattering does not reduce the correlation between the two pulses. Uncorrelated noise proportional to N_{at} could only arise from part of the atoms being in different and uncorrelated quantum states during the first and second probe pulse. The second piece of evidence is that the level of the reduced noise

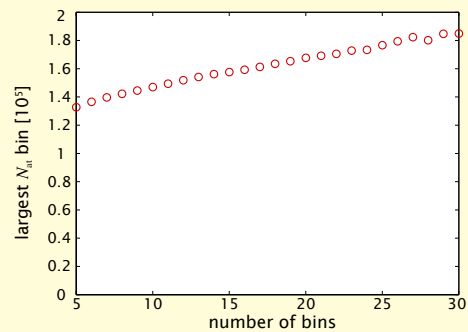
Box 12.1: Binning issues

When binning the data one must weigh two opposite concerns. Firstly, it is important that each bin contains enough data that the calculated



variances are statistically significant. From this one would advocate data to be put in few bins containing big portions of measurement data. On the other hand the fitting procedure requires bins to be spread out over a range of atom numbers. This then would speak for more bins, which unwillingly would contain fewer data. We have confirmed that within, a reasonable range of bin numbers the results of the fitting procedure agree. In the figures to the left we plot the reduced noise and degree of squeezing for different number of bins and pulse combinations. The noise reduction and squeezing obtained for different pulse combinations only varies a bit for the different number of bins. Moreover the variation is evidently not random. If instead we look at the dependence

on the number of bins there is a tendency of more noise reduction and squeezing the more bins we use. This is not due to any systematic change in the fitting, but due to the evaluation of the noise reduction at the bin with the largest N_{at} . The above figure shows that the more bins are used the higher is the mean atom number for the highest atom number bin. Hence, the noise reduction and squeezing increase because we evaluate it at a larger mean atom number. For the figures in the body text we use 11 bins as this number seemed to be the best match between having data points distributed well and them not being overly scattered because of too little statistical weight.



$\langle (\Delta(\tilde{\phi}_{\text{qnd},2} - \zeta\tilde{\phi}_{\text{qnd},1}))^2 \rangle$ is exactly at the level predicted by eq. (12.5). when to calculate the prediction we assumed that the linear scaling part of the atomic noise was all correlated. Finally, the correlation plot in fig. 12.10 reveals that the correlation is not reduced if we compare non-neighbouring pulses. That is, the

covariance $\langle\langle\Delta(\tilde{\phi}_{\text{qnd},j'}\tilde{\phi}_{\text{qnd},j})\rangle\rangle$ is more or less independent of which pulses i and j in the train one computes it for. To found this statement better, we plot the correlation between the first and all subsequent pulses, i.e., $\langle\langle\Delta(\tilde{\phi}_{\text{qnd},1'}\tilde{\phi}_{\text{qnd},i})\rangle\rangle$, vs. the pulse index i (see fig. 12.15). The spontaneous scattering is calculated

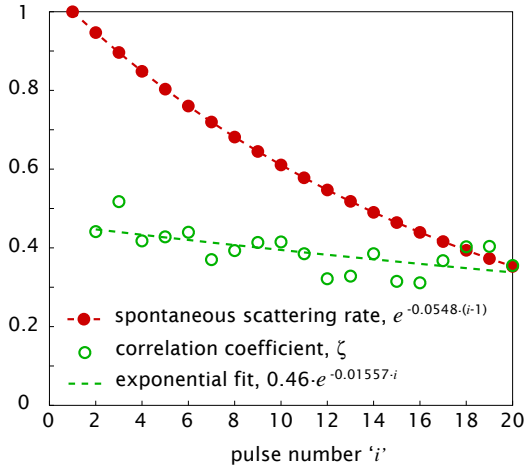


Figure 12.15: Correlation factor between first and subsequent pulses $\langle\langle\Delta(\tilde{\phi}_{\text{qnd},1'}\tilde{\phi}_{\text{qnd},i})\rangle\rangle$ together with spontaneous scattering rate. The 0.054 scattering rate per probe pulse is measured from a the reduction of the fringe in a Ramsey sequence.

as that occurring before the i 'th pulse, since this will gauge the degree to which the initial state has been "destroyed" at the point when it is measured by the i 'th pulse. The exponential fit to the correlation factors unveils that for every probe pulse about 1.5% of the correlation is lost. In contrast the spontaneous scattering affects about 5.5% of the atoms. This means that the spontaneous scattering only perturbs the mean value and second moment of the measured quantum state weakly. This was exactly the claim in sec. 4.5.1. The reduction in the correlation is partly due to the atoms being pumped in to high m_F levels which couple weaker to the probe. This supposition is supported by the single pulse variances also reducing moderately with the number of probe pulses. The effect of reduced coupling to the probe due to sub-level pumping was not included in the derivation in sec. 4.5.1.

Spontaneous scattering and dephasing The correct determination of the dephasing and decoherence of the pseudo-spin is *essential* for any claim of spin-squeezing. Therein lies also the rationale for devoting such a lengthy part of this work (chapt. 11) to the investigation of dephasing and decoherence. In the review of other experiments in sec. 16 we shall expatiate a bit on this issue. The values stated for the decoherence in this section were found by Ramsey spin-echo measurements with a probe pulse pair placed either both before or around the spin-echo pulse. The pulses power was set so that the two pulses combined would contain as close to the photon number as that used in the squeezing experiment. The measurements with pulses before or around the spin-echo always agreed within a 1-2%, which is the number stated as an uncertainty to the squeezing. Though, the two values agreed within the fit uncertainty, the lower Ramsey fringe amplitude was consistently obtained for the sequence with both pulses before, i.e., not being helped by re-phasing. This made it clear to us that the 2-input MZI is frightfully sensitive to the mode matching of the inputs — a task to be performed before every measurement run. From the careful, investigation of the cancellation in sec. 11.2.3 we were again enticed to re-configure the MZI to have the probes mode-matched in an optical fibre whereby they would enter the same input. Fortunately, we found in sec. 2.3.1 that the probes and the MZI could be set up so that even when entering the same port to the MZI, the probe fringes could be made to behave equivalent to the 2-input configuration.

That is, the probe fringes are out of phase. This we will investigate in the next section.

Correlation visualised As a conclusion to the 2-input MZI measurement section fig. 12.16 shows the plot that seems to have become a standard visualisation of pulse correlations [Takano09b, Appel09].¹¹ Admittedly a scatter plot gives a

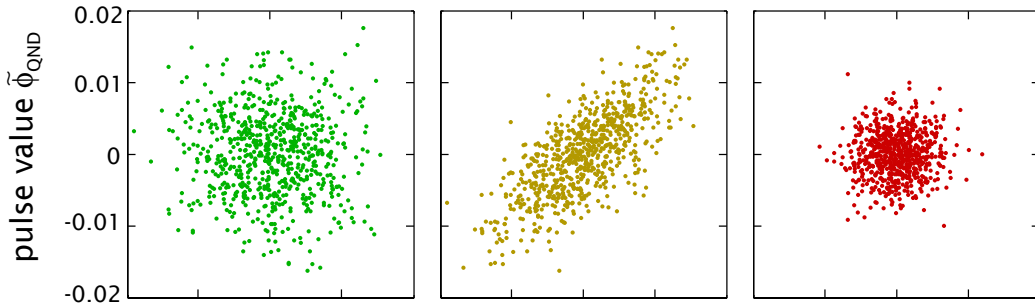


Figure 12.16: Correlation plot. a) scatter plot of $\tilde{\phi}_{\text{qnd},1}^j$ vs. $\tilde{\phi}_{\text{qnd},1}^{j+1}$ for ~ 800 data points with the highest atom number, revealing the atomic noise. b) scatter plot of $\tilde{\phi}_{\text{qnd},1}^j$ vs. $\tilde{\phi}_{\text{qnd},2}^j$ for ~ 800 data points with the highest atom number, revealing the correlation between subsequent measurements of the same atomic state. c) scatter plot of $\tilde{\phi}_{\text{qnd},1}^j$ vs. $\tilde{\phi}_{\text{qnd},2}^j$ for ~ 800 data points with no atoms in the sample, revealing the uncorrelated shot noise floor.

good feeling of what the QND measurement squeezing is all about. We include the shot noise plot, which neatly visualises the lower limit for the reduced noise.

12.4.4 Two-input equivalent MZI

Following the successful demonstration of spin-squeezing the aim was to characterise the squeezed state more carefully and attempt to introduce it in a clock-like sequence. All of these involve the experiment to be performed using different some set of sequences e.g. to observe the noise of the the different pseudo-spin components after the QND measurement so as to detect both squeezing and anti-squeezing. The ensuing experimental runs lasting up to one week, in turn, put even stronger demands on the stability of the experiment. In this respect, the 2-input configuration proved to fall short in a couple of ways. Firstly, the spatial separation of the probe inputs means that probe powers and fringe visibilities can drift independently and though the wiggler constantly ensures the fringe amplitudes to be equal, the optical power in the atoms can be different for the two probes. Secondly, a more serious effect arises when the spatial modes of the two probe colours do not match in the atomic sample. As a result the probes will couple differently to the sample. Say both are initially optimally overlapped with the atomic sample, but during the experiment the mode of one probe colour is misaligned. In this case the atomic signal from the probe that drifted will decrease and the atomic phase-shifts of the probes will no longer be equal. This makes the measurement sensitive to atom number fluctuations and laser frequency noise sec. 6.2. Moreover, the QND measurement signal will not be easily accommodated within the DSO range and may even become sufficiently

¹¹some version of this would also have appeared on the front page of this thesis if it were not for the many hours spent on the "PNAS cover attempt", which now adorns this work instead.

misbalanced to saturate the QND detector. Finally, there is the concern of the light-shift cancellation that we alluded to in the end of sec. 6.2. The aggregate of these problems provided enough impetus to launch yet another reconfiguration of the MZI to one of the setups equivalent to a 2-input MZI.

The first configuration took us to the setup where the probe colours were put in the same fibre with orthogonal polarisation modes. This is possible since in a single mode fibre the polarisation should be maintained for light on both the slow and fast fibre axis. We split half of each of the two polarisation into each of the MZI arms on the input BS, which in this case was a PBS. Because we can turn the probe polarisations with a wave-plate we can fine tune the splitting ratio so that the powers of the probes are exactly equal in the each arm. We then attenuate the probe arm using a polariser and split off part of the probe powers on to the power reference detector with a PBS. In the reference arm the probe polarisations are also purified with a polariser.

Ultimately this configuration suffered from many of the same problems as the configuration with two spatially separated inputs. By nature the spatial modes of the probe colours are perfectly matched, but the relative powers can drift because the polarisations are contaminated in the fibre. Only a little admixing of circular polarised light will change the splitting ratio on the MZI input PBS so that the fringe visibilities change. The wiggler compensates by the adjusting the probe powers, but this makes the powers in the probe arm slightly different. What is worse, is that the polarisation contamination causes small changes in the phases that the probe beams acquire upon reflection and transmission on the mirrors and BSs. Eventually, this can spoil the very fine balancing of the probe signals on the QND detector and force us to redo the balancing. This is possible, by using the memory wire attached to the wave-plate before the PBS that splits probes on to the two detector channels, but it is generally not desirable to make such an adjustment in the course of a measurement run.

Fortunately we were not out of options. In the, to date, final re-configuration we made use of the fact that by having different frequencies the two probes are already separated in two modes, which can be separated in the output signal by misaligning the MZI to a path-length difference of $c\pi/(\omega_{45'} - \omega_{32'})$ (see sec. 8.3). The probe polarisations can be set equal so all power drifts are almost perfectly in tune. With this configuration we are finally in a position to carry out detailed investigations.

Due to some major problems with the FORT trapping laser we had to re-align the optics for the FORT. One problem we noticed regarded the spatial mode of the FORT beam, which at certain powers developed a toroidal shape. This seemed to be a thermal lensing effect in the FORT switching AOM, and after re-alignment the FORT mode regained a Gaussian shape. We believe the FORT mode has been contaminated only for a short time following a re-alignment of the FORT laser cavity. In connection with solving the mode issue, we made some adjustments to the FORT beam spot-size in order to try different trapping confinements. After some trials, we decided that where we started out was not so bad, and the FORT beam was adjusted for a beam waist size of about $40 \mu\text{m}$. However, after making these adjustments we have not characterised the trap size and thus we have only vague idea of the sample to probe beam waist ratio. This will affect the absolute estimates of the noise, via the uncertainty on the appropriate geometric correction factor (see eq. (3.26)).

12.5 Squeezing lifetime

As with so many things in life, one of the most pressing questions about the generated squeezing is how long it lasts. From a pragmatic point of view we must examine if the correlation of the atomic noise between pulses degrades as the pulses are put farther apart. A hint to the answer may be drawn from fig. 12.15 where we saw that the correlation between the first QND measurement pulse and subsequent pulses did not reduce considerably. The temporal separation of the first and last pulse in that train was already $400 \mu\text{s}$. Of course, we cannot definitely state the lifetime of the squeezing until we have performed a measurement where we compare pulses of different separation *without* any intermediate pulses.

experimental settings The pulse sequence the same as in fig. 12.8 except for some of the QND pulses being absent. We set the probe powers so that they the coupling strength and spontaneous scattering in a single $10 \mu\text{s}$ pulse is close to optimal for the squeezing. To compare the lifetime over longer periods we skip a number of pulses after the first QND pulse e.g. skipping 4 pulses will allow us to compare the first QND pulse with one $(4 + 1)t_{\text{rep}} = 100 \mu\text{s}$ later. We take this approach of skipping pulses instead of displacing all the pulses after the first, because it allows us to use the same integration matrix for all the data. Besides removing some systematic errors due to small mismatches of the matrices' integration windows, the unified integration also makes it simple to analyse the data within the same analysis script. Another important step towards avoiding systematic biases of the data is to randomise the pulse skipping. That is to say, the acquisition program randomly picks a value from a preset range, passes this value to the relevant experiment control program (in this case the DIO-64 Lab-View program), which then configures its output to the given value. The value is held for 50-100 experimental cycles — so that we can do the subtraction of subsequent cycles c.f. sec. 12.2.2 — before being changed to another random value. Like this, the data for any particular setting will originate from cycles distributed over the whole duration of the experimental run, thereby hopefully eliminating any biases. To distinguish the data sets acquired for different settings we save the control value along with the data and use this value for selecting certain parameter values in the analysis. The remaining key parameters for the run are listed in table 12.3.

Δ_{32}	Δ_{45}	t_p	t_{rep}	$N_{\text{ph},a}$	$N_{\text{pha}}/N_{\text{phb}}$	$\tau_{\pi/2}$	$1 - e^{-\eta}$
MHz	MHz	μs	μs	–	–	μs	–
-84	-92	10	20*	$0.66 \cdot 10^7$	~ 12	5.6	0.135

Table 12.3: Probe settings for squeezing lifetime measurement with 2-input equivalent MZI. The photon number and decoherence correspond to a single probe pulse. *The repetition period corresponds to the pulse train with no pulses skipped.

Dissecting the noise To lay the ground for the analysis of the squeezing lifetime we will take a brief look at the noise scaling and establish the most important issues. As a starting point we pick the data where no QND pulses were skipped and chose to the combine pulses 2 to 20 in to a compound second QND pulse. The variances for this data are shown in fig. 12.17. The effect of combining pulses is to lower the shot-noise level, which in phase-units scales as $1/N_{\text{ph}}$. This constitutes an experimental demonstration of the increase of phase-resolution

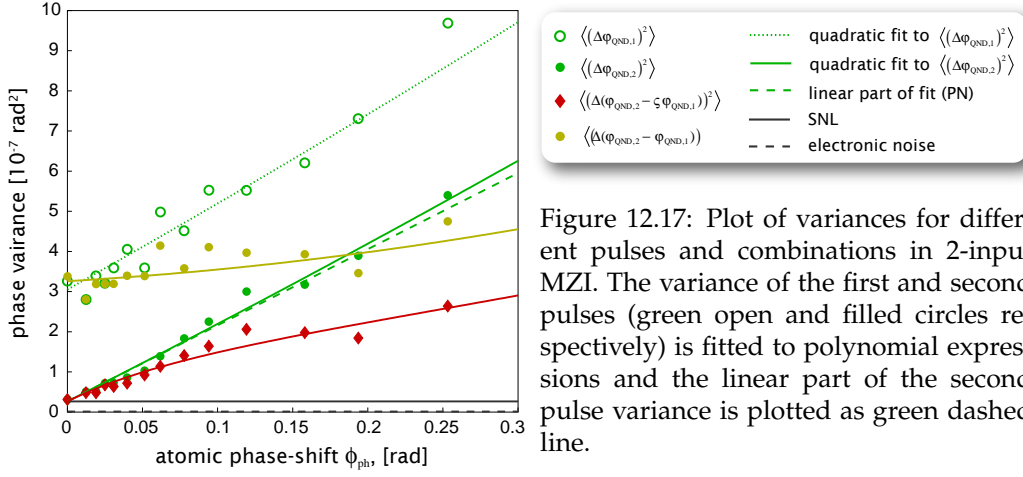


Figure 12.17: Plot of variances for different pulses and combinations in 2-input MZI. The variance of the first and second pulses (green open and filled circles respectively) is fitted to polynomial expressions and the linear part of the second pulse variance is plotted as green dashed line.

with increased photon numbers (see sec. 2.3.1). In the data this reduction causes the atomic noise $\langle(\Delta p_1)^2\rangle$ and $\langle(\Delta p_2)^2\rangle$ to be displaced, with the ratio of 1/19 between the shot-noise levels. Both $\langle(\Delta p_1)^2\rangle$ and $\langle(\Delta p_2)^2\rangle$ scale almost linearly with the atom number, as a sign being limited by the atomic projection noise. The reduced variance $\langle(\Delta(p_2 - \zeta p_1))^2\rangle$ reflects what we found in eq. (12.5), that combining the second pulse, which in some sense only verifies the squeezing induced by the first pulse, does not improve the noise reduction. We also remind, that the SNR in this plot should be found as the ratio of the first pulse shot noise and atomic noise, and not from the second pulse variance. The SNR in this measurement approaches 1.5 for the highest N_{at} bin.

Moving to the combined analysis of the variances and covariances we plot the $\langle(\Delta(p_2 - \zeta p_1))^2\rangle$ and $\langle(\Delta p_2)^2\rangle$ together with the fitted noise contributions. The

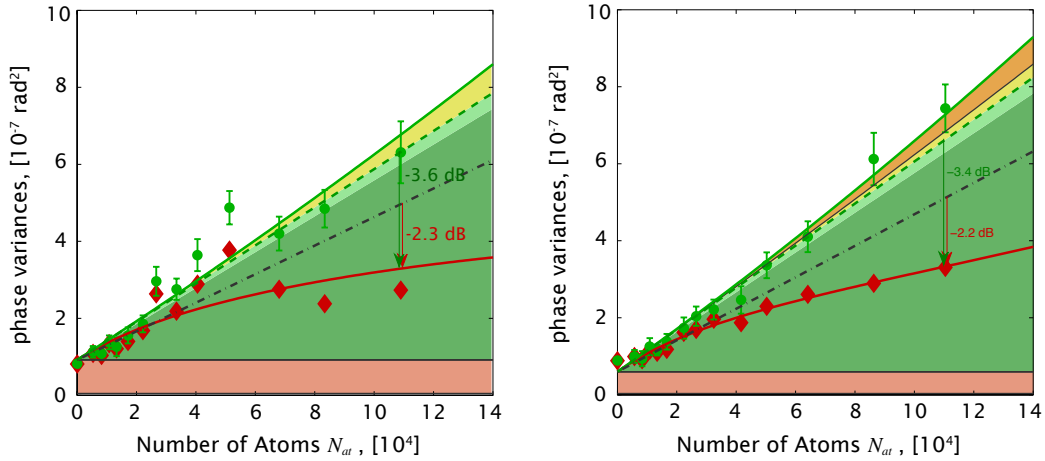


Figure 12.18: Plot of correlated and uncorrelated pulse variances with different atom-number scaling in 2-input MZI. The atom number is calculated from the mean bin phase-shift $\langle\tilde{\varphi}_{\text{ph}}\rangle$ c.f. eq. (12.10).

left hand plot of fig. 12.18 depicts the same data as in fig. 12.17 except for the second pulse being composed of 4 pulses now. We notice a small contribution of correlated classical noise which reduces the achievable noise reduction to 0.44 (-3.6 dB) and the squeezing to $\zeta_{\text{wineland}} = 0.59$ (-2.3 dB). However, we also notice that both the $\langle(\Delta p_2)^2\rangle$ and $\langle(\Delta(p_2 - \zeta p_1))^2\rangle$ values scatter quite a bit. The scattering is reduced by combining more pulses so clearly it is a result of a few bad second pulse measurement points that throw off the variances for some of the bins. The figure quite well illustrates the difficulties involved in sensibly analysing the data.

On the right hand plot we show the data from traces where 15 pulses have been skipped. The separation between the first and second measurement pulse is thus $320 \mu\text{s}$. The length of the total pulse train being 20 (also counting the skipped pulses), we are limited to combine only 4 pulses for the second compound pulse. The atomic noise is influenced by some amount of uncorrelated classical noise. Despite this, the fit predicts about 0.46 (-3.4 dB) noise reduction and $\xi_{\text{wineland}} = 0.60$ (-2.2 dB).

Altogether, the results derived from the two data sets agree rather convincingly, with special remarks to the projection noise slopes. However, we have had to impose some constraints on the fitting parameters for the r.h.s. data set. What we do is to let the fitting parameters for the covariance be limited to be no higher than those obtained from the fit to the first pulse variance. The rationale behind this constraint should be reasonably clear from eq. (12.8), but we will make a few comments. W.r.t. the N_{at} independent light-noise contribution the restraint makes no difference and we actually omit it. The linear scaling part of the variance is due to the projection noise, and there is no reason why it should be different for any of the traces. If the data-set is contaminated by some classical noise influence then that can only add quadratic noise. The correlation could decrease below the projection noise, whereby we would see some uncorrelated projection linear scaling noise. This we allow for since the lower bound on all parameters is just zero.

As a check of the fitted projection noise slope $\langle(\Delta p_1)^2\rangle$ for the data-set with no skipped pulses and using the maximal combination for the second pulse we get the slope in fig. 12.19. We compare this with the theoretical estimate

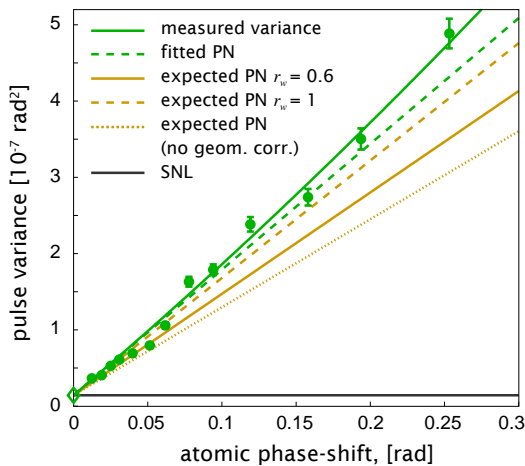


Figure 12.19: Plot of shot-noise and projection noise derived from pulse variances (green dashed) and phase-shift (yellow curves). The full yellow curve accounts for the geometry with a probe to sample waist ratio of $r_w = 0.6$, while the yellow dashed curve uses $r_w = 1$, and the yellow dotted line is without geometric correction.

as prescribed by eq. (12.10). The agreement of the measured projection noise variance (green dashed) with that expected for the measured phase-shift (yellow full line) is reasonable but not nearly as convincing as in fig. 12.14. The reason for the discrepancy can be due to a different sample size after the FORT realignment. If we take the disagreement at face value, we would predict the atomic sample to be narrower than before. As an indicator for this hypothesis we plot the expected noise for a sample to probe waist ratio of 1 (yellow dashed line). In any case, we are almost sure that the sample size is not exactly as before, since no matter how much we optimise we seem to get lower atomic phase-shifts now. On the other hand, the discrepancy may also be a sign of the fitted projection noise being too large. This can certainly not be ruled out, though the slope of the linear scaling part of the noise is similar to that obtain over several different squeezing measurements including some with larger and more unblemished data sets.

projection noise and squeezing for different pulse separations We have now presented some of the concern w.r.t. the analysis of the individual data sets and proceed with a more systematic comparison. When comparing the noise reduction for different pulse-separation we conventionally evaluate the number at the mean atomic phase-shift of the bin with the highest atom number. Since the data accumulated for different pulse-separation settings will comprise different distribution of atomic phase shifts, we risk adding noise to the estimated noise reduction (see box 12.1). To check the effect we plot the maximal mean atom number for the different pulse separation data sets in fig. 12.20, and verify that the variation is rather small.

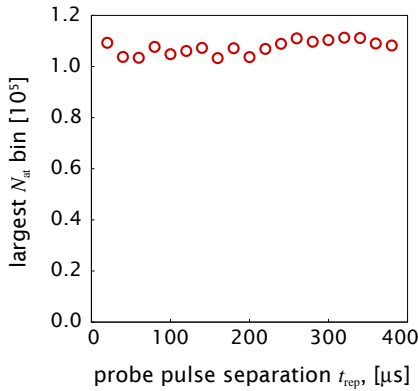


Figure 12.20: Highest mean atom number for different pulse separation data sets using 11 bins.

Now we plot the fitted projection noise level evaluated at the maximal N_{at} bin value in fig. 12.21. The three subfigures correspond to different pulse combining

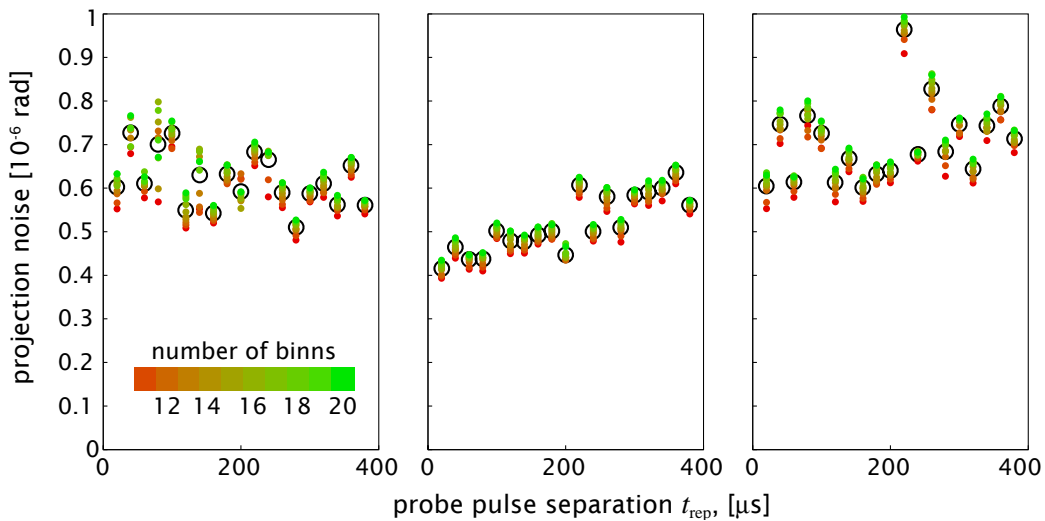


Figure 12.21: Projection noise for different pulse separations. The three plots correspond to different fitting constraints applied to the same data-set.

methods and fitting strategies. We also always show the outcome of the fits for different numbers of bins. In fig. 12.21a we do not make any constraints and the values are quite scattered. In fig. 12.21b we still do not make any constraints on the fit but combine as many pulses as possible for the second probe pulse. The resulting projection noise tends to be lower than that fitted for the other methods. Lastly, in fig. 12.21c we constrain the fit parameters as described above though this does not seem reduce the scattering.

We are now in a position to calculate the squeezing, with the result shown in fig. 12.22. Again the three figures correspond to imposing different constraints and pulse combination schemes. The error bars are calculated as the square-sum

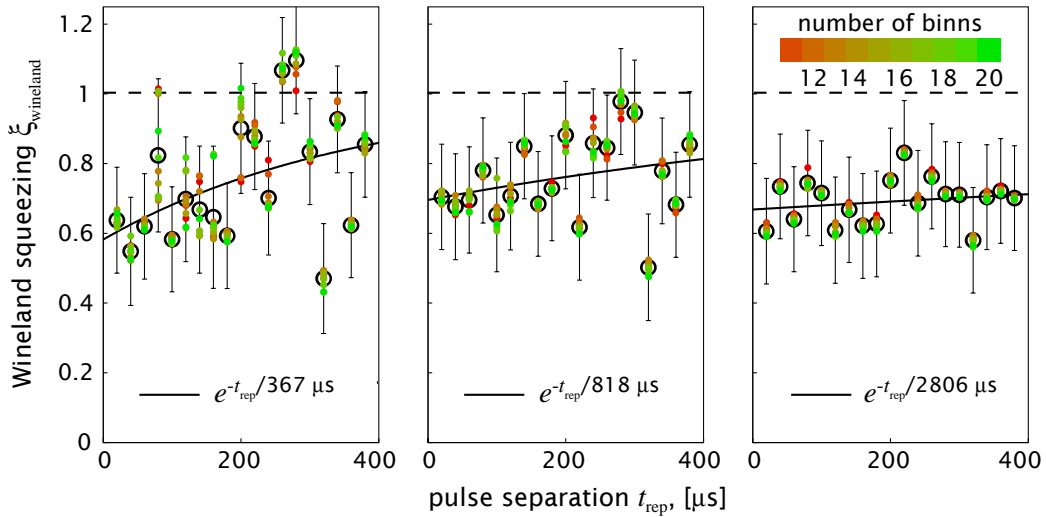


Figure 12.22: Squeezing for different pulse separations. The three plots correspond to different fitting constraints applied to the same data-set.

of several contributions; The first is the standard deviation of the projection noise value obtained for different binnings and three more account for the uncertainty in the atom number and decoherence measurements. The values in fig. 12.22 scatter considerably although one could possibly claim that the values up to around $200 \mu\text{s}$ lie at a reasonably constant level. We fit the squeezing to an exponential decay and achieve lifetimes of $367 \mu\text{s}$ and $818 \mu\text{s}$ for the fits in fig. 12.22a and b respectively. Due to the large scattering of the data these values should be taken with a handsome portion of scepticism. The last plot in fig. 12.22c displays a much more constant squeezing. It would appear that imposing the restrictions on the fit gives a more steady result, though this need not be taken as a proof of the procedure's validity. The decay constant of the squeezing in the last plot is fitted to $2806 \mu\text{s}$. We would like to believe this value, but when taking the squeezing life-time measurement as a whole we cannot yet make any definite claims. We see both in this section and from looking at the decay of the correlation in fig. 12.15 that the squeezing does not seem to degrade with time. In other less systematic measurements we have not observed any significant degrading of the squeezing. Sadly, we have not yet managed to make an experimental run that has been stable enough to get clear results on the lifetime — and we *have* made a number of attempts.

We should of course keep in mind that the inhomogeneous dephasing in the FORT happens at a rapid pace of around 1 ms . Hence, the noise reduction of the \hat{F}_z component may be preserved over long times but in the equatorial plane the spin-vector is washed out. Fortunately, a simple spin echo pulse could re-phase the broadening, but this on the other hand would not be useful in a spectroscopic measurement.

12.6 State tomography and anti-squeezing

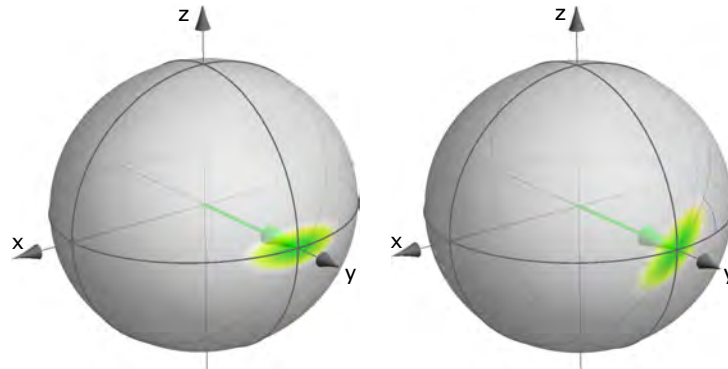
When characterising the spin-squeezing in the preceding sections we only measure the spin component that was squeezed, but this is not sufficient to disclose the whole atomic state. Essentially, we have no knowledge of the statistics of the pseudo-spin along the equator. This spin component is presumably anti-squeezed and it would be advantageous to measure the degree of anti-squeezing.

This is very relevant, since even for squeezing of one spin component if the anti-squeezed component is excessively noisy the state cannot be used for spectroscopy. Thus we want to characterise the complete statistics of the squeezed quantum state by performing a state tomography. In future applications where we propose the generation of more exotic quantum states we crucially rely on being able to faithfully reconstruct the atomic state by tomography. Hence, it pays off to get a good grasp of this type of measurement. There is one major catch, in that the manipulations of the quantum state, that are needed to observe the other spin components, can themselves introduce additional classical noise. Hence, the tomography of a squeezed state may very well show anti-squeezing well above the actual anti-squeezing. However, classical noise in the measurement of the anti-squeezed quadrature can also be a result of additional noise in that spin component. For example, classical laser intensity noise adds back-action noise to the atoms above the level set by the shot-noise of the probes.

Tomography approach 1 - simple The immediate idea for the tomography measurement of the squeezed state is to rotate the state by an angle θ around the y -axis after the first squeezing pulse (see fig. 12.23). This simple approach

Figure 12.23: Intuitive tomography approach.

a) A squeezed state is prepared by a QND measurement. b) A subsequent microwave pulse of varying duration and $\pi/2$ out of phase with the state preparing $\pi/2$ pulse, rotates the pseudo-spin around its own axis so that the a following measurement gives the squeezed or anti-squeezed pseudo-spin component.



turned out to suffer from a problem with the microwave coupling strength. As we increased the rotation angle, by making longer microwave pulses, we noticed that the mean of the signal oscillates (see fig. 12.24). These oscillations could not

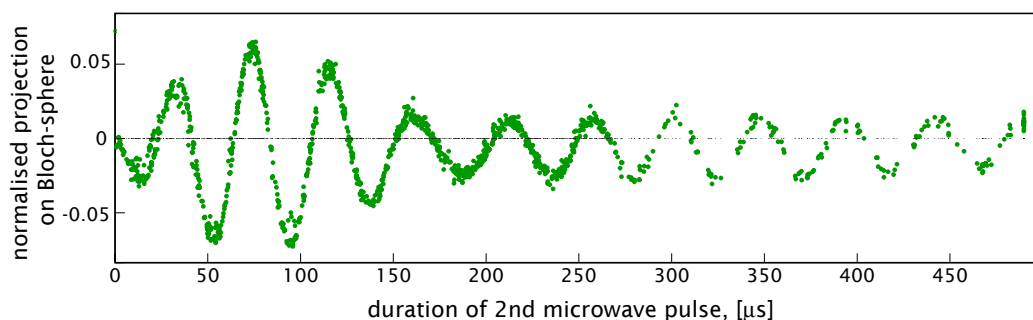


Figure 12.24: Oscillating mean population number difference in intuitive tomography sequence for different rotations of the Bloch-vector as shown in fig. 12.23.

be explained by power or frequency drifts during the microwave pulse. Rather it turned out to be rooted in an inhomogeneous distribution of microwave coupling strengths over the sample. This inhomogeneous spread of the coupling is partially explained by the FORT light shift, but the actual spatial intensity distribution of the microwaves seem also to play a role. The effect of this in-

homogeneous coupling is that the atoms actually experience different rotation angles when they are prepared in the coherent superposition along the y -axis. As illustrated in fig. 12.25, the result is that atoms at one spatial location have

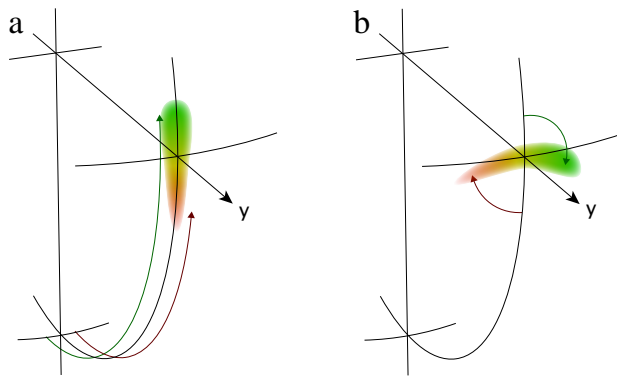


Figure 12.25: Illustration of microwave intensity spread influence on tomography. a) The inhomogeneous coupling smears out the atomic state in that atoms located in regions of low field intensity perform less than a $\pi/2$ rotation (red shade) while those located in high field-intensity regions perform more than a $\pi/2$ rotation (green shade). The microwave pulse length is thus chosen so that the spatial average of $\langle \hat{F}_z \rangle$ over the effective sample is 0.

b) The second, tomography microwave pulse causes the \hat{F} distribution to be twisted around the y -axis as the rotation angle of atoms in low field intensity lags behind that for atoms in high field intensity. We emphasise that the drawn distribution is deterministic and thus not the same as the uncertainty disk drawn on most other Bloch spheres in this thesis.

their pseudo-spin below the Bloch sphere equator, while others at a different place have the pseudo-spin mean above the equator. The average pseudo-spin projection over atoms at all positions is of course set to be zero. When the second tomography microwave pulse is applied the atoms located at the place of strongest coupling again rotate more than those at low coupling locations. This, causes a sort of spiral effect on the pseudo-spins where atoms on one side rotate more than those on the other side.

Tomography approach 2 - involved

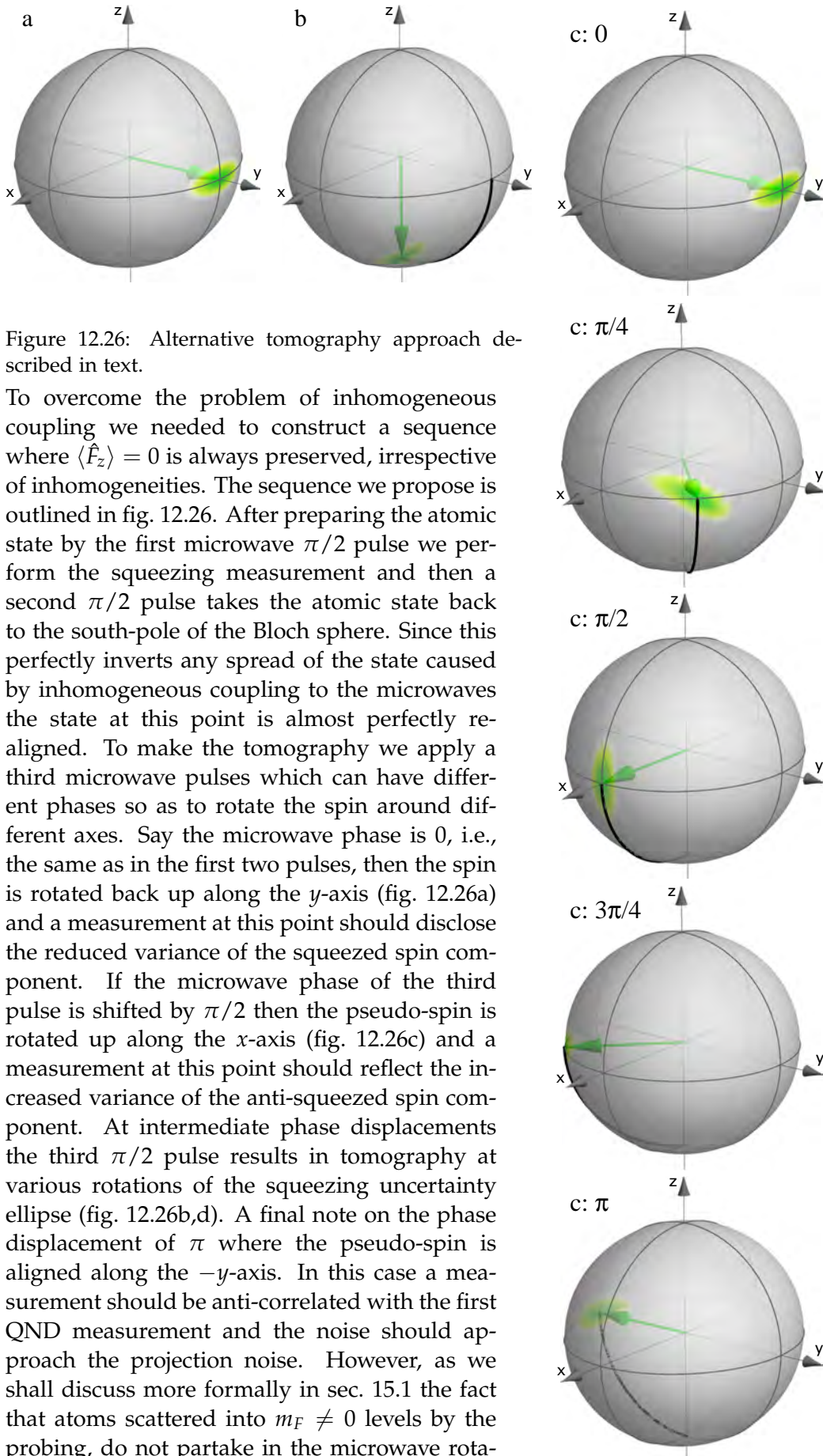


Figure 12.26: Alternative tomography approach described in text.

To overcome the problem of inhomogeneous coupling we needed to construct a sequence where $\langle \hat{F}_z \rangle = 0$ is always preserved, irrespective of inhomogeneities. The sequence we propose is outlined in fig. 12.26. After preparing the atomic state by the first microwave $\pi/2$ pulse we perform the squeezing measurement and then a second $\pi/2$ pulse takes the atomic state back to the south-pole of the Bloch sphere. Since this perfectly inverts any spread of the state caused by inhomogeneous coupling to the microwaves the state at this point is almost perfectly realigned. To make the tomography we apply a third microwave pulses which can have different phases so as to rotate the spin around different axes. Say the microwave phase is 0, i.e., the same as in the first two pulses, then the spin is rotated back up along the y -axis (fig. 12.26a) and a measurement at this point should disclose the reduced variance of the squeezed spin component. If the microwave phase of the third pulse is shifted by $\pi/2$ then the pseudo-spin is rotated up along the x -axis (fig. 12.26c) and a measurement at this point should reflect the increased variance of the anti-squeezed spin component. At intermediate phase displacements the third $\pi/2$ pulse results in tomography at various rotations of the squeezing uncertainty ellipse (fig. 12.26b,d). A final note on the phase displacement of π where the pseudo-spin is aligned along the $-y$ -axis. In this case a measurement should be anti-correlated with the first QND measurement and the noise should approach the projection noise. However, as we shall discuss more formally in sec. 15.1 the fact that atoms scattered into $m_F \neq 0$ levels by the probing, do not partake in the microwave rotations causes extra noise when the $m_F = 0$ atoms are not returned to their original value.

Δ_{32}	Δ_{45}	t_p	t_{rep}	$N_{\text{ph},a}$	$N_{\text{pha}}/N_{\text{phb}}$	$\tau_{\pi/2}$	$1 - e^{-\eta}$
MHz	MHz	μs	μs	–	–	μs	–
-84.3	-94.3	10	20	$0.483 \cdot 10^7$	~ 12	5.72	0.123

Table 12.4: Probe settings for tomography measurement with 2-input equivalent MZI. The photon number and decoherence correspond to a single probe pulse.

Now we shall present some preliminary tomography measurements using the sequence of fig. 12.26. The experimental settings are summarised in table 12.4. We randomly change the microwave phase between a set of phase values so that we avoid adding systematic effects. We take chunks of 50 experimental cycles for each phase-setting so that we can subtract subsequent cycles without loss of much data. The raw data for the first tomography probe pulse, i.e., the second pulse that follows after the squeezing pulse, is shown in fig. 12.27. We see that

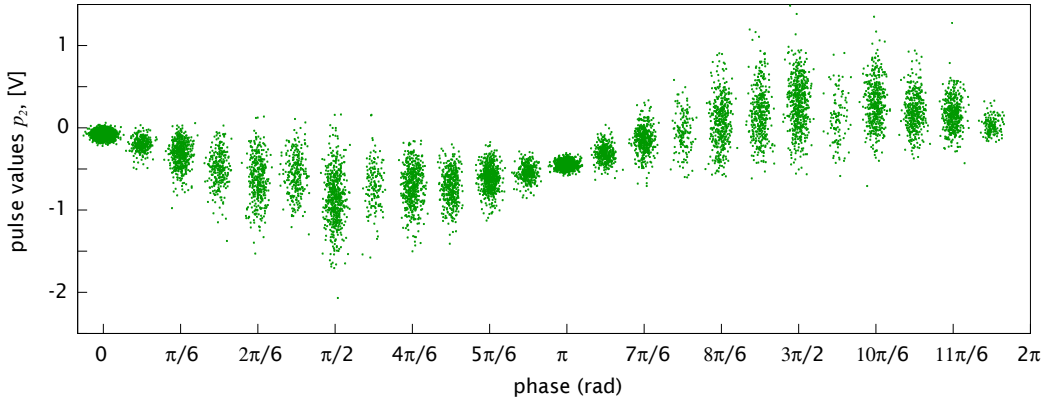


Figure 12.27: Raw high-atom number data points for tomography measurement. The data for each tomography angle is distributed over a small region to visualise the scattering. The number of points plotted at each setting varies from 100-500 for most angles except 0 and π where 2000-3000 points are plotted.

the mean value depends on the rotation angle. The cause of this can be that the cancellation of the inhomogeneous microwave field coupling is only perfect if atoms remain at the same position during the first and second $\pi/2$ pulses. Since the atoms are not stationary it is possible that they experience a slightly different coupling strength during the first and second pulses. We remove the harmonic dependency from the mean value by subtracting a sine function from all pulses. We will not show any of the noise-scaling curves as they do contribute with any new wisdom. Instead we focus on the data-point for the highest atom number bin where the SNR is highest and thus any effects should be most pronounced. First we plot the pulse variances $\langle (\Delta p_i)^2 \rangle$ normalised to the average projection noise, which is calculated as the mean variance of the first QND probe pulse $\langle (\Delta p_1)^2 \rangle$ (see fig. 12.28). We plot histograms of the variance of all 20 pulses in the train at all 24 rotation angles. A first observation is that the noise of the first (squeezing) pulse is constant and we take this as a sign of it being due to the quantum projection noise. This is supported by the first pulses always showing linear scaling with N_{at} . At the 0 rad angle the first half of the pulses stay projection noise limited, whereas at all other angles the noise is significantly increased. The noise is the largest at the angles where we should be probing the anti-squeezed spin component and achieves a local minimum when it is rotated by π . The apparent systematic change of the variance over the duration of the train is somewhat more confounding. We will seek for some answers shortly.

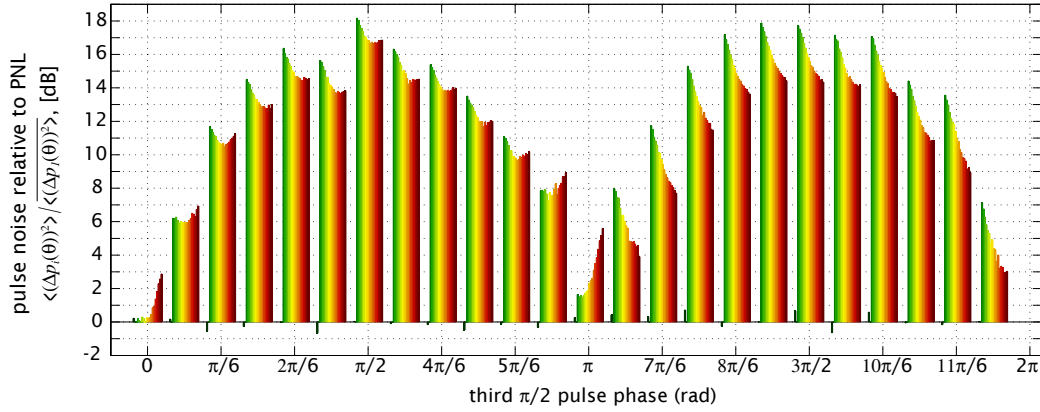


Figure 12.28: Total noise level of high atom number probe pulse trains for different tomography angles. Each coloured bar-plot corresponds to the pulse train at a given tomography angle.

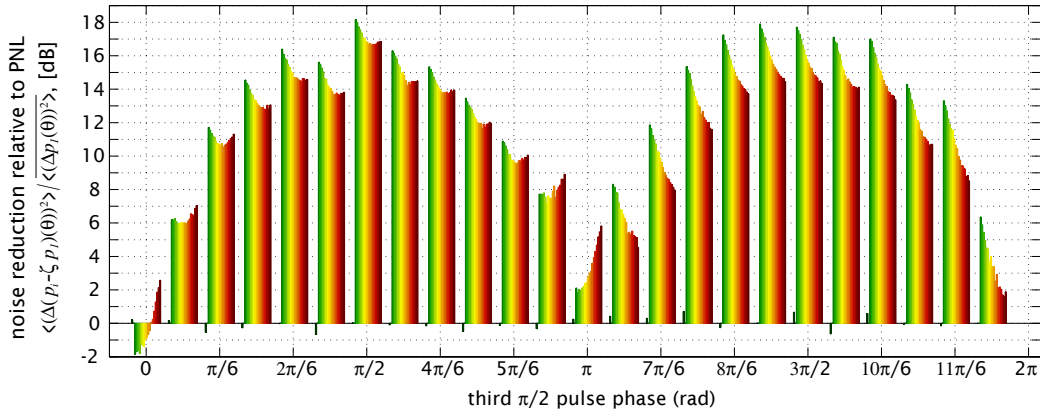


Figure 12.29: Noise reduction of high atom number probe pulse trains for different tomography angles. Each coloured bar-plot corresponds to the pulse train at a given tomography angle.

Our next move is to plot the noise reduction as a function of the rotation angle and pulse index within the train (see fig. 12.29). The overall pattern of course resembles that for the projection noise, and we see that a ~ 0.65 (~ 2 dB) reduction of the noise is only achieved at the zero rad angle. Since, the decoherence for a single pulse is 12% the squeezing is a modest ~ 0.8 (~ 0.9 dB). However, this noise reduction does not seem to survive the duration of the pulse train. The local minimum of the noise at the π angle corresponds to probing the squeezed pseudo-spin component. However, we actually do not expect the noise reduction to be as large as at zero rad angle. This is because not all scattered atoms end up back in the $m_F = 0$ levels. The atoms that end up in $m_F = \pm 1$ are not affected by the microwaves and thus do not make rotations around the Bloch sphere. For that reason, we always probe the $m_F = \pm 1$ atoms as if they were rotated around zero rad. Now, the scattering process is stochastic and though we may approximately take all atoms to decay back to their initial hyperfine level the fraction going in to $m_F = 0$ and $m_F = \pm 1$ fluctuates. When the $m_F = 0$ atoms rotated around a zero rad angle this is not important because all scattered atoms are put back in to the hyperfine state they spontaneously decayed in to. When the $m_F = 0$ atoms are rotated around a π rad we effectively interchange the hyperfine state of all $m_F = 0$ atoms. Hence, the fluctuations in the scattering process will now be amplified because the scattered $m_F = 0$ are not

only removed from their original hyperfine level but also add to the “opposite” signal from the other hyperfine level. This explanation is merely a qualitative account of scattering loss types in sec. 3.7.2 and quasi-elastic scattering in sec. 4.5. with approximately 10% spontaneously scattered atoms about half end up in the $m_F = 0$ level and we thus very roughly expect these to remove 0.05 units of projection noise from the noise reduction and add another 0.05 projection noise units of noise. This should still give a modest noise reduction whereas the data shows a noise increase.

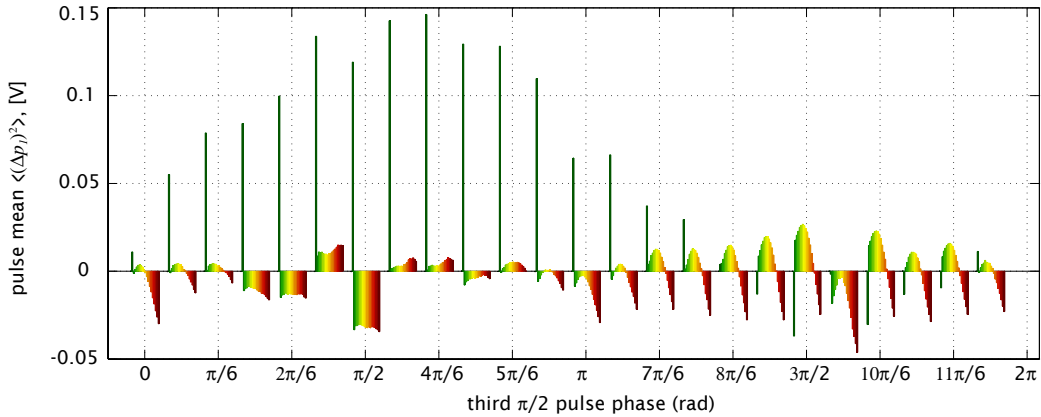


Figure 12.30: Mean values of high atom number probe pulse trains for different tomography angles. Each coloured bar-plot corresponds to the pulse train at a given tomography angle.

Finally, we take a look at the pulse mean values to see if they reveal anything about the peculiarities of the data (see fig. 12.30). Firstly, the mean values are well balanced for all pulses except the first one. The reason for the first pulse to be off is probably related to the MZI offsetting that compensates the mean atomic phase-shift and ensures the probes individually to be balanced during the QND measurement (see fig. 12.9).

A more serious concern is the change in mean values over the $400 \mu\text{s}$ duration of the pulse train. It almost appears as if the mean is performing some sort of oscillation. We have observed that the pattern of this mean value drift changes when the separation between the train and the microwave pulse is changed. Thus we conclude that the effect is connected to the microwave transitions. The relative change in atomic phase-shift as compared to the total atomic shift is about 2%. Very little power is needed to drive the microwave transition that little over such a long time. So we first ruled out that the DDS and filter cavity conspired to let a small amount of radiation pass through to the atoms. This we did by additionally gating the DDS pulses by the HP modulator, but it made no difference. At this point we believe that the fluctuations are caused by coherences between the atoms in $m_F \pm 1$ levels. To generate such coherences we need a coherent process of transferring the atoms to these levels. The process is of course just the microwaves. How this can be should be clear from fig. 10.24 showing the Rabi spectroscopy of microwave pulses of different duration. The figure shows that even non-resonant transitions are driven by the microwave radiation, albeit weakly. When we have $8 \mu\text{s}$ microwave π pulse durations the Fourier width of the pulse is roughly 125 kHz, which is not to far off from the ~ 350 kHz splitting between the $0 \rightarrow 0'$ clock transition and the $0 \rightarrow \pm 1'$ transitions. The latter requires circularly polarised microwave radiation, which ideally is not generated by the microwave antenna. However, as discussed in sec. 10.2.2 the metal enclosure of the setup along with the many metallic elements of the

setup it self, means that we very likely have anything but a pure microwave field polarisations. Hence, the $0 \rightarrow \pm 1'$ transitions are possible and can induce coherences between m_F levels. The way to suppress such transitions is to arrange the microwave power so that the π pulse duration gives a minimum in the Rabi spectrum in fig. 10.24 at the detuning corresponding to the $0 \rightarrow \pm 1'$ transition. This will be considered when we resume the tomography measurements.

Part III

Outlook and Applications

Conclusion

It is time to wrap up the results presented up to now. We have investigated the possibilities of engineering squeezed states by QND measurements of the atomic ensemble pseudo-spin constructed from the two clock-levels in Cs. The QND measurement has been implemented in several configurations of an MZI. We have concluded that in order to achieve the required coupling we must employ a dichromatic probe scheme in order to keep the optical power within the range where the MZI is shot-noise limited. We have thoroughly investigated the dephasing and decoherence of the pseudo-spin and come to a clear understanding of their dependence on trapping and probing parameters. We have found that the 2-input configuration affords better stability of the MZI detection and additionally enables almost perfect cancellation of the probe induced light-shift. Thus, we see a clear noise reduction of ~ 2 dB in a 1-input configuration, but even larger so (~ 6 dB) in a 2-input configuration where we also demonstrate spectroscopically relevant squeezing of ~ 3 dB. The observed projection noise level agrees well with that estimated from the atom number derived from the mean atomic phase-shift and the coupling parameters. The degree of squeezing is in fairly good agreement with that predicted from an optimal case theory where classical noise is absent. This supports the theoretical treatment where we argued the importance of correctly accounting for quasi-elastic photon scattering events. We have made preliminary investigations of the lifetime of the squeezing that indicate a decay in the ms range. We have hinted results of a full tomography of the squeezed state that show large noise in the anti-squeezed spin-components. With these conclusions the theses that formed the basis of this account have been affirmed.

Next steps and improvements

14.1 What to improve

Several parts of the setup are now in a form that we find optimal. The MZI has been reconfigured to enable light-shift cancellation and make it immune to acoustic noise. We have incorporated a host of features, such as probe power balancing by the wiggler and phase-offsetting the MZI to balance probes individually. The balanced QND detector delivers fully in terms of a high bandwidth and a low electronic noise level. The locking of the MZI is very stable and all together the MZI detection system seems to work extremely well.

FORT light shift The light-shift of the FORT trapping beam is a problem because it dephases the collective atomic state. From the observation that the irreversible dephasing time T_2^* is roughly 100 times longer than the reversible (inhomogeneous) dephasing time T_2 , there is really a lot to gain by reducing the FORT light shift. In most of the experiments shown in this thesis it is possible to interpose a spin-echo pulse to achieve coherence lifetimes given by T_2^* (see sec. 10.2.4). However, for a clock sequence this is not an option, as it also cancels the sensitivity to the microwave detuning that one wants to measure. Establishing, whether there exists a FORT polarisation setting which together with a certain bias magnetic field orientation cancels or, more likely, reduces the FORT light shift would be an important step. It would actually not be too hard to get some qualitative experimental observations of the light-shift dependence on the FORT polarisation, and we expect to commence some trials soon.

Removing the FORT light shift would also have an effect on the T_2^* as well as the reproducibility of the measurements. This is because the current VersaDisk FORT laser has a rather high intensity noise level. The T_2^* is affected by the irreversible fluctuations of the light-shift. Moreover, the light-shift on the probe transitions will also fluctuate, and since this translates in to variations of the effective probe laser detuning it adds noise to the output signal. Magic frequencies that cancel the differential light shift on the D2-line have been proven to exist [McKeever03] at 935.6 nm. Because of the specification on our dichroic mirrors it would, however, not be possible with our current setup to separate a laser at this frequency from the probe beams in the MZI. Another, option would simply be to acquire a new and less noisy laser at a frequency around the current 1030 nm. In light of the multiple breakdowns of either the VersaDisk power supply, and chiller we have investigated this option and are aware of several

concrete opportunities. All of these come at a steep cost, and for the moment we will see how far the current FORT laser will take us.

analysis Our data analysis works well as long as we have large data sets and are able to avoid spurious data points. For more moderate data set sizes the analysis is very vulnerable, mainly because we allow so many degrees of freedom. This freedom endows us with a lot of information on the origin of various noise sources, and as such has been a powerful tool for deciding where to improve the setup. On the other hand, we have in some cases had to impose certain restraints on the parameters in order to get sensible outcomes. The analysis of our measurements by making interdependent polynomial fits to the variances and covariances of the data binned with varying mean atom numbers basically attempts to pin down the statistical distribution of different noise sources. Another way of doing this is to specify certain distributions with different characteristics in terms of the dependence on atom number. From the distributions we can generate dummy data sets and test how close the dummy data resembles the recorded data. By iterating the parameters of the distributions of the different noise contributions we will at the end determine which parameter sets is the most likely to have generated the measured data. This type of *maximum likelihood* analysis has been implemented and tested on selected data sets. So far the results of the maximum likelihood analysis has agreed perfectly with our standard fitting analysis. An added advantage of this approach is that one can in principle add an infinite number of distributions that depend on various experimental parameters, e.g. the pulse-separation, spin-rotation angle etc. Thus a whole measurement can be analysed in one coherent process. The maximum likelihood analysis is unfortunately more computationally demanding and for that reason not a particularly versatile tool - at least not for now. We have not used the maximum likelihood analysis in this account, because the method has not been fully developed and so far has not added to our understanding of the results. In the future, we anticipate that we will be able to use the method for more reliable and coherent analysis of the complex measurements that we are attempting.

14.1.1 Limitations

Whereas, some issues are open for improvements, there are other that are beyond our capability to improve — at least without a complete refurbishing of the setup. We have found that the environment of the MZI setup is not very “microwave-friendly”. Due to reflections on the elements in the setup we have limited control over the polarisation and local intensity of the microwave field. This gives rise to spatially and temporally varying coupling strength and causes the field to drive transitions that should be forbidden with the intended pure polarisation.

We have worked hard on the microwave source and on stabilising the power fluctuations in the microwave field. We believe, we have come very close to the setup that is optimal, considering the cost that we can accept. However, when running a clock this is at most half of the equation. The other part is the isolation of the atomic sample from perturbations of the clock-levels. Some effects, such as the FORT intensity noise and light-shift, leave room for improvement, but other influences, such as background magnetic field fluctuations, are not easily amended.

Finally, we would love to have lasers that never make mode-jumps and never fall out of lock. This greatly reduce the amount of time spent unusable data and the amount of data discarded. It seems, however, that we must wait some time before such lasers come about.

14.2 What to do next

14.2.1 Running a squeezed clock

The first measurements with a full Ramsey clock sequence were taken almost one year from now. These showed excessive noise, which made it completely intractable to analyse the data meaningfully. This was one of the key reasons for upgrading the microwave source to a more stable version. With the new source, a couple of experiments have now been performed and the results of those have recently been documented in [Louchet-Chauvet09]. Due to time and space constraints the results of these measurements have not made it in to this thesis.

14.2.2 Single atom excitations

In the not so distant future the setup is supposed to be modified slightly so as to allow for the creation and detection of a single atomic excitation. This highly exotic quantum state is created by pumping atoms in to one of the hyper-fine ground states and subsequently the detection of single photon created by spontaneous decay. The spontaneous decay is induced by a weak "write" beam coupling the populated ground state to an excited state and should take an excited atom to the non-populated ground state. Hence, the experiment involves setting up single photon detection. Parts of this setup has been built and the current MZI configuration is compatible with the single excitation experiment up to rotations of probe polarisations and the bias magnetic field. A thorough discussion of this topic is far beyond the scope of this thesis.

Applications

15.1 Atomic clocks

It has been a general theme of this thesis that the generated spin squeezing would have applications for atomic microwave clocks. We found that according to the squeezing measure ζ_{wineland} we had generated a spin-squeezed state with improved spectroscopic resolution. Nevertheless, there is a bit more to the story than that. We need to account for the change in the mean value of the squeezed state. According to eqs. (5.10 and 5.16) the mean of the state changes according to the result of the QND measurement. This is of course obvious since that is exactly what makes the second measurement correlated with the first measurement. It is, however, not immediately clear how this effects the operation of the Ramsey clock sequence.

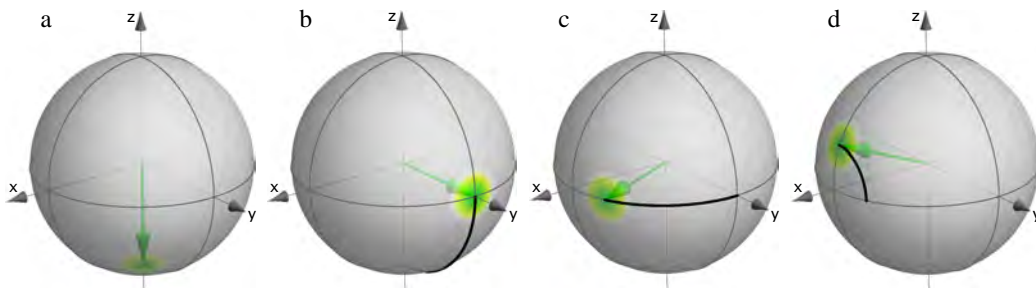


Figure 15.1: Ramsey clock-sequence with coherent pseudo-spin state

First we show a sketch of the standard clock sequence (fig. 15.1), in which a microwave $\pi/2$ pulse prepares the pseudo-spin in an equal superposition state along the Bloch-sphere y -axis (fig. 15.1b). If the microwave field is slightly detuned from the atomic clock frequency the pseudo-spin vector will precess around the equator and acquire a phase (fig. 15.1c). After waiting for as long as possible another $\pi/2$ pulse swaps the \hat{F}_y and \hat{F}_z components (fig. 15.1d) so that a measurement of the population difference on the two levels can reveal the phase acquired by the pseudo-spin during the precession. This is exactly the same as the Ramsey sequence describe by eq. (10.11) with the resulting fringes plotted in fig. 10.13.

Now we construct a clock sequence for the squeezed state. We start with the equal superposition state in fig. 15.1b. At this stage the QND measurement is performed and the resulting state has reduced noise in \hat{F}_z and increased noise in

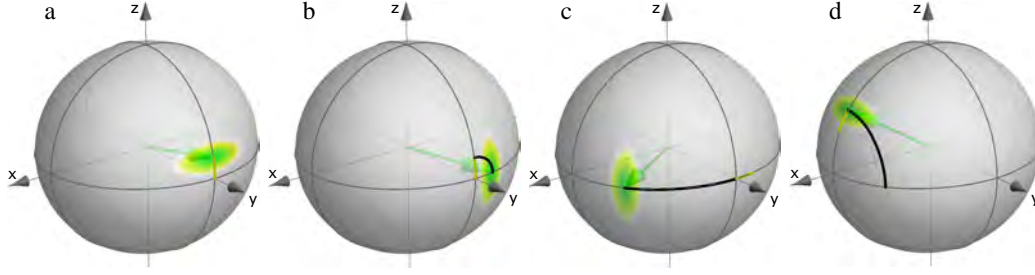


Figure 15.2: Ramsey clock-sequence with spin-squeezed state

\hat{F}_x (fig. 15.2b). Additionally, the measurement displaces the expectation value of \hat{F}_z slightly (marked by yellow line) so that it better agrees with the measurement outcome. We will tag this expectation value $\langle \hat{F}_z^{(\text{start})} \rangle$. Then next step differs from the normal clock sequence. We make another $\pi/2$ pulse, which is phase-shifted by $\theta = \pi/2$ w.r.t. the first $\pi/2$ pulse. Hence, the pseudo-spin is rotated around the y -axis and the measurement conditioned displacement $\langle \hat{F}_z^{(\text{start})} \rangle$ is converted into a displacement along the equator of the Bloch sphere. At the same time this takes \hat{F}_z to zero. Now follow only standard steps in the Ramsey sequence: free precession and a final $\pi/2$ pulse around the x -axis. The key feature is that the displacement of $\langle \hat{F}_z^{(\text{start})} \rangle$ is directly transferred into a displacement of the final $\langle \hat{F}_z^{(\text{end})} \rangle$ as compared to the value it would have attained without the QND measurement. In other words the described sequence of rotations preserves the correlation between the QND measurement result and the final state measurement following the Ramsey clock sequence.

written in terms of rotation matrices the sequence is described by

$$\begin{aligned} \overline{\mathbf{M}}_{\text{R, clock}}(\tau_{\text{R}}, \Delta_0) &= \mathbf{M}_{\mu\text{w}, \frac{\pi}{2}} \mathbf{M}_{\mu\text{w}}(\tau_{\text{R}}, 0, \Delta_0) \mathbf{M}_{\mu\text{w}, \frac{\pi}{2}} \mathbf{M}_{\mu\text{w}}(\theta_{\chi}) \\ &= \begin{pmatrix} -\hat{F}_z^{(\text{start})} \cos(\Delta_0 \tau_{\text{R}}) + \hat{F}_y^{(\text{start})} \sin(\Delta_0 \tau_{\text{R}}) \\ \hat{F}_x^{(\text{start})} \\ \sin(\Delta_0 \tau_{\text{R}}) \hat{F}_z^{(\text{start})} + \cos(\Delta_0 \tau_{\text{R}}) \hat{F}_y^{(\text{start})} \end{pmatrix}, \end{aligned} \quad (15.1)$$

where $\mathbf{M}_{\mu\text{w}}(\theta_{\chi})$ ensures the rotation about the y -axis of the first $\pi/2$ pulse (see eq. (10.6)). Again this confirms that $\hat{F}_z^{(\text{end})}$ is proportional to $\hat{F}_y^{(\text{start})}$ and $\hat{F}_z^{(\text{start})}$ and not $\hat{F}_x^{(\text{start})}$. At the precession angle $\Delta_0 \tau_{\text{R}}$ where the Ramsey sequence is most sensitive to frequency displacements we actually get $\hat{F}_z^{(\text{end})} = \hat{F}_z^{(\text{start})}$ as we said above. This invariance of \hat{F}_z means that all correlation induced in the atomic state just after the QND measurement are transferred to the end state.

The invariance of \hat{F}_z in the proposed clock sequence has another crucial implication bearing on the influence of the atoms that have been decohered by spontaneous scattering of QND probe photons. To recap the key point, that in our QND scheme each of the two probes couples predominantly to one ground level population. The selection rules restrict spontaneously scattered atoms to mostly decay back to the hyperfine level they were initially in. Since the two probes measure the populations in the whole hyperfine manifolds, i.e. one detects $N_{\text{at},4}(F = 4, \text{ all } m_F \text{ sub-levels})$ while the other detects $N_{\text{at},3}(F = 3, \text{ all } m_F \text{ sub-levels})$, the measured value of $\hat{F}_z = \frac{1}{2}(N_{\text{at},4} - N_{\text{at},3})$ is, to some extent, immune to spontaneous scattering. That is if the probes are closest to a cycling transition the spontaneous scattering will be mainly elastic and quasi-elastic, where the latter returns the atoms to the same hyperfine state but with $m_F \neq 0$.

The clock sequence for the squeezed state only affects atoms in $m_F = 0$ levels because atoms in all other m_F levels are shifted (by the bias field) w.r.t the microwave field frequency and thus do not perform any of the rotations. Therefore the contribution of these atoms to the measured \hat{F}_z is also invariant under the clock sequence. In order to maintain the correlation between the atoms scattered elastically in to $m_F = 0$ and those in $m_F \neq 0$ it is crucial that both sets of atoms transform equally under the clock sequence. In our case they actually do not transform, which is even more perfect. If instead the final rotation were a $3\pi/2$ pulse $\hat{F}_z^{(\text{start})} = -\hat{F}_z^{(\text{start})}$ and we would add anti-correlation between the atoms in $m_F = 0$ and in $m_F \neq 0$. The conclusion is that the total \hat{F}_z measured by the dichromatic QND method is invariant under the clock sequence eq. (15.1) irrespectively of the spontaneous emission, and hence its contribution to the noise of the clock measurement can be effectively reduced by this approach.

A deviation from the above description comes from the fact that the π -polarised probes couple slightly differently to $m_F = 0$ and $m_F = \pm 1$ levels. This adds some small extra noise to the spin squeezed state, which in principle could even be avoided by re-pumping all atoms with $m_F \neq 0$ into the according $m_F = 0$ state.

In our first illustration of the clock sequence [Oblak05] we had proposed a more involved sequence where we suggested to first do feedback with a microwave rotation around the x -axis so that the pseudo-spin would be put back in the equatorial plane along the y -axis. This would correspond to the creation of a unconditionally squeezed state¹, but as we have shown above this is not required for the clock measurement.

¹by this one simply means that one creates a specific pre-determined squeezed state, which does not depend on the QND measurement outcome as in our case (see eq. (5.10)).

Review of experiments

In this chapter we go into a bit extra detail with some of the experimental publications that have the closest relevance to the results treated in this work. Most of these turned up in the pre-print archive in the *cold atom spin-squeezing paper wave* of 2008.

Geremia et al. 2004 (Mabuchi group) The article [Geremia04] was the first publication to present an experimental realisation of spin-squeezing in a cold atomic sample. Moreover, the squeezing was obtained by a QND measurement, and thus seemed to beat our own efforts to reach the same goal. To make things worse it seemed unlikely that we would ever come close their whopping 10 dB of squeezing. By the end of 2007 we heard some rumours that doubts had been cast on the results and in the spring of 2008 article was retracted [Geremia08]. Carefully going through the experimental parameters part of the original authors had found the degree squeezing claimed in [Geremia04] to require an atomic density orders of magnitude above what had ever been achieved in any MOT setup. Additionally, all their subsequent attempts to reproduce the published results had been fruitless [Stockton07]. To date they have not found any explanation for the effect causing the apparent noise reduction¹ but in the note to the retraction they state *"We now have a technical understanding sufficient to rule out any possibility of spin-squeezing under the conditions of our 2004 experiment"*.

Esteve et. al. 2008 (Oberthaler group) In [Estève08] atom number squeezing is achieved between spatially separated BECs via the tunnelling interaction. Accounting for the phase-coherence between the squeezed BEC clouds they reach a spectroscopically relevant squeezing of $\xi_{\text{wineland}} = 0.42_{-0.17}^{+0.12}$, including all their stated statistical and systematic errors. The squeezing obtained in their experiment is different from our demonstration in two main ways. Firstly, the squeezing is generated by the coupling of the two BEC modes which results in atom number difference $N_a - N_b$ being evened out over time, and thus reducing $N_a - N_b$ variations between experimental realisations. Secondly, the squeezing is done with respect to number and phase of the entire BEC in two spatially separated modes a and b located in the potential wells of an optical lattice. This means that there is no direct dependence of the squeezing on the

¹In the words of [Geremia08], *Extensive efforts with revamped apparatus to reproduce the results published in our 2004 Science Report, "Real-time quantum feedback control of atomic spin-squeezing", have failed, as have attempts to develop a quantitative understanding of how those results could have arisen spuriously. We must therefore retract the Report.*

internal atomic state. As a final important note, the atom numbers $N_a + N_b$ used in the experiment are at most 2500 with a resulting relative projection noise $\langle(\Delta N_a - N_b)^2\rangle/(N_a + N_b)^2 \approx 0.5 \cdot 10^{-3}$. Thus in a spectroscopic application the squeezing improves the sensitivity to atom numbers from 2% to 1%, neither of which are particularly impressive. With these remarks, the results documented in [Estève08] are fascinating from a fundamental perspective and the experimental feat of producing them deserves high esteem.

Takano et al. 2009 (Takahashi group) In [Takano09b] they perform a QND measurement on a MOT cloud of ^{171}Yb , which is one of the potential candidates for an optical atomic frequency standard [Barber08]. Their setup is based on Faraday rotation of a beam linearly polarised along the x -direction by the collective spin of the atomic ensemble, which is optically pumped also to be polarised along the x -axis. The probe is detuned halfway between the hyperfine levels of the $^1S_0 \leftrightarrow ^1P_1$ line. The interaction is described in terms of Stokes operators $\hat{\mathbf{S}} = \{\hat{S}_x, \hat{S}_y, \hat{S}_z\}$ for light and collective spin-operators $\hat{\mathbf{J}} = \{\hat{J}_x, \hat{J}_y, \hat{J}_z\}$ for the atomic ensemble. These are normalised such that the input noise of all $\langle(\Delta\hat{S}_i)^2\rangle = \langle(\Delta\hat{J}_i)^2\rangle = 1/2$. The interaction transforms the Stokes vectors in much the same fashion as the Schwinger operators are affected in our experiment i.e. $\hat{S}_y^{\text{out}} = \hat{S}_y^{\text{in}} + \kappa_{\text{Yb}}\hat{J}_z$ while $\hat{S}_z^{\text{out}} = \hat{S}_z^{\text{in}}$ is unchanged. Two QND pulses are fired where the first serves to generate the squeezing and the second is to verify the noise reduction. For both pulses the output variances follow trivially as $\langle(\Delta\hat{S}_{yj}^{\text{out}})^2\rangle = (1 + \kappa_{\text{Yb}}^2)/2$ and $\langle(\Delta\hat{S}_{yj}^{\text{out}})^2\rangle = 1/2$, where j refers to the two pulses. When adding the results of the two successive measurements on the same ensemble they predict the variance $\langle(\Delta\hat{S}_{y,1+2})^2\rangle \equiv \langle(\Delta\hat{S}_{y1}^{\text{out}} + \hat{S}_{y2}^{\text{out}})^2\rangle = (1 + 2\kappa_{\text{Yb}}^2)/2$ because the atomic signal is essentially two times the same projected value whereas the shot noise is uncorrelated. For that same reason the variance of the subtracted signal is expected to be merely $\langle(\Delta\hat{S}_{y,1-2})^2\rangle \equiv \langle(\Delta\hat{S}_{y1}^{\text{out}} - \hat{S}_{y2}^{\text{out}})^2\rangle = 1/2$. Finally, when the ensemble is reinitialised in between the two pulses all noise contributions are uncorrelated and the noise becomes $\langle(\Delta\hat{S}_{y,1+2})^2\rangle = \langle(\Delta\hat{S}_{y,1-2})^2\rangle = (1 + \kappa_{\text{Yb}}^2)/2$.

Experimentally, the coupling strength is varied by changing the photon number, whereas the atom number is assumed to be roughly constant during the measurement sequence. For the maximal coupling strength $\kappa_{\text{Yb}} = 0.62$ achieved² a photon number of $N_L = 3.2 \cdot 10^6$ and a total MOT atom number of $N_A = 10^6$ are stated. With a probe beam waist of $58 \mu\text{m}$ it is however unlikely that the whole MOT is sampled. With this setting the paper reports the observation of the appropriate scaling of $\langle(\Delta\hat{S}_{y,1+2})^2\rangle$ and $\langle(\Delta\hat{S}_{y,1-2})^2\rangle$ with κ_{Yb} , notably the lack of any increase in the noise of the latter beyond the shot noise level. Utilising the experimental parameters and presumably an approximation of the number of atoms they calculate κ_{Yb} directly and use this to generate theoretical curves for the variances that fit nicely with the experimental data. Finally, the correlation between the two pulses are extracted and they arrive at a squeezing of $1.8_{-1.5}^{+2.4}$ dB, which in more transparent units reads $34 \pm 28\%$.

The pivotal shortcoming of this result is that the noise reduction is equated with squeezing without accounting for the measurement induced decoherence. Claiming spin squeezing either by Ueda's Eq. eq. (3.31) or Wineland's criterion Eq. eq. (3.33) is not well founded without direct inclusion of the decoherence.³ A theoretical estimate of the degree of the atomic state decoherence is obtained from the declared loss parameter $\epsilon_L = 9.3 \cdot 10^{-2}$ equalling $e^{-0.093} \approx 9\%$

²note this is κ_{Yb} so that $\kappa_{\text{Yb}}^2 = 0.38$.

³To be fair, nowhere in the article is the squeezing actually denoted by a ζ .

loss of spin polarisation. A subsequent experimental investigation yielded 9.8% spin depolarisation [Takano09a], thereby verifying the theoretical estimate. By Ueda's measure the squeezing is thus $26.8 \pm 31.1\%$ and by Wineland's measure $18.9 \pm 34.4\%$. According to both measures the result is thus not strictly statistically significant to claim spin squeezing. In conclusion, the reported experiment shows a significant noise reduction in repeated QND measurement with a strong, albeit not conclusive, indication of spin squeezing.

Schleier-Smith et al. 2009 (Vuletić group) *The discussion of [Schleier-Smith08] is in preparation*

Teper et al. 2008 (Kasevich group) In [Teper08] they make a cavity based QND measurement of the phase-shift from a MOT cloud of rubidium and observe anti-squeezing that agrees with their theoretical prediction. The probe mode is constituted by a sideband of an EOM modulated laser and the atomic phase-shift of the probe is detected by demodulating the beat note of the probe and the carrier in a similar fashion to what suggest in [Saffman09] (see sec. A.6). Compared with the proposal in [Saffman09] the use of a cavity increases the interaction strength of the QND measurement but also presents some additional complication in that it needs to be locked by reference to a locking laser. With the chosen probe detuning of 1.5 GHz the phase-shift will be have a component proportional to the total ground level population and thus be sensitive to fluctuations in the number of atoms loaded into the MOT. By recycling the MOT the atom number can presumably be kept more constant than in our setup. In the experimental sequence they fire one probe pulse of duration τ_{sq} , wait, make a microwave spin-echo π pulse, fire another probe pulse τ_{sq} long another $\pi/2$ pulse with a variable phase and then read out the result with a long probe pulse. The use of two probe pulses split by a spin-echo pulse overcomes the probe-induced light-shift as we also describe in [Windpassinger08c, Oblak08] (see sec. 11.2.1). They analyse the statistics of the fluctuations between the combined probe pulses and the read-out pulse for different phase of the final microwave pulse and thus establish the statistics of the different rotations angles of the spin state (see fig. 12.26). For 0 and π microwave phase-offsets the noise is at the projection noise level while at $\pi/2$ the noise is increased. Since the ratio of this increased noise w.r.t. the projection noise scales linearly with atom number they infer that the noise increase is caused by anti-squeezing c.f. eq. (5.11). Though they are unable to resolve a reduction in noise at 0 and π degrees from the anti-squeezing data one can infer a noise reduction of up to 0.02. They deserve much kudos for taking great care to characterise the loss of state-coherence due to spontaneous scattering and dephasing. This is done by looking at the loss of Rabi fringe amplitude. For the presented data the reduced amplitude amounts to 76% of the non-perturbed amplitude, which is somewhat less than what should be expected for the theoretically calculated $\leq 6\%$ decoherence due to spontaneous scattering. Comparing the inferred noise reduction with the loss of coherence one could estimate the inferred squeezing to be 0.026. These numbers are not spelled out in the paper, probably because they seem experimentally unattainable⁴. They state that for longer probe pulse duration they are able to directly observe a 3.8 dB noise reduction but without giving a number they write that the loss of coherence exceeds the noise reduction and thus squeezing cannot be claimed. In sum, [Teper08] outlines an experiment with some similarities

⁴compare with [Schleier-Smith08] where the inferred squeezing is also orders of magnitude higher than what they can observe.

with [Schleier-Smith08] but due to technical limitations can only claim indirect observation of spin-squeezing.

Part IV

Appendices

Optical field and operator transformations

A.1 Fields and operators

We introduce the field operators \hat{a} , \hat{b} , etc., and \hat{v} . All fields, except those labelled \hat{v} , may be coherent fields i.e. with $\langle \hat{a} \rangle = \alpha$, $\langle \hat{b} \rangle = \beta$ etc., where α and β are the coherent amplitudes of the fields such that $|\alpha|^2$ and $|\beta|^2$ are the respective photon number expectation values. Fields denominated \hat{v}_i are vacuum fields which have zero mean photon number, hence $\langle \hat{v} \rangle = 0$. We define the following Schwinger angular momentum operators

$$\begin{aligned} \hat{S}_x &\equiv \frac{1}{2} (\hat{a}^\dagger \hat{b} + \hat{b}^\dagger \hat{a}) , & \hat{S}_y &\equiv \frac{-i}{2} (\hat{a}^\dagger \hat{b} - \hat{b}^\dagger \hat{a}) , & \hat{S}_z &\equiv \frac{1}{2} (\hat{a}^\dagger \hat{a} - \hat{b}^\dagger \hat{b}) \\ \hat{S}_x^{a_i b_j} &\equiv \frac{1}{2} (\hat{a}_i^\dagger \hat{b}_j + \hat{b}_j^\dagger \hat{a}_i) , & \hat{S}_y^{a_i b_j} &\equiv \frac{-i}{2} (\hat{a}_i^\dagger \hat{b}_j - \hat{b}_j^\dagger \hat{a}_i) , & \hat{S}_z^{a_i b_j} &\equiv \frac{1}{2} (\hat{a}_i^\dagger \hat{a}_i - \hat{b}_j^\dagger \hat{b}_j) , \end{aligned}$$

where a convenient shorthand notation, omitting the field indexing, is chosen for the \hat{a} , \hat{b} combination. For other combinations the Schwinger operator symbol reflects the constituent fields e.g. $\hat{S}_x^{v_a c_1} \equiv \frac{1}{2} (\hat{v}_a^\dagger \hat{c}_1 + \hat{c}_1^\dagger \hat{v}_a)$.

A.2 Distribution in Fock-basis

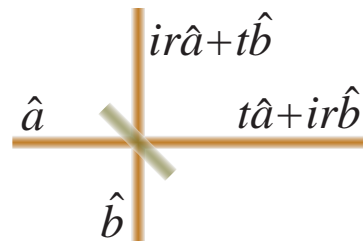
A.3 Elements

Next we derive the transformations due to various elements that the modes may encounter.

A.3.1 Beamsplitter

The field operator transformations on a beamsplitter (Fig. A.1) with field transmission t and reflection r are given by

$$\begin{aligned} \hat{a}' &= t\hat{a} + ir\hat{b} \\ \hat{b}' &= ir\hat{a} + t\hat{b} \end{aligned}$$



This can alternatively be expressed by the Schwinger operator transformation $\hat{\mathbf{S}}' = \mathbf{M}_\beta \hat{\mathbf{S}}$ with the transformation matrix

$$\mathbf{M}_\beta = \begin{pmatrix} 1 & 0 & 0 \\ 0 & r^2 - t^2 & 2rt \\ 0 & -2rt & r^2 - t^2 \end{pmatrix} = \begin{pmatrix} 1 & 0 & 0 \\ 0 & \cos \beta & \sin \beta \\ 0 & -\sin \beta & \cos \beta \end{pmatrix},$$

with the angle $\beta = \arctan\left(\frac{2rt}{r^2 - t^2}\right) = \arctan\left(\frac{2r\sqrt{(1-r^2)}}{2r^2 - 1}\right)$. The beamsplitter rotates the Schwinger operator around the x -axis.

A.3.2 Free propagation



Figure A.2: Fields propagating without disturbance

Free propagation results in accumulation of a phase difference $\tilde{\phi}$ between the fields

$$\begin{aligned} \hat{a}' &= e^{i\tilde{\phi}/2} \hat{a} \\ \hat{b}' &= e^{-i\tilde{\phi}/2} \hat{b} \end{aligned}$$

In terms of Schwinger operators this is expressed with the transformation matrix.

$$\mathbf{M}_{\tilde{\phi}} = \begin{pmatrix} \cos \tilde{\phi} & \sin \tilde{\phi} & 0 \\ -\sin \tilde{\phi} & \cos \tilde{\phi} & 0 \\ 0 & 0 & 1 \end{pmatrix}.$$

Hence, the phase accumulated by free propagation rotates the Schwinger operator by the angle corresponding to this phase.

A.3.3 Losses

The customary way to model losses of a light mode is by reflection on an imaginary beamsplitter. The fact that the vacuum field of the other beamsplitter input is admixed to the transmitted field ensures that the commutation relations are preserved correctly. If we start out with two modes \hat{a} and \hat{b} and only one of these are subjected to losses of magnitude ρ the resulting transformation is

$$\begin{aligned} \hat{a}' &= \tau \hat{a} + i\rho \hat{v} \\ \hat{b}' &= \hat{b} \end{aligned}$$

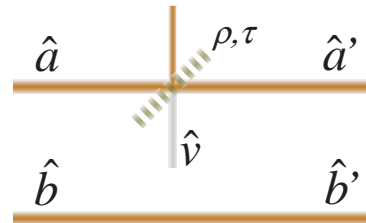


Figure A.3: Losses in one of a pair of fields

where $\tau = \sqrt{1 - \rho^2}$ is the transmission of the imagined beamsplitter and \hat{v} is the vacuum field operator with $\langle \hat{v} \rangle = 0$. The "lost" part of the mode $\hat{v}' = i\rho\hat{a} + \tau\hat{v}$ is not of interest as this is not necessarily in any mode one can detect. This results in the transformation

$$\begin{aligned}\hat{S}'_x &= \tau\hat{S}_x + \rho\hat{S}_y^{vb} \\ \hat{S}'_y &= \tau\hat{S}_y - \rho\hat{S}_x^{vb} \\ \hat{S}'_z &= \tau^2\hat{S}_z + \rho\tau\hat{S}_y^{va} + \rho^2\hat{S}_z^{vb},\end{aligned}$$

which alternatively can be expressed by the extended transformation matrix

$$\begin{pmatrix} \hat{S}'_x \\ \hat{S}'_y \\ \hat{S}'_z \\ \hat{S}'_{va} \\ \hat{S}'_{vb} \\ \hat{S}'_{va} \\ \hat{S}'_{vb} \\ \hat{S}'_{va} \\ \hat{S}'_{vb} \\ \hat{S}'_{va} \\ \hat{S}'_{vb} \end{pmatrix} = \begin{pmatrix} \tau & 0 & 0 & 0 & 0 & 0 & 0 & \rho & 0 \\ 0 & \tau & 0 & 0 & 0 & 0 & -\rho & 0 & 0 \\ 0 & 0 & \tau^2 & 0 & \rho\tau & 0 & 0 & 0 & \rho^2 \\ - & - & - & - & - & - & - & - & - \\ - & - & - & - & - & - & - & - & - \\ - & - & - & - & - & - & - & - & - \\ - & - & - & - & - & - & - & - & - \\ - & - & - & - & - & - & - & - & - \\ - & - & - & - & - & - & - & - & - \\ - & - & - & - & - & - & - & - & - \\ - & - & - & - & - & - & - & - & - \end{pmatrix} \begin{pmatrix} \hat{S}_x \\ \hat{S}_y \\ \hat{S}_z \\ \hat{S}_x^{va} \\ \hat{S}_y^{va} \\ \hat{S}_z^{va} \\ \hat{S}_x^{vb} \\ \hat{S}_y^{vb} \\ \hat{S}_z^{vb} \end{pmatrix} \quad (\text{A.1})$$

The expectation values of \hat{S}_x and \hat{S}_y are simply scaled down by τ because $\langle \hat{S}_x^{vb} \rangle = \langle \hat{S}_y^{vb} \rangle = 0$. On the other hand, $\langle \hat{S}_z \rangle$ attains an extra contribution $\rho^2 \langle \hat{S}_z^{vb} \rangle = -(1 - \tau^2) \langle \hat{b}^\dagger \hat{b} \rangle / 2$. Hence, we have the consistent result $\langle \hat{S}'_z \rangle = \tau^2 \langle \hat{a}^\dagger \hat{a} - \hat{b}^\dagger \hat{b} \rangle / 2 - (1 - \tau^2) \langle \hat{b}^\dagger \hat{b} \rangle / 2 = (\tau^2 \hat{a}^\dagger \hat{a} + \hat{b}^\dagger \hat{b}) / 2$, which is indeed proportional to the photon number difference after the probe arm attenuation.

A.3.4 Mode overlap

The overlap of the modes at the output beamsplitter of the MZI is rather good but not perfect. To model the imperfection we say that a fraction $\mathcal{R} = \sqrt{1 - \mathcal{T}^2}$ of the fields \hat{a} and \hat{b} are lost to another mode which are independently split on the beamsplitter and thus admixed with the vacuum field. Thus in each output we have three modes from the overlapped modes, the reflection of the non-overlapped part of one mode and the transmission of the non-overlapped part of the other mode. Written out this gives

$$\begin{aligned}\hat{a} &= t(\mathcal{T}\hat{a} + i\mathcal{R}\hat{v}_a) + r(i\mathcal{T}\hat{b} - \mathcal{R}\hat{v}_b) & \hat{b} &= t(\mathcal{T}\hat{b} + i\mathcal{R}\hat{v}_b) + r(i\mathcal{T}\hat{a} - \mathcal{R}\hat{v}_a) \\ \hat{a}_a &= t(i\mathcal{R}\hat{a} + \mathcal{T}\hat{v}_a) + ir\hat{v} & \hat{a}_a &= r(-\mathcal{R}\hat{a} + i\mathcal{T}\hat{v}_a) + t\hat{v} \\ & & & \\ \hat{a}_b &= r(-\mathcal{R}\hat{b} + i\mathcal{T}\hat{v}_b) + t\hat{v} & \hat{b}_b &= t(i\mathcal{R}\hat{b} + \mathcal{T}\hat{v}_b) + ir\hat{v}\end{aligned} \quad (\text{A.2})$$

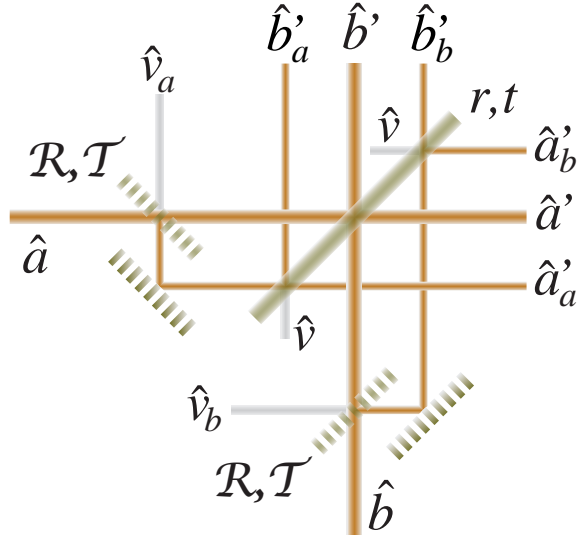


Figure A.4: Model of the imperfect mode overlap of two modes on a beamsplitter

Having only a small spatial separation, all three modes in each output impinge on the respective detector. Hence, it is indeed important to account for all six output modes. We combine the pairs of fields in Eq. eq. (A.2) into Schwinger operators and deduce the following transformations

$$\begin{aligned}\hat{S}'_x &= \mathcal{T}^2 \hat{S}_x + \mathcal{RT} \left(\hat{S}_y^{(v_b a)} + \hat{S}_y^{(v_a b)} \right) \\ \hat{S}'_y &= \mathcal{T}^2 \left(\sin \beta_2 \hat{S}_z - \cos \beta_2 \hat{S}_y \right) \\ &\quad + \mathcal{RT} \left(\sin \beta_2 \left(\hat{S}_y^{(v_a a)} - \hat{S}_y^{(v_b b)} \right) + \cos \beta_2 \left(\hat{S}_x^{(v_a b)} - \hat{S}_x^{(v_b a)} \right) \right) \\ \hat{S}'_z &= -\mathcal{T}^2 \left(\cos \beta_2 \hat{S}_z + \sin \beta_2 \hat{S}_y \right) \\ &\quad + \mathcal{RT} \left(\cos \beta_2 \left(\hat{S}_y^{(v_b b)} - \hat{S}_y^{(v_a a)} \right) + \sin \beta_2 \left(\hat{S}_x^{(v_a b)} - \hat{S}_x^{(v_b a)} \right) \right)\end{aligned}\quad (\text{A.3a})$$

$$\begin{aligned}\hat{S}_x^{(a)'} &= -\mathcal{R} \hat{S}_y^{(v a)} \\ \hat{S}_y^{(a)'} &= -\sin \beta_2 \left(\mathcal{RT} \hat{S}_y^{(v_a a)} + \mathcal{R}^2 \hat{S}_z^{(v a)} \right) + \cos \beta_2 \mathcal{R} \hat{S}_x^{(v a)} \\ \hat{S}_z^{(a)'} &= \cos \beta_2 \left(\mathcal{RT} \hat{S}_y^{(v_a a)} + \mathcal{R}^2 \hat{S}_z^{(v a)} \right) + \sin \beta_2 \mathcal{R} \hat{S}_x^{(v a)}\end{aligned}\quad (\text{A.3b})$$

$$\begin{aligned}\hat{S}_x^{(b)'} &= -\mathcal{R} \hat{S}_y^{(v b)} \\ \hat{S}_y^{(b)'} &= \sin \beta_2 \left(\mathcal{RT} \hat{S}_y^{(v_b b)} + \mathcal{R}^2 \hat{S}_z^{(v b)} \right) - \cos \beta_2 \mathcal{R} \hat{S}_x^{(v b)} \\ \hat{S}_z^{(b)'} &= -\cos \beta_2 \left(\mathcal{RT} \hat{S}_y^{(v_b b)} + \mathcal{R}^2 \hat{S}_z^{(v b)} \right) - \sin \beta_2 \mathcal{R} \hat{S}_x^{(v b)}.\end{aligned}\quad (\text{A.3c})$$

Here we have neglected all terms which exclusively contain vacuum fields. In the limit of perfect visibility ($R \rightarrow 0$) the $\hat{\mathbf{S}}^{(a)}, \hat{\mathbf{S}}^{(b)} \rightarrow 0$ and the expression for $\hat{\mathbf{S}}$ goes to the that of Eq. eq. (A.3.1) for a loss-less BS. For two detectors placed at the BS outputs the difference signal is thus given by $p_- = 2(\hat{S}'_z + \hat{S}_z^{(a)'} + \hat{S}_z^{(b)'})$.

A.4 Full MZI

Now that all transformations due to the single elements are known we combine them into MZIs of various complexities. For simplicity the Schwinger operators corresponding to the input fields \hat{c}_1, \hat{c}_2 and the output fields \hat{d}_1, \hat{d}_2 are termed $\hat{\mathbf{S}}^{in}$ and $\hat{\mathbf{S}}^{out}$ respectively. We get underway with the textbook case.

A.4.1 Ideal loss-less MZI

The transformation matrix for the full MZI without losses and with perfect mode overlap is found by matrix multiplication $\mathbf{M}_{MZI} = \mathbf{M}_{\beta_2} \mathbf{M}_{\tilde{\phi}} \mathbf{M}_{\beta_1}$ which results in

$$\mathbf{M}_{MZI} = \begin{pmatrix} \cos \tilde{\phi} & \sin \tilde{\phi} \cos \beta_1 & \sin \tilde{\phi} \sin \beta_1 \\ -\sin \tilde{\phi} \cos \beta_2 & \cos \tilde{\phi} \cos \beta_2 \cos \beta_1 - \sin \beta_2 \sin \beta_1 & \cos \tilde{\phi} \cos \beta_2 \sin \beta_1 + \sin \beta_2 \cos \beta_1 \\ \sin \tilde{\phi} \sin \beta_2 & -\cos \tilde{\phi} \sin \beta_2 \cos \beta_1 - \cos \beta_2 \sin \beta_1 & -\cos \tilde{\phi} \sin \beta_2 \sin \beta_1 + \cos \beta_2 \cos \beta_1 \end{pmatrix} \quad (\text{A.4})$$

The balanced detector signal p_- is equal to twice \hat{S}_z^{out} , which is the bottom row of the matrix. If we take the expectation value $\langle p_- \rangle$ assuming only \hat{c}_1 in a non-vacuum state we find

$$\frac{\langle p_- \rangle}{2} = \langle \hat{S}_z^{out} \rangle = (-\cos \tilde{\phi} \sin \beta_2 \sin \beta_1 + \cos \beta_2 \cos \beta_1) \langle \hat{S}_z^{in} \rangle,$$

The symmetric MZI, $\beta_1 = \beta_2 = \pi/2$, is most sensitive to phase-shifts between the probe and reference arms. Unequal splitting ratios of either of the beamsplitters will cause a reduction of the fringe amplitude. For there to be a DC offset of the output signal both BS must be non symmetric.

Using Eq. eq. (A.4) and eq. (2.10) the shot noise of \hat{S}_z^{out} is easily calculated to be

$$\begin{aligned} \langle (\Delta \hat{S}_z^{out})^2 \rangle &= (\sin \tilde{\phi} \sin \beta_2)^2 \langle (\Delta \hat{S}_x^{in})^2 \rangle \\ &\quad + (\cos \tilde{\phi} \sin \beta_2 \cos \beta_1 + \cos \beta_2 \sin \beta_1)^2 \langle (\Delta \hat{S}_y^{in})^2 \rangle \\ &\quad + (-\cos \tilde{\phi} \sin \beta_2 \sin \beta_1 + \cos \beta_2 \cos \beta_1)^2 \langle (\Delta \hat{S}_z^{in})^2 \rangle \\ &= \frac{n_{ph}}{4}, \end{aligned}$$

It is useful for later calculation to note that contribution from the cross-terms $\langle \hat{S}_i^{in} \hat{S}_j^{in} + \hat{S}_j^{in} \hat{S}_i^{in} \rangle = 0$, ($i \neq j$).

A.4.2 Loss-less MZI with imperfect mode overlap

We use Eqs. (A.3a-c) in place of the standard loss-less beamsplitter transformation to calculate the full MZI transformation matrix. As a change, I will stick to the necessary and state only the z-components output operators as this is what we measure at the end. First the mode matched output fields

$$\begin{aligned} \hat{S}_z^{out} &= \mathcal{T}^2 \left\{ \sin \tilde{\phi} \sin \beta_2 \hat{S}_x^{in} + (\cos \tilde{\phi} \sin \beta_2 \cos \beta_1 + \cos \beta_2 \sin \beta_1) \hat{S}_y^{in} \right. \\ &\quad \left. - (\cos \tilde{\phi} \sin \beta_2 \sin \beta_1 - \cos \beta_2 \cos \beta_1) \hat{S}_z^{in} \right\} \\ &\quad + \mathcal{RT} \left\{ - (t_1 \cos \beta_2 + r_1 \sin \beta_2) \hat{S}_y^{(v_a c_1)} + (r_1 \cos \beta_2 - t_1 \sin \beta_2) \hat{S}_x^{(v_b c_1)} \right. \\ &\quad \left. - (r_1 \cos \beta_2 - t_1 \sin \beta_2) \hat{S}_x^{(v_a c_2)} + (t_1 \cos \beta_2 + r_1 \sin \beta_2) \hat{S}_y^{(v_b c_2)} \right\} \end{aligned}$$

Non-interfering modes

$$\begin{aligned} \hat{S}_z^{out,a} &= \mathcal{R}^2 \cos \beta_2 \left\{ \frac{1}{2} \sin \beta_1 \hat{S}_y^{in} + t_1^2 \hat{S}_z^{(v c_1)} + r_1^2 \hat{S}_z^{(v c_2)} \right\} \\ &\quad + \mathcal{RT} \cos \beta_2 \left\{ t_1 \hat{S}_y^{(v_a c_1)} + r_1 \hat{S}_x^{(v_a c_2)} \right\} \\ &\quad + \mathcal{R} \sin \beta_2 \left\{ t_1 \hat{S}_x^{(v c_1)} - r_1 \hat{S}_y^{(v c_2)} \right\} \\ \hat{S}_z^{out,b} &= \mathcal{R}^2 \cos \beta_2 \left\{ \frac{1}{2} \sin \beta_1 \hat{S}_y^{in} - t_1^2 \hat{S}_z^{(v c_2)} - r_1^2 \hat{S}_z^{(v c_1)} \right\} \\ &\quad - \mathcal{RT} \cos \beta_2 \left\{ r_1 \hat{S}_y^{(v_b c_1)} + t_1 \hat{S}_x^{(v_b c_2)} \right\} \\ &\quad + \mathcal{R} \sin \beta_2 \left\{ r_1 \hat{S}_y^{(v c_1)} - t_1 \hat{S}_x^{(v c_2)} \right\} \end{aligned}$$

Note, that the expressions make no reference to the interferometer phase-shift $\tilde{\phi}$ as is expected for the non-interfering part of the fields. We may further wish to

combine all the operators that

$$\begin{aligned}
\frac{p_-}{2} &= \hat{S}_z^{out} + \hat{S}_z^{out,a} + \hat{S}_z^{out,b} \\
&= \mathcal{T}^2 \left\{ \sin \tilde{\phi} \sin \beta_2 \hat{S}_x^{in} + (\cos \tilde{\phi} \sin \beta_2 \cos \beta_1 + \cos \beta_2 \sin \beta_1) \hat{S}_y^{in} \right. \\
&\quad \left. - (\cos \tilde{\phi} \sin \beta_2 \sin \beta_1 - \cos \beta_2 \cos \beta_1) \hat{S}_z^{in} \right\} \\
&\quad - \mathcal{RT} \sin \beta_2 \left\{ r_1 \left(\hat{S}_y^{(v_{ac1})} - \hat{S}_y^{(v_{bc2})} \right) + t_1 \left(\hat{S}_x^{(v_{bc1})} - t_1 \hat{S}_x^{(v_{ac2})} \right) \right\} \\
&\quad + \mathcal{R} \sin \beta_2 \left\{ t_1 \left(\hat{S}_x^{(v_{c1})} - \hat{S}_x^{(v_{c2})} \right) + r_1 \left(\hat{S}_y^{(v_{c1})} - \hat{S}_y^{(v_{c2})} \right) \right\} \\
&\quad + \mathcal{R}^2 \cos \beta_2 \left\{ \sin \beta_1 \hat{S}_y^{in} + \cos \beta_1 \hat{S}_z^{in} \right\}
\end{aligned} \tag{A.5}$$

Most of the terms in this expression have expectation value zero and thus do not alter the detected mean output. On the other hand these terms do add shot noise to the detected signal. Taking the expectation value of Eq. eq. (A.5) and assuming that only one of the inputs, say \hat{c}_1 , are in a (non-vacuum) coherent state we get the measured output difference photo-current to be

$$\begin{aligned}
\frac{\langle p_- \rangle}{2} &= \langle \hat{S}_z^{out} \rangle + \langle \hat{S}_z^{out,a} \rangle + \langle \hat{S}_z^{out,b} \rangle \\
&= \mathcal{T}^2 (-\cos \tilde{\phi} \sin \beta_2 \sin \beta_1 + \cos \beta_2 \cos \beta_1) \langle \hat{S}_z^{in} \rangle + \mathcal{R}^2 \cos \beta_2 \cos \beta_1 \langle \hat{S}_z^{v_{c1}} \rangle
\end{aligned}$$

The interference fringe amplitude scales with \mathcal{T}^2 and if at least one of the beam-splitters has equal splitting ratio the fringe has no DC offset. Thus a balanced output, $\langle p_- \rangle = 0$ is achieved by setting the interferometer phase to $\tilde{\phi} = \pi/2$.

A.4.3 Near real life MZI

Alas, it is time to deal with the full interferometer setup with losses and imperfect mode overlap. To keep the expressions reasonably tidy we will make the assumption that we have an equal splitting ratio at the output BS such that $\beta_2 = \pi/2$. This is usually fulfilled as we need to have a balance signal in the outputs in order not to saturate the detector. As before we restrict our attention to \hat{S}_z^{out} , which can be traced back to the input Schwinger operators as

$$\begin{aligned}
\hat{S}_z^{out} &= \mathcal{T}^2 \left\{ \tau \sin \tilde{\phi} \hat{S}_x^{in} + \tau \cos \tilde{\phi} \cos \beta_1 \hat{S}_y^{in} \right. \\
&\quad \left. - \tau \cos \tilde{\phi} \sin \beta_1 \hat{S}_z^{in} \right. \\
&\quad \left. - \rho \left(r_1 \hat{S}_y^{(v_{c1})} - t_1 \hat{S}_x^{(v_{c2})} \right) \right\} \\
&\quad + \mathcal{RT} \left\{ \tau r_1 \left(\hat{S}_y^{(v_{bc2})} - \hat{S}_y^{(v_{ac1})} \right) + t_1 \left(\hat{S}_x^{(v_{ac2})} - \hat{S}_x^{(v_{bc1})} \right) \right\} \\
\hat{S}_z^{out,a} &= \mathcal{R} \tau \left\{ t_1 \hat{S}_x^{(v_{c1})} - r_1 \hat{S}_y^{(v_{c2})} \right\} \\
\hat{S}_z^{out,b} &= \mathcal{R} \left\{ r_1 \hat{S}_y^{(v_{c1})} - t_1 \hat{S}_x^{(v_{c2})} \right\}
\end{aligned}$$

Adding these modes up we get the combined output signal

$$\begin{aligned}
\frac{p_-}{2} &= \hat{S}_z^{out} + \hat{S}_z^{out,a} + \hat{S}_z^{out,b} \\
&= \mathcal{T}^2 \left\{ \tau \sin \tilde{\phi} \hat{S}_x^{in} + \tau \cos \tilde{\phi} \left(\cos \beta_1 \hat{S}_y^{in} - \sin \beta_1 \hat{S}_z^{in} \right) - \rho \left(r_1 \hat{S}_y^{(vc_1)} - t_1 \hat{S}_x^{(vc_2)} \right) \right\} \\
&\quad + \mathcal{RT} \left\{ \tau r_1 \left(\hat{S}_y^{(vb_2)} - \hat{S}_y^{(va_1)} \right) + t_1 \left(\hat{S}_x^{(va_2)} - \hat{S}_x^{(vb_1)} \right) \right\} \\
&\quad + \mathcal{R} \left\{ t_1 \left(\tau \hat{S}_x^{(vc_1)} - \hat{S}_x^{(vc_2)} \right) + r_1 \left(\hat{S}_y^{(vc_1)} - \tau \hat{S}_y^{(vc_2)} \right) \right\}
\end{aligned} \tag{A.6}$$

Finally, we may take the expectation value again assuming that only $\hat{c}_1^\dagger \hat{c}_1 \neq 0$, whereby we reach the very simple expression

$$\frac{\langle p_- \rangle}{2} = \langle \hat{S}_z^{out} \rangle + \langle \hat{S}_z^{out,a} \rangle + \langle \hat{S}_z^{out,b} \rangle = -\mathcal{T}^2 \tau \cos \tilde{\phi} \sin \beta_1 \langle \hat{S}_z^{in} \rangle \tag{A.7}$$

As discussed above, the equal splitting of the output coupler ensures that the difference signal has no DC-offset. For completeness the expectation value in the general case of arbitrary output BS rotation angle β_2 is

$$\begin{aligned}
\frac{\langle p_- \rangle}{2} &= \langle \hat{S}_z^{out} \rangle + \langle \hat{S}_z^{out,a} \rangle + \langle \hat{S}_z^{out,b} \rangle \\
&= \mathcal{T}^2 \left(\left[-\cos \tilde{\phi} \sin \beta_2 \sin \beta_1 \tau + \cos \beta_2 \cos \beta_1 \tau^2 \right] \langle \hat{S}_z^{in} \rangle - \cos \beta_2 \rho^2 r_1^2 \langle \hat{S}_z^{(vc_1)} \rangle \right).
\end{aligned}$$

The interference fringe amplitude scales with the mode mismatch squared \mathcal{T}^2 but importantly only goes linearly with the probe arm transmission τ . A non-offset interference fringe can still be achieved by an equal output BS ratio, however an equal splitting at the input BS is no longer sufficient.

The shot noise of the system is slightly more complicated than the for the previously examined configurations, the reason for this being that light is lost from the system in the probe arm. From Eq. eq. (A.6) we calculate

$$\langle (\Delta \hat{S}_z^{out})^2 \rangle = (1 - \rho^2 t_1^2) \frac{n_{ph}}{4}. \tag{A.8}$$

The shot noise in the output is thus proportional to the photon number transmitted through the interferometer independent of the phase-difference $\tilde{\phi}$ and the mode overlap τ . Naturally, Eq. eq. (A.8) is also valid for any output beamsplitter ratio.

A.5 MZI sensitivity to phase displacements

Interferometric spectroscopy is all about measuring the phase $\tilde{\phi}$ with as good a precision as possible. The phase $\tilde{\phi}$ is due to a difference in the *optical* path-length between the two arms — with emphasis on *optical*. This can be influenced by a whole range of things from physical displacements of the path-length to changes in the index of refraction in the beam path. The latter is essentially how an atomic sample placed in the probe arm will affect the $\tilde{\phi}$. For the moment we will not be concerned with the origin of the phase-shift, but just note that due to its origin it may fluctuate around some mean value i.e. we can write $\tilde{\phi} = \tilde{\phi}_0 + \Delta\tilde{\phi}$, where the mean of $\Delta\tilde{\phi}$ is zero. This will naturally add noise to the MZI output signal. How much this is, we can derive from eq. (A.6). Since the photon shot noise is completely uncorrelated we can neglect cross terms between the shot

noise and fluctuations $\Delta\tilde{\phi}$. The phase noise thus translates into noise in the output as

$$\begin{aligned} \langle (\Delta\hat{S}_z^{out})^2 \rangle &= \langle (\Delta\hat{S}_z^{out})^2 \rangle_{\text{SN}} + \langle (\Delta\hat{S}_z^{out})^2 \rangle_{\Delta\tilde{\phi}} \\ &= (1 - \rho^2 t_1^2) \frac{n_{\text{ph}}}{4} + T^4 \tau^2 \left[\cos^2 \tilde{\phi} \langle \hat{S}_x^{in} \rangle^2 + \sin^2 \tilde{\phi} \left(\cos \beta_1 \langle \hat{S}_y^{in} \rangle - \sin \beta_1 \langle \hat{S}_z^{in} \rangle \right)^2 \right] \langle (\Delta\tilde{\phi})^2 \rangle \\ &= (1 - \rho^2 t_1^2) \frac{n_{\text{ph}}}{4} + T^4 \tau^2 \sin^2 \tilde{\phi} \sin^2 \beta_1 \frac{n_{\text{ph}}^2}{4} \langle (\Delta\tilde{\phi})^2 \rangle, \end{aligned} \quad (\text{A.9})$$

where we have used that $\langle \hat{S}_x^{in} \rangle = \langle \hat{S}_y^{in} \rangle = 0$. Thus the ability of the MZI to detect phase-fluctuations depends heavily on the mode overlap. The sensitivity is affected by the first beamsplitter ratio and the probe arm loss to the same order as the shot noise is. Another observation is that the magnitude of phase-fluctuations scales with n_{at}^2 , whereas the shot noise only scales with n_{at} . Finally, the phase-fluctuations propagate most effectively to the output signal when the mean interferometer phase is set to $\tilde{\phi}_0 = \pi/2$ such that $\sin^2 \tilde{\phi} = 1$. This is of course because at $\tilde{\phi}_0 = \pi/2$ the MZI has the largest derivative w.r.t. changes to the phase (see eq. (A.7)).

A.6 Sideband interferometer configuration

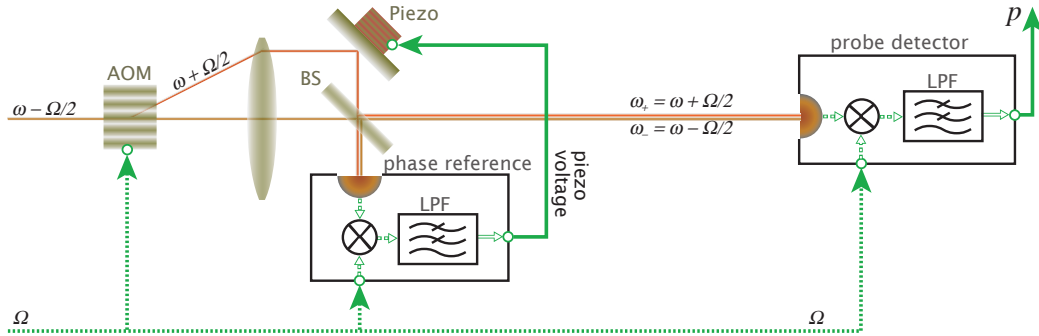


Figure A.5: Principle of the sideband interferometer setup.

From spatially separated modes we now turn our attention to the case of modes \hat{A}_+ and \hat{A}_- , which are only separated by frequency i.e. they have $\mathbf{k}_+ \parallel \mathbf{k}_-$ but $|\mathbf{k}_+| \neq |\mathbf{k}_-|$. The two frequencies correspond to sideband frequencies $\omega_{\pm} \equiv \omega \pm \Omega$, hence the mode labelling by plus/minus and the term sideband interferometer (SBI). The specific choice of frequencies will be discussed in a subsequent section (Sec. A.6.1). The setup including the way to generate the two fields is outlined in fig. A.5. A field with frequency $\omega - \Omega/2$ is incident on an AOM driven by a RF frequency Ω so that the 0'th and 1'st refracted orders obtain the frequencies $\omega_- = \omega - \Omega/2$ and $\omega_+ = \omega + \Omega/2$ respectively. We assume that the two fields have equal coherent amplitudes $\alpha_- + \alpha_+ = \alpha$. The fields are, then, put into the same spatial mode by mixing them on a 50/50 BS with the option of adjusting the phase-difference $\tilde{\phi}$ between the fields by tuning the path length difference of the two orders from the AOM to the BS. From the BS one output (probe output) goes to the probe detector while the other (reference output) goes to a phase-reference detector that is essentially the same as the probe detector, and which provides a feedback for locking the relative phase $\tilde{\phi}$ of the two orders. In the probe output we later wish to incorporate an atomic ensemble which may add an additional phase-shift between the two fields.

This case is significantly simpler to treat in the Schwinger operator picture as all optical elements affect the two modes equally and thus there are no transformations to account for. We simply define

$$\begin{aligned}\hat{S}_x &\equiv \frac{1}{2} \left(\hat{A}_+^\dagger \hat{A}_- + \hat{A}_-^\dagger \hat{A}_+ \right) = \cos(\Omega t + \tilde{\phi}) \hat{S}_x(0) - \sin(\Omega t + \tilde{\phi}) \hat{S}_y(0) \\ \hat{S}_y &\equiv -\frac{i}{2} \left(\hat{A}_+^\dagger \hat{A}_- - \hat{A}_-^\dagger \hat{A}_+ \right) = -\sin(\Omega t + \tilde{\phi}) \hat{S}_x(0) + \cos(\Omega t + \tilde{\phi}) \hat{S}_y(0) \\ \hat{S}_z &\equiv \frac{1}{2} \left(\hat{A}_+^\dagger \hat{A}_+ - \hat{A}_-^\dagger \hat{A}_- \right) = \frac{1}{2} (\hat{N}_{\text{ph}+} - \hat{N}_{\text{ph}-})\end{aligned}$$

Since the frequencies of the two fields differ the oscillating terms do not trivially cancel as in the MZI. As a consequence we explicitly draw out the time dependence of the fields and include the initial phase-difference $\tilde{\phi}$. Thus the $\langle \hat{S}_x(0) \rangle = N_{\text{ph}}/2$, $\langle \hat{S}_y(0) \rangle = 0$ and, $\langle \hat{S}_z \rangle = 0$. Additionally, we define the photon numbers $\hat{N}_{\text{ph}-} = \hat{A}_-^\dagger \hat{A}_-$, $\hat{N}_{\text{ph}+} = \hat{A}_+^\dagger \hat{A}_+$, and $\hat{N}_{\text{ph}} = \hat{N}_{\text{ph}-} + \hat{N}_{\text{ph}+}$. The advantage of resorting to the Schwinger operators in this setup is not immediately clear and indeed will not add much understanding until we commence our study of the interaction with the atomic ensemble.

After their merger on the BS the two fields propagate a distance before impinging on the probe detector generating a signal

$$\begin{aligned}p &= (\hat{A}_+^\dagger + \hat{A}_-^\dagger)(\hat{A}_- + \hat{A}_+) \\ &= \hat{N}_{\text{ph}} + 2\hat{S}_x \\ &= \hat{N}_{\text{ph}} + 2\cos(\Omega t + \tilde{\phi})\hat{S}_x(0) - 2\sin(\Omega t + \tilde{\phi})\hat{S}_y(0).\end{aligned}$$

This signal is subsequently mixed with the RF source of the AOM at Ω so that the output becomes

$$\begin{aligned}p' &= p \sin \Omega t \\ &= \hat{N}_{\text{ph}} \sin \Omega t + \hat{S}_x(0) [\sin(2\Omega t + 2\tilde{\phi}) - \sin 2\tilde{\phi}] - \hat{S}_y(0) [\cos(2\Omega t + 2\tilde{\phi}) + \cos 2\tilde{\phi}]\end{aligned}$$

The low pass filter removes most terms except for the DC signal $-\hat{S}_x(0) \sin 2\tilde{\phi} - \hat{S}_y(0) \cos 2\tilde{\phi}$, which is passed on from the QND detector. The signal has the expectation value

$$\langle p' \rangle = -N_{\text{ph}} \sin 2\tilde{\phi} \quad (\text{A.10})$$

As for the MZI, the detector signal measures the phase-difference between the two fields. When wishing to measure a small phase-shift ϕ_δ it is now advantageous to set $\tilde{\phi} = 0 \pmod{\pi/2}$. The phase-displacement then is computed from the signal as

$$\phi_\delta = -\frac{1}{2} \arcsin \left(\frac{2p'}{N_{\text{ph}}} \right) \approx -\frac{p'}{N_{\text{ph}}} \quad (\text{A.11})$$

The phase-reference detection only differs from the probe detection by the absence of any atomic ensemble in the beam path before the detector, ensuring sensitivity only to $\tilde{\phi}$.

The quantum shot-noise in the detector signal is simply equal to the combined photon number of the two impinging frequency modes $\langle (\Delta p')^2 \rangle = N_{\text{ph}-} + N_{\text{ph}+} = N_{\text{ph}}$. From Eq. (A.11) one easily calculates the corresponding phase-noise $\langle (\Delta \phi)^2 \rangle$ at the optimal phase-difference and the SNR becomes

$$\text{SNR} = \frac{\langle (\Delta \phi)^2 \rangle}{\langle (\Delta \phi)^2 \rangle_{\text{SN}}} = N_{\text{ph}} \langle (\Delta \phi)^2 \rangle$$

which is the same value as for the loss-less symmetric MZI (eq. (2.19)) with one extra twist; since now the modes are spatially degenerate they both pass through

the sample. Imposing a limit to the photon number interacting with the sample leads to the condition $N_{\text{ph}} = N_{\text{ph}0}$, which differs from the MZI case by a factor of two. In consequence the applicable photon number, and so the SNR, is half of what it is for the MZI. This drawback will be outweighed by the fact that both fields also interact with the atomic sample (Sec. A.6.1).

A.6.1 QND and squeezing in sideband interferometer

Atomic operator variances, correlations, and decoherence

B.0.2 Quantum projection noise

We now have a look at the PN for two realisations of the atomic ensemble that are of relevance to the experiment. First we take the product state in which the single atom states are in superpositions of the two ground states $e^{i\phi} \sin(\theta/2)|3\rangle + \cos(\theta/2)|4\rangle$. To deduce the variance we must find $\langle (\Delta \hat{f}_i(\mathbf{r}) \hat{f}_i(\mathbf{r}')) \rangle = \langle \hat{f}_i(\mathbf{r}) \hat{f}_i(\mathbf{r}') \rangle - \langle \hat{f}_i(\mathbf{r}) \rangle \langle \hat{f}_i(\mathbf{r}') \rangle$. The former term may be expanded as

$$\begin{aligned}
 \langle \hat{f}_i(\mathbf{r}) \hat{f}_i(\mathbf{r}') \rangle &= \left\langle \left(\sum_k \hat{f}_i^{(k)} \delta(\mathbf{r} - \mathbf{r}_k) \right) \left(\sum_l \hat{f}_i^{(l)} \delta(\mathbf{r}' - \mathbf{r}_l) \right) \right\rangle \quad (\text{B.1}) \\
 &= \sum_k \left\langle \left(\hat{f}_i^{(k)} \right)^2 \right\rangle \delta(\mathbf{r} - \mathbf{r}_k) \delta(\mathbf{r}' - \mathbf{r}_k) + \sum_{l \neq k} \left\langle \hat{f}_i^{(k)} \hat{f}_i^{(l)} \right\rangle \delta(\mathbf{r} - \mathbf{r}_k) \delta(\mathbf{r}' - \mathbf{r}_l) \\
 &= \sum_k \left\langle \left(\hat{f}_i^{(k)} \right)^2 \right\rangle \delta(\mathbf{r} - \mathbf{r}_k) \delta(\mathbf{r} - \mathbf{r}') + \sum_{l \neq k} \left\langle \hat{f}_i^{(k)} \right\rangle \left\langle \hat{f}_i^{(l)} \right\rangle \delta(\mathbf{r} - \mathbf{r}_k) \delta(\mathbf{r}' - \mathbf{r}_l) .
 \end{aligned}$$

Where in the last equality only holds when the atoms are uncorrelated as is the case for the product state. In sec. 3.6 we will discuss the very interesting case of correlated atoms. Note that the summation over l is done over one atom fewer than that over k . It is very reasonable to assume that the particles locally have identical properties or in other words exchanging two atoms would not change the value of the local operators so long as these refer to internal degrees of freedom. In this case we can simplify the expression

$$\begin{aligned}
 \langle \hat{f}_i(\mathbf{r}) \hat{f}_i(\mathbf{r}') \rangle &= \sum_k \left\langle \left(\hat{f}_i^{(k)} \right)^2 \right\rangle \delta(\mathbf{r} - \mathbf{r}_k) \delta(\mathbf{r}' - \mathbf{r}_k) + \sum_{l \neq k} \left\langle \hat{f}_i^{(k)} \hat{f}_i^{(l)} \right\rangle \delta(\mathbf{r} - \mathbf{r}_k) \delta(\mathbf{r}' - \mathbf{r}_l) \\
 &= \left\langle \left(\hat{f}_i^{(1)} \right)^2 \right\rangle \sum_k \delta(\mathbf{r} - \mathbf{r}_k) \delta(\mathbf{r}' - \mathbf{r}_k) + \left\langle \hat{f}_i^{(1)} \hat{f}_i^{(2)} \right\rangle \sum_{l \neq k} \delta(\mathbf{r} - \mathbf{r}_k) \delta(\mathbf{r}' - \mathbf{r}_l) \\
 &= \left\langle \left(\hat{f}_i^{(1)} \right)^2 \right\rangle n_{\text{at}}(\mathbf{r}) \delta(\mathbf{r} - \mathbf{r}') + \left\langle \hat{f}_i^{(1)} \hat{f}_i^{(2)} \right\rangle n_{\text{at}}(\mathbf{r}) (n_{\text{at}}(\mathbf{r}') - 1) , \quad (\text{B.2})
 \end{aligned}$$

where for uncorrelated states we can write $\langle \hat{f}_i^{(1)} \hat{f}_i^{(2)} \rangle = \langle \hat{f}_i^{(1)} \rangle^2$. Hereby, we have an expression where we base the expectation values on the single atom values and then extend to the continuous picture. We can now calculate the exact values for the pseudo-spins. The expectation values $\langle \hat{f}_i^{(k)} \rangle$ easily follow from eq. (3.16) and for all three components we get $\langle \hat{f}_i^{(k)} \rangle^2 = \frac{1}{4} (\hat{\rho}_{33}^{(k)} + \hat{\rho}_{44}^{(k)})$ and so

$\langle (\hat{f}_i^{(k)})^2 \rangle = 1/4$. This finally allows us to extract the variances e.g. for \hat{f}_z we get

$$\begin{aligned} \langle (\Delta \hat{f}_z(\mathbf{r}) \hat{f}_z(\mathbf{r}')) \rangle &= \frac{n_{\text{at}}(\mathbf{r}')}{4} \delta(\mathbf{r} - \mathbf{r}') + \frac{n_{\text{at}}(\mathbf{r})(n_{\text{at}}(\mathbf{r}') - 1)}{4} \cos^2 \theta - \frac{n_{\text{at}}(\mathbf{r})n_{\text{at}}(\mathbf{r}')}{4} \cos^2 \theta \\ &= \frac{n_{\text{at}}(\mathbf{r}')}{4} \sin^2 \theta \delta(\mathbf{r} - \mathbf{r}') . \end{aligned} \quad (\text{B.3})$$

Similarly we get for the other components

$$\begin{aligned} \langle (\Delta \hat{f}_x(\mathbf{r}) \hat{f}_x(\mathbf{r}')) \rangle &= \frac{n_{\text{at}}}{4} (1 - \sin^2 \theta \cos^2 \phi) \delta(\mathbf{r} - \mathbf{r}') \\ \langle (\Delta \hat{f}_y(\mathbf{r}) \hat{f}_y(\mathbf{r}')) \rangle &= \frac{n_{\text{at}}}{4} (1 - \sin^2 \theta \sin^2 \phi) \delta(\mathbf{r} - \mathbf{r}') . \end{aligned} \quad (\text{B.4})$$

We can now compare these product state uncertainties to the limit set by the uncertainty relation. We pick the uncertainty product for \hat{f}_x and \hat{f}_y . For these components the uncertainty relation forecasts

$$\langle (\Delta \hat{f}_x)^2 \rangle \langle (\Delta \hat{f}_y)^2 \rangle = \frac{n_{\text{at}}^2}{16} (1 - \sin^2 \theta \cos^2 \phi) \sin^2 \theta \geq \frac{n_{\text{at}}^2}{16} \sin^2 \theta ,$$

So, the product state of any superposition is not always a minimal uncertainty state for a particular combination of vector components [Wódkiewicz85a]. The difference between the actual and minimal uncertainty product is shown on fig. B.1. We see that the product state is, nevertheless, a minimal uncertainty

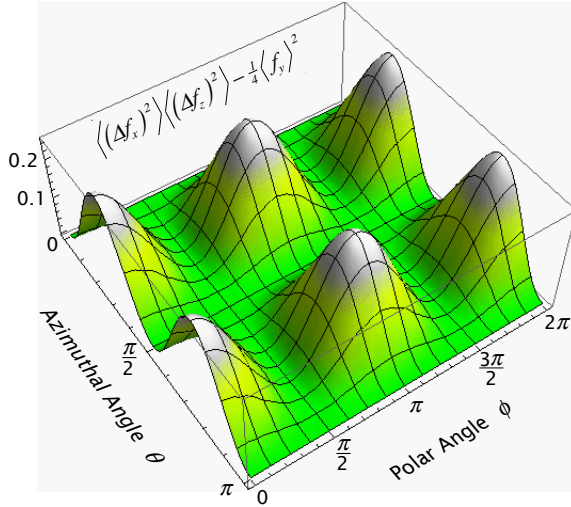


Figure B.1: Actual uncertainty minus the minimum uncertainty.

state when the pseudo-spin is aligned towards the poles or on the equator ($\theta = 0, \pi/2, \pi$) or when it is aligned in the yz -plane ($\phi = \pi/2, 3\pi/2$) of the Bloch sphere.

B.0.3 Squeezing affected by generic loss and decoherence

Decoherence is important for squeezing in a number of ways which we will discuss here. Firstly when an atom decoheres its correlation with all other atoms is erased; one can say that the atom is reset. Since squeezing is a result of interatomic correlations this means that overall the degree of squeezing of the ensemble is reduced. Secondly, the decoherence process is statistical and thus the randomness of the outcome of the decoherence process can add extra noise to the ensemble state. Finally, the decoherence affects the magnitude of the mean spin vector. This is because decohered atoms typically end up in a mixed state which has no mean spin amplitude. The first two effects that affect the noise of

the ensemble state will be treated together, whereas the last effect regarding the pseudo-spin magnitude can be treated independently.

Decoherence is modelled as an effect which takes a fraction η of the atoms into another state than the original one. Thus an initial density matrix $\hat{\rho}$ transforms into $(1 - \eta)\hat{\rho} + \eta\hat{\rho}'$, where the latter term is the density matrix for the decohered atom. We begin with the effect of decoherence on the mean spin $\langle \hat{f} \rangle$. We have the rather obvious equation

$$\begin{aligned} \langle \hat{f}_i^*(\mathbf{r}) \rangle &= \sum_k (1 - \eta) \langle \hat{f}_i^{(k)} \rangle \delta(\mathbf{r} - \mathbf{r}_k) + \sum_k \eta \langle \hat{f}_i^{(k)'} \rangle \delta(\mathbf{r} - \mathbf{r}_k) \\ &= (1 - \eta) \langle \hat{f}_i^{(1)} \rangle n_{\text{at}}(\mathbf{r}) + \eta \langle \hat{f}_i^{(1)'} \rangle n_{\text{at}}(\mathbf{r}) \\ &= (1 - \eta) \langle \hat{f}_i(\mathbf{r}) \rangle + \eta \langle \hat{f}_i'(\mathbf{r}) \rangle, \end{aligned} \quad (\text{B.5})$$

where $\hat{f}_i(\mathbf{r})$ refers to the unaffected atoms and $\hat{f}_i'(\mathbf{r})$ refers to the decohered atoms. The middle line is not required for reaching the last line, however, the form will be helpful below. In many cases the decohered atoms will have $\langle \hat{f}_i'(\mathbf{r}) \rangle = 0$.

Now we turn to the variance of the pseudo-spin components when some of the atoms decohere. Our treatment follows the approaches of [Mølmer03, Echaniz05, Saffman08] which is consistent with the results from [Madsen04]. First we recap eq. (B.2)

$$\langle \hat{f}_i(\mathbf{r}) \hat{f}_i(\mathbf{r}') \rangle = \left\langle \left(\hat{f}_i^{(1)} \right)^2 \right\rangle n_{\text{at}}(\mathbf{r}) \delta(\mathbf{r} - \mathbf{r}') + \left\langle \hat{f}_i^{(1)} \hat{f}_i^{(2)} \right\rangle n_{\text{at}}(\mathbf{r}) (n_{\text{at}}(\mathbf{r}') - 1).$$

The term $\langle \hat{f}_i^{(1)} \hat{f}_i^{(2)} \rangle$ contains the information on the inter-atomic correlations. For an uncorrelated state it can be re-written as $\langle \hat{f}_i^{(1)} \rangle^2$ and thus the value of the cross-term is exclusively determined by the mean value of the spin-component. For a squeezed state the cross-term may be non-zero even if the mean spins is zero, therein lies the inter-atomic correlations. We can isolate the correlation term and for $n_{\text{at}} \gg 1$ we get

$$\left\langle \hat{f}_i^{(1)} \hat{f}_i^{(2)} \right\rangle = \frac{\langle \hat{f}_i(\mathbf{r}) \hat{f}_i(\mathbf{r}') \rangle - \left\langle \left(\hat{f}_i^{(1)} \right)^2 \right\rangle n_{\text{at}}(\mathbf{r}) \delta(\mathbf{r} - \mathbf{r}')}{n_{\text{at}}(\mathbf{r}) n_{\text{at}}(\mathbf{r}')}. \quad (\text{B.6})$$

For a product state of equal superpositions $\langle \hat{f}_i(\mathbf{r}) \hat{f}_i(\mathbf{r}') \rangle = n_{\text{at}} \delta(\mathbf{r} - \mathbf{r}') / 4$ and for a spin $\frac{1}{2}$ system $\langle (\hat{f}_i^{(1)})^2 \rangle = 1/4$, so the numerator in eq. (B.6) is zero and thus there are no correlations as predicted. If on the other hand the collective spin has been squeezed the variance is reduced by ζ and the correlation term becomes

$$\left\langle \hat{f}_i^{(1)} \hat{f}_i^{(2)} \right\rangle_{\zeta} = \frac{\zeta \langle \hat{f}_i(\mathbf{r}) \hat{f}_i(\mathbf{r}') \rangle - \left\langle \left(\hat{f}_i^{(1)} \right)^2 \right\rangle n_{\text{at}}(\mathbf{r}) \delta(\mathbf{r} - \mathbf{r}')}{n_{\text{at}}(\mathbf{r}) n_{\text{at}}(\mathbf{r}')} < 0. \quad (\text{B.7})$$

If then a fraction η decoheres to another state we can rework eq. (B.2) in to

$$\begin{aligned} \langle \hat{f}_i^*(\mathbf{r}) \hat{f}_i^*(\mathbf{r}') \rangle &= (1 - \eta) \left\langle \left(\hat{f}_i^{(1)} \right)^2 \right\rangle n_{\text{at}}(\mathbf{r}) \delta(\mathbf{r} - \mathbf{r}') + \eta \left\langle \left(\hat{f}_i^{(1)'} \right)^2 \right\rangle n_{\text{at}}(\mathbf{r}) \delta(\mathbf{r} - \mathbf{r}') \\ &\quad + (1 - \eta)^2 \left\langle \hat{f}_i^{(1)} \hat{f}_i^{(2)} \right\rangle n_{\text{at}}(\mathbf{r}) n_{\text{at}}(\mathbf{r}') + \eta^2 \left\langle \hat{f}_i^{(1)'} \hat{f}_i^{(2)'} \right\rangle n_{\text{at}}(\mathbf{r}) n_{\text{at}}(\mathbf{r}') \\ &\quad + 2\eta(1 - \eta) \left\langle \hat{f}_i^{(1)} \hat{f}_i^{(2)'} \right\rangle n_{\text{at}}(\mathbf{r}) n_{\text{at}}(\mathbf{r}'), \end{aligned}$$

Here we have again used symmetry under particle exchange in the relation $\langle \hat{f}_i^{(1)} \hat{f}_i^{(2)'} \rangle = \langle \hat{f}_i^{(1)'} \hat{f}_i^{(2)} \rangle$. still taking $n_{\text{at}} \gg 1$. Inserting eq. (B.6) this can be

further rewritten

$$\begin{aligned} \langle \hat{f}_i^*(\mathbf{r}) \hat{f}_i^*(\mathbf{r}') \rangle &= (1 - \eta)^2 \langle \hat{f}_i(\mathbf{r}) \hat{f}_i(\mathbf{r}') \rangle \\ &+ \left[\eta(1 - \eta) \langle (\hat{f}_i^{(1)})^2 \rangle + \eta \langle (\hat{f}_i^{(1)'})^2 \rangle \right] n_{\text{at}}(\mathbf{r}) \delta(\mathbf{r} - \mathbf{r}') \\ &+ \left[\eta^2 \langle \hat{f}_i^{(1)' \dagger} \hat{f}_i^{(2)'} \rangle + 2\eta(1 - \eta) \langle \hat{f}_i^{(1)} \hat{f}_i^{(2)'} \rangle \right] n_{\text{at}}(\mathbf{r}) n_{\text{at}}(\mathbf{r}') , \end{aligned} \quad (\text{B.8})$$

Hereby, we can calculate the post decoherence variance of the continuous pseudo-spin

$$\begin{aligned} \langle (\Delta \hat{f}_i^*(\mathbf{r}) \hat{f}_i^*(\mathbf{r}')) \rangle &= \langle \hat{f}_i^*(\mathbf{r}) \hat{f}_i^*(\mathbf{r}') \rangle - \langle \hat{f}_i^*(\mathbf{r}) \rangle^2 \\ &= (1 - \eta)^2 \langle (\Delta \hat{f}_i(\mathbf{r}) \hat{f}_i(\mathbf{r}')) \rangle \\ &+ \left[\eta(1 - \eta) \langle (\hat{f}_i^{(1)})^2 \rangle + \eta \langle (\hat{f}_i^{(1)'})^2 \rangle \right] n_{\text{at}}(\mathbf{r}) \delta(\mathbf{r} - \mathbf{r}') \\ &+ \left[\eta^2 \left(\langle \hat{f}_i^{(1)' \dagger} \hat{f}_i^{(2)'} \rangle - \langle \hat{f}_i^{(1)'} \rangle^2 \right) \right. \\ &\quad \left. + 2\eta(1 - \eta) \left(\langle \hat{f}_i^{(1)} \hat{f}_i^{(2)'} \rangle - \langle \hat{f}_i^{(1)} \rangle \langle \hat{f}_i^{(1)'} \rangle \right) \right] n_{\text{at}}(\mathbf{r}) n_{\text{at}}(\mathbf{r}') , \end{aligned} \quad (\text{B.9})$$

Up till this point, we have made no assumptions and the above expression is completely general in that it is valid for any initial and final expectation values of \hat{f}_i and \hat{f}_i^2 . We note a few reductions that will be applied at various stages below. First, as mentioned earlier, the values of $\langle (\hat{f}_i^{(1)})^2 \rangle$ and $\langle (\hat{f}_i^{(1)'})^2 \rangle$ are both equal to $1/4$ in as long as the probing is only sensitive to two atomic levels i.e. we have a spin $\frac{1}{2}$ system. Secondly, if the decohered atoms are uncorrelated $\langle \hat{f}_i^{(1)' \dagger} \hat{f}_i^{(2)'} \rangle = \langle \hat{f}_i^{(1)'} \rangle^2$ and $\langle \hat{f}_i^{(1)} \hat{f}_i^{(2)'} \rangle = \langle \hat{f}_i^{(1)} \rangle \langle \hat{f}_i^{(1)'} \rangle$ the last terms proportional to $n_{\text{at}}(\mathbf{r})^2$ in eq. (B.9) cancel. Under these, quite lenient, assumptions eq. (B.9) becomes

$$\langle (\Delta \hat{f}_i^*(\mathbf{r}) \hat{f}_i^*(\mathbf{r}')) \rangle = (1 - \eta)^2 \langle (\Delta \hat{f}_i(\mathbf{r}) \hat{f}_i(\mathbf{r}')) \rangle + \eta(2 - \eta) \frac{1}{4} n_{\text{at}}(\mathbf{r}) \delta(\mathbf{r} - \mathbf{r}') \quad (\text{B.10})$$

If the input state is a coherent state with variance $\langle (\Delta \hat{f}_i(\mathbf{r}) \hat{f}_i(\mathbf{r}')) \rangle = \frac{n_{\text{at}}}{4} \delta(\mathbf{r} - \mathbf{r}')$ the output variance will be

$$\langle (\Delta \hat{f}_i^*(\mathbf{r}) \hat{f}_i^*(\mathbf{r}')) \rangle = \frac{n_{\text{at}}(\mathbf{r})}{4} \delta(\mathbf{r} - \mathbf{r}') . \quad (\text{B.11})$$

It is certainly worth noting that the decay of a coherent state does not add any additional noise to the system. The magnitude of the pseudo-spin will of course be reduced according to eq. (B.5) so that the resulting state provides a poorer angular resolution in spectroscopic applications (see eq. (3.32)). We now take a few examples of types of decay to aid the understanding of the equations.

Decay out of the system By this we mean that the atoms are lost out of the two level system either because the atoms leave the ensemble or because the decay goes to states that do not interact with the probe. In either case the decayed atoms are uncorrelated and $\langle \hat{f}_i' \rangle = \langle (\hat{f}_i')^2 \rangle = 0$. We get the simple result

$$\langle (\Delta \hat{f}_i^*(\mathbf{r}) \hat{f}_i^*(\mathbf{r}')) \rangle = (1 - \eta_l)^2 \langle (\Delta \hat{f}_i(\mathbf{r}) \hat{f}_i(\mathbf{r}')) \rangle + \frac{\eta_l(1 - \eta_l)}{4} n_{\text{at}}(\mathbf{r}) \delta(\mathbf{r} - \mathbf{r}') ,$$

where the subscript l on η_l testifies that we are specifically considering the loss process. Let $\hat{f}_i = f_{\perp}$ be the direction perpendicular to the mean spin that

has the smallest variance and $\langle \hat{f} \rangle = \langle \hat{f}_j \rangle$ i.e. the vector be aligned along the j -direction. The input state may be squeezed by ζ whereby the modified squeezing parameter following the decoherence is

$$\zeta'_1 = \frac{n_{\text{at}}(\mathbf{r}) \langle (\Delta \hat{f}_i^*(\mathbf{r}) \hat{f}_i^*(\mathbf{r}')) \rangle}{\langle \hat{f}_j^* \rangle^2} = \zeta + \frac{\eta_1}{(1 - \eta_1)} \quad (\text{B.12})$$

Decay to uncorrelated symmetric state As the decayed atoms are uncorrelated all correlation terms containing decay states are zero and since the state is symmetric w.r.t \hat{f}_i we have $\langle \hat{f}'_i \rangle = 0$. This process, though not necessarily symmetric, is really what one refers to by the term decoherence, hence we label the fraction of atoms subjected to this process η_{dc} . Thus the variance after decoherence becomes

$$\langle (\Delta \hat{f}_i^*(\mathbf{r}) \hat{f}_i^*(\mathbf{r}')) \rangle = (1 - \eta_{\text{dc}})^2 \langle (\Delta \hat{f}_i(\mathbf{r}) \hat{f}_i(\mathbf{r}')) \rangle + \frac{\eta_{\text{dc}}(1 - \eta_{\text{dc}}) + \eta_{\text{dc}}}{4} n_{\text{at}}(\mathbf{r}) \delta(\mathbf{r} - \mathbf{r}'),$$

from which we deduce the surviving degree of squeezing of the input to be

$$\zeta'_{\text{dc}} = \frac{n_{\text{at}}(\mathbf{r}) \langle (\Delta \hat{f}_i^*(\mathbf{r}) \hat{f}_i^*(\mathbf{r}')) \rangle}{\langle \hat{f}_j^* \rangle^2} = \zeta + \frac{\eta_{\text{dc}}}{(1 - \eta_{\text{dc}})} + \frac{\eta_{\text{dc}}}{(1 - \eta_{\text{dc}})^2} \quad (\text{B.13})$$

We observe that $\zeta'_{\text{dc}} > \zeta'_1$, which leads to the conclusion that decoherence is a more damaging effect than pure loss of atoms. This is perhaps not surprising because atoms lost out of the system no longer add any noise to the pseudo-spin, whereas decohered atoms sustainably affect the noise of the total combined pseudo-spin.

B.0.4 Decoherence due to probing

Due to selection rules for photon light absorption and spontaneous decay we can usually predict the excitation and decay channels. Combining this with the resulting expectation values of the pseudo-spin moments we can compute eq. (3.35). For the moment we use a heuristic picture sketched on fig. 4.5

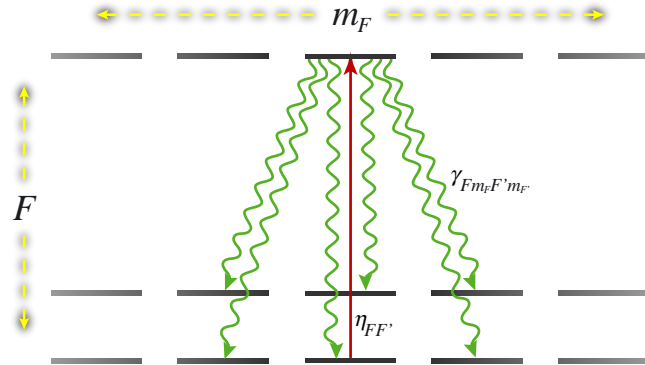


Figure B.2: Excitation and decay channels (see fig. 3.3)

find the branching ratios of the various decay channels. Each ground level labelled by F and m_F can be excited to a range of excited hyperfine-manifolds F' . The excitation will only go to a specific magnetic sublevel m'_F of each excited hyperfine level determined by the polarisation of the probe light. The fraction of atoms excited through this channel is labelled $\eta_{F,F'}$. From the excited states there is a number of channels through which the atom is allowed decay. The decay

rates are labelled by $\gamma_{F'm'_E, F''m_{E''}}$ and from each excited level we can determine the branching ratios of the allowed channels as

$$r_{F'm'_E, F''m_{E''}} = \gamma_{F'm'_E, F''m_{E''}} / \sum_{F^*, m_{F^*}} \gamma_{F'm'_E, F^*m_{F^*}} \quad (\text{B.14})$$

Hence the transition rate from an initial state $|F, m_F\rangle$ to a final state $|F'', m_{F''}\rangle$ is given by $\eta_{FF'} r_{F'm'_E, F''m_{E''}}$. If there are more than one excitation channel by which the atom can reach the same final state the correct transition rates must be calculated by the Kramers-Heisenberg formula, which includes a sum over the coupling to all intermediate levels $|F', m_{F'}\rangle$. Fortunately, for the experimentally relevant parameters the Kramers-Heisenberg formula yields nearly the same results as what is achieved by summing the transition rates $\eta_{FF'} r_{F'm'_E, F''m_{E''}}$ that share the same excited state $|F', m_{F'}\rangle$.

By summing over the two ground levels, the allowed excited manifolds and the possible magnetic sublevels in both groundlevels we calculate the effect of the decay on the pseudo-spin components. The mean spin component transforms as

$$\langle \hat{f}_i^*(\mathbf{r}) \rangle = (1 - \eta) \langle \hat{f}_i(\mathbf{r}) \rangle + \sum_{F, F'} \eta_{FF'} \sum_{m'_E, m_{E''}} r_{F'm'_E, F''m_{E''}} \langle \hat{f}_i^{(1)''} \rangle n_{\text{at}}(\mathbf{r}), \quad (\text{B.15})$$

where the value of $\langle \hat{f}_i^{(1)''} \rangle$ is fully determined by F'' and $m_{F''}$. For the second moment the expression based on eq. (B.8) is somewhat more cumbersome

$$\begin{aligned} \langle \hat{f}_i^*(\mathbf{r}) \hat{f}_i^*(\mathbf{r}') \rangle &= (1 - \eta)^2 \langle \hat{f}_i(\mathbf{r}) \hat{f}_i(\mathbf{r}') \rangle + \eta(1 - \eta) \left\langle \left(\hat{f}_i^{(1)} \right)^2 \right\rangle n_{\text{at}}(\mathbf{r}) \delta(\mathbf{r} - \mathbf{r}') \\ &+ \sum_{F, F'} \eta_{FF'} \sum_{m'_E, m_{E''}} r_{F'm'_E, F''m_{E''}} \left\langle \left(\hat{f}_i^{(1)''} \right)^2 \right\rangle n_{\text{at}}(\mathbf{r}) \delta(\mathbf{r} - \mathbf{r}') \quad (\text{B.16}) \\ &+ \sum_{E, F'} \sum_{F, F'} \eta_{FF'} \eta_{FF'} \sum_{m_{F'}, m_{F''}} \sum_{m_{F'}, m_{F''}} r_{F'm_{F'}, F''m_{F''}} r_{F'm_{F'}, F''m_{F''}} \left\langle \hat{f}_i^{(1)''} \hat{f}_i^{(2)''} \right\rangle n_{\text{at}}(\mathbf{r}) n_{\text{at}}(\mathbf{r}') \\ &+ (1 - \eta) \sum_{F, F'} \eta_{FF'} \sum_{m_{F'}, m_{F''}} r_{F'm_{F'}, F''m_{F''}} \left\langle \hat{f}_i^{(1)} \hat{f}_i^{(2)''} \right\rangle 2n_{\text{at}}(\mathbf{r}) n_{\text{at}}(\mathbf{r}'), \end{aligned}$$

In most circumstances we may focus on a limited number of excitation and decay channels since many $\eta_{FF'}$ and $r_{F'm_{F'}, F''m_{F''}}$ are zero or negligible.

Instead of including all the channels it may be possible to calculate the decay in terms of elastic (Rayleigh) and inelastic (Ramsey) scattering rates. Then the summation above can be reduced to a sum over the hyperfine changing scattering events and the hyperfine conserving events. In the latter case one has to argue that the final \hat{f}_z is the same as the initial because no information is gained about the \hat{f}_z of the individual atoms. For the inelastic events the appropriate terms must be calculated.

Full ensemble squeezing – influence of geometry

How can one say that the squeezing has a spatial distribution? After all we determine an atomic ensemble value of the operator \hat{F}_z based on the measurement of \hat{S}_x , which yields a single value. The reason is that the measured \hat{S}_x does not contain the same information about all sections of the atomic ensemble. Specifically the areas where the probe intensity is higher contribute more to the detected signal. Likewise the denser the atomic sample the more information is disclosed about the local operator. In sec. 5.4 we made a 1-D approximation and got the uniform coupling constant κ_{uni}^2 and squeezing factor ε_{uni} .

We now turn to the more rigorous approach where we the local squeezing is weighed by the local atomic density and probing intensity. Firstly, the noise reduction depends on the local densities such that

$$\varepsilon(\mathbf{r}) = \frac{1}{1 + \frac{\kappa^2}{c^2} \mathcal{N}(\mathbf{r}) U(\mathbf{r}) l_a \hat{n}_{\text{ph}} l_p} \quad (\text{C.1})$$

On fig. C.1 we plot the noise reduction either as the uniform ε_{uni} or the spatially

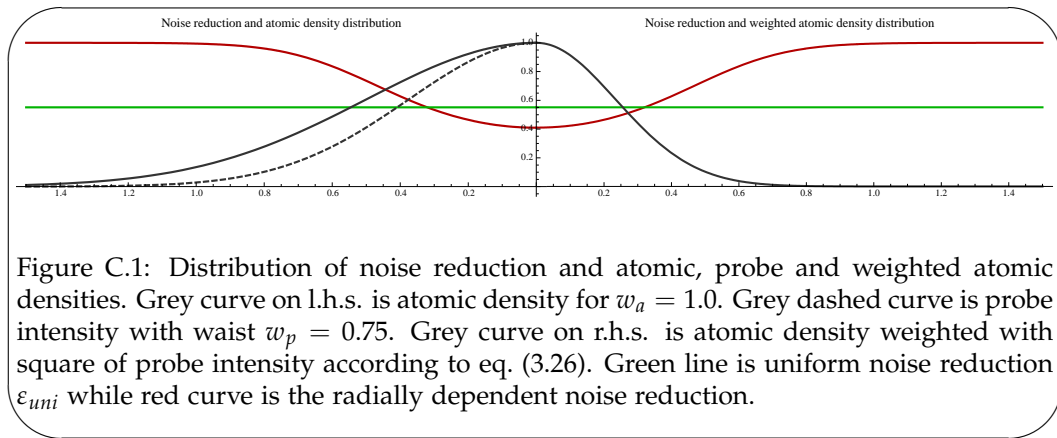


Figure C.1: Distribution of noise reduction and atomic, probe and weighted atomic densities. Grey curve on l.h.s. is atomic density for $w_a = 1.0$. Grey dashed curve is probe intensity with waist $w_p = 0.75$. Grey curve on r.h.s. is atomic density weighted with square of probe intensity according to eq. (3.26). Green line is uniform noise reduction ε_{uni} while red curve is the radially dependent noise reduction.

dependent $\varepsilon(\mathbf{r})$ and compare them to the pure or the weighted atomic density distributions. Obviously, $\varepsilon(0) > \varepsilon_{\text{uni}}$ since this is where the probe and atomic densities are the largest thus maximising the coupling strength. As this means that $\varepsilon(\mathbf{r})$ tends to be larger where the atomic density is largest we would expect that when integrating over the total (or effective) ensemble the estimate given by this method would be larger than that given by applying ε_{uni} . The reduced noise

of the effective ensemble \hat{F}_z is found as

$$\begin{aligned}
\langle (\Delta \hat{F}_z^{(out)})^2 \rangle &= \int_{R^3} \int_{R^3} \langle (\Delta \hat{f}_z^{(out)}(\mathbf{r}) \hat{f}_z^{(out)}(\mathbf{r}')) \rangle \mathcal{U}(\mathbf{r}) \mathcal{U}(\mathbf{r}') d^3 r d^3 r' \\
&= \int_{R^3} \int_{R^3} \frac{1}{1 + \kappa^2(\mathbf{r})} \langle (\Delta \hat{f}_z^{(in)}(\mathbf{r}) \hat{f}_z^{(in)}(\mathbf{r}')) \rangle \mathcal{U}(\mathbf{r}) \mathcal{U}(\mathbf{r}') d^3 r d^3 r' \\
&= \int_{R^3} \frac{1}{1 + \kappa^2(\mathbf{r})} \langle (\Delta \hat{f}_z^{(in)}(\mathbf{r}))^2 \rangle \mathcal{U}(\mathbf{r})^2 d^3 r \\
&= \frac{1}{4} \int_{R^2} \frac{1}{1 + \frac{\kappa^2}{c^2} \mathcal{N}(\mathbf{r}) \mathcal{U}(\mathbf{r}) l_a \hat{n}_{ph} l_p} \mathcal{N}(\mathbf{r}) \mathcal{U}(\mathbf{r})^2 l_a d^2 r \quad (C.2)
\end{aligned}$$

We attempt to illustrate this formula in fig. C.2 by plotting the argument of the integral and compare it to the projection noise of the uncorrelated ensemble. Strictly speaking this is done on fig. C.2b,d while on fig. C.2a,c we plot the total ensemble variant that is the argument of eq. (C.2) excluding the factor $\mathcal{U}(\mathbf{r})^2$. For

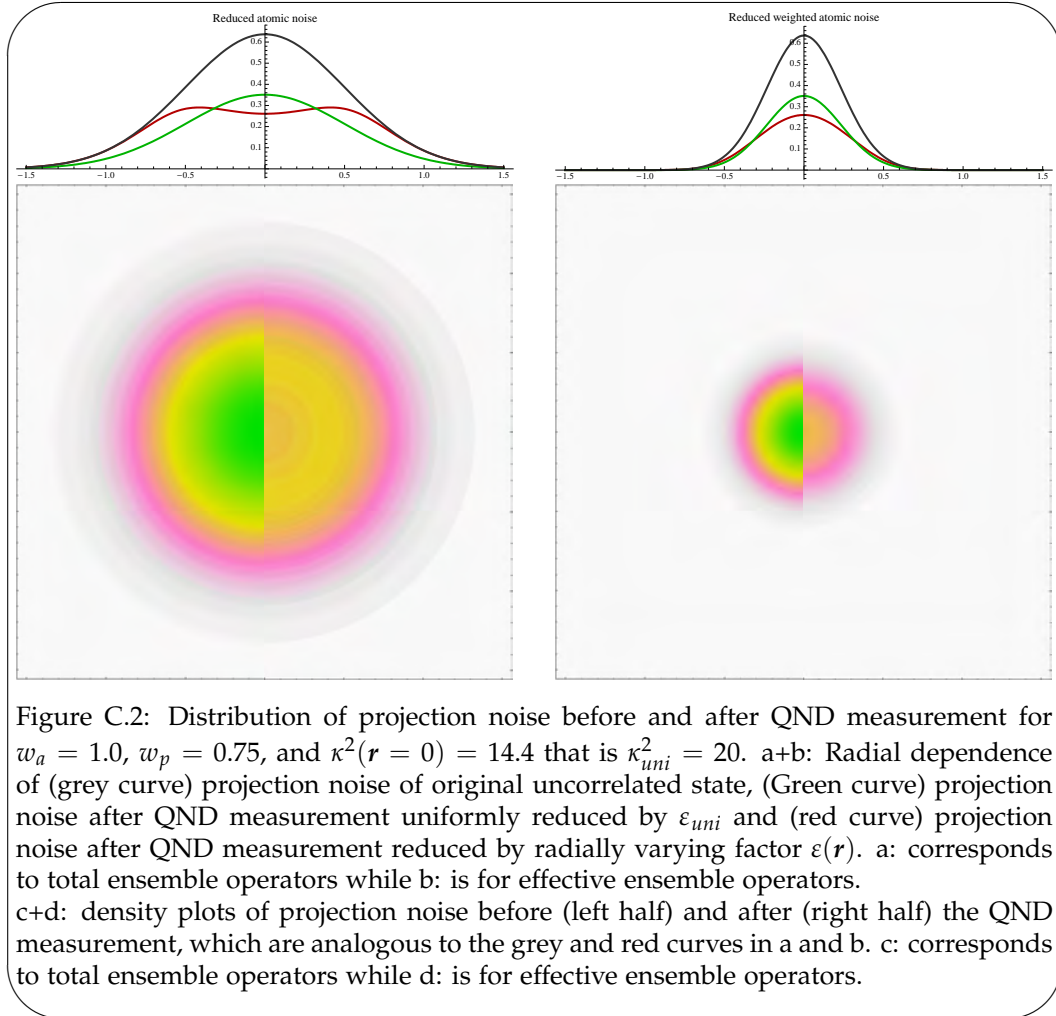


Figure C.2: Distribution of projection noise before and after QND measurement for $w_a = 1.0$, $w_p = 0.75$, and $\kappa^2(\mathbf{r} = 0) = 14.4$ that is $\kappa_{uni}^2 = 20$. a+b: Radial dependence of (grey curve) projection noise of original uncorrelated state, (Green curve) projection noise after QND measurement uniformly reduced by ε_{uni} and (red curve) projection noise after QND measurement reduced by radially varying factor $\varepsilon(\mathbf{r})$. a: corresponds to total ensemble operators while b: is for effective ensemble operators. c+d: density plots of projection noise before (left half) and after (right half) the QND measurement, which are analogous to the grey and red curves in a and b. c: corresponds to total ensemble operators while d: is for effective ensemble operators.

the illustration we chose a atomic sample to probe beam waist ratio of $r_w = 4/3$ so that the probing region is slightly smaller than the size of the sample. By this we wish to highlight the difference between the effective and total ensemble operators. Comparing fig. C.2a and b we see that the noise reduction is more pronounced when when utilising the effective ensemble operators. The total ensemble operators also count atoms that are not probed and thus never detected let alone noise-reduced.

Like the coupling strength the spontaneous scattering has a radial dependence according to the probe mode function. Using Wineland's criterion eq. (3.33) we

know that the SQL with which to compare the noise of the post-QND measurement ensemble is $(1 - \eta(\mathbf{r}))^2 \langle (\Delta \hat{F}_z^{(in)})^2 \rangle$, where $\eta(\mathbf{r}) \propto n_{\text{ph}} U(\mathbf{r})$. This may be compared to the uniform spontaneous scattering probability η_{uni} given above. On fig. C.3 we plot the reduced SQL as dashed lines. The remaining curves just reproduce the noise reduction fig. C.2. From both the effective and total ensemble

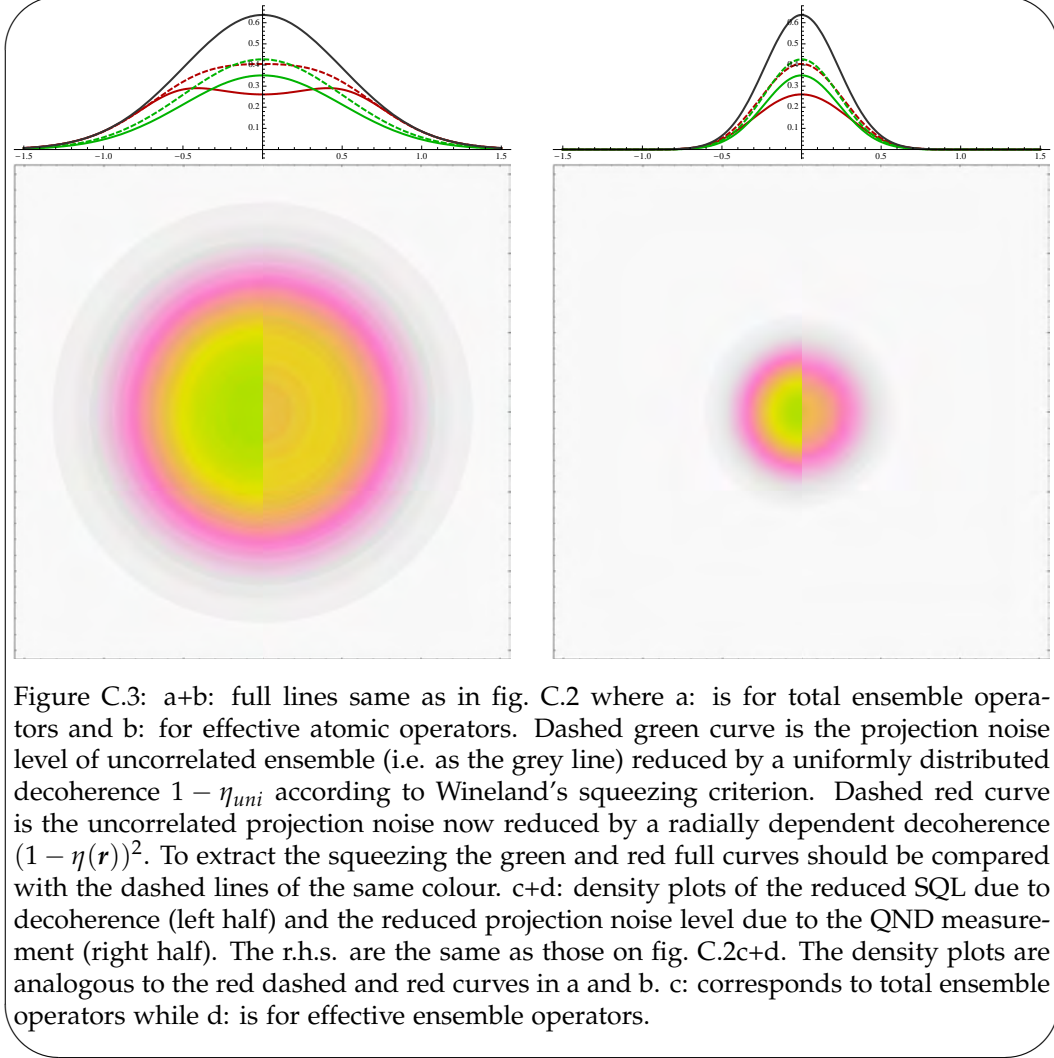


Figure C.3: a+b: full lines same as in fig. C.2 where a: is for total ensemble operators and b: for effective atomic operators. Dashed green curve is the projection noise level of uncorrelated ensemble (i.e. as the grey line) reduced by a uniformly distributed decoherence $1 - \eta_{\text{uni}}$ according to Wineland's squeezing criterion. Dashed red curve is the uncorrelated projection noise now reduced by a radially dependent decoherence $(1 - \eta(\mathbf{r}))^2$. To extract the squeezing the green and red full curves should be compared with the dashed lines of the same colour. c+d: density plots of the reduced SQL due to decoherence (left half) and the reduced projection noise level due to the QND measurement (right half). The r.h.s. are the same as those on fig. C.2c+d. The density plots are analogous to the red dashed and red curves in a and b. c: corresponds to total ensemble operators while d: is for effective ensemble operators.

picture it is clear that the spatially dependent treatment (red curves) predicts a larger squeezing (ratio of dashed to full lines) than the uniform treatment (green curves). By the same token, the effective ensemble operators, by accounting only for the atoms actually probed, foretell a larger squeezing. The combined effects of noise reduction and decoherence are synthesized in the squeezing factor which we define as

$$\mathcal{E} = \frac{\int_{R^2} \frac{1}{1 + \frac{1}{2} \mathcal{K}^2 \mathcal{N}(\mathbf{r}) U(\mathbf{r}) l_a \hat{n}_{\text{ph}} l_p} \mathcal{N}(\mathbf{r}) U(\mathbf{r})^2 l_a d^2 r}{\int_{R^2} e^{-2\eta_0 U(\mathbf{r}) \hat{n}_{\text{ph}} l_p} \mathcal{N}(\mathbf{r}) U(\mathbf{r})^2 l_a d^2 r}, \quad (\text{C.3})$$

or in terms of the total ensemble operators.

$$\mathcal{E}_{\text{tot}} = \frac{\int_{R^2} \frac{1}{1 + \frac{1}{2} \mathcal{K}^2 \mathcal{N}(\mathbf{r}) U(\mathbf{r}) l_a \hat{n}_{\text{ph}} l_p} \mathcal{N}(\mathbf{r}) l_a d^2 r}{\int_{R^2} e^{-2\eta_0 U(\mathbf{r}) \hat{n}_{\text{ph}} l_p} \mathcal{N}(\mathbf{r}) l_a d^2 r}, \quad (\text{C.4})$$

At this point we have defined all the quantities that we need to characterise the squeezing and it is time to perform the integrals and discuss the observed noise behaviour. We chose not to print analytical expressions for the solved integrals,

not the least because several of them have no simple solution. The plots are mostly based on numerical integration. We chose to investigate the noise for different ratios of the waists of the atomic sample and the probe beam. From this we can draw some conclusions about the optimal combination of sample and probe sizes. In accordance with the above expressions, the total number of atoms and photons is kept constant, whereby the peak atomic density and probe intensity will vary with the respective waists sizes. Naturally, in the limit of very small waist sizes the predictions become unrealistic and unphysical.

We first treat the effective ensemble noise and squeezing for different w_a and w_p , with all curves normalised to $N_{\text{at}}/4$. On fig. C.4a we plot the projection noise of the uncorrelated (input) state $\langle(\Delta\hat{F}_z^{(in)})^2\rangle$ c.f. eq. (3.26). For $r_w \gg 1$ only a small fraction of the atoms are probed and thus the projection noise in the detected meter is small. Fig. C.4b shows the projection noise of the input state reduced by the decoherence $\langle(\Delta\hat{F}_z^{(out)})^2\rangle_{SQL}$. According to eq. (3.33) this defines the SQL to which the noise reduced state should be compared in order to uncover if it is also a squeezed state. For w_a large there is little decoherence and $\langle(\Delta\hat{F}_z^{(out)})^2\rangle_{SQL}$ is close to $\langle(\Delta\hat{F}_z^{(in)})^2\rangle$. For $w_p \ll w_a$ the sample is probed by only a small fraction of the photons and thus the decoherence is also small, though this is hard to discern since the effective number of atoms probed is already small. Only when both waist sizes become sufficiently small, and thus the photon density and overlap becomes large, does the decoherence play a role. The projection noise reduced by the QND measurement $\langle(\Delta\hat{F}_z^{(out)})^2\rangle_{QND}$ as given by eq. (C.2) is shown on fig. C.4c. The output state noise is small when either of the waists are small, but it is only for small w_a that this noise is actually lower than the input noise. This is reflected in fig. C.4d where we plot the difference between the projection noise of the output state and the output SQL i.e. $\langle(\Delta\hat{F}_z^{(out)})^2\rangle_{QND} - \langle(\Delta\hat{F}_z^{(out)})^2\rangle_{SQL}$. It is clearly seen that the noise reduction is significant for small w_a i.e. for large atomic densities. Perhaps it is a bit surprising that, in the limit of infinitely dense atomic sample the noise reduction is always complete irrespective of the probe beam size. This is, however, a consequence of the noise reduction eq. (C.1) being proportional to the atomic density. From the above we are in a position to deduce the squeezing measures. We start out on fig. C.4e with the simple squeezing parameter $\zeta_{\text{simp}} = \langle(\Delta\hat{F}_z^{(out)})^2\rangle_{QND} / \langle(\Delta\hat{F}_z^{(in)})^2\rangle$ c.f. eq. (3.30). This criterion basically gauges the noise reduction normalised to the input projection noise level. The plot reveals that the simple squeezing is large for either w_a or w_p small. Again this is rooted in the coupling strength's proportionality with both the atomic density and the probe intensity together with the fact that we discount the atoms outside of the probe volume. Finally, we gauge the squeezing according to Wineland's criterion $\zeta_{\text{wineland}} = \langle(\Delta\hat{F}_z^{(out)})^2\rangle_{QND} / \langle(\Delta\hat{F}_z^{(out)})^2\rangle_{SQL}$ c.f. eq. (3.33). The plot on fig. C.4f goes to infinity in the limit of small probe waist size where the output state is completely decohered. The maximal squeezing is achieved in the limit of small w_a . Since the atomic sample size is in physical reality bounded from below, it is worth noting that the requirement for small w_a is more strict for large w_p . Hence, the limit of $w_p \gg w_a$ is not to be feasible. In essence it is desirable to combine the waist sizes so as to be located somewhere in the "trench" going in along the w_a axis on fig. C.4f. The position along the w_p axis of this "trench" depends on what might be called the overall coupling and decoherence. The former can be adjusted by changing probe detuning and the total number of atoms and photons. The latter depends only on the detuning and the photon number. Since a large number of atoms only contributes constructively to the squeezing it is always a goal to maximise this. Then the probe detuning and power can be used to facilitate an optimal choice of waists that is physically realisable.

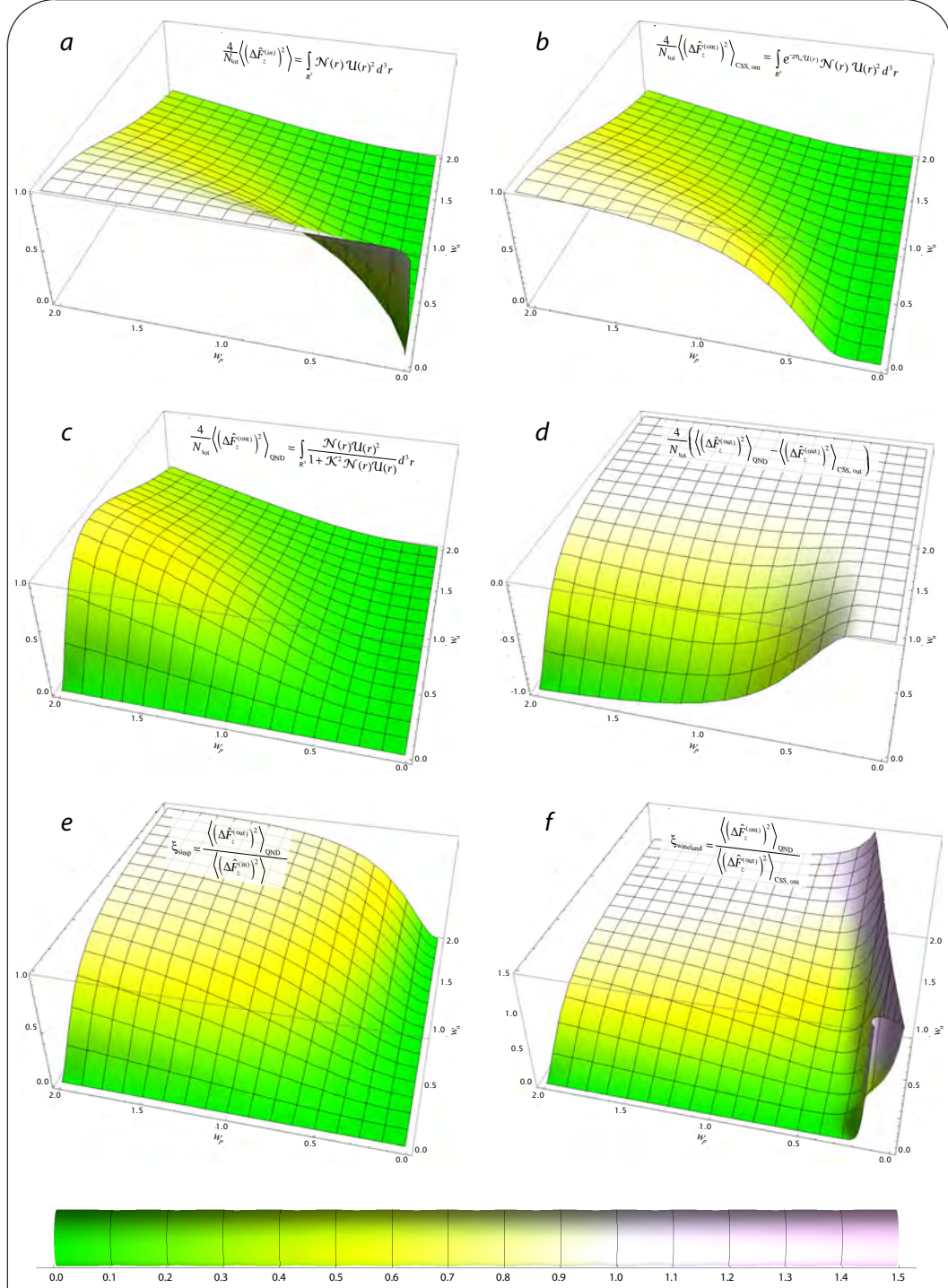


Figure C.4: effective ensemble noise and squeezing for different probe beam and atomic sample waists. All curves are normalised to $N_{\text{at}}/4$. a: Projection noise of uncorrelated (input) state $\langle (\Delta \hat{F}_z^{(in)})^2 \rangle = \int_{\mathbb{R}^2} \langle (\Delta \hat{f}_z^{(in)})^2 \rangle U(r)^2 d^2r$. b: Projection noise of input state reduced by the decoherence $\langle (\Delta \hat{F}_z^{(out)})^2 \rangle_{SQL} = \int_{\mathbb{R}^2} e^{-2\eta(r)} \langle (\Delta \hat{f}_z^{(in)})^2 \rangle U(r)^2 d^2r$. c: Projection noise reduction by the QND measurement $\langle (\Delta \hat{F}_z^{(out)})^2 \rangle_{QND} = \int_{\mathbb{R}^2} \langle (\Delta \hat{f}_z^{(in)})^2 \rangle U(r)^2 / (1 + \kappa^2) d^2r$. d: Projection noise difference between output state and output SQL $\langle (\Delta \hat{F}_z^{(out)})^2 \rangle_{QND} - \langle (\Delta \hat{F}_z^{(out)})^2 \rangle_{SQL}$. e: Squeezing according to simple criterion $\langle (\Delta \hat{F}_z^{(out)})^2 \rangle_{QND} / \langle (\Delta \hat{F}_z^{(in)})^2 \rangle$ c.f. eq. (3.30). f: Squeezing according to Wineland's criterion $\langle (\Delta \hat{F}_z^{(out)})^2 \rangle_{QND} / \langle (\Delta \hat{F}_z^{(out)})^2 \rangle_{SQL}$ c.f. eq. (3.33). Expanded formulae highlighting the spatial dependence of the local ensemble operators are printed on the individual figures.

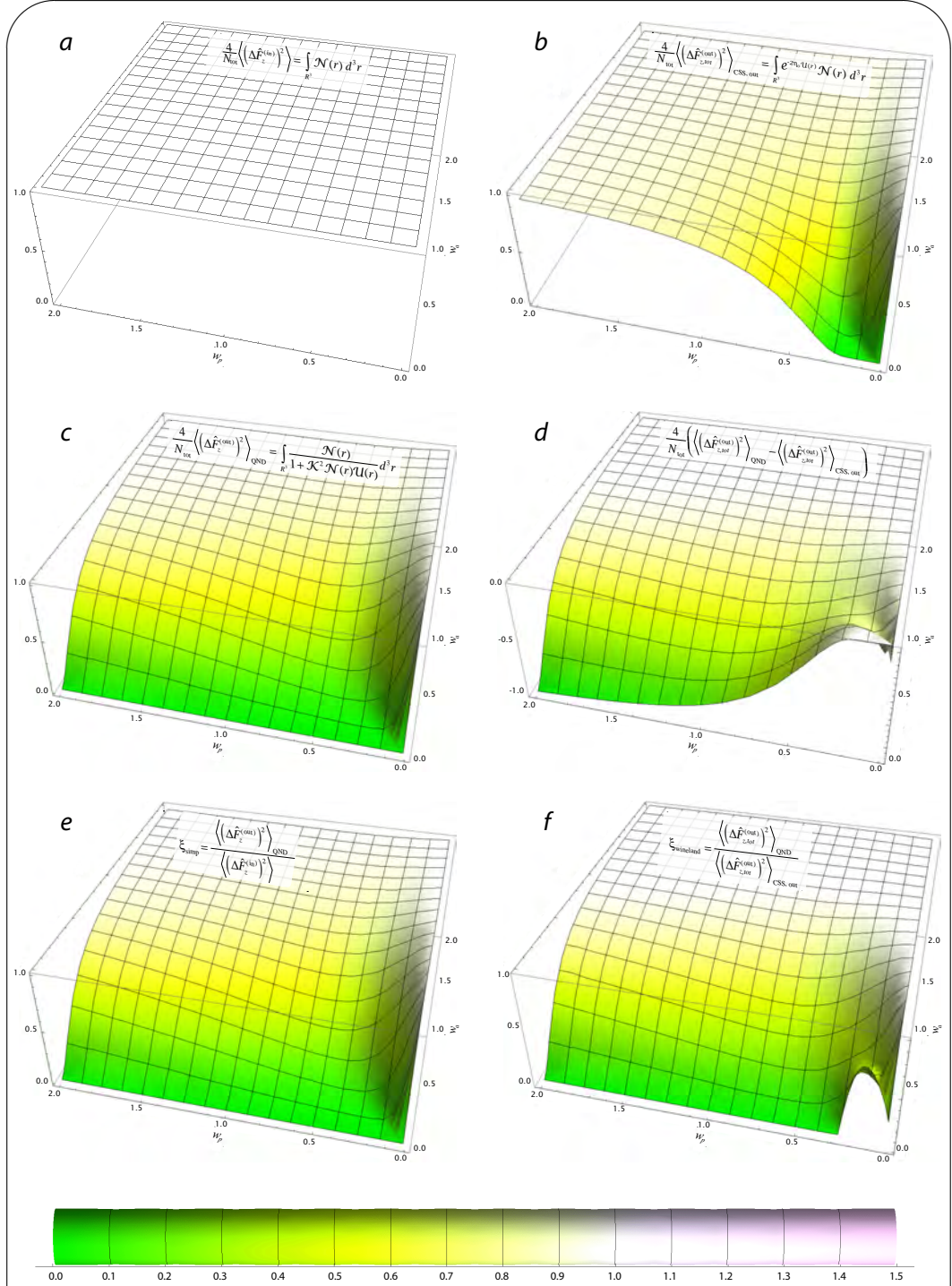


Figure C.5: Total ensemble noise and squeezing for different probe beam and atomic sample waists. All curves are normalised to $N_{\text{at}}/4$. a: Projection noise of uncorrelated (input) state $\langle (\Delta \hat{F}_z^{(in)})^2 \rangle = \int_{\mathbb{R}^2} \langle (\Delta \hat{f}_z^{(in)})^2 \rangle U(\mathbf{r})^2 l_a d^2 r$. b: Projection noise of input state reduced by the decoherence $\langle (\Delta \hat{F}_z^{(out)})^2 \rangle_{\text{SQL}} = \int_{\mathbb{R}^2} e^{-2\eta} \langle (\Delta \hat{f}_z^{(in)})^2 \rangle U(\mathbf{r})^2 l_a d^3 2$. c: Projection noise reduction by the QND measurement $\langle (\Delta \hat{F}_z^{(out)})^2 \rangle_{\text{QND}} = \int_{\mathbb{R}^2} \langle (\Delta \hat{f}_z^{(in)})^2 \rangle U(\mathbf{r})^2 l_a / (1 + \kappa^2) d^2 r$. d: Projection noise difference between output state and output SQL $\langle (\Delta \hat{F}_z^{(out)})^2 \rangle_{\text{QND}} - \langle (\Delta \hat{F}_z^{(out)})^2 \rangle_{\text{SQL}}$. e: Squeezing according to simple criterion $\langle (\Delta \hat{F}_z^{(out)})^2 \rangle_{\text{QND}} / \langle (\Delta \hat{F}_z^{(in)})^2 \rangle$ c.f. eq. (3.30). f: Squeezing according to Wineland's criterion $\langle (\Delta \hat{F}_z^{(out)})^2 \rangle_{\text{QND}} / \langle (\Delta \hat{F}_z^{(out)})^2 \rangle_{\text{SQL}}$ c.f. eq. (3.33). Expanded formulae highlighting the spatial dependence of the local ensemble operators are printed on the individual figures.

We will now recap the above in the picture of total ensemble operators. Since we chose to fix the total number of atoms the total ensemble projection noise of the uncorrelated (input) state $\langle(\Delta\hat{F}_z^{(in)})^2\rangle$ is constant (fig. C.5a). On fig. C.5b shows the input projection noise reduced by the decoherence $\langle(\Delta\hat{F}_z^{(out)})^2\rangle_{SQL}$. If w_a is large the decoherence only affects a small part of the atomic sample. If w_p is large the probe intensity is low. In either case the result is a small decoherence. There is, however, always a certain size of the probe and atomic sample size where the probe intensity is so large that any atoms contained in the probe area will experience complete decoherence. The projection noise reduced by the QND measurement $\langle(\Delta\hat{F}_z^{(out)})^2\rangle_{QND}$ (fig. C.5c), demonstrates that a high atomic density is essential to achieve large noise reduction. Again, for small probe waist sizes the requirement on the atomic waist size is less strict. The difference between the projection noise of the output state and output SQL $\langle(\Delta\hat{F}_z^{(out)})^2\rangle_{QND} - \langle(\Delta\hat{F}_z^{(out)})^2\rangle_{SQL}$, shows that the disadvantage of a small probe beam size is the large decoherence. However, given a certain realisable atomic sample size the optimal probe waist size may be at a finite value. Because of the constant input projection noise the squeezing according to simple criterion $\langle(\Delta\hat{F}_z^{(out)})^2\rangle_{QND} / \langle(\Delta\hat{F}_z^{(in)})^2\rangle$ (fig. C.5e) is identical to $\langle(\Delta\hat{F}_z^{(out)})^2\rangle_{QND}$ (fig. C.5c). Lastly the squeezing of the total ensemble operators according to Wineland's criterion $\langle(\Delta\hat{F}_z^{(out)})^2\rangle_{QND} / \langle(\Delta\hat{F}_z^{(out)})^2\rangle_{SQL}$ gives a very similar picture as for the effective atomic operators. The main difference is that for the total ensemble operators ξ_{wineland} only tends to infinity for the waist combinations were all atoms decohere i.e. not only those inside the effective probing volume. Note, that this region of the plot has been cut out so that it is easier to see the surface behind it.

Hereby, we conclude the somewhat lengthy discussion of the interaction geometry and its influence on the QND squeezing process.

Atomic constants and properties

D.1 Expressing the coupling-strength

In this section we will elaborate a bit on the expression for the coupling constant g_{ge} of the dipole interaction Hamiltonian eq. (4.1). This is a standard result of atomic physics and we do not find it necessary to go through all steps of the derivation. Detailed treatments can be found in e.g. [Loudon73, Sobelman06, Bransden83]. Based on these and [Steck08, Windpassinger08a] we will illustrate how the coupling constant can be expressed in terms of constants and the transition strengths tabulated in the below sections.

We want an expression for the per-photon Rabi frequency g_{ge} which was defined to be

$$g_{ge} = i\omega_{ge}\boldsymbol{\varepsilon} \cdot \hat{\mathbf{d}}_{ge} / \sqrt{2\hbar V\omega\epsilon_0} \quad (\text{D.1})$$

where ω_{ge} is the transition frequency, the magnitude of which will be very close to the frequency ω of the field.¹ The quantity ϵ_0 is the vacuum permittivity and V is the interaction volume [Duan02], which we take to be the effective interaction volume $\mathcal{V} = \pi l_a \frac{w_a^2}{2} \frac{r_w^2}{1+r_w^2}$ defined at the end of sec. 3.1. The remaining factor is $\boldsymbol{\varepsilon} \cdot \hat{\mathbf{d}}_{ge}$ the vector product of the field polarisation and the atomic dipole moment $\hat{\mathbf{d}}_{ge}$. We will account for the polarisation shortly, but first focus on $\hat{\mathbf{d}}_{ge}$. To find it we need to specify the states $|g\rangle$ and $|e\rangle$ a bit more carefully. From Sec. 3.2 we know that the states are fully determined by their F and m_F quantum number for the total atomic spin and it's projection respectively. Thus, the dipole matrix element can be expressed as $\hat{\mathbf{d}}_{ge} = \langle F_g \ m_{F_g} | e_0 \mathbf{r} | F_e \ m'_{F_e} \rangle$, where e_0 is the elementary charge and g marks the ground and e the excited state.

The atoms are spherically symmetric, so we conclude that $|\hat{\mathbf{d}}|^2 = e^2(|\hat{x}|^2 + |\hat{y}|^2 + |\hat{z}|^2) = 3|\hat{d}_z|^2 = 3|\hat{d}_q|^2$, where the q is the index of the irreducible vector operator [Sobelman06, Bransden83]. However, when we account for the light polarisation $\boldsymbol{\varepsilon}$, we must take the rotational average which cancels the factor of 3.

Since all final expressions involve the $|g_{ge}|^2$, we are only concerned with the norm-squared of the dipole matrix elements, and using the Wigner-Eckart theorem [Sobelman06, Bransden83], we can expand it as the product

$$|d_q|^2 = e_0^2 |\langle F_g \ m_{F_g} | r_q | F_e \ m_{F_e} \rangle|^2 = e_0^2 |\langle F_g || \mathbf{r} || F_e \rangle|^2 |\langle F_g \ m_{F_g} | F_e \ 1 \ m_{F_e} \ q \rangle|^2 \quad (\text{D.2})$$

¹For a red detuning of twice the hyperfine splitting their relative magnitude is $|\omega_{ge}/\omega| \approx 1.0000261$, so we will not hesitate to substitute ω for ω_{ge}

where the Clebsch-Gordan coefficient $\langle F_g m_{F_g} | F_e 1 m_{F_e} q \rangle$ will vanish unless $m_{F_e} = m_{F_g} - q$. If the atoms are unpolarised we can

For linearly polarised light we only have $q = 0$ transitions.

$$\sum_{m_{F_g}, m_{F_e}} |d_q|^2 = \sum_{m_{F_g}, m_{F_e}} |\langle F_g || e_0 \mathbf{r} || F_e \rangle|^2 |\langle F_g m_{F_g} | F_e 1 m_{F_e} 0 \rangle|^2 = \frac{1}{3} |\langle F_g || e \mathbf{r} || F_e \rangle|^2 \quad (\text{D.3})$$

which follows from the properties of the Clebsch-Gordan coefficients.

The reduced dipole matrix element can be further expanded. The first factor is

$$|\langle F_g || e \mathbf{r} || F_e \rangle|^2 = (2F_g + 1) \begin{Bmatrix} J_g & F_g & I \\ F_e & J_e & 1 \end{Bmatrix}^2 |\langle J_g || e \mathbf{r} || J_e \rangle|^2 \quad (\text{D.4})$$

written in terms of Wigner 6-j symbols [Sobelman06] while the second factor is the Clebsch-Gordan coefficient which can be written as

$$|\langle F_g m_{F_g} | F_e 1 m_{F_e} q \rangle|^2 = (2F_e + 1) \begin{pmatrix} F_g & 1 & F_e \\ m_{F_g} & q & m_{F_e} \end{pmatrix}^2 \quad (\text{D.5})$$

written in terms of Wigner 3-j symbols. As in Sec. 3.2 $J_g = 1/2$ and $J_e = 3/2$ ($J_e = 1/2$) for D2-line (D1-line) are the orbital angular momenta plus spin of the ground and excited state and $I = 7/2$ is the nuclear spin. We define the transition strength factor as

$$S_{F_g, F_e} \equiv (2F_g + 1)(2F_e + 1) \begin{Bmatrix} J_g & F_g & I \\ F_e & J_e & 1 \end{Bmatrix}^2 \begin{pmatrix} F_g & 1 & F_e \\ m_{F_g} & q & m_{F_e} \end{pmatrix}^2, \quad (\text{D.6})$$

so that $|d_q|^2 = S_{F_g, F_e} |\langle J_g || e \mathbf{r} || J_e \rangle|^2$. In table D.5-refAPPcgcoeff-D2-45 and D.4 below the Clebsch-Gordan coefficients and transition strength factors S_{F_g, F_e} are listed, respectively.

The dipole matrix elements are proportional to the natural linewidth through the formula from [Sobelman06, Loudon73]

$$|\langle J_g || e \mathbf{r} || J_e \rangle|^2 = (2J_e + 1) \frac{3\hbar c \epsilon_0 \lambda^2 \gamma_e}{2\pi \omega} \quad (\text{D.7})$$

If we collect the results and insert into Eq. eq. (D.1) we are able to write up a practical expression for the coupling constant g_{ge}

$$\begin{aligned} |g_{ge}|^2 &= (2J_e + 1) (2F_g + 1)(2F_e + 1) \begin{Bmatrix} J_g & F_g & I \\ F_e & J_e & 1 \end{Bmatrix}^2 \begin{pmatrix} F_g & 1 & F_e \\ m_{F_g} & q & m_{F_e} \end{pmatrix}^2 \frac{\lambda^2 c \gamma_e}{4\pi \mathcal{V} 2} \\ &= (2J_e + 1) S_{F_g, F_e} \frac{3\lambda^2 c \gamma_e}{4\pi \mathcal{V} 2} \end{aligned} \quad (\text{D.8})$$

For the D1-line with $J_e = 1/2$ the prefactor $(2J_e + 1)$ is 2 while for the D2-line with $J_e = 3/2$ it is 4. If we also express the interaction volume in terms of the probe and sample waists and the sample length we altogether get

$$|g_g|^2 = S_{F_g, F_e} \frac{3\lambda^2 c}{\pi^2 l_a w_a^2} \frac{1 + r_w^2}{r_w^2} \frac{\gamma_e}{2} \quad \text{D1 - line} \quad (\text{D.9})$$

$$|g_g|^2 = S_{F_g, F_e} \frac{6\lambda^2 c}{\pi^2 l_a w_a^2} \frac{1 + r_w^2}{r_w^2} \frac{\gamma_e}{2} \quad \text{D2 - line} \quad (\text{D.10})$$

property	symbol	Value
Atomic number	Z	55
Nuclear number	$Z + N$	133
Relative isotope abundance	-	100%
Atomic mass	m_{Cs}	$2.207 \cdot 10^{-25}$ kg
Density at 25°	\mathcal{N}_{Cs}	1.93 g/cm ³
Melting point	T_M	28.44°
Boiling point	T_B	671°
Vapour pressure at 25°	P_V	$1.3 \cdot 10^{-6}$ torr
Nuclear spin	I	7/2
Valence electrons		1

Table D.1: Dlines

D.2 Cs atom constants

D.2.1 D-line constants

The data presented is based on [Steck08] and is provided here mainly as a practical reference. The saturation intensity is the effective far detuned for π -polarised light i.e. corresponding to π -polarised light coupling to all hyperfine transitions simultaneously. Likewise the cross section is the effective for π -polarised light.

property	symbol	D1-line	D2-line
Wavelength	λ	894. nm	852. nm
Decayrate	γ	4.6 MHz	5.2 MHz
Saturation Intensity	I_{sat}	2.4981 mW/cm ²	1.6536 mW/cm ²
Resonant cross-section	σ_0	0.1531 μm^2	0.2313 μm^2

Table D.2: Dlines

Transition frequencies

$F_g \setminus F_e$	2	3	4	5
3	8589.18 MHz	8740.39 MHz	8941.63 MHz	-
4	-	-452.24 MHz	-251.00 MHz	0 MHz

Table D.3: Detunings relative to $\Delta 45$ [Steck08]

Interaction strength matrix elements

$F_g \setminus F_e$	2	3	4	5
3	$\frac{5}{14}$	$\frac{3}{8}$	$\frac{15}{56}$	0
4	0	$\frac{7}{72}$	$\frac{7}{24}$	$\frac{11}{18}$

Table D.4: Dipole transition strengths $S_{F_g F_e}$ for the D2-line [Steck08]

$m_{Fg} \setminus m_{Fe}$	-2	-1	0	1	2
-3	$\sqrt{\frac{5}{14}}$	0	0	0	0
-2	$\sqrt{\frac{5}{42}}$	$\sqrt{\frac{5}{21}}$	0	0	0
-1	$\sqrt{\frac{1}{42}}$	$\sqrt{\frac{4}{21}}$	$\sqrt{\frac{1}{7}}$	0	0
0	0	$\sqrt{\frac{1}{14}}$	$\sqrt{\frac{3}{14}}$	$\sqrt{\frac{1}{14}}$	0
1	0	0	$\sqrt{\frac{1}{7}}$	$\sqrt{\frac{4}{21}}$	$\sqrt{\frac{1}{42}}$
2	0	0	0	$\sqrt{\frac{5}{21}}$	$\sqrt{\frac{5}{42}}$
3	0	0	0	0	$\sqrt{\frac{5}{14}}$

Table D.5: Clebsh-Gordans: D2-line 3-2

$m_{Fg} \setminus m_{Fe}$	-3	-2	-1	0	1	2	3
-3	$-\sqrt{\frac{9}{32}}$	$\sqrt{\frac{3}{32}}$	0	0	0	0	0
-2	$\sqrt{-\frac{3}{32}}$	$-\sqrt{\frac{1}{8}}$	$\sqrt{\frac{5}{32}}$	0	0	0	0
-1	0	$-\sqrt{\frac{5}{32}}$	$-\sqrt{\frac{1}{32}}$	$\sqrt{\frac{3}{16}}$	0	0	0
0	0	0	$-\sqrt{\frac{3}{16}}$	0	$\sqrt{\frac{3}{16}}$	0	0
1	0	0	0	$-\sqrt{\frac{3}{16}}$	$\sqrt{\frac{1}{32}}$	$\sqrt{\frac{5}{32}}$	0
2	0	0	0	0	$-\sqrt{\frac{5}{32}}$	$\sqrt{\frac{1}{8}}$	$\sqrt{\frac{3}{32}}$
3	0	0	0	0	0	$-\sqrt{\frac{3}{32}}$	$\sqrt{\frac{9}{32}}$

Table D.6: Clebsh-Gordans: D2-line 3-3

$m_{Fg} \setminus m_{Fe}$	-4	-3	-2	-1	0	1	2	3	4
-3	$\sqrt{\frac{5}{24}}$	$-\sqrt{\frac{5}{96}}$	$\sqrt{\frac{5}{672}}$	0	0	0	0	0	0
-2	0	$\sqrt{\frac{5}{32}}$	$-\sqrt{\frac{5}{56}}$	$\sqrt{\frac{5}{224}}$	0	0	0	0	0
-1	0	0	$\sqrt{\frac{25}{224}}$	$-\sqrt{\frac{25}{224}}$	$\sqrt{\frac{5}{112}}$	0	0	0	0
0	0	0	0	$\sqrt{\frac{25}{336}}$	$-\sqrt{\frac{5}{42}}$	$\sqrt{\frac{25}{336}}$	0	0	0
1	0	0	0	0	$\sqrt{\frac{5}{112}}$	$-\sqrt{\frac{25}{224}}$	$\sqrt{\frac{25}{224}}$	0	0
2	0	0	0	0	0	$\sqrt{\frac{5}{224}}$	$-\sqrt{\frac{5}{56}}$	$\sqrt{\frac{5}{32}}$	0
3	0	0	0	0	0	0	$\sqrt{\frac{5}{672}}$	$-\sqrt{\frac{5}{96}}$	$\sqrt{\frac{5}{24}}$

Table D.7: Clebsh-Gordans: D2-line 3-4

$m_{Fg} \setminus m_{Fe}$	-3	-2	-1	0	1	2	3
-4	$\sqrt{\frac{7}{72}}$	0	0	0	0	0	0
-3	$\sqrt{\frac{7}{228}}$	$\sqrt{\frac{7}{96}}$	0	0	0	0	0
-2	$\sqrt{\frac{1}{288}}$	$\sqrt{\frac{1}{24}}$	$\sqrt{\frac{5}{96}}$	0	0	0	0
-1	0	$\sqrt{\frac{1}{96}}$	$\sqrt{\frac{5}{96}}$	$\sqrt{\frac{5}{144}}$	0	0	0
0	0	0	$\sqrt{\frac{1}{48}}$	$\sqrt{\frac{1}{18}}$	$\sqrt{\frac{1}{48}}$	0	0
1	0	0	0	$\sqrt{\frac{5}{144}}$	$\sqrt{\frac{5}{96}}$	$\sqrt{\frac{1}{96}}$	0
2	0	0	0	0	$\sqrt{\frac{5}{96}}$	$\sqrt{\frac{1}{24}}$	$\sqrt{\frac{1}{228}}$
3	0	0	0	0	0	$\sqrt{\frac{7}{96}}$	$\sqrt{\frac{7}{228}}$
4	0	0	0	0	0	0	$\sqrt{\frac{7}{72}}$

Table D.8: Clebsh-Gordans: D2-line 4-3

$m_{Fg} \setminus m_{Fe}$	-4	-3	-2	-1	0	1	2	3	4
-4	$-\sqrt{\frac{7}{30}}$	$\sqrt{\frac{7}{120}}$	0	0	0	0	0	0	0
-3	$-\sqrt{\frac{7}{120}}$	$-\sqrt{\frac{21}{160}}$	$\sqrt{\frac{49}{480}}$	0	0	0	0	0	0
-2	0	$-\sqrt{\frac{49}{480}}$	$-\sqrt{\frac{7}{120}}$	$\sqrt{\frac{21}{160}}$	0	0	0	0	0
-1	0	0	$-\sqrt{\frac{21}{160}}$	$-\sqrt{\frac{7}{480}}$	$\sqrt{\frac{7}{48}}$	0	0	0	0
0	0	0	0	$-\sqrt{\frac{7}{48}}$	0	$\sqrt{\frac{7}{48}}$	0	0	0
1	0	0	0	0	$-\sqrt{\frac{7}{48}}$	$\sqrt{\frac{7}{480}}$	$\sqrt{\frac{21}{160}}$	0	0
2	0	0	0	0	0	$-\sqrt{\frac{21}{160}}$	$\sqrt{\frac{7}{120}}$	$\sqrt{\frac{49}{480}}$	0
3	0	0	0	0	0	0	$-\sqrt{\frac{41}{480}}$	$\sqrt{\frac{21}{160}}$	$\sqrt{\frac{7}{120}}$
4	0	0	0	0	0	0	0	$-\sqrt{\frac{7}{120}}$	$\sqrt{\frac{7}{30}}$

Table D.9: Clebsh-Gordans: D2-line 4-4

$m_{Fg} \setminus m_{Fe}$	-5	-4	-3	-2	-1	0	1	2	3
-4	$\sqrt{\frac{1}{2}}$	$-\sqrt{\frac{1}{10}}$	$\sqrt{\frac{1}{90}}$	0	0	0	0	0	0
-3	0	$\sqrt{\frac{2}{5}}$	$-\sqrt{\frac{8}{45}}$	$\sqrt{\frac{1}{30}}$	0	0	0	0	0
-2	0	0	$\sqrt{\frac{14}{45}}$	$-\sqrt{\frac{7}{30}}$	$\sqrt{\frac{1}{15}}$	0	0	0	0
-1	0	0	0	$\sqrt{\frac{7}{30}}$	$-\sqrt{\frac{4}{15}}$	$\sqrt{\frac{1}{9}}$	0	0	0
0	0	0	0	0	$\sqrt{\frac{1}{6}}$	$-\sqrt{\frac{5}{18}}$	$\sqrt{\frac{1}{6}}$	0	0
1	0	0	0	0	0	$\sqrt{\frac{1}{9}}$	$-\sqrt{\frac{4}{15}}$	$\sqrt{\frac{7}{30}}$	0
2	0	0	0	0	0	0	$\sqrt{\frac{1}{15}}$	$-\sqrt{\frac{7}{30}}$	$\sqrt{\frac{14}{45}}$
3	0	0	0	0	0	0	0	$\sqrt{\frac{1}{30}}$	$-\sqrt{\frac{8}{45}}$
4	0	0	0	0	0	0	0	0	$\sqrt{\frac{1}{90}}$

Table D.10: Clebsh-Gordans: D2-line 4-5

Simulations of trapped atomic ensemble

In this section we will present the background and methods for simulating the time evolution of the individual atoms in the trapped sample. We need to discuss some result from statistical physics in order to derive expressions that are needed for the simulation. Thereby, we actually end up verifying some assumptions made in above chapters. This section is not without assumptions and approximations of its own. The most significant approximation is that we consider only the transverse motion and thus only express equations in this plane. This approximation is of course already implicitly included in the atomic density distribution eq. (3.5) stated above. The defect of the 2D approximation stems from the fact that any Gaussian beam will propagate with some divergence. As the atomic sample is centred in a location where all the relevant laser beams are focused, the task is to determine over which distance the radial beam profiles do not change too much. To this end, we calculate the Raleigh range which for the probe beam will be around $z_{1,0} = x$ mm and for the trapping beam $z_{t,0} \approx x$ mm. In comparison, images of the dipole trap show it to be no longer than 1 mm. The corresponding fractional change in beam-width of the laser beam is then x and x for the probe and trapping lasers respectively. We take this as a justification for reducing the scope to a 2D model. Finally, we point to [Oblak08] where some parts of the simulations have been presented.

E.1 Initial distribution

We describe the (external) motional state of the atom in terms of i_{\max} generalised coordinates q_i and momenta p_i , which together form a set of canonical variables in phase-space. Since our system is radially symmetric we parametrize the position in terms of the atom's radial r and angular ϕ positions with the corresponding radial p_r and angular p_ϕ momenta. Using these, we express the total energy of particle $H(q_1, p_1, \dots, q_{i_{\max}}, p_{i_{\max}})$, which for a radially symmetric potential $U(r)$ becomes

$$H(r, \phi, p_r, p_\phi) = \frac{1}{2m_{Cs}} \left(p_r^2 + \frac{p_\phi^2}{r^2} \right) + V(r) \quad (\text{E.1})$$

From statistical physics it is known that the probability of finding an atom in a state with phase-space coordinates in the range $q_i, q_i + dq_i$ and $p_i, p_i + dp_i$ for

$i = 1, \dots, i_{\max}$ is given by [Mandl88]

$$\mathcal{P}(q_1, p_1, \dots, q_{i_{\max}}, p_{i_{\max}}) = \frac{1}{Z} e^{-\frac{H(q_1, p_1, \dots, q_{i_{\max}}, p_{i_{\max}})}{k_B T}} \quad (\text{E.2})$$

where k_B is Boltzmann's constant, T the atom's thermodynamic temperature and the partition function $Z = \int_{R^{2i_{\max}}} e^{-\frac{H(q_1, p_1, \dots, q_{i_{\max}}, p_{i_{\max}})}{k_B T}} d^{i_{\max}} q d^{i_{\max}} p$. In the case of the radially symmetric potential we write

$$\mathcal{P}(r, \phi, p_r, p_\phi) = \frac{1}{Z} e^{-\frac{1}{k_B T} \left[\frac{1}{2mCs} \left(p_r^2 + \frac{p_\phi^2}{r^2} \right) + V(r) \right]} \quad (\text{E.3})$$

We are of course free to find the probability distribution only in terms of one or a few of the phase-space coordinates by integrating over the remaining degrees of freedom. For example we may wish to find the position distribution of the atoms in a trap and this becomes

$$\mathcal{P}(r, \phi) = \frac{\mathcal{N}(r)}{N_{\text{tot}}} = \frac{1}{Z_r} e^{-\frac{V(r)}{k_B T}} \quad (\text{E.4})$$

where the marginal partition function $Z_r = \int_{r=0}^{\infty} r e^{-\frac{1}{k_B T} V(r)} dr$.

Let us further specialise to the case of a Gaussian potential $V(r) = V_0 e^{-2r^2/w_t^2}$ c.f. eq. (9.1). The resulting marginal particle position distribution is then

$$\mathcal{P}(r, \phi) = \frac{\mathcal{N}(r)}{N_{\text{tot}}} = \frac{1}{Z_r} e^{-\frac{V_0}{k_B T} e^{-2r^2/w_t^2}} \quad (\text{E.5})$$

In the limit of $V_0 \ll k_B T$ the density is negligible for $r > w_t$ and we may expand the second exponential to second order

$$\mathcal{P}(r, \phi) = \frac{\mathcal{N}(r)}{N_{\text{tot}}} \approx \frac{k_B T 2}{\pi w_t^2 V_0} e^{-\frac{V_0}{k_B T} \frac{2r^2}{w_t^2}} \quad (\text{E.6})$$

This is the limit where the trapping potential is approximately harmonic and the resulting density distribution is Gaussian with a width $w_a = w_t^2 k_B T / V_0$ proportional to the width of the trapping potential width — The colder the ensemble the narrower the spatial extent of ensemble in the trap. In the opposite limit of $V_0 \gg k_B T$ the distribution becomes

$$\mathcal{P}(r, \phi) = \frac{\mathcal{N}(r)}{N_{\text{tot}}} \approx \frac{2}{\pi w_t^2} e^{-\frac{2r^2}{w_t^2}}. \quad (\text{E.7})$$

This is still a Gaussian, but it makes no explicit reference to the ensemble temperature.

Generating ensemble for simulation When generating an ensemble for the simulations of the time evolution we first pick random radial positions according to the marginal distribution for r i.e.

$$\mathcal{P}(r) = \frac{k_B T 2}{\pi w_t^2 V_0} r e^{-\frac{V_0}{k_B T} \frac{2r^2}{w_t^2}}, \quad (\text{E.8})$$

in analogous to the low temperature limit given by eq. (E.6). The angular distribution of particles is uniform from $0 \leq \phi \leq 2\pi$, but usually we will not be concerned with the angular coordinate as it does not affect any of the other

coordinates (see sec. E.2). The atoms are also given random momentum coordinates corresponding to the respective marginal distributions. These are both Gaussian and with widths $\sqrt{k_B T}$ and $r\sqrt{k_B T}$ for p_r and p_ϕ respectively. Computationally, the Gaussian-like distributed random values are selected by the rejection method [Press02]. For this to work we must specify cut-off values for the distributions, typically slightly bigger than the natural width of the distribution. If we use the radial coordinate as an example then we pick a cut-off value $r_{\max} \approx 2\omega_a$. Then we use standard algorithms to choose a pair of random numbers between 0 and 1, $\{x, y\}$. Next we multiply $2x - 1$ by r_{\max} and y by $\frac{\sqrt{2}}{\pi\omega_a}e^{-1}$ which is the maximal value of $\mathcal{P}(r)$ attained at $r = \omega_a/\sqrt{2}$. The final step is to determine if the rescaled values $\{x', y'\}$ lie below the curve $\mathcal{P}(r)$ i.e. if $y' < \mathcal{P}(x')$. If they do the points are accepted, otherwise they are rejected and another random pair is selected. When random positions and momenta are selected for an atom it is tested that the total energy $H(r, \phi, p_r, p_\phi) < V(r)$, that is the atom is trapped in the potential. If the atom turns out to be untrapped it is discarded and another random coordinate attempt is made. At the end we have generated a set of N_{tot} atoms characterised by their positions r_k and momenta p_k .

E.1.1 Detection

The atoms are detected by the phase-shift they impose on a probe beam. Since the probe beam has an inhomogeneous transverse profile the strength of the influence of each atom on the probe beam depends on that atom's transverse position within the probe beam. Since, both the probe and the atomic sample display cylindrical symmetry it is in fact only the radial position of the atom which matters. The probe intensity profile is described by the Gaussian $U(r) = \frac{2}{\pi w_p^2} e^{-2r^2/w_p^2}$. Thus, the phase-shift from the atomic ensemble is given by

$$\tilde{\phi}_{\text{ph}} = \tilde{\phi}_{\text{ph},0} \sum_{k=1}^{N_{\text{tot}}} U(r_k) \quad (\text{E.9})$$

where $\tilde{\phi}_{\text{ph},0} = \frac{3\lambda^2}{2\pi^3} (2J_e + 1) S_{F_g F_e} \frac{\Delta_{ge} \gamma_e}{\Delta_{ge}^2 + (\frac{\gamma_e}{2})^2} (\hat{\sigma}_{gg}^{(1)} - \hat{\sigma}_{ee}^{(1)})$ is the phase-shift imparted on the probe by a single atom c.f. eq. (4.15). In cases where we can specify an analytical form for $\mathcal{N}(r)$ we may of course perform an integral instead of the sum as e.g. the case of a Gaussian atomic density distribution in eq. (4.15). The shortcoming of the analytical approach is that it is difficult to express the time evolution of the ensemble except in a Harmonic trap limit. In several cases the movement of the individual

E.2 Single atom phase-space trajectories

The dynamics of an atom is easily deduced from the energy description in canonical phase-space variables. The evolution is described by the following differential equations [Hamilton34, Hamilton35].

$$\frac{dr}{dt} = \frac{\partial H}{\partial p_r} = \frac{p_r}{m} \quad \frac{d\phi}{dt} = \frac{\partial H}{\partial p_\phi} = \frac{p_\phi}{mr^2} \quad (\text{E.10})$$

$$\frac{dp_r}{dt} = \frac{\partial H}{\partial r} = -\frac{p_\phi^2}{mr^3} + \frac{\partial V(r)}{\partial r} \quad \frac{dp_\phi}{dt} = \frac{\partial H}{\partial \phi} = 0 \quad (\text{E.11})$$

where for convenience we have omitted the Cs-subscript from the mass. We see that the angular momentum is a constant of motion and that the angular position is completely de-coupled from the radial equations. Since at the same time, the angular position has no influence on any of the dynamics we observe we will concentrate our efforts to trace the radial degrees of freedom. Two potentials relevant for our experiment. First there is $V(r) = C$, where C is some constant value. This corresponds to untrapped atoms and the radial equations in this case reduces to

$$\frac{dr}{dt} = \frac{p_r}{m} \qquad \frac{dp_r}{dt} = -\frac{p_\phi^2}{mr^3} \quad (\text{E.12})$$

The other important potential is that generated by a Gaussian trapping laser beam $V(r) = \frac{V_0}{\pi w_0^2} e^{-2r^2/w_0^2}$

$$\frac{dr}{dt} = \frac{p_r}{m} \qquad \frac{dp_r}{dt} = -\frac{p_\phi^2}{mr^3} + \frac{4V_0 r}{w_0^2} e^{-\frac{2r^2}{w_0^2}} \quad (\text{E.13})$$

The numerical simulation is performed in MatLab[©] using the Störmer-Verlét velocity method [Störmer21, Verlet67], which we will not describe extensively here. It requires the velocity $v_r = p_r/m$ and acceleration $a_r = \frac{dp_r}{dt}/m$ at a given time-step so as to calculate the position at the subsequent time-step. We note that the simulation will introduce some errors that result in alteration of the atom's energy. This is likely to occur when an atom crosses the origin $r = 0$ where the equation for the radial momentum diverges. Hence, If the atomic energy at the end of the simulation differs too much from the energy at the beginning ($> 5\%$) the atom is disregarded. At the end of the simulation we get a triplet-array $\{r_k(t_i), p_{r,k}(t_i), t_i\}$ of computed values for different increments $0 \leq i \leq i_{\max}$ for each atom k . The simulation allows us to specify a different potentials for different times. Thereby, in sec. 9.2.2 we compute the evolution of an ensemble of atoms for which the potential is switched off and re-applied after some time, in order to model the observation of damped breathing oscillations at twice the characteristic trap frequency. Similarly, in sec. 9.2.3 we model the decrease in phase-shift as atoms are released from the trapping potential, so as to determine the sample's temperature. Finally, for use in sec. 11.2.1 we model the evolution of atoms that are imprinted with a spatially inhomogeneous light-shift phase that is subsequently detected in a Ramsey experiment.

We use a "manual" optimisation method to find the simulation parameters to that best reproduce the experimental data. We first simulate and store theoretical curves for a range of parameters. Following this, we compare the square deviation of the theoretical data points from the experimental. The set of simulation parameters that yield the smallest square deviation are taken to be optimal. One can refine the optimisation by calculating another set of simulations with smaller increments between the parameter values. Fig. E.1 is a plot of the errors associated with the trap oscillation data presented in fig. 9.10. The optimal set $\beta = 6$, $\omega_p/\omega_a = 0.6$, and $\omega_t = 1/3800 \mu\text{s}$ of parameter values stated for the data in the fig. 9.10 should be apparent from the above plot of the errors.

E.3 Light-shift phase imprints

Now we will study the situation where the atomic state receives a phase-shift from the energy perturbation by the probe field. Since the probe intensity is inhomogeneous over the atomic sample this light-shift will also be inhomogeneous. In Ramsey spectroscopy we exactly measure the time evolution of the

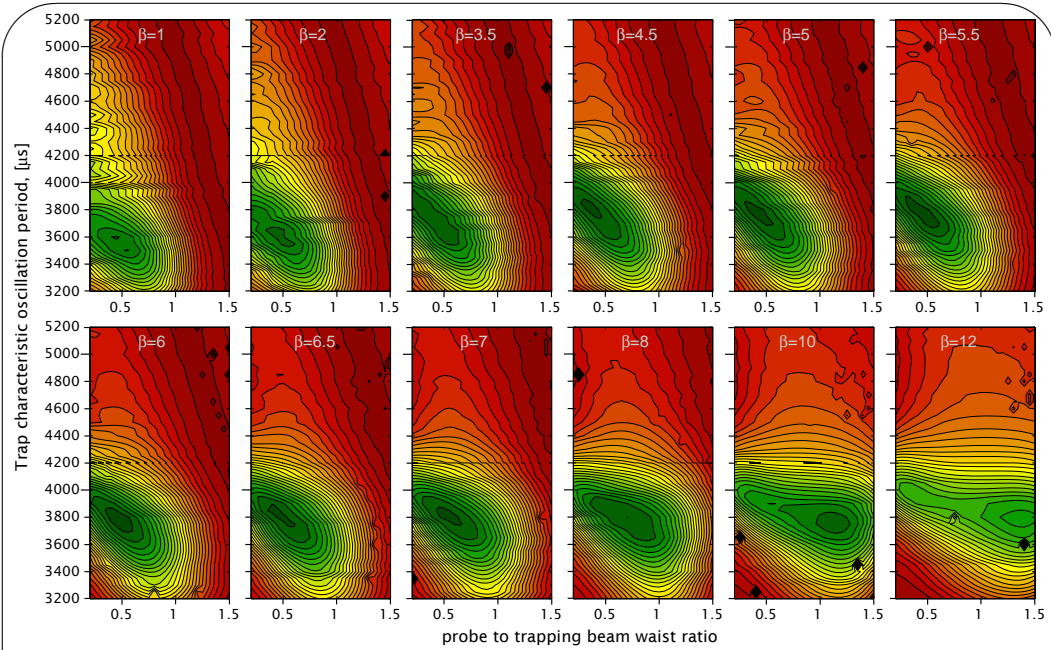


Figure E.1: Norm squared error between simulated and experimental trap oscillation data for different values of simulation parameters. The temperature parameter $\beta = 1/(k_b T)$ is stated in units of the trapping potential.

phase between the two ground-levels. the fringe amplitude is maximal when all atomic superposition states have an equal phase. Any distribution of the phases — coined dephasing — will decrease the Ramsey fringe amplitude. Hence, the Ramsey spectroscopy signal is direct related to the degree of light-shift dephasing.

To model the light shifts we simply add an additional degree of freedom to the atoms namely a state-phase ϕ' . We note that ϕ' is related to the internal state of the atoms and thus usually decoupled from the external motional degrees of freedom. The spatially inhomogeneous light shift thus couples the internal and external states of the atom. In the previous section we found the time evolution of the atomic position $\mathbf{r}_k(t)$. The light shift imparted on the atom by a probe pulse at time t_1 is given by

$$\tilde{\phi}'_{\text{at},k} = \tilde{\phi}_{\text{at},0} U(\mathbf{r}_k) \quad (\text{E.14})$$

where $\tilde{\phi}'_{\text{at},k}$ is the light shift induced by N_{ph} photons c.f. eq. (4.24). We note that if we have more probe colours the light shifts from these may add up or cancel depending on the probe frequencies. The combined light-shift from several pulses at times t_i is then $\tilde{\phi}'_{\text{at},k} = \sum_i \tilde{\phi}_{\text{at},0} U(\mathbf{r}_k(t_i))$. However, if a microwave π -pulse has been applied at some point the all the atomic phases will be inverted. This is equivalent to assigning the opposite sign to all light shifts imprinted after the π -pulse. Thus, for a pulse sequence as depicted in fig. E.2 the combined light-shift of the two probe pulses becomes

$$\tilde{\phi}'_{\text{at},k} = \tilde{\phi}_{\text{at},0} (U(\mathbf{r}_k(t_{p,1})) - U(\mathbf{r}_k(t_{p,2}))) \quad (\text{E.15})$$

We now take the Ramsey echo-spectroscopy into consideration starting with a single atom (a thorough explanation of Ramsey spectroscopy is provided in sec. 10.2.3). The microwave field is detuned by $\Delta_{\mu\text{w}}$ from the clock transition frequency and the time evolution of the atomic state is after the first $\pi/2$ pulse

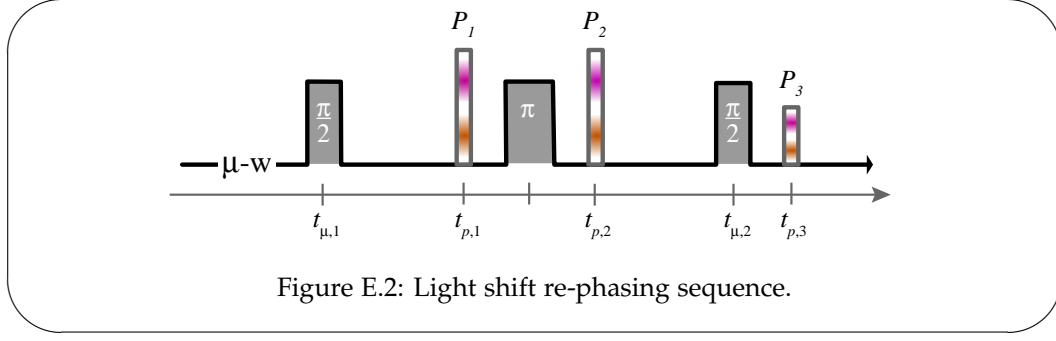


Figure E.2: Light shift re-phasing sequence.

is $|\psi_k\rangle = (|3\rangle e^{-i\Delta_{\mu w}t} + |4\rangle)/\sqrt{2}$. The two probe pulses surrounding the echo- π -pulse add a phase according to the state such that at the time of the final Ramsey $\pi/2$ -pulse the state has evolved to $(|3\rangle e^{-i\Delta_{\mu w}(t_{\mu,1}+t_{\mu,2})+\phi'_k} + |4\rangle)/\sqrt{2}$. The Ramsey signal of the atom is then

$$\tilde{\phi}_{\text{ph},0} U(\mathbf{r}_k(t_{p,3})) \cos\left(\Delta_{\mu w} \delta t_{\mu} + \tilde{\phi}_{\text{at},0} [U(\mathbf{r}_k(t_{p,1})) - U(\mathbf{r}_k(t_{p,2}))]\right) \quad (\text{E.16})$$

where $t_{p,3}$ is the time of the detection pulse, $\delta t_{\mu} = t_{\mu,1} + t_{\mu,2}$, and we have written out ϕ'_k . Thus the Ramsey signal depends on five different times of which three are linked to the position of the atom at the given moments. For the whole ensemble of atoms we simply sum over all atoms.

The simulation first calculates the particle trajectories according to sec. E.2 and then compute the phase-imprints at times $t_{p,1}$ and $t_{p,2}$. Next we calculate the Ramsey fringe from the combined phase-imprint ϕ'_k and the time separation $t_{\mu,1} + t_{\mu,2}$. Lastly, the atomic position at the detection moment is used to compute the Ramsey signal. In sec. 11.2.1 we present the experimental results of the measurement sequence in fig. E.2 and use the simulations to generate a theoretical comparison. The values of w_t , T , $\tilde{\phi}_{\text{at},0}$, w_p that produce the best simulation are found by the method described in sec. E.2.

Measures of oscillator (in)stability

In spectroscopy applications such as atomic clocks it is crucial to have a broadly recognised method to characterise the quality of the experiment. Here we aim to summarise some definitions and conventions that are relevant for our work. The treatment largely follows that found in [Barnes71].

An oscillator signal is a signal on the general form

$$A(t) = [A_0 + \alpha(t)] \sin[\omega_0 t + \phi(t)]$$

where A_0 is the signal's mean amplitude in the units of the signal, e.g. volts, current, intensity etc., and $\alpha(t)$ is the instantaneous departure of the amplitude from the mean value. Similarly, $\omega_0 = 2\pi\nu_0$ is the nominal (angular) frequency and $\phi(t)$ the instantaneous phase-offset. Thus, the instantaneous signal phase is simply the argument $\omega_0 t + \phi(t)$ while the instantaneous frequency is its derivative

$$\omega(t) = \omega_0 + \frac{d\phi(t)}{dt} \tag{F.1}$$

so that the frequency deviation plainly becomes $\omega(t) - \omega_0 = d\phi(t)/dt$. One then defines a fractional frequency deviation $y(t)$ as

$$y(t) = \frac{\omega(t) - \omega_0}{\omega_0} = \frac{1}{\omega_0} \frac{d\phi(t)}{dt} \tag{F.2}$$

Time domain - Allan variance The integral of $y(t)$ over some time τ starting at t_k represents the average frequency deviation over this time. From the definition eq. (F.2) we easily express this integral as

$$\bar{y}_k \equiv \frac{1}{\tau} \int_{t_k}^{t_k+\tau} y(t) dt = \frac{\phi(t_k + \tau) - \phi(t_k)}{\omega_0 \tau}$$

By measuring the phase of a signal at various times, thus, allows one to compute \bar{y}_k . The Allan or two-point variance is then defined as¹ [Allan66]

$$\sigma^2(\tau) = \frac{1}{2} \langle (\bar{y}_{k+1} - \bar{y}_k)^2 \rangle \tag{F.3}$$

¹the Allan variance is the $N = 2$ variant of the more general N -point variance $\sigma^2(\tau, N) \equiv \langle \frac{1}{N-1} \sum_{n=1}^N \left(\bar{y}_n - \frac{1}{N} \sum_{k=1}^N \bar{y}_k \right)^2 \rangle$.

Here the $\langle \cdot \rangle$ represents a temporal average over all possible values of t_k . The Allan variance thus characterises the oscillator stability over certain averaging times and is thus closely related to the power spectrum of the noise. The Allan variance is defined as a dimensionless measure, however, it is straight forward to relate it to e.g. (angular) frequency fluctuations $\nu_0\sigma^2(\tau)$ ($\omega_0\sigma^2(\tau)$). Additionally, by virtue of eq. (F.1) we can easily compute the expected phase-excursion on a certain time-scale as $\Delta\phi(\tau) = \omega_0\tau\sigma^2(\tau)$. It is worth noting that using eq. (F.2) we can re-write the Allan variance in terms of the instantaneous phase-offset

$$\sigma^2(\tau) = \frac{1}{2\omega_0^2\tau^2} \left\langle [\phi(t_k + 2\tau) - 2\phi(t_k + \tau) - \phi(t_k)]^2 \right\rangle \quad (\text{F.4})$$

This leads us to point to the connection of the Allan variance to the auto-covariance of the phase-signal defined as $C(\tau) = \langle \phi(t_k + \tau)\phi(t_k) \rangle$. Thereby, we can write

$$\sigma^2(\tau) = \frac{2}{2\omega_0^2\tau^2} [3C(0) - 4C(\tau) + C(2\tau)] \quad (\text{F.5})$$

This can be verified by expanding the square in eq. (F.3), noting that for stationary signals $\langle \phi(t_k)^2 \rangle = \langle \phi(t_k + \tau)^2 \rangle$ etc.

In an actual experimental situation one can not perform an infinite time average as prescribed by eq. (F.3) or eq. (F.4). An estimate of $\sigma^2(\tau)$ can be found by averaging $(\bar{y}_{k+1} - \bar{y}_k)^2$ a set of experimentally measured \bar{y}_k values. Specifically, the data acquisition will have a certain bandwidth ω_{BW} and a corresponding to the temporal resolution of the equipment $\tau_{BW} = 1/\omega_{BW}$. In this case the acquired phase-values are discretised as $\phi_k = \phi(t_k)$ and adjacent indices indicating a time separation $t_{k+1} = t_k + \tau_{BW}$. This intrinsic bandwidth of the apparatus is can be tuned by summing/combining the values of n successive values and, via eq. (F.4), this leads to the definition of a modified Allan variance [Allan81]

$$\sigma_M^2(\tau) = \frac{1}{2\omega_0^2\tau^2} \frac{1}{n^2} \left\langle \left[\sum_{i=1}^n (\phi_{i+2n} - 2\phi_{i+n} + \phi_i) \right]^2 \right\rangle$$

Since, much of our experiment deals with pulsed measurements the modified Allan variance is indeed the most relevant for our analysis.

Inventory

#	type	company	product no.	specifications
1	synthesized sweep generator	Agilent	HP8341B	0.01-20 GHz, output -110--+10 dBm
2	GPS Disciplined Oscillator	Jackson	Fury GPSDO	internal OXCO, outputs: 10 MHz sine, 10 MHz square, 1 Hz tick
3	analogue microwave phase-shifter	MCE/KDI (Aeroflex)	PQ-1867	0-360°, shift time 10 ns, 9-12 GHz, max input 10 dBm, IL 0.5-2 dB @ 9.12 GHz
4	microwave amplifier	Narda (L3)	DBS-0411N630	gain 43.6 dB, max input 20 dBm, max output 31.3 dBm
5	directional coupler	Meca	780-30-9.700	7-12.4 GHz, coupling 30 dB, directivity > 17 dB, IL 0.35 dB, max RF input 47 dBm [peak 65 dBm]
6	low-barrier Schottky diode detector	Agilent	HP33330B opt. 001 and 003	0.01-18 GHz, >0.5 mV/ μ W, max input 23 dBm
7	microwave pulse modulator	Agilent	HP11720A	TTL control, 2-18 GHz, rise time <10 ns, min pulse duration 50 ns, isolation >80 dB, IL 6 dB, max RF input 20 dBm
7*	single-pole-double-throw (SPDT) PIN-diode reflective switch	AMC	SWN-RRA-2DRH-COMDEV	TTL control, 8.74-9.66 GHz, rise delay 70 ns, rise time 30 ns, isolation 51.55 dB and 50.64 dB, IL 0.91 dB and 0.75 dB, max RF input 35 dBm
8	variable attenuator	Agilent	HP8496B	DC-18 GHz, 0-110 dB attenuation, max RF input 30 dBm
9	microwave power amplifier	Kuhne	KU PA 922 XL-226	gain 22 dB, max input 25 dBm, max output 41 dBm, monitor output 0.5 V/W
10	circulator	ATM	ATc8-12.4	8-12.4 GHz, isolation 22 dB, IL 0.35 dB, max RF input 33 dBm [peak 30 dBm]
11	high power RF 50 Ω resistor	ATM	TO516	DC-12.4 GHz, max RF input 7 dBm
12	low loss coaxial cable assembly	ATM	CF-300-SM-SMR	DC-18 GHz, 0.76 m, impedance 50 Ω , SMA connectorised, total losses in cable 0.56 dBm @ 9.192 GHz (0.22 dB in connector + 0.45 dBm/m in cable)
13	SMA to wave-guide adaptor	???	???	???

Table G.1: List of items in the microwave setup cf. Fig. 10.16

#	type	company	product no.	specifications
1	low loss coaxial cable assembly	Huber & Suhner	Sucoflex 104P	DC-26.5 GHz, m, impedance 50 Ω , SMA connectorised, losses in cable 1.04 dB/m @ 9 GHz
2	crystal detector	Agilent	HP423A	bla
3	microwave hermistor	Agilent	HP8438B	
4	power meter	Agilent	HP432A	
5				
6				

Table G.2: List of microwave items on stock in the lab

Experimental techniques

H.0.1 Background field nulling

We have tried two methods for cancelling or *nulling* the background magnetic field from the earth and magnetic elements in the setup. In both cases we monitor the splitting of the m_F levels of the $F = 4$ ground-state at various settings of the compensating coils along each spatial direction. The first approach is to monitor the frequency shift of particular microwave transition w.r.t. the clock frequency for different compensating coil currents and then deduce when the shift is minimal. At this coil setting the field is optimally compensated. Practically, we sweep the microwave frequency over some range ($\equiv 300$ kHz) where we expect the shifted transition frequency to be and mark the time during the sweep that the phase-shift makes a step. The step indicates that a fraction of the atoms have been transferred to the $F = 3$ ground level and from the time that it occurs we can infer the frequency of the transition. Ideally, we would observe transitions between high m_F states as these experience that largest shift $\delta\nu \propto m_F$, however these couple weakly and are hard to resolve. Instead we rely on π transitions between either $m_F = \pm 1$ or ± 2 levels. This in turn means that the frequency resolution is rather low and since the steps are still quite weak the method gives only a rough estimate of the compensation current.

We get a more precise estimate of the coil currents for the B-field nulling, by sweeping the microwave frequency over a somewhat larger range ($\equiv 1$ MHz) covering the whole multiplet of microwave transitions. The phase-shift of $F = 4$ atoms steadily reduces during the a period of the sweep as different m_F π transitions come into resonance (see fig. H.2). The duration of the “ $F = 4$ depletion period” indicates the frequency spread of the magnetic sub-levels, hence the shorter the period the smaller the B-field. We approximate the phase-shift step by an error-function¹.

¹ $\text{erf}(\sqrt{2}(x - x_0)/w) = \frac{2a}{\sqrt{2\pi}} \int_0^x e^{2(u-x_0)^2/w^2} du$

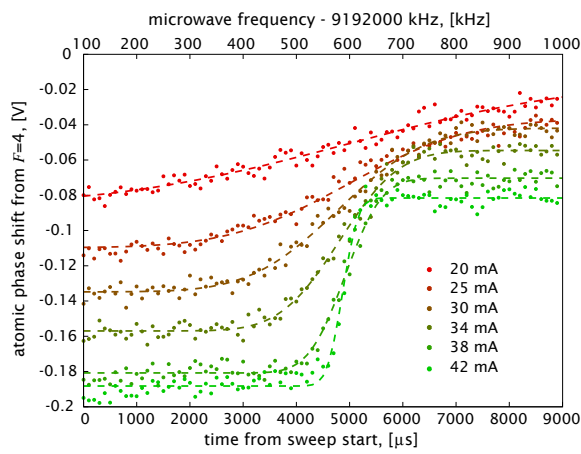


Figure H.1: Atomic phase-shift from $F=4$ atoms while microwave frequency is swept across the manifold of ground state transition frequencies.

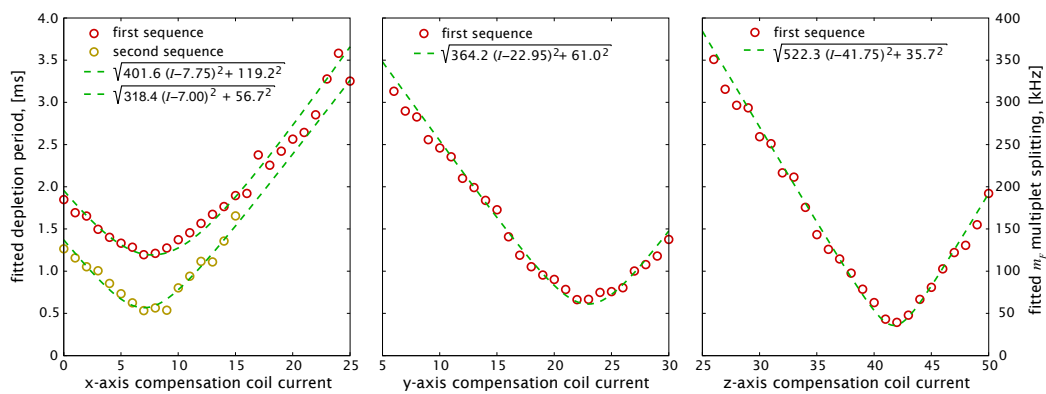
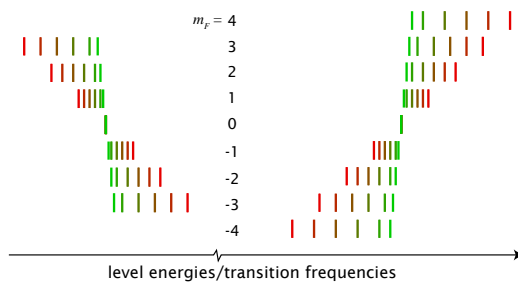


Figure H.2: Background magnetic field vs. compensating coil currents

List of Figures

1.1	Quantum uncertainty in spectroscopy	1
1.2	Quantum uncertainty in spectroscopy using a SSS	2
1.3	QND interaction between light and atoms	3
2.1	Probe beam geometry	19
2.2	Sketch of MZI	23
2.3	Photon pseudo-spin transformation in ideal MZI	25
2.4	Sketch of realistic MZI	27
2.5	Photon pseudo-spin transformation in a realistic MZI	28
2.6	MZI SNR scaling with probe arm loss	30
3.1	Atomic sample geometry	31
3.2	Realistic atomic sample and probe beam geometry	33
3.3	Cs level scheme	34
3.4	Bloch sphere representation	36
3.5	Projection noise on the Bloch Sphere	39
3.6	Dicke state decomposition of product states	40
3.7	Correction factor for total ensemble noise	41
3.8	Squeezed pseudo-spin state on the Bloch-sphere	42
3.9	Simple SSS criterion squeezed states	43
3.10	Pseudo-spin angular uncertainty	43
4.1	Diagram of the light-atom interaction	49
4.2	Phase-shift and absorption on D1-line	53
4.3	Phase-shift and absorption on D2-line	53
4.4	Evolution of level population during probing	55
4.5	Excitation and decay channels affecting decoherence	59
4.6	Proportions of quasi-elastic and inelastic scattering to total scattering on D1-line	63
4.7	Mean pseudo-spin change due to photon scattering on D1-line	64
4.8	Variance of pseudo-spin after photon scattering on D1-line	64
4.9	Proportions of quasi-elastic and inelastic scattering to total scattering on D2-line	65
4.10	Mean pseudo-spin change due to photon scattering on D2-line	65
4.11	Variance of pseudo-spin after photon scattering on D2-line	66
5.1	Joint atomic and photonic probability distribution after QND interaction: Different measurement outcomes	75
5.2	Joint atomic and photonic probability distribution after QND interaction: Different coupling strengths	76
5.3	Joint atomic and photonic probability distribution after QND interaction: Different SNL	76
5.4	Optimal decoherence and squeezing parameter for simplified relation for the coupling constant	78

5.5	Phase-shift and light-shift on D2-line with monochromatic MZI	79
5.6	Phase-shift and light-shift on D1-line	79
5.7	Phase-shift and light-shift on D2-line with dichromatic 1-input MZI	83
5.8	Phase-shift and light-shift on D2-line with dichromatic 2-input MZI	84
5.9	Coupling constant factor vs. probe detuning on D1-line for 1 and 2-input MZI	85
5.10	Coupling constant factor vs. probe detuning on D2-line for 1 and 2-input MZI	86
5.11	Noise of output \hat{f}_z vs. probe detunings on the D2-line in dichromatic 1-input MZI	87
5.12	Noise of output \hat{f}_z vs. probe detunings on the D2-line in dichromatic 2-input MZI	87
5.13	Squeezing vs. probe detunings on the D2-line in dichromatic 1-input MZI	87
5.14	Squeezing vs. probe detunings on the D2-line in dichromatic 2-input MZI	88
6.1	Shot noise influence on MZI fringe	90
6.2	Amplitude noise influence on MZI fringe	91
6.3	Phase noise influence on MZI fringe	92
6.4	Acoustic noise influence on MZI fringe	93
7.1	Screen-shot of DIO64 pulse timing program	102
7.2	Layout of control system	103
8.1	Probe laser spectra (23-24/08/07)	106
8.2	Intensity noise spectrum of dichromatic beam (19-20/05/08)	106
8.3	Probe laser layout for absorption saturation locking and 1-input MZI	107
8.4	Probe detunings/frequencies in absorption saturation locking scheme	108
8.5	Power spectrum of beat-note of two absorption saturation locked lasers	109
8.6	Beat-note locking scheme and test setup	110
8.7	Modified Allan deviation of phase-difference of two beat-note locked lasers	110
8.8	Power spectrum of beat-note signal of two beat-note locked lasers	111
8.9	Power spectrum of probe laser intensity noise	112
8.10	Probe laser layout for beat-note locking and 1 or 2-input MZI	113
8.11	Probe detunings/frequencies in beat note locking scheme	113
8.12	Raw detector traces recorded on DSO and integration matrices	115
8.13	Pulse detection power spectrum for symmetric integration windows	116
8.14	Pulse detection power spectrum for non-symmetric integration windows	117
8.15	Basic layout of 1-input MZI	120
8.16	Basic layout of 2-input MZI	121
8.17	Pulsed interference fringe (16/4/08)	123
8.18	Mode matching MZI inputs (2/4/07)	124
8.19	Pulsed interference fringes for two probe colours in 2-input MZI	125
8.20	Locking scheme with counter-propagating off-resonant CW locking laser	126
8.21	Locking scheme with co-propagating off-resonant modulated locking laser	127
8.22	Signal properties in MZI AC-locking circuits	128
8.23	Comparing the sum output signal in the 1 and 2-input MZI	128
8.24	Locking scheme with MZI path-length wiggling	129
8.25	Probe power balancing by MZI path-length wiggling (26/11/09)	130
8.26	Setup for generating reference pulses from locking laser beam	132

8.27	Raw detector traces of probe pulses with reference pulses (15/9/07)	133
8.28	Shot noise in 1-input MZI with and without reference pulses (15/9/07)	133
8.29	Shot noise scaling with photon number in 1-input MZI with reference pulses (15/9/07)	135
8.30	Shot noise scaling with photon number in 2-input MZI (1/8/08)	136
8.31	Shot noise scaling with photon number in 2-input MZI (29/9/09)	136
9.1	Vacuum setup	139
9.2	CAMOT screen-shot	140
9.3	MOT laser setup	141
9.4	MOT and FORT setup	142
9.5	Alignment of FORT waist	145
9.6	CCD camera fluorescence image of FORT	146
9.7	Dipole trap lifetime (05/06/08)	148
9.8	Directly measured optical depth (11/12/06)	148
9.9	Trap oscillations induced by release and recapture (10/6/05)	150
9.10	Trap oscillation frequency vs. trapping laser power (10/6/05)	151
9.11	Trap temperature measured by free expansion rate (8/6/05)	152
9.12	FORT laser light-shift on Probe transitions (12-13/2/08)	154
10.1	State preparation setup (optical pumping beam and microwave antenna)	158
10.2	Principle of optical pumping scheme	158
10.3	Optical pumping setup	159
10.4	Optical pumping sequence	160
10.5	Sloshing atomic sample after optical pumping (17/2/06)	160
10.6	Optical pumping efficiency vs. pumping time (4/12/07)	161
10.7	Optical pumping efficiency vs. laser detuning (4/12/07)	162
10.8	Optical pumping efficiency vs. pump beam polarisation (21/7/06)	163
10.9	Optical pumping efficiency vs. magnetic bias field strength (13/3/06)	163
10.10	Pseudo-spin rotations on the Bloch-sphere due to interaction with microwaves	166
10.11	Ramsey spectroscopy experimental sequence	167
10.12	Bloch vector rotations in a Ramsey sequence	167
10.13	Pseudo-spin z-component in frequency domain Ramsey spectroscopy	168
10.14	Ramsey spin-echo spectroscopy experimental sequence	169
10.15	Bloch vector rotations in a Ramsey sequence with spin-echo pulse	170
10.16	Layout of microwave setup	172
10.17	Microwave antenna radiation pattern (26/1/06)	173
10.18	Microwave phase-shifter characteristics	175
10.19	Schematic of new microwave source	176
10.20	Power drifts in cables	177
10.21	Allan deviations for beat signal between microwave sources (8/10/09)	179
10.22	Atomic phase-shift from $F = 4$ during sweep of microwave synthesiser frequency (29/7/06)	181
10.23	Rabi oscillations and frequency vs. microwave frequency (11/1/06)	182
10.24	Rabi spectroscopy of microwave transition (27/3/06 and 7/2/08)	183
10.25	State-purification (blow-away)	184
10.26	Ramsey fringes in frequency domain (5/2/08)	185
10.27	FORT light-shift of Ramsey fringe phase (5/2/08)	185
10.28	T_1 time measured as decay of Rabi fringe amplitude (10/2/06)	187
10.29	T_2 time measured as decay of Ramsey fringe amplitude (5/2/08)	188
10.30	T_2' and T_2^* times measured as decay of Ramsey spin-echo fringe amplitudes (22/2/08)	188

11.1	Long time non-destructive observation observation of Rabi oscillations (5/7/07)	191
11.2	Probe light-shift perturbation of Rabi oscillations (5/11/07)	193
11.3	Sequence for Rabi oscillations perturbed by probe pulse train	193
11.4	Theoretical pseudo-spin evolution during probed Rabi oscillations	194
11.5	Probe light shift perturbation of Rabi oscillations (5/7/07)	196
11.6	Ramsey spectroscopy sequence with probe light-shift	197
11.7	Probe light shift on Ramsey fringes (25/9/07)	198
11.8	Re-phasing of probe induced light-shift using Ramsey spin-echo technique	199
11.9	Probe light shift re-phasing in Ramsey spin-echo sequence (15/11/07)	200
11.10	Ramsey spin-echo fringes for different light-shift re-phasing pulse separations (31/1/08)	201
11.11	Light-shift re-phasing for determining trap-oscillation frequency (30/10/07)	203
11.12	Ramsey spin-echo amplitude vs. light-shift pulse separation for different pulse photon numbers (1/2/08)	204
11.13	Optimal simulation light-shift phase versus probe power (1/2/08)	205
11.14	Ramsey spin-echo sequence for characterising dichromatic probe light-shift cancellation	206
11.15	Light shift cancellation in Ramsey fringes in 2-input MZI for different relative probe detunings (11/11/08)	206
11.16	Light shift cancellation in Ramsey fringes in 1-input MZI for different relative probe detunings (18/11/08)	208
11.17	Surface plots of dichromatic probe cancellation of light-shift in different input configuration (11/11/08)	208
11.18	Surface plot of dichromatic probe cancellation of light-shift in same input configuration (18/11/08)	209
11.19	Ramsey spin-echo fringes for different probe powers	210
11.20	Estimating spontaneous scattering rate vs. probe power (3/3/08)	210
11.21	Estimating spontaneous scattering rate vs. probe detuning, relying on light-shift re-phasing (20/12/07)	210
11.22	Estimating spontaneous scattering rate vs. probe power, relying on light-shift cancellation (7/7/08)	211
12.1	Determining the $\pi/2$ pulse duration	214
12.2	Experimental sequence for the QND measurement	215
12.3	Recycling the atomic sample (14/11/07)	215
12.4	Predictions for analysis of correlated pulses	218
12.5	Raw QND and power reference detector signal for 1-input MZI configuration with reference pulses (19/11/07)	226
12.6	Plot of variances for different pulses and combinations in 1-input MZI (19/11/07)	227
12.7	Plot of correlated and uncorrelated pulse variances with different atom-number scaling in 1-input MZI (19/11/07)	228
12.8	Raw QND and power reference detector signal for 2-input MZI configuration (1/8/08)	230
12.9	Phase offset to balance probe signals in 2-input MZI	230
12.10	Correlation matrix for pulses within each segment (1/8/08)	231
12.11	Plot of variances for different pulses and combinations in 2-input MZI (1/8/08)	232
12.12	Plot of correlated and uncorrelated pulse variances with different atom-number scaling in 2-input MZI (1/8/08)	232
12.13	Experimental squeezing vs. decoherence (1/8/08)	234

12.14	Plot of shot-noise and projection noise derived from pulse variances and phase-shift (1/8/08)	234
12.15	Correlation factor between first and subsequent pulses together with spontaneous scattering rate (1/8/08)	236
12.16	Correlation plot (1/8/08)	237
12.17	Plot of variances for different pulses and combinations in 2-input equivalent MZI (27/11/09)	240
12.18	Plot of correlated and uncorrelated pulse variances with different atom-number scaling in 2-input equivalent MZI (27/11/09)	240
12.19	Plot of shot-noise and projection noise derived from pulse variances and phase-shift in 2-input equivalent MZI (27/11/09)	241
12.20	Highest mean atom number for different pulse separation data sets using 11 bins (27/11/09)	242
12.21	Projection noise for different pulse separations (27/11/09)	242
12.22	Squeezing for different pulse separations (27/11/09)	243
12.23	Intuitive tomography approach	244
12.24	Oscillating mean population number difference in intuitive tomography sequence (1/7/09)	244
12.25	Illustration of microwave intensity spread influence on tomography	245
12.26	Alternative tomography approach	246
12.27	Raw high-atom number data points for tomography measurement (3/11/09)	247
12.28	Total noise level in tomography measurement (3/11/09)	248
12.29	Noise reduction in tomography measurement (3/11/09)	248
12.30	Pulse mean values in tomography measurement (3/11/09)	249
15.1	Ramsey clock-sequence with coherent state	259
15.2	Ramsey clock-sequence with spin-squeezed state	260
A.1	Fields incident on a beamsplitter	269
A.2	Fields propagating without disturbance	270
A.3	Losses in one of a pair of fields	270
A.4	Model of the imperfect mode overlap of two modes on a beamsplitter	271
A.5	Sketch of SBI	276
B.1	Actual uncertainty of arbitrary product-state pseudo-spin components	280
B.2	Excitation and decay channels affecting decoherence	283
C.1	Distribution of noise reduction and atomic density	285
C.2	Original and reduced projection noise distribution	286
C.3	Distribution of noise reduction and non-decohered atomic density	287
C.4	effective ensemble noise and squeezing for different probe beam to atomic sample waist ratios	289
C.5	Total ensemble noise and squeezing for different probe beam and atomic sample waists	290
E.1	Norm squared error between simulated and experimental data for different values of simulation parameters	303
E.2	Light shift re-phasing sequence	304
H.1	Atomic phase-shift during microwave frequency sweep (10/11/06)	312
H.2	Background magnetic field vs. compensating coil currents (19/9/07)	312

Bibliography

- [Allan66] David W. Allan, *Statistics of Atomic Frequency Standards*, Proc. IEEE, **54**, 221 (1966)
- [Allan81] David W. Allan and James A. Barnes, *A modified "Allan variance" with increased oscillator characterization ability*, in *Proceedings of the 35th Annual Frequency Control Symposium* (1981), 470–474
- [Andersen04] Mikkel F. Andersen, Ariel Kaplan, Tzahi Grünzweig, and Nir Davidson, *Suppression of dephasing of optically trapped atoms*, Phys. Rev. A, **70**, 013405 (2004)
- [Appel07] Jürgen Appel, *A Light-Atom Quantum Interface based on Electromagnetically Induced Transparency*, Ph.D. thesis, Department of Physics and Astronomy, University of Calgary, Calgary, Alberta, Canada (2007)
- [Appel08] Jürgen Appel, Andrew MacRae, and Alex I. Lvovsky, *Versatile digital GHz phase lock for external cavity diode lasers*, arXiv:0809.3607 (2008)
- [Appel09] Jürgen Appel, Patrick J. Windpassinger, Daniel Oblak, Ulrich B. Hoff, Niels Kjærgaard, and Eugene S. Polzik, *Mesoscopic atomic entanglement for precision measurements beyond the standard quantum limit*, Proc. Natl. Acad. Sci. USA (2009)
- [Arditi78] Maurice Arditi, Isao Hirano, and Pierre Tougne, *Optical pumping of a caesium beam and detection of the 0-0 'clock' transition*, J. Phys. D: Applied Physics, **11**(18), 2465 (1978)
- [Audoin92] Claude Audoin, *Caesium Beam Frequency Standards: Classical and Optically Pumped*, Metrologia, **29**(2), 113 (1992)
- [Audoin01] Claude Audoin and Bernard Guinot, *The measurement of time: time, frequency, and the atomic clock*, Cambridge: Cambridge Univ. Press (2001)
- [Avila87] Gualberto Avila, Vincent Giordano, Vincent Candelier, Emeric de Clercq, Genevieve Theobald, and Pierre Cerez, *State selection in a cesium beam by laser-diode optical pumping*, Phys. Rev. A, **36**(8), 3719 (1987)
- [Aytür90] Orhan Aytür and Prem Kumar, *Pulsed twin beams of light*, Phys. Rev. Lett., **65**(13), 1551 (1990)
- [Bachor04] Hans A. Bachor and Timothy C. Ralph, *A Guide to Experiments in Quantum Optics*, Weinheim: Wiley-VCH, 2nd edn. (2004)

- [Barber08] Z. W. Barber, J. E. Stalnaker, N. D. Lemke, N. Poli, C. W. Oates, T. M. Fortier, S. A. Diddams, L. Hollberg, C. W. Hoyt, A. V. Taichenachev, and V. I. Yudin, *Optical Lattice Induced Light Shifts in an Yb Atomic Clock*, Phys. Rev. Lett., **100**(10), 103002 (2008)
- [Barnes71] James A. Barnes, Andrew R. Chi, Leonard S. Cutler, Daniel J. Healey, David B. Leeson, Thomas E. McGunigal, James A. Mullen Jr., Warren L. Smith, Richard L. Sydnor, Robert F. C. Vessot, and Gernot M. R. Winkler, *Characterization of Frequency Stability*, IEEE Transactions of Instrumentation and Measurement, **20**, 105 (1971)
- [Bertet02] Patrice Bertet, Alexia Auffeves, Paolo Maioli, Stefano Osnaghi, Tristan Meunier, Michel Brune, Jean-Michel Raimond, and Serge Haroche, *Direct Measurement of the Wigner Function of a One-Photon Fock State in a Cavity*, Phys. Rev. Lett., **89**(20), 200402 (2002)
- [Bjorklund80] Gary C. Bjorklund, *Frequency-modulation spectroscopy: a new method for measuring weak absorptions and dispersions*, Opt. Lett., **5**, 15 (1980)
- [Bjorklund83] Gary C. Bjorklund, Marc D. Levenson, W. Lenth, and C. Ortiz, *Frequency Modulation (FM) Spectroscopy*, Appl. Phys. B, **32**, 145 (1983)
- [Bloch46] Felix Bloch, *Nuclear Induction*, Phys. Rev., **70**(7-8), 460 (1946)
- [Bohm51] David Bohm, *Quantum Theory*, New York: Prentice Hall (1951)
- [Bouchoule02a] Isabelle Bouchoule and Klaus Mølmer, *Preparation of spin-squeezed atomic states by optical-phase-shift measurement*, Phys. Rev. A, **66**, 043811 (2002)
- [Bouchoule02b] —, *Spin squeezing of atoms by the dipole interaction in virtually excited Rydberg states*, Phys. Rev. A, **65**, 041803 (2002)
- [Braginsky74] Vladimir B. Braginsky and Yurii I. Vorontsov, *Quantum-mechanical limitations in macroscopic experiments and modern experimental technique*, Usp. Fiz. Nauk., **114**, 41 (1974)
- [Braginsky77] Vladimir B. Braginsky, Yurii I. Vorontsov, and Farid Ya Khalili, Zh. Eksp. Teor. Fiz., **73**, 1340 (1977)
- [Braginsky80] Vladimir B. Braginsky, Yuri I. Vorontsov, and Kip S. Thorne, *Quantum nondemolition measurements*, Science, **209**, 547 (1980)
- [Braginsky96] Vladimir B. Braginsky and Farid Ya Khalili, *Quantum nondemolition measurements: the route from toys to tools*, Rev. Mod. Phys., **68**(1), 1 (1996)
- [Bransden83] Brian Harold Bransden and Charles Jean Joachain, *Physics of Atoms and Molecules*, Harlow: Longman (1983)
- [Bruckmeier97] Robert Bruckmeier, Hauke Hansen, Stephan Schiller, and Jürgen Mlynek, *Realization of a Paradigm for Quantum Measurements: The Squeezed Light Beam Splitter*, Phys. Rev. Lett., **79**(1), 43 (1997)

- [Buchkremer00] F. B. J. Buchkremer, R. Dumke, Ch. Buggle, G. Birkl, and W. Ertmer, *Low-cost setup for generation of 3 GHz frequency difference phase-locked laser light*, *Review of Scientific Instruments*, **71**(9), 3306 (2000)
- [Chaudhury07] Souma Chaudhury, Seth Merkel, Tobias Herr, Andrew Silberfarb, Ivan H. Deutsch, and Poul S. Jessen, *Quantum Control of the Hyperfine Spin of a Cs Atom Ensemble*, *Physical Review Letters*, **99**(16), 163002 (2007)
- [Choi07] Jai Min Choi and D Cho, *Elimination of inhomogeneous broadening for a ground-state hyperfine transition in an optical trap*, *J. Phys. Conference Series*, **80**(1), 012037 (2007)
- [Chu86] Steven Chu, J. E. Bjorkholm, A. Ashkin, and A. Cable, *Experimental observation of optically trapped atoms*, *Phys. Rev. Lett.*, **57**, 2631 (1986)
- [Cirac93] J. Ignacio Cirac, A. Scott Parkins, Rainer Blatt, and Peter Zoller, *squeezed states of the motion of a trapped ion*, *Phys. Rev. Lett.*, **70**(5), 556 (1993)
- [Clercq84] Emeric de Clercq, Michel de Labachellerie, Gualberto Avila, Pierre Cerez, and Michel Tetu, *Laser diode optically pumped caesium beam*, *J. Phys. France*, **45**(2), 239 (1984)
- [Collett70] Edward Collett, *Stokes Parameters for Quantum Systems*, *Am. J. Phys.*, **38**(5), 563 (1970)
- [Dick90] G. J. Dick, J. D. Prestage, C. A. Greenhall, and L. Maleki, *Local Oscillator Induced Degradation of Medium-Term Stability in Passive Atomic Frequency Standards*, in *Proceedings of the 22nd Annual Precise Time and Time Interval (PTTI) Applications and Planning Meeting, Vienna, Virginia (1990)*, no. No. 3116 in NASA Conference Publication, p. 487
- [Dicke54] Robert H. Dicke, *Coherence in Spontaneous Radiation Processes*, *Phys. Rev.*, **93**(1), 99 (1954)
- [Dirac58] Paul A.M. Dirac, *Quantum Mechanics*, Oxford Univ. Press (1958)
- [Drever83] Ron W. P. Drever, Jan L. Hall, F. V. Kowalski, J. Hough, G. M. Ford, A. J. Munley, and H. Ward, *Laser phase and frequency stabilization using an optical resonator*, *Appl. Phys. B: Lasers and Optics*, **31**(2), 97 (1983)
- [Drewsen94] Michael Drewsen, Philippe Laurent, Aziz Nadir, Giorgio Santarelli, Andre Clairon, Yvan Castin, Delphine Grison, and Christophe Salomon, *Investigation of sub-Doppler cooling effects in a cesium magneto-optical-trap*, *Appl. Phys. B*, **59**, 283 (1994)
- [Duan02] Lu-Ming Duan, J. Ignacio Cirac, and Peter Zoller, *Three-dimensional theory for interaction between atomic ensembles and free-space light*, *Phys. Rev. A*, **66**, 023818 (2002)
- [Echaniz05] Sebastian R. de Echaniz, Morgan W. Mitchell, Marcin Kubasik, Marco Koschorreck, Herbert Crepaz, Jürgen Eschner, and Eugene S. Polzik, *Conditions for spin squeezing in a cold 87Rb ensemble*, *J. Opt. B*, **7**, S548 (2005)

- [Estève08] Jerome Estève, Christian Gross, Andreas Weller, Stefano Giovanazzi, and Markus Oberthaler, *Squeezing and entanglement in a Bose-Einstein condensate*, *Nature*, **455**, 1216 (2008)
- [EU88] EU, *Commission Regulation (EEC) No 1677/88 laying down quality standards for cucumbers*, *Official Journal of the European Union*, **L150**, 21 (1988)
- [Featonby98] P. D. Featonby, C. L. Webb, G. S. Summy, C. J. Foot, and K. Burnett, *Observation of light-induced coherence loss in a caesium atomic fountain*, *J. Phys. B*, **31**, 375 (1998)
- [Feynman57] Richard P. Feynman, Jr. Frank L. Vernon, and Robert W. Hellwarth, *Geometrical Representation of the Schrödinger Equation for Solving Maser Problems*, *J. Appl. Phys.*, **28**(1), 49 (1957)
- [Figl06] Cristina Figl, Laurent Longchambon, Matthew Jeppesen, Michael Kruger, Hans A. Bachor, Nicholas P. Robins, and John D. Close, *Demonstration and characterization of a detector for minimally destructive detection of Bose condensed atoms in real time*, *Appl. Opt.*, **45**, 3415 (2006)
- [Flambaum08] Victor V. Flambaum, Vladimir A. Dzuba, and Andrei Derevianko, *Magic Frequencies for Cesium Primary-Frequency Standard*, *Phys. Rev. Lett.*, **101**(22), 220801 (2008)
- [Fock28] Vladimir A. Fock, *Verallgemeinerung und Lösung der Diracschen statistischen Gleichung*, *Zeitschrift für Physik*, **49**(5-6), 339 (1928)
- [Fraleigh95] John B. Fraleigh and Raymond A. Beauregard, *Linear Algebra*, Reading: Addison-Wesley, 3rd edn. (1995)
- [Freeman93] Michael J. Freeman, Hailin Wang, Duncan G. Steel, Richard R. Craig, and Don R. Scifres, *Wavelength-tunable amplitude-squeezed light from a room-temperature quantum-well laser*, *Opt. Lett.*, **18**, 2141 (1993)
- [Friberg92] Stephen R. Friberg, Susumu Machida, and Yoshihisa Yamamoto, *Quantum-nondemolition measurement of the photon number of an optical soliton*, *Phys. Rev. Lett.*, **69**(22), 3165 (1992)
- [gam06] *Ion Pumping of Cesium and Rubidium*, Tech. Rep. 00.003.971, Gamma Vacuum (2006)
- [Gerbier06] Fabrice Gerbier, Simon Fölling, Artur Widera, Olaf Mandel, and Immanuel Bloch, *Probing Number Squeezing of Ultracold Atoms across the Superfluid-Mott Insulator Transition*, *Physical Review Letters*, **96**(9), 090401 (2006)
- [Geremia04] John M. Geremia, John K. Stockton, and Hideo Mabuchi, *Real-Time Quantum Feedback Control of Atomic Spin-Squeezing*, *Science*, **304**(5668), 270 (2004), <http://www.sciencemag.org/cgi/reprint/304/5668/270.pdf>
- [Geremia08] —, *Retraction*, *Science*, **321**(5888), 489a (2008)
- [Glauber63a] Roy J. Glauber, *Coherent and Incoherent States of the Radiation Field*, *Phys. Rev.*, **131**(6), 2766 (1963)

- [Glauber63b] —, *The Quantum Theory of Optical Coherence*, Phys. Rev., **130**(6), 2529 (1963)
- [Grangier91] Philippe Grangier, Jean-Francois Roch, and Gérard Roger, *Observation of backaction-evading measurement of an optical intensity in a three-level atomic nonlinear system*, Phys. Rev. Lett., **66**(11), 1418 (1991)
- [Grimm00] Rudi Grimm, Matthias Weidemüller, and Yurii B. Ovchinnikov, *Optical Dipole Traps for Neutral Atoms* (2000)
- [Hahn50] Erwin L. Hahn, *Spin Echoes*, Phys. Rev., **80**(4), 580 (1950)
- [Hald99] Jan Hald, Jens L. Sørensen, Christian Schori, and Eugene S. Polzik, *Spin squeezed atoms: A macroscopic entangled ensemble created by light*, Phys. Rev. Lett., **83**(7), 1319 (1999)
- [Hald00] Jan Hald, *Spin Squeezing in a Cold Atomic Ensemble*, Ph.D. thesis, University of Aarhus (2000)
- [Hall81] John L. Hall, Leo Hollberg, Thomas Baer, and Hugh G. Robinson, *Optical heterodyne saturation spectroscopy*, Appl. Phys. Lett., **39**(9), 680 (1981)
- [Hamilton34] William R. Hamilton, *On a General Method in Dynamics; by which the Study of the Motions of all free Systems of attracting or repelling Points is reduced to the Search and Differentiation of one central Relation, or characteristic Function*, Philosophical Transactions of the Royal Society, **part II**, 247 (1834)
- [Hamilton35] —, *Second Essay on a General Method in Dynamics*, Philosophical Transactions of the Royal Society, **part I**, 94 (1835)
- [Hammerer09] Klemens Hammerer, Anders S. Sørensen, and Eugene S. Polzik, *Quantum interface between light and atomic ensembles* (2009), submitted to Rev. Mod. Phys.
- [Hansen01] Hauke Hansen, Thomas Aichele, Christian Hettich, Peter Lodahl, Alex I. Lvovsky, Jürgen Mlynek, and Stephan Schiller, *Ultrasensitive pulsed, balanced homodyne detector: application to time-domain quantum measurements*, Opt. Lett., **26**(21), 1714 (2001)
- [Heidmann87] Antoine Heidmann, R. J. Horowicz, Serge Reynaud, Elisabeth Giacobino, Claude Fabre, and G. Camy, *Observation of Quantum Noise Reduction on Twin Laser Beams*, Phys. Rev. Lett., **59**(22), 2555 (1987)
- [Heinzen90] Daniel J. Heinzen and David J. Wineland, *Quantum-limited cooling and detection of radio-frequency oscillations by laser-cooled ions*, Phys. Rev. A, **42**(5), 2977 (1990)
- [Holland90] Murray J. Holland, Matthew J. Collett, Daniel F. Walls, and Marc D. Levenson, *Nonideal quantum nondemolition measurements*, Phys. Rev. A, **42**(5), 2995 (1990)
- [Imoto85] Nobuyuki Imoto, Hermann A. Haus, and Yoshihisa Yamamoto, *Quantum nondemolition measurement of the photon number via the optical Kerr effect*, Phys. Rev. A, **32**(4), 2287 (1985)

- [Inoue92] Shuichiro Inoue, Hitoshi Ohzu, Susumu Machida, and Yoshihisa Yamamoto, *Quantum correlation between longitudinal-mode intensities in a multimode squeezed semiconductor laser*, Phys. Rev. A, **46**(5), 2757 (1992)
- [Itano93] Wayne M. Itano, James C. Bergquist, John J. Bollinger, Jonathan M. Gilligan, Daniel J. Heinzen, Fred L. Moore, Mark G. Raizen, and David J. Wineland, *Quantum projection noise: Population fluctuations in two-level systems*, Phys. Rev. A, **47**(5), 3554 (1993)
- [Jackson99] John David Jackson, *Classical Electrodynamics*, New York: John Wiley & Sons, Inc, 3rd edn. (1999)
- [Jau04] Y.-Y. Jau, E. Miron, A. B. Post, N. N. Kozuma, and W. Happer, *Push-Pull Optical Pumping of Pure Superposition States*, Phys. Rev. Lett., **93**(16), 160802 (2004)
- [Jo07] G.-B. Jo, J.-H. Choi, C. A. Christensen, Y.-R. Lee, T. A. Pasquini, W. Ketterle, and D. E. Pritchard, *Matter-Wave Interferometry with Phase Fluctuating Bose-Einstein Condensates*, Physical Review Letters, **99**(24), 240406 (2007)
- [Julsgaard01] Brian Julsgaard, Alexander Kozhekin, and Eugene S. Polzik, *Experimental long-lived entanglement of two macroscopic objects*, Nature, **413**, 400 (2001)
- [Kaplan02] Ariel Kaplan, Mikkel F. Andersen, and Nir Davidson, *Suppression of inhomogeneous broadening in rf spectroscopy of optically trapped atoms*, Phys. Rev. A, **66**(4), 045401 (2002)
- [Katori99] Hidetoshi Katori, Tetsuya Ido, and Makoto Kuwata-Gonokami, *Optimal Design of Dipole Potentials for Efficient Loading of Sr Atoms*, J. Phys. Soc. Japan, **68**(8), 2479 (1999)
- [Kitagawa93] Masahiro Kitagawa and Masahito Ueda, *Squeezed spin states*, Phys. Rev. A, **47**, 5138 (1993)
- [Kjærgaard08] Niels Kjærgaard, *Effective Atomic Number* (2008), work Note
- [Kuhr05] Stefan Kuhr, Wolfgang Alt, Igor Dotsenko, Yevhen Miroshnychenko, Arno Raushenbeutel, and Dieter Meschede, *Analysis of dephasing mechanisms in a standing-wave dipole trap*, Phys. Rev. A, **72**, 023406 (2005)
- [Kuzmich98] Alex Kuzmich, Nicholas P. Bigelow, and Leonard Mandel, *Atomic quantum non-demolition measurements and squeezing*, Eur. Phys. Lett., **42**(5), 481 (1998)
- [Kuzmich99] Alex Kuzmich, Leonard Mandel, John Janis, York E. Young, Renato Ejnisman, and Nicholas P. Bigelow, *Quantum nondemolition measurements of collective atomic spin*, Phys. Rev. A, **60**(3), 2346 (1999)
- [Kuzmich00] Alex Kuzmich, Leonard Mandel, and Nicholas P. Bigelow, *Generation of Spin Squeezing via Continuous Quantum Nondemolition Measurement*, Phys. Rev. Lett., **85**(8), 1594 (2000)

- [Lambrecht95] Astrid Lambrecht, Jean Michel Courty, Serge Reynaud, and Elisabeth Giacobino, *Cold atoms: A new medium for quantum optics*, Appl. Phys. B., **60**(2-3), 129 (1995)
- [Landau31] Lev D. Landau and Rudolf Peierls, *Erweiterung des Unbestimmtheitsprinzips für die relativistische Quantentheorie*, Z. Phys., **69**, 56 (1931)
- [Leibfried04] D. Leibfried, M. D. Barrett, T. Schaetz, J. Britton, J. Chiaverini, W. M. Itano, J. D. Jost, C. Langer, and D. J. Wineland, *Toward Heisenberg-Limited Spectroscopy with Multiparticle Entangled States*, Science, **304**(5676), 1476 (2004), <http://www.sciencemag.org/cgi/reprint/304/5676/1476.pdf>
- [Leroux09] Ian D. Leroux, Monika H. Schleier-Smith, and Vladan Vuletić, *Implementation of Cavity Squeezing of a Collective Atomic Spin*, arXiv.org:0911.4065v1 (2009), 0911.4065v1
- [Levenson85] Marc D. Levenson, Robert M. Shelby, and Stephen H. Perlmuter, *Squeezing of classical noise by nondegenerate four-wave mixing in an optical fiber*, Opt. Lett., **10**, 514 (1985)
- [Levenson93] Juan Ariel Levenson, Izo Abram, Thomas Rivera, P. Fayolle, Jean Claude Garreau, and Philippe Grangier, *Quantum optical cloning amplifier*, Phys. Rev. Lett., **70**(3), 267 (1993)
- [Lodewyck09] Jérôme Lodewyck, Philip G. Westergaard, and Pierre Lemonde, *Nondestructive measurement of the transition probability in a Sr optical lattice clock*, Phys. Rev. A, **79**(6), 061401 (2009)
- [Louchet-Chauvet09] Anne Louchet-Chauvet, Jürgen Appel, Jelmer J. Renema, Daniel Oblak, and Eugene S. Polzik, *Entanglement-assisted atomic clock beyond the projection noise limit* (2009), 0912.3895v1
- [Loudon73] Rodney Loudon, *The Quantum Theory of Light*, Oxford: Oxford Univ. Press (1973)
- [Ludlow06] Andrew D. Ludlow, Martin M. Boyd, Tanya Zelevinsky, Seth M. Foreman, Sebastian Blatt, Mark Notcutt, Tetsuya Ido, and Jun Ye, *Systematic Study of the [sup 87]Sr Clock Transition in an Optical Lattice*, Physical Review Letters, **96**(3), 033003 (2006)
- [Ludlow08] A. D. Ludlow, T. Zelevinsky, G. K. Campbell, S. Blatt, M. M. Boyd, de M. H. G. Miranda, M. J. Martin, J. W. Thomsen, S. M. Foreman, Jun Ye, T. M. Fortier, J. E. Stalnaker, S. A. Diddams, Y. Le Coq, Z. W. Barber, N. Poli, N. D. Lemke, K. M. Beck, and C. W. Oates, *Sr Lattice Clock at 1×10^{-16} Fractional Uncertainty by Remote Optical Evaluation with a Ca Clock*, Science, **319**(5871), 1805 (2008), <http://www.sciencemag.org/cgi/reprint/319/5871/1805.pdf>
- [Lye03] Jessica E. Lye, Joseph J. Hope, and John D. Close, *Non-destructive, dynamic detectors for Bose-Einstein condensates*, Phys. Rev. A, **67**, 043609 (2003)
- [MacAdam92] K. B. MacAdam, A. Steinbach, and C. Wieman, *A narrow-band tunable diode laser system with grating feedback, and a saturated absorption spectrometer for Cs and Rb*, Am. J. of Phys., **60**(12), 1098 (1992)

- [Madsen04] Lars B. Madsen and Klaus Mølmer, *Spin squeezing and precision probing with light and samples of atoms in the Gaussian description*, Phys. Rev. A, **70**, 052324 (2004)
- [Mandel95] Leonard Mandel and Emil Wolf, *Optical Coherence and Quantum Optics*, Cambridge: Cambridge Univ. Press (1995)
- [Mandl88] Franz Mandl, *Statistical Physics*, Chichester: John Wiley & Sons, Inc, 2nd edn. (1988)
- [McKeever03] J. McKeever, J. R. Buck, A. D. Boozer, A. Kuzmich, H.-C. Nägerl, D. M. Stamper-Kurn, and H. J. Kimble, *State-Insensitive Cooling and Trapping of Single Atoms in an Optical Cavity*, Phys. Rev. Lett., **90**(13), 133602 (2003)
- [Meiser08] Dominic Meiser, Jun Ye, and Murray J. Holland, *Spin squeezing in optical lattice clocks via lattice-based QND measurements*, New J. of Phys., **10**, 073014 (2008)
- [Metcalf99] Harold J. Metcalf and Peter van der Straten, *Laser Cooling and Trapping*, New York: Springer (1999)
- [Meyer01] V. Meyer, M. A. Rowe, D. Kielpinski, C. A. Sackett, W. M. Itano, C. Monroe, and D. J. Wineland, *Experimental Demonstration of Entanglement-Enhanced Rotation Angle Estimation Using Trapped Ions*, Phys. Rev. Lett., **86**(26), 5870 (2001)
- [Milburn87] Gerard J. Milburn, Marc D. Levenson, Robert M. Shelby, Stephen H. Perlmutter, Ralph G. DeVoe, and Daniel F. Walls, *Optical-fiber media for squeezed-state generation*, J. Opt. Soc. Am. B, **4**, 1476 (1987)
- [Milonni88] Peter W. Milonni and Joseph H. Eberly, *Lasers*, New York: John Wiley & Sons, Inc (1988)
- [Mølmer03] Klaus Mølmer, *Reduction of spin squeezing by atomic decay* (2003), private communications
- [Nabors90] Charles D. Nabors and Robert M. Shelby, *Two-color squeezing and sub-shot-noise signal recovery in doubly resonant optical parametric oscillators*, Phys. Rev. A, **42**(1), 556 (1990)
- [Neumann32] John von Neumann, *Mathematische Grundlagen der Quantenmechanik*, Berlin: Springer (1932)
- [Oblak04] Daniel Oblak, *Non-Destructive, Interferometric Quantum Noise Limited Measurements on Cold Caesium Atoms*, Master's thesis, Institute of Physics and Astronomy, University of Aarhus (2004)
- [Oblak05] Daniel Oblak, Plamen G. Petrov, Carlos L. Garrido Alzar, Wolfgang Tittel, Anton K. Vershovski, Jens K. Mikkelsen, Jens L. Sørensen, and Eugene S. Polzik, *Quantum-noise-limited interferometric measurement of atomic noise: Towards spin squeezing on the Cs clock transition*, Phys. Rev. A, **71**, 043807 (2005)
- [Oblak08] Daniel Oblak, Jürgen Appel, Patrick J. Windpassinger, Ulrich Busk Hoff, Niels Kjærgaard, and Eugene S. Polzik, *Echo spectroscopy of atomic dynamics in a Gaussian trap via phase imprints*, Eur. Phys. J. D, **50**, 67 (2008)

- [Orozco87] Luis A. Orozco, Mark G. Raizen, Min Xiao, Robert J. Brecha, and H. Jeff Kimble, *Squeezed-state generation in optical bistability*, J. Opt. Soc. Am. B, **4**, 1490 (1987)
- [Orzel01] C. Orzel, A. K. Tuchman, M. L. Fenselau, M. Yasuda, and M. A. Kasevich, *Squeezed States in a Bose-Einstein Condensate*, Science, **291**(5512), 2386 (2001), <http://www.sciencemag.org/cgi/reprint/291/5512/2386.pdf>
- [Pereira88] Sylvania F. Pereira, Min Xiao, H. Jeff Kimble, and Jan L. Hall, *Generation of squeezed light by intracavity frequency doubling*, Phys. Rev. A, **38**(9), 4931 (1988)
- [Petermann91] Klaus Petermann, *Laser Diode Modulation and Noise*, Klüwer academic press (1991)
- [Petrov06] Plamen G. Petrov, *Quantum noise limited light interferometry with cold trapped atoms*, Ph.D. thesis, Niels Bohr Institute (2006)
- [Petrov07] Plamen G. Petrov, Daniel Oblak, Carlos L. Garrido Alzar, Niels Kjærgaard, and Eugene S. Polzik, *Nondestructive interferometric characterization of an optical dipole trap*, Phys. Rev. A, **75**, 033803 (2007)
- [Poizat93] Jean-Philippe Poizat and Philippe Grangier, *Experimental realization of a quantum optical tap*, Phys. Rev. Lett., **70**(3), 271 (1993)
- [Poizat94] Jean-Philippe Poizat, Jean-Francois Roch, and Philippe Grangier, *Characterization of quantum non-demolition measurements in optics*, Ann. Phys. Fr., **19**, 265 (1994)
- [Press02] William H. Press, Saul A. Teukolsky, William T. Vetterling, and Brian P. Flannery, *Numerical Recipes in C++*, Cambridge: Cambridge Univ. Press, 2nd edn. (2002)
- [Ravetz05] Jerome Ravetz, *No-Nonsense Guide to Science*, New Internationalist (2005)
- [Raymer81] Michael G. Raymer and Jan Mostowski, *Stimulated Raman scattering: Unified treatment of spontaneous initiation and spatial propagation*, Phys. Rev. A, **24**(4), 1980 (1981)
- [Ricci95] L. Ricci, Matthias Weidemüller, Tilman Esslinger, A. Hemmerich, C. Zimmermann, Vladan Vuletić, W. König, and Theodor W. Hänsch, *A compact grating-stabilized diode laser system for atomic physics*, Opt. Comm., **117**(5-6), 541 (1995)
- [Richardson91] Wayne H. Richardson and Yoshihisa Yamamoto, *Quantum correlation between the junction-voltage fluctuation and the photon-number fluctuation in a semiconductor laser*, Phys. Rev. Lett., **66**(15), 1963 (1991)
- [Ries03] Jonas Ries, Björn Brezger, and Alex I. Lvovsky, *Experimental vacuum squeezing in rubidium vapor via self-rotation*, Phys. Rev. A, **68**(2), 025801 (2003)
- [Roch97] Jean-Francois Roch, Karine Vigneron, Philippe Grelu, Alice Sinatra, Jean-Philippe Poizat, and Philippe Grangier, *Quantum Nondemolition Measurements using Cold Trapped Atoms*, Phys. Rev. Lett., **78**(4), 634 (1997)

- [Roos04] Christian F. Roos, Mark Riebe, Hartmut Haffner, Wolfgang Hansel, Jan Benhelm, Gavin P. T. Lancaster, Christoph Becher, Ferdinand Schmidt-Kaler, and Rainer Blatt, *Control and Measurement of Three-Qubit Entangled States*, *Science*, **304**(5676), 1478 (2004), <http://www.sciencemag.org/cgi/reprint/304/5676/1478.pdf>
- [Rosenbusch09] P. Rosenbusch, S. Ghezali, V. A. Dzuba, V. V. Flambaum, K. Belyoy, and A. Derevianko, *ac Stark shift of the Cs microwave atomic clock transitions*, *Physical Review A (Atomic, Molecular, and Optical Physics)*, **79**(1), 013404 (2009)
- [Saffman08] Mark Saffman, *private communications* (2008)
- [Saffman09] Mark Saffman, Daniel Oblak, Jürgen Appel, and Eugene S. Polzik, *Optimal spin squeezing of atomic ensembles by multi-colour quantum nondemolition measurements*, *Phys. Rev. A*, **79**, 023831 (2009)
- [Sakurai94] Jun John Sakurai, *Modern Quantum Mechanics*, Reading: Addison-Wesley, revised edn. (1994)
- [Santarelli94] Giorgio Santarelli, Andre Clairon, Stephen N. Lea, and Guglielmo M. Tino, *Heterodyne optical phase-locking of extended-cavity semiconductor lasers at 9 GHz*, *Opt. Comm.*, **104**(4-6), 339 (1994)
- [Santarelli99] Giorgio Santarelli, Philippe Laurent, Pierre Lemonde, Andre Clairon, Anthony G. Mann, Sheng Chang, Andre N. Luiten, and C. Salomon, *Quantum Projection Noise in an Atomic Fountain: A High Stability Cesium Frequency Standard*, *Phys. Rev. Lett.*, **82**, 4619 (1999)
- [Schiller96] Stephan Schiller, Robert Bruckmeier, Manfred Schalke, Klaus Schneider, and Jürgen Mlynek, *Quantum nondemolition measurements and generation of individually squeezed twin beams by a degenerate optical parametric amplifier*, *Eur. Phys. Lett.*, **36**, 361 (1996)
- [Schleier-Smith08] Monica Schleier-Smith, Ian D. Leroux, and Vladan Vuletić, *Generating Reduced-Quantum-Uncertainty States for an Atomic Clock*, arXiv:0810.2582v1 (2008)
- [Schleier-Smith09] Monika H. Schleier-Smith, Ian D. Leroux, and Vladan Vuletić, *Squeezing the Collective Spin of a Dilute Atomic Ensemble by Cavity Feedback*, arXiv:0911.3936 (2009)
- [Schmidt94] O. Schmidt, K. M. Knaak, R. Wynands, and Dieter Meschede, *Cesium saturation spectroscopy revisited: How to reverse peaks and observe narrow resonances*, *Appl. Phys. B: Lasers and Optics*, **59**(2), 167 (1994)
- [Schünemann99] U. Schünemann, H. Engler, R. Grimm, M. Weidemüller, and M. Zielonkowski, *Simple scheme for tunable frequency offset locking of two lasers*, *Rev. Sci. Instr.*, **70**(1), 242 (1999)
- [Schwinger52] Julian S. Schwinger, *On angular momentum*, report NYO-3071, U.S. Atomic Energy Commission (1952)

- [Shapiro80] Jeffrey H. Shapiro, *Optical waveguide tap with infinitesimal insertion loss*, *Opt. Lett.*, **5**(8), 351 (1980)
- [Slusher85] Richard E. Slusher, Leo W. Hollberg, Bernard Yurke, Jerome C. Mertz, and J. F. Valley, *Observation of Squeezed States Generated by Four-Wave Mixing in an Optical Cavity*, *Phys. Rev. Lett.*, **55**(22), 2409 (1985)
- [Smith06] Greg A. Smith, Andrew Silberfarb, Ivan H. Deutsch, and Poul S. Jessen, *Efficient Quantum-State Estimation by Continuous Weak Measurement and Dynamical Control*, *Physical Review Letters*, **97**(18), 180403 (2006)
- [Sobelman06] Igor I. Sobelman, *Theory of Atomic Spectra*, Oxford: Alpha Science Intl. (2006)
- [Sørensen01a] Anders S. Sørensen, Lu-Ming Duan, J. Ignacio Cirac, and Peter Zoller, *Many-particle entanglement with Bose-Einstein condensates*, *Nature*, **409**, 63 (2001)
- [Sørensen01b] Anders S. Sørensen and Klaus Mølmer, *Entanglement and extreme spin squeezing*, *Phys. Rev. Lett.*, **86**(20), 4431 (2001)
- [Sørensen08] Martin W. Sørensen and Anders S. Sørensen, *Three-dimensional theory for light-matter interaction*, *Phys. Rev. A*, **77**, 013826 (2008)
- [Steck08] Daniel A. Steck, *Cesium D Line Data*, 2.1 edn. (2008)
- [Stockton07] John K. Stockton, *Continuous quantum measurement of cold alkali-atom spins*, Ph.D. thesis, California Institute of Technology (2007)
- [Stokes52] George G. Stokes, *Composition and resolution of streams of polarized light from multiple sources*, *Trans. Cambridge Philos. Soc.*, **9**, 399 (1852)
- [Størmer21] F. Carl M. Størmer, *Methode d'integration numerique des equations differentielles ordinaires.*, in *Comptes rendus du Congres international des Mathematiciens*, Strasbourg, 22-30 sept. 1920 (1921), 243–257
- [Takano09a] Tetsushi Takano, *private communications* (2009)
- [Takano09b] Tetsushi Takano, Miho Fuyama, Ryo Namiki, and Yoshiro Takahashi, *Spins squeezing of a cold atomic ensemble with the nuclear spin of one half*, *Phys. Rev. Lett.*, **102**, 033601 (2009)
- [Takano09c] Tetsushi Takano, Shin-Ichi-Ro Tanaka, Ryo Namiki, and Yoshiro Takahashi, *Manipulation of Non-classical Atomic Spin States*, arXiv:0909.2423 (2009)
- [Targat06] Rodolphe Le Targat, Xavier Baillard, Mathilde Fouché, Anders Brusch, Olivier Tcherbakoff, Giovanni D. Rovera, and Pierre Lemonde, *Accurate Optical Lattice Clock with [sup 87]Sr Atoms*, *Physical Review Letters*, **97**(13), 130801 (2006)
- [Telle93] H. R. Telle, *Stabilization and modulation schemes of laser diodes for applied spectroscopy*, *Spechtrochimica Acta Rev.*, **15**(5), 301 (1993)

- [Teper08] Igor Teper, Geert Vrijsen, Jongmin Lee, and Mark A. Kasevich, *Backaction noise produced via cavity-aided nondemolition measurements of an atomic clock state*, Phys. Rev. A, **78**, 051803 (2008)
- [Tey08] Meng Khoon Tey, Zilong Chen, Syed Abdullah Aljunid, Brenda Chng, Florian Huber, Gleb Maslennikov, and Christian Kurtsiefer, *Strong interaction between light and a single trapped atom without the need for a cavity*, Nat Phys, **4**(12), 924 (2008)
- [Thorne78] Kip S. Thorne, Ronald W. P. Drever, Carlton M. Caves, Mark Zimmermann, and Vernon D. Sandberg, *Quantum Nondemolition Measurements of Harmonic Oscillators*, Phys. Rev. Lett., **40**(11), 667 (1978)
- [Unruh78] William G. Unruh, *Analysis of quantum-nondemolition measurement*, Phys. Rev. D, **18**(6), 1764 (1978)
- [Vanier89] Jacques Vanier and Claude Audoin, *The Quantum Physics of Atomic Frequency Standards*, Bristol: Adam Hilger (1989)
- [Varcoe00] Benjamin T. H. Varcoe, Simon Brattke, Matthias Weidinger, and Herbert Walther, *Preparing pure photon number states of the radiation field*, Nature, **403**(6771), 743 (2000)
- [Verlet67] Loup Verlet, *Computer "Experiments" on Classical Fluids. I. Thermodynamical Properties of Lennard-Jones Molecules*, Phys. Rev., **159**(1), 98 (1967)
- [Wang93] Hailin Wang, Michael J. Freeman, and Duncan G. Steel, *Squeezed light from injection-locked quantum well lasers*, Phys. Rev. Lett., **71**(24), 3951 (1993)
- [Windpassinger08a] Patrick J. Windpassinger, *Quantum non-destructive measurements and noise squeezing*, Ph.D. thesis, Niels Bohr Institute, University of Copenhagen, Blegdamsvej 17, 2100 Copenhagen OE, Denmark (2008)
- [Windpassinger08b] Patrick J. Windpassinger, Daniel Oblak, Ulrich Busk Hoff, J. Appel, Niels Kjærgaard, and Eugene S. Polzik, *Inhomogeneous Light Shift effects on Atomic Quantum State Evolution in Non-Destructive Measurements*, New J. of Phys., **10**, 053032 (2008)
- [Windpassinger08c] Patrick J. Windpassinger, Daniel Oblak, Plamen G. Petrov, Marcin Kubasik, Mark Saffman, Carlos L. Garrido Alzar, Jürgen Appel, Jörg H. Müller, Niels Kjærgaard, and Eugene S. Polzik, *Non-Destructive Probing of Rabi Oscillations on the Cesium Clock Transition near the Standard Quantum Limit*, Phys. Rev. Lett., **100**, 103601 (2008)
- [Windpassinger09a] Patrick J. Windpassinger, Marcin Kubasik, Marco Koschorreck, Axel Boisen, Niels Kjærgaard, Eugene S. Polzik, and Jörg H. Mueller, *Ultra low noise differential AC-coupled photodetector for sensitive pulse detection applications*, Meas. Sci. Technol., **20**, 055301 (2009)
- [Windpassinger09b] Patrick J. Windpassinger, Daniel Oblak, Ulrich B. Hoff, Anne Louchet, Jürgen Appel, Niels Kjærgaard, and Eugene S.

- Polzik, *Squeezing of Atomic Quantum Projection Noise*, J. Mod. Opt., **56**, 1993 (2009)
- [Wineland92] David J. Wineland, John J. Bollinger, Wayne M. Itano, Fred L. Moore, and Daniel J. Heinzen, *Spin squeezing and reduced quantum noise in spectroscopy*, Phys. Rev. A, **46**, R6797 (1992)
- [Wineland94] David J. Wineland, John J. Bollinger, Wayne M. Itano, and Daniel J. Heinzen, *Squeezed atomic states and projection noise in spectroscopy*, Phys. Rev. A, **50**(1), 67 (1994)
- [Wódkiewicz85a] Krzysztof Wódkiewicz, *Reduced quantum fluctuations in the Josephson junction*, Phys. Rev. B, **32**(7), 4750 (1985)
- [Wódkiewicz85b] Krzysztof Wódkiewicz and Joseph H. Eberly, *Coherent states, squeezed fluctuations, and the $SU(2)$ and $SU(1,1)$ groups in quantum-optics applications*, J. Opt. Soc. Am. B, **2**(3), 458 (1985)
- [Wu86] Ling-An Wu, H. Jeff Kimble, Jan L. Hall, and Huifa Wu, *Generation of Squeezed States by Parametric Down Conversion*, Phys. Rev. Lett., **57**(20), 2520 (1986)
- [Yurke86] Bernard Yurke, *Input States for Enhancement of Fermion Interferometer Sensitivity*, Phys. Rev. Lett., **56**(15), 1515 (1986)
- [Zoller03] Peter Zoller, *Squeezed and Coherent State* (2003), private communications



Quantum mechanics is characterised by several strange features, which include quantum uncertainty, quantum measurements, and entanglement. This thesis involves all three of these. The quantum uncertainty poses a fundamental standard quantum limit (SQL) in applications where quantum systems are used to gauge some quantity. A prime example is that of atomic frequency standards, which with unprecedented precision measure an atomic quantum state. Quantum measurements in the form of Quantum Non-Demolition (QND) measurements can be engineered so as to overcome the SQL by redistributing quantum uncertainty amongst different variables of the system. Such squeezed spin-states rely on inter-atomic correlation, which goes by the name of entanglement.

In this work we present a detailed description of how we have implemented a QND measurement with laser pulses in a Mach-Zehnder Interferometer (MZI) and demonstrate that we can engineer a squeezed state in a cold trapped ensemble of Cs atoms. We verify that the squeezing is useful for improving the precision of atomic clocks. Along the way, we also investigate several remarkable features of the interaction, by which atoms and light-particles (photons) exchange phase-shifts.

(Sammendrag på dansk forefindes på side iii)

(Sažetak na hrvatskom jeziku se nalazi na iv. stranici)